DEEP-SEA RESEARCH II

http://www.elsevier.com/locate/dsr2

Volume 177, 2020

Deep–Sea Research II 177 (2020) 104850

Contents lists available at ScienceDirect

Deep-Sea Research Part II

journal homepage: http://www.elsevier.com/locate/dsr2

Integrated ecosystem research in the Pacific Arctic – understanding ecosystem processes, timing and change

A B S T R A C T

Arctic marine ecosystems are experiencing substantial changes associated with sea ice loss and surface warming. The most obvious and dramatic changes include earlier ice retreat and a longer ice-free season, particularly on Arctic inflow shelves, including the Barents Sea in the Atlantic Arctic and the northern Bering Sea and Chukchi Sea in the Pacific Arctic. The extreme variability observed in recent years in the Pacific Arctic is unparalleled in recorded history. This volume is devoted to studies that integrate research across various components of the Arctic marine ecosystem to better characterize these changes. The intent of this integrated approach is to better understand the linkages and interactions that shape ecosystem processes, influence timing and phenology of events, and inform predictions of future conditions. The studies presented in this Special Issue investigate processes in the Bering Sea, Chukchi Sea, and Beaufort Sea. The data derive from remote sensing, ship-based surveys, and integrated data products. The research presented includes time-series analyses on environmental change across the greater Pacific Arctic, heat flux, stratification and mixing dynamics, vertical structure, and wind and current patterns. It explores the influence of physical processes on, and seasonal and annual variability in, primary production, nutrient distribution, and the export of biogenic matter. It also examines the effects of oceanographic variability on zooplankton taxa, the distribution of larval fishes, age and growth in Arctic fishes, responses of salmon to warming, and variability in cetacean occurrence. These studies are designed to provide new insights on integrated ecosystem research in the Pacific Arctic, with a focus on improving understanding of ecosystem processes, timing and change. This volume marks the first in a series of research volumes supported by the North Pacific Research Board to integrate ecosystem research in the Pacific Arctic and to inform our collective understanding of the rapid transformation in this region.

1. Pacific Arctic system

The Pacific Arctic region encompasses the broad interconnected continental shelf systems of the Bering and Chukchi Seas in addition to the contiguous marine systems of the East Siberian and Beaufort Seas. Arctic marine ecosystems generally (IPCC, 2013), and this region in particular (Grebmier and Maslowski, 2014; Woodgate, 2018; Huntington et al., 2020; Polyakov et al., 2020), appear to be in a period of rapid transition. Recent observations suggest that the region is entering a new normal (Jeffries et al., 2013; Wood et al., 2015). Sea ice is a defining feature of the Arctic and recent decades have seen significant changes in sea-ice cover (Stroeve et al., 2012), particularly in the northern portion of the Pacific Arctic (Frey et al., 2015; Wang et al., 2018). More recently, these changes appear evident throughout the region (Mueter et al., 2017; Stabeno and Bell, 2019) and sea surface temperatures in the region show a pronounced rise. Implications for warmer conditions include a progressively later date of sea-ice formation, shorter duration of ice cover, thinner winter ice conditions (Stabeno and Bell, 2019), and the near complete loss of multiyear sea ice (Kwok, 2018). Both the Pacific Decadal Oscillation and the Arctic Oscillation appear to influence the persistence of sea ice in the Bering Sea (Frey et al., 2015). Transport anomalies in the Bering Strait also influence regions immediately north (Woodgate, 2018) and are associated with broad-scale atmospheric circulation patterns, including the Beaufort High and Aleutian Low atmospheric pressure systems (Danielson et al., 2014). Reduced sea-ice extent has led to positive feedback mechanisms (Wang and Overland, 2015), as the longer seasonal ice-free period increases oceanic solar heating (Woodgate et al., 2012; Wood et al., 2015). Heat stored in the upper ocean early in the summer is now persisting until the return of ice in winter (Lu et al., 2020). Reduced ice concentrations and anomalous wind conditions are transforming the region into an open water environment for a greater portion of the year (Frey et al., 2015; Wood et al., 2015; Thomson et al., 2016). Open water allows for increased fetch, surface waves, and wind-driven mixing and advection (Thomson and Rogers, 2014; Smith and Thomson, 2019). These shifts in the physical system have already had profound effects on the production (Arrigo and van Dijken, 2015), biological communities (Grebmier et al., 2006; Moore et al., 2014), and ecology of these systems (Carmack and Wassman, 2006; Moore and Stabeno, 2015; Moore et al., 2018).

In response, scientific research has increased in the Pacific Arctic with expanded trawl and acoustic survey efforts, new deployments of increasingly sophisticated ice-adapted moorings, and advanced monitoring technologies. This region has also witnessed the increased use of autonomous vehicles, as well as further prospects for opportunistic sampling and attention to historical, satellite, and community-based data and Indigenous knowledge. These research activities and their findings are reflected in several recent compendia examining physical, biogeochemical, and biological patterns and trends in this rapidly changing environment (Arrigo and van Dijken, 2015; Grebmeier and Maslowski, 2014; Moore and Stabeno, 2015; Mueter et al., 2017).

This Special Issue provides important new insights into how changing environmental conditions influence ecosystem dynamics in this

https://doi.org/10.1016/j.dsr2.2020.104850

Available online 18 August 2020

region. It also provides important new findings related to the mechanisms that influence ecosystem processes and the implications for shifts in the phenology and interactions in the region. Research presented here leverages a variety of data sources, including remote sensing, ship-based surveys and integrated data products. The research developed in the manuscripts of this Special Issue includes time-series analyses on environmental change in the greater Pacific Arctic. The research characterizes physical oceanography in the region with a focus on heat flux, stratification and mixing dynamics, vertical structure of the water column, and regional wind and current patterns. New insights to biological oceanography and production dynamics, including seasonal and annual variability in primary production, nutrient distribution, and the export of biogenic matter are presented. Finally, dynamics of zooplankton taxa, the effects of oceanographic variability on the distribution of larval fishes, age and growth patterns in Arctic fishes, the response of salmonids to warming trends, and variability in cetacean occurrence in response to environmental conditions are examined.

Research on human dimensions, coastal community perspectives, and engagement with Alaska Native communities is a critical component of research in the Pacific Arctic. This Arctic Integrated Ecosystem Research Program (IERP) was developed in partnership with the North Slope Borough Baselines Studies Program and was informed by initial consultations in 2013 with five Arctic communities (Utqiaġvik, Kotzebue, Nome, Gambell and Savoonga) in the Pacific Marine Arctic Synthesis (PacMARS) program theme: Subsistence Lifestyles in Times of Climate Change (Grebmier, 2014, 2015). The Arctic IERP has also been informed through engagement with Arctic community leaders in a variety of fora (e.g. Arctic Waterways Safety Committee, Alaska Eskimo Whaling Commission), as well as subsequent (2016–2017), regional hub meetings in Utqiaġvik, Kotzebue, and Nome, coordinated with the North Slope Borough Department of Wildlife Management, the Northwest Arctic Borough, and Kawerak Inc. These meetings and engagements served as an important mechanism to understand research needs and priorities as perceived by local residents, coordinate research efforts with local communities, inform communities about research activities, and solicit insights from subsistence hunters and local residents. As part of the Arctic IERP, a Local and Traditional Knowledge (LTK) team was funded consisting of residents of eight coastal communities (Savoonga, Diomede, Buckland, Kotzebue, Kivalina, Point Hope, Point Lay, Utqiaġvik) as well as two non-Native researchers from the Anchorage area; community participants were selected for experience with scientific-LTK collaborations as well as the depth of their own LTK and also included professional researchers and managers. This group considered the results of literature and archive reviews and analyzed new information, including personal experience and LTK, to address the hypotheses of the program, collaborate on research, and appraise results and conclusions (Arctic IERP Integrated Workplan, https://www.nprb.org/arctic-program/about-the-program/#arctic_integrated). The research products related to this focus will be published in subsequent Special Issues or in alternate media more likely to reach the intended audiences, at the discretion of the authors of that research. Products that develop from community engagement will be referenced in subsequent Special Issue publications, as available.

The research presented here marks the first in a series of Special Issue volumes supported by the North Pacific Research Board (NPRB) to integrate ecosystem research in the Pacific Arctic and to inform our collective understanding of the rapid transformation in this region.

2. Integrated research

2.1. Arctic Integrated Ecosystem Research Program

The Arctic IERP was initiated in 2016 to bring together a multidisciplinary group of Arctic scientists and Alaskan coastal community residents to gather and integrate information and observations from marine-focused studies in the Pacific Arctic region. This program builds on a model for integrated ecosystem research (Baker and Smith, 2018) that has been applied in other regions of the North Pacific (Wiese et al., 2012; Dickson and Baker, 2016; Ormseth et al., 2019). The goal is to improve understanding of the relationships between oceanographic conditions, ocean productivity, lower trophic level benthic and pelagic species, and upper trophic species, including marine fish, birds and mammals.

This program is specifically structured to address the question of how reductions in Arctic sea ice and the associated changes in the physical environmental might influence the flow of energy through the ecosystem in the Chukchi Sea. The program supports research on mechanisms and processes that structure the Arctic marine ecosystem and influence the distribution and interactions of marine fishes and the phenology of ecosystem processes. More broadly, this program aims to: (i) increase scientific understanding of the biophysical environment in this region; (ii) enhance capability to predict future conditions; and (iii) effectively communicate research findings to local residents, resource managers, the research community, and the general public. The program (2016–2021) is sponsored by NPRB, the Collaborative Alaskan Arctic Studies Program (formerly the North Slope Borough/Shell Baseline Studies Program), the Bureau of Ocean Energy Management (BOEM), and the Office of Naval Research (ONR) Marine Mammals and Biology Program. In-kind support was contributed by the National Oceanic and Atmospheric Administration (NOAA) and the University of Alaska Fairbanks (UAF). This coordinated program was developed in cooperation with the Interagency Arctic Research Policy Committee (IARPC) Chukchi and Beaufort Sea Ecosystem Collaboration Team and the U.S. Arctic Research Commission (USARC). The research in this program built extensively on preceding coordinated research programs. The 12 peer-reviewed papers presented in this volume of Deep-Sea Research II represent research that was, in many cases, initiated and supported though the aforementioned research programs. This Special Issue represents the first of three anticipated Special Issue volumes resulting from the Arctic IERP.

2.2. Integrated research and multi-institution coordination

In recent years, multiple programs have focused on this important region. Coordinated research programs in the area include the Distributed Biological Observatory (DBO; https://www.pmel.noaa.gov/dbo/), Study of Environmental Arctic Change (SEARCH; https://www.searcharcticscience.org/), Arctic Observing Network (AON; https://www.nsf.gov/div/index.jsp?org=OPP), Arctic Ecosystem Integrated Survey (IES; http://web.cfos.uaf.edu/wordpress/arcticeis/), Sustaining Arctic Observing Networks (SAON; https://iasc.info/data-observations/saon), Synthesis of Arctic Research (SOAR; https://www.pmel.noaa.gov/soar/), the Russian-US Long-term Census of the Arctic (RUSALCA, https://www.pmel.noaa.gov/rusalca), NOAA Ecosystem Monitoring Assessment (EMA; https://www.fisheries.noaa.gov/alaska/ecosystems/alaska-ecosystem-monitoring-and-assessment), and fisheries-oceanographic surveys through the Bering-Aleutian Salmon International Survey (BASIS; https://www.afsc.noaa.gov/ABL/MESA/Archives/mesa_occ_basis.htm), the Marine Arctic Ecosystem Study (MARES; https://www.nopp.org/projects/mares/), and the NPRB-led Marine Arctic Regional Synthesis (PacMARS; http://pacmars.eol.ucar.edu/) and Arctic IERP (https://www.nprb.org/arctic-program/about-the-program/).

The research presented here represents research conducted by the following institutions: Finnish Meteorological Institute, Fisheries and Oceans Canada (DFO), Japan Agency for Marine-Earth Science and Technology (JAMSTEC), NOAA Alaska Fisheries Science Center (AFSC), NOAA Pacific Marine Environmental Laboratory (PMEL), Native Village of Diomede, NPRB, North Slope Borough Department of Wildlife Management, Oregon State University, Russian Federal Research Institute of Fisheries and Oceanography (TINRO/VNIRO), Russian Academy of Science Shirshov Institute of Oceanology, UAF International Arctic

Research Center, UAF College of Fisheries and Ocean Sciences, University of Maryland Center for Environmental Sciences, University of Toronto, University of Washington Joint Institute for the Study of the Atmosphere and Ocean and Applied Physics Laboratory, Université Laval Amundsen Science, and the Woods Hole Oceanographic Institute. Data collected in integrated ecosystem surveys conducted in 2017–2019 will be covered in subsequent Special Issue publications in Deep Sea Research II.

3. Data and models

Multiple data sources informed the analyses and models contained in this volume, including satellite and remote sensing data, *in situ* sampling in oceanographic cruises, autonomous underwater sampling platforms, aerial surveys, oceanographic and acoustic moorings, fixed gear deployments, and the use of archival data.

3.1. Remote sensing data

3.1.1. Sea ice

Remote sensing satellite data on sea-ice extent and areal concentration were accessed from multiple sources and compiled products. Sea-ice data included 6.25 km (Escajeda et al., 2020, This Issue) and 12.5 km (Logerwell et al., 2020, This Issue; Stabeno et al., 2020, This Issue) resolution data from the Advanced Microwave Scanning Radiometer for EOS (AMSR-E), 6.25 km resolution data from the Integrated Climate Date Center (ICDC; Spear et al., 2020), and 12.5 km and 25 km resolution data from the National Aeronautics Space Agency (NASA) Scanning Multichannel Microwave Radiometer (SMMR), Special Sensor Microwave Imager (SSM/I), and Special Sensor Microwave Imager and Sounder (SSMIS) passive microwave radiometers available through the National Snow and Ice Data Center (http://nsidc.org/data/; Baker et al., 2020, This Issue; Churnside et al., 2020, This Issue; Escajeda et al., 2020, This Issue; Spear et al., 2020, This Issue; Stabeno and McCabe, 2020, This Issue). Data (12.5 km resolution) were also accessed from the Center ERS d'Archivage et de Traitement (CERSAT) service of the French Research Institute for Exploitation of the Sea (http://cersat.ifremer.fr/; Lalande et al., 2020, This Issue), as were estimates of snow depth on sea ice at a 25-km resolution from the Northern Hemisphere snow depth files, derived from SMMR and SSM/I (https://neptune.gsfc.nasa.gov/). Hindcasts on sea ice were also accessed via the ECMWF ERA5 (C3S, 2017) dataset (Danielson et al., 2020, This Issue). These data were used to examine and analyze associations relevant to daily, monthly, and annual patterns in areal coverage and thickness.

3.1.2. Sea surface temperature and atmospheric temperature

Sea surface temperature (SST) data were accessed through the NOAA Optimum Interpolation Sea-Surface Temperature (OISST, https://www.esrl.noaa.gov) as a gridded product with a 0.25° spatial resolution (Baker et al., 2020, This Issue; Escajeda et al., 2020, This Issue; Spear et al., 2020, This Issue). Data from the Coral Reef Watch version 3.1 operational global satellite were also applied, accessed via the Pacific Islands Ocean Observing System ERDDAP site (https://pae-paha.pacioos.hawaii.edu/erddap/index.html). Danielson et al. (2020, This Issue) applied the European Center for Medium-Range Weather Forecasts ERA5 (ECMWF; Haiden et al., 2017) dataset to assess surface heat fluxes and provide supporting wind, ice cover, and air temperature data, as well as the reconstructed SST (ERSST, version 5; Huang et al., 2017) and the NASA Surface Temperature Analysis (GISTEMP, version 4; Lenssen et al., 2019) datasets. Atmospheric temperatures were estimated via the ECMWF-ERA5 dataset (Danielson et al., 2020, This Issue) and the National Weather Service (NWS; https://w2.weather.gov/climate/xmacis.php?wfo = pafg; Farley et al., 2020, This Issue).

3.1.3. Sea level pressure and wind

Wind velocity data were obtained from the National Center for Environmental Prediction (NCEP) North American Regional Reanalysis (NARR; https://www.esrl.noaa.gov/psd; Churnside et al., 2020, This Issue; Escajeda et al., 2020, This Issue; Spear et al., 2020, This Issue; Stabeno and McCabe, 2020, This Issue) and the ECMWF-ERA5 reanalysis (Danielson et al., 2020, This Issue; Stabeno et al., 2020, This Issue). Comparisons were also made with observed wind from the Barrow Atmospheric Baseline Observatory near Utqiaġvik, Alaska, downloaded from the NOAA ESRL Global Monitoring Division (https://www.esrl.noaa.gov/gmd/obop/brw/; Stabeno and McCabe, 2020, This Issue). Sea level pressure fields and 10-m winds were constructed with the ECMWF-ERA5 atmospheric reanalysis (https://www.ecmwf.int/en/forecasts/datasets/archive-datasets/reanalysis-datasets/era5; Baker et al., 2020, This Issue).

3.2. Moorings and deployed instrumentation

3.2.1. Physical oceanographic data

Overwinter moorings (C1–C8) on the Chukchi Shelf (70.5–72.5° N, 166-158° W; see Stabeno et al., 2020, This Issue) were used to collect physical and chemical oceanographic data, supporting multiple studies (Logerwell et al., 2020, This Issue; Mordy et al., 2020, This Issue; Stabeno et al., 2020, This Issue). Instruments on these moorings measured temperature and salinity (SBE-37, 107 SBE-39 SeaCat; Sea-Bird Electronics, Inc., Bellevue, WA), currents (ADCP-RCM-9), chlorophyll fluorescence (SBE/WET Labs DLSB ECO Fluorometer), nitrate (SBE, ISUS or SUNA), and photosynthetically active radiation (PAR). Dissolved inorganic nitrate was measured using automated continuous flow analysis. Instruments at mooring C9 were deployed 2014–2017 at a depth of 1000 m on the Chukchi continental slope northwest of Barrow Canyon (Stabeno and McCabe, 2020, This Issue) This mooring design included three RCM current meters, an upward looking 75 kHz ADCP, and a SBE Microcat. Moorings associated with the Chukchi Sea Environmental Observatory (CEO; 71.4° N, 161.3° W) monitored subsurface oceanographic parameters used in analyses of export fluxes in Lalande et al. (2020, This Issue). This array autonomously recorded year-round high-resolution data on nutrient and carbonate chemistry, particle deposition, zooplankton, fish and marine mammal observations as well as fluctuations in currents, waves, winds, light, and ice. Mooring data from the Bering Strait climate monitoring mooring A3 (66.7° N, 171.5° W; Woodgate, 2018) were used by Danielson et al. (2020, This Issue) to quantify water properties in Bering Strait, including hourly temperature, salinity, and velocity. Data were used to derive estimates of oceanic volume and heat flux. Spear et al. (2020, This Issue) also acquired Bering Strait volume transport data from moored ADCP measurements (Woodgate et al., 2015; Woodgate, 2018). Pop-up buoys, developed at NOAA-PMEL (Langis et al., 2018) provided under-ice measurements on temperature, fluorescence and PAR (Stabeno et al., 2020, This Issue). Collectively, these moored arrays provide reference observations to evaluate and improve models of ice-ocean circulation and biogeochemical, fisheries, and ecosystem dynamics.

3.2.2. Acoustic data

Acoustic data were used by Escajeda et al. (2020, This Issue) to monitor cetacean vocalizations (2009–2015). Data were collected from three AURAL-M2 hydrophones (Autonomous Underwater Recorder for Acoustic Listening-Model 2, Multi-Électronique, Inc.) attached to oceanographic moorings positioned in the eastern channel of the Bering Strait (A2, A4) and approximately 35 km north of the strait in the Chukchi Sea (A3). Each hydrophone was positioned 4–8 m above the seafloor and sampled at 8192 Hz or 16,384 Hz. Environmental variables were also recorded *in situ*, including: near-bottom temperature and salinity (40–55 m depth); near-surface temperature and salinity (14–19 m depth) measured by the ISCAT system developed at the University of Washington (see Woodgate et al., 2015), and water velocity and direction measured by Teledyne's Workhorse ADCPs.

3.2.3. Satellite-tracked drifters

Satellite-tracked drifters were deployed by the NOAA Ecosystem Fisheries Oceanographic Coordinated Investigations (EcoFOCI) program in the Chukchi Sea (2012–2018). Data were used by Stabeno and McCabe (2020, This Issue) to analyze vertical structure and temporal variation over the Chukchi Sea continental slope. Lagrangian velocities were determined by centered differences using hourly drifter positions.

3.3. Surveys

3.3.1. Physical oceanography survey data and shipboard hydrography

Data from several research cruises and oceanographic and aerial surveys were used to support analyses in this volume. Data on surface and bottom temperatures (SBE-39 datalogger) were integrated from NOAA-AFSC bottom trawl surveys in the EBS and NBS continental shelves (Baker et al., 2020, This Issue). Water density profiles were measured using the NOAA Prawler and by CTD casts from the USCGC Healy and CCGS Sir Wilfrid Laurier (Churnside et al., 2020, This Issue); a 150 kHz ADCP was also operated from these vessels. Stabeno et al. (2020, This Issue) also used data from USCGC Healy cruise HE1501 on CTD, oxygen, and chlorophyll fluorescence. Hydrographic data were collected along the Icy Cape transect line (2010–2018; Mordy et al., 2020, This Issue) in conjunction with mooring recovery and re-deployment. Profile data were collected using a SBE 911plus CTD instrument. Dissolved inorganic nitrate was measured using automated continuous flow analysis and discrete calibration samples for salinity and nutrient samples were collected from Niskin bottles. Temperature and salinity data were also collected from a cruise on the R/V Ocean Starr (2017; Stabeno and McCabe, 2020, This Issue). CTD profiles were collected using a SBE-911plus system as well as oxygen (SBE-43), chlorophyll fluorescence (WETStar, WS3S) and PAR (QSP-200 L4S or QSP-2300).

3.3.2. Fish and plankton survey data

A variety of survey and research cruise transects were used by Spear et al. (2020, This Issue) to collect zooplankton samples using 126 μm and 505 μm mesh nets. For smaller taxa, a 150 μm mesh net was used to profile the full water column. Physical data and hydrographic data were collected using SBE 911plus and FastCAT SBE 49 systems. Logerwell et al. (2020, This Issue) used ichthyoplankton and oceanographic data collected over a survey grid that spanned the U.S. northeastern Bering Sea and Chukchi Sea shelves (157–170° W, 60–72° N, 2012–2013). Sampling used a 60 cm bongo sampler fitted with two 0.505 mm mesh nets. Quantitative oblique tows were made to develop vertically integrated estimates of larval fish abundance. Salinity (SBE16) and current speed and direction (Aanderaa RCM-9, SeaGuard and/or Teledyne RD ADCP; Stabeno et al., 2018) were collected across the survey footprint. Förster et al. (2020, This Issue) accessed fish data from a variety of demersal and pelagic trawl deployments in the Chukchi and Beaufort Seas (174E-156° W, 66–76° N, 2007–2015). Research surveys coordinated through the IES (60°N to 65°N; 2003–2018) provided data on Arctic fishes and water column characteristics used in analyses on salmonids conducted by Farley et al. (2020, This Issue).

3.3.3. Airborne lidar

Stratification, plankton layers, and mixing in the Chukchi Sea and Beaufort Sea were measured with airborne oceanographic lidar (Churnside et al., 2020, This Issue), using a NOAA Twin Otter aircraft.

3.4. Integrated data products

3.4.1. Hydrographic data

Hydrographic data used by Danielson et al. (2020, This Issue) were assembled from the National Centers for Environmental Information World Ocean Database 2018. This archive provides water column CTD and profiling float soundings, with data collected since 1922 in the Chukchi Sea and 1966 in the Bering Sea. Additional profiles were compiled from US oceanographic expeditions in recent years in the NOAA-PMEL and NOAA-AFSC hydrographic databases, the UAF-Institute of Marine Science hydrographic database, and CTD data compiled by SOAR (Moore et al., 2018). Additional data were accessed from institutional archives at TINRO, DFO, and JAMSTEC.

3.4.2. Bathymetric data

Danielson et al. (2020, This Issue) used the soundings-based Alaska Region Digital Elevation Model (ARDEM; Danielson et al., 2015) and ETOPO1 (Eakins and Sharman, 2010) to analyze data relative to seafloor depths across the Bering and Chukchi shelves. Bathymetric data used by Churnside et al. (2020, This Issue) were obtained from the International Bathymetric Chart of the Arctic Ocean (IBCAO) Version 3.0 (Jakobsson et al., 2012). Stabeno and McCabe (2020, This Issue) used historical CTD profiles taken from an accumulated data set provided by Corlett and Pickart (2017).

4. Research results – physical processes and system change

4.1. Physical processes

Recent system changes in the Pacific Arctic Region have been rapid and extensive. Understanding these changes requires historical perspective and comparison against previous conditions. Several manuscripts in this Special Issue analyze these recent changes in the context of historical baselines and provide further mechanistic understanding of the processes and interactions that influence the Pacific Arctic marine environment.

Danielson et al. (2020, This Issue) assemble and evaluate a temperature and salinity hydrographic profile climatology to assess seasonal and annual changes in the Bering and Chukchi Sea continental shelves. This research provides a new reference for the spatial and temporal evolution of water masses in this region and quantifies changes in the magnitude and throughput of heat and fresh water. While the Chukchi Sea shows a linear warming trend of 0.14 °C decade^{-1} (1922–2018) and an increase in the rate of warming (1990–2018), decadal-scale variability in the Bering Sea has obscured clear trends (1966–2018). Danielson et al. (2020, This Issue) conclude by examining recent trends (2014–2018) and show an acceleration of the heat engine in both the Bering Sea and Chukchi Sea, with increased surface heat flux exchanges and oceanic heat advection. A conceptual model is presented to propose feedback controls related to heat content, sea ice, fresh water distribution, and heat flux.

Baker et al. (2020, This Issue) characterize these more recent changes in physical processes, including shifts in seasonal ice cover and water temperatures. Results suggest the conditions observed in 2017–2019 are unprecedented and highlight important shifts in the phenology and magnitude of physical variables, including sea-ice extent, concentration, and duration, as well as extreme reduction in the extent and intensity of the related Bering Sea cold pool. Baker et al. (2020, This Issue) also analyze regional dynamics in the Bering-Chukchi system, distinguishing western, eastern and northern areas of the Bering Sea. Results suggest the strength and position of the Aleutian Low has an important role in large-scale circulation and may drive warm and cold phases in the region. This international collaboration highlights opportunities to integrate data across Russian and US waters to more fully represent system-wide processes, contrast regional trends, and understand physical interactions. This effort also underscores the importance of, and addresses increasing calls for, international collaboration in the Arctic (Drinkwater and Pepin, 2013; Hollowed and Sundby, 2014; Van Pelt et al., 2017; Baker et al., 2018).

Due to rapid and dramatic seasonal transitions (Woodgate, 2018), strong currents and advection (Stabeno et al., 2018), the confluence of distinct water masses (Pisareva, 2018), and local-scale topography (Pickart et al., 2016), conditions and processes may be very different at

local scales in the Bering-Chukchi region. Certain areas may be particularly important in determining larger system attributes and conditions or particularly important as hotspots of productivity and ecological interactions (Banas et al., 2018). At the northern edge of the Chukchi Sea, Stabeno and McCabe (2020, This Issue) provide new insights on the vertical structure and temporal variability of currents along the continental slope. Flow in this area divides into three depth ranges. In the upper 200 m, mean along slope flow associated with the Chukchi Slope Current was northwestward and strongest in summer, weakening or reversing in winter. Flow at 200–850 m was directed southeastward and weak, advecting Atlantic Water in the Arctic Ocean Boundary Current. Mean flow at 900 m was weak and associated with Arctic deep water. Stabeno and McCabe (2020, This Issue) hypothesize that the northwestward Chukchi Slope Current is associated with the dynamics of the Beaufort Gyre.

4.2. Primary and secondary production

Changes in the physical system of the Arctic have profound implications for nutrient availability, stratification and production dynamics. Mordy et al. (2020, This Issue) consider the influence of rapid changes in sea ice and ocean properties in the Chukchi Sea and their influence on nutrient distributions and primary productivity. Results provide new insights on seasonal and interannual variability of nitrate, particularly wintertime replenishment of nitrate. This study examines hourly measurements of nitrate at mooring locations off Icy Cape between 2010 and 2018, with a focus on winter replenishment in relation to transport. Nitrate concentrations were lowest in newly formed winter water, and local nitrate replenishment appears low relative to the nutrient flux through Bering Strait. The considerable interannual variability in transport over the northeastern shelf of the Chukchi Sea is driven by northerly (weakens transport) and southerly (strengthens transport) winds. Results suggest that, in the presence of southerly wind events, nutrient measurements in the northern Bering Sea can be used to forecast pre-bloom nitrate concentrations in the eastern Chukchi Sea.

Hydrographic structure, the presence and absence of ice, and origin and mechanisms of production are important factors determining how and what forms of production are available to fuel ecosystem dynamics. Using nearly 5 million vertical profiles of optical backscattering measured by airborne lidar in the Chukchi and Beaufort Seas, Churnside et al. (2020, This Issue) examine ice conditions and the characteristics of subsurface plankton layers. The authors note that the prevalence of subsurface plankton layers exponentially decreases with increasing ice cover, with layers in open water deeper than those in the pack ice. Results suggest differences in layer thickness may be caused by current shear and that the level of turbulence and its vertical distribution are affected by local upwelling winds. To characterize a more comprehensive system perspective, Stabeno et al. (2020, This Issue) advance a Multiple Production Layers (MPL) hypothesis that suggests that the shallow depths of the Chukchi Sea facilitate multiple persistent layers of production, including surface open water, bottom mixed layer, under-ice algae and disassociated ice algae at the bottom. Near-bottom blooms follow ice retreat, where the intensity of light at the seafloor is similar to under-ice levels, allowing disassociated ice algae to continue to photosynthesize near bottom. Results suggest that even in a changing system, with shifts in the timing of the retreat and advance of sea ice, the shallow nature of the shelf and the export of ice algae to the seafloor will sustain these multiple levels of production.

Lalande et al. (2020, This Issue) provide new insights to sympagic and pelagic algal production, the seasonal development of the zooplankton community, pelagic-benthic coupling, and particulate matter export in relation to snow and sea ice cover on the Chukchi Sea continental shelf. Results indicate substantial autumn production. While pelagic copepods were abundant, meroplanktonic stages of benthic organisms displayed the largest abundances and reflected mixing and resuspension events on the shallow Chukchi Sea shelf. High chlorophyll-a, diatom and particulate organic carbon fluxes during these periods suggest strong pelagic-benthic coupling in the northeast Chukchi Sea. Persistent summer and autumn production suggests that local benthic communities benefit from a sustained food supply, rather than episodic flux events. These observations provide new insights to year-round dynamics and the phenology of production and set a baseline for understanding the impact of environmental changes on Arctic marine ecosystems.

Spear et al. (2020, This Issue) examine the impacts of increased water temperatures, increased advection of water from the Bering Sea, declines in sea-ice concentration, and shorter periods of ice coverage on trophic food webs and ecosystem attributes in the Chukchi Sea. This analysis provides new insights on the role of advective forcing on zooplankton distributions in the context of the highly connected Bering Sea and Chukchi Sea complex (Moore et al., 2018). A series of research surveys (2011–2015) allowed the authors to examine the influence of physical and biological forcing on the abundance of large zooplankton. Results revealed that amphipods, mysids, and euphausiids were more abundant near the bottom. Known development times of stages of zooplankton, along with their location within the study area, suggest that only a fraction of the zooplankton standing stock was the result of local production. While advection from the Bering Sea appeared to influence adult large zooplankton abundance, this influence was less apparent in the earlier stages. Decreased advection and later ice retreat resulted in higher abundances of *Calanus glacialis*. Warmer conditions with increased advection from the Bering Sea resulted higher abundances of euphausiids. These results provide new insights to the consequences of warming, sea-ice melt, and increased transport to Chukchi Sea lower trophic dynamics.

4.3. Responses of fishes and marine mammals

One of the important distinctions between Arctic and sub-Arctic marine communities in the Pacific Arctic is the dominance of benthic versus pelagic pathways. Nearly all fishes have an important larval pelagic stage. While much of the research in the Arctic system has focused on benthic conditions, the pelagic environment is also critical to marine fishes (Doyle and Mier, 2016). Logerwell et al. (2020, This Issue) provide new insights on pelagic habitat requirements of Arctic larval fish and the effects of interannual variability of ocean conditions on their distribution. This research focuses on both groundfish and pelagic species, including larval Arctic cod, Bering flounder, yellowfin sole and capelin. Despite examining these species over years with differing oceanographic conditions and water mass distributions, distributions of larval fishes were not significantly different. Arctic cod and Bering flounder were found in cold, high salinity shelf waters advected from the south and influenced by winter cooling (Chukchi Winter Water and Anadyr Water mix), whereas yellowfin sole and capelin were found in warm, low salinity Alaska Coastal Water. Cold, high salinity water masses had high large copepod biomass and the Alaska Coastal Water had high small copepod biomass. These findings suggest that these water masses provided different but productive foraging habitat and that the

timing and location of spawning of these species may have evolved, such that larvae are distributed to suitable foraging habitat, despite interannual variability in ocean conditions. This study provides a baseline of Arctic larval fish distribution and insight to potential climate impacts to early life history stages of larval fish.

Understanding the dynamics and fluctuations of Arctic fishes and their resilience to changing conditions and potential encroachment of subarctic species from the south requires better understanding of species life history. Basic life history parameters of Arctic fishes have not been well characterized for many species in the Chukchi and Beaufort Seas. The impact of increasing environmental and anthropogenic changes in the Arctic on the biology of Arctic fishes requires baseline data. Förster et al. (2020, This Issue) used data from over 45,000 individual fishes to determine length and weight relationships of 28 species, and further determined ages of 17 species of Arctic fishes. Specimens tended to be small in size and generally showed positive allometric growth. Despite their small sizes, many individuals were long-lived, reaching ages of up to 26 years. In the Chukchi Sea, individuals were shorter-lived and tended to be larger and longer-at-age than those in the Beaufort Sea. Growth variation can have a large effect on management reference points and this study provides insights on species-specific parameters important to informing potential future fisheries management in the region (2009 Arctic Fisheries Management Plan).

Although often considered in isolation, Pacific salmon (*Oncorhychus spp*.) have important interactions with other marine fishes, especially at larval and juvenile stages (Daly et al., 2019). Pacific salmon have also been one of the species groups most able to capitalize on environmental shifts in the Arctic. Evidence of this includes colonization of new natal spawning habitat (Pitman et al., 2020), prevalence in Arctic sampling (DeRobertis et al., 2017; Marsh et al., 2017) and emergence and observation in estuarine and coastal environments by Arctic communities (Dunmall et al., 2018; Carothers et al., 2019). Farley et al. (2020, This Issue) used juvenile Pink salmon (*Oncorhynchus gorbuscha*) relative abundance in the northern Bering Sea to provide insight into production dynamics for adult Pink salmon returning to rivers around Norton Sound and the Yukon River. Adult returns of Pink salmon to rivers in the Alaskan Arctic have reached record levels in recent years. Research explored whether warming and shifts in seasonal ice extent and thickness might benefit pelagic production in summer months and improve growth and survival of local Pink salmon stocks in freshwater and early marine life history stages. Farley et al. (2020, This Issue) found a positive, significant relationship between annual juvenile Pink salmon relative abundance and annual average summer air temperatures, suggesting warming conditions in river and streams may improve freshwater survival. Significant relationships between juvenile abundance and adults returns indicate that much of the variability in survival may occur during early marine life-history stages. The juvenile northern Bering Sea Pink salmon index presented in this study may help to inform future production and management of adult salmon returning to the region.

Higher trophic level dynamics often serve as important indicators of marine ecosystem status (Hazen et al., 2019; Moore and Gulland, 2014) and are of critical interest in Arctic coastal communities that rely on marine mammals as subsistence resources (Harcharek et al., 2018). Escajeda et al. (2020, This Issue) focus on fin whales (*Balaenoptera physalus*), a cetacean present in the summer in the Pacific Arctic, migrating north through Bering Strait to feed on seasonally-abundant prey. Using acoustic recordings from three hydrophones moored in the Bering Strait region, this research identified fin whale calls during the open-water season (2009–2015) and investigated environmental drivers of interannual variability in fin whale detections. Most detections were recorded at the mooring site nearest the confluence of the nutrient-rich Anadyr and Bering Shelf water masses, approximately 35 km north of Bering Strait. Years with the highest fin whale detections had contrasting temperatures and water flow velocities, suggesting that there may be other environmental factors or ecosystem interactions that determine fin whale seasonal abundance in this region.

4.4. Insights from and impacts on human communities in the Pacific Arctic

As an integrated ecosystem study, the Arctic IERP endeavors to integrate the insights and perspectives of Alaska Native communities and to communicate relevant results through an iterative and ongoing process of exchange. More work is required to determine how to integrate multiple perspectives towards understanding Arctic marine ecosystems. Specifically, efforts are ongoing to better understand and predict impacts on human communities in the Arctic (Huntington et al., 2019) and to strengthen the relevance and depth of understanding of research results through integration of traditional ecological knowledge (Huntington, 2000), engagement with indigenous communities (Eekes-Medrano et al., 2019), and co-production of knowledge (Robards et al., 2018). The Arctic IERP has developed a program component explicitly directed towards investigating the impacts of ecosystem change on human communities in the region. This LTK team works in collaboration with other program components and is dedicated to questions of relevance to Alaska Native Arctic communities. We encourage researchers operating in the region to reference ongoing research developed by or in collaboration with the North Slope Arctic Borough (https://www.north-slope.org), Northwest Arctic Borough (https://www.nwabor.org), and Kawerak Inc. (https://kawerak.org).

5. Reference to past and future research in the Pacific Arctic

Previous research in this region provides important reference and context for the changes observed and reported in this volume. In 2005, NPRB and the National Science Foundation (NSF) developed a multiyear integrated ecosystem research partnership (http://www.nprb.org/bering-sea-project; Van Pelt., 2016) to address potential implications of climate change to the Bering Sea. A consistent finding was that physical conditions drive an important ecosystem transition that divides the Bering Sea into northern and southern regions and delineates an important boundary between sub-Arctic and Arctic ecosystems (Stabeno et al., 2012; Baker and Hollowed, 2014; Ortiz et al., 2016). This division is driven primarily by the extent and persistence of sea ice. While previous research suggested the northern Bering Sea shelf would retain extensive ice cover in winter (Sigler et al., 2010), recent data (2017–2020) and analyses of conditions in recent years (Stabeno et al., 2019) no longer anticipate extensive winter sea ice as a consistent feature of the physical environment south of Bering Strait. This suggests a region in transformation.

Results in this volume provide indications that the Pacific Arctic is no longer exempt from trends in sea-ice declines evident elsewhere in the Arctic region. These findings signal a potential new physical regime in the Pacific Arctic (Huntington et al., 2020). These new physical processes and dynamics will have significant ecological implications. It is expected that changes to the physical environment, if persistent, will substantially influence important biological processes and their phenology, including primary production, benthic-pelagic coupling, and carbon and energy transfer. These conditions, in turn, will influence the abundance, distribution, and life history of many species in this region. This has important implications for ecosystem structure, resource availability, and food security to Alaska Native communities in the region. Subsequent Special Issue volumes in Deep-Sea Research II are planned to document and synthesize continued and ongoing research in this important and transforming region. This research is anticipated to further increase our collective understanding of the important processes linking various components of the ecosystems of the Bering and Chukchi seas and adjacent marine systems.

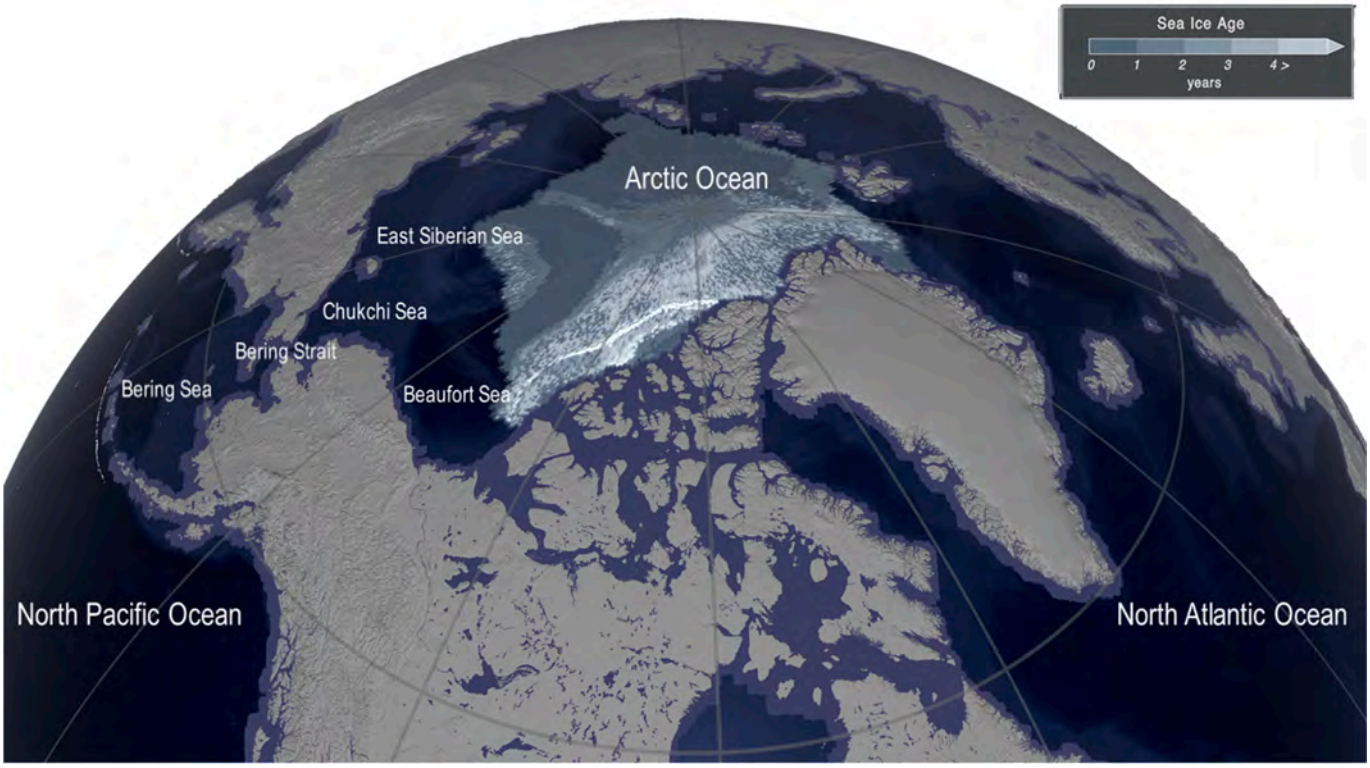

Fig. 1. The Pacific Arctic region at historical minimum sea-ice extent in September 2019, estimated at 4.15 million square km [source data: NASA Goddard Scientific Visualization Studio]. The greater Arctic Ocean is shown, as well as the constituent parts of the Pacific Arctic, including the Bering Sea, Chukchi Sea, Beaufort Sea and East Siberian Sea. Sea ice is shown in the central Arctic, displayed according to estimated sea-ice age.

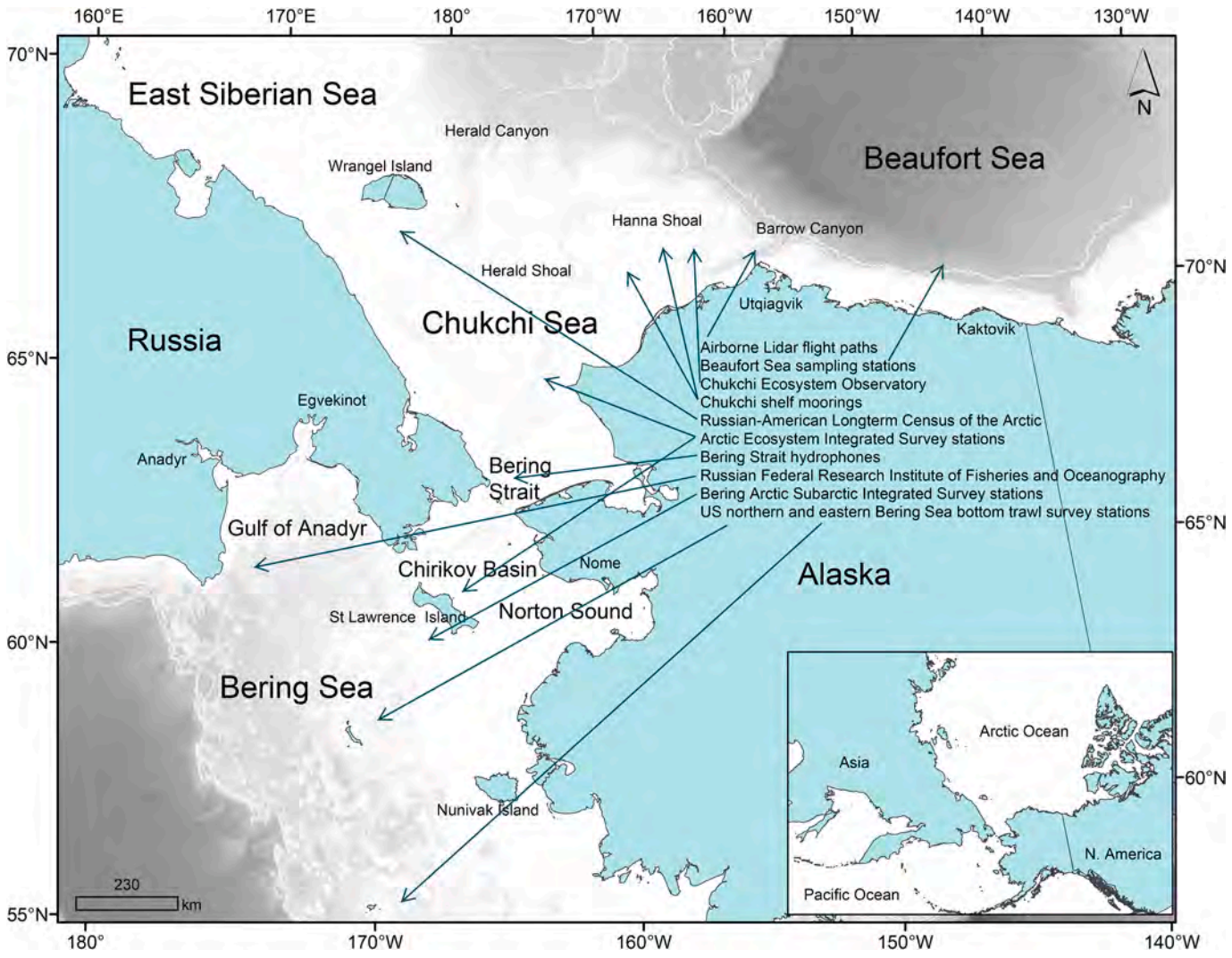

Fig. 2. Main Map: Approximate location of research, survey efforts and mooring arrays conducted and/or deployed in the Pacific Arctic region in recent years. Inset Map: Arctic Ocean and North Pacific Ocean, including the Gulf of Alaska, Aleutian and Commander Islands and Kuril Islands, and the Sea of Okhotsk.

Acknowledgements

We thank all the contributing authors and external reviewers that contributed to the development of this Special Issue publication. We also acknowledge the sponsors of and contributors to this program, including the North Pacific Research Board (NPRB), Collaborative Alaskan Arctic Studies Program (formerly the North Slope Borough/Shell Baseline Studies Program), Bureau of Ocean Energy Management (BOEM), and the Office of Naval Research (ONR) Marine Mammals and Biology Program. Generous in-kind support was provided by the National Oceanic and Atmospheric Administration (NOAA) and the University of Alaska Fairbanks (UAF). This coordinated program was developed in cooperation with the Interagency Arctic Research Policy Committee (IARPC) Chukchi and Beaufort Sea Ecosystem Collaboration Team and the U.S. Arctic Research Commission (USARC). The program benefitted from and was informed by consultations with Alaska Native communities and regional and tribal associations, and coordinated in partnership with Alaska Sea Grant, the North Slope Borough, the village of Kotzebue and Northwest Arctic Borough, and the city of Nome and Kawerak Inc. We thank Ken Drinkwater and Kishore Sivakolundu for their work to edit and support the research presented in this Special Issue. The scientific results and conclusions, as well as any views or opinions expressed herein, are those of the authors and do not necessarily reflect those of NOAA or the Department of Commerce. This manuscript is a product of the NPRB Arctic Integrated Ecosystem Research Program [NPRB publication number: ArcticIERP-01].

References

Arrigo, K.R., van Dijken, G.L., 2015. Continued increases in Arctic Ocean primary productivity. Prog. Oceanogr. 136, 60–70.

Baker, M.R., Hollowed, A.B., 2014. Delineating ecological regions in marine systems: integrating physical structure and community composition to inform spatial management in the eastern Bering Sea. Deep-Sea Res. II 109, 215–240.

Baker, M.R., Smith, B. (Eds.), 2018. North Pacific Research Board Science Plan. North Pacific Research Board, Anchorage, AK, ISBN 978-0-9772670-2-6, 132 p. Library of Congress Control Number: 2018911595.

Baker, M.R., Kivva, K.K., Pisareva, M., Watson, J., Selivanova, J., 2020. Shifts in the physical environment in the Pacific Arctic and implications for ecological timing and conditions. Deep-Sea Res. II (this issue).

Baker, M.R., Kivva, K.K., Eisner, L., 2018. In: Workshop – the Role of the Northern Bering Sea in Modulating the Arctic II: International Interdisciplinary Collaboration, vol.26. PICES Press, pp. 15–19.

Banas, N., Ashjian, C.J., Campbell, R.G., Laidre, K.L., Møller, E.F., Nielsen, T.G., Simon, M., 2018. Are Arctic productivity hotspots sources or sinks? A trait-based approach to mesozooplankton life history and energetics along advective corridors. In: 2018 Ocean Sciences Meeting.

Carmack, E., Wassmann, P., 2006. Food webs and physical–biological coupling on pan-Arctic shelves: unifying concepts and comprehensive perspectives. Prog. Oceanogr. 71, 446–477.

Carothers, C., Sformo, T.L., Cotton, S., George, J.C., Westley, P.A., 2019. Pacific salmon in the rapidly changing Arctic: exploring local knowledge and emerging fisheries in Utqiaġvik and Nuiqsut. Alaska. Arctic 72 (3), 273–288.
Churnside, J.H., Marchbanks, R.D., Vagle, S., Bell, S.W., Stabeno, Phyllis J., 2020. Stratification, plankton layers, and mixing measured by airborne lidar in the Chukchi and Beaufort seas. Deep-Sea Res. II (this issue).
Corlett, W.B., Pickart, R.S., 2017. The Chukchi slope current. Prog. Oceanogr. 153, 50–65.
Daly, E.A., Moss, J.H., Fergusson, E., Brodeur, R.D., 2019. Potential for resource competition between juvenile groundfishes and salmon in the eastern Gulf of Alaska. Deep-Sea Res. II 165, 150–162.
Danielson, S.L., Dobbins, E.L., Jakobsson, M., Johnson, M.A., Weingartner, T.J., Williams, W.J., Zarayskaya, Y., 2015. Sounding the northern seas. Eos 96.
Danielson, S.L., Weingartner, T.J., Hedstrom, K.S., Aagaard, K., Woodgate, R., Curchitser, E., Stabeno, P.J., 2014. Coupled wind-forced controls of the Bering-Chukchi shelf circulation and the Bering Strait throughflow: ekman transport, continental shelf waves, and variations of the Pacific-Arctic sea surface height gradient. Prog. Oceanogr. 125, 40–61.
Danielson, S.L., Ahkinga, O., Ashjian, C., Basyuk, E., Cooper, L.W., Eisner, L., Farley, E., Iken, K.B., Grebmeier, J.M., Juranek, L., Khen, G., Jayne, S.R., Kikuchi, T., Ladd, C., Lu, K., McCabe, R.M., Moore, G.W.K., Nishino, S., Ozenna, F., Pickart, R.S., Polyakov, I., Stabeno, P.J., Thoman, R., Williams, W.J., Wood, K., Weingartner, T.J., 2020. Manifestation and consequences of warming and altered heat fluxes over the Bering and Chukchi Sea continental shelves. Deep-Sea Res. II (this issue).
De Robertis, A., Taylor, K., Wilson, C.D., Farley, E.V., 2017. Abundance and distribution of arctic cod (Boreogadus saida) and other pelagic fishes over the US continental shelf of the northern bering and Chukchi seas. Deep-Sea Res. II 135, 51–65.
Dickson, D., Baker, M.R., 2016. Introduction to the north pacific research board Gulf of Alaska integrated ecosystem research program (GOAIERP): volume I. Deep-Sea Res. II 132, 1–5.
Doyle, M.J., Mier, K.L., 2016. Early life history pelagic exposure profiles of selected commercially important fish species in the Gulf of Alaska. Deep-Sea Res. II 132, 162–193.
Drinkwater, K., Pepin, P., 2013. Comparison of climate forcing on the marine ecosystems of the Northeast and Northwest Atlantic: a synthesis of the NORCAN Project. Prog. Oceanogr. 114, 3–10.
Dunmall, K.M., McNicholl, D.G., Reist, J.D., 2018. Community-based monitoring demonstrates increasing occurrences and abundances of Pacific Salmon in the Canadian Arctic from 2000 to 2017. N. Pac. Anadr. Fish Comm. Tech. Rep 11, 87–90.
Eakins, B.W., Sharman, G.F., 2010. Volumes of the World's Oceans from ETOPO1. NOAA National Geophysical Data Center, Boulder, p. 1.
Eerkes-Medrano, L., Huntington, H.P., Castro, A.O., Atkinson, D.E., 2019. Engaging northern indigenous communities in biophysical research: pitfalls and successful approaches. Arctic 72, 2.
Escajeda, E., Stafford, K.M., Woodgate, R.A., Laidre, K.L., 2020. Variability in fin whale (Balaenoptera physalus) occurrence in the Bering Strait and southern Chukchi Sea in relation to environmental factors. Deep-Sea Res. II (this issue).
Farley, E.V., Murphy, J.M., Cieciel, K., Yasumiishi, E.M., Dunmall, K.M., Sformoe, T., Rand, P., 2020. Response of Pink salmon to climate warming in the northern Bering Sea. Deep-Sea Res. II (this issue).
Forster, C.E., Norcross, B.L., Spies, I., 2020. Documenting growth parameters and age in Arctic fish species in the Chukchi and Beaufort seas. Deep-Sea Res. II (this issue).
Frey, K.E., Moore, G.W.K., Cooper, L.W., Grebmeier, J.M., 2015. Divergent patterns of recent sea ice cover across the bering, Chukchi, and Beaufort seas of the pacific arctic region. Prog. Oceanogr. 136, 32–49.
Grebmeier, J.M. (Ed.), 2014. Pacific Marine Arctic Regional Synthesis (PacMARS) Community Meetings during February-March 2013. PacMARS report, p. 30.
Grebmeier, J.M., Maslowski, W. (Eds.), 2014. The Pacific Arctic Region: Ecosystem Status and Trends in a Rapidly Changing Environment. Springer, Dordrecht, p. 50.
Grebmeier, J.M., Overland, J.E., Moore, S.E., Farley, E.V., Carmack, E.C., Cooper, L.W., Frey, K.E., Helle, J.H., McLaughlin, F.A., McNutt, S.L., 2006. A major ecosystem shift in the northern Bering Sea. Science 311, 1461–1464.
Grebmeier, J.M., Cooper, L.W., Ashjian, C.A., Bluhm, B.A., Campbell, R.B., Dunton, K.E., Moore, J., Okkonen, S., Sheffield, G., Trefry, J., Pasternak, S.Y., 2015. Pacific Marine Arctic Regional Synthesis (PacMARS) Final Report. North Pacific Research Board, p. 259.
Haiden, T., Janousek, M., Bidlot, J., Ferranti, L., Prates, F., Vitart, F., Bauer, P., Richardson, D.S., 2017. Evaluation of ECMWF Forecasts, Including 2016-2017 Upgrades. European Centre for Medium Range Weather Forecasts, p. 56.
Harcharek, Q., Kayotuk, C.S., George, J.C., Pederson, M., 2018. Qaaktuġvik/Kaktovik, Subsistence Harvest Report 2007-2012. Technical Report Prepared by the North Slope. Borough Department of Wildlife Management, Barrow, Alaska, p. 63.
Hazen, E.L., Abrahms, B., Brodie, S., Carroll, G., Jacox, M.G., Savoca, M.S., Scales, K.L., Sydeman, W.J., Bograd, S.J., 2019. Marine top predators as climate and ecosystem sentinels. Front. Ecol. Environ. 17 (10), 565–574.
Hollowed, A.B., Sundby, S., 2014. Change is coming to the northern oceans. Science 344, 1084–1085.
Huang, B., Thorne, P.W., Banzon, V.F., Boyer, T., Chepurin, G., Lawrimore, J.H., Menne, M.J., Smith, T.M., Vose, R.S., Zhang, H.M., 2017. Extended reconstructed sea surface temperature, version 5 (ERSSTv5): upgrades, validations, and intercomparisons. J. Clim. 30 (20), 8179–8205.
Huntington, H.P., 2000. Using traditional ecological knowledge in science: methods and applications. Ecol. Appl. 10, 1270–1274.
Huntington, H.P., Carey, M., Apok, C., Forbes, B.C., Fox, S., Holm, L.K., Ivanova, A., Jaypoody, J., Noongwook, G., Stammler, F., 2019. Climate change in context: putting people first in the Arctic. Reg. Environ. Change 19 (4), 1217–1223.
Huntington, H.P., Danielson, S.L., Wiese, F.K., Baker, M.R., Boveng, P., Citta, J.J., De Robertis, A., Dickson, D.M., Farley, E., George, J.C., Iken, K., 2020. Evidence suggests potential transformation of the Pacific Arctic ecosystem is underway. Nat. Clim. Change 1–7.
Jakobsson, M., Mayer, L., Coakley, B., Dowdeswell, J.A., Forbes, S., Fridman, B., Hodnesdal, H., Noormets, R., Pedersen, R., Rebesco, M., Schenke, H.W., 2012. The international bathymetric chart of the Arctic Ocean (IBCAO) version 3.0. Geophys. Res. Lett. 39 (12).
Jeffries, M.O., Overland, J.E., Perovich, D.K., 2013. The arctic shifts to a new normal. Phys. Today 10, 35–40.
Kwok, R., 2018. Arctic sea ice thickness, volume, and multiyear ice coverage: losses and coupled variability (1958-2018). Environ. Res. Lett. 13, 10.
Langis, D., Stabeno, P.J., Meinig, C., Mordy, C.W., Bell, S.W., Tabisola, H.M., 2018. October. Low-cost expendable buoys for under ice data collection. In: OCEANS 2018 MTS/IEEE Charleston. IEEE, pp. 1–9.
Lalande, C., Grebmeier, J.M., Hopcroft, R.R., Danielson, S.L., 2020. Annual cycle of export fluxes of biogenic matter near Hanna Shoal in the northeast Chukchi Sea. Deep-Sea Res. II (this issue).
Lenssen, N.J., Schmidt, G.A., Hansen, J.E., Menne, M.J., Persin, A., Ruedy, R., Zyss, D., 2019. Improvements in the GISTEMP uncertainty model. J. Geophys. Res. Atmos. 124 (12), 6307–6326.
Logerwell, E.A., Busby, M., Mier, K.L., Tabisola, H., Duffy-Anderson, J., 2020. The effect of oceanographic variability on the distribution of larval fishes of the northern Bering and Chukchi seas. Deep-Sea Res. II (this issue).
Lu, K., Danielson, S., Hedstrom, K., Weingartner, T., 2020. Assessing the role of oceanic heat fluxes on ice ablation of the central Chukchi Sea Shelf. Prog. Oceanogr., 102313
Marsh, J.M., Mueter, F.J., Iken, K., Danielson, S., 2017. Ontogenetic, spatial and temporal variation in trophic level and diet of Chukchi Sea fishes. Deep-Sea Res. II 135, 78–94.
Moore, S.E., Stabeno, P.J., Grebmeier, J.M., Okkonen, S.R., 2018. The Arctic Marine Pulses Model: linking annual oceanographic processes to contiguous ecological domains in the Pacific Arctic. Deep-Sea Res. II 152, 8–21.
Moore, S.E., Stabeno, P.J., 2015. Synthesis of arctic research (SOAR) in marine ecosystems of the pacific arctic. Prog. Oceanogr. 136, 1–11.
Moore, S.E., Gulland, F.M., 2014. Linking marine mammal and ocean health in the 'New Normal'. Arctic Ocean Coast. Man. 102, 55–57.
Moore, S.E., Logerwell, E., Eisner, L., Farley, E.V., Harwood, L., Kuletz, K., Lovvorn, J., Murphy, J., Quakenbush, L., 2014. Marine fishes, birds and mammals as sentinels of ecosystem variability and reorganization in the Pacific Arctic region. In: Grebmeier, J.M., Maslowski, W. (Eds.), The Pacific Arctic Region: Ecosystem Status and Trends in a Rapidly Changing Environment. Springer, Dordrecht, pp. 337–392.
Mordy, C., Bell, S., Cokelet, E., Ladd, C., Lebon, G., Proctor, P., Stabeno, P.J., Strausz, D., Wisegarver, E., Wood, K., 2020. Seasonal and interannual variability of nitrate in the eastern Chukchi sea: transport and winter replenishment. Deep-Sea Res. II this issue).
Mueter, F.J., Weems, J., Farley, E.V., Sigler, M.F., 2017. Arctic ecosystem integrated survey (Arctic Eis): marine ecosystem dynamics in the rapidly changing Pacific Arctic Gateway. Deep-Sea Res. II 135, 1–6.
Ormseth, O.A., Baker, M.R., Hopcroft, R.R., Ladd, C., Mordy, C.W., Moss, J.H., Mueter, F. J., Shotwell, S.K., Strom, S.L., 2019. Introduction to understanding ecosystem processes in the Gulf of Alaska. Deep-Sea Res. II 165, 1–6.
Ortiz, I., Aydin, K., Hermann, A.J., Gibson, G.A., Punt, A.E., Wiese, F.K., Eisner, L.B., Ferm, N., Buckley, T.W., Moffitt, E.A., Ianelli, J.N., 2016. Climate to fish: synthesizing field work, data and models in a 39-year retrospective analysis of seasonal processes on the eastern Bering Sea shelf and slope. Deep-Sea Res. II 134, 390–412.
Pickart, R.S., Moore, G.W.K., Mao, C., Bahr, F., Nobre, C., Weingartner, T.J., 2016. Circulation of winter water on the Chukchi shelf in early Summer. Deep-Sea Res. II 130, 56–75.
Pisareva, M.N., 2018. An overview of the recent research on the Chukchi Sea water masses and their circulation. Russ. J. Earth Sci. 18 (4).
Pitman, K.J., Moore, J.W., Sloat, M.R., Beaudreau, A.H., Bidlack, A.L., Brenner, R.E., Hood, E.W., Pess, G.R., Mantua, N.J., Milner, A.M., Radić, V., 2020. Glacier retreat and pacific salmon. Bioscience 70 (3), 220–236.
Polyakov, I.V., Alkire, M.B., Bluhm, B.A., Brown, K.A., Carmack, E.C., Chierici, M., Danielson, S.L., Ellingsen, I., Ershova, E.A., Gårdfeldt, K., Ingvaldsen, R.B., Pnyushkov, A.V., Slagstad, D., Wassmann, P., 2020. Borealization of the Arctic Ocean in response to anomalous advection from sub-arctic seas. Front. Mar. Sci. 7, 491.
Robards, M.D., Huntington, H.P., Druckenmiller, M., Lefevre, J., Moses, S.K., Stevenson, Z., Watson, A., Williams, M., 2018. Understanding and adapting to observed changes in the Alaskan Arctic: actionable knowledge co-production with Alaska Native communities. Deep-Sea Res. II 152, 203–213.
Sigler, M.F., Harvey, H.R., Ashjian, J., Lomas, M.W., Napp, J.M., Stabeno, P.J., Van Pelt, T.I., 2010. How does climate change affect the Bering Sea ecosystem? Eos Trans. Am. Geophys. Union 91 (48), 457–458.
Smith, M., Thomson, J., 2019. Ocean surface turbulence in newly formed marginal ice zones. J. Geophys. Res. Oceans 124 (3), 1382–1398.
Spear, A., Napp, J., Ferm, N., Kimmel, D., 2020. Advection and in situ processes as drivers of change for the abundance of large zooplankton taxa in the Chukchi sea. Deep-Sea Res. II (this issue).
Stabeno, P.J., Farley Jr., E.V., Kachel, N.B., Moore, S., Mordy, C.W., Napp, J.M., Overland, J.E., Pinchuk, A.I., Sigler, M.F., 2012. A comparison of the physics of the northern and southern shelves of the eastern Bering Sea and some implications for the ecosystem. Deep-Sea Res. II 65, 14–30.
Stabeno, P.J., Bell, S.W., 2019. Extreme conditions in the Bering Sea (2017–2018): record-breaking low sea-ice extent. Geophys. Res. Lett. 46, 8952–8959.

Stabeno, P., Kachel, N., Ladd, C., Woodgate, R., 2018. Flow patterns in the eastern Chukchi sea: 2010–2015. J. Geophys. Res. Oceans 123 (2), 1177–1195.
Stabeno, P.J., Bell, S.W., Bond, N.A., Kimmel, D.G., Mordy, C.W., Sullivan, M.E., 2019. Distributed biological observatory region 1: physics, chemistry and plankton in the northern Bering Sea. Deep-Sea Res. II 162, 8–21.
Stabeno, P.J., Mordy, C., Sigler, M.F., 2020. Seasonal patterns of primary production at the seafloor in the eastern Chukchi Sea based upon in-situ chlorophyll fluorescence measurements. Deep-Sea Res. II 2010–2018 (this issue).
Stabeno, P.J., McCabe, R.M., 2020. Vertical structure and temporal variability of currents over the Chukchi Sea continental slope. Deep-Sea Res. II (this issue).
Stroeve, J.C., Serreze, M.C., Holland, M.M., Kay, J.E., Malanik, J., Barrett, A.P., 2012. The Arctic's rapidly shrinking sea ice cover: a research synthesis. Climatic Change 110, 1005–1027.
Thomson, J., Rogers, W.E., 2014. Swell and sea in the emerging Arctic Ocean. Geophys. Res. Lett. 41 (9), 3136–3140.
Thomson, J., Fan, Y., Stammerjohn, S., Stopa, J., Rogers, W.E., Girard-Ardhuin, F., Ardhuin, F., Shen, H., Perrie, W., Shen, H., Ackley, S., 2016. Emerging trends in the sea state of the Beaufort and Chukchi seas. Ocean Model. 105, 1–12.
Van Pelt, T.I., Napp, J.M., Ashjian, C.J., Harvey, H.R., Lomas, M.W., Sigler, M.F., Stabeno, P.J., 2016. An introduction and overview of the Bering Sea project: volume IV. Deep-Sea Res. II. 134, 3–12.
Van Pelt, T.I., Huntington, H.P., Romanenko, O.V., Mueter, F.J., 2017. The missing middle: central Arctic Ocean gaps in fishery research and science coordination. Mar. Pol. 85, 79–86.
Wang, M., Overland, J.E., 2015. Projected future duration of the sea-ice-free season in the Alaskan Arctic. Prog. Oceanogr. 136, 50–59.
Wang, M., Yang, Q., Overland, J.E., Stabeno, P.J., 2018. Sea-ice cover timing in the Pacific Arctic: the present and projections to mid-century by selected CMIP5 models. Deep-Sea Res. II 152, 22–34.
Wiese, F.K., Wiseman, W.J., Van Pelt, T.I., 2012. Bering sea linkages. Deep-Sea Res. II 65, 2–5.
Wood, K.R., Bond, N.A., Danielson, S.L., Overland, J.E., Salo, S.A., Stabeno, P.J., Whitefield, J., 2015. A decade of environmental change in the Pacific Arctic region. Prog. Oceanogr. 136, 12–31.
Woodgate, R.A., Weingartner, T.J., Lindsay, R., 2012. Observed increases in Bering Strait oceanic fluxes from the Pacific to the Arctic from 2001 to 2011 and their impacts on the Arctic Ocean water column. Geophys. Res. Lett. 39, L24603.
Woodgate, R.A., 2018. Increases in the Pacific inflow to the Arctic from 1990 to 2015, and insights into seasonal trends and driving mechanisms from year-round Bering Strait mooring data. Prog. Oceanogr. 160, 124–154.

Matthew R. Baker*
North Pacific Research Board, 1007 West Third Avenue, Anchorage, AK, 99501, USA

Edward V. Farley
NOAA, Alaska Fisheries Science Center, Ted Stevens Marine Research Institute, Juneau, AK, USA

Carol Ladd
NOAA Pacific Marine Environmental Laboratory, Seattle, WA, USA

Seth L. Danielson
University of Alaska Fairbanks, College of Fisheries and Ocean Sciences, Fairbanks, AK, USA

Kathleen M. Stafford
Applied Physics Laboratory, University of Washington, Seattle, WA, USA

Henry P. Huntington
Huntington Consulting, Eagle River, AK, USA

Danielle M.S. Dickson
North Pacific Research Board, 1007 West Third Avenue, Anchorage, AK, 99501, USA

* Corresponding author.
E-mail address: Matthew.Baker@nprb.org (M.R. Baker).

Deep–Sea Research II 177 (2020) 104781

Contents lists available at ScienceDirect

Deep-Sea Research Part II

journal homepage: http://www.elsevier.com/locate/dsr2

Manifestation and consequences of warming and altered heat fluxes over the Bering and Chukchi Sea continental shelves

S.L. Danielson [a,*], O. Ahkinga [b], C. Ashjian [c], E. Basyuk [d], L.W. Cooper [e], L. Eisner [f], E. Farley [g], K. B. Iken [a], J.M. Grebmeier [e], L. Juranek [h], G. Khen [d], S.R. Jayne [c], T. Kikuchi [i], C. Ladd [j], K. Lu [a], R. M. McCabe [k], G.W.K. Moore [l], S. Nishino [i], F. Ozenna [b], R.S. Pickart [c], I. Polyakov [m,p], P. J. Stabeno [j], R. Thoman [n], W.J. Williams [o], K. Wood [k], T.J. Weingartner [a]

[a] University of Alaska Fairbanks (UAF), College of Fisheries and Ocean Sciences, Fairbanks, AK, USA
[b] Native Village of Diomede, Diomede, AK, USA
[c] Woods Hole Oceanographic Institute, Woods Hole, MA, USA
[d] Russian Federal Research Institute of Fisheries and Oceanography, Pacific Branch of VINRO, TINRO, Vladivostok, Russia
[e] University of Maryland Center for Environmental Sciences, Chesapeake Biological Laboratory, Solomons, MD, USA
[f] National Oceanographic and Atmospheric Administration, Alaska Fisheries Science Center, Seattle, WA, USA
[g] NOAA, Alaska Fisheries Science Center, Ted Stevens Marine Research Institute, Juneau, AK, USA
[h] College of Earth, Ocean and Atmospheric Science, Oregon State University, Corvallis, OR, USA
[i] Institute of Arctic Climate and Environment Research (IACE), Research Institute for Global Change (RIGC), Japan Agency for Marine-Earth Science and Technology (JAMSTEC), Yokosuka, Kanagawa, Japan
[j] National Oceanographic and Atmospheric Administration (NOAA), Pacific Marine Environmental Laboratory, Seattle, WA, USA
[k] University of Washington, Joint Institute for the Study of the Atmosphere and Ocean, Seattle, WA, USA
[l] University of Toronto Mississauga, Mississauga, ON, Canada
[m] UAF International Arctic Research Center and College of Natural Science and Mathematics, 930 Koyukuk Drive, Fairbanks, AK, 99775, USA
[n] UAF, Alaska Center for Climate Assessment and Policy, Fairbanks, AK, USA
[o] Institute of Ocean Sciences, Fisheries and Oceans Canada, Sidney, BC, Canada
[p] Finnish Meteorological Institute, Erik Palménin aukio 1, 00560, Helsinki, Finland

ARTICLE INFO

Keywords:
Pacific arctic
Chukchi sea
Bering sea
Temperature
Trend
Heat flux
Climate
Change
Sea ice
Budget

ABSTRACT

A temperature and salinity hydrographic profile climatology is assembled, evaluated for data quality, and analyzed to assess changes of the Bering and Chukchi Sea continental shelves over seasonal to century-long time scales. The climatology informs description of the spatial distribution and temporal evolution of water masses over the two shelves, and quantification of changes in the magnitude and throughput of heat and fresh water. For the Chukchi Shelf, linear trend analysis of the integrated shelf heat content over its 1922–2018 period of record finds a significant summer and fall warming of 1.4 °C (0.14 ± 0.07 °C decade^{-1}); over 1990–2018 the warming rate tripled to 0.43 ± 0.35 °C decade^{-1}. In contrast, the Bering Shelf's predominantly decadal-scale variability precludes detection of a water column warming trend over its 1966–2018 period of record, but sea surface temperature data show a significant warming of 0.22 ± 0.10 °C decade^{-1} over the same time frame. Heat fluxes over 1979–2018 computed by the European Centre for Medium-Range Weather Forecast (ECMWF) ERA5 reanalysis exhibit no record-length trend in the shelf-wide Bering surface heat fluxes, but the Chukchi Shelf cooling season (October–March) has a trend toward greater surface heat losses and its warming season (April–September) has a trend toward greater heat gains. The 2014–2018 half-decade exhibited unprecedented low winter and spring sea-ice cover in the Northern Bering and Chukchi seas, changes that coincided with reduced springtime surface albedo, increased spring absorption of solar radiation, and anomalously elevated water column heat content in summer and fall. Consequently, the warm ocean required additional time to cool to the freezing point in fall. Fall and winter ocean-to-atmosphere heat fluxes were anomalously large and associated with enhanced southerly winds and elevated surface air temperatures, which in turn promoted still lower sea-ice production, extent, and concentration anomalies. Likely reductions in sea-ice melt were associated with positive salinity anomalies on the Southeast Bering Shelf and along the continental slope over 2014–2018. Negative

* Corresponding author.
E-mail address: sldanielson@alaska.edu (S.L. Danielson).

https://doi.org/10.1016/j.dsr2.2020.104781
Received 30 July 2019; Received in revised form 7 April 2020; Accepted 7 April 2020
Available online 25 May 2020

salinity anomalies during 2014–2018 on the central and northern Bering Shelf may be related to a combination of 1) long-term declines in salinity, 2) an increase of ice melt, and 3) a decline of brine production. We hypothesize that freshening on the Bering Shelf and in Bering Strait since 2000 are linked to net glacial ablation in the Gulf of Alaska watershed. We show that the heat engines of both the Bering and Chukchi shelves accelerated over 2014–2018, with increased surface heat flux exchanges and increased oceanic heat advection. During this time, the Chukchi Shelf delivered an additional 5–9 x 10^{19} J yr^{-1} (50–90 EJ yr^{-1}) into the Arctic basin and/or sea-ice melt, relative to the climatology. A similar amount of excess heat (60 EJ yr^{-1}) was delivered to the atmosphere, showing that the Chukchi Sea makes an out-sized contribution to Arctic amplification. A conceptual model that summarizes the controlling feedback loop for these Pacific Arctic changes relates heat content, sea ice, freshwater distributions, surface heat fluxes, and advective fluxes.

1. Introduction

Oceanic and atmospheric transport of heat from low to high latitudes contributes to global thermal regulation (Trenberth et al., 2009), but greenhouse warming regionally perturbs heat content and fluxes (Stocker et al., 2013), causing the earth's climate system and biological systems to adjust in response. These adjustments include alterations to sea ice (Stroeve et al., 2005; Perovich et al., 2008), permafrost (Osterkamp and Romanovsky, 1999), precipitation (Groves and Francis, 2002), and many components of both terrestrial and marine ecosystems (Walther et al., 2002; Doney et al., 2011). At high latitudes in the Northern Hemisphere, reinforcing feedback loops induce faster rates of atmospheric warming than elsewhere, resulting in the "Arctic amplification" of global climate warming (Serreze and Francis, 2006; Hansen

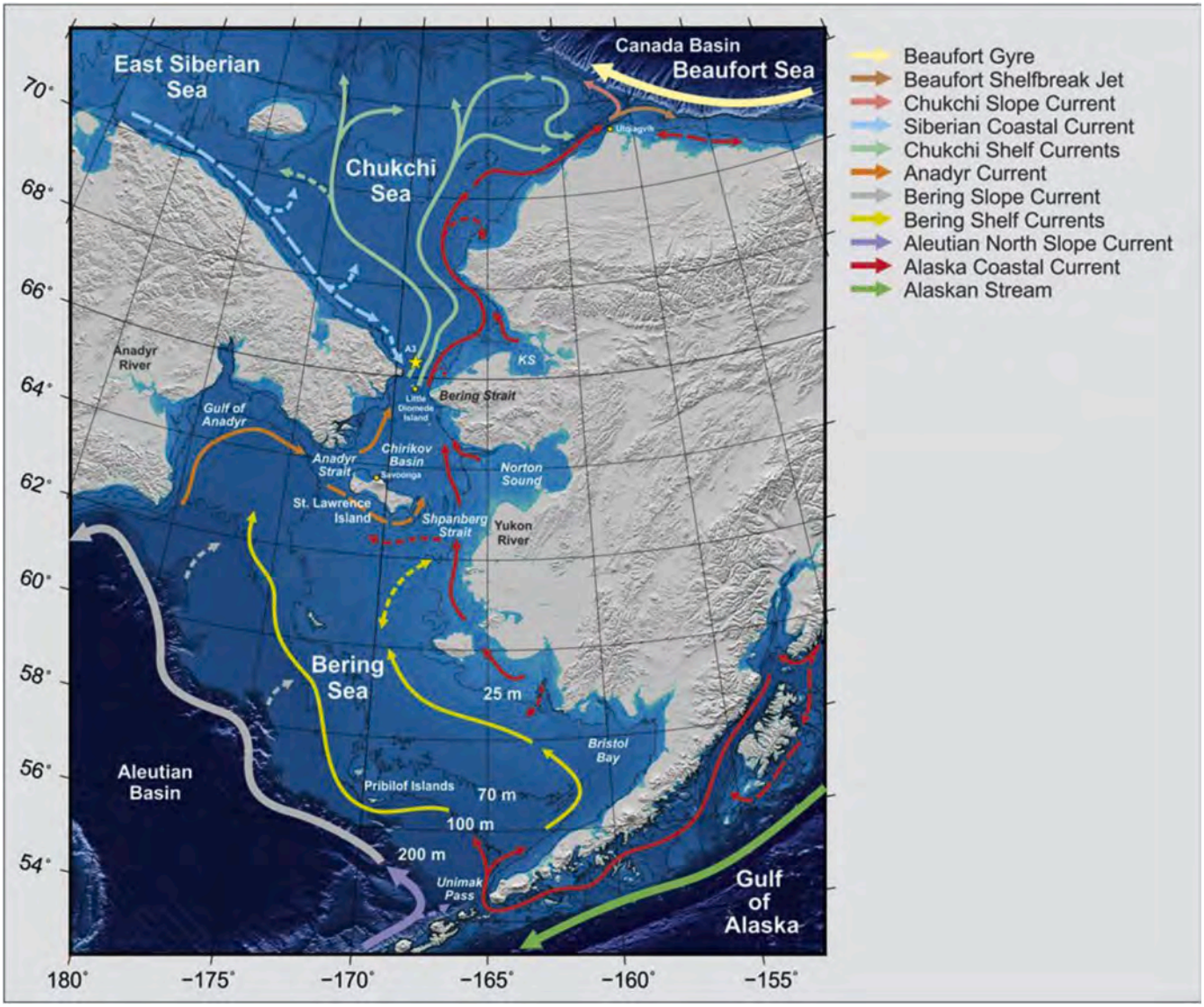

Fig. 1. Location map of the Pacific Arctic region with water body and place names. Persistent currents are shown with solid arrows; intermittent or poorly known flows are denoted with dashed arrows. Bering Strait mooring A3 is marked with a yellow star. Abbreviation KS denotes Kotzebue Sound. Depth isopleths are contoured with thin black lines at 25, 70, 100 and 200 m. (For interpretation of the references to color in this figure legend, the reader is referred to the Web version of this article.)

et al., 2010; Overland and Wang, 2010; Screen and Simmonds, 2010; Serreze and Barry, 2011). In this study, we quantify recent (years) and long-term (decades to century) changes in shelf temperatures, salinities, and air-sea heat exchanges over the Bering and Chukchi continental shelves (Fig. 1), examining the local manifestation and consequences of Arctic amplification within the context of the prior period of record.

Marine ecosystems of the Bering-Chukchi shelves encompass economically important fishing grounds (Van Vorhees and Lowther, 2010), productive benthos (Grebmeier et al., 2015), and subsistence resources for Indigenous coastal communities (Suydam et al., 2006), all of which derive fundamental structure from the regional environmental conditions (Hare and Mantua, 2000; Benson and Trites, 2002; Hunt et al., 2011). For example, oceanic heat content (Walsh et al., 2018) is important to sea-ice extent and duration (Woodgate et al., 2010; Frey et al., 2015; Danielson et al., 2017; Polyakov et al., 2017), which in turn affect trophic exchanges (Coyle et al., 2011), prevalence of harmful algal blooms (Natsuike et al., 2017), and species distributions (Mueter and Litzow, 2008). Temperature is by itself an important control on growth rates (Eppley, 1972) and oxygen respiration (Ikeda, 1985, 2001). A better understanding of ongoing and past environmental change is a first step to exploring how bottom-up forcing may propagate through the Arctic ecosystem in the future.

In the 2013/2014 winter, the North Pacific experienced surface and subsurface warming that resulted from a persistent atmospheric blocking ridge located over western North America (Bond et al., 2015) and meridional modes of atmospheric teleconnections that directed heat away from the tropics (Di Lorenzo and Mantua, 2016). This was followed by a strong 2015 El Niño (McPhaden, 2015) and additional atmospheric blocking patterns that extended the marine heat wave. The Bering Sea also experienced previously undocumented and unprecedented high sea surface temperatures in 2014 (Stabeno et al., 2017), which by sea surface temperature (SST) and heat content metrics have continued to persist into 2018 (Thoman et al., 2020) and 2019 (Cornwall, 2019; Stabeno and Bell, 2019). The upper ocean heat content (0–300 m integration) for the eastern Bering Sea exhibited warm anomalies that were correlated with SST variations (Walsh et al., 2018). The recent warm anomalies are superimposed upon longer term warming trends previously identified for the Bering and Chukchi seas (Steele et al., 2008; Woodgate et al., 2010; Woodgate et al., 2012; Tokinaga et al., 2017).

Recent weather patterns and sea ice conditions in the northern Bering and southern Chukchi seas are challenging long-held understanding of what constitutes winter norms. The two Diomede Islands, in the past connected by shorefast ice through the winter months (sufficient to support commercial airline service on an ice runway), were exposed in January and February 2018 to long fetch open water and unconsolidated sea ice that allowed massive waves to roll ashore in a late February 2018 storm (Fig. 2). Mid-winter conditions of 2019 brought similarly low sea-ice extents to the region (Cornwall, 2019). These unprecedented observations are illustrative of conditions at the epicenter of Arctic amplification over the Pacific sector: sea ice loss over the Bering-Chukchi shelves.

The broad eastern Bering and Chukchi Sea continental shelves, connected by the narrow (~85 km) Bering Strait, comprise the shallow expanse (average < 70 m) across which Pacific waters carrying heat, fresh water and nutrients are transported into the Arctic (Coachman and Aagaard, 1966; Stigebrandt, 1984; Walsh et al., 1989). Based on oceanographic mooring data, the annual mean volume flux northward through Bering Strait is thought to be approximately 1 Sv ($1\ \text{Sv} = 10^6\ \text{m}^3\ \text{s}^{-1}$) (Woodgate, 2018), having increased to this level from roughly 0.8 Sv in the 1990s and early 2000s (Roach et al., 1995; Woodgate et al., 2005a, 2015; Woodgate, 2018). The increasing volume transport (~0.2 Sv decade^{-1}) and a weakly increasing trend in the observed temperature (0.27 ± 0.23 °C decade^{-1}) both contribute to an increasing trend in the

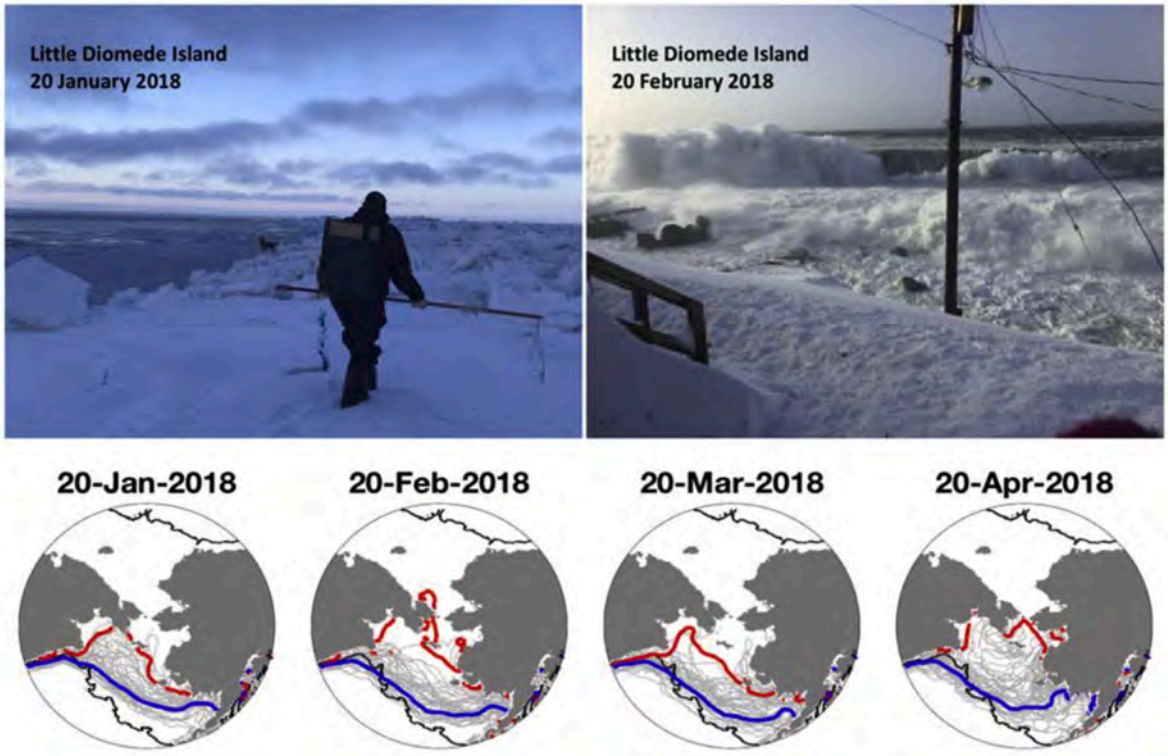

Fig. 2. Open water seen in late January (top left) and February (top right) 2018 from Little Diomede Island, which was historically located far north of the ice edge at this time of year. Satellite-derived ice edge locations (bottom) show the 1979–2018 climatological (blue) and 2018 (red) 15% concentration contours for the 20th of January, February, March, and April. Corresponding ice edges for all years over 1979–2017 are shown with gray contours. The 200 m isobath (black contour) shows the shelf break location. Photographs by O. Ahkinga (left) and F. Ozenna (right). (For interpretation of the references to color in this figure legend, the reader is referred to the Web version of this article.)

northward heat flux (Woodgate, 2018). Measurements also document a modest freshening of ~0.14±0.10 decade^{-1} over 1991–2015 that together with the increasing transport have increased the Pacific origin freshwater flux into the Arctic by ~40% or more (Woodgate, 2018). It is worth noting that the Bering Strait throughflow is the only oceanic inflow to the Arctic showing significant change in volume transport over 1993–2015 but the trend magnitude in Bering Strait is smaller than the trend uncertainty of other inflow pathways (Østerhus et al., 2019), leaving the system-wide balance unclear. In the absence of wind forcing, vorticity constraints confine much of the Bering Strait inflow to an advective pathway that circumscribes the Gulf of Anadyr in a clockwise fashion and enters the Bering Strait region via Anadyr Strait (Kinder et al., 1986), leaving the bulk of the eastern Bering Sea shelf as a secondary feed to the Bering Strait throughflow via Shpanberg Strait, east of St. Lawrence Island (Danielson et al., 2012a). Variations in these currents can alter Pacific-Arctic exchanges and the seasonal evolution of sea ice and water properties.

Processes that perturb the mean circulation and spatial distributions of water properties vary temporally and regionally across these shelves. For example, on interannual and longer time scales, variations in the Bering Strait throughflow have been ascribed to a combination of local wind stress (Aagaard et al., 1985; Woodgate et al., 2012; Danielson et al., 2014; Woodgate, 2018), wind stress over the adjoining basin and adjoining shelves (Danielson et al., 2014), variability in regional pressure gradients, especially in relation to the western Chukchi and East Siberian Sea (Danielson et al., 2014; Peralta-Ferriz and Woodgate, 2017; Okkonen et al., 2019), and thermohaline variations (Aagaard et al., 2006). Regional wind and buoyancy forces drive the seasonally warm Alaskan Coastal Current (ACC) (Paquette and Bourke, 1974; Ahlnäs and Garrison, 1984; Gawarkiewicz et al., 1994; Wiseman and Rouse, 1980; Woodgate and Aagaard, 2005) and the cool but fresh Siberian Coastal Current (Weingartner et al., 1999), which is present only in some years in the Chukchi Sea. Both coastal currents are near-shore and low-salinity features of the high latitude riverine coastal domain continuum (Carmack et al., 2015). Baroclinically unstable fronts separating ice-melt plumes from denser and warmer shelf waters (Lu et al., 2015) may be important to ocean-ice-atmosphere feedbacks and the seasonal melt-back of the Chukchi sea ice. Energetic eddies in the Bering Slope Current (Ladd, 2014), tidal energy fluxes (Foreman et al., 2006) and wind-driven exchanges, especially upwelling within shelfbreak canyons (Bourke and Paquette, 1976; Woodgate et al., 2005b; Danielson et al., 2012b) may impact cross-slope exchanges.

Although all consequences of thermal, haline, and advective variations over the Bering and Chukchi shelves are not well understood, under a warming climate it is reasonable to anticipate altered lateral and vertical property gradients that in turn will impact local and downstream habitats and potentially feed-back on the processes mentioned above. The Bering Shelf is downstream of heat and fresh water on the Gulf of Alaska shelf via Unimak Pass (Weingartner et al., 2005a). The Canada Basin is downstream of the Chukchi Shelf, which, in turn, is downstream of the Bering Sea via Bering Strait. The flows connecting these two shelves do not drain all parts of the Bering Sea shelf equally (e.g. Danielson et al., 2012a, 2012b), nor are all parts of the Chukchi uniformly flushed (e.g. Weingartner et al., 2005b; Woodgate et al., 2005c; Lin et al., 2019). The fate of Pacific-origin heat and fresh water is important to the Arctic Ocean's thermohaline structure (Aagaard et al., 1981; Shimada et al., 2005; Woodgate et al., 2012; Timmermans et al., 2014, 2018); the thickness of sea ice (Kwok and Untersteiner, 2011) and the timing with which it forms and melts (Steele et al., 2008; Jackson et al., 2012; Woodgate et al., 2010; Serreze et al., 2016); and the Arctic atmospheric heat budget (Serreze et al., 2007). Ice-related processes are critically dependent on the local heat balance so alterations to advective heat fluxes carry the potential for profoundly reorganizing the ecosystem. Given these roles for the Bering Strait throughflow in relation to a changing Arctic, an important goal for this paper is to develop an improved understanding of long-term changes in the Bering and Chukchi Seas' heat and freshwater budgets.

For the present study, we compiled temperature and salinity hydrographic profiles for the Bering and Chukchi shelves from 1922 to 2018, from which we estimate changes in heat content and freshwater content. Atmospheric reanalysis model outputs from the European Centre for Medium-Range Weather Forecast (ECMWF) ERA5 model (Copernicus Climate Change Service (C3S), 2017) provide estimates of surface heat fluxes from 1979 to 2018, and we use oceanographic mooring data from Bering Strait (Woodgate, 2018) from 1990 to 2016 to constrain oceanic advective heat fluxes from the Bering Shelf into the Chukchi Sea. Gridded surface air temperature (SAT) (Lenssen et al., 2019) and sea surface temperature (SST) (Huang et al., 2017) datasets give alternate multi-decadal perspectives of thermal conditions.

2. Data and methods

2.1. Geography

The soundings-based Alaska Region Digital Elevation Model (ARDEM; Danielson et al., 2015) provides seafloor depths on a ~1 km grid across the Bering and Chukchi shelves (Fig. 1). Using the ARDEM grid and ETOPO1 (Eakins and Sharman, 2010) digital elevation model results, we compile geographic statistics (Table 1) that summarize our primary domains of interest and are used to scale area-averaged surface fluxes, heat content, and freshwater anomaly estimates. The ARDEM depth estimates are also used to help validate hydrographic profiles and form full water column estimates of fresh water and heat contents.

2.2. Hydrography

The archive of water column profile data covering the largest number of years (first samples taken in 1922 in the Chukchi Sea and in 1966 in the Bering Sea) and providing the largest number of conductivity-temperature-depth (CTD), bottle and profiling float soundings is the National Centers for Environmental Information (NCEI) World Ocean Database 2018 (WOD18) (Boyer et al., 2018). Additional profiles come from US oceanographic expeditions in recent years for which the hydrographic data are not yet incorporated into WOD18, and archives from non-US institutions. These include data from the US National Oceanographic and Atmospheric Administration (NOAA) Pacific Marine Environmental Laboratory (PMEL) and NOAA Alaska Fisheries Science Center (AFSC) hydrographic databases, the University of Alaska Fairbanks Institute of Marine Science (UAF IMS) hydrographic database, and CTD data compiled by the Synthesis for Arctic Ocean Research (Moore et al., 2018). Additional data come from archives at the Russian Federal Research Institute of Fisheries and Oceanography (TINRO), the Fisheries and Oceans Canada's Institute of Ocean Sciences (IOS) and the Japan Agency for Marine-Earth Science and Technology (JAMSTEC). Temporal and spatial coverage of these data are shown in Fig. 3.

A data reduction scheme was implemented to minimize platform-associated bias and maximize consistency in handling profiles collected by discrete bottle casts, shipboard CTDs, tow-yo CTD systems, and autonomous float and glider profilers. Only profile data from the Chukchi and eastern Bering continental shelves were used, confined to stations located in less than 200 m water depth. Data locations were screened for position and depth errors, and data from stations with

Table 1
Regional depth, area, and volume statistics for the Eastern Bering Sea shelf (i.e. the shelf region shown in Fig. 1) and the Chukchi Sea continental shelf. Shelves are defined here as the region with depths less than 200 m.

	Average Depth (m)	Surface Area (km^2)	Volume (km^3)
Arctic Ocean	1205	15,558,000	18,750,000
Chukchi Shelf	57	553,842	31,478
Bering Shelf	66	915,385	60,423

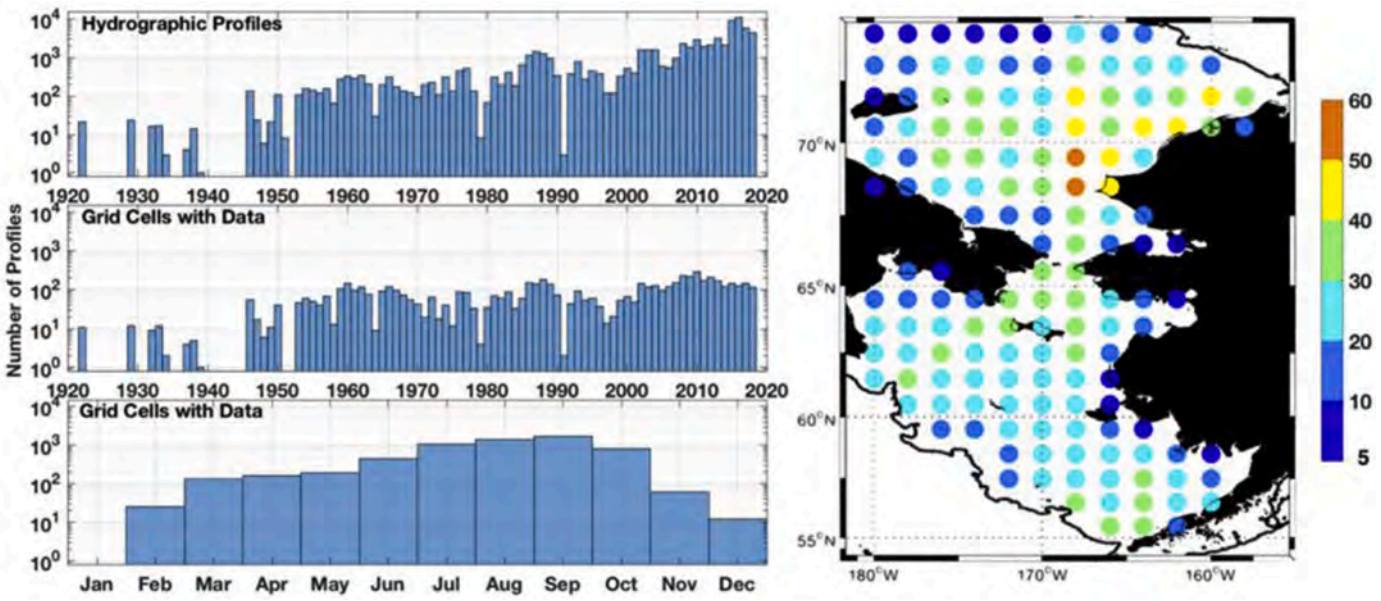

Fig. 3. Temporal and spatial coverage of gridded hydrographic profile data. The map shows the number of years represented within each grid cell. Thick black contours denote the 200 m isobath.

coordinates on land were presumed to have erroneous positions and discarded. Station data having measurements deeper than 140% of the local ARDEM bottom depth were discarded, again signaling a possible location error (errors in the ARDEM grid could also lead to spurious data discards especially in regions of steep bottom slopes). Rejecting partial profiles, we required that measurements extend at least 75% of way to the seafloor from the surface. Casts were also discarded if their shallowest measurements were from deeper than 10 m depth. Temperature data were constrained to a range of −2 to +25 °C and salinities to a range of 0–38. Any station having salinity of less than 20 at 75 m depth or deeper was assumed to be spurious and was discarded. We computed the freezing point for all data and removed casts showing data that were supercooled by more than 0.1 °C (suggesting problems with sensor calibration). Data profiles that included vertical density gradient inversions greater than 0.5 kg m^{-4} were also discarded. Following this initial screening and identification of usable profiles, we then linearly interpolated all profiles to 1 m depth intervals, extrapolated data from the deepest measurement depth to the shallower of the seafloor or 200 m, and extrapolated data from the shallowest measurement depth to the surface. Throughout, we employ the Practical Salinity Scale, using the dimensionless practical salinity units (PSU) for reporting all salinities.

The resulting data screened as described above were then gridded monthly from 1922 to 2018 on a 1° latitude by 2° longitude grid spanning 55 °N to 74 °N and 179 °E to 152 °W. Grid cells on the shelf containing fewer than 5 years of data were excluded from the climatology and analysis. In total, we reduced 69,224 hydrographic profiles into 6235 gridded profiles for an average of about 11 data points per resolved grid cell. Approximately 1600, 4500, and 27,000 of the profiles were taken from profiling floats, discrete bottles, and gliders, respectively.

At each grid cell, we evaluated the mean monthly temperature, heat content, salinity and density for the near-surface (0–10 m) layer, and for the near-bottom layer (within 10 m of the shallower of the bottom or 200 m depth). Following Woodgate et al. (2006) and others, we selected −1.9 °C (approximately the freezing point of Pacific Arctic waters) as a reference for heat content computations. Stratification was assessed by differencing water density between the near-bottom and near-surface levels. Recognizing a strong bias toward open water (summer) data collections, we generated monthly and seasonal climatological averages with winter, spring, summer and fall means created by combining data from January to March, April to June, July to September and October to December, respectively.

2.3. Moorings

Mooring data from the Bering Strait climate monitoring mooring A3 (Woodgate, 2018) have been shown to give a useful measure of the mean water properties of the flow through the Bering Strait. This site (66.7 °N, 171.5 °W) is located ~100 km north of the Diomede Islands. The instruments record hourly temperature, salinity and velocity approximately 15 m above the bottom. From these data, estimates of volume, heat flux and freshwater flux are calculated (Woodgate, 2018). As sensors are located near the seafloor, alone these measurements underestimate heat and freshwater fluxes. Thus, simple corrections are made based either on sea surface temperature data or climatological estimates of stratification to include the effects of the seasonally present warmer surface layer and the Alaskan Coastal Current (Woodgate, 2018). The Bering Strait mooring period of record begins in 1990, missing many known cooler years during the 1970s (e.g. Overland et al., 2012). Mooring data from more recent extremely warm years from mid-2016 through 2018 are not available yet. For this reason, our initial heat budget estimates using the Bering Strait mooring data provide lower bound estimates of changes to the shelf heat budgets.

2.4. Gridded surface temperatures

For another perspective on temperature changes through time, we use the reconstructed sea surface temperature (ERSST) (Huang et al., 2017) version 5 and the NASA Surface Temperature Analysis (GISTEMP) version 4 (Lenssen et al., 2019) datasets. These compilations also provide an opportunity to examine changes over the Bering and Chukchi shelves relative to changes over larger spatial domains. The ERSST is a coarsely gridded (2° × 2°) global monthly mean SST dataset that combines historical and recent ocean surface temperature records. GISTEMP is a globally and monthly gridded dataset that provides estimates of land and ocean surface temperatures (using ERSST v5 over the ocean) based on other compilations of historical and recent weather and ocean platform data. Both datasets extend to the mid-1800s; we restrict our examinations to 1900–2018. Missing data in each compilation are replaced using statistical methods; in high latitudes records of sea-ice cover help

constrain SST estimates (Huang et al., 2017). Many early ERSST observations are based on ships logs. In the Bering and Chukchi seas, sea ice and temperature observations were commonly made from 19th and early 20th century whaling ships and patrol vessels such as those of the U.S. Revenue Cutter Service (Freeman et al., 2017).

We average the ERSST and GISTEMP data over four integration domains: the whole globe, the Arctic (latitudes $\geq$ 66 °N), the Chukchi Sea (66 °N $\leq$ latitudes $\leq$ 74 °N, 180 $\leq$ longitudes $\leq$ 156 °W), and the eastern Bering Sea (55 °N $\leq$ latitudes $\leq$ 66 °N, 180 $\leq$ longitude $\leq$ 160 °W). Selecting a reference baseline common to the profile data coverage on both shelves, we compute annual anomalies relative to the half-century covering 1966–2016.

2.5. Surface heat fluxes

We use the ECMWF ERA5 (Copernicus Climate Change Service (C3S), 2017) dataset to assess surface heat fluxes and provide supporting wind, ice cover, and air temperature data. ERA5 is a recent version release and due to higher spatial resolution, a better data assimilation scheme, and other improvements (Haiden et al., 2017), we anticipate accuracy and precision improvements relative to the prior version, ERA-Interim (Dee et al., 2011). We are unaware of an Arctic-focused assessment of ERA5 performance but evaluation of seven reanalysis products in the Arctic found that ERA-Interim was one of the three best performing reanalyses, with this product consistently scoring well for surface precipitation, shortwave and longwave fluxes, bias of air temperature at 2 m above the surface, and both temperature and wind speed correlations (Lindsay et al., 2014). Seasonally, bias in individual heat flux terms can be as large as 20–40 W m^{-2} but in aggregate the net heat flux bias was found to be < 2 W m^{-2} relative to the Lindsay et al. (2014) analyzed models' median. Many of the heat flux analyses in our study are based on differencing seasonal means that are aggregated across multiple years. For such analyses, the differencing procedure removes much of the stationary bias and we think that the resulting anomalies primarily reflect alterations in the heat exchange balance rather than nonstationary bias.

The net surface heat flux (Q_N) is computed as $Q_N = Q_{SW} + Q_{LW} + Q_{LH} + Q_{SH}$. Terms include the net shortwave (Q_{SW}), net longwave (Q_{LW}), latent (Q_{LH}) and sensible (Q_{SH}) fluxes. Because our main focus is the ocean, we assign a sign convention such that positive heat fluxes represent oceanic heat gain and negative fluxes denote oceanic heat loss.

2.6. Computation of anomalies and trends

Our results are not very sensitive to the differing climatological base periods amongst the various datasets because alternate options for multi-decade baselines of the hydrography appear more similar to each other than to the mean conditions observed over the 2014–2018 period. An advantage of including extra decades (prior to the start of the ERA5 integration or the Bering Strait mooring record) within the hydrographic baseline is that it facilitates building a more robust hydrographic climatology to help ameliorate sparse data limitations.

We compute time series anomalies relative to long-term means to facilitate unbiased assessments of change across space or time where different data subsets have differing means or variances. At each grid cell these include monthly anomalies $X' = X - \overline{X_j}\Big|_{j=1}^{j=12}$ where the long term (climatological) monthly mean $\overline{X_j}$ for each month ($j \in [1 \ldots 12]$) is subtracted from the monthly mean parameter X to create monthly anomaly X' time series with mean zero. The monthly standard anomaly computation $X_j'' = (X - \overline{X_j})/\sigma_j\Big|_{j=1}^{j=12}$ normalizes each monthly anomaly by its corresponding monthly standard deviation σ, creating a time series with zero mean and unity variance. Anomalies retain units of parameter X and standard anomalies are non-dimensional.

Temporal trend analyses are based on linear regression of anomalies and standard anomalies versus year of observation, with error estimates representing the 95% confidence interval. Statistical significance of trends that are statistically distinguishable from zero is ascribed for p-values < 0.05.

3. Results

Below, we describe the mean thermohaline structure over the two shelves and quantify changes in heat and freshwater contents over seasons and interannually. This is followed by assessment of surface heat fluxes, and finally heat budgets for the two shelves. To assess changes since the onset of the recent North Pacific marine heat wave (Bond et al., 2015), the half-decade of 2014–2018 is compared to the period of record prior to 2014.

3.1. Hydrography: climatology

We begin with temperature and salinity data, constructing a coarsely gridded seasonal climatology of the vertical profiles (Figs. S1 and S2) using water mass definitions (Table 2) that apply to both shelves and all four seasons (Fig. 4). The gridding and averaging operations smooth out spatial and temporal extremes and numerous small-scale features but nevertheless capture much of the basic hydrographic structure and its seasonal evolution, depicted with maps of water mass distributions (Fig. 5). Examinations of water masses on the Bering and Chukchi shelves typically take one of two approaches to classification. Either they follow the standard nomenclature provided by Coachman et al. (1975) describing Anadyr Water (AnW), Bering Sea Water (BSW) and Alaskan Coastal Water (ACW), or they develop an alternate classification, often necessitated by the large swing in salinities from one year to the next, that is more closely tuned to a particular dataset compilation or thermal/haline processes under consideration (e.g. Pisareva et al., 2015; Gong and Pickart, 2016; Danielson et al., 2017; Lin et al., 2019; Pickart et al., 2019). In this manuscript we develop a minimal set of classifications that can be applied across both shelves and in all seasons (but again the classification resolution lacks ability to distinguish many water mass sub-classes). We deviate from the Coachman et al. (1975) water mass designations because for the large shelf regions under consideration and our multi-season perspective the classifications BSW and ACW do not describe all water mass residence locations or natal formation regions. For example, fresh waters of the riverine coastal domain may well be termed ACW along the Alaskan coast but not in the Gulf of Anadyr. We distinguish between warm Coastal Water (wCW) and cool Coastal Water (cCW) because properties in the coastal domain vary greatly over the course of the year and alternately reflect the impact of runoff, heating, cooling, melting and freezing processes. Similarly, our warm Shelf Water

Table 2
Water mass definitions (see also Fig. 4 and the color scheme in Fig. 5).

Water Mass	Abbreviations	Temperature Range	Salinity Range
Anadyr Water	AnW	$0 < T < 3$	$32.5 < S < 33.8$
Ice Melt Water & cool Coastal Water	IMW cCW	$-2 < T < 3$	$22 < S < 30.8$
cool Shelf Water	cSW	$0 < T < 3$	$30.8 < S < 32.5$
warm Coastal Water	wCW	$3 < T < 14$	$18 < S < 30.8$
warm Shelf Water	wSW	$3 < T < 14$	$30.8 < S < 33.4$
Modified Winter Water	MWW	$-1 < T < 0$	$30.8 < S < 33.8$
Winter Water	WW	$-2 < T < -1$	$30.8 < S < 35$
Atlantic Water & Bering Basin Water	AtlW & BBW	$-1 < T < 3$ $3 < T < 5$	$34 < S < 35$ $33.8 < S < 35$

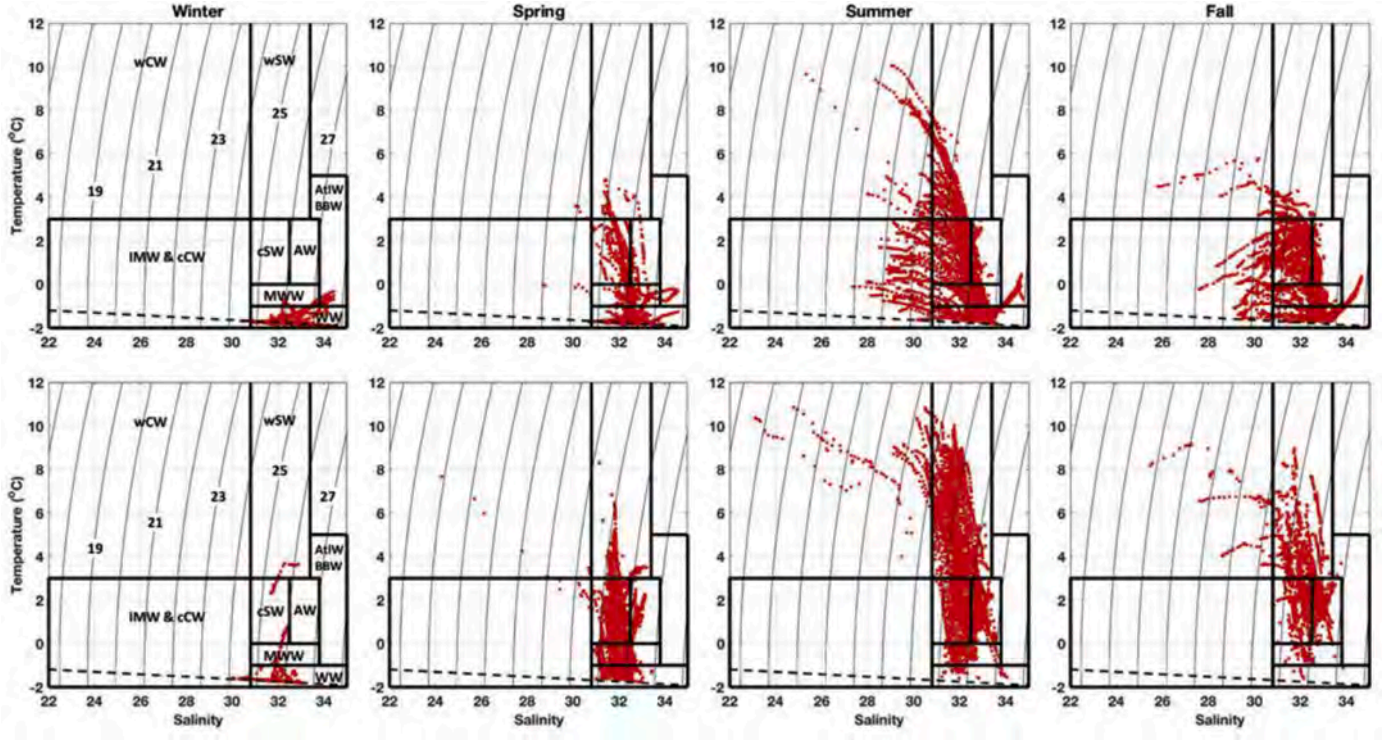

Fig. 4. Seasonal climatology T-S distributions for the Chukchi Shelf (top) and the Bering Shelf (bottom). Water masses shown in Fig. 5 are outlined by black lines and definitions are given in Table 2. The freezing point curve is marked with a dashed line. Sigma-t contours are labeled in the lower left panel. Abbreviations include wCW = warm Coastal Water; wSW = warm Shelf Water; IMW = Ice Melt Water; cCW = cool Coastal Water; cSW = cool Shelf Water; AnW = Anadyr Water; WW = Winter Water; AtlW = Atlantic Water; BBW = Bering Basin Water.

(wSW) and cool Shelf Water (cSW) designations encompass the BSW category of Coachman et al. (1975).

Winter months are the most sparsely sampled and many grid cells lack any profiles at all. For those cells containing data, most show Winter Water (WW) characteristics with temperatures close to the freezing point ($T < -1$ °C), although modestly elevated temperatures (-1.0 °C $< T < 1.0$ °C) are found at depth along the outer Bering Shelf and near the Chukchi Slope, including some waters at the edge of the Arctic basin below 150 m depth that exhibit contributions of Atlantic Water (AtlW). The southernmost few grid points in the Bering Sea have the warmest waters in winter ($T > 2.0$ °C), suggesting heat entering the Bering Shelf via advection up Bering Canyon from the North Aleutian Slope Current (Stabeno et al., 2009) or coming through Unimak Pass (Stabeno et al., 2002, 2017). Relatively high salinities (>32.5) are observed in or near to known dense water formation regions, including over much of the southern Chukchi Sea and near the St. Lawrence Island polynya (Danielson et al., 2006). In winter, riverine influence (CCW) is detected in Norton Sound and along the Chukchi Siberian coastline (Fig. 5). We note that cold and fresh coastal runoff is not readily distinguishable from Ice Melt Water (IMW) or the cold fresh water of the SCC in summer (Weingartner et al., 1999) using only temperature and salinity tracers but isotopic tracers can separate them readily (e.g. Cooper et al., 2005).

Spring data show that cSW is prevalent in the upper portion of the water column on both shelves due to the combined effects of seasonal warming and freshening from ice melt. IMW is found at some stations near coasts, but low salinity ice-melt plumes (e.g. $S < 28$) are not generally observed across the middle of either shelf in spring. The latter point suggests that ice melt ($S \sim 7$) quickly mixes and is diluted by mixing with ambient shelf waters, or possibly that interannual variability in the ice extent combined with the climatology averaging obscures the ice melt signal. We detect little IMW in the Bering Sea in the climatology, but it is a dominant surface water mass across the northern and northwestern Chukchi Sea in summer and fall. The Bering Shelf upper water column at this time of year mostly contains wSW except for low-salinity wCW of the riverine coastal domains, especially within the large river-fed embayments: the Gulf of Anadyr, Bristol Bay, Norton Sound and Kotzebue Sound. Possibly shunted offshore by winds or bathymetry, wCW is also found offshore south of St. Lawrence Island and relatively far offshore in the northeast Chukchi Sea.

Low temperature waters (<2 °C) of the Bering Sea cold pool extend from the northwest portion of the eastern Bering Shelf along the mid-shelf region (e.g. along the 70-m isobath), past the Pribilof Islands, and into the southern reaches of the southeast Bering Sea in years with extensive ice cover (Takenouti and Ohtani, 1974). The cold pool region contains near-bottom waters classified as WW or cSW through all seasons. These temperature-salinity characteristics also occupy the lower portion of the water column across much of the northern and northeastern Chukchi Shelf in summer.

Following the main pathway of nutrient-rich currents feeding the highly productive portions of the Pacific Arctic, saline ($S > 32.5$) AnW can be traced from the upper Bering slope counter-clockwise around the Gulf of Anadyr, into Chirikov Basin and through Bering Strait (orange color in Fig. 5). AnW can be found close to the seafloor at many stations in the western Chukchi Sea in summer and fall months, showing that at least some of the high-nutrient AnW entering the Pacific Arctic is not strongly mixed with the lower-salinity shelf and coastal waters in the energetic Anadyr Strait, Chirikov Basin, and Bering Strait mixing zones. However, the high level of nutrients characteristic of AnW entering Bering Strait may not be retained as the AnW crosses the Chukchi Shelf because nutrient draw-down can occur from the surface to the seafloor on this shallow shelf. It should be noted that south of the Gulf of Anadyr the orange color indicates basin/slope dichothermal water (Miura et al., 2002) having temperature and salinity characteristics close to AnW. In the future, AnW should be separated from the dichothermal water by nutrient parameters. The AnW flow pathway has been modeled in many studies (Kinder et al., 1986; Overland and Roach, 1987; Clement et al.,

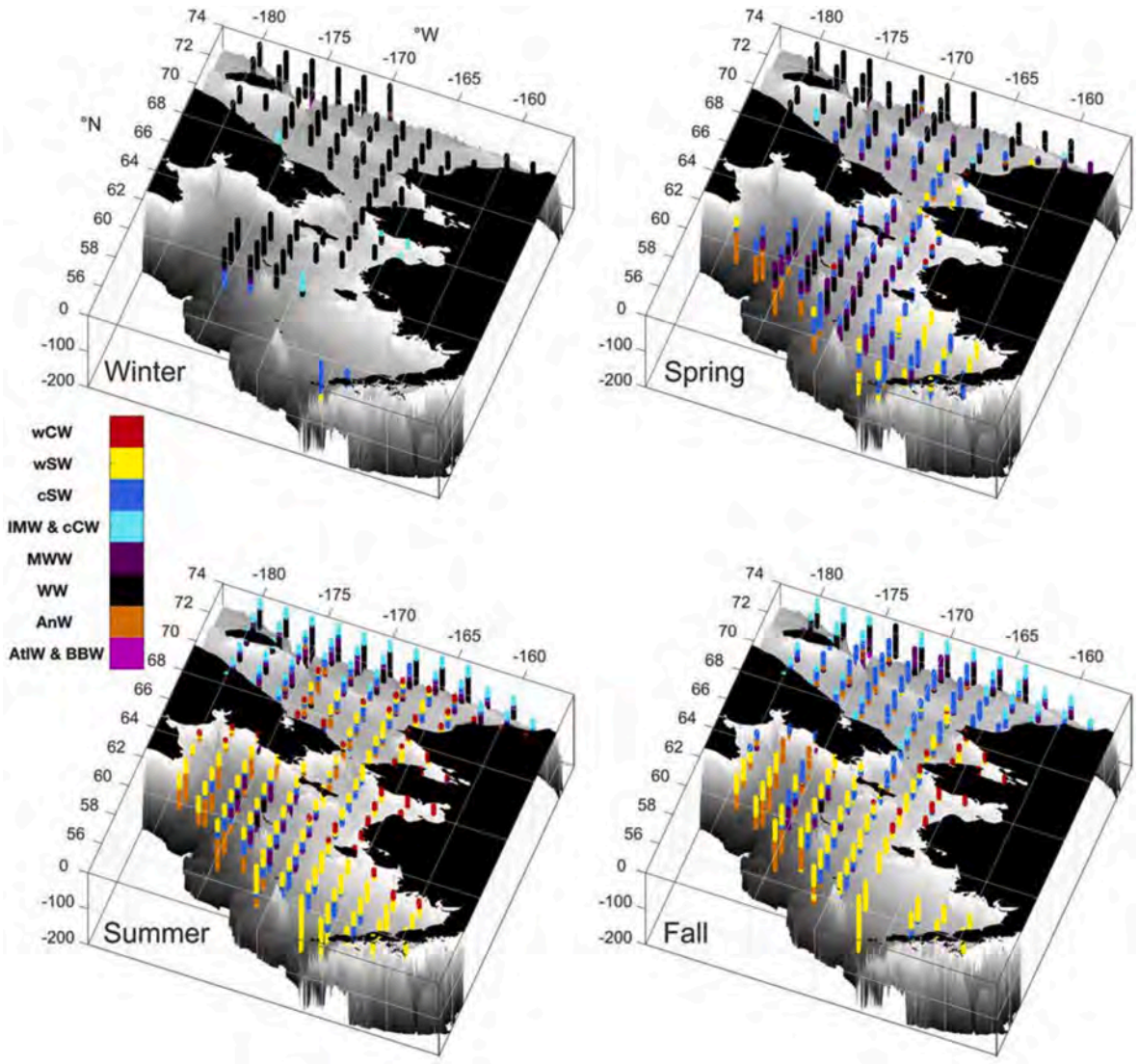

Fig. 5. Perspective view of the water seasonal climatology water mass distribution on the Bering and Chukchi shelves for winter (upper left), spring (upper right), summer (lower left) and fall (lower right) using data from before 2014. The AtlW water mass is mostly hidden behind the seafloor of the northward-facing Chukchi slope due to the perspective view. Seafloor topography (gray shading) is shown only for depths shallower than 200 m. Latitude and longitude markings are associated with the −200 depth level. Abbreviations include wCW = warm Coastal Water; wSW = warm Shelf Water; IMW = Ice Melt Water; cCW = cool Coastal Water; cSW = cool Shelf Water; AnW = Anadyr Water; WW = Winter Water; AtlW = Atlantic Water; BBW = Bering Basin Water. Note that water mass colors do not correspond to the colors of the flow field shown in Fig. 1. (For interpretation of the references to color in this figure legend, the reader is referred to the Web version of this article.)

2005; Danielson et al., 2012b, 2014) but direct observations of the Anadyr Current are few (Coachman and Shigaev, 1992; Overland et al., 1996). Our climatology supports prior diagnoses of this pathway location because the near-bottom waters flowing through Bering Strait have relatively high summer salinities (S ~ 32.5) (Woodgate, 2018), while cold pool waters and waters farther east are for the most part considerably fresher (S < 32) (Fig. S2). Hence, the fresher waters of the cold pool cannot be the source for the high-salinity component of the flow field entering Bering Strait. Although moorings (Danielson et al., 2006) and shipboard data (Grebmeier and Cooper, 1995) show the presence of a mean west-to-east current on the south side of St Lawrence Island, AnW does not appear in the climatology here, suggesting that eastward advection of AnW in the St. Lawrence Current is diluted by westward-flowing low salinity surface waters from the Alaskan coastal domain (Danielson et al., 2006, 2012a).

The seasonal evolution of the water masses on these shelves (Figs. 4 and 5) reveals a few fundamental differences between the Bering and Chukchi shelves and their adjoining slope regions. In the summer and fall, Bering Shelf WW exists in the climatology only as remnants in the northern portion of the cold pool but can be found in significant quantities year-round in the northern Chukchi Sea. IMW is prevalent in the Chukchi Sea but nearly absent from the Bering Shelf year-round. High salinity (>34) basin waters exist at shallower depths along the upper Chukchi Slope than along the Bering Sea Slope (not shown). Our examination of the seasonal climatology provides an assessment of typical water mass characteristics and locations through the year but any individual year may look considerably different (Coachman et al., 1975). To better understand temporal variations, we turn to anomalies relative to this climatology.

3.2. *Hydrography: anomalies and trends*

Using our long-term climatology as a reference and motivated by our interest in placing recent conditions into the context of the prior record, we examine spatial and temporal variations of the water column hydrography. Warming is evident throughout the water column of most grid cells in the 2014–2018 average summer conditions (Fig. 6, left panel). There is less extensive sampling coverage in spring and fall, but a

similar warming is also found at most grid cells sampled in these seasons (not shown). Even in the presence of top-to-bottom warming (Fig. 6), a few locations depict a mid-depth cool anomaly, reflective of a thermocline shoaled relative to the climatology. We also observe enhanced warming in the upper water column. Strong wind-induced mixing generally resets shelf stratification with water column homogenization to a depth of at 70–100 m in winter (e.g. Kinder and Schumacher, 1981; Stabeno et al., 1998), although data from recent years suggest that the maximum depth of winter mixing may be declining (Stabeno and Bell, 2019). Lower water column properties are set annually prior to the spring onset of ice melt and surface heating that forms the characteristic two-layer Bering Shelf hydrographic structure, in which the lower water column is relatively isolated from direct atmospheric exchange (Coachman, 1986). Together, these observations suggest that the deeper warm anomalies are in place before summer stratification sets in and that heat gains through the surface during spring and summer months subsequently reinforce the surface warm anomaly.

The distribution of salinity anomalies is more complex than for temperature but they exhibit organized spatial structure (Fig. 6, right panel). We find a slight freshening (negative salinity anomaly) in the southernmost portion of the Bering Sea. A positive salinity anomaly extends from inner Bristol Bay to the outer slope in the band of latitudes from 57 to 59 °N and then continues to the northwest along the continental slope. Freshening exists from ~60 °N northward through Bering Strait and across much of the nearshore Alaskan Chukchi Sea. In contrast, farther offshore in the northeast, central, and southwest portions of the shelf, near-surface salinities are considerably higher than in the climatology. Despite somewhat sparse data in any given year, examination of monthly anomalies suggests that the seasonal mean depictions of Fig. 6 are not artifacts of the gridding or uneven sampling efforts.

Seasonally aggregated monthly standard anomalies (Fig. 7) and annually averaged monthly anomalies (Fig. 8) of temperature and salinity integrated through the water column and across each shelf reveal that the two shelves do not change in tight temporal synchrony, despite being advectively linked via Bering Strait. Each shelf forms its own set of thermohaline balances consistent with its local thermohaline inputs, sinks, and property modifications.

The Bering Shelf exhibits a record-length (1966–2018) summer freshening of -0.13 ± 0.13 (Fig. 7), which contrasts with a 1990–2018 0.08 ± 0.07 decade^{-1} salinization of the Bering Shelf (Fig. 8), a 1991–2015 increase of freshwater transport through Bering Strait (260 ± 170 km^3 decade^{-1}) (Woodgate, 2018) and a 1991–2015 decline in the Bering Strait salinity of -0.14 ± 0.10 decade^{-1} (Woodgate, 2018).

The Bering Shelf thermal anomaly is dominated by approximately decadal-scale variability of alternating warm and cold intervals (Stabeno et al., 2012). Many of the warm/cold transitions align with qualitatively similar decadal scale alternating warm and cold atmospheric conditions in the Bering Sea (Overland et al., 2012) but a full understanding of the causes of transition between the two phases is lacking. We note that from the 1990s to the present the amplitude of each successive warm interval peak has increased (Fig. 8) and that the 2014–2018 warm interval duration of five years has matched the previous warm phase duration maximum. Continued warm conditions in 2019 suggest that the warm phase will extend at least into a sixth consecutive year for the first time since the beginning of the Bering Sea hydrographic profile record.

Both shelves show indications of warming over their record length but the linear trend is only significant in the Chukchi Sea, where we compute a 1922–2018 summer season increasing temperature trend of 0.14 ± 0.07 °C decade^{-1}. This rate increased to 0.43 ± 0.35 °C decade^{-1} starting in 1990, the first year of the Bering Strait mooring deployment. Over 1991–2015 the Bering Strait mooring shows a temperature increase of 0.27 ± 0.23 °C decade^{-1} (Woodgate, 2018). During 2014–2018, each shelf shows anomalies that lie 1–2 standard deviations higher than the mean, corresponding to shelf-wide monthly average temperature anomalies of up to 3 °C. Relative to the climatology for the Chukchi, we find 2014–2018 mean monthly anomalies for spring, summer and fall of 3.2, 0.5 and 0.7 °C. In the Bering, corresponding anomalies for these three seasons are 1.3, 1.1 and 1.2 °C. The mean annual temperature anomaly over 2014–2018 for the two shelves combined is 1.2 °C. The highest observed 5-year average spring anomalies in the Bering Sea occurred in 2014–2018. On an annually aggregated basis, seven of the warmest ten Chukchi Shelf years have occurred

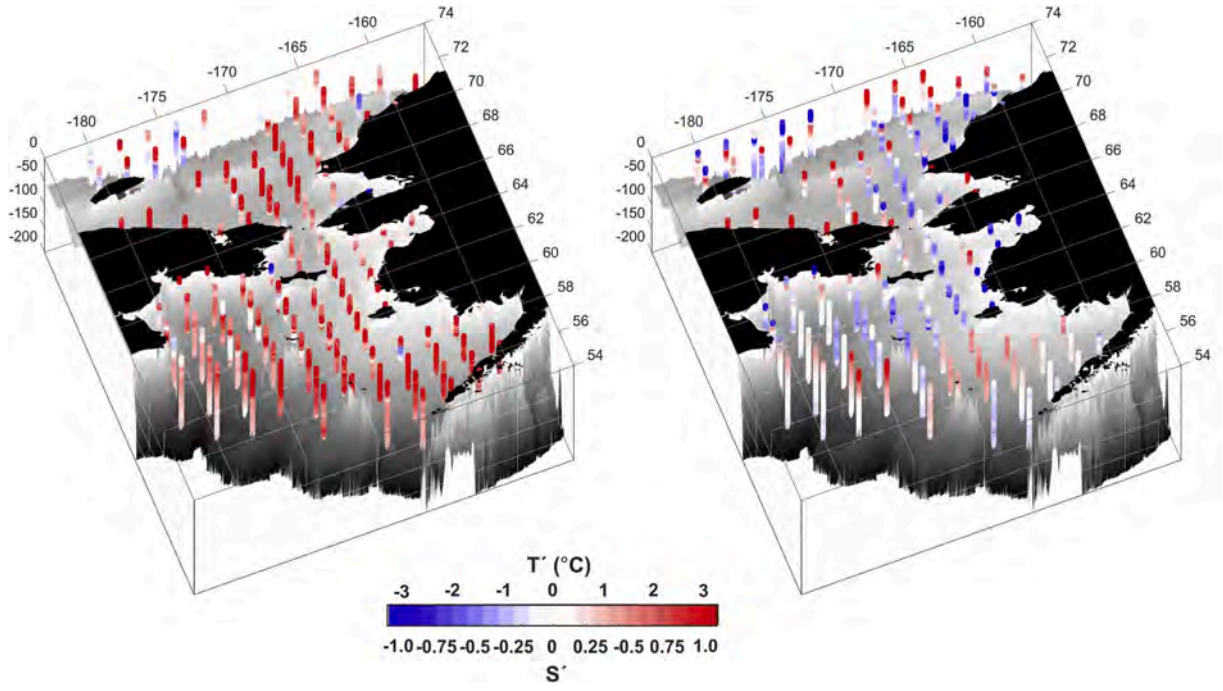

Fig. 6. Perspective view showing profiles of summer season temperature anomalies (T'; left) and salinity anomalies (S′, right) for 2014–2018 relative to data collected prior to 2014. Seafloor topography (gray shading) is shown only for depths shallower than 200 m.

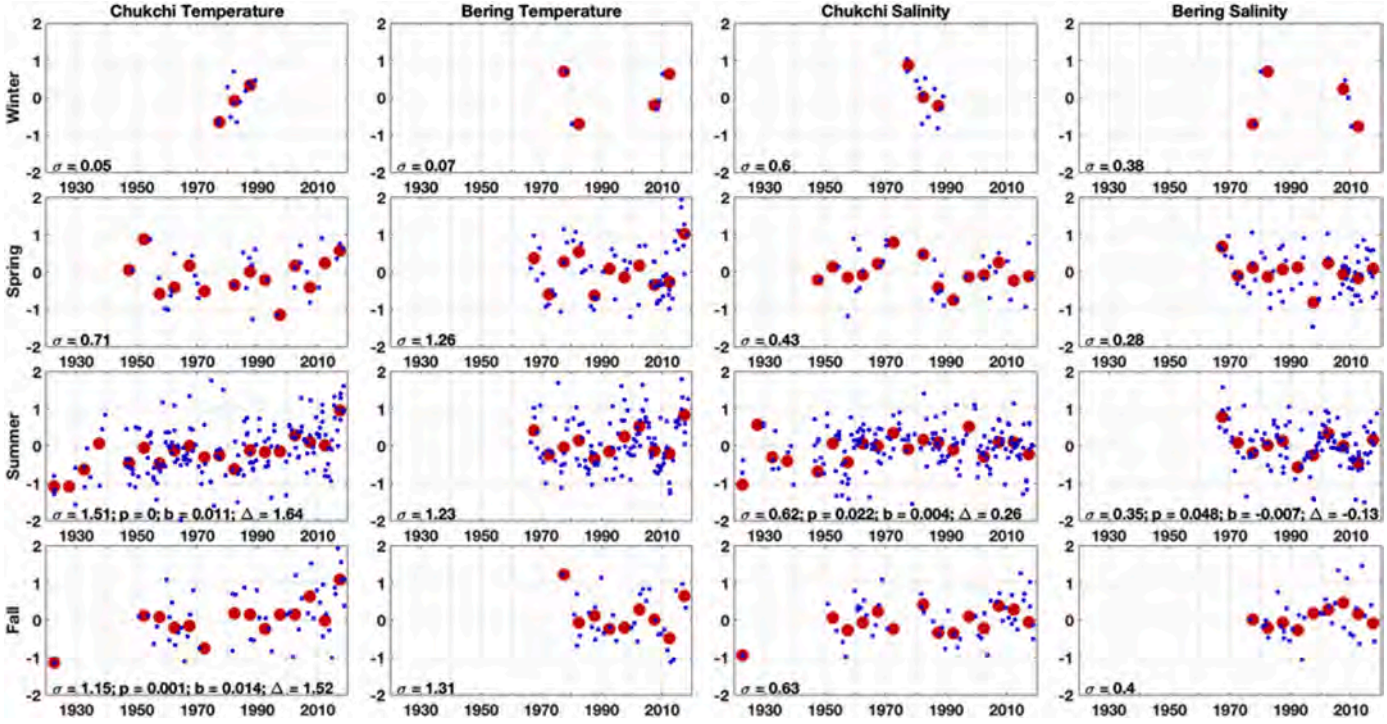

Fig. 7. Seasonally-aggregated monthly normalized temperature and salinity anomaly time series of the vertically integrated gridded profile data for the Chukchi and Bering shelves. From top to bottom, rows show seasonal aggregations for winter, spring, summer and fall, respectively. Large red dots depict 5-year averages. The standard deviation (σ) for each parameter and season is given in the lower-left corner of each panel. For records longer than 20 years that exhibit significant long-term linear trends at the 95% confidence level, the regression p-value, slope (b) and record-length change (Δ) are given. (For interpretation of the references to color in this figure legend, the reader is referred to the Web version of this article.)

since 2007 (Fig. 8), which at the time was a record-low sea-ice extent year for the Arctic as a whole (Lindsay et al., 2009). In contrast, the ten coldest anomalies are fairly evenly distributed between 1922 and 1999. We note that especially for the Chukchi Shelf, sampling is generally biased to open water areas.

There exist many more records of SST and SAT than water column profiles, so for additional context we compare our gridded temperature profile data to the gridded ERSST (Huang et al., 2017) and GISTEMP (Lenssen et al., 2019) datasets, averaging over the eastern Bering Sea, the Chukchi Shelf, the Arctic, and the globe (Fig. 8 and Supplementary Table S1). Linear trend analysis shows that all four of the integration regions and time frames have significantly increasing SST and SAT trends over each of the selected integration intervals. Over 1900–2018, the SST trend for the Bering, Chukchi, Arctic and globe are 0.10 ± 0.0, 0.08 ± 0.02, 0.05 ± 0.01, and 0.07 ± 0.01 °C decade^{-1}, respectively. Over 1990–2018, these four regions exhibit SAT trends of 0.34 ± 0.28, 0.35 ± 0.14, 0.27 ± 0.05, and 0.13 ± 0.03 °C decade^{-1}, showing that in recent decades the Pacific Arctic is warming both in the atmosphere and the ocean more quickly than the globe as a whole.

Water column thermal anomalies are correlated ($p < 0.05$) with SST variations for both shelves, with correlation coefficients of $r = 0.52$ and 0.63, respectively, for the Chukchi and Bering shelves (Fig. 8). A trend from 1922 to 2018 of an increase of 0.14 ± 0.07 °C decade^{-1} for the summer/fall water column average temperature for the Chukchi Sea (Fig. 8) is consistent with the 0.11 ± 0.02 °C decade^{-1} ERSST trend over the same period. By comparison, the Bering Sea SST trend is 0.13 ± 0.04 °C decade^{-1} over 1922–2018, lending support to the notion that the Bering Sea heat content is likely increasing significantly but that decadal scale variability obscures the long-term trend.

Anomalies of data restricted to only July through October (Fig. 9) bear close resemblance to the annually averaged anomalies shown in Fig. 8. For the three extremely warm recent years of 2015, 2017 and 2018, the mean July through October temperature anomaly of 1.80 ± 0.19 °C stands 2.26 °C higher than the average anomaly, −0.46 ± 0.24 °C, for these months in all sampled years prior to 2000. These three years are 2.86 °C higher than the average anomaly of the cold 1970s decade (−1.06 ± 0.72 °C).

To summarize, trend analyses show warming of the Chukchi Shelf over the last 96 years (Figs. 7–9), and the rate of warming has increased in recent decades. This contrasts with the decadal scale variability characteristic of the Bering Shelf, which mostly masks a likely long-term warming trend in water column average temperature over 1966–2018, although the 1922–2018 Bering Sea SST record does depict a warming trend. The Pacific Arctic is warming faster than the globe as a whole and the half-decade of 2014–2018 brought previously unobserved high temperatures to both shelves that were associated with a significantly altered sea ice regime and with this, alterations to salinity distributions (Fig. 6).

3.3. Surface heat fluxes

The shelf temperature anomalies described in Sections 3.1 and 3.2 motivate us to better understand the role of atmospheric heat fluxes in setting the temperature, salinity and sea ice anomalies described above.

The Bering and Chukchi both function as high-latitude oceanic radiators, but surface heat exchanges are not spatially or temporally uniform. For the region shown in Fig. 10a, four oceanographically distinct zones of heat loss emerge in the annual averages: the central Chukchi Shelf, the Gulf of Anadyr, the eastern Bering Sea outer shelf and slope, and the Aleutian Basin (the Bering Sea Basin). Both shelves are oceanic sources of heat to the atmosphere for six months of the year and oceanic heat sinks for about four months, gaining heat from the atmosphere in spring and summer and losing heat to the atmosphere in fall and winter. April and September are transitional months, with net cooling at higher latitudes often coincident with net warming at lower latitudes. Hence, we aggregate months into quarterly and semi-annual seasonal averages.

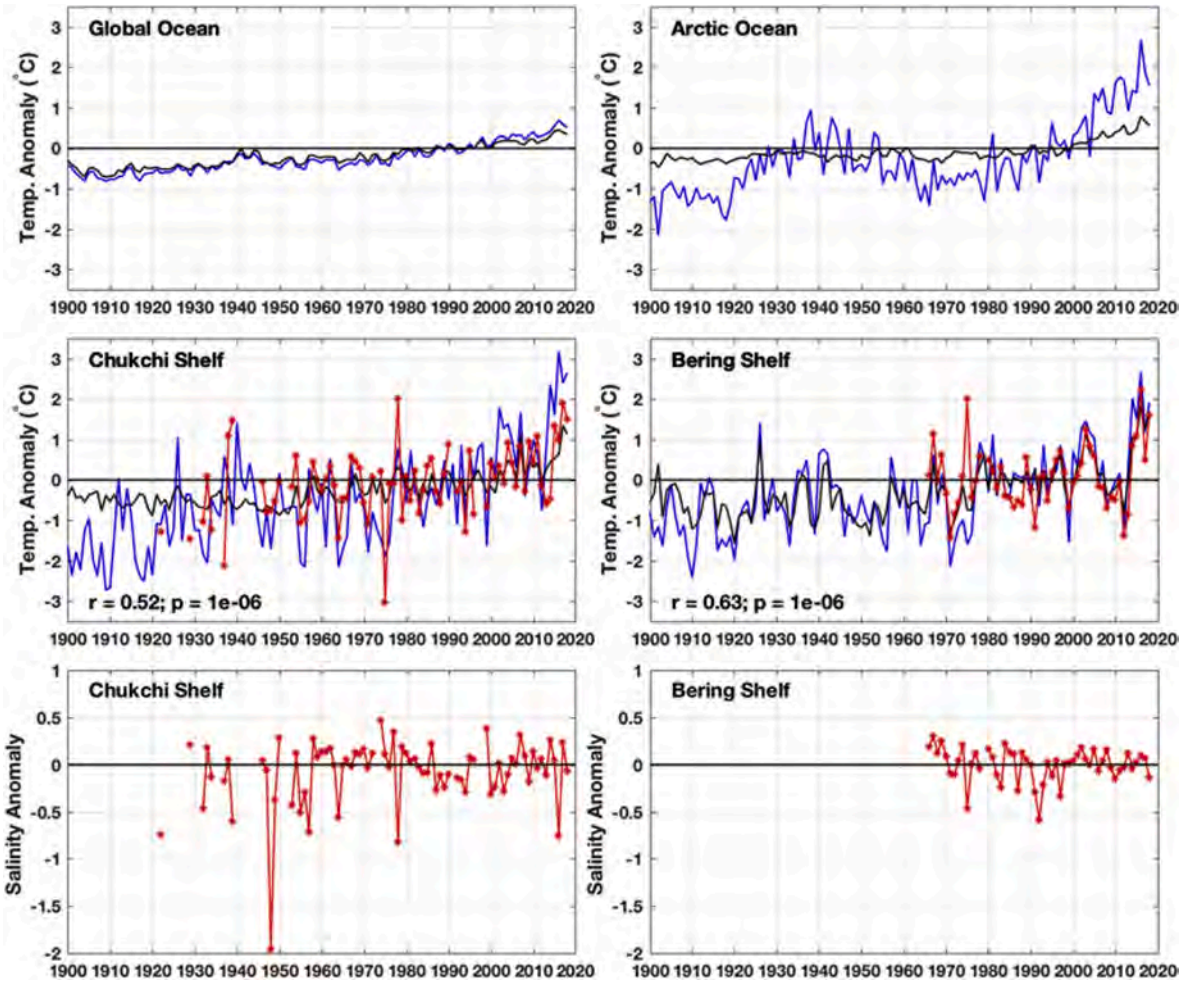

Fig. 8. Annual anomaly time series for the whole globe (upper left), the Arctic (upper right), the Chukchi Shelf (middle and lower left) and Bering Shelf (middle and lower right). Parameters include SAT (blue), SST (black), and water column temperature and salinity (both red). Correlation r and p-value statistics for the relation between the water column temperature and the SST are shown in the two middle panels. All anomalies are plotted with respect to baselines spanning the 1966–2015 half-century. (For interpretation of the references to color in this figure legend, the reader is referred to the Web version of this article.)

Comparing the climatological (1979–2013) surface heat fluxes on a quarterly basis (Table 3), we note strong seasonality in magnitude and sign and note that the Bering and Chukchi shelves have statistically different mean rates of heat exchange with the atmosphere in all seasons. Our primary focus is on the continental shelf regions but the deeper Aleutian Basin is also important to the regional heat balance so we begin there. On a per square meter basis, the Aleutian Basin is the North Pacific sub-region responsible for the greatest oceanic heat loss to the atmosphere during fall and winter months. Factors that contribute to this characteristic include the deep-water column, low winter air temperatures (Rodionov et al., 2005), energetic wind (Moore and Pickart, 2012) and tidal (Foreman et al., 2006) mixing, and the Bering Slope Current's continual advective supply of warm waters from the south (Johnson et al., 2004; Ladd, 2014). While ice is regularly advected over the northern portion of the basin and along the Kamchatka Shelf in winter, these factors keep the Aleutian Basin mostly ice-free. Open water and thin ice allow ocean-atmosphere heat exchange to occur much more readily than from a water column covered with even a few tens of centimeters of ice (Maykut, 1978; Wettlaufer, 1991; Martin et al., 2004), so Aleutian Basin waters effectively transfer available heat to the atmosphere in winter months. Despite lower air temperatures over the Chukchi through winter, the Bering Shelf loses more heat to the atmosphere in winter (-94 W m^{-2}) than the Chukchi (-43 W m^{-2}) because of the Bering's higher heat content at the start of fall and lower average winter ice concentrations and thicknesses. Similarly, the Bering Shelf gains more heat from the atmosphere in spring and summer, a consequence of higher solar angle and because the Bering maintains a lower average surface albedo, so a larger fraction of the incoming shortwave radiation is absorbed.

By differencing the mean surface heat fluxes before and after 2013, we find that the northern Chukchi Shelf in the last half-decade lost appreciably more heat to the atmosphere than in years past, and the Bering Sea lost less heat (Fig. 10b and Table 3). The Chukchi Shelf increased its net cooling by ~25% (from -14 to -18 W m^{-2} on annual average), while the Bering Shelf remained essentially unchanged (-20 to -18 W m^{-2}) and the Aleutian Basin lost nearly 20% of its net cooling (-27 to -22 W m^{-2}). The potential of these changes to alter cyclogenesis, surface moisture transport, and other important meteorological processes is unclear but worthy of further investigation. The Chukchi Shelf and Aleutian Basin mean heat fluxes over 2014–2018 both lie outside of the 95% confidence interval for the mean of the 1979–2013 annual means. The changes over the two shelves do not balance, suggesting that the system is not just redistributing heat gains and losses and that net warming, cooling, and/or oceanic advective contributions must be significant. To the extent that some of the regional ocean-atmosphere heat exchange was effectively redistributed from the sub-Arctic Aleutian Basin into the Arctic Chukchi Sea, this represents a mechanism whose impact in part likely promotes reduced latitudinal gradients in air temperature.

Differences in the seasonal net surface heat fluxes (Fig. 11 and

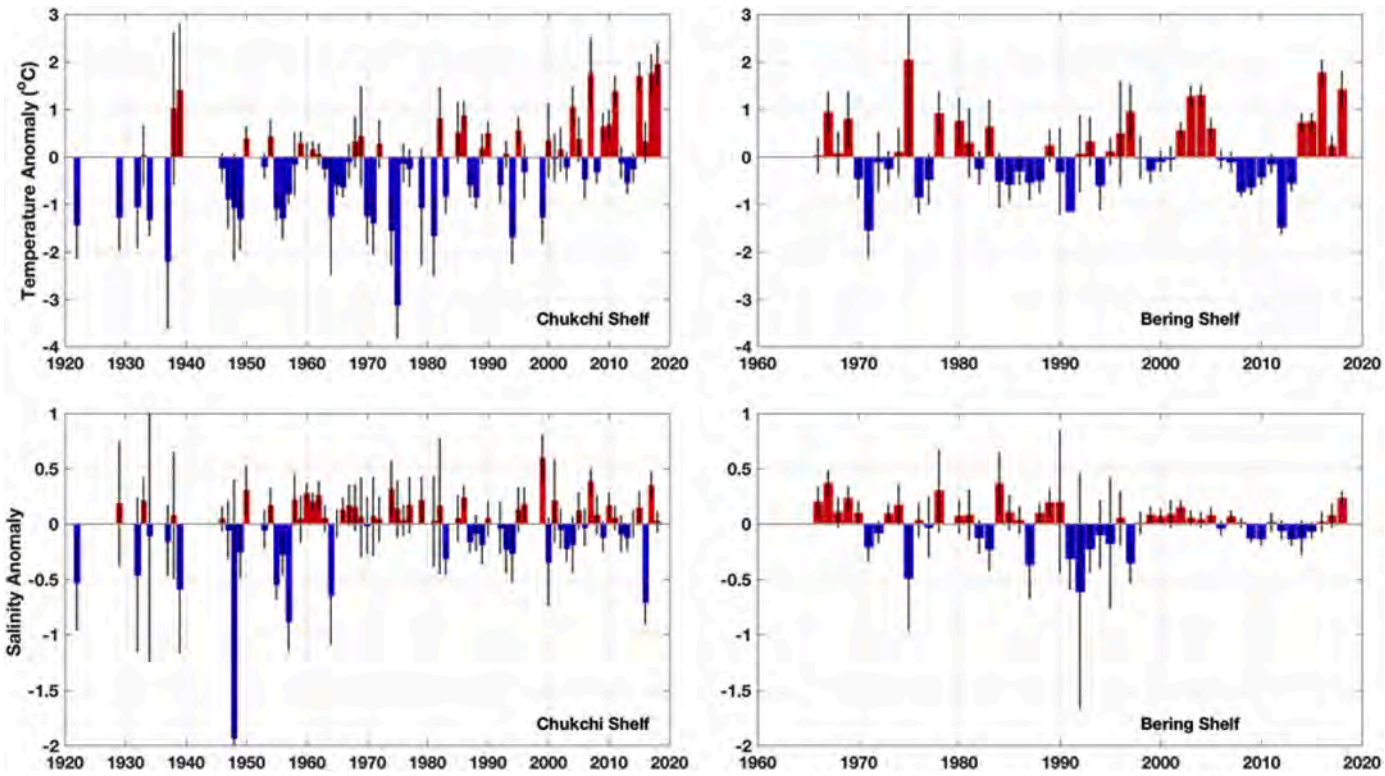

Fig. 9. Annually averaged July through October thermal (top) and haline (bottom) anomalies over the Chukchi (left) and Bering (right) continental shelves. Error bar whiskers depict 95% confidence limits on the mean for each year's anomaly.

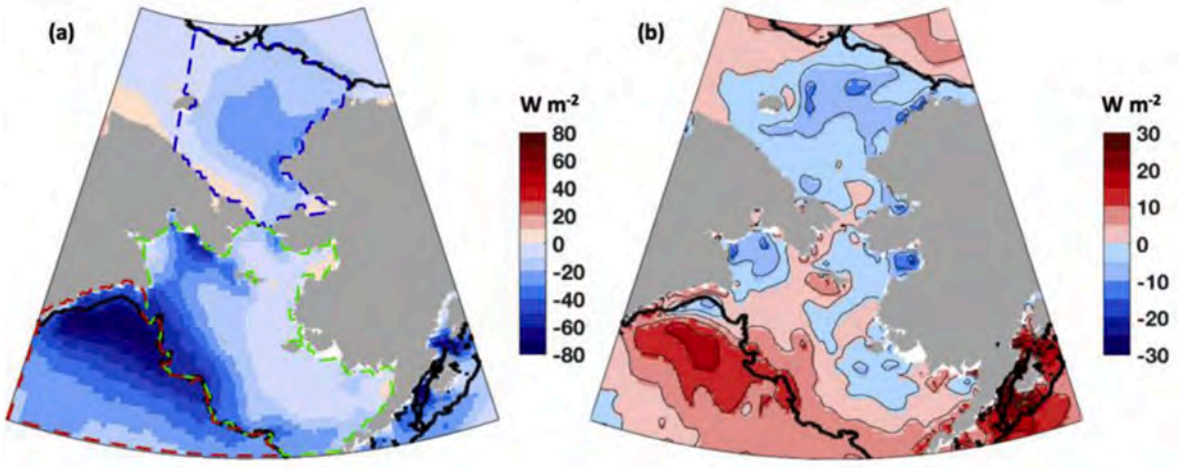

Fig. 10. (a) Mean annual surface heat flux for 1979–2013 and (b) the difference between 2014–2018 and the earlier interval, computed as the latter interval minus the earlier. Note different color bar scaling for the two panels. Edges of the continental shelves (200 m depth) are marked with a black contour. Chukchi Shelf, Bering Shelf, and Aleutian Basin integration zones discussed in the text are marked in panel (a) with blue, green and red dashed lines, respectively. (For interpretation of the references to color in this figure legend, the reader is referred to the Web version of this article.)

Table 3) for 2014–2018 relative to the climatology reveal spatial structures and temporal evolutions not apparent in the annually averaged fields, including large (often > 5 W m^{-2}) and significant changes in the mean seasonal surface heat exchanges. With the exception of summer for the Bering Shelf and Aleutian Basin, all three integration regions had 2014–2018 surface flux means that exceeded the 95% confidence limits of the 35-year climatological mean.

Over 2014–2018 the fall Chukchi heat loss increased by 30% to -129 ± 15 W m^{-2}, a consequence of the delayed onset of ice cover and higher oceanic heat content in the fall. Given typical rates of heat loss for the ice-free ocean in fall (Table 3), a warming of about 1.3 °C for the Bering and Chukchi shelves would require an additional month to cool the water column to the freezing point. Hence, the Chukchi Shelf now requires more time to cool to the freezing point because the shelf begins the cooling season (near the fall equinox) with a higher heat content (Section 3.2). Furthermore, the southern Bering Shelf shows a positive heat flux anomaly in the recent years that manifests in fall and winter. Diagnosis of this signal (not shown here) suggests that it is tied to decreases in the sensible and latent heat fluxes, reflecting reconfigured balances between the air-sea temperature gradient, wind speeds, and the relative humidity.

In winter, the Chukchi Shelf shows modest yet statistically significant

Table 3
Mean ERA5 net surface heat fluxes (W m^{-2}) for seasonal and year-long averaging intervals for 1979–2013 and 2014–2018 over the three integration regions denoted in Fig. 10. Limits denote 95% confidence limit on the mean for the respective interval. Positive values denote oceanic heat gain from the atmosphere; negative values are oceanic heat loss. Bold type shows when the 2014–2018 mean value lies outside of the 95% confidence interval for the 1979–2013 mean. Non-overlapping 95% confidence intervals are shown in italics.

Region	Interval	Winter JFM	Spring AMJ	Summer JAS	Fall OND	Annual Mean
Chukchi Shelf	1979–2013	*−43 ± 1*	31 ± 3	53 ± 2	*−99 ± 5*	−14 ± 1
	2014–2018	***−36 ± 4***	**44 ± 11**	**49 ± 8**	***−129 ± 15***	**−18 ± 4**
Bering Shelf	1979–2013	−94 ± 7	96 ± 3	67 ± 2	−146 ± 5	−19 ± 3
	2014–2018	**−102 ± 15**	**111 ± 7**	64 ± 7	−146 ± 11	−18 ± 6
Aleutian Basin	1979–2013	*−138 ± 7*	95 ± 2	77 ± 2	−144 ± 5	−27 ± 3
	2014–2018	***−116 ± 15***	**101 ± 6**	79 ± 2	**−154 ± 16**	**−22 ± 8**

(−43 to −36 W m^{-2}) reduction of heat loss during 2014–2018 relative to the 1979–2013 base period. Note that the Aleutian Basin loses much less heat in winter compared to previous years (−138 to −116 W m^{-2}). Examination of the individual heat flux terms for this case shows that the difference is driven primarily by anomalous sensible heat fluxes, with additional contributions from latent and longwave fluxes.

In spring, both the Bering and Chukchi shelves exhibited strong positive surface heat flux anomalies during 2014–2018, a consequence of lower ice concentrations (e.g. Fig. 2) that directly led to lower average surface albedo and greater oceanic shortwave heat absorption (see also correlations in Supplementary Tables S2–S5). In the northernmost reaches of the analysis domain (e.g. north of about 72 °N) the spring ice cover has not changed greatly, nor have the ocean-atmosphere heat fluxes changed there in the spring season.

Semi-annually aggregated surface heat flux trends over 1979–2018 show that the Bering and Chukchi shelves follow contrasting trajectories through time (Fig. 12). The Chukchi Shelf shows significant trends ($p < 0.05$) whereby in recent years more heat is gained in the heating season and more heat lost in the cooling season, and the cooling season standard anomaly is nearly twice larger in magnitude. These trends provide additional evidence that the Chukchi Shelf heat engine is accelerating, consistent with faster rates of transition from winter to summer ice cover conditions as identified by Danielson et al. (2017). In contrast, the Bering Shelf does not exhibit a significant trend at either time of year, in part because different portions of the Bering Shelf exhibit contrasting responses in surface heat fluxes during times of warm water and low ice, such as over 2014–2018 (see Fig. 10b).

Cross-correlations between the two shelves' seasonally averaged heat fluxes provide insights into drivers and responses. Heating season anomalies over the Chukchi Sea are correlated ($r = 0.49$, $p = 0.001$) with heating season anomalies in the Bering Sea, reflecting in part the fact that Pacific Arctic atmospheric pressure systems have typical decorrelation length scales of many hundreds or thousands of km. More importantly, surface flux anomalies of the Chukchi Sea cooling season are inversely correlated to both Chukchi ($r = -0.67$, $p < 0.001$) and Bering ($r = -0.45$, $p = 0.003$) anomalies of the prior heating season, showing that heat loss follows accumulated heat gain. In contrast, cooling season surface flux anomalies are not good predictors ($p > 0.05$) for the following summer season's heat flux because the freezing point provides a nearly invariant lower temperature re-set each winter.

The ERA5 reanalysis reports a 2017 October to December heat flux anomaly for the Chukchi Shelf of about 41 W m^{-2}, or nearly 200 EJ (1 EJ = 10^{18} J) integrated over three months. For a typical atmospheric heat capacity of 1 J g^{-1} °C^{-1}, this massive heat exchange would be sufficient to warm the entire Arctic troposphere by more than 1 °C. The Chukchi Shelf occupies only about 3% of the Arctic Ocean area (Table 1). This scaling shows how, through ice cover mediated feedbacks of spring heat gain and fall heat loss, the Chukchi Sea delivers an out-sized contribution to Arctic amplification. The trends of Fig. 12 show increasing frequency of large surface heat losses from the Chukchi Sea, with five of the most recent eight years exhibiting an annually averaged anomalous flux of greater than one standard deviation away

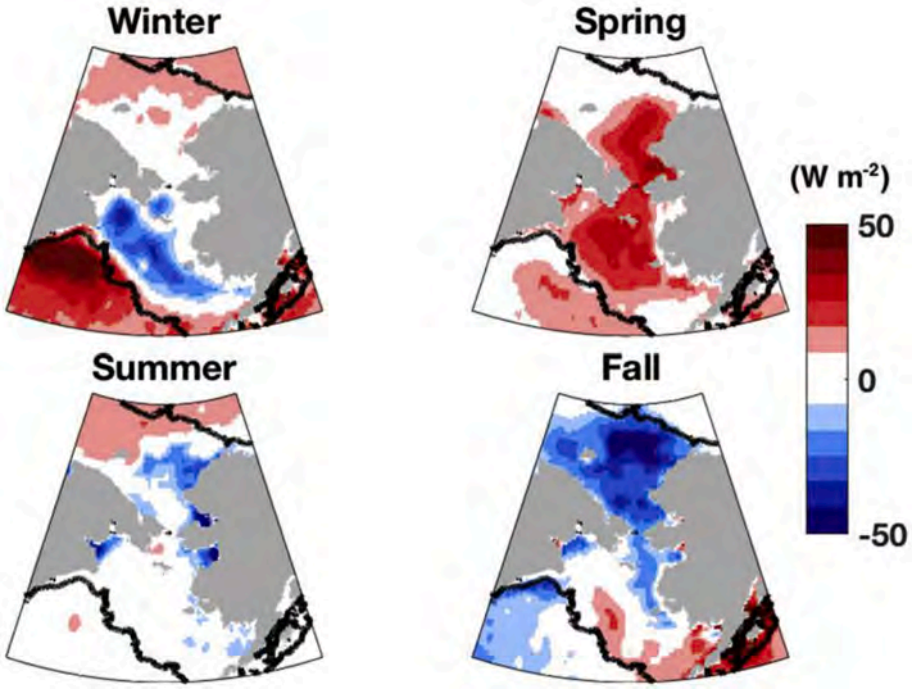

Fig. 11. Seasonal surface heat flux anomalies (W m^{-2}) for 2014–2018 relative to 1979–2013. Edges of the continental shelves (200 m depth) are marked with a black contour.

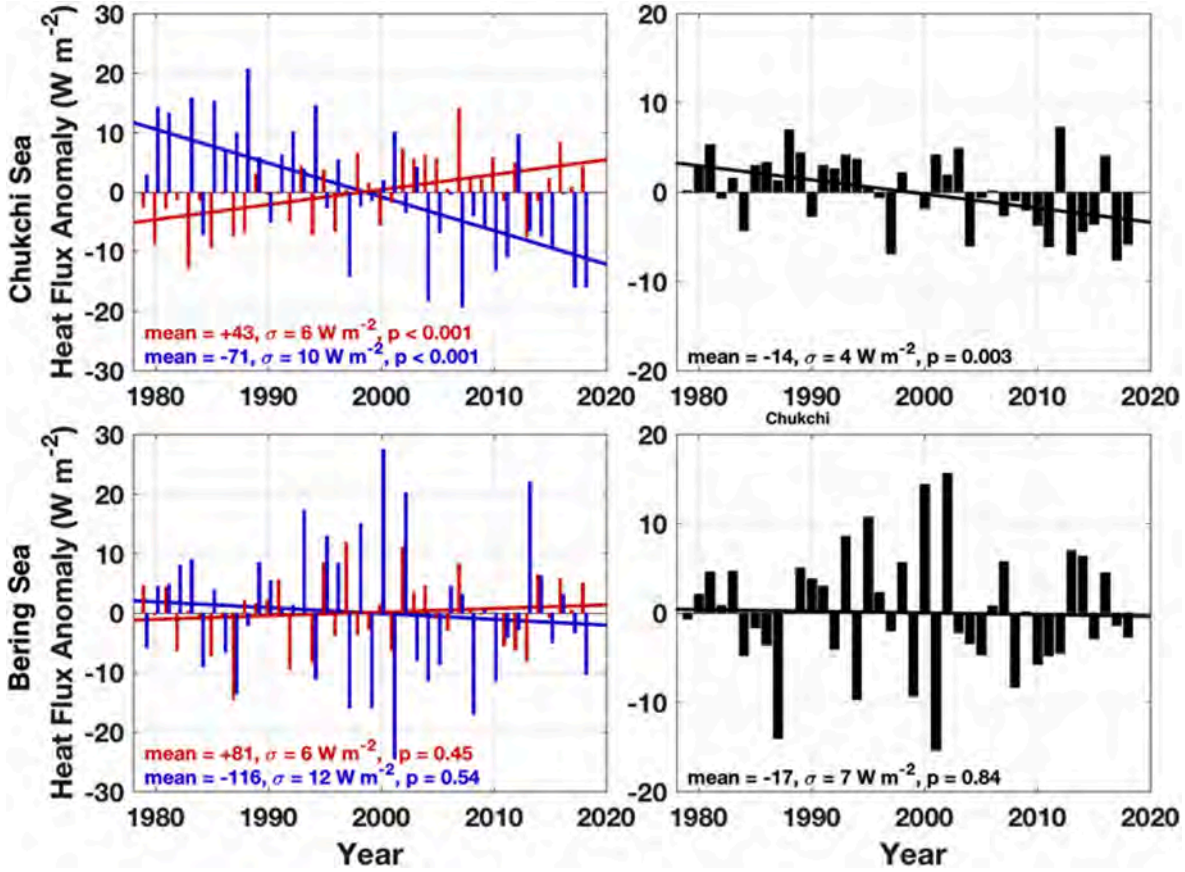

Fig. 12. Seasonally (left) and annually (right) averaged ERA5 surface heat flux anomalies for the Chukchi (top) and Bering (bottom) shelves, computed relative to a 1979–2018 record length baseline. Red bars and trend lines denote the heating spring and summer months (April–September); blue is used for the cooling fall and winter months (January–March plus October–December of the same year). Corresponding mean, standard deviations (σ) and linear trend p-values are shown at the bottom of each panel. Note different axis scales for the annual and seasonal plots. (For interpretation of the references to color in this figure legend, the reader is referred to the Web version of this article.)

from the mean (1 standard deviation = 4 W m^{-2} = 70 EJ yr^{-1} for the year).

In summary, we find statistically significant trends over the 1979–2018 period of record in the ERA5 seasonal surface heat fluxes over the Chukchi Shelf, whereby spring months are absorbing more shortwave energy, and with the lack of sea ice and a warmer ocean, fall and winter months exhibit accelerated heat losses. In contrast, the Bering Shelf does not show temporal trends in the surface heat fluxes over the last 40 years, but recent winters have lost anomalously large amounts of heat and recent spring months have absorbed more heat. The Aleutian Basin also exhibits large anomalous heat fluxes seasonally, and in recent years has delivered considerably less heat to the atmosphere than in years past. Increased heat losses to the atmosphere from the Chukchi Sea are large enough to contribute appreciably to Arctic amplification.

3.4. Bering and Chukchi Shelf heat budgets

In this section, we apply estimates of heat content, surface heat flux, and oceanic heat transport through Bering Strait to form balanced heat budgets for the Chukchi and Bering shelves. For the spring and fall, data coverage is fairly sparse so we conservatively estimate heat content changes by starting with gridded observations from 2014 to 2018 and then inserting the previously computed climatological hydrography at grid cells lacking data. Hence, heat content changes for these seasons represent a lower bound because the computation is biased toward the climatology at many grid points. We are unable to make reliable estimates for the 2014–2018 winter heat content due to lack of observations at this time of year.

A steady state solution is obtained by integrating heat fluxes over the course of the year (Table 4 and Fig. 13). The annual integration allows us to neglect ice formation, ice melt, and the work of seasonally changing oceanic heat content because integration through one climatological (or 2014–2018 mean) calendar year exhibits zero net change in ice cover or temperature. The surface heat exchanges shown in Fig. 13 come from the annual time integrations of the ERA5 net surface heat flux shown in Table 4. The heat flux through Bering Strait is based on Bering Strait mooring A3, adjusted for instrument depths and dropouts and the mean transport in Alaskan Coastal Current transport of heat assuming a 15 m surface mixed layer (Woodgate, 2018).

The steady-state solution (Fig. 13) exhibits characteristics consistent with the heat content and surface heat flux changes described in Sections 3.1-3.3. Heat loss over the Bering Shelf exceeds that of the Chukchi by about a factor of two, primarily a consequence of the Bering Shelf's greater surface area (Table 1). The Bering Shelf is a large (~900 EJ) sink for advectively sourced heat in the North Pacific. The Chukchi Sea net surface heat flux removes from the ocean a sizeable majority (two-thirds to three-quarters) of the heat transported northward through Bering Strait.

The analysis residual represents two heat budget contributions that we cannot separate from one another: oceanic sensible heat fluxed onto or off of the shelf and the contribution of net sea ice advection - because import of sea ice to the shelves represents a potential heat sink. Lacking adequate data about changes in the sea ice flux, if we want to assess changes in sensible heat flux to the adjoining basin we are forced to assume that the advection of sea ice onto the shelf has not appreciably

Table 4
Seasonal and annual estimates of heat content and surface heat exchanges for the Bering and Chukchi continental shelves, and the northward heat flux through Bering Strait over 2014–2018, the prior period of record for each dataset, and differences between the two time periods. Annual summaries are given as net values for the fluxes and means for the heat contents. We were unable to make estimates of the winter heat content for the recent interval so conservatively assume no change.

			Winter	Spring	Summer	Fall	Annual Mean
Oceanic Heat Content (EJ)	Chukchi Shelf	1922–2013	60	130	210	200	180
		2014–2018	60	140	260	210	200
		Difference	0	10	50	10	20
	Bering Shelf	1960–2013	520	920	1200	1200	980
		2014–2018	520	1000	1500	1300	1090
		Difference	0	120	300	100	110
			Winter	**Spring**	**Summer**	**Fall**	**Annual Net**
Bering Strait Heat Advection (EJ)	Bering Strait	1990–2013	0	60	220	70	350
		2014–2016	0	80	290	100	460
		Difference	0	20	70	30	120
Ocean-Atmosphere Heat Exchange (EJ)	Chukchi Shelf	1979–2013	−180	130	240	−430	−250
		2014–2018	−160	190	220	−570	−310
		Difference	20	60	−20	−130	70
	Bering Shelf	1979–2013	−670	690	480	−1100	−560
		2014–2018	−730	800	470	−1100	−520
		Difference	−60	110	−10	0	40

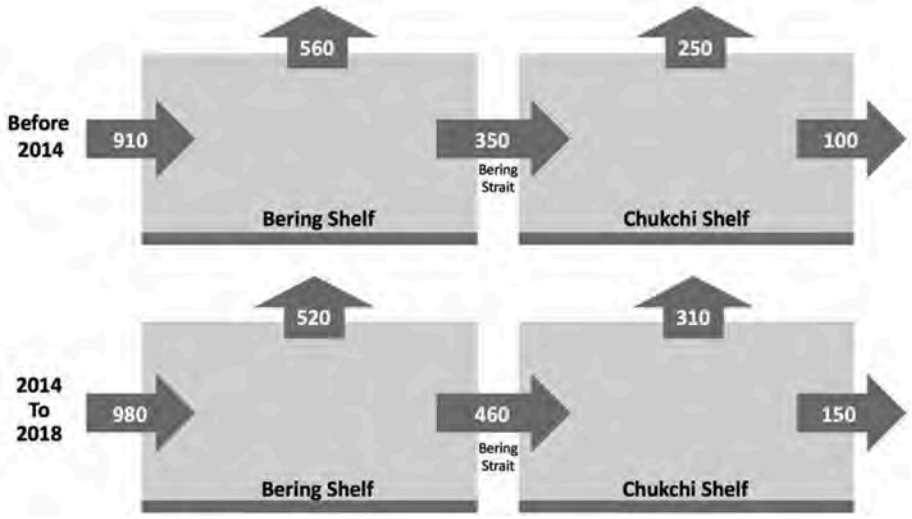

Fig. 13. Steady-state solution to the heat balance for the Bering-Chukchi Shelf system. Residual terms at the lateral shelf boundaries represent the sum of net basin-shelf sensible heat exchanges and heat budget contributions from advected sea ice. Orientation is such that the Gulf of Alaska and the Aleutian Basin are located to the left, the Canada Basin to the right and the atmosphere/ocean interface is at the top. All values reported in EJ.

changed over time. This assumption is assuredly invalid for some years so the approach has limitations but it is a useful starting point. The Chukchi Shelf annual heat budget residual is ~100 EJ, suggesting that in past decades the amount of heat fluxed off the shelf and directed into melting imported ice comprised about one quarter of the heat input northward through Bering Strait. Whether the Chukchi Shelf is a source or sink of ice varies seasonally and interannually (Howell et al., 2016) and this term is difficult to estimate. Ice can enter the Chukchi Shelf from Bering Strait (Woodgate and Aagaard, 2005), Long Strait (Weingartner et al., 1999), across the Chukchi Slope (Hutchings and Rigor, 2012) or from the Beaufort Shelf (Petty et al., 2016; Weingartner et al., 2017). In addition to the potentially significant impact of sea ice advection on the Chukchi heat budget, warm waters exiting Barrow Canyon (Itoh et al., 2015) may at times be carried back onto the Chukchi Shelf in summer and fall months, examples of which are shown with satellite tracked drifter observations by Danielson et al. (2017). Heat sourced farther offshore in the Beaufort Gyre may also be carried onto the NE Chukchi Shelf. Over the Bering Shelf, the typical ice volume near winter's end is ~1.3×10^{12} m^3 (Zhang et al., 2010), representing 400 EJ of extracted heat, or two-thirds of the Bering heat loss from summer to winter. If only 10% of the Bering ice is advected northward through Bering Strait, its latent heat of fusion would represent a 40 EJ heat sink in the Chukchi Shelf, a relatively minor term in this shelf's heat budget, but a large fraction of the annual residual. The net export of ice through Bering Strait is estimated at ~100 km^3 yr^{-1} (Woodgate and Aagaard, 2005); we lack any good estimate of the ice transport through the other boundaries.

Relative to the earlier time interval, during 2014–2018 the Bering Strait northward heat flux increased by 30% (110 EJ), the Chukchi Shelf net (outgoing) surface heat flux increased by 25% (60 EJ) and the net heat flux residual increased by 50% (50 EJ). Simultaneously, the Bering Shelf surface heat loss diminished by 7% (40 EJ) and the advective contribution to the Bering Shelf increased (70 EJ). This advective increase represents two-thirds of the observed increase in the northward Bering Strait oceanic heat flux. Hence, the heat budget shows that the remaining 1/3 of the Bering Strait heat flux increase over 2014–2018 derives from the net decrease in the Bering Shelf surface heat exchange.

We note that the 110 EJ yr^{-1} increase of the Bering Strait heat flux during 2014–2018 is a likely lower bound for this value because the mooring record used here misses 2017 and 2018, two of the warmest years on each shelf. Using the relation $Q = C_p{*}\Delta T{*}V{*}\rho{*}dt$ for typical annual average values of heat capacity (C_p = 4000 J kg^{-1} °C^{-1}), density

($\rho = 1025$ kg m^{-3}) Bering Strait transport ($V = 1$ Sv), and from Fig. 8 the average annual temperature anomaly ($\Delta T = 1.2$ °C) for the two shelves over 2014–2018, we estimate a more probable Chukchi throughput increase of 150 EJ for an annual mean of 500 EJ. The impact on the annual heat budget would be an increase in the 2014–2018 Bering Shelf and Chukchi Shelf residuals to 1020 EJ yr^{-1} and 190 EJ yr^{-1}, respectively. This estimate could grow further if the Bering Strait throughflow during these years continues its increasing trend (Woodgate, 2018).

The steady state approach obscures numerous potentially important factors so we turn to a seasonally explicit solution (Fig. 14). In this analysis, we separately balance the heating season and cooling season, maintaining continuity for each season at Bering Strait. Because the seasonal heat content changes (from spring to fall and then fall to spring) are approximately equal and opposite, any change in the seasonal amplitude of shelf temperatures triggers a commensurate adjustment in the residual terms. The heat balance shows that during the cooling season the warm ocean acts as a heat source, buffering the advective supply of heat and surface heat losses. In the heating season, the large heat capacities of these expansive shelves act as heat sinks. The 2014–2018 data do not show a significant change in the spring-to-fall temperature amplitude for either shelf relative to the climatology, showing that changes in heat throughput dominate over changes in heat content. This balance also shows that oceanic and atmospheric contributions to the Chukchi Shelf heat content in the heating season are similar in magnitude, but dominated by the atmospheric contribution, and that the oceanic input over 2014–2018 increased twice as fast as the atmospheric increase.

The Bering Shelf balance suggests that the increased northward heat flux through Bering Strait comes from both increase in heat gain through the ocean surface during the heating season and increase of heat supplied via advection during the cooling season. In addition to radiating advectively sourced heat, the Bering Shelf supplies a significant amount of heat (~600 EJ) back into the Aleutian basin during the heating season. For a 100 m winter mixed layer and the whole of the Aleutian Basin (~2×10^6 km^2), 30 EJ – the increase of Bering Shelf heat export to the basin – represents a potentially significant 0.30 °C decade^{-1} Aleutian Basin upper water column warming. While removed from the Bering Shelf at least in the short term, this heat may have another opportunity to influence the Bering Shelf heat budget if it is eventually advected back onto the eastern Bering Sea shelf. In contrast, oceanic heat delivered to the Arctic through Bering Strait is lost subsequently from the Bering Sea system for many centuries.

The seasonal heat balance findings suggest that the heating season advective heat loss from the Chukchi Shelf increased by 120 EJ relative to the prior climatology. This value, more than twice the magnitude of the steady state balance increase (50 EJ), is dependent upon the magnitude of the spring-to-fall change in heat content and the influence of summer ice advection onto the Chukchi Shelf from elsewhere. Nonetheless, both heat balances describe a Chukchi Sea advective throughput that has increased appreciably. Note that Timmermans et al. (2018) document a 2014–2017 increase of heat content in the Beaufort Gyre thermocline of ~150 EJ relative to observations made over 1987–2002.

A cross-correlation analysis of the time series assembled above can provide insight into the relations between the heat fluxes, shelf temperatures and salinities, and the Bering Strait mooring data. Correlation matrices (Supplemental Tables 2–5) show the tightly interlinked nature of the various variables and the manner in which these relations evolve with the passing seasons and their adjusting heat budget balances. For example, the Chukchi ice concentration most closely co-varies with the latent heat flux in winter, the net surface heat flux in spring, and the air temperature and latent fluxes nearly equally in fall. The correlation between Chukchi latent heat flux and the ice concentration anomaly has a very high coefficient of regression in fall ($r^2 = 0.71$, $p < 0.01$) and winter ($r^2 = 0.79$, $p < 0.01$). The winter Bering ice concentration is most strongly correlated with the inverse of air temperature and shortwave

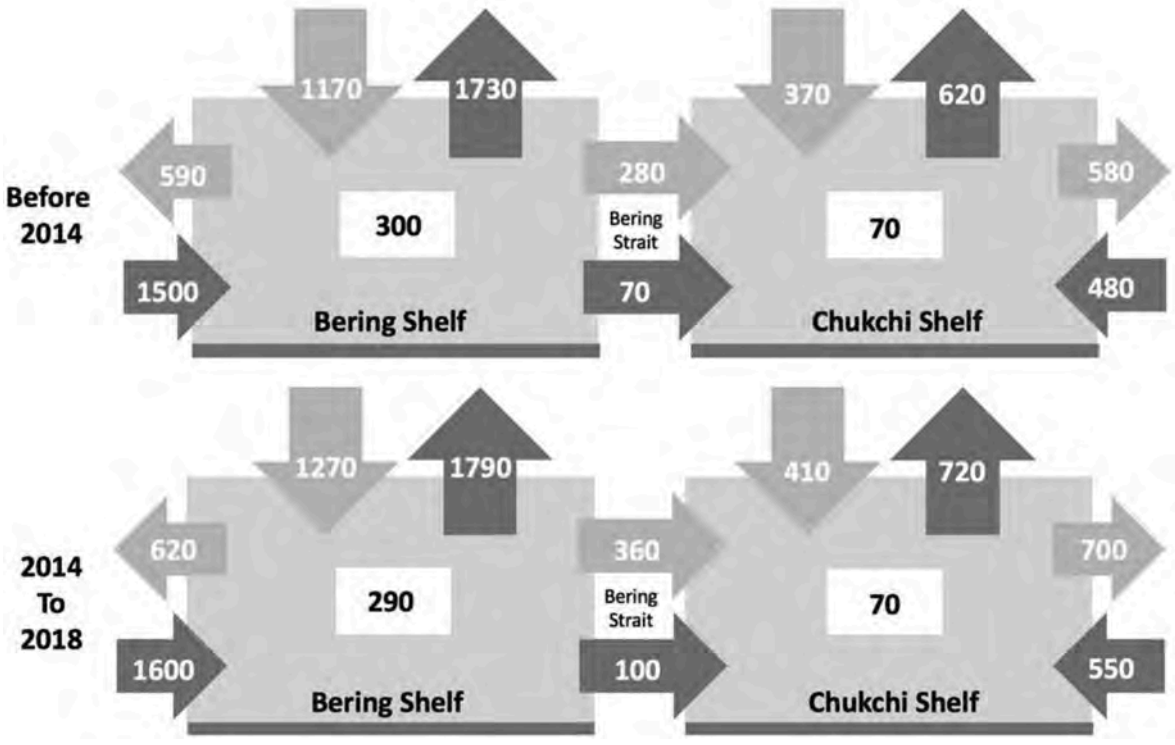

Fig. 14. Semi-annual solution of the Bering-Chukchi Shelf heat budget for the two integration intervals. Light and dark arrows denote heating and cooling season fluxes, respectively. Values in the central white boxes show the seasonal change in oceanic heat content across the heating and cooling seasons (from spring to fall and vice-versa). Figure orientation is such that the Gulf of Alaska and the Aleutian Basin are located to the left, the Canada Basin is to the right, and the atmosphere/ocean interface is at the top. All values reported in EJ.

radiation fluctuations. The Bering Sea spring ice concentration is positively correlated with the Bering Strait mooring salinity, showing that years with high ice concentrations exhibit higher salt flux to the Chukchi Sea, presumably due to enhanced brine production. The Chukchi ice concentration is negatively correlated with the Bering Strait heat flux.

Low ice anomalies in the Chukchi Sea appear to generate southerly wind anomalies (wind blowing anomalously from the south to the north) that could potentially advect ice and/or oceanic heat northward in a positive feedback relation (Tachibana et al., 2019). Thus, we examine regional wind field anomalies for 2014–2018 and correlations between monthly wind anomalies and our other variables of interest (Supplemental Tables 2–5). For the Chukchi Sea, we find that the 2014–2018 anomalous heat fluxes of winter were associated with southerly wind anomalies (Fig. 15). The net Chukchi Sea surface heat flux variations are significantly correlated ($r^2 = 0.45$, $p < 0.01$) with the meridional wind component in winter and weakly, but still significantly correlated, in fall ($r^2 = 0.08$, $p < 0.05$). The surface heat flux versus meridional wind relation in the Bering Sea is significant in both fall ($r^2 = 0.42$, $p < 0.05$) and winter ($r^2 = 0.33$, $p < 0.05$). Furthermore, the correlation analysis shows that southerly wind anomalies are significantly correlated to northward flow anomalies in Bering Strait. These findings are all consistent with the hypothesis proposed by Tachibana et al. (2019); namely, that low sea ice concentrations and excess ocean-to-atmosphere heat fluxes in the Pacific Arctic are associated with wind anomalies that also help promote reduced ice cover. Stabeno and Bell (2019) identify southerly winds in conjunction with the positive air temperature anomalies advected by these winds as key factors in driving the low ice concentrations of recent years.

In this section, we documented altered heat exchanges between these shelves, the overlying atmosphere, and the adjacent basins over 2014–2018 relative to the prior 35-year climatology. We found that the Chukchi Shelf heat engine significantly accelerated over this time, with larger heat gains in spring, larger heat content in summer in fall, and greater heat throughput to the high Arctic (110–150 EJ yr^{-1}). Anomalously high heat content of the shelves entering fall results in high oceanic heat loss to the atmosphere in fall and winter, triggering southerly wind anomalies that in turn advect warm air northward and drive water and sea ice northward.

4. Summary and discussion

Our results provide evidence for recent acceleration of the Pacific Arctic heat engine and show that the ocean plays multiple roles in the ocean-ice-atmosphere feedback loop, which are depicted schematically in Fig. 16. Relative to prior decades, the 2014–2018 heat balance is one in which the shelves absorbed more heat in the spring because of low ice concentrations and lost more heat in the fall because they begin the fall warmer and thus must lose more heat in order to reach the freezing point. Chukchi Sea surface heat fluxes trigger southerly wind anomalies that in turn promote northward advection of ice, water, and warm air, all of which lead to further reductions in winter and spring ice cover. The year-round shelf heat content has increased and the advective throughput of heat has increased. These changes are all consistent with recent observations of low ice concentrations, warm North Pacific and Pacific Arctic waters, and unusual winter storms in the northern Bering Sea. Some of these process changes were anticipated recently but have been obscured in the noise of interannual variability (see Stroeve et al. (2012) for a detailed discussion). The changes documented here help explain why the rate of warming in the Pacific Arctic has increased in recent decades, and why the Arctic is warming faster than the globe on average.

We think that some of the haline anomalies of Fig. 6, both fresh and salty, are mechanistically linked to an altered sea-ice regime, although some of the freshening is also likely due in part to the long-term decline of salinity recorded by the Bering Strait moorings (Woodgate, 2018). In the past, advection from the north carried ice southward across the Bering Sea shelf each winter and its subsequent melt at the edge of the ice pack represented a significant freshwater contribution to the shelf in water depths greater than about 70 m and especially between latitudes 56–60 °N (Zhang et al., 2010). We suggest that in recent years, the diminished southward advection effectively removed this freshwater input, resulting in the positive salinity anomalies seen near 57–59 °N. We find a typical water-column salinization of ~0.4 on the mid-shelf here (in ~70 m of water), which represents a freshwater deficit of ~0.9 m and appears reasonable relative to the expected accumulation of ~1.5 m of ice melt in a three-month winter season predicted by Zhang et al. (2010). In the northern Bering Sea and possibly the Chukchi Sea, we speculate that compounding factors likely account for the observed freshening: reduced brine production due to reduced sea-ice growth and extent (Fig. 2), and sea-ice melt along the leading (southern) ice edge

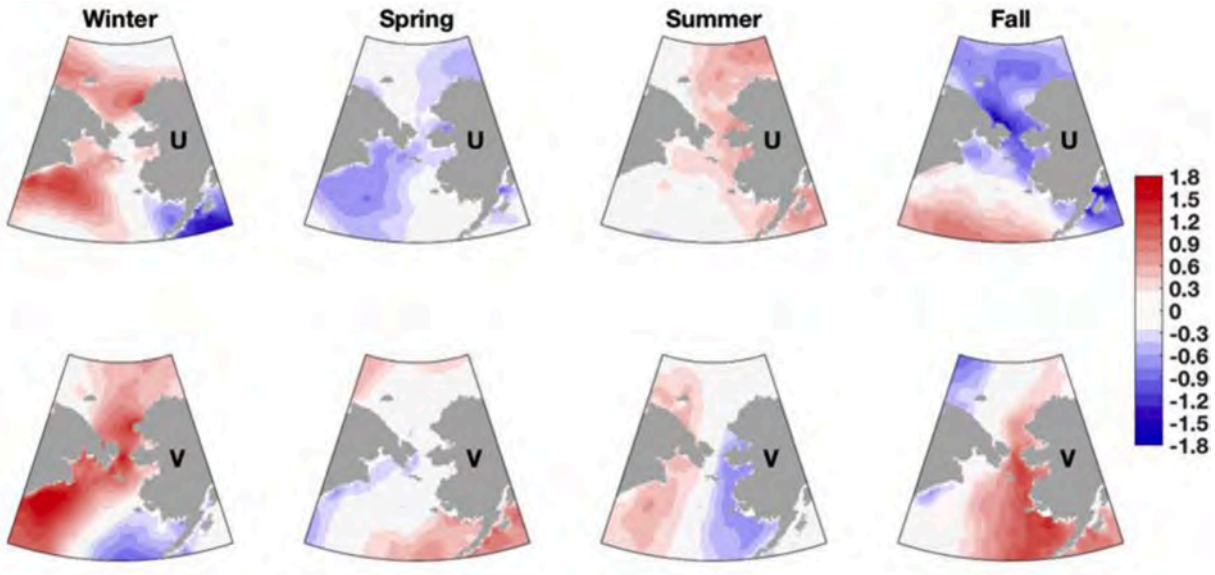

Fig. 15. Differences of seasonally averaged ERA5 wind vector components U (top row) and V (2014–2018 minus 1979–2013), units of m s-1. Note the fall and winter wind V anomalies over the Bering and Chukchi seas.

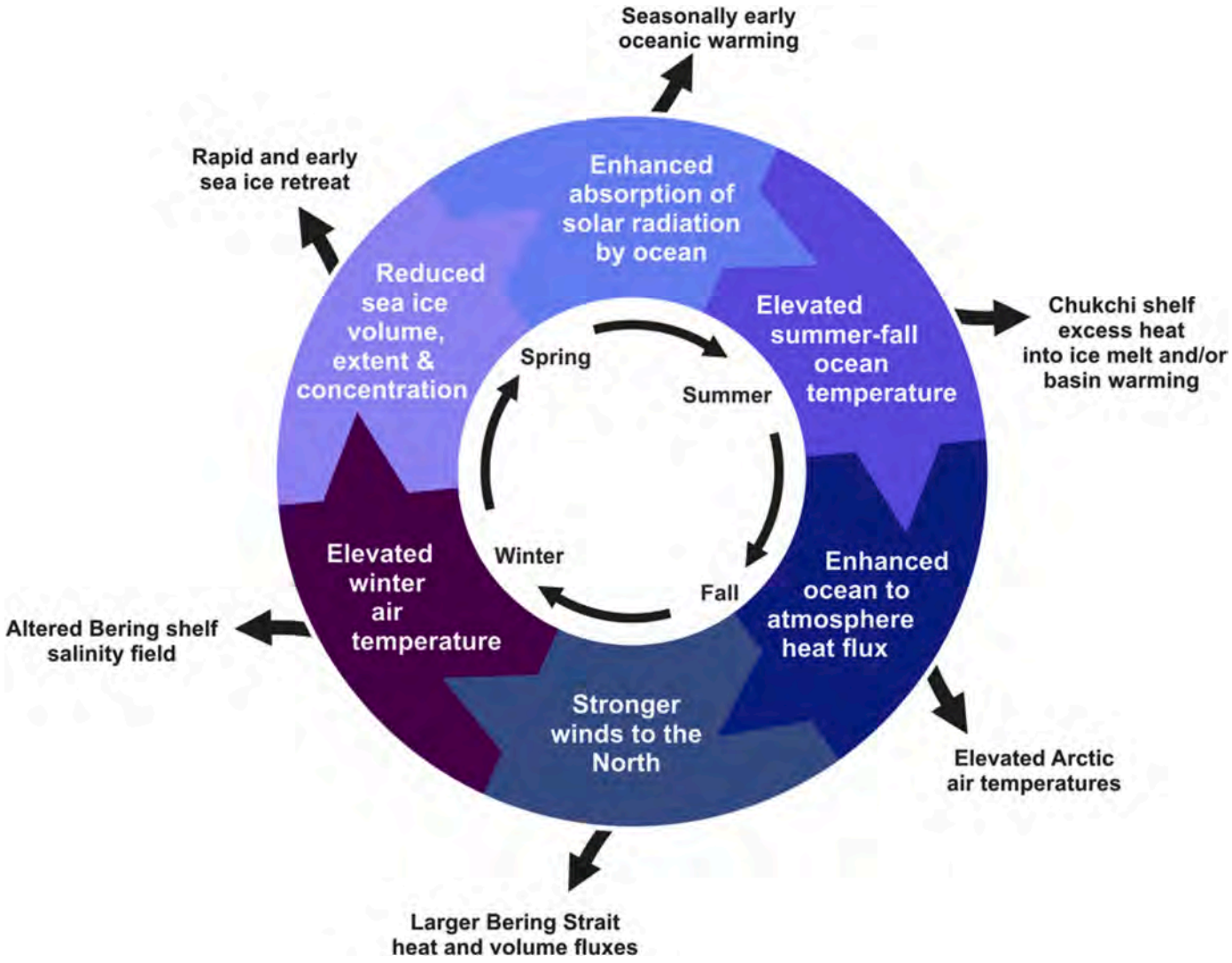

Fig. 16. The ocean-ice-atmosphere feedback loop for the Pacific Arctic's role in contributing to the Arctic amplification of air and ocean temperatures. The approximate seasonal sequence of events is shown with the inner loop (black). Physical consequences of the altered heat balances (black) include both local and remote impacts. The feedback loop promotes cascading effects on the regional physical system; not depicted here are equally important consequences for the ecosystem, for biogeochemical cycles, and for climate teleconnections that may influence weather far from the Pacific Arctic.

occurring farther north than in years past (in association with a northward-displaced freezing isotherm). Farther north, the positive salinity anomaly found near the surface in the northeast Chukchi Sea may result from at least two sources. Thinner arctic sea ice (e.g. Kwok and Rothrock, 2009; Zhang et al., 2018) would contribute less fresh water upon melting in summer. A positive saline anomaly could also develop in the ice edge plume region if the relative orientation between the winds and the ice edge is altered to promote northward ice advection. Lu et al. (2020) finds that winds from the southwest, south or east should trigger positive salinity anomalies in the meltwater plumes associated with the Chukchi marginal ice zone, so a salinization of the meltwater plume is consistent with observations of enhanced polar easterlies (e.g. Pickart et al., 2013). Further diagnosis of the sea-ice regime in relation to the shelf salinity field is clearly warranted.

Warming permafrost, outflow timing, and other hydrological changes are impacting Yukon River discharges into the Bering Sea and increasing winter season discharge rates, but annual discharge trends have not been well established for this river (Brabets and Walvoord, 2009). Since 2000, the Yukon has discharged on average 209 $km^3\ yr^{-1}$: an increase of 3 $km^3\ yr^{-1}$, or 1.5% above the period of record mean (Holmes et al., 2018). On the other hand, temperate glaciers around the northern and eastern rim of the Gulf of Alaska are rapidly losing 57 ± 11 $km^3\ yr^{-1}$ of volume (Hill et al., 2015), a rate maintained since at least the early part of this century (Jacob et al., 2012; Hill et al., 2015). Long-term declines in salinity have been identified in the coastal Gulf of Alaska (Royer and Grosch, 2006) and oceanic realms of the North Pacific (Freeland, 2013). The magnitude of net glacier melt represents more than a quarter of the annual Yukon River outflow and more than 15% of all river systems that discharge onto the eastern Bering Sea shelf (Aagaard et al., 2006). Might the glacier melt in the Gulf of Alaska be partially responsible for the 2000 to present freshening observed in Bering Strait (Woodgate, 2018) and over the shelf?

We can estimate the Gulf of Alaska glaciers' potential contribution to declining Bering Shelf salinity since 2000 with the relation $S_{GF} = (S_S{*}V_S)/(V_S + V_G)$, where S_{GF} is the shelf salinity under the influence of glacial freshening, S_S and V_S are the unfreshened shelf salinity and shelf volume, and V_G is the volume of glacial melt. Given the volume of the Bering Shelf (Table 1) and a typical shelf salinity of ~32, if only one-quarter of the Gulf of Alaska net glacial ablation were to enter the Bering Sea shelf via Unimak pass, we can account for a shelf-wide freshening of $0.015 \pm 0.003\ yr^{-1}$ (or about five times greater than the amount of freshening that the Yukon River appears to be contributing).

We conclude that the freshening signal observed in Bering Strait is at least consistent with a terrestrial discharge source from Gulf of Alaska glacial ablation.

Altered latitudinal atmospheric temperature gradients and the changing Arctic ice cover may play a role in triggering baroclinic perturbations to the atmospheric polar vortex, and with it, alterations to mid-latitude weather (Serreze and Francis, 2006; Francis and Vavrus, 2012). While a complete understanding and description of mid-to-high latitude ocean-atmosphere-climate-weather linkages is still needed, the concept is supported by theoretical considerations and evidence derived from observations, reanalysis hindcast models, and idealized process-oriented models (e.g. Holland and Bitz, 2003; Johannessen et al., 2004; Taylor et al., 2018). Very likely, when these linkages are fully resolved, our understanding will hinge on the roles played by sea ice, heat content, and heat fluxes within and between both the ocean and the atmosphere.

Tachibana et al. (2019) propose that the very presence of severely reduced ice cover over the Chukchi Shelf triggers a flow of warm southerly wind over the Bering Sea, a reinforcing feedback mechanism. Their focus was on winter, but our analysis suggests that this component of the feedback loop may be just as important in fall when the surface heat flux anomalies are the largest over the Chukchi Sea. Such feedbacks may be particularly difficult to disrupt once strongly established. As the fall warm ocean conditions become more common in a warmer world, we speculate that such winds could provide a potentially important control on the phase of polar vortex meanders (Serreze and Francis, 2006; Francis and Vavrus, 2012). If so, then improved understanding of this mechanism could lead to better predictability of atmospheric weather systems beyond the Pacific Arctic.

Only time will tell if these recent conditions represent a "new normal" as the data record shows that decadal scale variability exerts a fundamental influence. Our results suggest that to return to the pre-2014 heat balances, the cycle of low spring ice concentrations and associated low albedos must be interrupted. The heat balance suggests that such an interruption could result from advection of cooler waters onto the Bering Sea Shelf and/or winters having particularly strong and cold northerly winds. We have not determined exactly how the system entered the present state; it may have been a combination of both oceanic advection of warm waters and anomalously large surface heat fluxes.

There are physical limits to how much additional solar radiation the ocean can absorb as ice diminishes: the maximum addition available is the difference between that absorbed under current ice conditions and that reflected. As the system approaches the limit, the incoming shortwave radiation influence on the rate of change now observed in the Pacific Arctic will slow. However, continued atmospheric warming will continue to impact the oceanic heat content, latent, longwave, and sensible surface heat fluxes, and the regional heat balances. Thoman et al. (2020) find that the anomalously sparse winter sea ice conditions of 2018 will likely become the norm by the 2040s, suggesting that the 2014–2018 conditions will become increasingly common and eventually expected in any given year.

Declaration of competing interest

The authors declare that they have no known competing financial interests or personal relationships that could have appeared to influence the work reported in this paper.

CRediT authorship contribution statement

S.L. Danielson: Formal analysis, Writing - original draft, Data curation. **O. Ahkinga:** Writing - original draft, Visualization. **C. Ashjian:** Writing - original draft, Data curation. **E. Basyuk:** Writing - original draft, Data curation. **L.W. Cooper:** Writing - original draft, Data curation. **L. Eisner:** Writing - original draft, Data curation. **E. Farley:** Writing - original draft, Data curation. **K.B. Iken:** Writing - original draft, Data curation. **J.M. Grebmeier:** Writing - original draft, Data curation. **L. Juranek:** Writing - original draft, Data curation. **G. Khen:** Writing - original draft, Data curation. **S.R. Jayne:** Writing - original draft, Data curation. **T. Kikuchi:** Writing - original draft, Data curation. **C. Ladd:** Writing - original draft, Data curation. **K. Lu:** Writing - original draft, Data curation. **R.M. McCabe:** Writing - original draft, Data curation. **G.W.K. Moore:** Writing - original draft, Data curation. **S. Nishino:** Writing - original draft, Data curation. **F. Ozenna:** Writing - original draft, Visualization. **R.S. Pickart:** Writing - original draft, Data curation. **I. Polyakov:** Writing - original draft, Data curation. **P.J. Stabeno:** Writing - original draft, Data curation. **R. Thoman:** Writing - original draft, Data curation. **W.J. Williams:** Writing - original draft, Data curation. **K. Wood:** Writing - original draft, Data curation. **T.J. Weingartner:** Writing - original draft, Data curation.

Acknowledgements

The authors thank the many scientists and mariners whose work and dedication have contributed to the massive field efforts that this century-long climatology represents. We thank Shaun Bell, Liz Dobbins, Jeanette Gann, Leah Trafford McRaven, Stephen Okkonen and Hank Statscewich for assistance in assembling the CTD climatology. We thank the editors and two anonymous reviewers for comments that improved the manuscript. Data in this manuscript come from multiple sources and are available online and by request from the host institutions as noted below. ECMWF ERA5 data are archived and available online at https://www.ecmwf.int/en/forecasts/datasets/reanalysis-datasets/era5. NSIDC sea ice data are archived online and available at https://nsidc.org/data/nsidc-0051. Data sourced from Japan's R/V Mirai are archived online and available online at http://www.godac.jamstec.go.jp/darwin/e/. The R/V Mirai cruises were supported by the Green Network of Excellence (GRENE) Program/Arctic Climate Change Research Project and the Arctic Challenge for Sustainability (ArCS) Project, which were funded by the Ministry of Education, Culture, Sports, Science and Technology of Japan (MEXT). ALAMO float data are available online at http://argo.whoi.edu/alamo/. Data sourced from Russia are archived at the TINRO Center (http://www.tinro-center.ru/) and available upon request for permitted uses. Data from Fisheries and Oceans Canada's Institute of Ocean Science can be accessed by request via https://www.pac.dfo-mpo.gc.ca/science/index-eng.html. WOD18 can be accessed online at https://www.nodc.noaa.gov/OC5/WOD/pr_wod.html. Bering Strait mooring data are available from NCIS (www.nodc.noaa.gov) and the Bering Strait project page (psc.apl.washington.edu/BeringStrait.html) which also carries various data products (e.g., annual and monthly means). Data from NOAA-PMEL can be accessed online at https://www.pmel.noaa.gov/epic/ewb/. Data from NOAA-AFSC (https://www.fisheries.noaa.gov/alaska/commercial-fishing/alaska-physical-and-oceanographic-research) are available upon request. Data from the SOAR project, the ARDEM bathymetric grid, and the UAF-IMS database are available online at the Alaska Ocean Observing System, http://www.aoos.org. SLD assembled CTD data, performed analyses and the initial draft. OA and FO provided photographs and contextual background information. GWKM assembled ERA5 data; RT assembled GISTEMP and ERSSTv5 data. CA, EB, LWC, LE, EF, KBI, JMG, LJ, GK, SJ, TK, CL, KL, GWKM, RMM, SN, RSP, IP, PJS, RT, WJW, KW and TJW provided CTD data. All authors contributed to writing and/or discussion of the analytical approach. SRJ was supported by ONR grant N000141812475. LWC and JMG acknowledge support from multiple NSF and NOAA grants. RMM acknowledges support from NPRB grants A92-02a and A92-02b; and from JISAO under NOAA Cooperative Agreement NA15OAR4320063. SLD was supported by NPRB grants A91-99a and A91-00a and NSF grants OPP 1603116 and OPP 1708427. This manuscript is PMEL contribution #4997 and JISAO contribution #2019–1049. This manuscript is a product of the North Pacific Research Board Arctic Integrated Ecosystem Research Program, NPRB publication

number ArcticIERP-04.

Appendix A. Supplementary data

Supplementary data to this article can be found online at https://doi.org/10.1016/j.dsr2.2020.104781.

References

Aagaard, K., Coachman, L.K., Carmack, E., 1981. On the halocline of the Arctic Ocean. Deep Sea Res. Pt. A. Oceanogr. Res. Pap. 28 (6), 529–545.

Aagaard, K.A.T.R., Roach, A.T., Schumacher, J.D., 1985. On the wind-driven variability of the flow through Bering Strait. J. Geophys. Res.: Oceans 90 (C4), 7213–7221.

Aagaard, K., Weingartner, T.J., Danielson, S.L., Woodgate, R.A., Johnson, G.C., Whitledge, T.E., 2006. Some controls on flow and salinity in Bering Strait. Geophys. Res. Lett. 33 (19).

Ahlnäs, K., Garrison, G.R., 1984. Satellite and oceanographic observations of the warm coastal current in the Chukchi Sea. Arctic 244–254.

Benson, A.J., Trites, A.W., 2002. Ecological effects of regime shifts in the Bering Sea and eastern North Pacific ocean. Fish Fish. 3 (2), 95–113.

Bond, N.A., Cronin, M.F., Freeland, H., Mantua, N., 2015. Causes and impacts of the 2014 warm anomaly in the NE Pacific. Geophys. Res. Lett. 42 (9), 3414–3420.

Bourke, R.H., Paquette, R.G., 1976. Atlantic water on the Chukchi shelf. Geophys. Res. Lett. 3 (10), 629–632.

Boyer, T.P., Baranova, O.K., Coleman, C., Garcia, H.E., Grodsky, A., Locarnini, R.A., Mishonov, A.V., O'Brien, T.D., Paver, C.R., Reagan, J.R., Seidov, D., Smolyar, I.V., Weathers, K., Zweng, M.M., 2018. World Ocean Database 2018. National Centers for Environmental Information Ocean Climate Laboratory, Silver Spring, MD.

Brabets, T.P., Walvoord, M.A., 2009. Trends in streamflow in the Yukon River basin from 1944 to 2005 and the influence of the pacific decadal oscillation. J. Hydrol 371 (1–4), 108–119.

Carmack, E., Winsor, P., Williams, W., 2015. The contiguous panarctic Riverine Coastal Domain: a unifying concept. Prog. Oceanogr. 139, 13–23.

Clement, J.L., Maslowski, W., Cooper, L.W., Grebmeier, J.M., Walczowski, W., 2005. Ocean circulation and exchanges through the northern Bering Sea—1979–2001 model results. Deep Sea Res. Pt. II 52 (24–26), 3509–3540.

Coachman, L.K., 1986. Circulation, water masses, and fluxes on the southeastern Bering Sea shelf. Continent. Shelf Res. 5 (1–2), 23–108.

Coachman, L.K., Aagaard, K., 1966. On the water exchange through Bering Strait. Limnol. Oceanogr. 11 (1), 44–59.

Coachman, L.K., Shigaev, V.V., 1992. Northern bering-chukchi ecosystem: the physical basis. In: Nagel, P. (Ed.), Results of the Third Joint US-USSR Bering & Chukchi Sea Expedition (BERPAC), U.S. Fish and Wildlife Service.

Coachman, L.K., Coachman, L.K., Aagaard, K., Tripp, R.B., 1975. Bering Strait: the Regional Physical Oceanography. Univ. Washington Press.

Cooper, L.W., Benner, R., McClelland, J.W., Peterson, B.J., Holmes, R.M., Raymond, P.A., Hansell, D.A., Grebmeier, J.M., Codispoti, L.A., 2005. Linkages among runoff, dissolved organic carbon, and the stable oxygen isotope composition of seawater and other water mass indicators in the Arctic Ocean. J. Geophys. Res.: Biogeosciences 110 (G2).

Copernicus Climate Change Service (C3S), 2017. ERA5: fifth generation of ECMWF atmospheric reanalyses of the global climate. Copernicus Climate Change Service Climate Data Store (CDS). https://cds.climate.copernicus.eu/cdsapp#!/home.

Cornwall, W., 2019. Vanishing Bering Sea ice threatens one of the richest U.S. seafood sources. Science.

Coyle, K.O., Eisner, L.B., Mueter, F.J., Pinchuk, A.I., Janout, M.A., Cieciel, K.D., Farley, E. V., Andrews, A.G., 2011. Climate change in the southeastern Bering Sea: impacts on pollock stocks and implications for the oscillating control hypothesis. Fish. Oceanogr. 20 (2), 139–156.

Danielson, S., Aagaard, K., Weingartner, T., Martin, S., Winsor, P., Gawarkiewicz, G., Quadfasel, D., 2006. The St. Lawrence polynya and the Bering Shelf circulation: new observations and a model comparison. J. Geophys. Res.: Oceans 111 (C9).

Danielson, S., Weingartner, T., Aagaard, K., Zhang, J., Woodgate, R., 2012a. Circulation on the central Bering Sea shelf. J. Geophys. Res.: Oceans 117 (C10). July 2008 to July 2010.

Danielson, S., Hedstrom, K., Aagaard, K., Weingartner, T., Curchitser, E., 2012b. Wind-induced reorganization of the Bering Shelf circulation. Geophys. Res. Lett. 39 (8).

Danielson, S.L., Weingartner, T.J., Hedstrom, K.S., Aagaard, K., Woodgate, R., Curchitser, E., Stabeno, P.J., 2014. Coupled wind-forced controls of the Bering–Chukchi Shelf circulation and the Bering Strait throughflow: ekman transport, continental shelf waves, and variations of the Pacific–Arctic sea surface height gradient. Prog. Oceanogr. 125, 40–61.

Danielson, S.L., Dobbins, E.L., Jakobsson, M., Johnson, M.A., Weingartner, T.J., Williams, W.J., Zarayskaya, Y., 2015. Sounding the Northern Seas, 96. Eos.

Danielson, S.L., Eisner, L., Ladd, C., Mordy, C., Sousa, L., Weingartner, T.J., 2017. A comparison between late summer 2012 and 2013 water masses, macronutrients, and phytoplankton standing crops in the northern Bering and Chukchi Seas. Deep Sea Res. Pt. II 135, 7–26.

Dee, D.P., Uppala, S.M., Simmons, A.J., Berrisford, P., Poli, P., Kobayashi, S., Andrae, U., Balmaseda, M.A., Balsamo, G., Bauer, D.P., Bechtold, P., 2011. The ERA-Interim reanalysis: configuration and performance of the data assimilation system. Q. J. R. Meteorol. Soc. 137 (656), 553–597.

Di Lorenzo, E., Mantua, N., 2016. Multi-year persistence of the 2014/15 North Pacific marine heatwave. Nat. Clim. Change 6 (11), 1042–1047.

Doney, S.C., Ruckelshaus, M., Duffy, J.E., Barry, J.P., Chan, F., English, C.A., Galindo, H. M., Grebmeier, J.M., Hollowed, A.B., Knowlton, N., Polovina, J., 2011. Climate Change Impacts on Marine Ecosystems.

Eakins, B.W., Sharman, G.F., 2010. Volumes of the World's Oceans from ETOPO1, 7. NOAA National Geophysical Data Center, Boulder, CO.

Eppley, R.W., 1972. Temperature and phytoplankton growth in the sea. Fish. Bull. 70 (4), 1063–1085.

Foreman, M.G.G., Cummins, P.F., Cherniawsky, J.Y., Stabeno, P., 2006. Tidal energy in the Bering Sea. J. Mar. Res. 64 (6), 797–818.

Francis, J.A., Vavrus, S.J., 2012. Evidence linking Arctic amplification to extreme weather in mid-latitudes. Geophys. Res. Lett. 39 (6).

Freeland, H.J., 2013. Evidence of change in the winter mixed layer in the Northeast Pacific Ocean: a problem revisited. Atmos.-Ocean 51 (1), 126–133.

Freeman, E., Woodruff, S.D., Worley, S.J., Lubker, S.J., Kent, E.C., Angel, W.E., Berry, D. I., Brohan, P., Eastman, R., Gates, L., Gloeden, W., 2017. ICOADS Release 3.0: a major update to the historical marine climate record. Int. J. Climatol. 37 (5), 2211–2232.

Frey, K.E., Moore, G.W.K., Cooper, L.W., Grebmeier, J.M., 2015. Divergent patterns of recent sea ice cover across the bering, Chukchi, and Beaufort seas of the pacific arctic region. Prog. Oceanogr. 136, 32–49.

Gawarkiewicz, G., Haney, J.C., Caruso, M.J., 1994. Summertime synoptic variability of frontal systems in the northern Bering Sea. J. Geophys. Res.: Oceans 99 (C4), 7617–7625.

GISTEMP Team, 2019. GISS Surface Temperature Analysis (GISTEMP). NASA Goddard Institute for Space Studies. Dataset accessed 2019-07-20 at. https://data.giss.nasa.gov/gistemp/.

Gong, D., Pickart, R.S., 2016. Early summer water mass transformation in the eastern Chukchi Sea. Deep Sea Res. Pt. II 130, 43–55.

Grebmeier, J.M., Cooper, L.W., 1995. Influence of the St. Lawrence Island polynya upon the Bering Sea benthos. J. Geophys. Res.: Oceans 100 (C3), 4439–4460.

Grebmeier, J.M., Bluhm, B.A., Cooper, L.W., Danielson, S.L., Arrigo, K.R., Blanchard, A. L., Clarke, J.T., Day, R.H., Frey, K.E., Gradinger, R.R., Kędra, M., 2015. Ecosystem characteristics and processes facilitating persistent macrobenthic biomass hotspots and associated benthivory in the Pacific Arctic. Prog. Oceanogr. 136, 92–114.

Groves, D.G., Francis, J.A., 2002. Variability of the Arctic atmospheric moisture budget from TOVS satellite data. J. Geophys. Res. Atmos. 107 (D24). ACL-18.

Haiden, T., Janousek, M., Bidlot, J., Ferranti, L., Prates, F., Vitart, F., Bauer, P., Richardson, D.S., 2017. Evaluation of ECMWF Forecasts, Including 2016-2017 Upgrades (56). European Centre for Medium Range Weather Forecasts.

Hansen, J., Ruedy, R., Sato, M., Lo, K., 2010. Global surface temperature change. Rev. Geophys. 48, RG4004.

Hare, S.R., Mantua, N.J., 2000. Empirical evidence for North Pacific regime shifts in 1977 and 1989. Prog. Oceanogr. 47 (2–4), 103–145.

Hill, D.F., Bruhis, N., Calos, S.E., Arendt, A., Beamer, J., 2015. Spatial and temporal variability of freshwater discharge into the Gulf of Alaska. J. Geophys. Res.: Oceans 120 (2), 634–646.

Holland, M.M., Bitz, C.M., 2003. Polar amplification of climate change in coupled models. Clim. Dynam. 21 (3–4), 221–232.

Holmes, R.M., Shiklomanov, A.I., Suslova, A., Tretiakov, M., McClelland, J.W., Spencer, R.G.M., Tank, S.E., 2018. River discharge. In: Arctic Report Card 2018.

Howell, S.E., Brady, M., Derksen, C., Kelly, R.E., 2016. Recent changes in sea ice area flux through the Beaufort Sea during the summer. J. Geophys. Res.: Oceans 121 (4), 2659–2672.

Huang, B., Thorne, P.W., Banzon, V.F., Boyer, T., Chepurin, G., Lawrimore, J.H., Menne, M.J., Smith, T.M., Vose, R.S., Zhang, H.M., 2017. Extended reconstructed sea surface temperature, version 5 (ERSSTv5): upgrades, validations, and intercomparisons. J. Clim. 30 (20), 8179–8205.

Hunt Jr., G.L., Coyle, K.O., Eisner, L.B., Farley, E.V., Heintz, R.A., Mueter, F., Napp, J.M., Overland, J.E., Ressler, P.H., Salo, S., Stabeno, P.J., 2011. Climate impacts on eastern Bering Sea foodwebs: a synthesis of new data and an assessment of the Oscillating Control Hypothesis. ICES J. Mar. Sci. 68 (6), 1230–1243.

Hutchings, J.K., Rigor, I.G., 2012. Role of ice dynamics in anomalous ice conditions in the Beaufort Sea during 2006 and 2007. J. Geophys. Res.: Oceans 117 (C8).

Ikeda, T., 1985. Metabolic rates of epipelagic marine zooplankton as a function of body mass and temperature. Mar. Biol. 85 (1), 1–11.

Ikeda, T., Kanno, Y., Ozaki, K., Shinada, A., 2001. Metabolic rates of epipelagic marine copepods as a function of body mass and temperature. Mar. Biol. 139 (3), 587–596.

Itoh, M., Pickart, R.S., Kikuchi, T., Fukamachi, Y., Ohshima, K.I., Simizu, D., Arrigo, K.R., Vagle, S., He, J., Ashjian, C., Mathis, J.T., 2015. Water properties, heat and volume fluxes of Pacific water in Barrow Canyon during summer 2010. Deep Sea Res. Pt. I: Oceanogr. Res. Pap. 102, 43–54.

Jackson, J.M., Williams, W.J., Carmack, E.C., 2012. winter sea-ice melt in the Canada basin, Arctic Ocean. Geophys. Res. Lett. 39 (3).

Jacob, T., Wahr, J., Pfeffer, W.T., Swenson, S., 2012. Recent contributions of glaciers and ice caps to sea level rise. Nature 482 (7386), 514–518.

Johannessen, O.M., Bengtsson, L., Miles, M.W., Kuzmina, S.I., Semenov, V.A., Alekseev, G.V., Nagurnyi, A.P., Zakharov, V.F., Bobylev, L.P., Pettersson, L.H., Hasselmann, K., 2004. Arctic climate change: observed and modelled temperature and sea-ice variability. Tellus Dyn. Meteorol. Oceanogr. 56 (4), 328–341.

Johnson, G.C., Stabeno, P.J., Riser, S.C., 2004. The Bering slope current system revisited. J. Phys. Oceangr. 34 (2), 384–398.

Kinder, T.H., Schumacher, J.D., 1981. Hydrographic Structure over the Continental Shelf of the Southeastern Bering Sea, the Eastern Bering Sea Shelf: Oceanography and

Resources, 1 DW Hood, JA Calder, 31–52. Oceanic and Atmos. Admin., Washington, DC.
Kinder, T.H., Chapman, D.C., Whitehead Jr., J.A., 1986. Westward intensification of the mean circulation on the Bering Sea shelf. J. Phys. Oceangr. 16 (7), 1217–1229.
Kwok, R., Rothrock, D.A., 2009. Decline in Arctic sea ice thickness from submarine and ICESat records: 1958–2008. Geophys. Res. Lett. 36 (15).
Kwok, R., Untersteiner, N., 2011. The thinning of Arctic sea ice. Phys. Today 64 (4), 36–41.
Ladd, C., 2014. Seasonal and interannual variability of the bering slope current. Deep Sea Res. Pt. II 109, 5–13.
Lenssen, N.J., Schmidt, G.A., Hansen, J.E., Menne, M.J., Persin, A., Ruedy, R., Zyss, D., 2019. Improvements in the GISTEMP uncertainty model. J. Geophys. Res. Atmos. 124 (12), 6307–6326.
Lin, P., Pickart, R.S., McRaven, L.T., Arrigo, K.R., Bahr, F., Lowry, K.E., Stockwell, D.A., Mordy, C.W., 2019. Water mass evolution and circulation of the northeastern Chukchi Sea in summer: implications for nutrient distributions. J. Geophys. Res.: Oceans 124 (7), 4416–4432.
Lindsay, R.W., Zhang, J., Schweiger, A., Steele, M., Stern, H., 2009. Arctic sea ice retreat in 2007 follows thinning trend. J. Clim. 22 (1), 165–176.
Lindsay, R., Wensnahan, M., Schweiger, A., Zhang, J., 2014. Evaluation of seven different atmospheric reanalysis products in the Arctic. J. Clim. 27 (7), 2588–2606.
Lu, K., Weingartner, T., Danielson, S., Winsor, P., Dobbins, E., Martini, K., Statscewich, H., 2015. Lateral mixing across ice meltwater fronts of the Chukchi Sea shelf. Geophys. Res. Lett. 42 (16), 6754–6761.
Lu, K., Danielson, S.L., Weingartner, T.J., 2020. Impacts of short-term wind events on Chukchi hydrography and sea ice retreat. Deep Sea Res. II (this volume).
Martin, S., Drucker, R., Kwok, R., Holt, B., 2004. Estimation of the thin ice thickness and heat flux for the Chukchi Sea Alaskan coast polynya from Special Sensor Microwave/Imager data, 1990–2001. J. Geophys. Res.: Oceans 109 (C10).
Maykut, G.A., 1978. Energy exchange over young sea ice in the central Arctic. J. Geophys. Res.: Oceans 83 (C7), 3646–3658.
McPhaden, M.J., 2015. Playing hide and seek with El Niño. Nat. Clim. Change 5 (9), 791.
Miura, T., Suga, T., Hanawa, K., 2002. Winter mixed layer and formation of dichothermal water in the Bering Sea. J. oceanography 58 (6), 815–823.
Moore, G.W.K., Pickart, R.S., 2012. Northern Bering Sea tip jets. Geophys. Res. Lett. 39 (8).
Moore, S.E., Stabeno, P.J., Grebmeier, J.M., Okkonen, S.R., 2018. The Arctic Marine Pulses Model: linking annual oceanographic processes to contiguous ecological domains in the Pacific Arctic. Deep Sea Res. Pt. II 152, 8–21.
Mueter, F.J., Litzow, M.A., 2008. Sea ice retreat alters the biogeography of the Bering Sea continental shelf. Ecol. Appl. 18 (2), 309–320.
Natsuike, M., Matsuno, K., Hirawake, T., Yamaguchi, A., Nishino, S., Imai, I., 2017. Possible spreading of toxic Alexandrium tamarense blooms on the Chukchi Sea shelf with the inflow of Pacific summer water due to climatic warming. Harmful Algae 61, 80–86.
Okkonen, S., Ashjian, C., Campbell, R.G., Alatalo, P., 2019. The encoding of wind forcing into the Pacific-Arctic pressure head, Chukchi Sea ice retreat and late-summer Barrow Canyon water masses. Deep Sea Res. Pt. II 162, 22–31.
Østerhus, S., Woodgate, R., Valdimarsson, H., Turrell, B., de Steur, L., Quadfasel, D., Olsen, S.M., Moritz, M., Lee, C.M., Larsen, K.H.M., Jónsson, S., Johnson, C., Jochumsen, K., Hansen, B., Curry, B., Cunningham, S., Berx, B., 2019. Arctic Mediterranean exchanges: a consistent volume budget and trends in transports from two decades of observations. Ocean Sci. 15 (2), 379–399.
Osterkamp, T.E., Romanovsky, V.E., 1999. Evidence for warming and thawing of discontinuous permafrost in Alaska. Permafr. Periglac. Process. 10 (1), 17–37.
Overland, J.E., Roach, A.T., 1987. Northward flow in the bering and Chukchi seas. J. Geophys. Res.: Oceans 92 (C7), 7097–7105.
Overland, J.E., Wang, M., 2010. Large-scale atmospheric circulation changes are associated with the recent loss of Arctic sea ice. Tellus 62 (1), 1–9.
Overland, J.E., Stabeno, P.J., Salo, S., 1996. Direct evidence for northward flow on the northwestern Bering Sea shelf. J. Geophys. Res.: Oceans 101 (C4), 8971–8976.
Overland, J.E., Wang, M., Wood, K.R., Percival, D.B., Bond, N.A., 2012. Recent Bering Sea warm and cold events in a 95-year context. Deep Sea Res. Pt. II 65, 6–13.
Paquette, R.A., Bourke, R.H., 1974. Observations on the coastal current of Arctic Alaska. J. Mar. Res. 32 (2), 195–207.
Perovich, D.K., Richter-Menge, J.A., Jones, K.F., Light, B., 2008. Sunlight, water, and ice: extreme Arctic sea ice melt during the summer of 2007. Geophys. Res. Lett. 35 (11).
Peralta Ferriz, C., Woodgate, R.A., 2017. The dominant role of the east Siberian Sea in driving the oceanic flow through the Bering Strait—conclusions from GRACE Ocean mass satellite data and in situ mooring observations between 2002 and 2016. Geophys. Res. Lett. 44 (22), 11–472.
Petty, A.A., Hutchings, J.K., Richter-Menge, J.A., Tschudi, M.A., 2016. Sea ice circulation around the Beaufort Gyre: the changing role of wind forcing and the sea ice state. J. Geophys. Res.: Oceans 121 (5), 3278–3296.
Pickart, R.S., Moore, G.W.K., Weingartner, T.J., Danielson, S.L., Frey, K.E., 2013. Physical drivers of the Chukchi, Beaufort, and northern bering seas. Developing a Conceptual Model of the Arctic Marine Ecosystem 2.
Pickart, R.S., Nobre, C., Lin, P., Arrigo, K.R., Ashjian, C.J., Berchok, C., Cooper, L.W., Grebmeier, J.M., Hartwell, I., He, J., Itoh, M., 2019. Seasonal to mesoscale variability of water masses and atmospheric conditions in Barrow Canyon, Chukchi Sea. Deep Sea Res. Pt. II 162, 32–49.
Pisareva, M.N., Pickart, R.S., Spall, M.A., Nobre, C., Torres, D.J., Moore, G.W.K., Whitledge, T.E., 2015. Flow of pacific water in the western Chukchi sea: results from the 2009 RUSALCA expedition. Deep Sea Res. Pt. I: Oceanogr. Res. Pap. 105, 53–73.
Polyakov, I.V., Pnyushkov, A.V., Alkire, M.B., Ashik, I.M., Baumann, T.M., Carmack, E. C., Goszczko, I., Guthrie, J., Ivanov, V.V., Kanzow, T., Krishfield, R., 2017. Greater role for atlantic inflows on sea-ice loss in the eurasian basin of the Arctic Ocean. Sci. Asia 356 (6335), 285–291.
Roach, A.T., Aagaard, K., Pease, C.H., Salo, S.A., Weingartner, T., Pavlov, V., Kulakov, M., 1995. Direct measurements of transport and water properties through the Bering Strait. J. Geophys. Res.: Oceans 100 (C9), 18443–18457.
Rodionov, S.N., Overland, J.E., Bond, N.A., 2005. The Aleutian low and winter climatic conditions in the Bering Sea. Part I: Classification. J. Clim. 18 (1), 160–177.
Royer, T.C., Grosch, C.E., 2006. Ocean warming and freshening in the northern Gulf of Alaska. Geophys. Res. Lett. 33 (16).
Screen, J.A., Simmonds, I., 2010. The central role of diminishing sea ice in recent Arctic temperature amplification. Nature 464 (7293), 1334–1337.
Serreze, M.C., Barry, R.G., 2011. Processes and impacts of Arctic amplification: a research synthesis. Global Planet. Change 77 (1–2), 85–96.
Serreze, M.C., Francis, J.A., 2006. The Arctic amplification debate. Climatic Change 76 (3–4), 241–264.
Serreze, M.C., Holland, M.M., Stroeve, J., 2007. Perspectives on the Arctic's shrinking sea-ice cover. Sci. Asia 315 (5818), 1533–1536.
Serreze, M.C., Crawford, A.D., Stroeve, J.C., Barrett, A.P., Woodgate, R.A., 2016. Variability, trends, and predictability of seasonal sea ice retreat and advance in the Chukchi Sea. J. Geophys. Res.: Oceans 121 (10), 7308–7325.
Shimada, K., Itoh, M., Nishino, S., McLaughlin, F., Carmack, E., Proshutinsky, A., 2005. Halocline structure in the Canada basin of the Arctic Ocean. Geophys. Res. Lett. 32 (3).
Stabeno, P.J., Bell, S.W., 2019. Extreme conditions in the Bering Sea (2017–2018): record-breaking low sea-ice extent. Geophys. Res. Lett. 46 (15), 8952–8959.
Stabeno, P.J., Schumacher, J.D., Davis, R.F., Napp, J.M., 1998. Under-ice observations of water column temperature, salinity and spring phytoplankton dynamics: eastern Bering Sea shelf. J. Mar. Res. 56 (1), 239–255.
Stabeno, P.J., Reed, R.K., Napp, J.M., 2002. Transport through Unimak pass, Alaska. Deep Sea Res. Pt. II 49 (26), 5919–5930.
Stabeno, P.J., Ladd, C., Reed, R.K., 2009. Observations of the aleutian north slope current, Bering Sea, 1996–2001. J. Geophys. Res.: Oceans 114 (C5).
Stabeno, P.J., Farley Jr., E.V., Kachel, N.B., Moore, S., Mordy, C.W., Napp, J.M., Overland, J.E., Pinchuk, A.I., Sigler, M.F., 2012. A comparison of the physics of the northern and southern shelves of the eastern Bering Sea and some implications for the ecosystem. Deep Sea Res. Pt. II 65, 14–30.
Stabeno, P.J., Duffy-Anderson, J.T., Eisner, L.B., Farley, E.V., Heintz, R.A., Mordy, C.W., 2017. Return of warm conditions in the southeastern Bering Sea: physics to fluorescence. PloS One 12 (9).
Steele, M., Ermold, W., Zhang, J., 2008. Arctic Ocean surface warming trends over the past 100 years. Geophys. Res. Lett. 35 (2).
Stigebrandt, A., 1984. The North Pacific: a global-scale estuary. J. Phys. Oceangr. 14 (2), 464–470.
Stocker, T.F., Qin, D., Plattner, G.K., Tignor, M., Allen, S.K., Boschung, J., Nauels, A., Xia, Y., Bex, V., Midgley, P.M., 2013. Climate Change 2013: the Physical Science Basis. Contribution of Working Group I to the Fifth Assessment Report of the Intergovernmental Panel on Climate Change, p. 1535.
Stroeve, J.C., Serreze, M.C., Fetterer, F., Arbetter, T., Meier, W., Maslanik, J., Knowles, K., 2005. Tracking the Arctic's shrinking ice cover: another extreme September minimum in 2004. Geophys. Res. Lett. 32 (4).
Stroeve, J.C., Serreze, M.C., Holland, M.M., Kay, J.E., Malanik, J., Barrett, A.P., 2012. The Arctic's rapidly shrinking sea ice cover: a research synthesis. Climatic Change 110 (3–4), 1005–1027.
Suydam, R., George, J.C., Rosa, C., Person, B., Hanns, C., Sheffield, G., Bacon, J., 2006. Subsistence Harvest of Bowhead Whales (Balaena Mysticetus) by Alaskan Eskimos during 2010. Unpubl. paper to the IWC Scientific Committee.
Tachibana, Y., Komatsu, K.K., Alexeev, V.A., Cai, L., Ando, Y., 2019. Warm hole in Pacific Arctic sea ice cover forced mid-latitude Northern Hemisphere cooling during winter 2017–18. Sci. Rep. 9 (1), 1–12.
Takenouti, A.Y., Ohtani, K., 1974. Currents and water masses in the Bering Sea: a review of Japanese work. Oceanogr. Bering Sea 2, 39–57.
Taylor, P.C., Hegyi, B.M., Boeke, R.C., Boisvert, L.N., 2018. On the increasing importance of air-sea exchanges in a thawing Arctic: a review. Atmosphere 9 (2), 41.
Thoman, R.L., Bhatt, U.S., Bieniek, P.A., Brettschneider, B.R., Brubaker, M., Danielson, S. L., Labe, Z., Lader, R., Meier, W.N., Sheffield, G., Walsh, J.E., 2020. The record low Bering Sea ice extent in 2018: context, impacts, and an assessment of the role of anthropogenic climate change. Bull. Am. Meteorol. Soc. 101 (1), S53–S58.
Timmermans, M.L., Proshutinsky, A., Golubeva, E., Jackson, J.M., Krishfield, R., McCall, M., Platov, G., Toole, J., Williams, W., Kikuchi, T., Nishino, S., 2014. Mechanisms of Pacific summer water variability in the Arctic's Central Canada Basin. J. Geophys. Res.: Oceans 119 (11), 7523–7548.
Timmermans, M.L., Toole, J., Krishfield, R., 2018. Warming of the interior Arctic Ocean linked to sea ice losses at the basin margins. Sci. Adv. 4 (8), 6773.
Tokinaga, H., Xie, S.P., Mukougawa, H., 2017. Early 20th-century Arctic warming intensified by Pacific and Atlantic multidecadal variability. Proc. Natl. Acad. Sci. Unit. States Am. 114 (24), 6227–6232.
Trenberth, K.E., Fasullo, J.T., Kiehl, J., 2009. Earth's global energy budget. Bull. Am. Meteorol. Soc. 90 (3), 311–324.
Van Vorhees, D., Lowther, A., 2010. Fisheries of the United States 2009. Current Fishery Statistics No. 2009. National Marine Fisheries Service, Silver Spring, MD, p. 103.
Walsh, J.J., McRoy, C.P., Coachman, L.K., Goering, J.J., Nihoul, J.J., Whitledge, T.E., Blackburn, T.H., Parker, P.L., Wirick, C.D., Shuert, P.G., Grebmeier, J.M., 1989. Carbon and nitrogen cycling within the Bering/Chukchi Seas: source regions for organic matter effecting AOU demands of the Arctic Ocean. Prog. Oceanogr. 22 (4), 277–359.

Walsh, J.E., Thoman, R.L., Bhatt, U.S., Bieniek, P.A., Brettschneider, B., Brubaker, M., Danielson, S., Lader, R., Fetterer, F., Holderied, K., Iken, K., 2018. The high latitude marine heat wave of 2016 and its impacts on Alaska. Bull. Am. Meteorol. Soc. 99 (1), S39–S43.
Walther, G.R., Post, E., Convey, P., Menzel, A., Parmesan, C., Beebee, T.J., Fromentin, J. M., Hoegh-Guldberg, O., Bairlein, F., 2002. Ecological responses to recent climate change. Nature 416 (6879), 389.
Weingartner, T.J., Danielson, S., Sasaki, Y., Pavlov, V., Kulakov, M., 1999. The Siberian Coastal Current: a wind-and buoyancy-forced Arctic coastal current. J. Geophys. Res.: Oceans 104 (C12), 29697–29713.
Weingartner, T.J., Danielson, S.L., Potter, R.A., Trefry, J.H., Mahoney, A., Savoie, M., Irvine, C., Sousa, L., 2017. Circulation and water properties in the landfast ice zone of the Alaskan Beaufort Sea. Continent. Shelf Res. 148, 185–198.
Weingartner, T.J., Danielson, S.L., Royer, T.C., 2005a. Freshwater variability and predictability in the Alaska coastal current. Deep Sea Res. Pt. II 52 (1–2), 169–191.
Weingartner, T., Aagaard, K., Woodgate, R., Danielson, S., Sasaki, Y., Cavalieri, D., 2005b. Circulation on the north central Chukchi Sea shelf. Deep Sea Res. Pt. II 52 (24–26), 3150–3174.
Wettlaufer, J.S., 1991. Heat flux at the ice-ocean interface. J. Geophys. Res.: Oceans 96 (C4), 7215–7236.
Wiseman Jr., W.J., Rouse Jr., L.J., 1980. A coastal jet in the Chukchi Sea. Arctic 21–29.
Woodgate, R.A., 2018. Increases in the Pacific inflow to the Arctic from 1990 to 2015, and insights into seasonal trends and driving mechanisms from year-round Bering Strait mooring data. Prog. Oceanogr. 160, 124–154.
Woodgate, R.A., Aagaard, K., 2005. Revising the Bering Strait freshwater flux into the Arctic Ocean. Geophys. Res. Lett. 32 (2).
Woodgate, R.A., Aagaard, K., Weingartner, T.J., 2005a. Monthly temperature, salinity, and transport variability of the Bering Strait through flow. Geophys. Res. Lett. 32 (4).
Woodgate, R.A., Aagaard, K., Swift, J.H., Falkner, K.K., Smethie Jr., W.M., 2005b. Pacific ventilation of the Arctic Ocean's lower halocline by upwelling and diapycnal mixing over the continental margin. Geophys. Res. Lett. 32 (18).
Woodgate, R.A., Aagaard, K., Weingartner, T.J., 2005c. A year in the physical oceanography of the Chukchi Sea: moored measurements from autumn 1990–1991. Deep Sea Res. Pt. II 52 (24–26), 3116–3149.
Woodgate, R.A., Aagaard, K., Weingartner, T.J., 2006. Interannual changes in the Bering Strait fluxes of volume, heat and freshwater between 1991 and 2004. Geophys. Res. Lett. 33 (15).
Woodgate, R.A., Weingartner, T., Lindsay, R., 2010. The 2007 Bering Strait oceanic heat flux and anomalous Arctic sea-ice retreat. Geophys. Res. Lett. 37 (1).
Woodgate, R.A., Weingartner, T.J., Lindsay, R., 2012. Observed increases in Bering Strait oceanic fluxes from the Pacific to the Arctic from 2001 to 2011 and their impacts on the Arctic Ocean water column. Geophys. Res. Lett. 39 (24).
Woodgate, R.A., Stafford, K.M., Prahl, F.G., 2015. A synthesis of year-round interdisciplinary mooring measurements in the Bering Strait (1990–2014) and the RUSALCA years (2004–2011). Oceanography 28 (3), 46–67.
Zhang, J., Woodgate, R., Moritz, R., 2010. Sea ice response to atmospheric and oceanic forcing in the Bering Sea. J. Phys. Oceangr. 40 (8), 1729–1747.
Zhang, J., Schweiger, A., Webster, M., Light, B., Steele, M., Ashjian, C., Campbell, R., Spitz, Y., 2018. Melt pond conditions on declining Arctic sea ice over 1979–2016: model development, validation, and results. J. Geophys. Res.: Oceans 123 (11), 7983–8003.

Deep–Sea Research II 177 (2020) 104802

Contents lists available at ScienceDirect

Deep-Sea Research Part II

journal homepage: http://www.elsevier.com/locate/dsr2

Shifts in the physical environment in the Pacific Arctic and implications for ecological timing and conditions

Matthew R. Baker [a,*], Kirill K. Kivva [b], Maria N. Pisareva [c], Jordan T. Watson [d], Julia Selivanova [b,c]

[a] North Pacific Research Board, 1007 West Third Avenue, Anchorage, AK, 99501, USA
[b] Russian Federal Research Institute of Fisheries and Oceanography, 17 V. Krasnoselskaya, Moscow, 107140, Russia
[c] Shirshov Institute of Oceanology, Russian Academy of Sciences, 36 Nakhimovsky Prospekt, Moscow, 117997, Russia
[d] National Oceanic and Atmospheric Administration, Alaska Fisheries Science Center, Auke Bay Laboratories, 17109 Pt. Lena Loop Road, Juneau, AK, 99801, USA

ARTICLE INFO

Keywords:
US
Russia
Bering Sea
Chukchi Sea
Marine system
Sea ice
Sea surface temperature
Hydrography
Water masses
Wind
Phenology
Climate
International collaboration

ABSTRACT

The northern Bering Sea and Chukchi Sea represent the gateway from the Pacific to the Arctic. This contiguous marine system encompasses one of the largest continental shelves in the world and serves as the sole point of connection between the North Pacific and Arctic Ocean. This region has unique attributes and complex dynamics, driven by the convergence of distinct water masses, dynamic currents, advection between Pacific and Arctic systems, and important latitudinal gradients relevant to stratification and water mass structure, water temperature, and seasonal ice cover. Many processes and interactions in the region appear to be changing with important implications for both hydrography and ecology. Our analyses access remote and local data sources in US and Russian waters to characterize oceanographic conditions and analyze the implications of dramatic shifts in recent years. Previously, this region appeared resistant to trends apparent elsewhere in the greater Arctic. Now, the Pacific Arctic also appears to be in rapid transition. The conditions observed in 2017–2019 are unprecedented. We note important shifts in the phenology and magnitude of physical variables, including sea-ice extent, concentration, and duration, as well as extreme reduction in the extent and intensity of the related Bering Sea cold pool. We also note distinct regional dynamics in sea surface temperature in the Bering-Chukchi system, distinguishing western, eastern and northern areas of the Bering Sea. Specifically, our analyses distinguish the northern Bering Sea as an important transition zone between the Pacific and Arctic with higher frequency variability in sea surface temperature anomalies. Our results suggest that the strength and position of the Aleutian Low may be linked to warm and cold phases in the Bering Sea and has an important role in large-scale circulation. While cold winds out of the north are necessary to form ice in the northern Bering Sea, strong winds may be associated with weak sea ice, as wind action may break ice and enhance vertical mixing, counteracting enhanced sea-ice production from the advection of cold air. Research in this important region is complicated by international borders but may be enhanced through international collaboration. This analysis represents an attempt to integrate data across Russian and US waters to more fully represent system-wide processes, to contrast regional trends, and to better understand physical interactions.

1. Introduction

1.1. Pacific-Arctic system

The Pacific Arctic region, spanning the Bering-Chukchi complex (Fig. 1), encompasses the sole ocean conduit between the Pacific and the Arctic, linked by the narrow (85 km) and shallow (50 m) Bering Strait. Despite annual mean northerly winds (Woodgate et al., 2005), mean transport though the Bering Strait is 0.8 Sv northward (Sv, Sverdrup, is a non-SI unit of flow; 1 Sv = 10^6 m^3 s^{-1}; Ratmanov, 1937; Natarov, 1963; Coachman et al., 1975; Woodgate et al., 2005), though recent analyses indicate sustained increases (~1.2 Sv) in Bering Strait inflow to the Arctic (Woodgate, 2018). Transport is highly variable and reversible with a range of -2 to 3 Sv (Roach et al., 1995). Northward transport of Pacific waters imports carbon, nutrients, and plankton into the Arctic (Asahara et al., 2012; Torres-Valdes et al., 2013); it also transports heat

* Corresponding author.
E-mail address: Matthew.Baker@nprb.org (M.R. Baker).

https://doi.org/10.1016/j.dsr2.2020.104802
Received 1 August 2019; Received in revised form 13 May 2020; Accepted 13 May 2020
Available online 27 May 2020

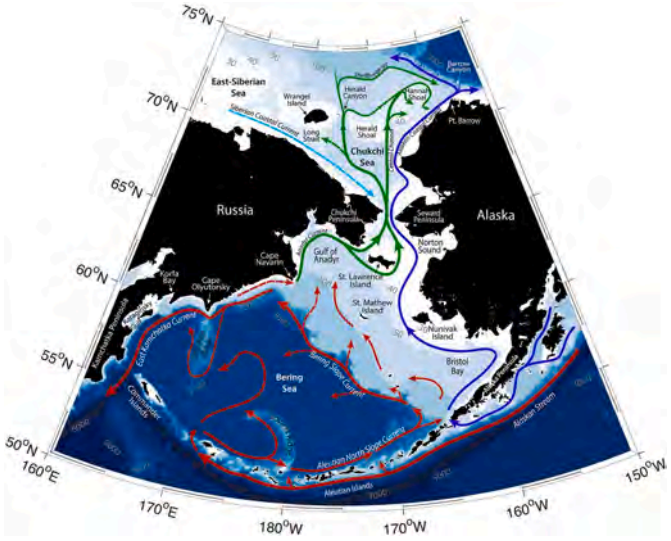

Fig. 1. Map of the Pacific Arctic (50–75N, 160E-150W), including the Bering Sea and Chukchi Sea. Important regional areas and broadscale circulation patterns are detailed. Solid arrows indicate observed currents and dashed arrows indicate modeled or quasi-permanent flow; circulation patterns and current vectors in the Chukchi Sea were informed by Pisareva et al., (2015) and Pickart et al., (2016).

and has important influences on Arctic sea ice (Woodgate et al., 2010) and global hydrologic (Aagaard and Carmack, 1989) and thermal-haline circulation (Hu et al., 2010). Throughout this region, there are important and distinctive north-south gradients. These latitudinal gradients, however, appear to be shifting with important implications for each regional system, as well as for broader Pacific-Arctic interactions. Each system in the study area is briefly described below.

1.1.1. *Western Bering Sea and Basin*

The western Bering Sea (WBS) shelf is narrow (40–130 km), extending from Cape Navarin in the north to the Commander Islands and southern Kamchatka Peninsula (Kivva et al., In Press). Flow is southward along the shelf break (Natarov, 1963), dominated by the East Kamchatka Current (referred to as the 'Kamchatka Current' in some literature), a western boundary current driven by gyre dynamics associated with the adjacent Bering Sea Basin (Verkhunov and Tkachenko, 1992; Verkhunov, 1995). This flow accelerates in winter (Nov–Mar) and slows in summer (May–Aug). In contrast to temperature gradients, salinity increases through the water column. The narrow WBS shelf has higher per-unit-area pelagic production, compared with other regions in the Bering and Chukchi seas (Aydin et al., 2002; Aydin and Mueter, 2007). The vertical structure in the WBS includes an upper mixed layer (0–25 m), cold intermediate layer (55–250 m), warm intermediate layer (250–500 m), and deep Pacific water mass (>500 m; Khen et al., 2015). The depth of convection depends on winter heat loss. The bottom of this active layer is deepest along the Kamchatka Peninsula (Luchin, 2007, Luchin et al., 2009). North of Cape Navarin, flow drives northward to the Gulf of Anadyr, over the northern Bering Sea shelf and subsequently through the Bering Strait (Khen, Pacific Research Fisheries Center, TINRO, Vladivostok, Russia, personal communication). There are as many as 11 distinct water masses that converge in the area north of Cape Navarin (Danielson et al., 2011), including Bering Shelf Water, Anadyr Water, shelf and shallow basin waters, and coastal waters.

1.1.2. *Eastern Bering Sea*

The eastern Bering Sea is defined by a broad (~500 km wide) highly productive continental shelf that extends from the Alaska Peninsula to the Bering Strait, typically defined by three oceanographic depth domains (Inner: 0–50 m, middle: 50–100 m, and outer: 100–200 m). There is also a distinct separation north-south defined by temperature. A 'cold pool' of bottom water <2 °C extends southwards through the middle domain (Wyllie-Echeverria, 1995; Wyllie-Echeverria and Wooster, 1998; Stabeno et al., 2016). This oceanographic feature represents the footprint of winter sea ice and usually persists throughout the summer. In warm years, the cold pool is restricted to the north. In cold years, it may extend to the Alaska Peninsula (Stabeno et al., 2012a). The cold pool serves as both a barrier and thermal refuge to fish and invertebrate populations and contributes to a strong latitudinal gradient in physical dynamics and ecosystem structure (Mueter and Litzow, 2008; Baker and Hollowed, 2014; Ortiz et al., 2016). The southeastern Bering Sea (EBS) is a subarctic system with significant groundfish populations and significant pelagic and benthic energy pathways (Aydin et al., 2002; Aydin and Mueter, 2007). This is in stark contrast to the Arctic systems of the northern Bering Sea (NBS) and Chukchi Sea, which are dominated by benthic invertebrates and benthic energy pathways (Grebmeier et al., 1988; Grebmeier et al., 2006; Whitehouse et al., 2014). Previous studies have demonstrated that not only physical properties, but also species distribution and community composition are distinct in the EBS and NBS (Mueter and Litzow, 2008; Stevenson and Lauth, 2012; Baker and Hollowed, 2014) with the relative extent of each biogeographic area reflective of temperature regimes (Baker and Hollowed, 2014). While the conditions of the EBS shelf generally reflect a subarctic system, the cold pool of the middle EBS shelf more closely resembles an Arctic system (Wyllie-Echeverria, 1995) and therefore represents a variable extension of Arctic conditions associated within the NBS and into the EBS area.

1.1.3. *Northern Bering Sea*

The seasonally ice-covered NBS encompasses the continental shelf north of 60°N (Sigler et al., 2017), and includes areas north of the Anadyr River and Yukon River drainages (Andriashev, 1939). This system ranges from Russian coast in the west to the Alaska Coast in the east (Golikov et al., 1990) and north to the Bering Strait. Mean current flow is northward into the Arctic Ocean most of the year (Coachman, 1993; Danielson et al., 2014) and transport plays an important role in exchange and advection of production from the Pacific to Arctic (Panteleev et al., 2012). This ecosystem is characterized by distinct regional dynamics in wind stress and circulation, the integration of various water masses, fluctuating sea ice, highly seasonal production, and benthic-dominated trophic transfer (Grebmeier et al., 2006). Historically, important differences in water column physics have been noted between the otherwise contiguous northern and southern sectors of the Bering Sea Shelf, with an Arctic-Subarctic temperature front (Stabeno et al., 2012b) and distinct nutrient loading (Kivva, 2016) at approximately 60°N. Until recently, the NBS has been more closely connected in hydrographic and biological characteristics to the Chukchi Sea to the north than to the southern portions of the Bering Sea (Walsh et al., 1997; Grebmeier et al., 2006; Stabeno et al., 2012b; Sigler et al., 2017). Distinct attributes related to physical oceanography, biogeography, species distributions and community structure in the NBS, EBS and WBS are further detailed in Baker (In Press), Siddon (In Press) and Kivva et al. (In Press).

1.1.4. *Bering Strait*

Northward flow is the defining hydrographic feature in the Bering Strait. Mean northward transport is caused by the pressure head between the Pacific and Arctic Oceans (Coachman and Aagaard, 1966; Woodgate et al., 2012) and wind effects. This transports a significant volume of freshwater (Aagaard and Carmack, 1989; Woodgate et al., 2012) and heat (Woodgate et al., 2007; Steele et al., 2008) and has strong influence on the circulation, physical processes and ecosystem structure of the Arctic (Pickart et al., 2005). Peak northward flow occurs in June–July. In the summer, warm fresh waters are at the surface, while in autumn, temperature inversion occurs with colder waters overlying warmer saltier waters. Homogenization occurs in winter as a result of

wind-driven or flow-related mixing, convection due to heat fluxes, and brine rejection due to ice formation (Woodgate et al., 2015).

1.1.5. Chukchi Sea

The Chukchi Sea is an important transition region for Pacific waters entering the Arctic Basin (Pisareva, 2018). It is also one of the most productive areas of the world's oceans (Walsh et al., 2005). North of Bering Strait, seafloor topography directs flow along Herald Canyon in the west, Barrow Canyon in the east, and the Central Channel (Woodgate et al., 2005). Residence time and water properties are heavily influenced by the throughflow from the Bering Sea (Woodgate et al., 2015). These Pacific waters are detectable in parts of the upper Arctic Ocean (Steele et al., 2008) and influence recession of sea ice in the Arctic. In summer, Pacific Water adds subsurface heat. In winter, Pacific Water forms a protective layer between the winter sea ice and warmer Atlantic waters (Francis and Hunter, 2006; Shimada et al., 2006; Woodgate et al., 2010).

1.1.6. Integrated Pacific-Arctic System

The systems within the Pacific Arctic region, while distinct, are strongly interconnected and trends in each should be considered in assessing northern hemispheric ecosystem change (Brown and Arrigo, 2012). Importantly, attributes that have historically distinguished these regions (particularly the thermal barrier between the southern and northern Bering Sea shelf), appear to be eroding at a rate and to an extent that far exceed predictions made only a few years ago (Stabeno et al., 2012b; Lomas and Stabeno, 2014).

1.2. Sea ice, cold pool and thermal regimes

Historically, the Bering Sea has been ice-free in summer and covered with extensive sea ice in winter, with mean maximum sea-ice extent in March (range = Jan–Apr; Wendler et al., 2014). In winter, atmospheric forcing and ocean circulation drive a sea-ice advance that is unparalleled in the northern hemisphere (Sigler et al., 2010). The Bering Sea cold pool represents the summer footprint of this seasonal sea-ice cover. Recently there has been a series of distinct thermal phases recognized in the EBS (Stabeno et al., 2001, 2007; 2012a,b; 2017, Stevenson and Lauth, 2019). Following a period of high interannual variability (1982–2000), the system transitioned into multi-year stanzas of warm (2000–2005, 2014–2016) and cold periods (2007–2013). These trends (April–August) have also been recognized in the WBS (Glebova et al., 2009), related to negative temperature anomalies in 2006–2013 correlated with cold winters and extensive sea ice (Khen et al., 2013). Khen and Zavolokin (2015) also showed differences in circulation between 2002-2006 and 2007–2011 related to changes in spring sea level pressure (SLP) patterns and Kivva et al. (In Press) notes that alternating cold (2006–2013) and warm (2000–2005, 2014–2016) phases were prevalent. A recent warm period initiated in 2014 throughout the Bering Sea, with 2014–2016 bottom temperatures well above the long-term mean (Conner and Lauth, 2017). In winter 2017–2018 the maximum extent of sea ice in the Bering Sea was the lowest on record.

1.3. Evidence of system change

In the past 50 years, the Arctic Ocean has experienced unprecedented and accelerating sea-ice loss (Walsh and Chapman, 2001; Stroeve et al., 2007; Comiso, 2012), with predictions for an ice-free Arctic (summer minimum) by mid-century (Wang and Overland, 2009). Multiple factors are driving reductions in sea-ice extent, concentration, and duration, including rising air temperature (Lindsay and Zhang, 2005), increased flux of warm water into the Arctic (Maslowski et al., 2001), and advection of ice out of the Arctic (Serreze et al., 2007). This reduction of sea ice has also initiated positive feedbacks (Perovich et al., 2007). Until recently, these processes appeared absent in the Pacific Arctic, especially the Bering Sea (Brown et al., 2011; Brown and Arrigo, 2012).

Prior to 2017, no significant trend in sea-ice extent in the Bering Sea was evident and it was assumed that seasonal sea ice would continue to form in the NBS (Walsh et al., 2017). Oceanographic conditions observed in 2017–2019, however, contradict these assumptions. Reductions in extent and duration of sea ice were evident in the satellite record, with virtually no sea ice in the EBS in winter 2017–2018 ($<0.2 \times 10^6$ km^2) and winter 2018–2019 ($<0.4 \times 10^6$ km^2; Stabeno et al., 2019). These conditions reflect the lowest sea-ice cover on record (Stabeno and Bell, 2019) and the first recorded absence of the cold pool. Shifts in salinity and nutrient dynamics (Stabeno et al., 2019), northward movement of sub-Arctic groundfish stocks (Stevenson and Lauth, 2019; Baker, In Press), and notable marine bird mortality events (Duffy-Anderson et al., 2019) were associated with these anomalous conditions. Pressing questions include whether this represents a phase or regime shift (Huntington et al., 2020) and the extent to which these processes and properties vary over decadal and interannual timeframes (Overland et al., 2012; Woodgate et al., 2015).

Documentation and analysis of trends and variability in sea ice are essential to project future trajectories and understand ecosystem implications (Walsh et al., 2017). The post-1979 satellite record provides insight into decadal variability. Our analysis explored this at various timeframes, comparing consecutive warm (2001–2005, 2014–2016) and cold (2007–2012) years, the preceding period of interannual variability (1982–1999), and recent anomalous conditions (2017–2018).

1.4. Integrated research and international coordination

Scientific access across the Bering-Chukchi complex is complicated by the political boundary between the United States and Russia (Kinney et al., 2014). Nevertheless, this region is also an area of active research for many Arctic states, including US, Russia, Japan, Korea, China, and Canada. Several international marine research and management organizations have been active in the region, including the Arctic Council, International Arctic Science Committee (IASC), North Pacific Marine Science Organization (PICES), Intergovernmental Consultative Committee (ICC), Ecosystem Studies of the Subarctic and Arctic Seas (ESSAS), and Pacific Arctic Group (PAG) (Van Pelt et al., 2017). Directed collaborative research between the US and Russia has occurred in the form of coordinated cruise transects in the long-term ecological investigations of the Bering Sea and other Pacific Ocean ecosystems (BERPAC, 1977–1995; Grebmeier et al., 2006) and the Russian American Long-term Census of the Arctic (RUSALCA, 2004–2011; Crane and Ostrovsky, 2015; Pisareva et al., 2015), joint mooring deployments (Woodgate et al., 2015), US-Russian cooperative surveys in the NBS and Gulf of Anadyr (1990; Sample and Nichol, 1994), Bering Aleutian Salmon International Surveys (BASIS), https://npafc.org/working-groups/#basis), and in the North Pacific Research Board (NPRB) Arctic Integrated Ecosystem Research program (Arctic IERP; Baker et al., This Issue).

Our analysis is part of an ongoing attempt to integrate scientific data from Russian and US surveys and moorings with region-wide satellite coverage to: (1) highlight recent trends relative to historical baseline conditions; and (2) investigate potential mechanisms and implications for the dramatic shifts in the physical conditions of this important Pacific-Arctic gateway. Observations are informed by research supported by NPRB, US National Oceanic and Atmospheric Administration (NOAA), Russian Federal Research Institute of Fisheries and Oceanography (VNIRO) and by discussions and exchange at the 2016 and 2017 PICES workshops on data sharing in the Northern Bering Sea (Eisner et al., 2017; Baker et al., 2018) and North Pacific Ecosystem Status Report (https://meetings.pices.int/projects/npesr).

2. Data and methods

Our analyses consider data at various resolutions and spatial scales, consistent with different sources of remote sensing and in situ data. We examine sea ice, sea surface and bottom temperature data along north-

south gradients within the Bering Sea and Chukchi Sea complex. We also examine east-west gradients, use patterns in sea surface temperatures (SST) to identify areas of statistical convergence and differentiation, and examine the influence of wind and atmospheric processes. We then apply these results to identify sub-regional patterns in the shelf-basin system and to provide insight as to how regional properties influence system-scale processes.

2.1. Regional delineation of the Pacific Arctic – cluster analysis

2.1.1. Data

To evaluate the entire Bering-Chukchi Sea complex (50–76°N, 162E-156°W), the NOAA Optimum Interpolation Sea-Surface Temperature V2 monthly data product was used. This dataset has spatial resolution of 1° × 1°, with temporal coverage from 1981 to present (https://www.esrl.noaa.gov/; Reynolds et al., 2002). Data for complete years from 1982-2018 were used in our analysis. Clustering was performed to group grid nodes with similar variability in sea surface temperature anomalies (SSTA). Correlation was chosen as a measure of similarity instead of Euclidian distance. This allowed us to group grid nodes with similar SSTA dynamics (patterns over time), rather than absolute values, and delineate regions of synchronous SSTA. The dimensionality of the initial data was 860 × 444 (grid nodes × monthly SST or SSTA values). Annual mean SSTA values were calculated to reduce dimensionality of the data. Monthly SST values were averaged over every year (1982–2011) and the 30-yr mean was calculated for every grid node. This 30-year mean was subsequently subtracted from annual mean SST time-series for every grid node. Data normality was checked with the Shapiro-Wilk test. Annual mean SSTA values of many grid nodes for 1982–2011 could not be treated as normally distributed (160 of 860 data points had W-values < 0.927 with p-values < 0.05). Data were positively skewed in areas close to Cape Navarin, Cape Olyutorsky and Karaginsky Gulf and negatively skewed in Norton Sound. Areas north of 72° N were covered by sea ice almost permanently until recent years. This resulted in SST values (SST = −0.4 to +0.1 °C) close to the freezing point for sea water (SST ~ −1.7 °C) in most of the time series, whereas many grid nodes in this area were seasonally ice-free in recent years (SSTA = +0.5–1.0 °C). To account for this skewed distribution, we used the non-parametric Spearman correlation coefficient.

2.1.2. Clustering approach

The DBSCAN algorithm (Density-Based Clustering for Applications with Noise; Ester et al., 1996) and the "dbscan" package in R [https://cran.r-project,org/web/packages/dbscan/dbscan.pdf] were used to identify clusters of similar SSTAs for grid cells in the Bering-Chukchi regions. This approach searched for data points with more than N nearest neighbors ('minPts') within a certain radius (ε, 'eps'). Those data points are assigned 'core points'. All neighbors of core point within ε radius were considered to belong to the same cluster ('direct density reachable' points). The DBSCAN result depends on the choice of eps and minPts parameters and should balance the signal to noise ratio (Schubert et al., 2017). For our purpose, we limited 'noise' to values between 0.1-0.3. We performed clustering for all combinations of minPts between 5-70 and eps between 0.04-0.18 with step 0.02 and documented the number of clusters and noise ratio for every combination (Appendix, Fig. A-1), and visualized all results (Appendix, Fig. A-2, A-3). Results were similar and we choose minPts = 31 for subsequent analysis and set eps = 0.1. Data included 1982–2018 (444 months). Clustering was based on annual SSTA values as it was difficult to perform clustering on monthly values without dimensionality reduction.

2.1.3. Regional monthly SSTA calculation

Regional SSTA values (1982–2018) were calculated as the monthly value minus the mean value for the month of interest from a 30-year baseline reference period (1982-2011), excluding periods of recent warming. This allowed us to remove variance related to seasonal cycle and focus on relative cold and warm events. The SSTA time series were averaged across every region, weighting by the cosine of the latitude of the grid nodes. The annual SSTA values were calculated as January–December means. All months were divided into five categories based on the standard deviation (SD). Months with absolute SSTA values > 2SD were considered extremely cold or extremely warm (depending on the sign of SSTA value). Absolute SSTA values between 1 SD and 2 SD were classified as cold or warm, and months with values between -1SD and +1SD were considered normal.

2.2. Bering Sea – sea surface temperature

To evaluate regional differences at higher resolution within the Bering Sea, SST data from the NOAA Coral Reef Watch version 3.1 operational global satellite (pacioos.hawaii.edu/metadata/dhw_5km.htm) were applied. Data were accessed via the Pacific Islands Ocean Observing System ERDDAP site (https://pae-paha.pacioos.hawaii.edu/erddap/index.html) and spanned 01 January 1986–31 December 2019. These data include daily satellite information with a 5-km spatial resolution. Data were spatially apportioned to the EBS, NBS, and WBS using the PICES NPESR Working Group 35 spatial boundaries for regions 13, 14, and 16, respectively (https://meetings.pices.int/projects/npesr). Because we were primarily interested in shelf habitats, data were limited to locations with depths between 10 m and 200 m, as determined from Amante and Eakins (2009), accessed via the *marmap* package (Pante and Simon-Bouhet, 2013) in R. The spatial extent of each system (EBS, WBS, NBS) as defined for this analysis is shown in Appendix (Fig. A-4). Seasonal components were removed from time series using an additive decomposition with a frequency of 365 using the *fpp2* package (Hyndman and Athanasopoulos, 2018) in R Statistical Software (version 3.5.0). In addition to an analysis of trends in the time series of the EBS, NBS, and WBS during different climatic phases (e.g. warm, cool), we also directly compared the EBS and NBS, decomposing the time series as a reflection of their difference in temperature (also see Watson, 2019).

2.3. Sea-ice concentration

Sea-ice concentration (SIC) data were obtained from the Climate Data Record (CDR) of the National Snow and Ice Data Center (NSIDC) (Meier et al., 2017a). Data were derived from Special Sensor Microwave Imager (SSM/I) and Special Sensor Microwave Imager and Sounder (SSMIS) passive microwave radiometers and processed with a bootstrap algorithm (Peng et al., 2013). CDR is currently limited to the years 1979–2017. Version 1 of the near-real time Climate Data Record (NRT-CDR) was used for 2018 (Meier et al., 2017b). This product is based on SSMIS data, produced using bootstrapping and NASA algorithms. Both data sets are based on the polar stereographic grid of nominal resolution 25 × 25 km.

2.4. Sea-ice retreat

Similar to many previous studies, we used the SIC threshold approach to define the date of sea-ice retreat (DOR) (e.g. Stroeve et al., 2016; Lebrun et al., 2019). Different thresholds (e.g. 0.15, 0.30, and 0.50 fractional areal coverage) revealed similar results in previous studies; we chose 0.15 as a threshold. Data were smoothed by a 7-day running mean to filter out high-frequency synoptic variability, following Peng et al. (2018). While most previous studies used the first day when SIC fell below the threshold level as the DOR, our study focused on how changes in physical environment may alter biological processes. Thus, we determined the best metric to signal the shift to an ice-free state would be the last date on which SIC reached the 0.15 threshold.

2.5. Ice extent and open water index

Areal extent of open water in the Bering Sea and Chukchi Sea was

calculated using the National Snow and Ice Data Center [https://nsidc.org/data] regional monthly sea ice data index [Sea Ice Index Regional Monthly Data G02135_v3.0], using 15% SIC. Data were compiled using passive microwave estimates of Arctic sea-ice extent (1979-present). Regional extent for the Bering Sea and Chukchi Sea were comprehensive and defined by the NSIDC (https://nsidc.org/data/masie/browse_regions; Appendix, Fig. A-5). In the Bering Sea, our index of interest was the extent of sea-ice coverage. We measured sea ice at a standard reference date of March 15 (approximate mid-point for the timeframe of mean annual maximal ice extent in February–April; Appendix, Fig. A-6). We calculated an annual index of open water as a function of the deviation of March 15 ice extent in each year from maximum March 15 sea-ice extent in the timeseries. In the time series, maximum sea-ice extent occurred in 2012 (817,752 km^2). In the Chukchi Sea, our interest was spring melt and the location of ice edge at peak primary production. We used a standard reference date of May 15, which historically coincides with the initiation of sea-ice retreat, the onset of open water production (Wang et al., 2005; Zhang et al., 2015), and chlorophyll a (chl-a) maximum associated with under-ice blooms (Brown et al., 2015). We calculated open water as the difference between the full areal extent of Chukchi Sea (800,000 km^2) minus the areal extent of sea ice within that region on May 15. Regression analyses were performed in SigmaPlot (Systat Software). All other statistical applications were applied using R statistical computing software (R Development Core Team, 2019; http://www.r-project.org/index.htm).

2.6. Bering Sea cold pool

The annual extent of the Bering Sea cold pool (bottom temperatures ≤ 2 °C; Stevenson and Lauth, 2019; Thorson, 2019) was estimated via data collected in the annual NOAA bottom trawl surveys of the EBS and NBS conducted during the summer months of 1982–2018 (Stevenson and Lauth, 2019). In all years, the survey covered the EBS shelf from the Alaska Peninsula to approximately 61°N. Surveys conducted in 2010, 2017 and 2018 also encompassed US waters within the NBS. Bottom water temperatures were recorded using a Sea-Bird SBE-39 datalogger (Sea-Bird Electronics, Inc., Bellevue, WA) attached to the trawl headrope. Bottom temperatures were recorded at each survey station. Maps of the cold pool area were developed in ArcGIS using Inverse Distance Weighting (IDW) interpolation. Statistical analyses were developed in R statistical computing software (R Development Core Team 2019). Differences in the areal extent of the cold pool were assessed using analysis of variance (ANOVA) and Tukey's HSD test on pairwise comparisons.

2.7. Sea surface pressure and wind vectors

Composite maps of mean sea level pressure (SLP) fields and 10-m winds were constructed for winter months (November–March) with the use of 1 h ERA5 atmospheric reanalysis with 0.25° spatial resolution. The ERA5 reanalysis data were downloaded from the European Centre for Medium-Range Weather Forecasts (ECMWF) website https://www.ecmwf.int/en/forecasts/datasets/archive-datasets/reanalysis-datasets/era5.

3. Results

3.1. Delineation of regions in the Pacific Arctic

To identify regional boundaries according to patterns in mean monthly SSTA, we set the minPts parameter of DBSCAN to 31 and varied the eps parameter to choose the best spatial organization of clusters and minimize noise. Setting eps = 0.12 resulted in three clusters with noise ratio of 0.18 (Fig. 2a, left plot). A decrease in eps (eps = 0.10) resulted in an increase of the noise ratio and a simultaneous decrease of cluster areas (Fig. 2a, center plot). Further reduction in eps values resulted in the separation of the Chukchi-Siberian cluster into two clusters with an increase in noise to 0.4 (Fig. 2a, right plot). Values of eps between 0.1334-0.1344 resulted in collapsing three clusters into two clusters (Appendix A; Fig. A-2), and eps >0.1345 resulted in only one cluster with very few points assigned as 'noise'. Results for eps of 0.08–0.12 reflected meaningful physical boundaries. Areas north of Bering Strait usually experienced more severe ice conditions (i.e. higher concentrations, greater ice thickness, and longer duration of ice cover) than other regions. Due to more extensive ice cover, annual mean SSTs were low and interannual variability was lower than south of Bering Strait. The area of the Chukchi and East-Siberian seas (CS-ESS) divided into two clusters roughly along the boundary between those two seas. This is probably a reflection of different processes controlling thermal conditions in each sea; the Chukchi Sea is more strictly controlled by the inflow of the warm Bering Sea waters than the East-Siberian Sea. All combinations of eps and minPts resulted in the separation of the Bering Sea into at least two clusters: western, and eastern. Larger eps values resulted in closer geographic location of margins of those clusters, while lower values led many of those grid nodes to be assigned as 'noise'. The final analysis (epsilon radius = 0.10; nearest neighbor minPts = 31) identified four regions in the Bering-Chukchi complex (Fig. 2b). The NBS (areas north of 60 °N) was comprised of areas assigned as 'noise' in the DBSCAN analysis. Those 'noise' regions were treated as a transition area between neighboring clusters. It is anticipated that NBS SSTA variability may at times match patterns of variability in the EBS, but at other times match patterns of variability in the Chukchi Sea, depending on atmospheric and marine circulation.

3.2. Regional patterns in SSTA in the Pacific Arctic

The final evaluation of SSTA variability 1982–2011 distinguished regionally coherent patterns in the CS-ESS, WBS, and EBS. We also identified the NBS as the area of high variability between 60-66 °N and 175°E -165°W (Fig. 2b). The NBS is a region of higher spatial and temporal SSTA variability and may be treated as transition region between three other regions. The CS-ESS region had generally low SSTA values, but anonymously warm spring-autumn conditions since 2016. The WBS and EBS regions behaved similarly, but with very different duration of cold/warm periods. For instance, 1998–2002 were substantially colder in the WBS, but only 1999 was cold in the EBS (2007–2012 were quite cold in the EBS, but only 2012 was cold in the WBS). Detailed results on each system are provided below.

3.2.1. Region 1 – CS-ESS

The north (CS-ESS) SSTA cluster (region1; Fig. 3, panel 1) exhibited little variability in SSTA in winter months because ocean water annually reaches the freezing point and SSTA values are therefore relatively constant. The highest interannual and within-region SSTA variability is seen in this region during summer. The SSTA time-series in this region may be roughly divided into three intervals: 1982–1989, 1989–2003, and 2004–2019. Before 1989, summer SST values were similar to winter values (e.g. the freezing point). This resulted in low SSTA values compared to later intervals. Between 1989 and 2003 many areas in the region started to experience ice-free conditions, which resulted in warmer SST and positive SSTA values. At the same time, most of the northern part of the cluster was still ice-covered even in summer. Exceptions occurred in 1990, 1993, and 1997, where SST values in most of the region were above the freezing point, which resulted in positive summer SSTA values. Since 2003, summer SSTA values have been mostly positive, with exceptions of high variability in the summers of 2006, 2008, and 2012–2013. Since 2004, the frequency of monthly SSTA values larger than the monthly standard deviation for the time series has increased, with several extremely warm months in spring and autumn.

3.2.2. Region 2 – WBS

Several distinct thermal regimes were observed in the WBS (region 2;

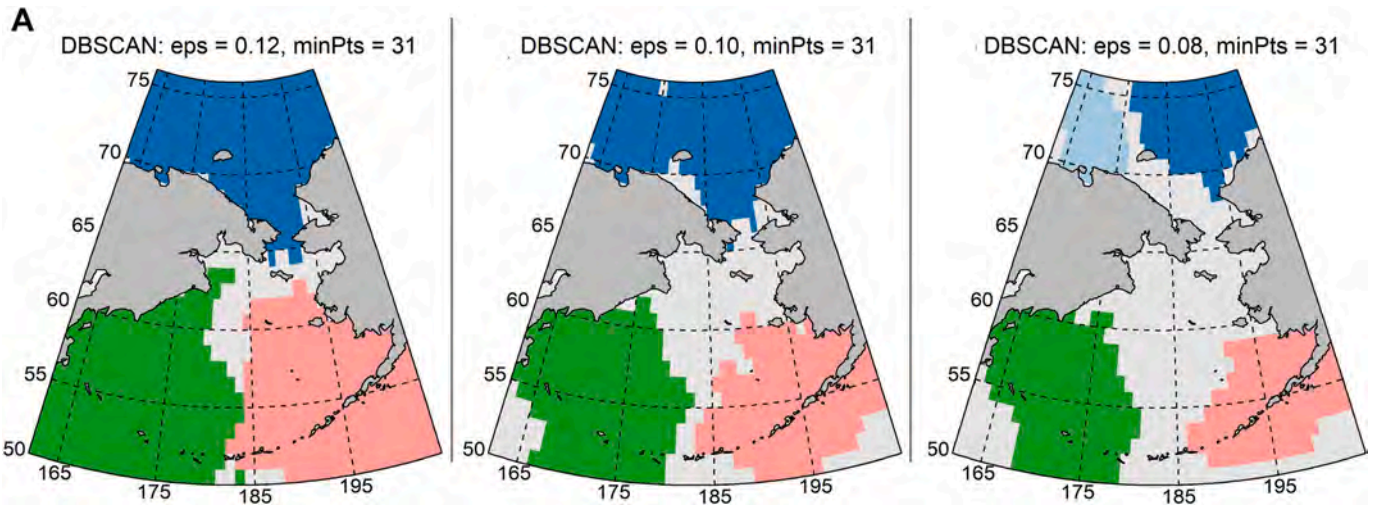

Fig. 2a. Annual mean SSTA clusters for regional delineation according to various input parameters in the DBSCAN analysis. The threshold for the number of neighbors (minPts) was set to 31. Radius ε (eps) varied between 0.12 (left), 0.10 (middle), and 0.08 (right).

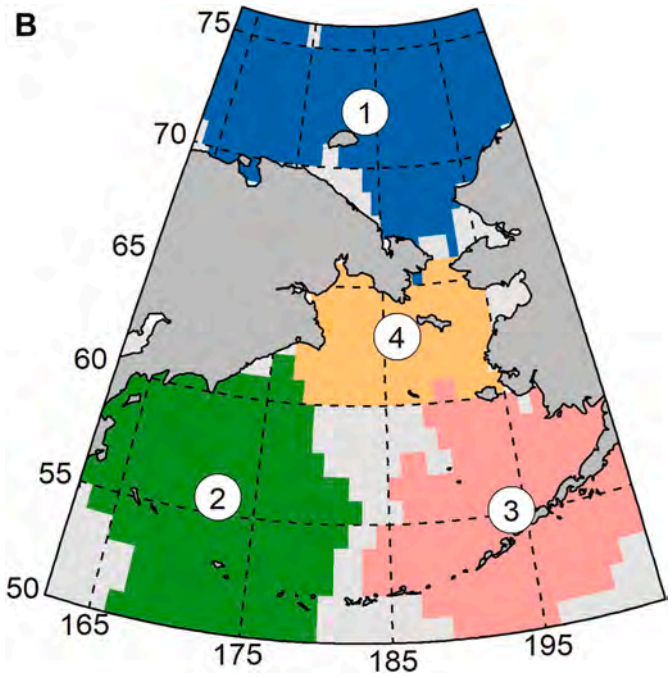

Fig. 2b. Regions delineated via DBSCAN (final analysis): Region 1 – Chukchi and East Siberian Seas (CS-EES, dark blue), Region 2 – western Bering Sea (WBS, green), Region 3 – eastern Bering Sea (EBS, pink), Region 4 – northern Bering Sea (NBS, orange). Note regions 1–3 are based on clustering of annual mean SSTA values with DBSCAN algorithm. Region 4 is the remaining grid nodes of this region assigned as 'noise' in the DBSCAN analysis. When eps = 0.10 is chosen (not eps = 0.08 or less) the dark blue region clearly includes large part of the East Siberian sea. (For interpretation of the references to color in this figure legend, the reader is referred to the Web version of this article.)

Fig. 3, panel 2). Normal-cold conditions characterized the early time series (1982–1995), followed by several warm years (1996–1998), then cold conditions (1999–2002), and then a prolonged warm phase (2003–2019) with a slight deviation toward colder conditions in 2012. The most extreme monthly temperatures in both warm (1996–1998) and cold (1999–2002) periods occurred in winter and spring. This suggests that winter-spring SST conditions may determine the thermal regime for the year (e.g. if winter/spring conditions are cold, the rest of the year will likely also be cold). Since 2003, warm conditions have predominated in the WBS, with few exceptions (though with large inter-annual SSTA variability). Mean annual SSTA values for all years except 2009 and 2012 were positive, and many months exhibited extremely warm conditions, particularly in summer. Since 2017, winter and spring conditions have been extremely warm. Thus 2003–2016 may be viewed as a period of variable warm conditions with a transition to extremely warm conditions in 2017–2019.

3.2.3. Region 3 – EBS

The EBS exhibited patterns in SST variability similar to the WBS, but with substantially shifted margins for the time intervals (region 3; Fig. 3, panel 3). Moreover, while the range of variability was similar in the WBS and EBS prior to 2006, the very cold period in the EBS (2007–2013) had no analog in the WBS. In the EBS, years 1982–1999 were highly variable without a distinct pattern, characterized by a series of transitions from relatively cold to relatively warm conditions with most monthly SSTA values falling between 0 ± 1 SD. This situation changed in 2000, followed by a relatively warm phase (2001–2005), a cold phase (2007–2013), and subsequent warm phase (2014–2019). In contrast to the WBS region, the EBS region exhibited extremely warm conditions in both winter and spring, starting in 2015.

3.2.4. Region 4 – NBS

According to our analysis, the NBS is a region of 'noise' meaning all grid nodes there experienced SSTA dynamics that substantially differed both from the dynamics of any grid node in previously described areas (regions 1–3) as well as from the dynamics of any neighboring nodes within this 'noise' region (region 4). While monthly regional mean SSTA in the WBS and EBS exhibited a series of cold-to-warm transitions, dynamics in the NBS exhibited higher frequency variability, on the scale of months (region 4; Fig. 3, panel 4). This is a region of high inter-annual temporal and within-cluster spatial SSTA variability. Still, patterns reflect those observed in other regions with relatively warm (2001–2003, 2014–2019) and cold (2008–2012) phases. This region may be characterized as a transition region with substantially higher spatial-temporal SST variability.

3.3. Identification of distinct climatic phases via SST

High-resolution satellite-based SST data confirm a sequence of distinct phases in the Bering Sea (Fig. 4, top panel). In the EBS, a period of high interannual variability (1987–2000), transitioned into multi-year stanzas of warm (2000–2005, 2014–2016, 2017–2019) and cold periods (2006–2013). These trends were roughly mirrored in the NBS

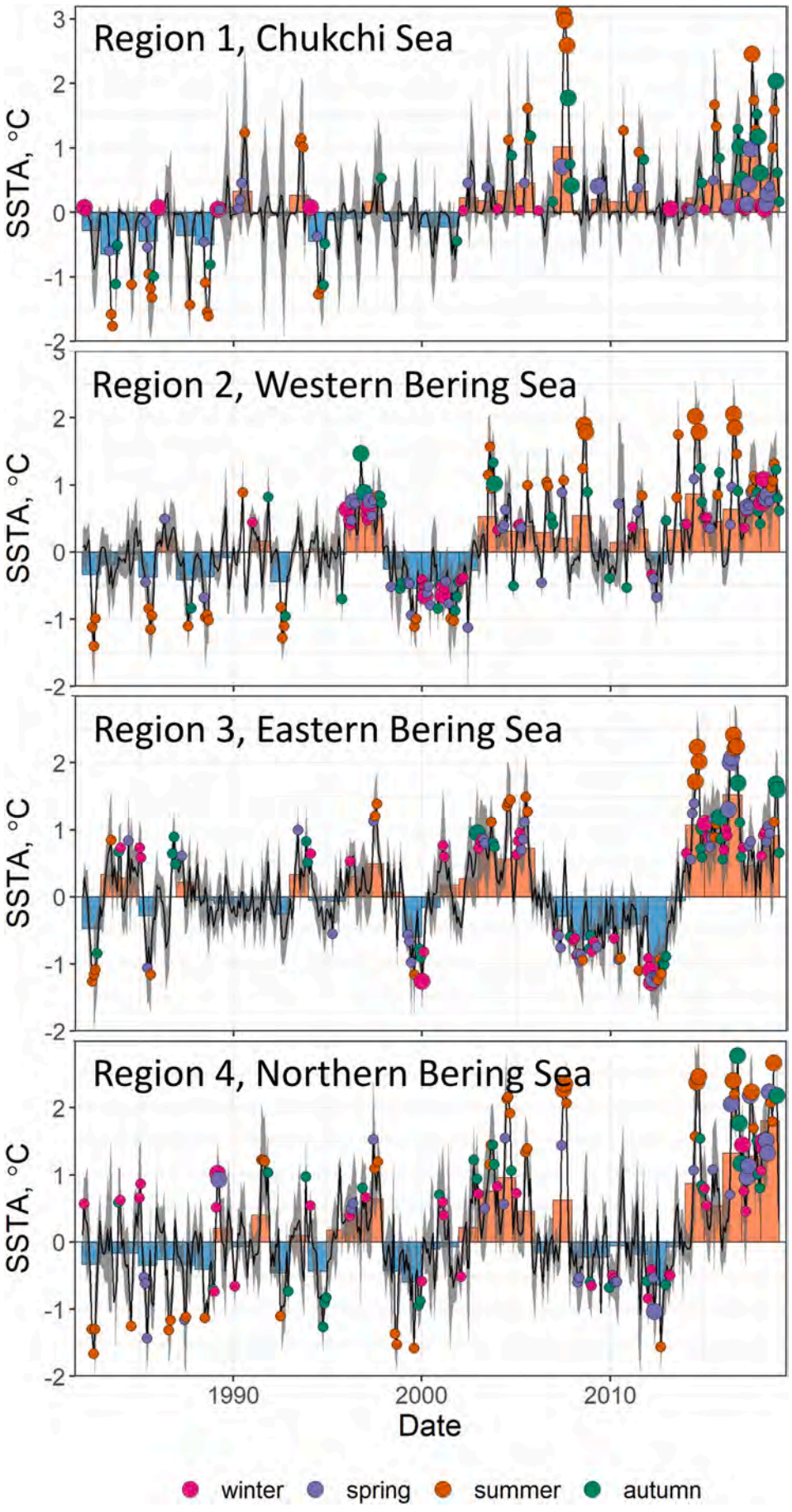
Region 1, Chukchi Sea
Region 2, Western Bering Sea
Region 3, Eastern Bering Sea
Region 4, Northern Bering Sea
SSTA, °C
3
2
1
0
-1
-2
1990
2000
2010
Date
winter
spring
summer
autumn

Fig. 3. Sea surface temperature anomalies (SSTA). Trends correspond to the 4 regions defined through cluster analyses (Fig. 2b), including (top plot to bottom plot) CS-ESS (region 1), WBS (region 2), EBS (region 3), and NBS (region 4). The solid black line depicts the monthly regional mean SSTA. Gray semi-transparent shading illustrates the monthly regional standard deviation (i.e., the measure of monthly spatial variability of SSTA in each region). Bars represent annual region mean SSTA. Cold periods relative to the time series mean are shown in blue and warm periods in red. Dots denote months with absolute SSTA values > 1 standard deviation of the monthly regional mean (12 values different for every month); larger dots denote absolute SSTA values > 2 standard deviations. Dots are color-coded according to seasons (winter – JFM, spring – AMJ, summer – JAS, autumn – OND) [data = OISST]. (For interpretation of the references to color in this figure legend, the reader is referred to the Web version of this article.)

(though see differences between EBS and NBS sea surface temperatures; Fig. 4, bottom panel). Trends in SST differed substantially in the WBS. Alternating cold and warm phases were also prevalent, but according to a different pattern, such that the temporal bounds of these thermal phase shifts were offset. The WBS was characterized by relatively warmer temperatures in 1996–1998 and 2003–2016, colder temperatures in 1999–2002, and anomalously warmer temperatures in 2017–2019. In general, the WBS is colder than the EBS, though temperatures converged in 1996–1998 (warm period in the WBS) and 2006–2013 (overlap of a warm period in the WBS and a cold period in the EBS). Since 2014, the water column 0–100m in the WBS has been warmer, relative to 1950–2003. In all sub-regions of the Bering Sea (EBS, WBS, NBS), the conditions of 2017–2019 exceeded values observed in the recent warm stanzas and represent the warmest conditions in the historical record in each respective system (Fig. 4, upper panel). It should be noted that the relative increase in temperature in this recent warming period (2017–2019) was greatest in the NBS. This is reflected in the reduced temperature differential between the EBS and NBS in this timeframe (Fig. 4, lower panel). In both 2006–2013 and 2017–2019, the difference in mean SST values between the EBS and NBS was reduced. In the former period (2006–2013), this was due to cold phase in the EBS, such that conditions in the EBS more closely resembled those typical of the NBS. In the later period (2017–2019), this reflects warming in both systems, but greater relative warming in the NBS, such that the conditions in the NBS more closely resemble those typical of the EBS.

3.4. Annual sea-ice extent and concentration

Analysis of the relationship between maximum annual sea-ice extent and a standardized annual index of sea-ice extent on March 15 suggested that the seasonal timing of maximum sea-ice extent varied greatest in years of greatest extensive sea-ice extent; the relationship was strongest in the timeframe of warm and cold phases analyzed (2000–2019, $R^2 = 0.57$, $P < 0.001$; Appendix, Fig. A-6). It should be noted that mid-March was used to develop a standardized index of annual ice extent and that the seasonal timing of maximum ice extent will vary between years. Also, while mid-March sea-ice extent is well correlated with maximum ice extent, it is a significant underestimation. This standardized index was used to examine patterns of change in sea-ice extent over the timeseries, 1979–2018 (Appendix, Fig. A-7). Sea-ice extent and configuration varied greatly over this period with mid-March sea-ice extent ranging 55°N-60°N in the EBS (Alaska Peninsula to north of Nunivak Island) and 60°N-63°N in the WBS (south of Cape Olyutosky to north of Cape Navarin). There was extensive retreat in sea-ice extent in the Gulf of Anadyr in recent years (2017–2018). Maximum mid-March Bering Sea ice extent was observed in 2012 (2937×10^3 km^2); minimum mid-March Bering Sea ice extent was observed in 2018 (2318×10^3 km^2). The marginal ice zone (areas with sea-ice concentration 15%–80%; http://seaiceatlas.snap.uaf.edu/) was highly variable; its greatest mid-March extent was observed in 1984 (332×10^3 km^2) and lowest in 2016 (125×10^3 km^2). While there were no significant trends in total mid-March sea-ice extent 1979–2018, the area of the marginal ice zone exhibited a steady decrease over the 40-year period (-13.6% per decade). Mean sea-ice extent on March 15 in each of the climatic stanzas identified in this analysis was visualized (Fig. 5); the greatest sea-ice extent occurred in the EBS cold period 2006–2013 (2738×10^3 km^2), versus reduced areas in the EBS 2000–2005 (2500×10^3 km^2) and 2014–2016 (2573×10^3 km^2) warm periods.

The western part of the Bering Sea is consistently less ice covered in winter than the eastern shelf. Sea ice covers only a narrow coastal band along the Koryak and Kamchatka coasts. Sea ice starts to form in the Gulf of Anadyr in the middle of October. Outside the Gulf of Anadyr, sea ice forms in the embayments of the Koryak coast (Cape Olyutorsky to Cape Navarin) and inner part of the Korfa Bay in mid-November. In December, the rate of ice growth accelerates and peaks in February (Plotnikov and Vakulskaya, 2012). The area is totally ice free by the middle of June. In cold years (e.g. winter of 2011–2012) sea-ice growth may continue until the end of April. In contrast, ice cover in warm years (e.g. winter of 2002–2003) starts to disappear in February. Interannual variability of mean sea-ice cover of the western portion for the Bering Sea (WBS extent shown; Appendix, Fig. A-4) generally mimics that for the total Bering Sea ice cover (correlation coefficient, $R = 0.6$, $P < 0.001$; Gennady Khen, personal correspondence; Kivva et al., In Press).

3.5. Annual sea-ice retreat

The date of sea-ice retreat (DOR) was highly variable during the 40-year period (Appendix, Fig. A-8). Ice melt initiated in the end of February and was complete by the end of August. Mean DOR was May 22 in the Bering Sea and July 20 in the Chukchi Sea. The trend in mean day of spatial retreat in the Bering-Chukchi complex was positive (6.5 days later per decade). Mean DOR for sea ice in each of the identified climatic stanzas was visualized (Fig. 6). For annual areal extent in ice retreat timing in the Bering and the Chukchi Sea, see supplementary

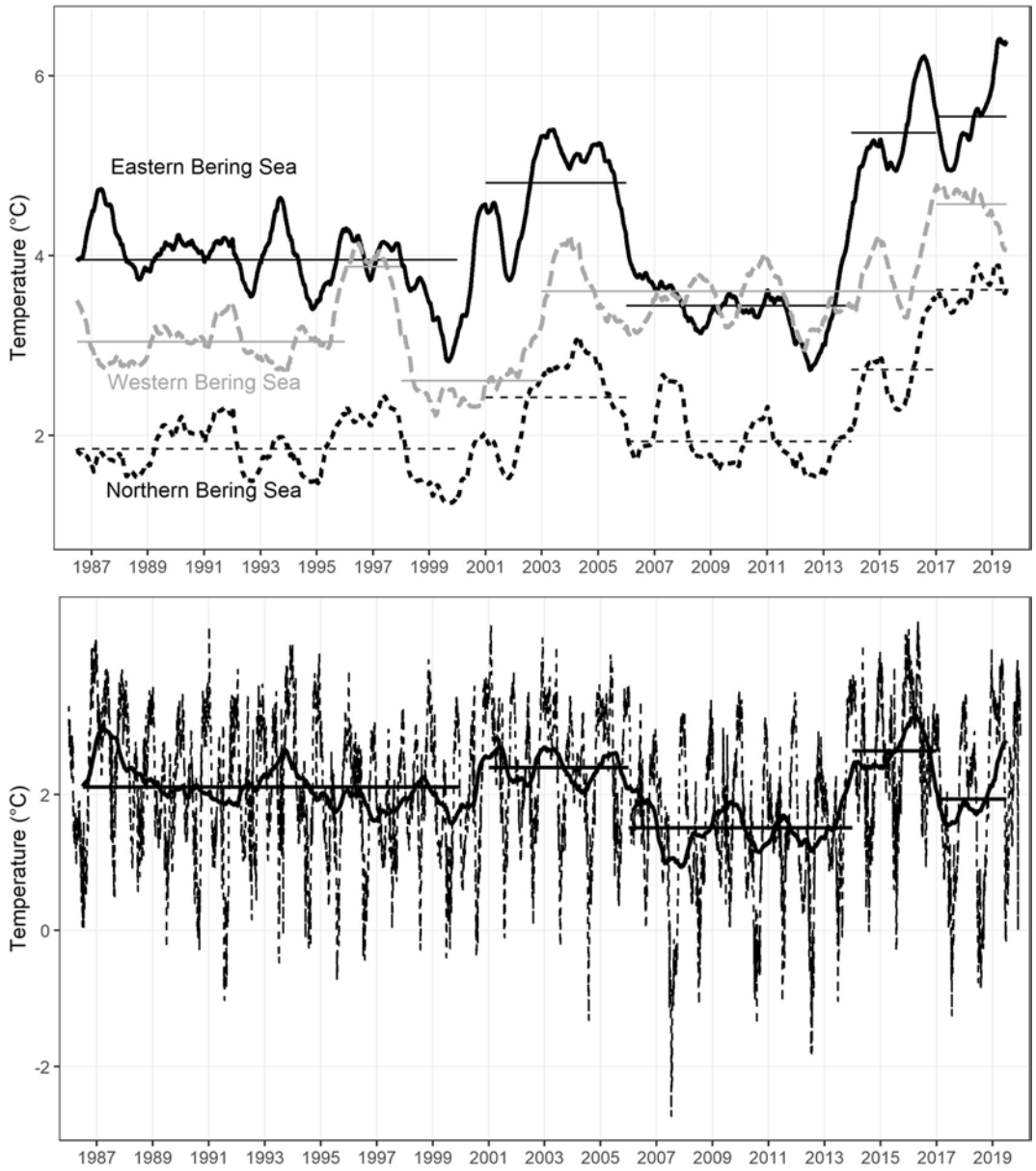

Fig. 4. Top panel: Sea surface temperature (decomposed trend or time series adjusted to remove seasonality) in the EBS (black solid line), WBS (gray dashed line), and NBS (black dashed line). Bottom panel: difference between EBS and NBS sea surface temperatures (dashed line; positive values indicate greater temperatures in the EBS) and time series trend (solid line; seasonality removed). Horizontal lines are the mean temperatures during each of the respective stanzas [data: NOAA Coral Reef Watch version 3.1 operational global satellite daily sea surface temperature 5 km resolution].

figure (Appendix, Fig. A-9).

3.6. Ice extent and open water

Differences in the annual areal ice extent are apparent and differences are notable between the warm, cold, and variable periods (Fig. 7, Table 1). As a consequence, the areal extent of open water in the Bering Sea on March 15 and in the Chukchi Sea on May 15 varied considerably across the time series (Fig. 8). Differences in the extent of open water were noted across identified climatic stanzas (Fig. 9; Table 1) in both the Bering Sea (ANOVA, $F_{4,36} = 2.63$, $P < 0.001$) and Chukchi Sea (ANOVA $F_{4,36} = 6.67$, $P < 0.001$).

3.7. Annual areal coverage of the Bering Sea cold pool

Annual areal extent of the cold pool varied across the time series (Fig. 10, Table 2) and differences were noted between climatic stanzas (1982–1999, 2000–2005, 2006–2013, 2014–2016, 2017–2018; ANOVA $F_{3,33} = 2.89$, $P = 0.001$). Post Hoc tests (Tukey HSD) noted significant differences between warm (2000–2005, 2014–2016) and cold (2006–2013) years ($P < 0.022$). The cold period was also distinct from the 1982–1999 variable period ($P = 0.081$). No differences were noted between recent warm periods (2000–2005, 2014–2016, $P = 0.999$), nor between warm years and the variable period (1982–1999; $P>0.555$). The most recent anomalous year, 2018, was significantly different from both the cold period 2006–2012 ($P = 0.013$), as well as the initial part of the timeseries,1982–1999 ($P = 0.038$). As the cold pool may be defined at different temperature thresholds, we also examined differences in the mean areal extent of the cold pool between climatic stanzas, as defined as bottom temperatures colder than 2 °C, 1 °C, 0 °C, and -1 °C; all were significant ($P < 0.046$). The most recent year of analysis (2018) had an extreme reduction in cold pool extent. Cold pool areal coverage as a percentage of the total survey area declined from a mean of 38.7% (1982–2018) to 1.4% in 2018. Temperatures within the cold pool were

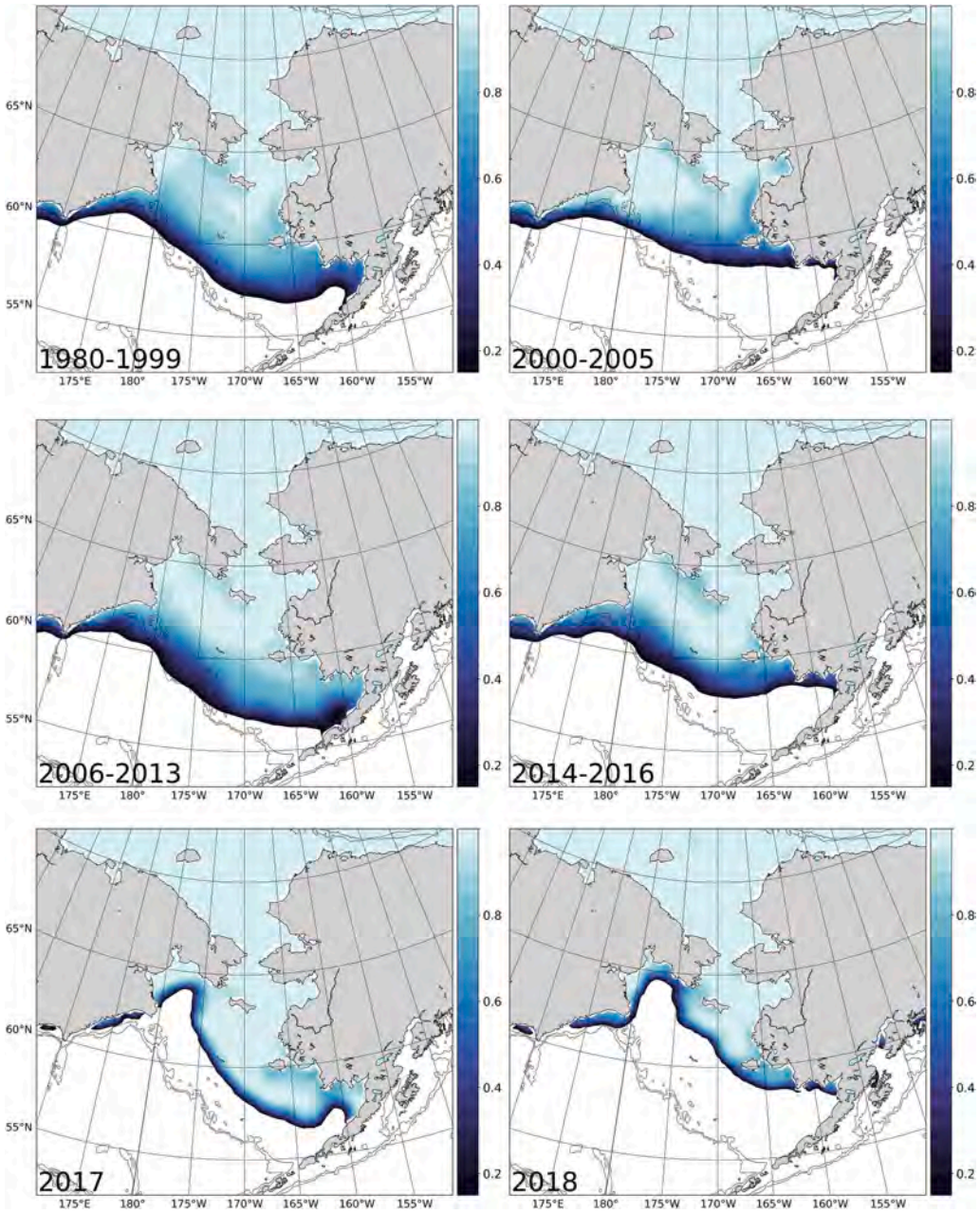

Fig. 5. Mean sea-ice extent on March 15, compiled in discrete temperature phases: 1980–1999 (high interannual variability), 2000–2005 (warm), 2006–2013 (cold), 2014–2016 (warm), and 2017 and 2018 (anomalously warm). Annual maps for all individual years are available in supplementary materials (Appendix Fig. A-7).

also warmer than previously observed; no area in the 2018 survey had bottom temperature <0 °C, compared to a mean coverage of 11.7% for bottom temperatures <0 °C 1989–2018 (22% in cold years, 2006–2013; 5–6% in warm periods, 2000–2005 and 2014–2018). No temperatures <1 °C were observed in the NOAA EBS survey area in 2018, a phenomenon not previously observed.

3.8. Climate and wind

Mean composite winter SLP and wind patterns for November–March provide further insight into mechanisms (Fig. 11). In each of the warm periods (2000–2005, 2014–2016), both the Aleutian Low and the high-pressure system of Beaufort High and Siberian High were strong, with Aleutian Low located over the Aleutian Islands. These time intervals also exhibited slightly enhanced winds. In the later warm period (2014–2016), the Aleutian Low shifted to the east, altering the direction of the wind field over the islands. Alternatively, in the cold phase (2006–2013), while the high-pressure system still developed, the Aleutian Low was much weaker, with two centers - one in the Gulf of Alaska, another close to Russia. This resulted in weaker winds over the central Bering Sea, while the winds in the southeastern part of the EBS shelf were slightly enhanced, due to the longitudinal shift of the Aleutian Low. In the most recent period of anomalous warming (2017–2018), there was a significant shift of the Aleutian Low towards Russia, and prominent weakening of both systems. Composite annual SLP and winter wind anomalies (Fig. 12) demonstrate the substantial difference between 1979-2018 climatology and 2017–2018, including both the position shift and weakening of the Aleutian Low.

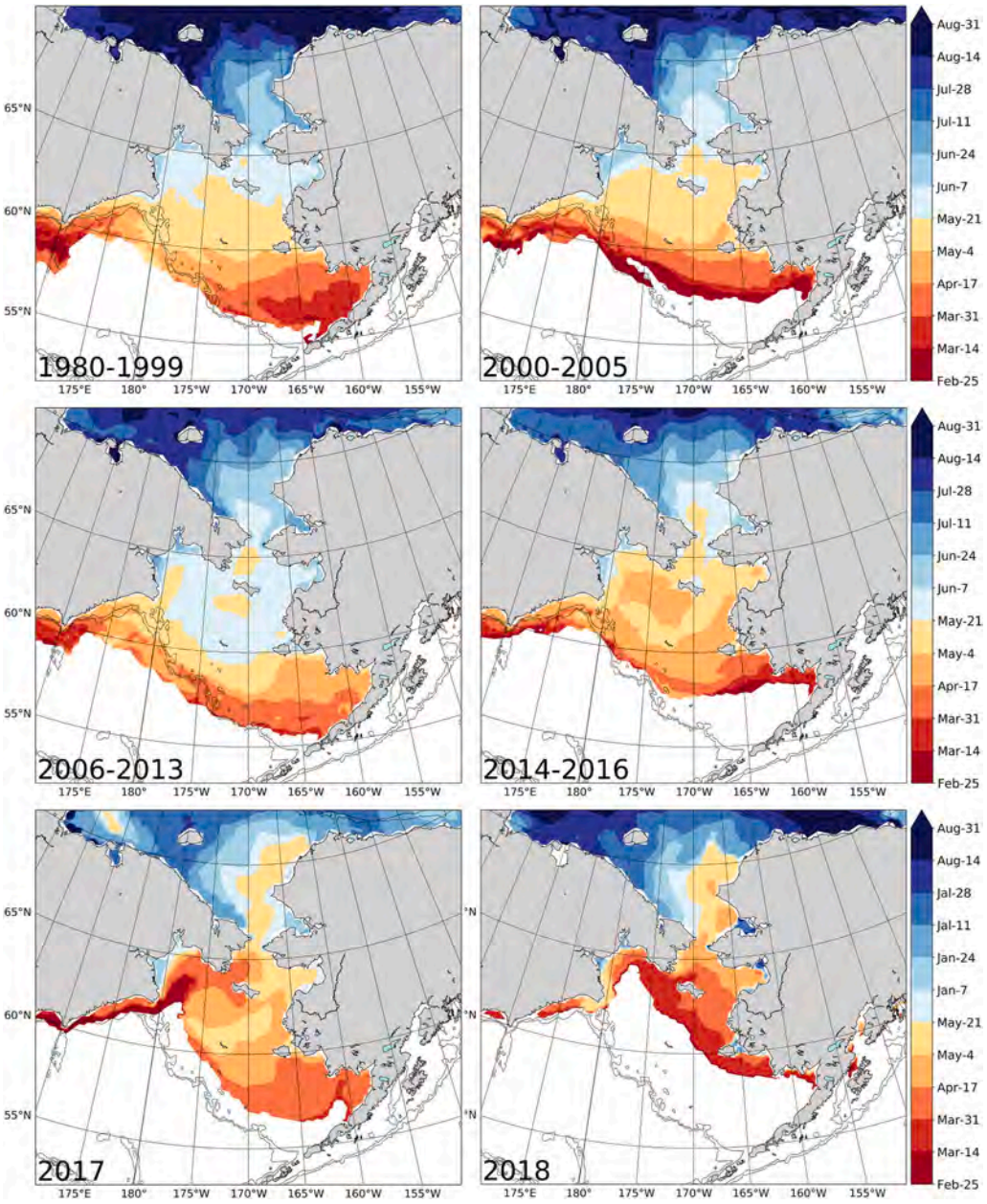

Fig. 6. Mean date of sea-ice retreat, compiled in discrete temperature phases: 1980–1999 (high interannual variability), 2000–2005 (warm), 2006–2013 (cold), 2014–2016 (warm), and 2017 and 2018 (anomalously warm). Annual maps for all individual years are available in supplementary materials (Appendix Fig. A-9).

4. Discussion

4.1. New state of the Pacific Arctic

While sea-ice extent, concentration and duration exhibited extensive reduction in the broader Arctic Ocean (Walsh and Chapman, 1990; Chapman and Walsh, 1993; Levitus et al., 2000; Rigor and Wallace, 2004; Nghiem et al., 2007; Kinnard et al., 2011; SWIPA, 2011; 2012) and in the Chukchi Sea (Wood et al., 2015), the same trend had not been evident in the Bering Sea (Wendler et al., 2014; Peng et al., 2018). Recent data (2014–2019, particularly (2017–2019), however, has revealed similar trends in the Bering Sea as well. Both models and observations note increasing sea-ice loss, decreasing sea-ice thickness, shorter duration, and reduced extent of ice coverage in this region. This suggests a new state of the Pacific Arctic. The shift in pressure and weather patterns and the associated shift in sea-ice dynamics (Stabeno and Bell, 2019) have altered the timing and magnitude of heat exchange in this region. One result is that the thermal barriers (e.g., cold pool) previously evident in the Bering and Chukchi shelf have eroded. This has important implications for connectivity between Pacific and Arctic systems.

4.2. Phase shifts

The North Pacific is known as a region of decadal variations (Mantua et al., 1997; Overland et al., 1999; Di Lorenzo et al., 2008). Decadal variability is also apparent in the Bering Sea ice record, including historical analyses that extend to the 1800s (Walsh et al., 2017). Such variability is expected to continue in the future (Hollowed et al., 2013). The Bering Sea differs from the high Arctic in that its sea-ice cover is seasonal. Phases identified in our analysis match those of other studies of the region (Barbeaux and Hollowed, 2018; Stabeno et al., 2017). In the period 2000–2006, the EBS was characterized by reduced sea ice and above average ocean temperatures, while in 2007–2013, it was

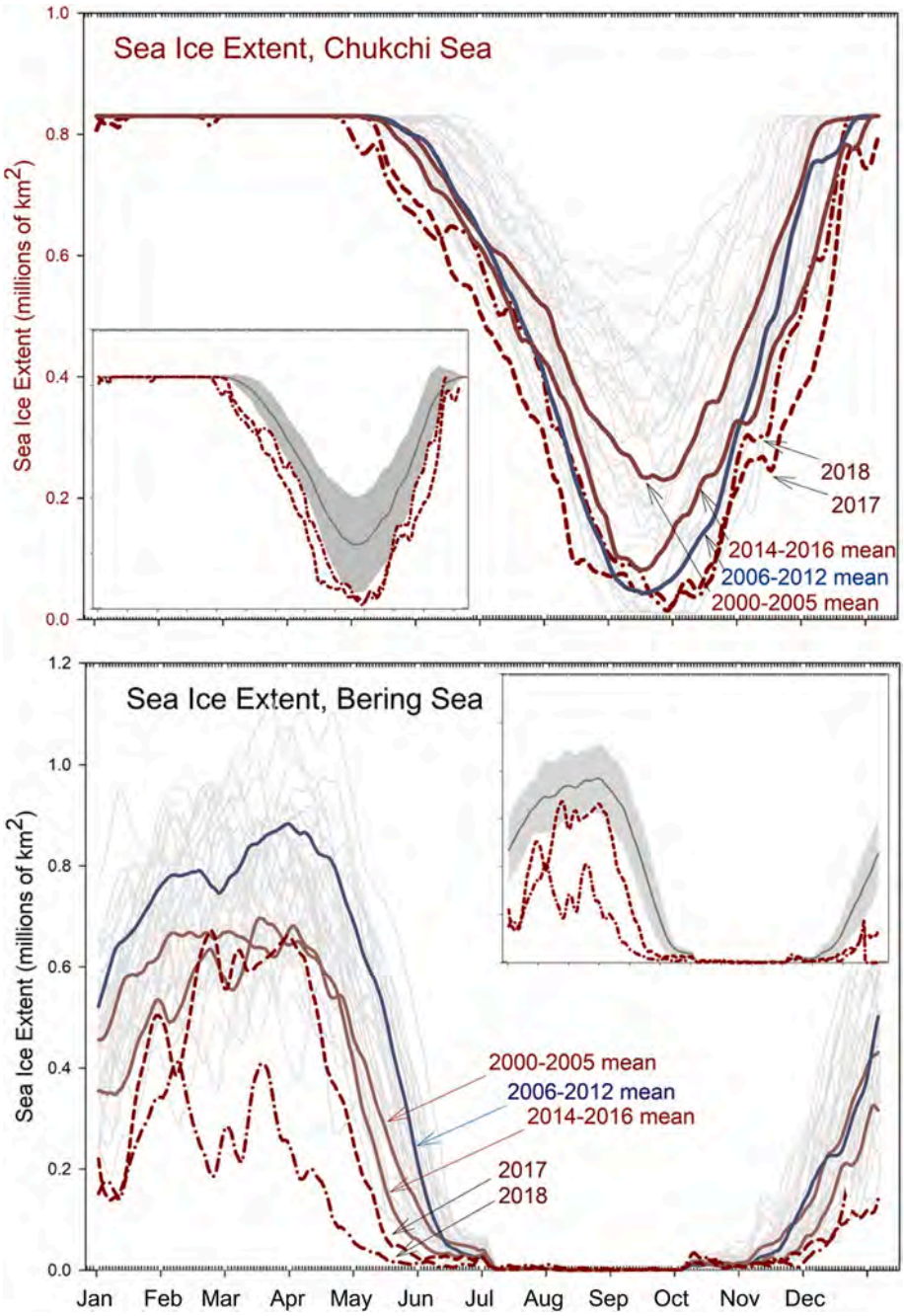

Fig. 7. Seasonal progression of sea-ice extent (millions of km^2) in the Bering Sea and Chukchi Sea (January–December 1982–2018). Time intervals for warm (2000–2005 and 2014–2016, —) and cold periods (2006–2012, —) and 2017 (- - -) and 2018 (- • -) are contrasted against all other years (1980–1999, —). Inset plot display 2017 (- - -) and 2018 (- • -) contrasted against the 1980–2016 mean (—) and standard deviation (gray area plot).

characterized by extensive ice and below average ocean temperatures. In the period 2014–2016, there was another shift to reduced sea ice and above average temperatures. Recent conditions (2017–2019) exceed anything witnessed in the historical record. Still, ice cover in the current winter (2019/2020) has been more extensive (more like a "cold year"). It is uncertain whether recent conditions represent an anomaly or the start of a fundamental transition (Stevenson and Lauth, 2019; Huntington et al., 2020).

4.3. Sea ice

Sea ice is the dominant driver of physical conditions in the Bering Sea. Historically, sea ice begins to form on the northern shelf in December with strong cold northerly winds, advecting ice southward (Pease, 1980). In years with limited sea ice on the southern Bering Sea shelf (2001–2005, 2014–2018), depth-averaged temperature was correlated to the previous summer ocean temperature (Stabeno et al., 2017). Winter sea ice had been expected to continue to form in the NBS and Chukchi Sea and a summer cold pool had been expected to form at depth (Stabeno et al., 2012a; Hollowed et al., 2013). In these systems, timing matters, both for ice arrival and retreat. A late ice arrival allows less time for ice formation and advection south. This alters both the influence and the character of the ice. The Chukchi has been freezing ~0.7 days later per year on average (1920–2019; Stabeno et al., 2019). In the NBS, no trend had been apparent through 2014. Recently (2014–2019), however, this region has also been freezing later (Stabeno

Table 1
Sea ice extent and sea ice area.

Bering Sea (March 15)		
Time Interval	Extent, Mean ± SD (km^2)	Area, Mean ± SD (km^2)
1979–1999	753,786 ± 103,689	298,719 ± 89,944
2000–2005	648,574 ± 52,652	372,470 ± 41,362
2006–2013	850,977 ± 149,819	201.389 ± 134,204
2014–2016	641,753 ± 80,119	402,340 ± 54,478
2017–2019	402,637 ± 191,671	568,946 ± 153,904
Chukchi Sea (May 15)		
Time Interval	Extent, Mean ± SD (km^2)	Area, Mean ± SD (km^2)
1979–1999	823,708 ± 9095	771,239 ± 23,819
2000–2005	813,072 ± 15,336	746,736 ± 38,737
2006–2013	816,247 ± 8123	758,523 ± 16,303
2014–2016	798,425 ± 3908	703,902 ± 4739
2017–2019	734,284 ± 24,341	625,182 ± 55,788

Notes: Values for sea-ice extent describe the edges of the sea ice and is inclusive of all area within that expanse. Sea-ice extent therefore encompassed all portions of a region determined to be ice-covered, based on a threshold of 15%. If a data cell had greater than 15% ice concentration, the cell was considered ice covered; less than that was determined to be ice-free. Values for sea-ice area reflect the portion of area within that extent that is truly ice covered, accounting for gaps. Sea-ice area values were determined as a function of the percentage of sea ice within each data cells, summed across the full extent to report how much of the total area is covered by ice.
Data Source: National Snow and Ice Data Center, Sea Ice Regional Monthly Index, version 3.0.

et al., 2019). As the NBS begins to warm and reflect patterns evident in the greater Arctic, this will have important implication for other areas within the Bering Sea.

4.4. Sea surface temperature and cold pool

Oceanographic conditions observed in 2017–2019 are unprecedented. On the northern Bering Sea shelf, there was a near-complete lack of sea ice and no sea ice in the southeastern shelf in the winter 2017–2018 and in winter 2018–2019. Consequently, there was almost no cold pool in summer 2018 (Stabeno and Bell, 2019). To monitor bottom temperatures and to continue comparisons of cold pool areal extent, regular extension of surveys to northern areas are required. Research should continue to focus on important and complex dynamics related to the extent and timing of sea-ice cover, wind and stratification dynamics. While winters 2016–2017 and 2017–2018 were both warm, there was extensive, if weak, cold pool extent in summer 2017 due to a late winter freeze.

4.5. Salinity and stratification

Lack of sea ice has implications for stratification. In winter (Dec–Apr) the water column is uniformly cold. In spring ice melt develops a cold low-salinity layer at the surface that then gradually warms over the summer, in isolation from the bottom cold layer. In fall, storms and cooling breaks the stratification. Both salinity and temperature contribute to this dynamic. Without ice melt, there will be a reduced salinity gradient and thus weaker stratification; bottom temperatures may warm over the summer due to reduced stratification. Winter 2018 had the lowest ice year on record in the Bering Sea, primarily because of warm, southerly winds (Stabeno and Bell, 2019). Reduced sea ice resulted in warmer bottom temperatures and weaker stratification allowed warming of the bottom water during summer. The extreme reduction of the cold pool in 2018 may be partially explained by this increased mixing at depth due to reduced salinity (Stabeno and Bell, 2019).

There are several indications that these conditions may be more prevalent in the future. Regional oceanographic models predict the reduced footprint of the Bering Sea cold pool observed in 2018 may be typical rather than anomalous by mid-century (A. Hermann, Joint Institute for the Study of the Atmosphere and Ocean, unpublished data). Winds out of the south are predicted to increase (Stabeno, unpublished data), setting conditions similar to those observed in 2017–2018. Conditions in the Chukchi Sea will also have implications for the Bering Sea. Delays in freezing in the southern Chukchi may delay freezing in the NBS, which in turn may reduce the time available for sea ice to be advected southward (P. Stabeno, NOAA Pacific Marine Environmental Laboratory, personal communication).

4.6. Mechanisms for reduced sea ice and elevated temperatures

While the trends seem clear, the mechanisms and interactions are complicated. Physical conditions are governed by exchange between the ocean and air masses of Arctic and Pacific origin, advection from the Pacific to the Arctic, formation and retreat of sea ice, related stratification and mixing dynamics, and redistribution of water masses. Heat flux through the Bering Strait and Chukchi shelf appears to influence not only the distribution, but also the thickness of sea ice (Coachman et al., 1975; Shimada et al., 2006; Woodgate et al., 2010). The dominant parameters that control winter sea-ice extent in the Bering Sea are wind and air temperature, with persistent northerly winds in winter and spring leading to extensive sea ice (Stabeno et al., 2017). The factors recognized as contributing to the rapid loss of sea ice in the Arctic include warmer air temperatures (SWIPA, 2011), wind forcing (Rigor et al., 2002; Ogi et al., 2010), radiative forcing (Francis and Hunter, 2007; Perovich et al., 2007) and oceanic heat flux from below (Shimada et al., 2006; Polyakov et al., 2011). Until recently, the Bering Sea has appeared exempt from loss of sea ice. Sea ice in the Bering Sea 1979–2012 demonstrated an increasing trend (Parkinson, 2014). Weather patterns in November 2017 through early January 2018 were unusual, most notably the duration of the southerly winds. While ice extent during winter months in 2017–2018 was well below previous years, early in the 2018–2019 ice season, ice extent was near normal, only declining to record lows after January. The interplay between air temperatures and wind direction has important implications and trends in this region will have influence beyond the Pacific Arctic. Transport of Pacific waters into the Arctic Ocean play an important role in the exchange of properties between these two systems (Panteleev et al., 2012) and freshwater inflow from the Bering Sea into the Chukchi Sea is an important influence on stratification and maintenance of the Arctic Ocean halocline (Aagaard and Carmack, 1989).

4.7. Winds and atmospheric forcing

Ice cover on the eastern Bering Sea shelf is strongly influenced by the direction of winter winds. Winter winds transport Arctic air southwards. Air temperatures typical of Arctic-origin are necessary to cool the surface waters and allow the formation of ice (Stabeno et al., 2007). Until recently, these winter winds had remained relatively constant (Brown and Arrigo, 2012), allowing the continued formation of winter sea-ice cover in the Bering sea at approximately 465,000 km^2 over the satellite record, in contrast to significant reductions in summer sea ice in the Arctic Ocean. The seasonal Bering Sea ice pack between 1980-2010 showed no sign of reduction (Brown et al., 2011), with warming trends limited to the summer, when the Bering Sea is ice free. Wendler et al. (2014) identified an association between extensive ice extent and decreased atmospheric pressure over mainland Alaska and increased atmospheric pressure in eastern Siberia. These conditions lead to northerly wind vectors for years with heavy ice, which push ice south.

We found that the strength and position of the Aleutian Low differs between warm phases and cold phases in the Bering Sea. The position of the Aleutian Low was relatively constant in warm years. Cold years were characterized by a more variable position of the center of the Aleutian Low system. Similar phenomena have been noted in the Bering-Chukchi

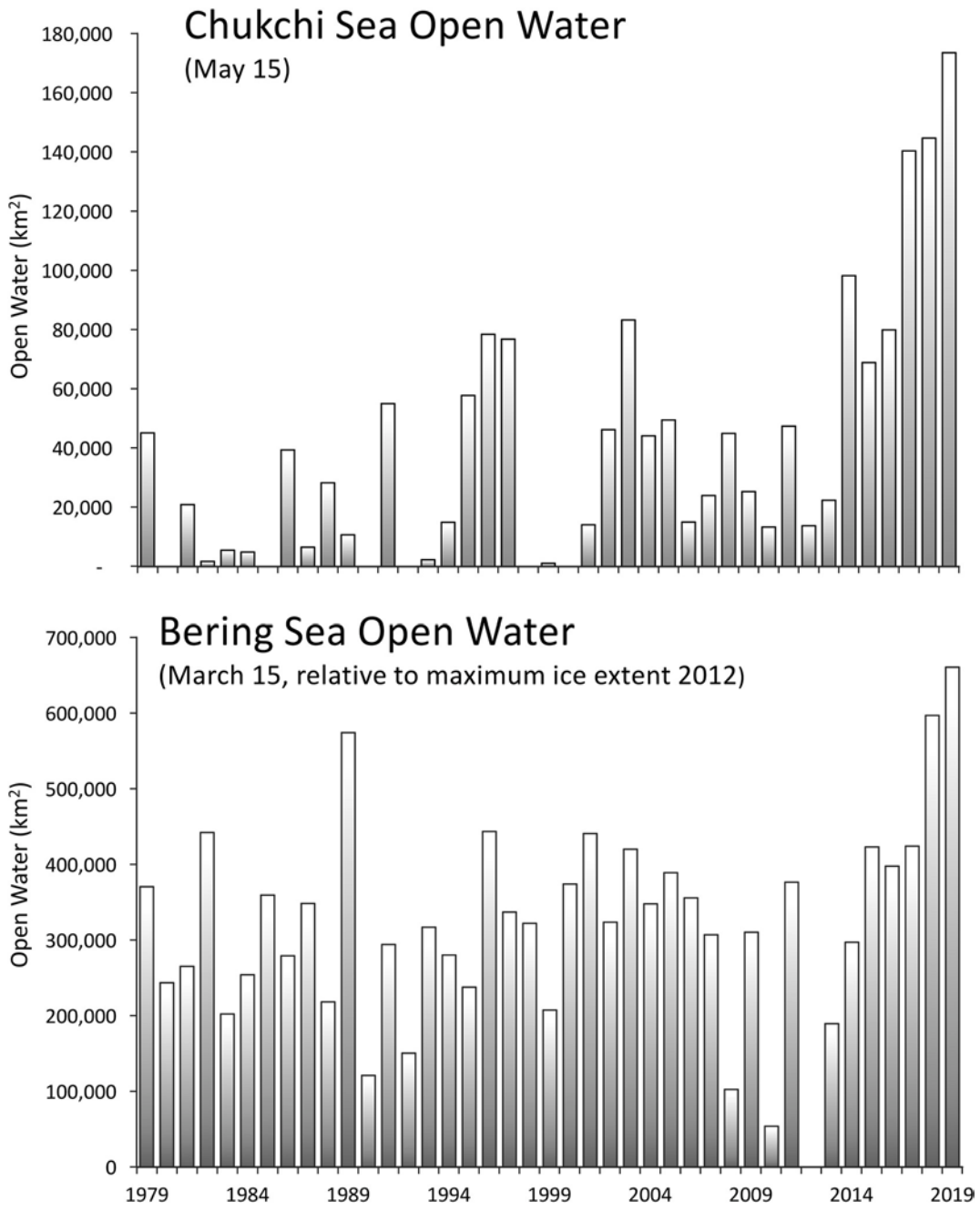

Fig. 8. Annual extent of open water in the Chukchi Sea on May 15 (top plot). Annual extent of open water in the Bering Sea on March 15 (bottom plot). In the Chukchi Sea, values represent the absolute area of open water within the LME. In the Bering Sea, values are relative to the area of Bering Sea ice extent in 2012, the year of maximal ice extent in the timeseries.

circulation field (Rodionov et al., 2007; Overland et al., 1999). Danielson et al. (2014) also noted that mean winter position of the Aleutian Low shifted eastward in 2006–2011 relative to a more westward position in 2000–2005 and in recent warm years.

In the Chukchi Sea, the Aleutian Low position is known to be largely responsible for wind-driven upwelling (Pickart et al., 2009; Pisareva et al., 2019). Our results suggest that it also has important effects on circulation and thermal dynamics in the Bering Sea.

4.8. The distinct nature of the NBS

Results of the DBSCAN cluster analysis confirm past analyses that distinguish the NBS (>60°N) from other regions of the Bering Sea. Many regional studies that distinguish marine systems also separate the NBS from other parts of the Bering Sea, often including it in the Chukchi Sea large marine ecosystem (e.g. the United National Intergovernmental Oceanographic Commission; Fanning et al., 2015; Chandler and Yoo, In Press). Many of these important distinctions may be less evident absent sea ice.

The 60°N latitude marks the historical minimum southern extent of maximum sea-ice cover in the Bering Sea. Until recently, areas north of this latitude were covered with sea ice every year, while areas south were characterized by variable annual sea-ice extent (Sigler et al., 2010). This had important implications for atmospheric-oceanic interactions, wind mixing, wave activity, salinity, heat content, stratification, and phenology and pathways of primary productivity (planktonic production and ice algal pathways). These observations are supported by historical data 1958–1980 (Overland and Pease, 1982), as

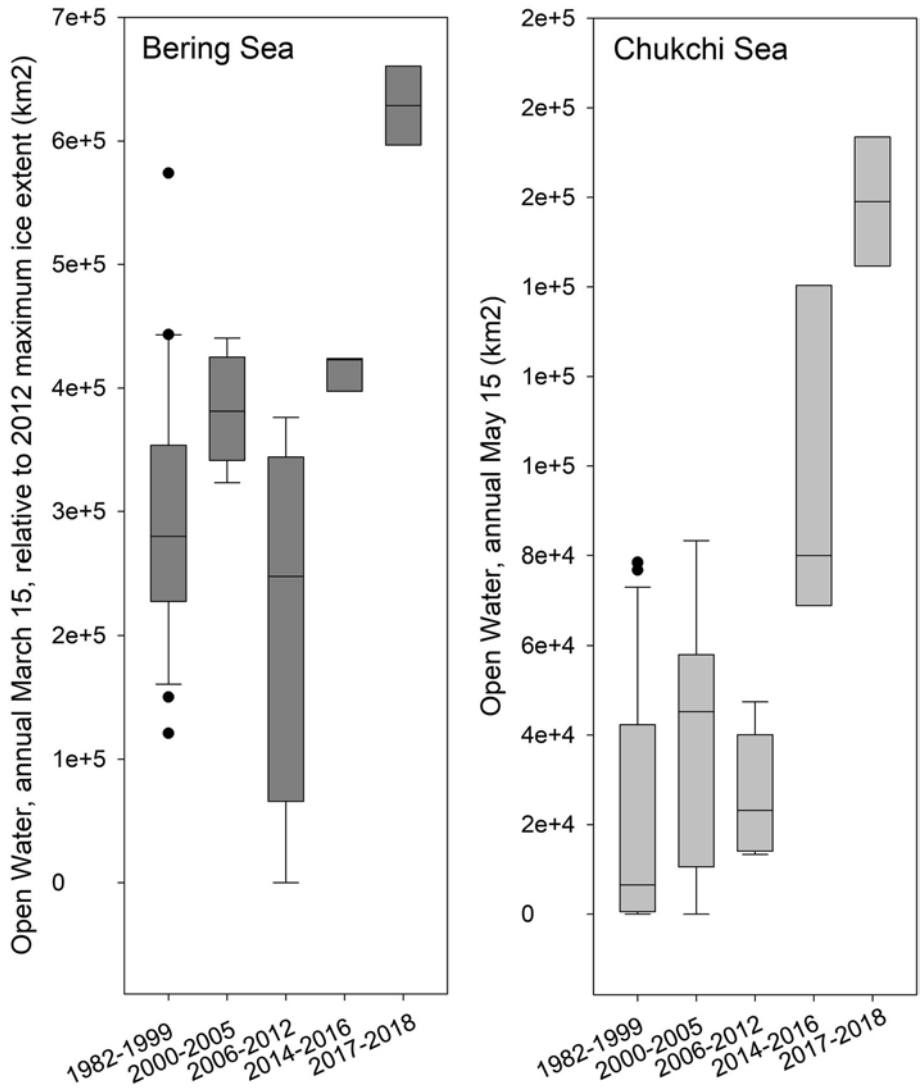

Fig. 9. Boxplots of annual areal extent of open water in the Bering Sea (March 15) and the Chukchi Sea (May 15) for the intervals of analyses, 1982–1999 (high interannual variability), 2000–2005 (warm), 2006–2012 (cold), 2014–2016 (warm), 2017–2018 (anomalously warm). The box represents the interquartile range of the data, the whiskers contain 90% of the data. Horizontal lines within each box display the median value. Points indicate outliers.

well as more recent analyses (Sigler et al., 2014). In physical terms, there are some distinct dynamics that are likely to permanently distinguish areas north of 60°N. This is the approximate point where the Bering Slope current turns off-shelf to flow westward (Ladd, 2014), where flow intensifies along the east coast of Siberia (creating the Anadyr Current, Kinder et al., 1986), and where geostrophic velocity vectors and circulation patterns on the shelf diverge (Cokelet, 2016; Hollowed et al., 2012). This latitude also features influx of freshwater inputs via the Yukon and Kuskokwim rivers. Distinct patterns in upper-to-lower density differences on the shelf are also pronounced at approximately 60°N (Cokelet, 2016). Intensified northward flow occurs in the approach to Bering Strait (Woodgate and Aagaard, 2005) and differences are noted in bottom and surface velocity vectors (Zhang et al., 2013). Other attributes of physical oceanography, however, appear to be in transition. Evident breaks in vertical hydrographic, temperature, and salinity profiles (Goes et al., 2014) and distinct patterns in stratification (Ladd and Stabeno, 2012) are likely to change in the absence of ice. ROMS model results that formerly suggest significant difference in patterns at 60°N for sea surface temperature, ice cover, and wind stress (Hermann et al., 2016) are not apparent in more recent model predictions (Hermann, Pacific Marine Environmental Laboratory, NOAA, Seattle, USA, personal communication).

It is important to monitor how shifts in the physical system might influence the ecology of the systems (Post et al., 2013). Notable differences north and south of 60°N have been noted in phytoplankton community production and trends (Mordy et al., 2012) and in large crustacean zooplankton abundance and species composition (Eisner et al., 2015; Hermann et al., 2016; Siddon and Stephani Zador, 2019). These patterns are also noted in larval fish assemblages (Eisner et al., 2015; Parker-Stetter et al., 2016; Siddon and Stephani Zador, 2019) forage fishes, (Andrews et al., 2016; Baker, In Press), and adult fishes and invertebrate communities (Stevenson and Lauth 2012, 2019; Mueter and Litzow, 2008; Baker and Hollowed, 2014). Subsistence harvest and community dynamics are also distinct north and south of 60°N (Renner and Huntington, 2014).

4.9. Implications of reduced sea ice and the erosion of thermal barriers in Bering- Chukchi system

Ice thickness, age, and extent have changed rapidly in the Arctic (Comiso, 2012). Reductions in sea-ice duration and declines in multi-year ice cover are leading to extensive open water in the Central Arctic Ocean, particularly in summer and fall, increasing availability for commercial activity, especially international shipping (Van Pelt et al.,

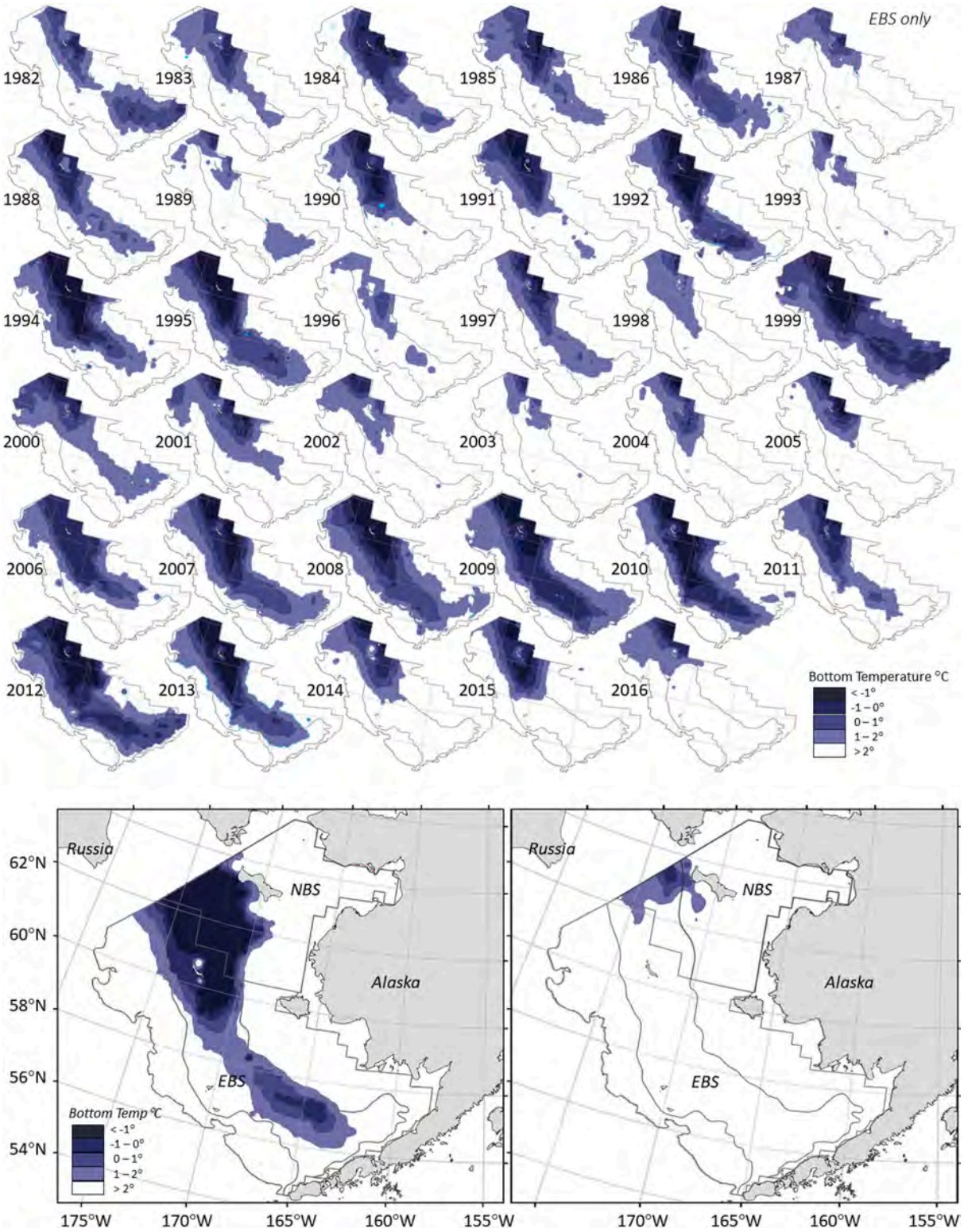

Fig. 10. Areal extent of the Bering Sea cold pool in mid-summer, calculated via bottom temperatures sampled in the NOAA bottom trawl survey. Images 1982–2016 display the area surveyed in the EBS survey grid. Images for 2017 and 2018 show an enlarged sample area that reflects increased survey coverage in those years that included the both the full EBS survey area and also the NBS survey area. Gray lines within the shelf denote the 50 m and 100 m isobaths. The cold pool typically concentrates in the middle shelf, depths 50–100 m. [data: NOAA Alaska Fisheries Science Center, Resource Assessment and Conservation Engineering Division, Groundfish Assessment Program].

Table 2
Cold pool extent.

Time Interval	1982–1999	2000–2005	2006–2013	2014–2016	20172018	
Cold Pool Proportional Area	40% ± 30	25% ± 20	58% ± 2	24% ± 4	35%	1.4%

Notes: Total areal coverage of the cold pool as a proportion of the standard EBS survey area.

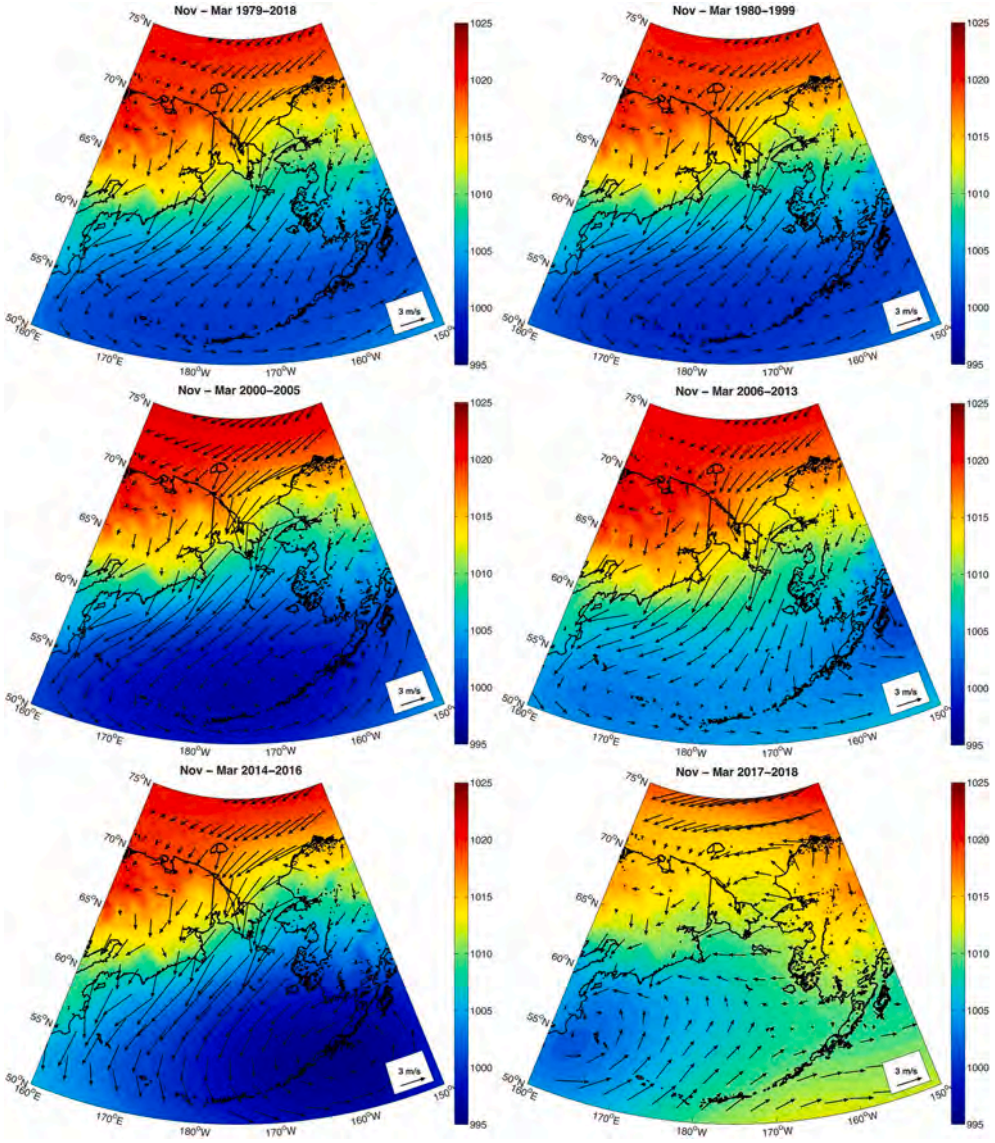

Fig. 11. Maps of mean sea level pressure (hPa, color) and 10-m winds (m/s, vectors) for winter months (Nov–Mar) in the Pacific Arctic region [data: ERA5 reanalysis - 1979–2018]. (For interpretation of the references to color in this figure legend, the reader is referred to the Web version of this article.)

2017). Continued sea-ice loss will ensure the Arctic is increasingly accessible for oil and gas exploration and developments and marine shipping (United States Navy, 2014). Increased expanse of open water also increases fetch and wave action (Thomson and Rogers, 2014). This may break up the ice that is present, changing the character of that ice, with implications for human transport (i.e., subsistence activities) and marine mammal use (e.g., ice seals, walrus, polar bears). These trends, evident in the broader Arctic should be closely monitored in the Pacific-Arctic gateway.

4.10. Prospects for increased international collaboration and data sharing

Despite several coordinated international efforts, the ability to access and visualize data in a unified data portal is limited. Data sharing is often dependent on personal correspondence between colleagues (Van Pelt et al., 2017). An integrated Arctic Ocean Observing System has emerged to complement regional networks, but none are comprehensive. International science institutions such as PICES and regional networks such as PAG have been instrumental in promoting information standardization and information sharing (Eisner et al., 2017; Baker et al., 2018) and research institutions such as NPRB have been effective in coordinating scientific efforts across diverse institutions and internationally. Further collaboration between national science agencies including NOAA (USA), VNIRO (RUS), Fisheries and Oceans Canada (DFO-CAN), Japan Agency for Marine-Earth Science and Technology (JAMSTEC-JPN), the Korea Institute of Ocean Science and Technology (KIOST-KOR), and the State Oceanic Administration (SOA-CHN) are promising. Continued efforts to integrate data and perspectives across

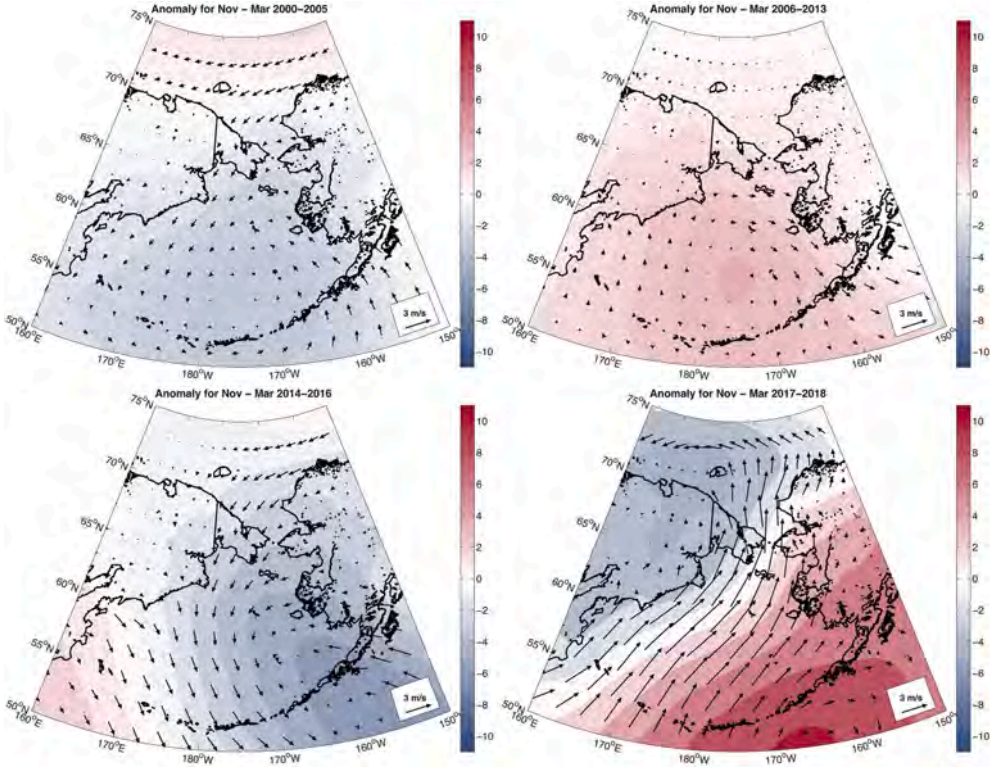

Fig. 12. Maps of mean sea level pressure (hPa, color) and 10-m winds (m/s, vectors) anomalies from climatology (1979–2018) for winter months (Nov–Mar) in the Pacific Arctic region [data: ERA5 reanalysis - 1979–2018]. (For interpretation of the references to color in this figure legend, the reader is referred to the Web version of this article.)

national boundaries are increasingly necessary.

Declaration of competing interest

The authors declare that they have no known competing financial interests or personal relationships that could have appeared to influence the work reported in this paper.

CRediT authorship contribution statement

Matthew R. Baker: Supervision, Conceptualization, Methodology, Data curation, Formal analysis, Visualization, Writing - original draft, Writing - review & editing. **Kirill K. Kivva:** Supervision, Conceptualization, Methodology, Data curation, Formal analysis, Visualization, Writing - original draft. **Maria N. Pisareva:** Methodology, Data curation, Formal analysis, Visualization, Writing - original draft. **Jordan T. Watson:** Methodology, Data curation, Formal analysis, Writing - original draft. **Julia Selivanova:** Data curation, Visualization.

Acknowledgements

This research was initiated in discussions related to the 2016 and 2017 North Pacific Marine Science Organization (PICES) Annual Science Meeting workshops on data sharing and collaboration in the northern Bering Sea in San Diego and Vladivostok, Russia, convened by M. Baker, K. Kivva and L. Eisner. Analyses were further developed through subsequent discussion and collaboration, related to the development of the PICES North Pacific Ecosystem Status Report in 2018 in Yokohama, Japan. The dedicated efforts of A. Bychkov, H. Batchelder, S. Batten, P. Mundy, P. Chandler, and S. Yoo to coordinate these meetings is also greatly appreciated. We also thank L. Eisner, V. Lobanov, Y. Zuenko, V. Kulik, E. Siddon, E. Farley, and S. Danielson for their contributions to these discussions. Support provided to these efforts by PICES, NPRB, NOAA, and VNIRO is greatly appreciated. Analyses were also supported by the Ministry of Science and Education of Russia, theme 0149-2019-0004. This research was further informed by the NPRB Arctic Integrated Ecosystem Research Program, which has facilitated and continued US-Russian collaborative research. This work builds on the extensive and continued efforts of the NOAA Alaska Fisheries Science Center and Pacific Marine Environmental Laboratory and we thank P. Stabeno, R. Lauth, A. Hollowed, A. Hermann, and K. Holsman for conversations that informed this analysis. We also thank J. Gann, A. Gray, P. Stabeno, and C. Ladd for review of the manuscript and K. Drinkwater for editing and facilitating the publication. The findings and conclusions are those of the authors and do not necessarily represent those of the associated institutions. This is NPRB publication ArcticIERP-05.

Appendix A. Supplementary data

Supplementary data to this article can be found online at https://doi.org/10.1016/j.dsr2.2020.104802.

Appendix

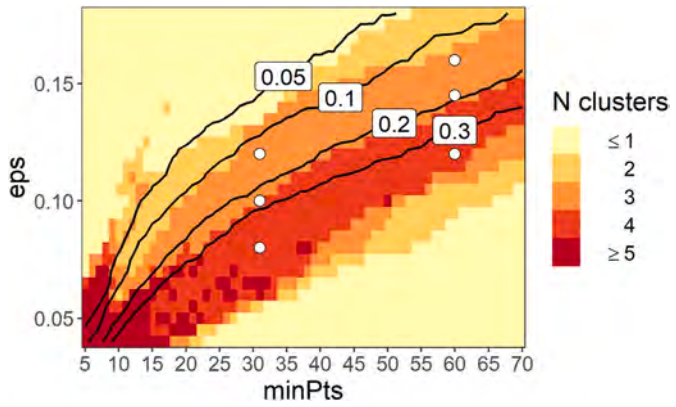

Fig. A1. Number of clusters (shading) and proportion of noise nodes (only isolines of 0.05, 0.1, 0.2, and 0.3 are shown) for different combinations of eps and minPts parameters for annual mean SSTA (1982–2011) clustering with DBSCAN algorithm. White dots represent values of the parameters investigated.

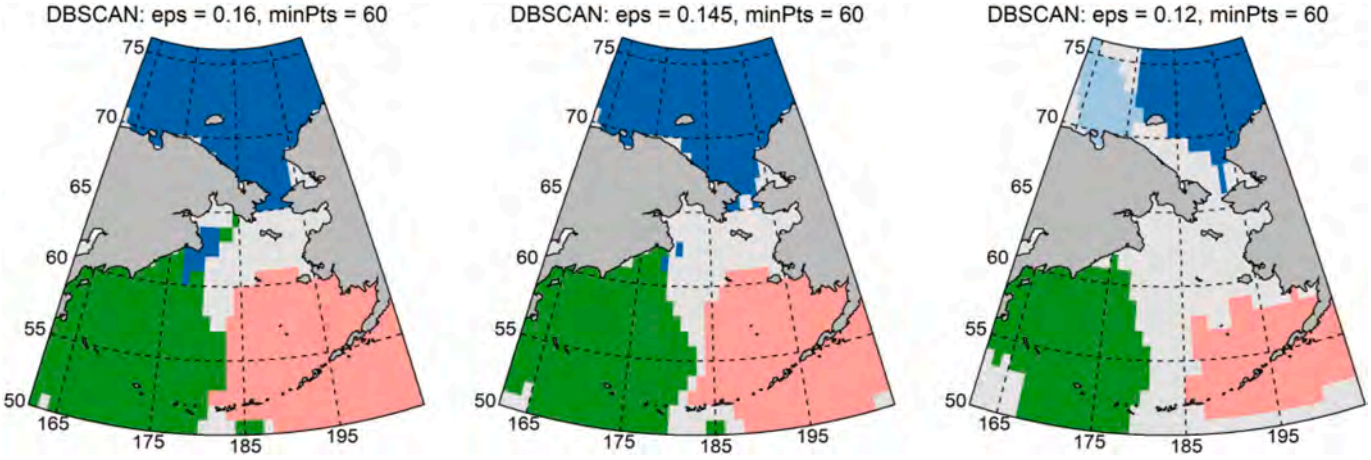

Fig. A2. Annual mean SSTA (1982–2011) clusters distribution according to DBSCAN. The threshold for the number of neighbors (minPts) was set to 60. Radius ε (eps) varied between 0.16 (left), 0.45 (middle), and 0.12 (right panel). Note this case of minPts = 60 has patchy distribution of clusters around Cape Navarin and Gulf of Anadyr for eps values between 0.145-0.16.

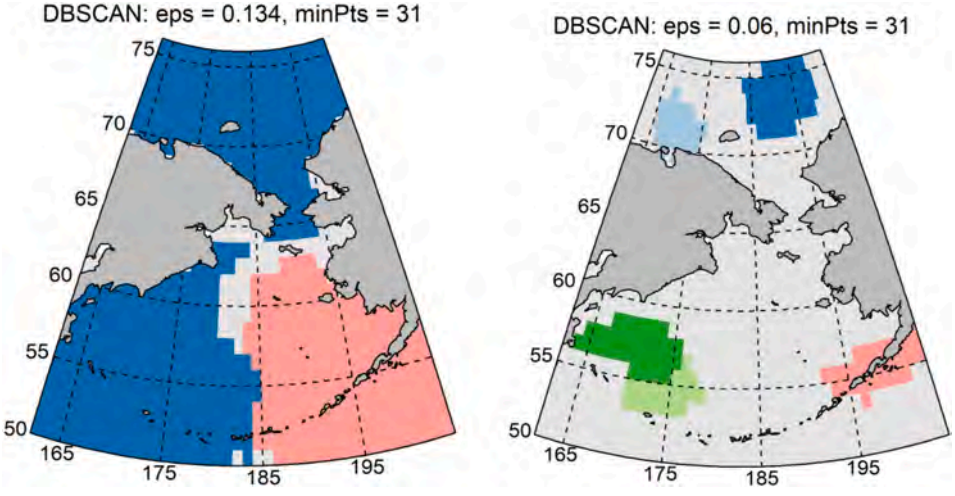

Fig. A3. Annual mean SSTA (1982–2011) clusters distribution according to DBSCAN. The threshold for the number of neighbors (minPts) was set to 31. Radius ε (eps) varied between 0.134 (left), and 0.06 (right panel). Note Chukchi-Siberian and western Bering Sea clusters are merged when eps = 0.134. On the other hand, all clusters are smaller and western Bering Sea cluster is divided into two clusters with eps = 0.06. This was not useful for regional delineation, but may be useful for identification of smaller regional coherence in SSTA dynamics..

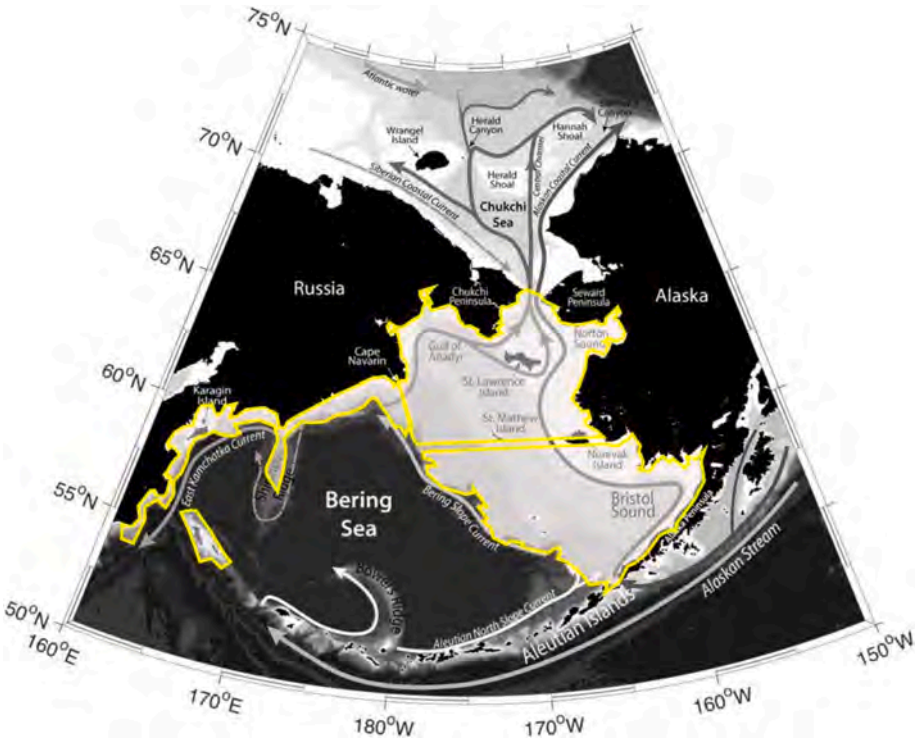

Fig. A4. Regional boundaries used for the shelf systems of the Bering Sea (EBS, WBS, and NBS). Analyses of sea surface temperatures (SST) used data from the NOAA Coral Reef Watch version 3.1 operational global satellite (pacioos.hawaii.edu/metadata/dhw_5km.html). These data include daily satellite information with a 5 km spatial resolution. The data were accessed via the Pacific Islands Ocean Observing System ERDDAP site (https://pae-paha.pacioos.hawaii.edu/erddap/index.html). Data were limited to spatial coordinates between 10m and 200m of depth as shown in this outline for the western Bering Sea (WBS). This spatial extent for the WBS was also used in analyses of interannual variability of mean sea-ice cover of the western portion for the Bering Sea.

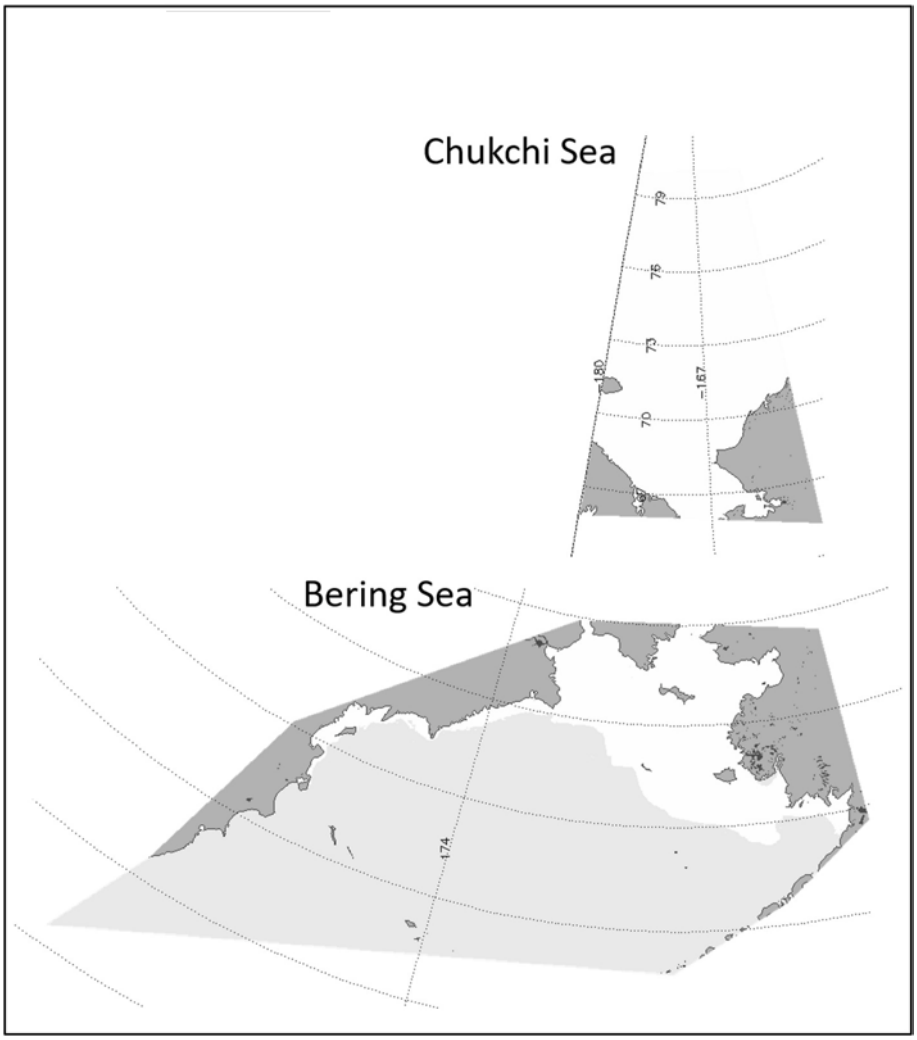

Fig. A5. Spatial extent coverages for data and analyses of sea ice in the Chukchi (top) and Bering (bottom) seas. Spatial extents were defined and data were accessed via the National Snow and Ice Data Center [https://nsidc.org/data/masie/browse_regions].

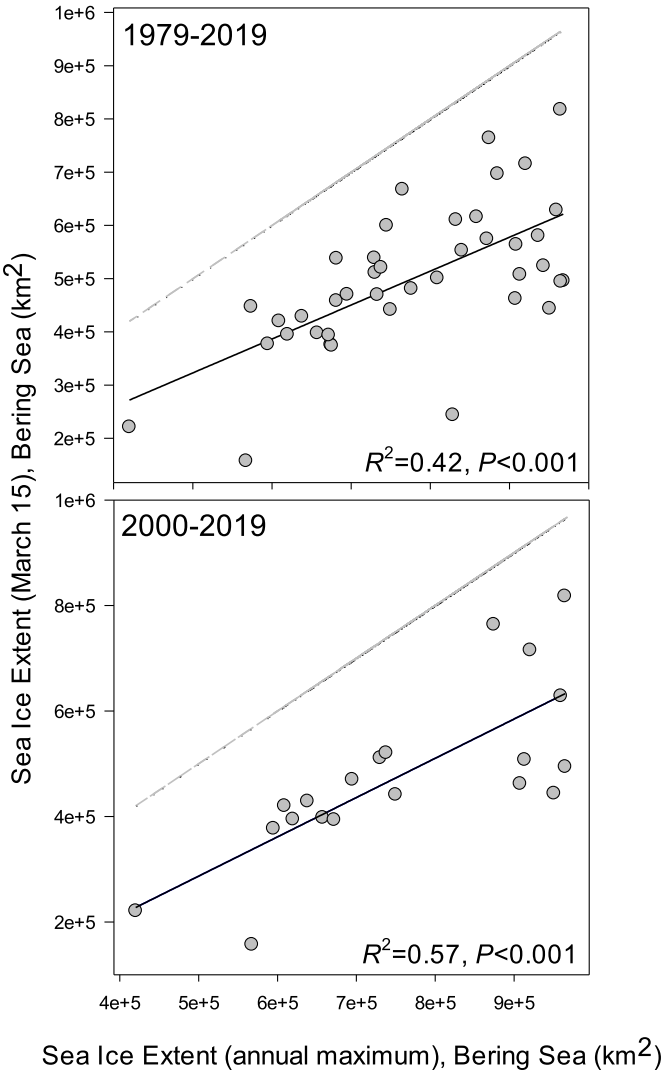

Fig. A6. Correlation of Bering Sea annual maximum ice extent versus annual ice extent on March 15 (date used as a standard index for annual ice extent; black solid line represents the regression, gray dashed line represents the 1-to-1 line.) Variation was greatest in years of extensive ice extent and the relationship was strongest in the timeframe of warm and cold phases analyzed (2000–2019, $R^2 = 0.57$, $P < 0.001$). While mid-March sea-ice extent is well-correlated with annual maximum ice extent, it is a significant underestimation (34% reduction from maximum; mean 1979–2019).

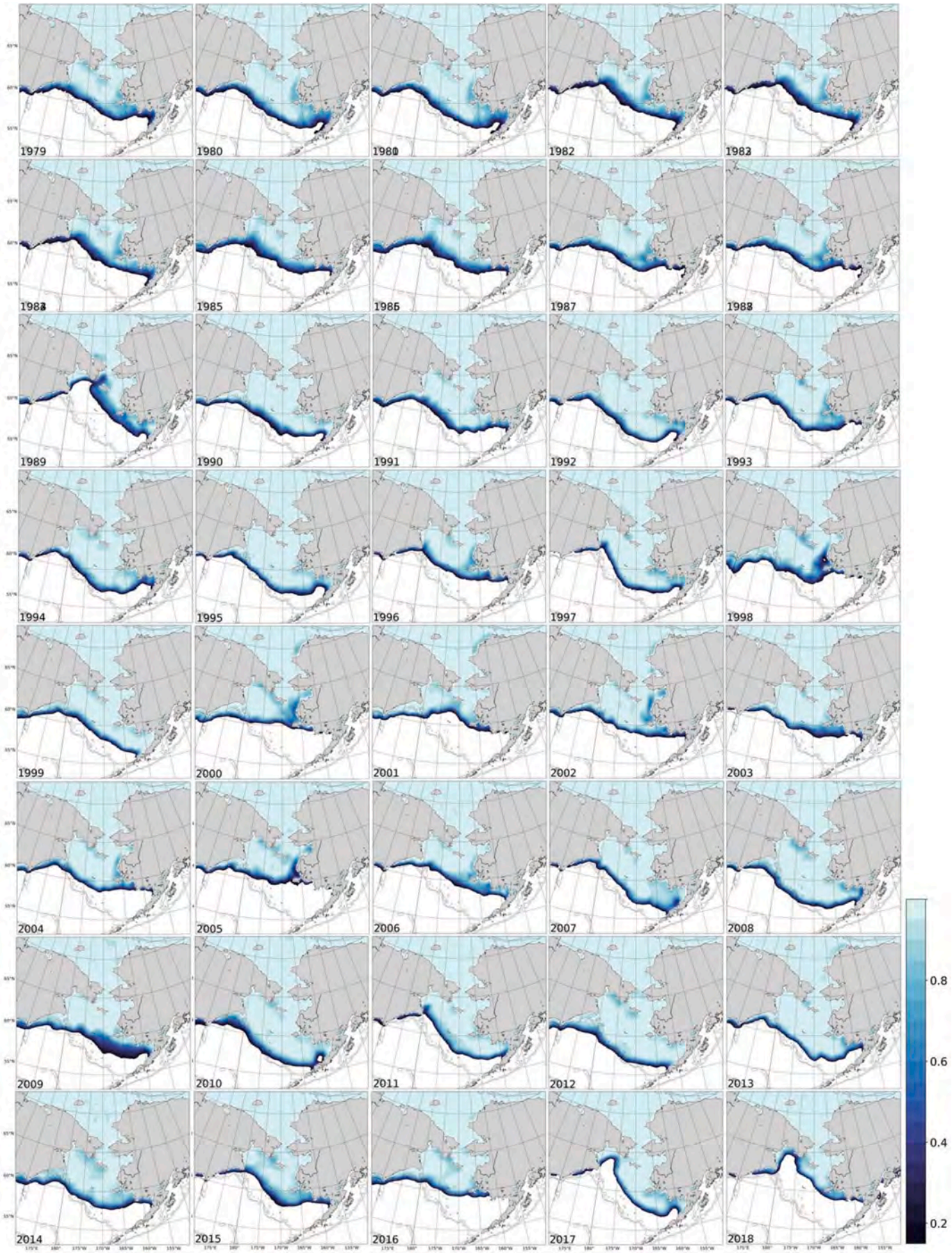
1979
1980
1981
1982
1983
1984
1985
1986
1987
1988
1989
1990
1991
1992
1993
1994
1995
1996
1997
1998
1999
2000
2001
2002
2003
2004
2005
2006
2007
2008
2009
2010
2011
2012
2013
2014
2015
2016
2017
2018
0.8
0.6
0.4
0.2

Fig. A7. Annual sea-ice extent at the approximate point of season maximum, March 15 (1979–2018). Shading indicates sea-ice concentration.

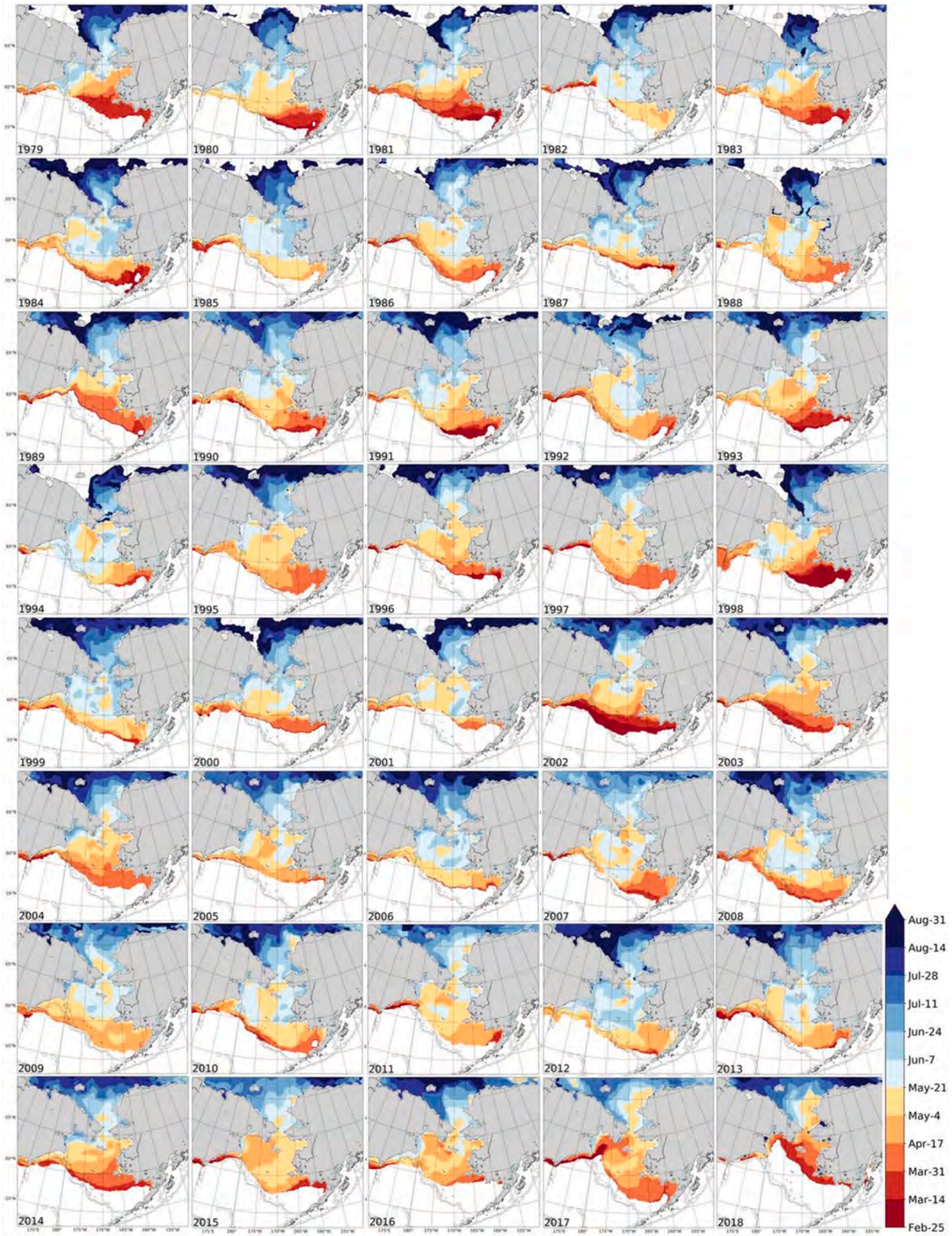
1979
1980
1981
1982
1983
1984
1985
1986
1987
1988
1989
1990
1991
1992
1993
1994
1995
1996
1997
1998
1999
2000
2001
2002
2003
2004
2005
2006
2007
2008
2009
2010
2011
2012
2013
2014
2015
2016
2017
2018
Aug-31
Aug-14
Jul-28
Jul-11
Jun-24
Jun-7
May-21
May-4
Apr-17
Mar-31
Mar-14
Feb-25

Fig. A8. Date of sea-ice retreat (1979–2018). For a given grid node and a given year, the day of retreat was the day of last transition of the sea-ice concentration from above 0.15 to below 0.15. In years prior to 2002, some areas in the Chukchi Sea remained ice-covered beyond Aug-31 (shown in white).

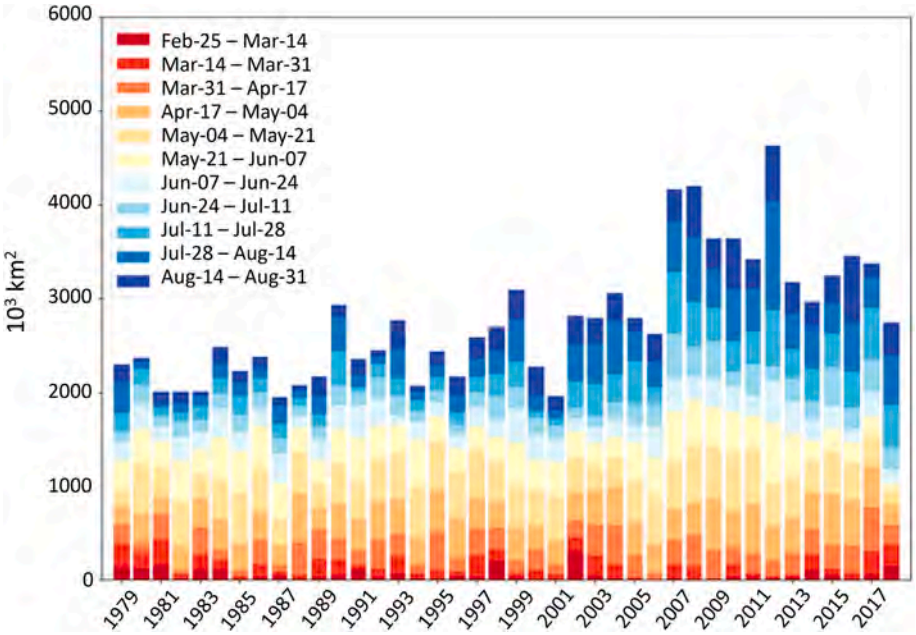

Fig. A9. Timeseries of annul areal extent in ice retreat in the Bering and the Chukchi Sea. Bars represent area (km^2) of ice retreat. Colors represent 17-day intervals.

References

Aagaard, K., Carmack, E.C., 1989. The role of sea ice and other fresh water in the Arctic circulation. J. Geophys. Res. Oceans 94, 14485–14498.

Amante, C., Eakins, B.W., 2009. Etopo1 1 arc-minute global relief model: procedures, data sources and analysis. NOAA Tech. Memo. NESDIS NGDC 24, 1–19.

Andrews, A.G., Strasburger, W.W., Farley, E.V., Murphy, J.M., Coyle, K.O., 2016. Effects of warm and cold climate conditions on capelin (*Mallotus villosus*) and Pacific herring (*Clupea pallasii*) in the eastern Bering Sea. Deep-Sea Res. II 134, 235–246.

Andriashev, A.P., 1939. Zoogeography and origin of the fish fauna of the Bering Sea and adjacent waters. Leningr. Gos. Univ. 1–187.

Asahara, Y., Takeuchi, F., Nagashima, K., Harada, N., Yamamoto, K., Oguri, K., Tadai, O., 2012. Provenance of terrigenous detritus of the surface sediments in the Bering and Chukchi Seas as derived from Sr and Nd isotopes: implications for recent climate change in the Arctic regions. Deep-Sea Res. II 61, 155–171.

Aydin, K.Y., Lapko, V.V., Radchenko, V.I., Livingston, P.A., 2002. A Comparison of the Eastern Bering and Western Bering Sea Shelf and Slope Ecosystems through the Use of Mass-Balance Food Web Models, vol. 130. NOAA Technical Memorandum NMFS-AFSC.

Aydin, K., Mueter, F., 2007. The Bering Sea—a dynamic food web perspective. Deep-Sea Res. II 54, 2501–2525.

Baker, M.R., Farley, E.V., Danielson, S.L., Ladd, C., Stafford, K.M., Dickson, D.M.S., In Press. Understanding ecosystem processes, timing, and change in the Pacific Arctic. Deep-Sea Res. II. In this issue.

Baker, M.R., Hollowed, A.B., 2014. Delineating ecological regions in marine systems: integrating physical structure and community composition to inform spatial management in the eastern Bering Sea. Deep-Sea Res. II 109, 215–240.

Baker, M.R., Kivva, K.K., Eisner, L., 2018. Workshop – the Role of the Northern Bering Sea in Modulating the Arctic II: International Interdisciplinary Collaboration, vol. 26. PICES Press, pp. 15–19. https://search.proquest.com/openview/37716f6583252e708e1825d84c0f2dd0/1?pq-origsite=gscholar&cbl=666306.

Baker, M.R., In press. Contrast of warm and cold phases in the Bering sea to understand spatial distributions of Arctic and subarctic gadids. Special issue: Arctic gadids in a changing climate. Polar Biol. In press.

Baker, M.R., (in press). The northern Bering sea. North Pacific ecosystem Status report. North Pacific Marine Science Organization (PICES). Special Publication. https://meetings.pices.int/projects/npesr.

Barbeaux, S.J., Hollowed, A.B., 2018. Ontogeny matters: climate variability and effects on fish distribution in the eastern Bering Sea. Fish. Oceanogr. 27, 1–15.

Brown, Z.W., Van Dijken, G.L., Arrigo, K.R., 2011. A reassessment of primary production and environmental change in the Bering Sea. J. Geophys. Res. Oceans 116, C8.

Brown, Z.W., Arrigo, K.R., 2012. Contrasting trends in sea ice and primary production in the Bering Sea and Arctic Ocean. ICES J. Mar. Sci. 69, 1180–1193.

Brown, Z.W., Lowry, K.E., Palmer, M.A., van Dijken, G.L., Mills, M.M., Pickart, R.S., Arrigo, K.R., 2015. Characterizing the subsurface chlorophyll a maximum in the Chukchi sea and Canada basin. Deep-Sea Res. II 118, 88–104.

Chandler, P., Yoo, S., (in press). reportNorth Pacific Ecosystem Status Report. North Pacific Marine Science Organization. PICES, Special Publication.

Chapman, W., Walsh, J., 1993. Recent variations in sea ice and air temperature at high latitudes. BAMS 74, 33–48.

Coachman, L.K., Aagaard, K., 1966. On the water exchange through Bering Strait. Limnol. Oceanogr. 11, 44–59.

Coachman, L.K., 1993. On the flow field in the Chirikov Basin. Continent. Shelf Res. 13, 481–508.

Coachman, L.K., Aagaard, K., Tripp, R.B., 1975. Bering Strait: the Regional Physical Oceanography. University of Washington Press.

Cokelet, E.D., 2016. 3-D water properties and geostrophic circulation on the eastern Bering Sea shelf. Deep-Sea Res. II 134, 65–85.

Comiso, J.C., 2012. Large decadal decline of the arctic multiyear ice cover. J. Clim. 25, 1176–1193.

Conner, J., Lauth, R.R., 2017. Results of the 2016 Eastern Bering Sea Continental Shelf Bottom Trawl Survey of Groundfish and Invertebrate Resources. US Dep. Comm. NOAA Tech Memo NMFSAFSC-352, p. 159. US Dep. Comm. NOAA Tech Memo NMFSAFSC-352, 159 (2017).

Crane, K., Ostrovsky, A., 2015. Introduction to the special issue: Russian-American long-term Census of the Arctic (RUSALCA). Oceanography 28. https://doi.org/10.5670/oceanog.2015.54, 18–3.

Danielson, S., Curchitser, E., Hedstrom, K., Weingartner, T., Stabeno, P., 2011. On ocean and sea ice modes of variability in the Bering Sea. J. Geophys. Res. Ocean 116, C12.

Danielson, S.L., Weingartner, T.J., Hedstrom, K.S., Aagaard, K., Woodgate, R., Curchitser, E., Stabeno, P.J., 2014. Coupled wind-forced controls of the Bering–Chukchi shelf circulation and the Bering Strait throughflow: Ekman transport, continental shelf waves, and variations of the Pacific–Arctic sea surface height gradient. Prog. Oceanogr. 125, 40–61.

Di Lorenzo, E., Schneider, N., Cobb, K.M., Franks, P.J.S., Chhak, K., Miller, A.J., McWilliams, J.C., Bograd, S.J., Arango, H., Curchitser, E., Powell, T.M., 2008. North Pacific Gyre Oscillation links ocean climate and ecosystem change. Geophys. Res. Lett. 35, 8. http://www.pmel.noaa.gov/dbo/about.

Duffy-Anderson, J.T., Stabeno, P., Andrews III, A.G., Cieciel, K., Deary, A., Farley, E., Fugate, C., Harpold, C., Heintz, R., Kimmel, D., Kuletz, K., 2019. Responses of the northern Bering Sea and southeastern Bering Sea pelagic ecosystems following record-breaking low winter sea ice. Geophys. Res. Lett. 46, 9833–9842.

Eisner, L.B., Siddon, E.C., Strasburger, W.W., 2015. Spatial and temporal changes in assemblage structure of zooplankton and pelagic fish in the eastern Bering Sea across varying climate conditions. TINRO 181, 141–160.

Eisner, L., Kivva, K., Baker, M., 2017. Workshop 9 – the role of the northern Bering Sea in modulating arctic environments: towards international interdisciplinary efforts. In: PICES science in 2016: A note from the Science Board Chairman, 25, p. 23. https://meetings.pices.int/publications/pices-press/volume25/issue1/PPJan2017.pdf#page=23.

Ester, M., Kriegel, H.P., Sander, J., Xu, X., 1996. A density-based algorithm for discovering clusters in large spatial databases with noise. In Kdd 96, 226–231.

Fanning, L., Mahon, R., Baldwin, K., Douglas, S., 2015. Transboundary Waters Assessment Programme (TWAP) Assessment of Governance Arrangements for the Ocean, Volume 1: Transboundary Large Marine Ecosystems. IOC-UNESCO, vol. 119. IOC Technical Series, Paris, p. 80.
Francis, J.A., Hunter, E., 2007. Changes in the fabric of the Arctic's greenhouse blanket. Environ. Res. Lett. 2, 045011.
Francis, J.A., Hunter, E., 2006. New insight into the disappearing Arctic sea ice. Eos Trans. Am. Geophys. Union 87, 509–511.
Glebova, S., Ustinova, E., Sorokin, Y., 2009. Long-term tendencies of atmospheric processes and thermal regime in Far-Eastern Seas of Russia in the last three decades. TINRO 159, 285–298.
Goes, J.I., do Rosario Gomes, H., Haugen, E.M., McKee, K.T., D'Sa, E.J., Chekalyuk, A.M., Stoecker, D.K., Stabeno, P.J., Saitoh, S.I., Sambrotto, R.N., 2014. Fluorescence, pigment and microscopic characterization of Bering Sea phytoplankton community structure and photosynthetic competency in the presence of a Cold Pool during summer. Deep-Sea Res. II 109, 84–99.
Golikov, A.N., Dolgolenko, M.A., Maximovich, N.V., Scarlato, O.A., 1990. Theoretical approaches to marine biogeography. Mar. Ecol. Progr. Ser. Oldendorf 63, 289–301.
Grebmeier, J.M., McRoy, C.P., Feder, H.M., 1988. Pelagic-benthic coupling on the shelf of the northern Bering and Chukchi seas. Food supply source and benthic biomass. Mar. Ecol. Prog. Ser. 48, 57–67.
Grebmeier, J.M., Cooper, L.W., Feder, H.M., Sirenko, B.I., 2006. Ecosystem dynamics of the Pacific-influenced northern Bering and Chukchi seas in the Amerasian Arctic. Prog. Oceanogr. 71, 331–361.
Hermann, A.J., Gibson, G.A., Bond, N.A., Curchitser, E.N., Hedstrom, K., Cheng, W., Wang, M., Cokelet, E.D., Stabeno, P.J., Aydin, K., 2016. Projected future biophysical states of the Bering Sea. Deep-Sea Res. II 134, 30–47.
Hollowed, A.B., Barbeaux, S.J., Cokelet, E.D., Farley, E., Kotwicki, S., Ressler, P.H., Spital, C., Wilson, C.D., 2012. Effects of climate variations on pelagic ocean habitats and their role in structuring forage fish distributions in the Bering Sea. Deep-Sea Res. II 65, 230–250.
Hollowed, A.B., Barange, M., Beamish, R.J., Brander, K., Cochrane, K., Drinkwater, K., Foreman, M.G., Hare, J.A., Holt, J., Ito, S.I., Kim, S., 2013. Projected impacts of climate change on marine fish and fisheries. ICES J. Mar. Sci. 70, 1023–1037.
Hu, A., Meehl, G.A., Otto-Bliesner, B.L., Waelbroeck, C., Han, W., Loutre, M.F., Lambeck, K., Mitrovica, J.X., Rosenbloom, N., 2010. Influence of Bering Strait flow and North Atlantic circulation on glacial sea-level changes. Nat. Geosci. 2, 118.
Huntington, H.P., Danielson, S.L., Wiese, F.K., Baker, M.R., Boveng, P., Citta, J.J., De Robertis, A., Dickson, D.M.S., Farley, E.V., George, J.C., Iken, K., Kimmel, D.G., Kuletz, K., Ladd, C., Levine, R., Quakenbush, L., Stabeno, P., Stafford, K.M., Stockwell, D., Wilson, C., 2020. Evidence suggests potential transformation of the Pacific Arctic ecosystem is underway. Nat. Clim. Change 1–7.
Khen, G.V., Basyuk, E.O., Vanin, N.S., Matveev, V.I., 2013. Hydrography and biological resources in the western Bering Sea. Deep-Sea Res. II 94, 106–120.
Hyndman, R.J., Athanasopoulos, G., 2018. Forecasting: principles and practice. OTexts.
Khen, G.V., Basyuk, E.O., Matveev, V.I., 2015. Parameters of the upper mixed layer and thermocline layer and chlorophyll-a in the western deep basin of the Bering Sea in summer and fall of 2002–2013, 2015 Izv. TINRO. 182, 115–131 [In Russian].
Khen, G.V., Zavolokin, A.V., 2015. The change in water circulation and its implication for the distribution and abundance of salmon in the western Bering Sea in the early 21st century. Russ. J. Mar. Biol. 41 (7), 528–547.
Kinder, T.H., Chapman, D.C., Whitehead Jr., J.A., 1986. Westward intensification of the mean circulation on the Bering Sea shelf. J. Phys. Oceanogr. 16, 1217–1229.
Kinnard, C., Zdanowicz, C.M., Fisher, D.A., Isaksson, E., de Vernal, A., Thompson, L.G., 2011. Reconstructed changes in Arctic sea ice over the past 1,450 years. Nature 479, 509.
Kinney, J.C., Maslowski, W., Aksenov, Y., de Cuevas, B., Jakacki, J., Nguyen, A., Osinski, R., Steele, M., Woodgate, R.A., Zhang, J., 2014. On the flow through Bering Strait: a synthesis of model results and observations. In: The Pacific Arctic Region. Springer, Dordrecht, pp. 167–198.
Kivva, K.K., 2016. Delineation of ecological regions in the Bering Sea based on oceanographic data. Trudy VNIRO 164, 62–74 [In Russian].
Ladd, C., Stabeno, P.J., 2012. Stratification on the eastern Bering sea shelf revisited. Deep-Sea Res. II 65, 72–83.
Kivva, K.K., Basyuk, E.O., Khen, G.V., Matyushenko, L.Y., Kubriakov, A.A., Somov, A.A., Klovach, N.V., Zolotov, A.O., Nadtochii, V.A., Kolpakov, N.V., Simokon, M.V., Kovekovdova, L.T., In Press. The Western Bering Sea. North Pacific Ecosystem Status Report. In: North Pacific Marine Science Organization, (PICES). Special Publication. In press.
Ladd, C., 2014. Seasonal and interannual variability of the Bering slope current. Deep-Sea Res. II 109, 5–13.
Lebrun, M., Vancoppenolle, M., Madec, G., Massonnet, F., 2019. Arctic sea-ice-free season projected to extend into autumn. Cryosphere 13, 79–96.
Levitus, S., Antonov, J.I., Boyer, T.P., Stephens, C., 2000. Warming of the world ocean. Science 287, 2225–2229.
Lindsay, R.W., Zhang, J., 2005. The thinning of Arctic sea ice, 1988–2003: have we passed a tipping point? J. Clim. 18, 4879–4894.
Lomas, M.W., Stabeno, P.J., 2014. Introduction to the Bering sea project: volume III. Deep-Sea Res. II 109, 1–4.
Luchin, V.A., 2007. Seasonal variability of water temperature in the active layer of the Far Eastern seas. In: Akulichev, V.A. (Ed.), Far Eastern Seas of Russia: in 4 Books. Book 1. Oceanological Studies. Nauka, Moscow, Russia, pp. 232–253 ([In Russian]).
Luchin, V., Kruts, A., Sokolov, O., Rostov, V., Rudykh, N., Perunova, T., Zolotukhin, E., Pischalnik, V., Romeiko, L., Hramushin, V., Shustin, V., 2009. Climatic Atlas of the north Pacific seas 2009: Bering sea, sea of Okhotsk, and sea of Japan. In: Akulichev, V., Volkov, Yu, Sapozhnikov, V., Levitus, S. (Eds.), NOAA Atlas NESDIS 67. US Gov. Printing Office, Wash. DC.
Mantua, N.J., Hare, S.R., Zhang, Y., Wallace, J.M., Francis, R.C., 1997. A Pacific interdecadal climate oscillation with impacts on salmon production. Bull. Am. Meteorol. Soc. 78, 1069–1080.
Maslowski, W., Marble, D.C., Walczowski, W., Semtner, A.J., 2001. On large-scale shifts in the Arctic Ocean and sea-ice conditions during 1979– 98. Ann. Glaciol. 33, 545–550.
Meier, W.N., Fetterer, F., Savoie, M., Mallory, S., Duerr, R., Stroeve, J., 2017. NOAA/NSIDC Climate Data Record of Passive Microwave Sea Ice Concentration. NSIDC: National Snow and Ice Data Center, Boulder, Colorado USA. https://doi.org/10.7265/N59P2ZTG, Version 3, 10 July 2019.
Meier, W.N., Fetterer, F., Windnagel, A.K., 2017. Near-real-time NOAA/NSIDC climate data record of passive microwave sea ice concentration. Version 1. https://doi.org/10.7265/N5FF3QJ6. July 2019.
Mordy, C.W., Cokelet, E.D., Ladd, C., Menzia, F.A., Proctor, P., Stabeno, P.J., Wisegarver, E., 2012. Net community production on the middle shelf of the eastern Bering Sea. Deep-Sea Res. II 65, 110–125.
Mueter, F.J., Litzow, M.A., 2008. Sea ice retreat alters the biogeography of the Bering Sea continental shelf. Ecol. Appl. 18, 309–320.
Natarov, V.V., 1963. On the water masses and currents of the Bering Sea [O vodnykh massakh i techeniyakh Beringova moray] (On Water Masses and Currents in the Bering Sea). Trudy VNIRO 48 (1). In Russian.
Nghiem, S., Rigor, R., Perovich, D., Clemente-Colon, P., Wetherly, J., Neumann, G., 2007. Rapid reduction of Arctic perennial sea ice. JGR Lett. 34, GL031480.
Ogi, M., Yamazaki, K., Wallace, J.M., 2010. Influence of winter and summer surface wind anomalies on summer Arctic sea ice extent. Geophys. Res. Lett. 39, L08502.
Ortiz, I., Aydin, K., Hermann, A.J., Gibson, G.A., Punt, A.E., Wiese, F.K., Eisner, L.B., Ferm, N., Buckley, T.W., Moffitt, E.A., Ianelli, J.N., 2016. Climate to fish: synthesizing field work, data and models in a 39-year retrospective analysis of seasonal processes on the eastern Bering Sea shelf and slope. Deep-Sea Res. II 134, 390–412.
Overland, J.E., Pease, C.H., 1982. Cyclone climatology of the Bering Sea and its relation to sea ice extent. Mon. Weather Rev. 110, 5–13.
Overland, J., Adams, J., Bond, N., 1999. Decadal variability of the Aleutian Low and its relation to high-latitude circulation. J. Clim. 12, 1542–1548.
Overland, J., Wang, M., Wood, K., Percival, D., Bond, N., 2012. Recent Bering Sea warm and cold events in a 95-year context. Deep-Sea Res. II 6–13.
Pante, E., Simon-Bouhet, B., 2013. Marmap: a package for importing, plotting and analyzing Bathymetric and topographic data in R. PLoS One 8 (9), e73051. https://doi.org/10.1371/journal.pone.0073051.
Panteleev, G., Yaremchuk, M., Luchin, V., Nechaev, D., Kukuchi, T., 2012. Variability of the Bering sea circulation in the period 1992-2010. J. Oceanogr. 68, 485–496. https://doi.org/10.1007/S10872-012-0113-O.
Parker-Stetter, S., Urmy, S., Horne, J., Eisner, L., Farley, E., 2016. Factors affecting summer distributions of Bering Sea forage fish species: assessing competing hypotheses. Deep-Sea Res. II 134, 255–269.
Pickart, R.S., Weingartner, T.J., Pratt, L.J., Zimmermann, S., Torres, D.J., 2005. Flow of winter-transformed Pacific water into the western Arctic. Deep-Sea Res. II 52, 3175–3198.
Pickart, R.S., Moore, G.W.K., Torres, D.J., Fratantoni, P.S., Goldsmith, R.A., Yang, J., 2009. Upwelling on the continental slope of the Alaskan Beaufort Sea: storms, ice, and oceanographic response. J. Geophys. Res. Ocean 114, C00A13. https://doi.org/10.1029/2008JC005009.
Pisareva, M.N., 2018. An overview of the recent research on the Chukchi Sea water masses and their circulation. Russ. J. Earth Sci. 18, 4.
Pisareva, M.N., Pickart, R.S., Spall, M.A., Nobre, C., Torres, D.J., Moore, G.W.K., Whitledge, T.E., 2015. Flow of Pacific water in the western Chukchi sea: results from the 2009 RUSALCA expedition. Deep-Sea Res. II 105, 53–73.
Pisareva, M.N., Pickart, R.S., Lin, P., Fratantoni, P., Weingartner, T.J., 2019. On the nature of wind-forced upwelling in Barrow Canyon. Deep-Sea Res. II. https://doi.org/10.1016/j.dsr2.2019.02.002.
Parkinson, C.L., 2014. Spatially mapped reductions in the length of the Arctic sea ice season. Geophys. Res. Lett. 41, 4316–4322.
Pease, C.H., 1980. Eastern Bering sea ice processes. Mon. Weather Rev. 108, 2015–2023.
Peng, G., Meier, W.N., Scott, D.J., Savoie, M.H., 2013. A long-term and reproducible passive microwave sea ice concentration data record for climate studies and monitoring. Earth Syst. Sci. Data 5, 311–318.
Peng, G., Steele, M., Bliss, A., Meier, W., Dickinson, S., 2018. Temporal means and variability of Arctic sea ice melt and freeze season climate indicators using a satellite climate data record. Rem. Sens. 10, 1328.
Perovich, D.K., Light, B., Eicken, H., Jones, K.F., Runciman, K., Nghiem, S.V., 2007. Increasing solar heating of the Arctic Ocean and adjacent seas, 1979-2005: Attribution and the role of the ice-albedo feedback. Geophys. Res. Lett. 34, L19505.
Pickart, R.S., Moore, G.W.K., Mao, C., Bahr, F., Nobre, C., 2016. Circulation of winter water on the Chukchi shelf in early summer. Deep-Sea Res. II 130, 56–75.
Plotnikov, V.V., Vakulskaya, N.M., 2012. Variability of ice conditions in the Bering Sea in the second half of 20 century and the beginning of 21 century//Izv. TINRO 170, 220–228. In Russian.
Polyakov, I., Alexeev, V.A., Ashik, I.M., Bacon, S., Beszynska-Moller, A., Carmack, E.C., Dmitrenko, I.A., Fortier, L., Gascard, J.C., Hansen, E., Holemann, J., Ivanov, V.V., Kikuchi, T., Kirillov, S., Lenn, Y.D., McLaughlin, F.A., Piechura, J., Repina, I., Timokhov, L.A., Walczoowski, W., Woodgate, R., 2011. Fate of the early 2000's Arctic warm water pulse. Bull. Am. Meteorol. Soc. 92, 561–566.

Post, E., Bhatt, U.S., Bitz, C.M., Brodie, J.F., Fulton, T.L., Hebblewhite, M., Kerby, J., Kutz, S.L., Stirling, I., Walker, D.A., 2013. Ecological consequences of sea ice decline. Science 341, 519–524.
Development Core Team, R, 2019. A Language and Environment for Statistical Computing. R Foundation for statistical computing, Vienna.
Ratmanov, G.E., 1937. On the hydrology of the Bering and Chukchi seas. Explor. Far-East Seas 5, 10–18.
Renner, M., Huntington, H.P., 2014. Connecting subsistence harvest and marine ecology: a cluster analysis of communities by fishing and hunting patterns. Deep-Sea Res. II 109, 293–299.
Reynolds, R.W., Rayner, N.A., Smith, T.M., Stokes, D.C., Wang, W., 2002. An improved in situ and satellite SST analysis for climate. J. Clim. 15, 1609–1625.
Rigor, I., Wallace, J., 2004. Variation in the age of Arctic sea ice and summer sea ice extent. JGR Lett. 31, GL019492.
Rigor, I.G., Wallace, J.M., Colony, R.L., 2002. Response of sea ice to the Arctic oscillation. J. Clim. 15, 2648–2663.
Roach, A.T., Aagaard, K., Pease, C.H., Salo, S.A., Weingartner, T., Pavlov, V., Kulakov, M., 1995. Direct measurements of transport and water properties through the Bering Strait. J. Geophys. Res. 100, 18443–18457.
Rodionov, S., Bond, N., Overland, J., 2007. The Aleutian low. Stormtracks, and winter climate variability in the Bering sea. Deep-Sea Res. II 54, 2560–2577.
Sample, T.M., Nichol, D.G., 1994. Results of the 1990 US-USSR Cooperative Bottom Trawl Survey of the Eastern and Northwestern Bering Sea Continental Shelf.
Schubert, E., Sander, J., Ester, M., Kriegel, H.P., Xu, X., 2017. DBSCAN revisited, revisited: why and how you should (still) use DBSCAN. ACM Trans. Database Syst. 42, 19.
Serreze, M., Holland, M., Stroeve, J., 2007. Perspectives on the Arctic's shrinking sea-ice cover. Science 315, 1533–1536.
Shimada, K., Kamoshida, T., Itoh, M., Hishino, S., Carmack, E., McLaughlin, F., Zimmerman, S., Proshutinsky, A., 2006. Pacific Ocean inflow: influence on catastrophic reduction of sea ice cover in the Arctic Ocean. Geophys. Res. Lett. 33, l08605.
Siddon, E., (in press). reportThe Eastern Bering Sea. North Pacific Ecosystem Status Report. North Pacific Marine Science Organization (PICES). Special Publication.
Siddon, E., Stephani Zador, S., 2019. Ecosystem Status report - eastern Bering sea. NPFMC Bering sea and Aleutian islands SAFE report. https://access.afsc.noaa.gov/REFM/REEM/ecoweb/pdf/2019EBSecosys.pdf.
Sigler, M.F., Harvey, H.R., Ashjian, C.J., Lomas, M.W., Napp, J.M., Stabeno, P.J., Van Pelt, T.I., 2010. How does Climate change affect the Bering Sea ecosystem? Trans. Am. Geophys. Union 91, 457–458.
Sigler, M.F., Stabeno, P.J., Eisner, L.B., Napp, J.M., Mueter, F.J., 2014. Spring and fall phytoplankton blooms in a productive subarctic ecosystem, the eastern Bering Sea, 1995–2011. Deep-Sea Res. II 109, 71–83.
Sigler, M.F., Mueter, F.J., Bluhm, B.A., Busby, M.S., Cokelet, E.D., Danielson, S.L., De Robertis, A., Eisner, L.B., Farley, E.V., Iken, K., Kuletz, K.J., 2017. Late summer zoogeography of the northern Bering and Chukchi seas. Deep-Sea Res. II 135, 168–189.
Stabeno, P.J., Bond, N.A., Kachel, N.B., Salo, S.A., Schumacher, J.D., 2001. On the temporal variability of the physical environment over the south-eastern Bering Sea. Fish. Oceanogr. 10, 81–98.
Stabeno, P.J., Bond, N.A., Salo, S.A., 2007. On the recent warming of the southeastern Bering Sea Shelf. Deep-Sea Res. II 54, 2599–2618. https://doi.org/10.1016/j.dsr2.2007.08.023.
Stabeno, P.J., Kachel, N.B., Moore, S.E., Napp, J.M., Sigler, M., Yamaguchi, A., Zerbini, A.N., 2012a. Comparison of warm and cold years on the southeastern Bering Sea shelf and some implications for the ecosystem. Deep-Sea Res. II 65 (70), 31–45. https://doi.org/10.1016/j.dsr2.2012.02.019.
Stabeno, P.J., Farley, E.V., Kachel, N.B., Moore, S., Mordy, C.W., Napp, J.M., Overland, J. E., Pinchuk, A.I., Sigler, M.F., 2012b. A comparison of the physics of the northern and southern shelves of the eastern Bering Sea and some implications for the ecosystem. Deep-Sea Res. II 65–70, 14–30.
Stabeno, P.J., Danielson, S.L., Kachel, D.G., Kachel, N.B., Mordy, C.W., 2016. Currents and transport on the eastern Bering Sea shelf: An integration of over 20 years of data. Deep-Sea Res. II 134, 13–29.
Stabeno, P.J., Duffy-Anderson, J.T., Eisner, L.B., Farley, E.V., Heintz, R.A., Mordy, C.W., 2017. Return of warm conditions in the southeastern Bering Sea: physics to fluorescence. PLoS One 12, e0185464. https://doi.org/10.1371/journal.pone.0185464.
Stabeno, P.J., Bell, S.W., Bond, N.A., Kimmel, D.G., Mordy, C.W., Sullivan, M.E., 2019. Distributed biological observatory region 1: physics, chemistry and plankton in the northern Bering sea. Deep-Sea Res. II 162, 8–21. https://doi.org/10.1016/j.dsr2.2018.11.006.
Stabeno, P.J., Bell, S.W., 2019. Extreme conditions in the Bering sea (2017–2018): record-breaking low sea-ice extent. Geophys. Res. Lett. 46, 8952–8959.
Stevenson, D.E., Lauth, R.R., 2012. Latitudinal trends and temporal shifts in the catch composition of bottom trawls conducted on the eastern Bering Sea shelf. Deep-Sea Res. II 65, 251–259. https://doi.org/10.1016/j.dsr2.2012.02.021.
Stevenson, D.E., Lauth, R.R., 2019. Bottom trawl surveys in the northern Bering Sea indicate recent shifts in the distribution of marine species. Polar Biol. 42, 407–421.
Steele, M., Ermold, W., Zhang, J., 2008. Arctic Ocean surface warming trends over the past 100 years. Geophys. Res. Lett. 35, L02614. https://doi.org/10.1029/2007GL031651.
Stroeve, J., Holland, M.M., Meier, W., Scambos, T., Serreze, M., 2007. Arctic sea ice decline: faster than forecast. Geophys. Res. Lett. 34, 9.
Stroeve, J.C., Crawford, A.D., Stammerjohn, S., 2016. Using timing of ice retreat to predict timing of fall freeze-up in the Arctic. Geophys. Res. Lett. 43, 6332–6340.
SWIPA, 2011. Snow, Water, Ice and Permafrost in the Arctic. Cambridge University Press Executive Summary, Cambridge, p. 16. Oslo: Arctic Monitoring and Assessment Program.
SWIPA, 2012. Snow, Water, Ice and Permafrost in the Arctic. Cambridge University Press Executive Summary, Cambridge, p. 16. Oslo: Arctic Monitoring and Assessment Program.
Thomson, J., Rogers, W.E., 2014. Swell and Sea in the emerging Arctic Ocean. Geophys. Res. Lett. 41, 3136–3140.
Thorson, J.T., 2019. Measuring the impact of oceanographic indices on species distribution shifts: the spatially varying effect of cold-pool extent in the eastern Bering Sea. Limnol. Oceanogr. 64, 2632–2645.
Torres-Valdés, S., Tsubouchi, T., Bacon, S., Naveira-Garabato, A.C., Sanders, R., McLaughlin, F.A., Whitledge, T.E., 2013. Export of nutrients from the Arctic Ocean. J. Geophys. Res. 118, 1625–1644.
United States Navy, 2014. The United States Navy Artic Roadmap for 2014 to 2030. Department of the Navy, Washington, D.C, p. 38. Available at: www.navy.mil/docs/USN_arctic_roadmap.pdf.
Van Pelt, T.I., Huntington, H.P., Romanenko, O.V., Mueter, F.J., 2017. The Missing Middle: central Arctic Ocean gaps in fishery research and science communication. Mar. Pol. 85, 79–86.
Verkhunov, A.V., Tkachenko, Y.Y., 1992. Recent observations of variability in the western Bering Sea current system. J. Geophys. Res. Ocean 97, 14369–14376.
Verkhunov, A.V., 1995. The role of hydrological and hydrochemical processes in the formation of bioproductivity of the Bering Sea shelf. Moscow, VNIRO. In: Kotenev, B. N., Sapozhnikov, V.V. (Eds.), Complex Studies of the Bering Sea Ecosystem, pp. 52–78 ([In Russian]).
Walsh, J.J., Dieterle, D.A., Muller-Karger, F.E., Aagaard, K., Roach, A.T., Whitledge, T.E., Stockwell, D., 1997. CO2 cycling in the coastal ocean. II. Seasonal organic loading of the Arctic Ocean from source waters in the Bering Sea. Continent. Shelf Res. 17, 1–3.
Walsh, J.E., Chapman, W.L, 2001. 20th-century sea-ice variations from observational data. Ann. Glaciol. 33, 444–448.
Walsh, J.J., Dieterle, D.A., Maslowski, W., Grebmeier, J.M., Whitledge, T.E., Flint, M., Sukhanova, I.N., Bates, N., Cota, G.F., Stockwell, D., Moran, S.B., 2005. A numerical model of seasonal primary production within the Chukchi/Beaufort Seas. Deep-Sea Res. II 52, 3541–3576.
Walsh, J.E., Fetterer, F., Scott, S.J., Chapman, W.L., 2017. A database for depicting Arctic sea ice variations back to 1850. Geogr. Rev. 107, 89–107.
Walsh, J., Chapman, W., 1990. Short-term climatic variability of the Arctic. J. Clim. 3, 237–250.
Watson, J.T., 2019. Spatial and temporal visualizations of satellite-derived sea surface temperatures for Alaska fishery management areas. Pac. States E J Sci. Visual. PSESV. https://doi.org/10.28966/PSESV.2019.003. Article 003.
Wendler, G., Chen, L., Moore, B., 2014. Recent sea ice increase and temperature decrease in the Bering Sea area, Alaska. Theor. Appl. Climatol. 117, 393–398.
Wang, M., Overland, J.E., 2009. A sea ice free summer Arctic within 30 years? Geophys. Res. Lett. 36, 7.
Wang, J., Cota, G.F., Comiso, J.C., 2005. Phytoplankton in the Beaufort and Chukchi Seas: distribution, dynamics, and environmental forcing. Deep-Sea Res. II 24, 3355–3368.
Whitehouse, G.A., Aydin, K., Essington, T.E., Hunt, G.L., 2014. A trophic mass balance model of the eastern Chukchi Sea with comparisons to other high-latitude systems. Polar Biol. 37, 911–939.
Wood, K.R., Bond, N.A., Danielson, S.L., Overland, J.E., Salo, S.A., Stabeno, P.J., Whitefield, J., 2015. A decade of environmental change in the Pacific Arctic region. Prog. Oceanogr. 136, 12–31.
Woodgate, R.A., Aagaard, K., 2005. Revising the Bering Strait freshwater flux into the Arctic Ocean. Geophys. Res. Lett. 32, 2.
Woodgate, R.A., Aagaard, K., Weingartner, T.J., 2005. Monthly temperature, salinity, and transport variability of the Bering Strait through flow. Geophys. Res. Lett. 32, 4.
Woodgate, R.A., Weingartner, T., Lindsay, R., 2007. The 2007 Bering Strait oceanic heat flux and anomalous Arctic sea-ice retreat. Geophys. Res. Lett. 37, 0094-8276.
Woodgate, R.A., Weingartner, T., Lindsay, R., 2010. The 2007 Bering Strait oceanic heat flux and anomalous Arctic sea-ice retreat. Geophys. Res. Lett. 37, 1. https://doi.org/10.1029/2009GL041621.
Woodgate, R.A., Weingartner, T.J., Lindsay, R., 2012. Observed increases in Bering Strait oceanic fluxes from the Pacific to the Arctic from 2001 to 2011 and their impacts on the Arctic Ocean water column. Geophys. Res. Lett. 39, 24.
Woodgate, R.A., Stafford, K.M., Prahl, F.G., 2015. A synthesis of year-round interdisciplinary mooring measurements in the Bering Strait (1990–2014) and RUSALCA (2004–2011). Oceanography 28, 46–67.
Woodgate, R.A., 2018. Increases in the Pacific inflow to the Arctic from 1990 to 2015, and insights into seasonal trends and driving mechanisms from year-round Bering Strait mooring data. Prog. Oceanogr. 160, 124–154.
Wyllie-Echeverria, T., 1995. Seasonal Sea Ice, the Cold Pool and Gadid Distribution on the Bering Sea Shelf (Doctoral Dissertation).
Wyllie-Echeverria, T.I.N.A., Wooster, W.S., 1998. Year-to-year variations in Bering Sea ice cover and some consequences for fish distributions. Fish. Oceanogr. 7, 159–170.
Zhang, J., Lindsay, R., Schweiger, A., Steele, M., 2013. The impact of an intense summer cyclone on 2012 Arctic sea ice retreat. Geophys. Res. Lett. 40, 720–726.
Zhang, J., Ashjian, C., Campbell, R., Spitz, Y.H., Steele, M., Hill, V., 2015. The influence of sea ice and snow cover and nutrient availability on the formation of massive under-ice phytoplankton blooms in the Chukchi Sea. Deep-Sea Res. II 118, 122–135.

Deep–Sea Research II 177 (2020) 104805

Contents lists available at ScienceDirect

Deep-Sea Research Part II

journal homepage: http://www.elsevier.com/locate/dsr2

Vertical structure and temporal variability of currents over the Chukchi Sea continental slope

Phyllis J. Stabeno [a,*], Ryan M. McCabe [b]

[a] NOAA Pacific Marine Environmental Laboratory (PMEL), Ocean Environment Research Division, 7600 Sand Point Way NE, Seattle, WA, 98115-6349, USA
[b] Joint Institute for the Study of the Atmosphere and Ocean (JISAO), University of Washington, 3737 Brooklyn Ave NE, Seattle, WA, 98195, USA

A B S T R A C T

Observations from a single mooring site on the northern Chukchi Sea continental slope near the 1000-m isobath are presented. This site was occupied consecutively for three years (spanning September 2014–August 2017). Vertically the flow divides into three depth ranges: the upper ~200 m, ~200–~850 m and near-bottom flow. In the upper ~200 m, the mean flow was northwestward and strongest in the summer months. During winter months, currents decreased in magnitude, and in some years even reversed in direction. Satellite-tracked drifter trajectories (drogue depth ~30 m) show this along-slope flow persists at least from 156 to 165 °W, with an average velocity of ~17 cm s^{-1}. This northwestward flowing current is the Chukchi Slope Current. From ~250 m to ~850 m, the flow reversed; this weak flow is the Arctic-wide cyclonic boundary current advecting Atlantic Water. The mean flow at ~900 m is weak and on an annual time scale not significantly different from 0 cm s^{-1}. It consists of Arctic deep water. In the upper two layers, currents vary on the scale of days to seasons, with short-term reversals common. Currents below 40 m were not significantly correlated with local winds nor wind stress curl. We hypothesize that the northwestward flowing Chukchi Slope Current is a consequence of dynamics associated with the Beaufort Gyre.

1. Introduction

The Chukchi Sea consists of a broad shallow (<80 m) shelf, extending >800 km northward from its southern boundary at Bering Strait to the shelf break bounding the Arctic basin (Fig. 1). Approximately 1×10^6 m^3 s^{-1} (1 Sverdrup [Sv]) of Pacific water enters the shelf through Bering Strait (Woodgate et al., 2005a, 2012) and continues generally northward following the bathymetry (Woodgate et al., 2005b). Most of this flow exits the Chukchi Shelf through two canyons—Barrow Canyon in the east (Coachman et al., 1975; Weingartner et al., 2005) and Herald Canyon in the west (Coachman et al., 1975; Pickart et al., 2010). The flow exiting via Barrow Canyon is a combination of the northward flow through Central Channel that joins the coastal flow offshore of Icy Cape. Exiting Herald Canyon, there is a relatively narrow eastward flowing shelfbreak jet (Linders et al., 2017; Corlett and Pickart, 2017; Li et al., 2019).

As Pacific water transits the Chukchi Shelf northward, it is modified through local physical and biological processes. In summer, when sea-ice coverage is marginal or absent, water over the shallow Chukchi Shelf gains heat. A portion of this excess summer heat is advected north from the Bering Sea through Bering Strait (e.g., Woodgate et al., 2012), but the heat gained locally over the Chukchi Shelf through solar radiation can also be substantial (Tsukada et al., 2018). The modified shelf water then flows off the shelf and into the Canada Basin (Shimada et al., 2001; Steele et al., 2004; Watanabe et al., 2017; Fine et al., 2018) where it contributes to the observed accumulation of heat (Timmermans et al., 2014, 2018). Excess subsurface heat, as far west as the Chukchi Abyssal Plain (just to the west of the Chukchi Borderland), was recently identified to have a Pacific origin (Watanabe et al., 2017). Such subsurface heat anomalies can persist for years (Watanabe et al., 2017; Fine et al., 2018) and likely lead to delays in winter freeze-up and an overall decline of sea ice (Steele et al., 2008; Jackson et al., 2012; Timmermans, 2015; Serreze et al., 2016). The pathways of Pacific Water after exiting Barrow Canyon are not well known.

The basin in the vicinity of the Chukchi and Beaufort shelves is influenced by the anti-cyclonic Beaufort Gyre (Aagaard and Carmack, 1989; Regan et al., 2019), which dominates surface flow in the Canada Basin. Along the slope and beneath the Beaufort Gyre is the Arctic Ocean Boundary Current (AOBC; Woodgate et al., 2001), which moves Atlantic water cyclonically around the Arctic basin. The westward flowing Chukchi Slope Current (CSC) resides along the slope from Barrow Canyon to Herald Canyon (Corlett and Pickart, 2017; Stabeno et al., 2018; Li et al., 2019). The recently identified CSC appears to vary seasonally, with the strongest flow in the summer months and weak or even eastward flow dominating in the winter months. From earlier results, it appears to be confined to the upper ~300 m, with an eastward

* Corresponding author.
E-mail address: phyllis.stabeno@noaa.gov (P.J. Stabeno).

https://doi.org/10.1016/j.dsr2.2020.104805
Received 26 August 2019; Received in revised form 8 May 2020; Accepted 23 May 2020
Available online 17 June 2020

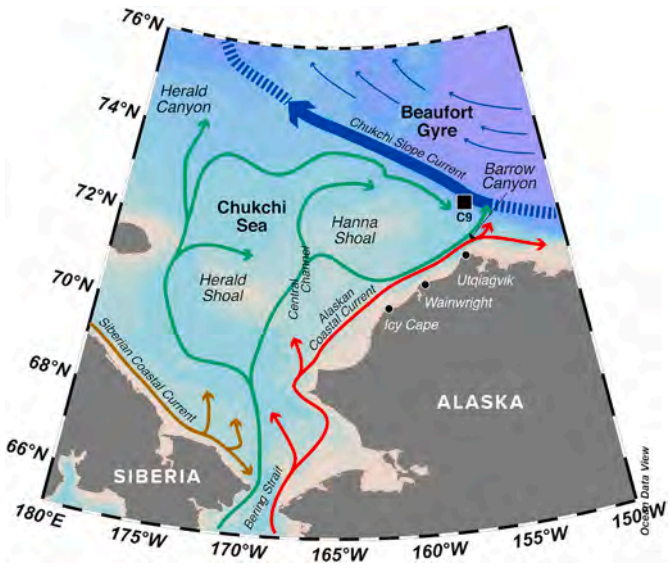

Fig. 1. Schematic map of surface flow patterns over the Chukchi Sea continental shelf and slope (adapted from Stabeno et al., 2018). The location of the C9 mooring, near the 1000-m isobath, is indicated with the black square.

reversal at deeper depths (Stabeno et al., 2018). Analysis by Corlett and Pickart (2017) indicates that it is baroclinically unstable and meanders along the slope. Satellite-tracked drifter trajectories show that the CSC extends from at least Barrow Canyon to near Herald Canyon (Stabeno et al., 2018). Watanabe et al. (2017) used observations and a high-resolution numerical ocean model to demonstrate that Pacific-origin heat gets transported in the CSC as far west as the Chukchi Borderland.

This paper concentrates on a 34-month time series of currents, temperature and salinity collected at a single mooring site on the Chukchi continental slope. A single mooring was deployed in each of three years (2014, 2015 and 2016) in the late summer, near the 1000-m isobath at a site (C9; 72.46°N, 156.55°W) north of Utqiaġvik (previously Barrow), Alaska. The goal of these deployments was to better understand the flow along the slope and the fate of Chukchi Shelf water exiting Barrow Canyon. Data and handling methods are described in section 2. Results are presented in section 3, including: vertical structure and temporal variability of currents and temperature at C9, relationship of sea ice and winds to flow patterns, variability of Atlantic water and the strength of the AOBC. Section 4 provides a discussion of the results, summary and conclusions.

2. Data sources and methods

2.1. Atmospheric variables

Two different reanalysis products were considered in order to provide a comprehensive record of wind over our region of interest. The first is the European Centre for Medium-Range Weather Forecasts (ECMWF) ERA5 reanalysis (https://climate.copernicus.eu/climate-reanalysis), which is the latest update to the ERA-Interim reanalysis (Dee et al., 2011). Like ERA-Interim, ERA5 solutions are based on a 4D-Var data assimilation routine, but the ERA5 model implements substantial improvements relative to ERA-Interim and includes hourly output at 31 km horizontal resolution (Haiden et al., 2017; Hersbach et al., 2018). At present, no thorough validation exists for ERA5 in the Alaskan Arctic, but we note that an Arctic-focused comparison of seven reanalysis products found that ERA-Interim was among the top-performing models for a number of key parameters (Lindsay et al., 2014). For 10-m winds, which is our focus, ERA-Interim had low biases of $\leq$0.5 m s^{-1} as well as the highest correlations ($\geq$0.85) among the seven different reanalysis models when compared to independent daily-averaged wind records measured from drifting ice stations (Lindsay et al., 2014). Belmonte Rivas and Stoffelen (2019) discuss improvements of ERA5 wind relative to ERA-Interim in comparisons with Advanced Scatterometer satellite wind on a global scale, including a 20% improvement in root mean square wind speed agreement, and reductions in divergence and curl biases; the Arctic, however, was not part of that analysis. Given the model and resolution improvements of ERA5 relative to ERA-Interim, we anticipate model skill that is at least on par with that of ERA-Interim in the Arctic.

The second reanalysis product that we considered is the National Center for Environmental Prediction (NCEP) North American Regional Reanalysis (NARR). It is an extension of the NCEP Global Reanalysis that is run over the North American Region with improvements in both resolution (~32 km) and accuracy (Mesinger et al., 2006). Stegall and Zhang (2012) reported moderate agreement between coastal land- and ocean-based wind observations in northern Alaska and the NARR winds, with correlations of 0.66 for speed and 0.71 for direction. NARR wind variance was close to observed wind variance, but NARR wind speeds were biased low (by as much as 2.5 m s^{-1}). Moore et al. (2008) and Renfrew et al. (2009) reported somewhat better performance in comparisons to buoy and aircraft measurements off southern Greenland (correlations of 0.88 for speed and $\geq$0.92 for direction with a ~1.5 m s^{-1} low bias). NARR data are available eight times daily from 1979 to present. Three-hourly winds at 10 m were obtained from the NOAA Earth System Research Laboratory, Physical Sciences Division in Boulder, Colorado, USA, from their website (https://www.esrl.noaa.gov/psd/).

For both reanalysis products, data spanning 2014–2017 were downloaded and then linearly interpolated onto desired locations or averaged over specific regions as discussed in the text. Because grid-scale noise is present in NARR wind, we first applied a two-dimensional Gaussian filter (standard deviation = 1; 5 grid points wide) to the spatial wind fields before calculating wind stress curl. We then re-gridded the smoothed NARR wind fields onto a regularly spaced 0.2° latitude by 0.6° longitude grid. Wind stress for both NARR and ERA5 was then estimated at each grid point following Large and Pond (1981), and wind stress curl was calculated using a centered-difference approach.

Comparisons with observed wind from the Barrow Atmospheric Baseline Observatory near Utqiaġvik, Alaska, were also made. Hourly averaged meteorological data recorded at the Barrow Observatory were downloaded from the NOAA ESRL Global Monitoring Division website at https://www.esrl.noaa.gov/gmd/obop/brw/.

2.2. Sea ice

Sea-ice concentration data (2014–2017) used herein were the daily Version 3 Sea-Ice Concentrations from Nimbus-7 SMMR and DMSP SSM/I-SSMIS and were obtained from the National Snow and Ice Data Center (http://nsidc.org/data/nsidc-0079). These data are calculated using NASA's Earth Observing System AMSR-E bootstrap algorithm. Average ice concentrations in a 50 km × 50 km square around the mooring site (72.5°N, 156.5°W) were calculated.

2.3. Moorings

Moorings at C9 were deployed in three consecutive years (spanning September 2014–July 2017) in ~1000 m of water on the Chukchi continental slope northwest of Barrow Canyon (Fig. 1, Table 1). For reference, this site was ~9.8 km offshore of the seaward-most mooring (deployed during the previous year) discussed in Li et al. (2019). Because of the steepness of the slope and the interference of sea ice during deployment, actual C9 bottom depths ranged from 870 m to 970 m. The mooring design included three RCM current meters near ~900 m, ~600 m and ~300 m; an upward looking 75 kHz acoustic Doppler current profiler (ADCP) at a depth of ~300 m; and a Sea-Bird Electronics

Table 1
The duration of deployment, location and bottom depth are indicated in the first column. The instrumentation and depth of instruments are indicated in columns 2–4. MTR refers to miniature temperature recorders.

Deployment/ Recovery Info	Instrument	Measurement	Deployment Depth (m)	Comments
14C9	75 kHz ADCP	Currents	345	16-m bins
10/1/14–9/ 15/15	SBE-37	Temp, Sal	349	
72° 27.5′ N	RCM-9	Currents, Temp	350	Inst. at 645 m failed
156° 33.9′ W	RCM-11	Currents, Temp	895	
950 m				
15C9	75 kHz ADCP	Currents	372	8-m bins
9/15/15–9/8/ 16	SBE-37	Temp, Sal	382	
72°28.0′ N	RCM-9	Currents, Temp	378, 672	
156°33.0′ W	RCM-11	Currents, Temp	922	
970 m				
16C9	75 kHz ADCP	Currents	290	16-m bins
9/8/16–8/3/ 2017	MTR	Temp	90, 101, 120, 150, 180, 210, 240, 270	
72°27.8′ N	SBE-37	Temp, Sal	45, 460	
156°32.9W	RCM-9	Currents, Temp	311	
870 m	RCM-11	Currents, Temp	467, 822	

(SBE) Microcat near a depth of 400 m (actual instrument depths are listed in Table 1). Additional temperature sensors (miniature temperature recorders or MTRs, and SBE-37 which also measures conductivity) were added in the upper 300 m for the 2016 deployment. Data were collected at hourly intervals except for the ADCP deployed in 2014, which recorded data at 2 h intervals. All instruments were calibrated prior to deployment and data were processed according to manufacturers' specifications. Current meter time series were low-pass filtered with a 35 h, cosine-squared, tapered Lanczos filter to remove tidal and higher-frequency variability, and then resampled at 6 h intervals. Additional analyses were completed using other filters as described in the text (e.g., section 3.4.1). Final processed time series data are accurate to at least ±0.002 °C, ±0.0005 S/m and ±0.5 cm s^{-1} (temperature, conductivity and currents, respectively).

Wavelet analysis was used to examine the dominant frequencies of the low-pass filtered current data. The wavelet function used here was the Morlet wavelet with non-dimensional frequency six, consisting of a sinusoid modulated by a Gaussian. The wavelet power spectra were normalized by the variance of each time series. The 95% significance levels were calculated by comparing each wavelet power spectrum to a red noise background spectrum, modeled as univariate lag-1 autoregressive (AR-1) processes generated with variance equal to that of each time series (Torrence and Compo, 1998).

2.4. Satellite-tracked drifters

From 2012 to 2018, the National Oceanographic and Atmospheric Administration's Ecosystem Fisheries Oceanographic Coordinated Investigations (EcoFOCI) program deployed 45 satellite-tracked drifters in the Chukchi Sea. Drifters were drogued at a depth of 25–35 m using a 10-m long "holey sock" drogue. Each drifter reported position and sea surface temperature via Argos approximately 14 times per day. Data were examined and spurious points were removed by inspection, as were data collected after drogues were lost (as indicated by a sensor), and after drifters grounded or entered into ice (determined from satellite maps of sea-ice extent). The resulting data were linearly interpolated to hourly intervals.

Lagrangian velocities were determined by centered differences using the hourly drifter positions. A low-pass filter (25-h running mean) was applied to the drifter location data. Spatially gridded mean velocities were then calculated following Stabeno and Reed (1994) and Stabeno et al. (2016b). In this analysis, each 2-day period within a grid area was considered an independent estimate. Each rectangular grid cell was 1° latitude by 3° longitude. In addition, three rhomboids of a similar size abutted the slope (Fig. 2).

2.5. Shipboard hydrography

In this paper, temperature and salinity data from a cruise aboard the R/V *Ocean Starr* in late summer 2017 are presented. Conductivity, temperature, depth (CTD) profiles were collected using a Sea-Bird Electronics (SBE) 911*plus* system with dual temperature, conductivity (for salinity) and oxygen (SBE-43) sensors, and single chlorophyll fluorescence (WET Labs WETStar WS3S) and photosynthetically active radiation (PAR; Biospherical Instruments QSP-200 L4S or QSP-2300) sensors. Data were recorded during the downcast, with a descent rate of

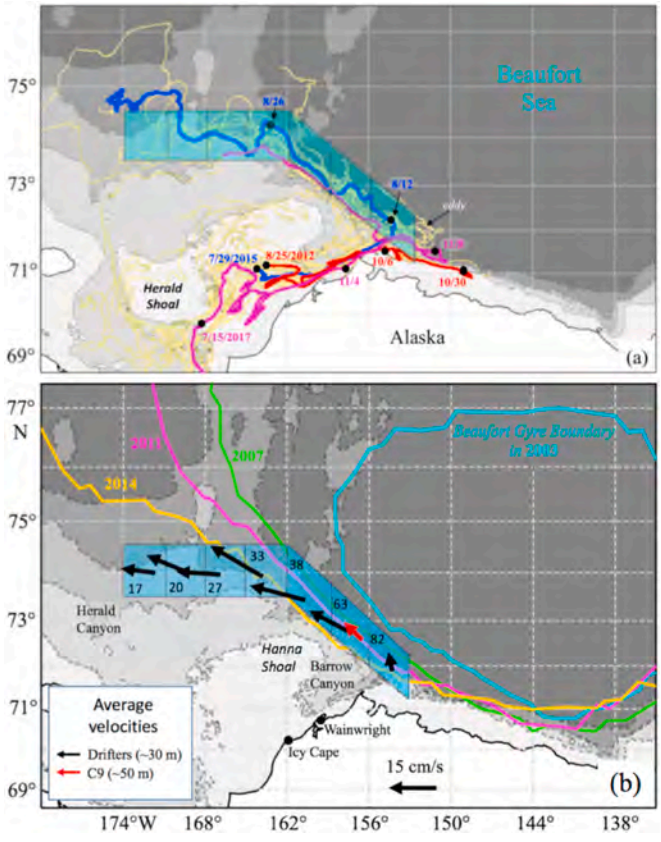

Fig. 2. (a) Drifter trajectories (drogue depth ~30 m). The yellow trajectories indicate drifters deployed in the region. Three pathways are shown in different colors: (1) eastward flow on the Beaufort Shelf (red); (2) first eastward flow and then northwestward flow (magenta); and (3) northwestward flow upon exiting Barrow Canyon (blue). Selected dates are indicated along each trajectory. (b) The position of the edge of the Beaufort Gyre during four different years (adapted from Regan et al., 2019, their Fig. 3). The mean Lagrangian velocity of the drifters in each box (black arrows), with the number of independent estimates that contributed to the mean (black numerals). The red arrow is the mean velocity at ~50 m from the three C9 mooring deployments. (For interpretation of the references to color in this figure legend, the reader is referred to the Web version of this article.)

15 m min^{-1} to a depth of ~30 m, and 30 m min^{-1} at deeper depths. Salinity calibration samples were taken on approximately one-third of the 135 casts and analyzed on a laboratory salinometer. The bottle samples were then used to post-calibrate the CTD data.

In addition to the 2017 R/V *Ocean Starr* data, historical CTD profiles collected aboard a variety of other vessels that were seaward of the shelf-break, within 200 km of the C9 mooring location, and at least 400 m deep are used to describe mean water properties over the Chukchi continental slope. Those historical profiles were taken from the much larger accumulated data set provided by Corlett and Pickart (2017).

3. Results and discussion

3.1. Patterns of variability of flow in the Chukchi Slope Current

3.1.1. Spatial patterns of flow

Trajectories from satellite-tracked drifters (yellow lines Fig. 2a) provide information on general flow patterns during the ice-free season. Drifters deployed in the southern Chukchi Sea (south of 70°N), generally followed one of two trajectories, one northward through Central Channel and the other westward then turning northward through Herald Canyon. Most of the drifters did not enter onto Hanna nor Herald shoals (Fig. 2a). Stabeno et al. (2018) calculated that ~40% of the transport through Bering Strait exits through Barrow Canyon as part of the Alaskan Coastal Current (ACC). The ACC has a buoyant low salinity core, but similar to the Alaska Coastal Current in the Gulf of Alaska (Stabeno et al., 2004, Stabeno et al., 2016), it is wind driven and extends beyond the freshwater core. The strongest transport is in the summer when northward winds dominate the Chukchi Sea. Only about half of the drifters deployed in the Chukchi Sea exited the shelf. The remainder failed to reach the northern boundary before sea ice arrived or before the shifting winds weakened the northward flow. Strong wind-driven reversals are evident in the 2017 (magenta) trajectory (Fig. 2a). It must be noted that except for the low-salinity Alaskan Coastal Water, the water in the ACC is more saline and denser than the melt water that typically resides along the slope. When exiting Barrow Canyon, the ACC water sinks to ~40 m (Stabeno et al., 2018). Thus, once seaward of Barrow Canyon the drifters are not tracking shelf water.

Most of the drifters deployed over the eastern Chukchi continental shelf traveled northward through Central Channel and turned eastward south of Hanna Shoal (Fig. 2; Stabeno et al., 2018). This flow intensifies between Icy Cape and Wainwright into a narrow current (the ACC) that exits the shelf via Barrow Canyon (Stabeno et al., 2018). The trajectories of flow, once the drifters have exited Barrow Canyon, fall into three patterns (Fig. 2a): (1) a sharp westward turn and then continuing along the slope (blue); (2) an eastward turn for a short period (days) followed by a westward trajectory along the slope (magenta); and (3) eastward flow on the Beaufort shelf or along the shelf break (red). Of the 22 drifters that passed through Barrow Canyon, nine followed the first pathway and an equal number followed the second pathway traveling eastward for ~8 days (on average) before turning westward; only four followed the third pathway. The remainder of the 45 drifters that were deployed in the Chukchi Sea did not leave the shelf.

Of the satellite-tracked drifters that joined the westward flowing CSC, most continued northwestward along the slope until sea ice arrived. The remaining drifters ceased transmitting or lost their drogue before the arrival of sea ice. Mean Lagrangian velocities of all of the satellite-tracked drifters that transited along the continental slope were calculated as described in section 2.4, with an integral time scale of 48 h. Velocity was calculated in seven boxes (three rhomboids and four rectangles; Fig. 2). The outflow from Barrow Canyon dominates in the easternmost box. The velocity estimated in this box is biased, because all drifters were deployed on the shelf, so northward flow out of Barrow Canyon dominates the mean flow. The next three boxes (moving westward) all show a well-defined CSC (black arrows, Fig. 2b). Mean velocities from east to west were 14.9 ± 2.7 (mean ± standard error), 19.4 ± 2.5, and 17.3 ± 2.9 cm s^{-1}, respectively. Fewer drifters survived long enough to travel west of 165°W, and the velocities decreased from 14 ± 3.0 to 9.2 ± 1.6 cm s^{-1} in that region. The mean velocity (at 50 m) from the moorings (red arrow) was weaker than that calculated from the drifters for three reasons. Drogue depths were typically shallower than the uppermost ADCP bin; the Lagrangian velocities were primarily during the summer and early fall months (July–November) when the CSC is at its strongest; and the drifters only entered the CSC when the currents were westward.

The trajectories of drifters in the CSC were often characterized by meanders (wavelength ~100 km). Eddies also were apparent in two trajectories (one is illustrated in Fig. 2a) with radii of 25–50 km. The drifters remained near the slope in a ~70 km wide band, which is similar to the width of the CSC observed by Corlett and Pickart (2017).

It must be noted that the drifter trajectories reveal flow that is limited to the ice-free period. Once entering the ice field the drifters move with the sea ice. A few drifters transmitted locations sporadically during the winter, but most drifters caught in the sea ice were damaged and failed during winter or in spring/summer with the melting of the sea ice.

3.1.2. Temporal variability and vertical structure of flow at C9

Year-long deployments of each C9 mooring were made in late summer of 2014, 2015, and 2016, resulting in 34-month long velocity, temperature and salinity records at a variety of depths (Table 1; Figs. 3–5). During the first two deployments, sea ice arrived in the vicinity of C9 (50 km × 50 km box centered on the mooring site) in October and reached >80% areal ice cover within a month (Figs. 3 and 4, top panels). In the fall of 2016, sea ice arrived a month later in November, with >80% areal cover occurring ~3 weeks later (Fig. 5). Each year, the ice retreat began in June, with areal ice coverage falling below 20% from mid-July to early August.

The current meter records reveal a well-organized flow (Figs. 3–5). In the upper 100 m, the net direction ranged from 300 to 324° (Table 2), which is approximately the along-slope direction at C9. The principal axes were in a similar direction, indicating that most of the variance was also in the along-slope direction. Contours of monthly mean along-slope currents (toward 310°) reveal the mean structure of the surface-intensified CSC (Fig. 6a). During the warm months, the CSC extended to depths of approximately 200–250 m depending on the year, which is consistent with the mean geostrophic description constructed from historical hydrographic profiles by Corlett and Pickart (2017), the modeling results of Watanabe et al. (2017) and the results presented in Li et al. (2019). There was a strong seasonality in the flow, with northwestward flow most common in the warm season, and reversals occurring below 200 m in the cold seasons of 2015 and 2016. September through November of 2016 showed southeastward flow from the surface to at least 500 m (Figs. 5 and 6).

The current measurements deeper in the water column (>250 m) reveal the existence of an along-slope undercurrent that flows southeastward for at least part of the year (Figs. 3–5, Table 2). At C9, daily magnitudes of this southeastward flowing undercurrent were ≤10 cm s^{-1}. At ~300 m, there was a strong seasonality in the flow, with northwestward flow during spring shifting to southeastward flow in September 2015, June 2016 and July 2017 (Fig. 6b, solid line).

While the areal sea-ice concentration, and the flow in the upper 200 m and at 300 m all have annual signals, it is not clear that they are related. Depth-averaged flow in the upper 200 m ($V_{0\text{-}200}$) begins to increase before ice retreats in the summer and begins to weaken before the arrival of sea ice in the fall. The relationship between flow in the upper 200 m and at 300 m also appears to be somewhat out of phase, with northwestward flow at 300 m (Fig. 6b, solid line) tending to reverse just as the depth-averaged flow in the upper 200 m reaches its maximum.

On shorter time scales (days to weeks), variability, including flow reversals, was common in both the CSC and the flow below ~200 m (the AOBC; Figs. 3–5). The near-bottom (~900 m) flow was extremely weak during the first two deployments and not statistically different from 0

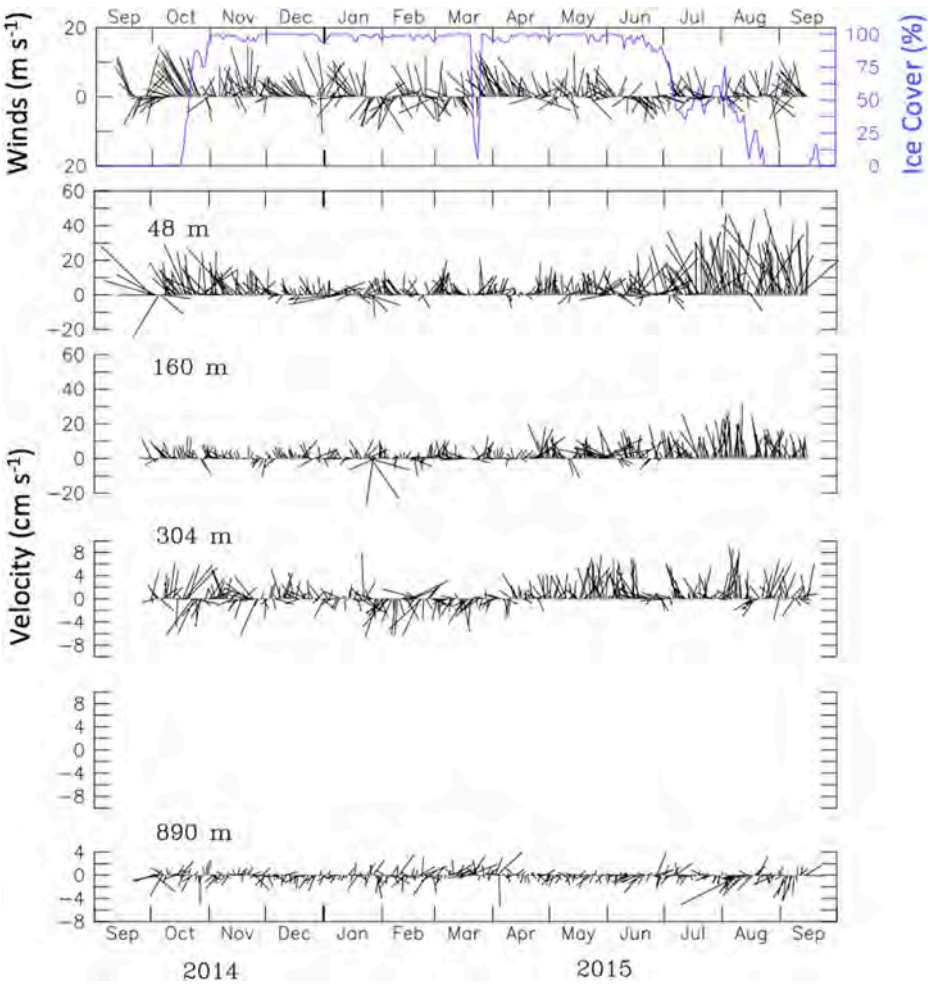

Fig. 3. (top panel) Daily ERA5 wind vectors interpolated onto the C9 mooring location and percent areal ice cover (blue) in a ~50 km × 50 km box centered on C9. (bottom panel) Low-pass filtered current velocities (daily) measured at C9 spanning September 2014–September 2015. The depths of each time series of currents are indicated. Both the wind and velocity were rotated 310° so that upward is approximately northwestward along the continental slope. Note the different velocity scales. (For interpretation of the references to color in this figure legend, the reader is referred to the Web version of this article.)

cm s^{-1}. In the third deployment, the bottom instrument was almost 100 m shallower than during the first two years. During this last year, near-bottom currents were stronger and appeared to be related to the flow above (Fig. 5).

3.1.3. Vertical variability

To examine the vertical structure of the currents in more detail, we divide the time series into two parts—the warm (ice free) season (1 July – 31 October) and the cold (ice-covered) season (1 December – 31 May). During the warm season, currents in the upper 200 m were much stronger in 2015 than they were in either of the other years (Fig. 7a). During the cold season, the three years were all comparable (Fig. 7b). A comparison of average flows during the warm and cold seasons shows that currents in the upper 200 m were stronger in the warm season compared to the cold season, as were the reversals below 300 m (Fig. 7c). Reversals were evident below 300 m in the warm season. During the cold season, average currents below 300 m were weak and were not significantly different from zero.

The currents fall into three vertical groups: (1) 0–200 m; (2) 200–850 m; and (3) below 850 m (Fig. 8). Currents in the upper 200 m were well correlated and in phase during each deployment, and the rotation between different depths was near zero. The second vertical group was also in phase and well correlated, with a slightly larger angle of rotation among depths. Currents in groups 1 and 2 were significantly correlated at zero lag, but with a rotation angle of 15–30°. The final group consists of the bottom instrument in the first two deployments. Here the correlations between group 3 and the other two groups were weak, with significant correlation largely limited to group 2. Perhaps more importantly, there was significant rotation of ~140° counterclockwise and a lag of 2 days between the currents at ~900 m and those at depths >200 m. The third deployment was approximately 70–100 m shallower than the other two deployments and the bottom two depths were significantly, albeit weakly, correlated and in phase with group 2.

This same vertical pattern appears in the empirical orthogonal functions (EOFs) of the along slope component (along 310°) of the time series for each deployment (Fig. 9). There were two significant modes, EOF1 and EOF2. EOF1 accounted for 69%, 51% and 62% of the variability in the 2014, 2015 and 2016 deployments, respectively, and EOF2 accounted for 17%, 33% and 22% of the variability in the 2014, 2015 and 2016 deployments, respectively. EOF1 represents the upper ~250 m of the water column, and EOF2 represents the flow patterns between ~250 and ~850 m. The bottom time series of the 2014 and 2015 deployments were not represented in neither EOF1 nor EOF2 and appeared as a mode by itself that was not statistically significant.

3.2. Temperature and salinity at the mooring site

Several water types are recognized on the Chukchi Shelf (Coachman et al., 1975; Gong and Pickart, 2016; Corlett and Pickart, 2017) and are indicated in Fig. 10a. Melt water (MW) results from melting ice earlier in summer. The source of fresh, relatively warm Alaskan Coastal Water (ACW), and the colder more saline Bering Sea Water (BSW) originates in the Bering Sea, entering the Chukchi Sea through Bering Strait. The cold, saline Winter Water (WW) forms locally through cooling and brine rejection during the previous winter. Remnant Winter Water (RWW)

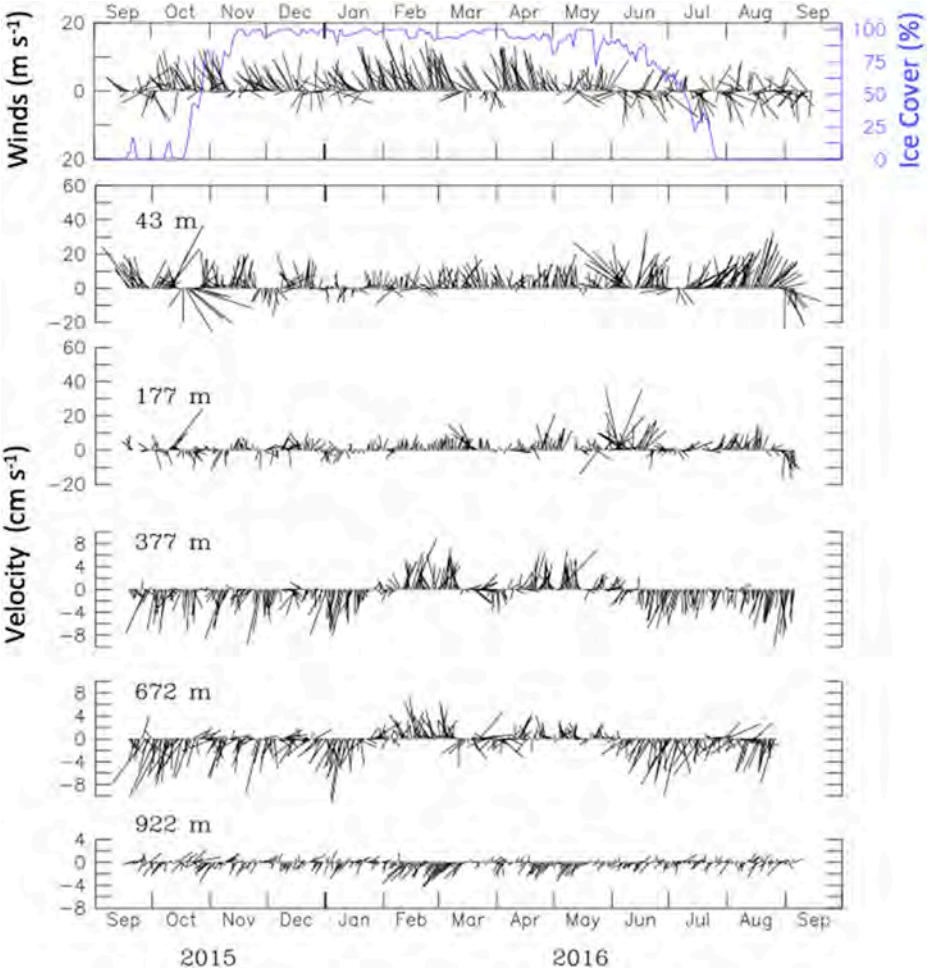

Fig. 4. Same as Fig. 3 except for September 2015–September 2016.

forms as WW warms through heating and mixing processes in the Chukchi Sea. Finally, the relatively warm and saline Atlantic Water (AW) originates in the Atlantic, as its name suggests, flowing cyclonically around the Arctic basin and, occasionally, flows onto the Chukchi Shelf via Barrow Canyon (Bourke and Paquette, 1976; Ladd et al., 2016; Wood et al., 2018; Pisareva et al., 2019).

The C9 data at 45 m in 2016 showed large variability in temperature and salinity, indicating multiple water types (MW, RWW, BSW; cyan dots, Fig. 10a). Salinity varies from <30 to >32, with the least saline water occurring in early December, almost a month after the arrival of sea ice (Fig. 11a), and likely is the result of local ice melt. So, it was not surprising that the water type for this least saline, cold (<-1 °C) water is categorized as MW (Fig. 10a).

While measurements of salinity were limited to a few depths, in the 2016–2017 deployment 11 temperature sensors were distributed between 45 m and 460 m (Fig. 11b). In the upper 100 m, temperature ranges from −1.8 °C in winter to 3.5 °C in July 2017 after ice retreat (Fig. 10a). Between 100 m and 200 m, there was a band of relatively cold (approximately −1 °C) water. At ~200 m, the temperature begins to increase from approximately −1 °C reaching 0 °C at 258 m ± 10 m (average ± standard deviation) and continuing to warm to a depth of ~400 m. This relatively warm, saline (~0.5 °C, 34.8; Fig. 10b) water below 200 m is Atlantic Water (AW).

Atlantic Water generally inhabits intermediate depths (200–1000 m) over the continental slope in the western Arctic (Corlett and Pickart, 2017). AW contains a large amount of heat (enough to melt all the ice in the Arctic, if it came into direct contact with sea ice; Polyakov et al., 2017). At the C9 location the core of this water mass, with maximum subsurface temperature ~0.65 °C (0.57–0.80 °C) and practical salinities in the range of 34.73–34.86, was consistently found near a depth of 400 m (Fig. 10b) as expected from the historical data (Fig. 10 c–d). The C9 instrument depths varied from 345 m to 460 m dependent upon the year. The 2016 deployment was the deepest (~460 m), and the 2014 deployment was shallowest (~345 m), with the 2015 deployment falling in between (~382 m). All three time series were near the relative maximum in temperature of AW, and varied as expected along the long-term temperature-salinity line. The greatest variability was in the 2014 deployment, which was at the upper edge of the depth of the local temperature maximum. The least variability was at 460 m, while the two shallower instruments showed periods of colder temperatures.

3.3. Temporal variability in the depth of Atlantic Water

To examine the temporal variability in the depth of the warmer Atlantic Water, we chose the 0 °C isotherm (Fig. 11b). There was insufficient vertical instrumentation near 350 m, where the relative maximum of temperature occurs and the water column at the relative minimum (depth <200 m) is influenced by surface processes. The character of the isotherm varies in time. From September through March, there was much higher variability in the depth of the 0° isotherm than later during April–July. This coincides with the variability of the currents (Fig. 5, bottom). At depths shallower than 170 m, prior to mid-March, the currents were highly variable and largely southeastward. This transition was not related to sea-ice cover, since sea-ice cover was extensive (>90%) from mid-January through April (Fig. 5, top).

There are two sharp increases in the depth of the 0 °C isotherm, one

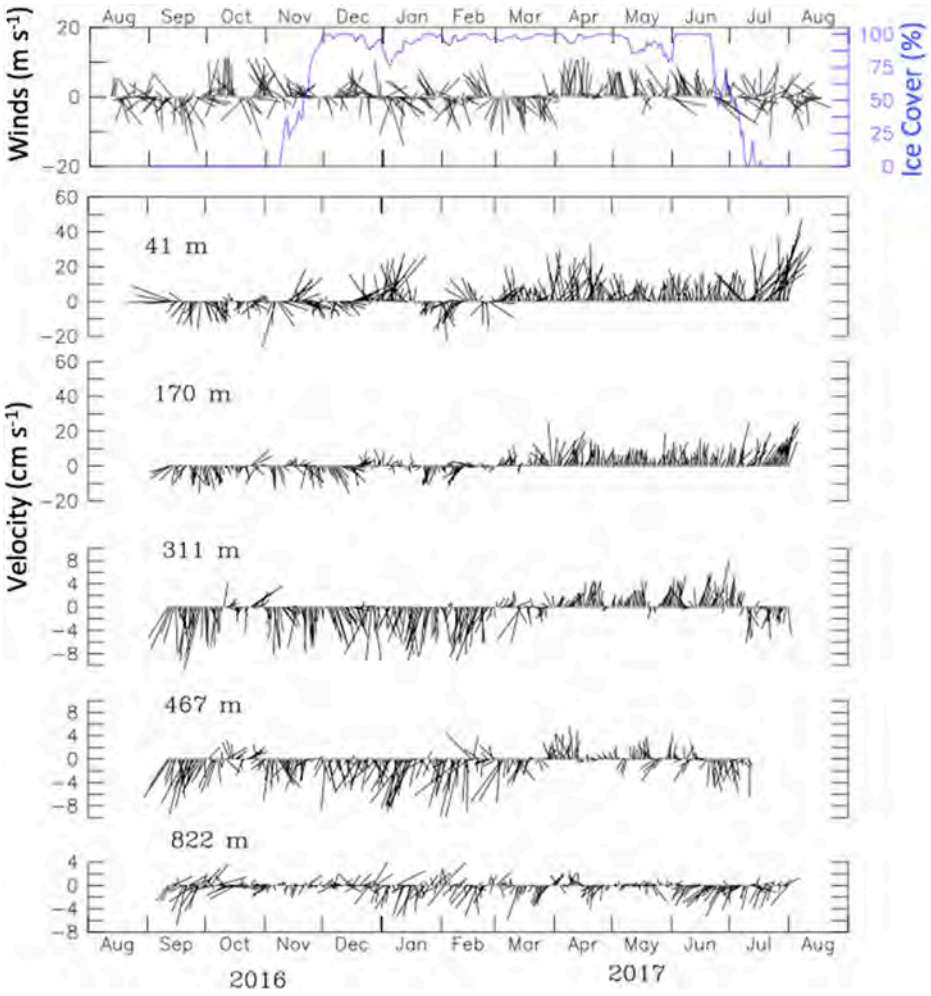

Fig. 5. Same as Fig. 3 except for September 2016–August 2017.

Table 2
Velocity statistics at selected depths distributed through the water column. Maximum speed was calculated from the hourly velocities, while net speed and principal axis were calculated from the low-pass filtered data (35-hr Lanczos).

Mooring	Depth (m)	Maximum Speed (cm s^{-1})	Net speed (Direction) (cm s^{-1} [°])	Prin. Axis (% var) (° [%])
14C9	48	72.1	10.6 (300)	302 (62)
	96	59.1	9.5 (302)	298 (62)
	192	31.1	3.4 (306)	320 (66)
	304	11.5	1.0 (291)	318 (75)
	895	11.4	0.5 (159)	359 (75)
15C9	35	58.6	8.0 (320)	306 (56)
	99	57.8	5.2 (327)	312 (58)
	195	35.9	1.7 (335)	318 (69)
	299	21.6	1.2 (129)	323 (79)
	672	17.0	1.4 (148)	330 (73)
	922	9.1	0.7 (160)	358 (75)
16C9	41	54.5	6.1 (324)	322 (70)
	105	48.7	4.7 (322)	320 (68)
	201	23.1	0.8 (10)	321 (75)
	265	17.4	1.6 (124)	320 (80)
	467	13.2	1.9 (148)	322 (77)
	822	14.4	0.8 (156)	319 (82)

in late October and the second in late December (Fig. 11b). The first event was during a period of no ice and the second during extensive ice cover. Both events had temporal scales consistent with those of longitudinal waves (3–5-day periods; Fig. 12). Interestingly, the greatest depth of the 0° isotherm in October (on the 24th) occurred when the currents were northwestward and the greatest depth of the 0° isotherm in December (on the 27th) occurred when currents were southeastward, but both were during a period of maximum wave amplitude (~20 cm s^{-1}).

Energy in the 3–5 day band is fairly common in the along slope currents at ~240 m (Fig. 13b). It does not appear to be strongly related to the presence of sea ice nor to variations in the winds. At periods >12 days there are only a couple of events in the fall of 2015 and 2016 with significant energy. In contrast, the spectra of the depth-averaged along-slope currents in the upper 200 m appears to be more energetic when sea-ice concentrations are <85% areal coverage (Fig. 13a). There are several periods (e.g. late March 2015) when a sharp decrease in sea ice is associated with an increase in energy at 1–5 days. There also is more energy in the 10- to 20-day band, but once again no significant peaks in energy are present at lower frequencies.

3.4. Forcing mechanisms

3.4.1. Wind

Given the lack of buoy measurements of wind in the Chukchi-Beaufort region, the ECMWF ERA5 reanalysis product was chosen for our analysis. While we also evaluated the NCEP NARR reanalysis,

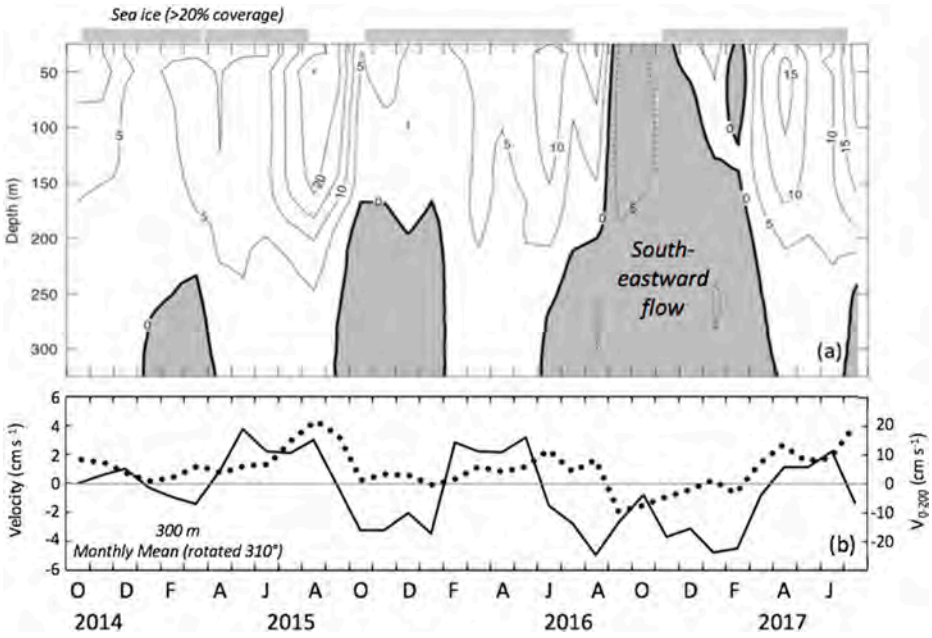

Fig. 6. (a) Contours of monthly mean currents (rotated 310°) measured by the three ADCPs deployed at C9. Positive is approximately northwestward. At the top is the areal sea-ice cover (>20%) in the vicinity of C9. The shaded region represents negative (nominally southeastward) flow. (b) Monthly mean currents at ~300 m (solid line) and depth-averaged velocity, $V_{0\text{-}200}$, in the upper 200 m (dotted line). Positive is northwestward.

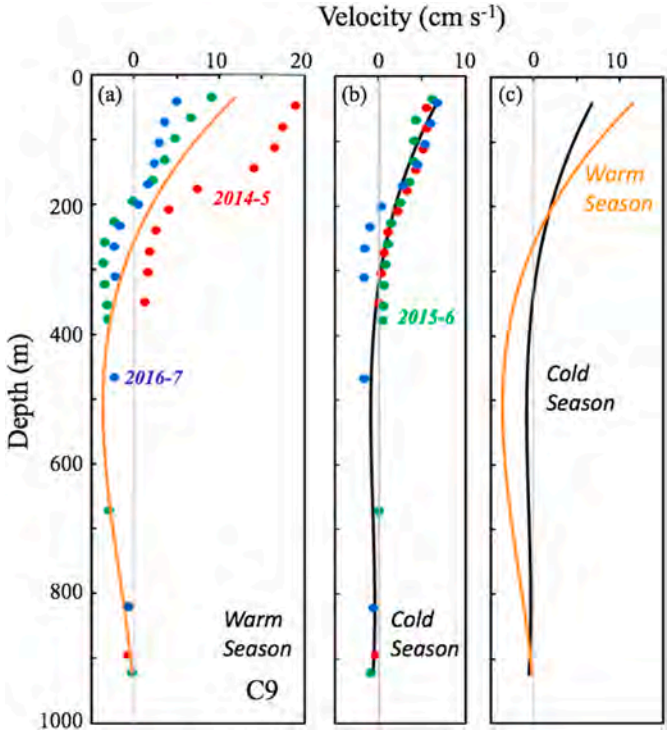

Fig. 7. Mean alongshore flow in (a) the warm season, 1 July – 31 October, and (b) the cold season, 1 December – 31 May. Positive is approximately northwestward (310°). Colored dots represent averages for different deployment years (2014 is red, 2015 is green, 2016 is blue). Solid lines in (a) and (b) represent 3-year seasonal means and are least squares fits of a third-degree polynomial. (c) The 3-year seasonal means are shown separately to facilitate comparison. (For interpretation of the references to color in this figure legend, the reader is referred to the Web version of this article.)

comparisons with observed wind from the Barrow Atmospheric Baseline Observatory near Utqiaġvik, Alaska, indicated that ERA5 more faithfully reproduced the observations. Zero-lag correlation coefficients for the east-west (north-south) components of 10-m winds spanning the 2014–2017 C9 record were r = 0.96 (0.85) for ERA5 compared to 0.90 (0.70) for NARR. Complex (vector) correlations were r = 0.94 with a 4° clockwise rotation for ERA5 wind compared to observed wind, while NARR wind had r = 0.89 with a 17° clockwise rotation relative to the Barrow observations. As is discussed later, the use of a reanalysis product such as ERA5 further allows for an examination of the spatial structure of the wind field.

We attempted a number of different lagged correlation analyses between both observed and ERA5 winds and the along-slope currents measured at the C9 mooring. For simplicity, we first chose to use currents from the shallowest ADCP bin (52 m, 36 m and 44 m depth for the 2014, 2015 and 2016 deployments, respectively). Correlations between year-long records of low-pass filtered 10-m ERA5 wind interpolated to the C9 location and the low-pass filtered near-surface along-slope current were poor, even when the current was lagged relative to the wind. The highest correlation coefficient (r = 0.36 at zero lag for the cross-slope wind component) was in 2015. This was the year with the shallowest (36 m) current data. Using observed wind or wind stress from the Barrow observatory did not markedly improve the wind-current correlations. Similarly, when we restricted the analysis to the largely ice-free summer season (or conversely to the ice-covered winter season), wind-current correlations remained poor or not significant, despite the ice-free periods generally resulting in stronger relationships. The highest correlation coefficient during an ice-free period was r = 0.46 for the along-slope wind in fall 2014. Correlations between near-surface currents at C9 and remote ERA5 winds at selected sites (e.g. in the East Siberian Sea as suggested by Danielson et al., 2014; Peralta-Ferriz and Woodgate, 2017) were generally lower than with local winds, even with lags.

We next examined wind-current correlations using successively low-frequency filters (5, 10, 15 and 30 day Hanning windows) for both the observed wind and along-slope current records. Again, highest correlations were in 2015, but the values remained low (e.g. r = 0.42 for the cross-slope component of wind with a 15-day Hanning filter applied).

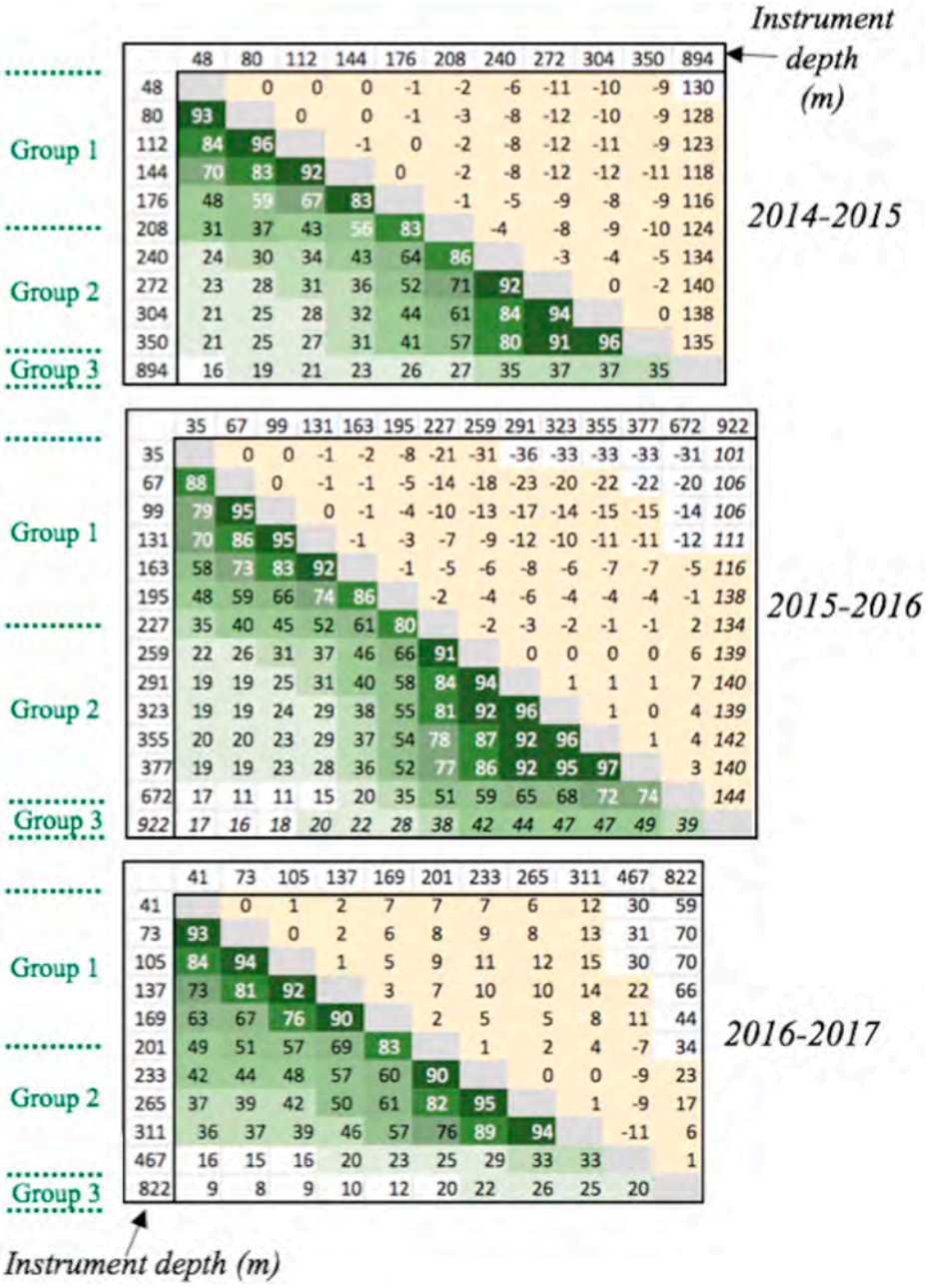

Fig. 8. Complex correlations (below diagonal) and correlation angles (above diagonal) for currents for each of the three mooring deployments: (top) 2014 with 1350 data points; (middle) 2015 with 1372 data points; and (bottom) 2016 with 1200 data points. Instrument depths are in meters. The correlations are color coded from dark (high) to light (low) correlations. Shaded correlations are significant at $p < 0.01$. All lags are zero except for the 922-m record in 2014–15, and the 894-m record in 2015–16. For both of those deployments the deep current record lags the shallower records by 2 days. Divisions into three vertical groups are indicated at the left. (For interpretation of the references to color in this figure legend, the reader is referred to the Web version of this article.)

Unsurprisingly, correlations between ERA5 wind and the 200-m depth-averaged along-slope current, $V_{0\text{-}200}$, over the entire 3-year record (also using 5, 10, 15 and 30-day Hanning window filters) were also poor. Thus, near-surface along-slope flows at C9 do not appear to be significantly correlated with local wind nor with ERA5 wind at select remote sites.

There are specific events, however, in the C9 200-m depth average current record, $V_{0\text{-}200}$, that appear to be in response to local wind forcing (Fig. 14c). For example, the onset of a period of sustained southeastward along-slope flow in September 2016 begins during a reasonably strong southeastward wind event (Fig. 14). Interestingly, such strong along-slope wind events are somewhat rare in the 3-year record, with the September 2016 event being the strongest during an ice-free period. Similarly, the enhancement of northwestward slope flows in April 2017 may be related to the northwestward component of winds at that time. Recall that it is evident from the wavelet analysis (Fig. 13a) that more energy is found in the currents (2–10 day band; 0–200 m average) when areal ice concentrations are <85% and wind can directly force the ocean surface. April through June 2017 was a period of relatively sustained upwelling favorable winds (Fig. 5, top) with corresponding low variability in the depth of 0° isotherm (as mentioned in the previous section; Fig. 11b) and a period of reduced 3–5 day energy in the currents (Fig. 13a). During this time, correlation between the winds and depth of 0° isotherm were significant ($r = 0.48$, $p < 0.01$) with the isotherm depth lagging the winds by 1 day with a decrease in depth of 1.8 m per 1 m s^{-1} increase in wind toward 310° (approximately northwestward). The winds were not well correlated ($r = 0.22$, $p > 0.10$) with the depth of the 0° isotherm for the first part of the record (September 2016–February 2017). We note that Li et al. (2019) also found no correlation between local wind forcing and upwelling events on the Chukchi continental slope at their nearby array site. Watanabe et al. (2017) similarly noted the lack of correspondence between local winds and the current flowing west along the Chukchi Slope in their model.

To briefly summarize, although more synoptic energy (2–10 day

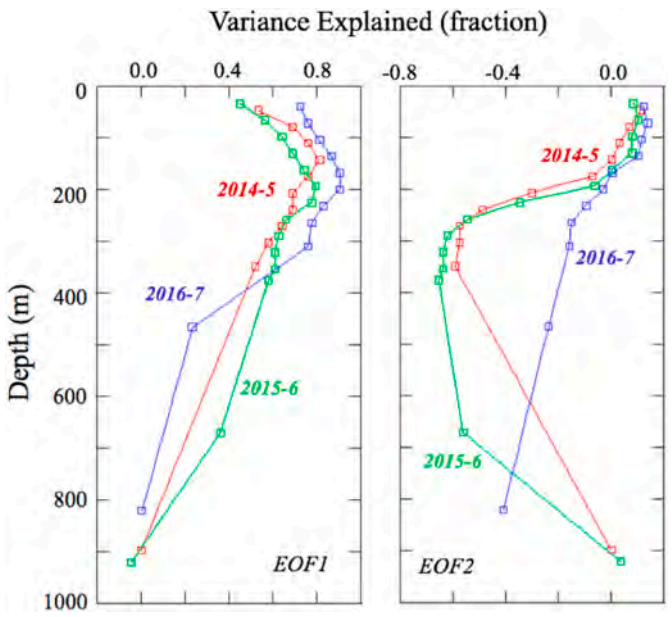

Fig. 9. The first two EOF modes of variability of the along-shelf flow (rotation of 310°) colored by deployment year. The time series were normalized by their respective standard deviations. (a) The fraction of the variance of each time series represented by the first EOF mode (EOF1). (b) The fraction of the variance of each time series represented by the second EOF mode (EOF2). Note that a negative fraction indicates negative correlations between the EOF mode and the time series and positive indicates a positive correlation.

band) is found in the upper water column currents during ice-free periods, on average, local wind does not appear to exert a primary influence on the upper water column along-slope current at the C9 site. Evidence suggests that particularly strong wind events may enhance upper water column currents over the slope, consistent with the findings of Corlett and Pickart (2017). For at least a portion of the C9 data record in 2017, wind influences were instead more readily observed in variation of the depth of the 0° isotherm.

3.4.2. Wind stress curl

Because the C9 mooring was located >100 km from shore, it is unlikely that coastal divergence of surface Ekman transport would be an important mechanism there. Wind stress curl, however, could lead to transport divergence or convergence that, in turn, could drive flow along the continental slope. Using composite averages over multiple northwestward flow events, Li et al. (2019) showed relationships between strong along-slope flows and the wind stress curl averaged over a region of the northeast Chukchi Shelf, suggesting that wind stress curl is a primary forcing agent for strong and weak states of the CSC. Although such extreme states comprised only ~23% of their record, their dominant EOF mode appeared to reflect that variability, suggesting it may be important.

To investigate whether or not wind stress curl impacts currents at C9, we plotted the time variation of mean wind stress curl calculated over a similar portion of the northeast Chukchi Sea shelf (as in Li et al., 2019, Fig. 14a) and compared it with the upper 200-m depth-averaged along-slope current, $V_{0\text{-}200}$, (Fig. 14 d,g). A few characteristics stand out. First, wind stress curl averaged over the northeast Chukchi Shelf is highly variable, often changing sign in as little as three days. On average, the mean wind stress curl is negative, although a few positive events are apparent such as in August 2015, February 2016, and January 2017. Negative wind stress curl over the northeast Chukchi Shelf would lead to flow convergence and geostrophic sea level set-up. Interestingly, high sea level over the shelf (relative to sea level offshore) would tend to force southeastward along-shelf/slope flow, which is opposite to the mean northwestward flow observed at the C9 location (Fig. 14g) and as previously observed for the CSC (Corlett and Pickart, 2017; Stabeno et al., 2018; Li et al., 2019). Thus, on average, it does not appear that the mean wind stress curl over the northeast Chukchi Shelf is itself adequate to explain the observed northwestward flowing CSC at the C9 site. Still, as with some of the wind events described earlier, and in agreement with Li et al. (2019), there is a suggestion of a relationship between portions of the wind stress curl record and the mean along slope currents. For instance, the current decreases and briefly turns southeastward in October and December 2015 when the wind stress curl is strongly negative. Similarly, the current increases to the northwest in early January 2017 when the wind stress curl is significantly positive. Other

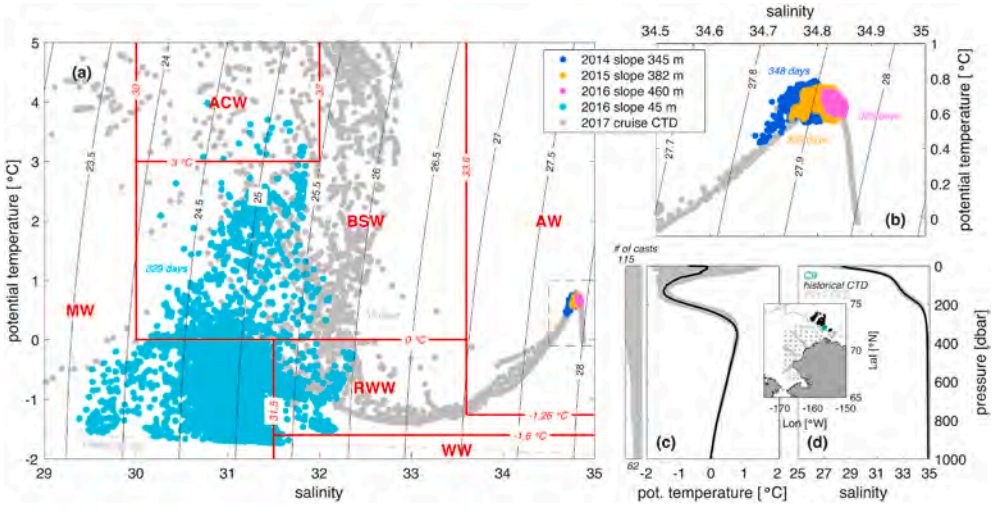

Fig. 10. (a) Potential temperature–salinity diagram, with potential density contours in black, for the Chukchi Shelf and continental slope. Red lines indicate nominal water mass boundaries (after Corlett and Pickart, 2017), and include: melt water (MW), Alaskan Coastal Water (ACW), Bering Sea Water (BSW), Winter Water (WW), Remnant Winter Water (RWW) and Atlantic Water (AW). Hydrographic data from a summer 2017 cruise are shown (gray) for context, with data (45 m) at C9 in 2016–2017 (cyan). Three years of moored data near the core depth of the AW are colored by deployment year, which is expanded in (b). The mean (c) potential temperature and (d) salinity profiles near the C9 location from historical profiles are drawn in black; gray shading represents the standard deviation. The number of profiles used to construct the means is shown to the left of (c). The inset map shows the locations of: C9 (green); the 2017 cruise data (gray) used in (a) and (b); and the historical profiles (black) used to calculate (c) and (d). (For interpretation of the references to color in this figure legend, the reader is referred to the Web version of this article.)

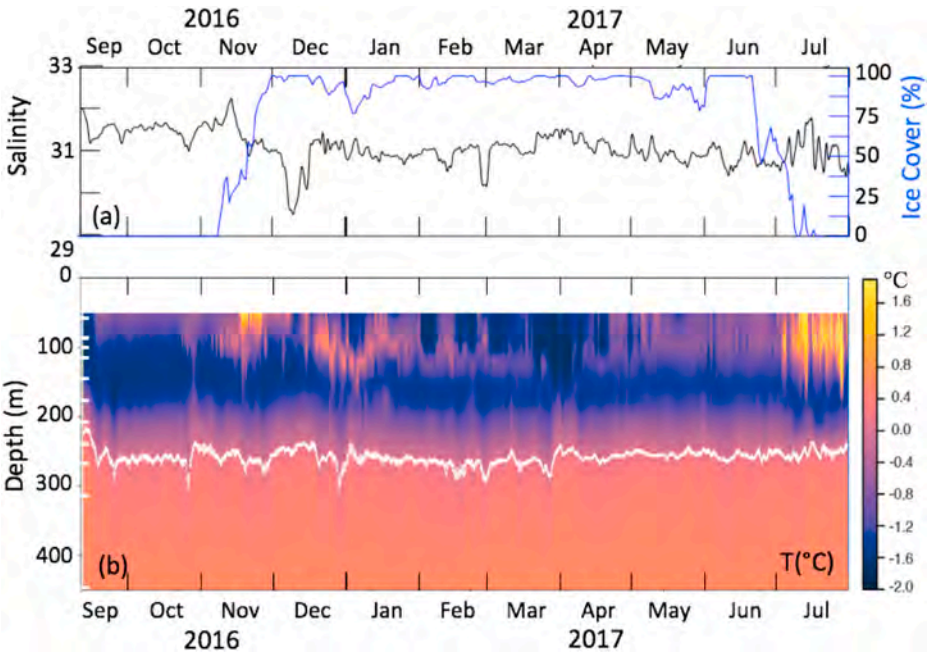

Fig. 11. (a) Time series of salinity at 45 m (black) and the daily percent ice cover (blue) in a 50 km × 50 km box centered at C9. (b) Contours of temperature at the C9 mooring spanning 50–450 m depth from September 2016 to July 2017 (color). Depth of the 0° isotherm is overlaid (white contour). Instrument depths are indicated by the white bars at the left. (For interpretation of the references to color in this figure legend, the reader is referred to the Web version of this article.)

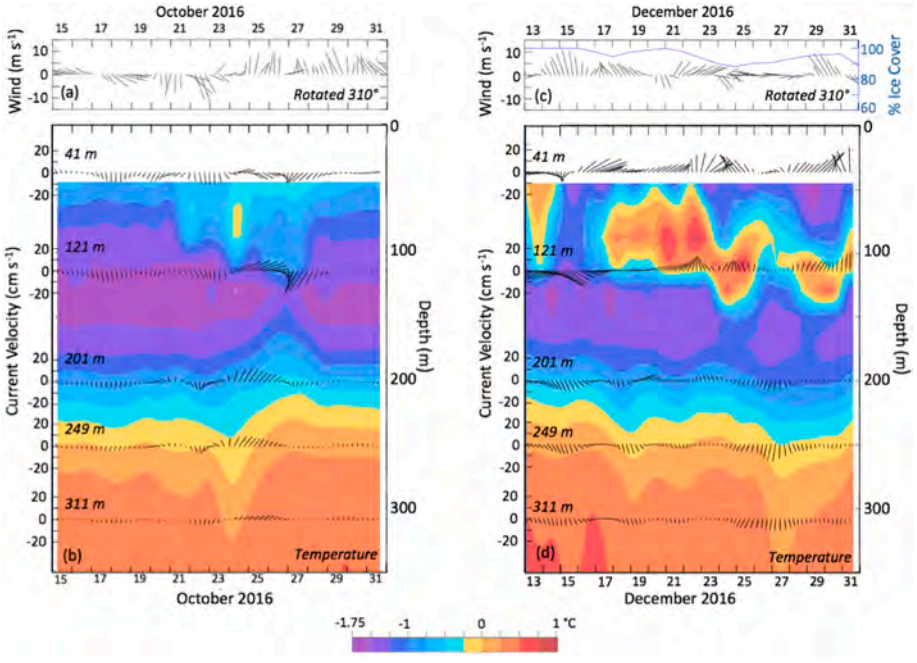

Fig. 12. (a) ERA5 winds at C9, and (b) contours of ocean temperature (color) and current velocity (vectors) at indicated depths during 15–31 October 2016. No ice was near C9 in October. (c) As in (a) during 13–31 December 2016, with percent ice cover indicated in blue. (d) As in (b) except for 13–31 December 2016. The currents are low pass filtered and rotated 310° (upward is approximately northwestward) and ice is percent cover in the 50 km × 50 km box centered on C9. (For interpretation of the references to color in this figure legend, the reader is referred to the Web version of this article.)

events exist, however, that defy such a simple one-to-one explanation. The strengthening of the current in July 2015, a time when the wind stress curl over the northeast Chukchi Shelf was in opposition, is not clearly explained by shelf-average curl. Also, the positive current events spanning June–August 2016 do not appear to be related to wind stress curl over the shelf.

An examination of monthly averaged spatial patterns of wind and wind stress curl throughout the region suggests the possibility of large gradients in wind stress curl near the Chukchi continental slope (not shown); in some cases, positive/negative wind stress curl over the shelf was accompanied by negative/positive wind stress curl offshore. Thus, the induced across-slope geostrophic sea level gradient could potentially be enhanced or diminished as a result of changes in the sign of the wind stress curl across the continental slope. To test this possibility, we averaged wind stress curl over two adjacent boxes: one including a small region of the Chukchi Shelf west of Barrow Canyon parallel to the continental slope, and the other immediately offshelf including the continental slope (Fig. 14a). The difference in mean wind stress curl over these two boxes (shelf value – offshelf value) is illustrated in Fig. 14e. The mean wind stress curl difference is negative, meaning that the wind stress curl induced geostrophic sea level in the offshore box is higher than that over the shelf box (ignoring any otherwise pre-existing shelf-

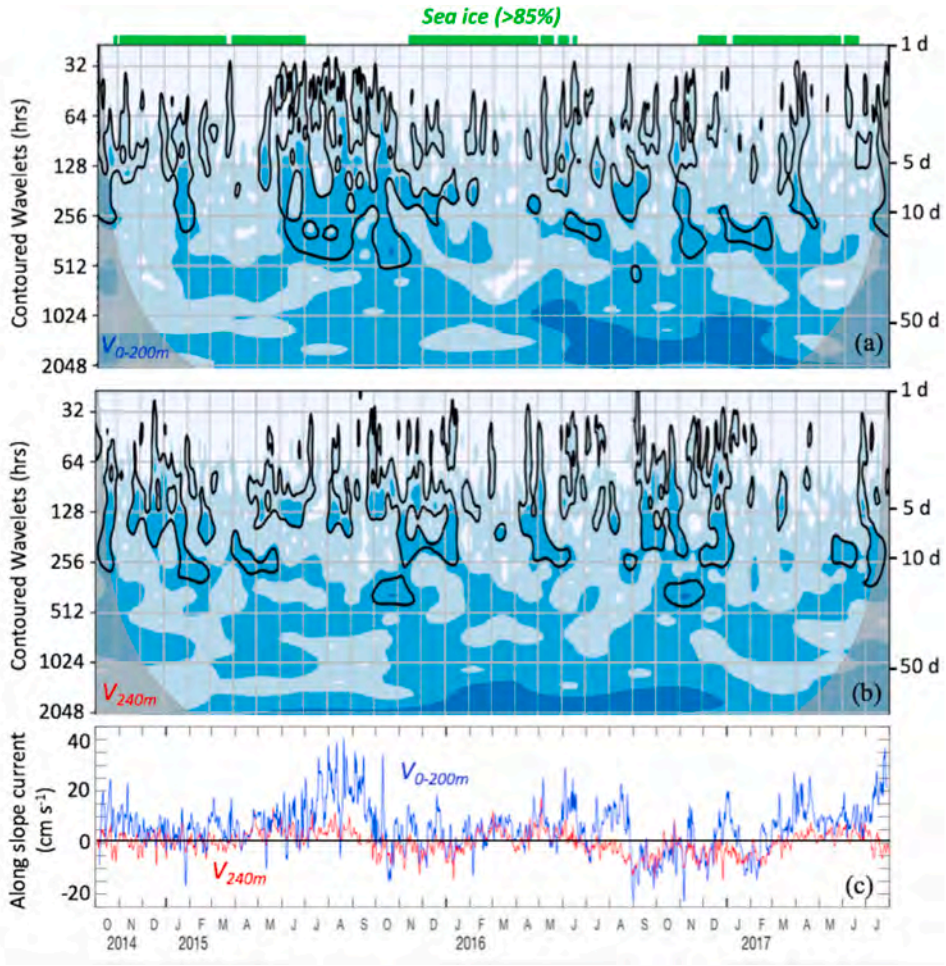

Fig. 13. Wavelet analysis for (a) along slope (rotated 310°), depth average (0–200 m) flow at C9, and (b) along-slope flow at ~240 m for October 2014–July 2017. The blue-shaded contours are quartiles. Closed black contours denote peaks of significant energy. Areal sea-ice concentration (>85%) in a 50 km × 50 km box centered on C9 is indicated in green above (a). (c) Time series used to create (a) and (b) are shown. (For interpretation of the references to color in this figure legend, the reader is referred to the Web version of this article.)

slope sea level gradient), a condition that would favor the northwestward flowing CSC. There is also the suggestion of correspondence between events in the wind stress curl difference and the mean along slope currents. For example, the along-slope current is strong from August through September 2015 when the curl difference is favorable, and then decreases as the curl difference changes sign in late September 2015. A similar series of events occurred during fall 2016. Nevertheless, correlation between the shelf-offshelf curl difference and the 200-m depth-averaged current remains poor over the entire record, even when considering low-pass filtered time series (Fig. 14e, g).

3.4.3. The Beaufort Gyre

The Beaufort Gyre (BG) is a relatively shallow (~250 m), anticyclonic circulation that dominates the Canadian Basin and is driven by the Beaufort Sea High pressure system (e.g. Giles et al., 2012; Moore, 2012). The low salinity (<30) core of the BG sits above more saline Atlantic Water. It is of interest that the depth of the BG along its edge shoals to ~200 m (Doddridge et al., 2019; see their Fig. 1), which is the depth between our observed current groups 1 and 2 discussed in section 3.1.3. The size and strength of the gyre varies on seasonal through interannual time scales. Using sea surface height data from satellite altimetry during the period 2003–2014, the area of gyre and its strength were greatest in the fall and smallest in the summer (Regan et al., 2019). In addition, the size and strength of the BG increased during this time period. Although care must be taken in interpreting dynamic ocean topography near shore and complex bathymetry, it is noteworthy that the edge of the gyre extends in recent years along the continental slope from 130°W westward to the Chukchi Borderland (Fig. 2b).

The location of C9 is at the southern edge of the BG, so it could be argued that the currents measured at C9 are likely related to the BG. The largest slope of dynamic ocean topography is in the region of C9 westward to the Chukchi Borderland (Regan et al., 2019; see their Figs. 4 and 5), where the outer edge of the gyre crosses lines of latitude. This is reminiscent of a western boundary current. Here the bathymetry of the shelf crosses lines of latitude effectively reducing the strength of β, the rate of change of the Coriolis parameter (f) with latitude, to ~20% of its value at a latitude of 45°. Yang et al. (2016) suggest that even though β is small at these latitudes a western boundary current could be supported.

Since the BG is driven by the large-scale wind stress curl it is possible that variability in upper 200-m depth-averaged current at C9 would also be related to variability in the basin-scale wind stress curl. A time series of wind stress curl averaged over the Canada Basin is illustrated in Fig. 14f. As with other wind metrics, correlation of this low-pass filtered quantity with low-pass filtered currents was poor ($r = 0.12$ at 37-day lag with a 30-day Hanning filter applied). We also attempted to correlate the currents with running cumulative sums of basin-averaged curl (e.g. summations over 60 days and 90 days), but this too gave similarly poor results.

3.4.4. The Alaskan Coastal Current exiting Barrow Canyon

Using both an idealized model and the year-long moored array observations of Li et al. (2019), Spall et al. (2018) found a relationship between flow in Barrow Canyon and the CSC, with monthly-averaged CSC transport lagging the transport through Barrow Canyon by roughly 2–3 months. Using the Barrow Canyon transport and velocities measured at C9, our results are more ambiguous.

The mean northeastward flow out of Barrow Canyon is ~0.5 Sv (Itoh et al., 2013; Stabeno et al., 2018), with a seasonal signal. The monthly

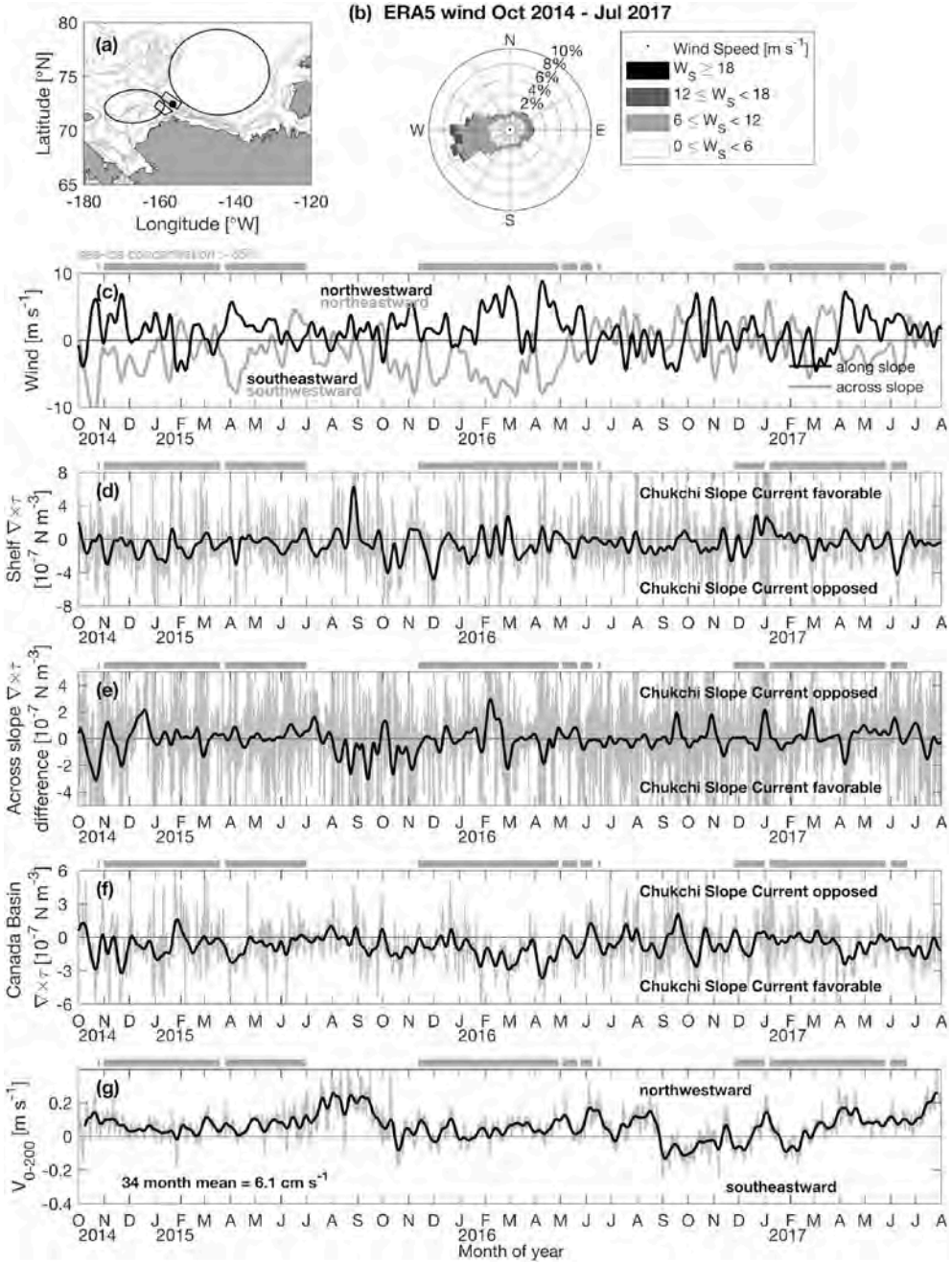

Fig. 14. (a) Map of the Chukchi Sea with the location of the C9 mooring (black dot) and the regions over which wind and wind stress curl were averaged. (b) Histogram of hourly 10-m ERA5 wind averaged over the offshore rectangle encompassing C9 in (a). Wind blows toward the direction indicated. (c) Along- and across-slope components of 10-m ERA5 winds (rotated 310°). Values were averaged over the offshore box encompassing C9 as shown in (a) and low-pass filtered with a 15.5 day Hanning window. (d) Wind stress curl (gray) calculated from the hourly ERA5 winds averaged over the ellipse spanning the northeast Chukchi Sea in (a), and low-pass filtered with a 15.5 day Hanning window (black). (e) Across slope difference of wind stress curl, as a proxy for an across slope sea-surface deformation, calculated from averages over the offshore and shelf boxes in (a). The hourly ERA5 data are gray and the 15.5-day Hanning window filtered time series is black. (f) ERA5 wind stress curl averaged over the Canada Basin as indicated by the large black circle in (a). Hourly values are gray and the 15.5-day Hanning window filtered values are black. (g) The upper 200 m depth average along-slope current measured by the C9 mooring (hourly values - gray, 15.5-day Hanning window filtered values - black).

mean transports in Stabeno et al. (2018) were calculated from hourly currents measured at three mooring sites located off Icy Cape. The number of instruments available varied from three ADCPs deployed in September 2010, 2016, 2017 and 2018 to only one instrument at the central site in 2012. Details of the calculations can be found in Stabeno et al. (2018). The monthly mean northeastward transport along the Chukchi Shelf is strongest in the summer months and weakest in the winter months. As the flow exits Barrow Canyon much of it continues northwestward in the CSC, while a smaller portion turns east forming the Beaufort shelf break current (Nikolopoulos et al., 2009). There is a significant correlation between the monthly mean transport in Barrow Canyon and the upper 200-m depth-averaged velocity, $V_{0\text{-}200}$, observed at C9 ($r = 0.5$, $p < 0.01$; Fig. 15). This significant correlation, however, is a result of six individual months during which the flow in the CSC is above average (Fig. 15a). That is, when monthly mean flow in the CSC is strong, the transport exiting the shelf through Barrow Canyon is also strong. There are even more instances, however, when the Barrow Canyon transport is just as strong yet the monthly averaged flow in the CSC is weak (<10 cm s^{-1}).

As alluded to above, we do not observe a 2–3 month lag between the peaks of monthly-averaged Barrow Canyon transport and currents at C9, although the variability in our record is substantial (Fig. 15). Given an approximate distance of 100 km from Barrow Canyon to the C9 mooring, currents leaving Barrow Canyon should pass the C9 location in 6–17 days, assuming typical speeds of ~6 cm s^{-1} from C9 (Fig. 14g) and ~15 cm s^{-1} from the drifters (drogue depth ~30 m; Fig. 2b).

Thus, using the C9 and Icy Cape current observations the flow out Barrow Canyon does not appear to drive the CSC. Once again there does appear to be an intermittent relationship between possible forcing mechanisms and the magnitude of flow at C9. While the ACC does not drive the CSC, it is a major contributor as discussed in the next section.

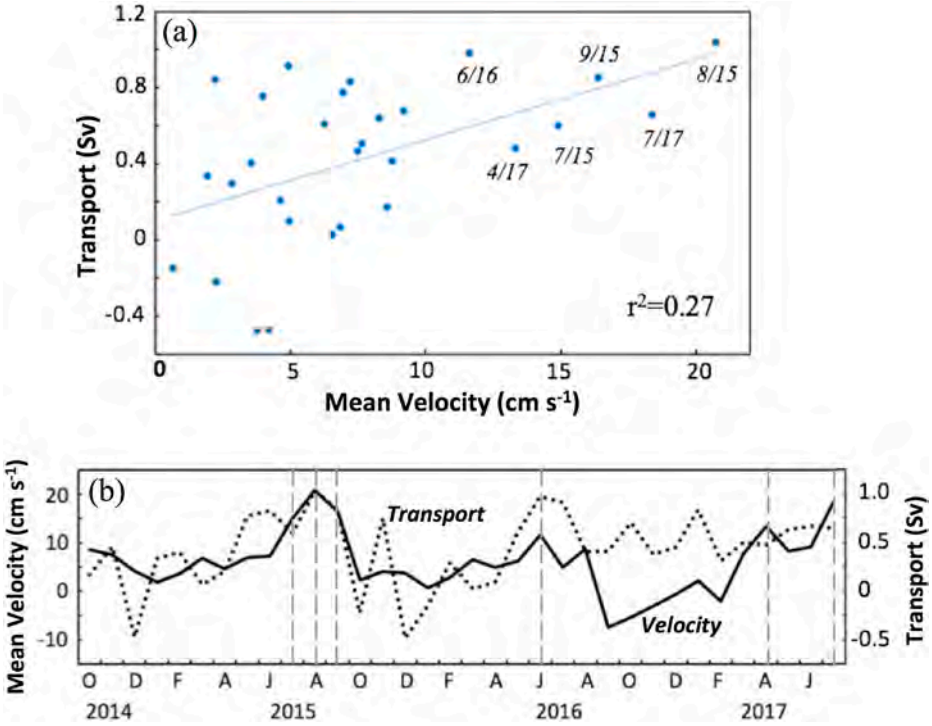

Fig. 15. (a) Monthly depth-averaged (0–200 m) velocity at C9 versus transport at Icy Cape using only data when the mean velocity at C9 was positive (toward the northwest). Best fit line and associated r^2 value are shown. (b) Time series of the depth-averaged (0–200 m) monthly mean velocity at C9 (solid line; left axis) and the monthly mean transport at Icy Cape (dotted line; right axis). The vertical dashed lines represent the timing of the strong velocity events identified in (a).

3.4.5. Volume transport in the CSC

The transport estimate for the CSC can be updated using results from Li et al. (2019) and our C9 results presented herein. Li et al. (2019) estimated transport in the CSC using three year-long moorings deployed in 2013 (spanning 163–356 m bottom depths) and covering an off-slope distance of ~30 km. Their estimate of transport over this area appears to be ~0.35 Sv (their "non-mirrored" value). As noted earlier, our C9 mooring was on the same line of moorings, and ~10 km beyond their outermost site. If we assume that the measurements at C9 are representative of the 20 km beyond the Li et al. (2019) moorings and note that the mean along-slope current in the upper 250 m at C9 was ~5 cm s^{-1}, transport in this region is estimated at 0.25 Sv (width × velocity × depth = 20,000 m × 0.05 m s^{-1} × 250 m). This is likely an under-estimation since the satellite-tracked drifter trajectories provided a width estimate of ~70 km for the CSC. If we do the same calculation assuming that the C9 average velocity is representative of 40 km instead, we obtain an estimate of 0.5 Sv. Although this is likely an over-estimation, it provides a range of transport (including the Li et al., 2019 estimate of 0.35 Sv) in the CSC of 0.60–0.85 Sv.

The mean transport at the Icy Cape moorings for September 2014–August 2017 was 0.42 Sv (following Stabeno et al., 2018). Nikolopoulos et al. (2009) estimated that the eastward transport of Pacific water exiting Barrow Canyon was 0.13 Sv, meaning that 0.29 Sv of the water exiting Barrow Canyon would flow westward. Using these values, the volume of outflow from Barrow Canyon provides between ~34% ([0.42–0.13]/0.85) to ~48% ([0.42–0.13]/0.60) of the CSC volume transport, which as a percentage is less than what was estimated by Li et al. (2019). Alternately, if we use the values explicitly measured from the mooring array, Li et al. (2019) estimated 0.28 Sv of Pacific water in the CSC (their "non-mirrored" value), which is essentially identical to our 0.29 Sv that exits Barrow Canyon and turns westward.

4. Discussion and conclusions

Three years of moored current meter and water property data confirm a well-defined, seasonally varying northwestward surface-intensified flow (the CSC) along the northern Chukchi continental slope. This flow was best defined in the upper 200–250 m of the water column. Below this surface layer was an undercurrent (the AOBC) that flowed predominantly southeastward. Temperature and salinity in this undercurrent (~200 m–~850 m) classified it as Atlantic Water. Vertical correlations among current time series in the AOBC were strong, as were correlations among current time series in the CSC. Only temperature was measured at 900 m in the 2014 and the 2015 deployments, and the average potential temperature at 900 m (below the AOBC) was ~0.0 °C (standard deviation of 0.03 °C), which is typical of Arctic deep water in the Canada Basin.

The C9 mooring site was unknowingly positioned on the southern boundary of the BG (Regan et al., 2019). The BG intensified from 2003 through 2012, reaching a maximum in 2013 and 2014 the end of the analysis period described by Regan et al. (2019). In recent years, the geostrophic transport in the vicinity of C9 has stabilized (Armitage et al., 2017; Zhang et al., 2016), although there remains strong monthly variability in the system, particularly in the fall (Regan et al., 2019). Northwestward velocity appears to be largest in the fall (Regan et al., 2019), but variability also appears to be strongest at that time. In contrast, the flow in the upper 200 m at C9 increased from June through September and then appeared to weaken in the fall. It is unclear whether this apparent disagreement is a result of temporal variability in the system or other mechanisms. For instance, C9 was a single mooring, making it difficult to differentiate between spatial oscillations, such as cross-slope meanders, and temporal variability in the current system. As noted in section 3.1.2, meanders in the system are apparent in the satellite-tracked drifter trajectories. The northwestward trajectory of the drifters followed the trajectory of the southern edge of the BG in 2013 and 2014 (Regan et al., 2019).

The appearance of the CSC has been most evident to the west of Utqiaġvik, AK (Corlett and Pickart, 2017; Stabeno et al., 2018; Li et al., 2019). According to the analysis by Regan et al. (2019) this is also the region of greatest slope of dynamic ocean topography. Evidence for a

similar current flowing along the Beaufort continental slope is currently lacking. However, we note that the ~1400 m depth mooring of Nikolopoulos et al. (2009) did capture a weak (~2 cm s^{-1}) mean northwestward near-surface flow. Interestingly, the Beaufort mooring array analyzed by Nikolopoulos et al. (2009) was deployed in 2002–2004 before the recent expansion and increase in strength of the BG (Armitage et al., 2017; Regan et al., 2019). It remains unknown whether a more recent mooring array would detect a similar relatively weak northwestward flowing current off the Beaufort continental slope. It should also be noted that the model fields of Watanabe et al. (2017) showed northwestward flow all along the Beaufort continental slope. That the strength of the CSC varied substantially over the three years of our deployment is not surprising, in that the strength and size of the BG also varies interannually (Armitage et al., 2017; Regan et al., 2019).

Recent updates to the freshwater content volume in the BG region indicate that 2015–2017 have the largest total freshwater content volumes on record, with particularly large spatial gradients near the Chukchi continental slope (Proshutinsky et al., 2019; see their Figs. 4 and 5). Thus, our three years of observations at C9 were during a period where the BG was particularly strong.

Li et al. (2019) built upon the results of Corlett and Pickart (2017) by suggesting that wind stress curl over the shelf, rather than westward winds alone, primarily drive variability in the CSC. Our findings indicate that while this may be true in an episodic sense, it is generally not the case over our three-year C9 record. The along-slope currents at C9 were not significantly correlated with local winds, except at depths <40 m. There are several possibilities for this.

One potential explanation for the lack of strong correlations between winds and currents at C9 could be meandering of the current. As mentioned, from a single mooring location, it is difficult to distinguish between temporal variability in currents and inherent spatial changes such as cross-slope meandering of the current.

Secondly, the winds were typically weak, often <10 m s^{-1} (Fig. 14b and c). At present, we remain uncertain about how skillfully the ERA5 reanalysis reproduces the true wind stress curl. Belmonte Rivas and Stoffelen (2019) suggest improvements in ERA5 relative to its predecessor model, but additional ground-truthing is needed, particularly in the Arctic where data for assimilation is sparse.

Remote forcing could provide another possible explanation for the lack of correlation between currents and winds or between the depth of the 0° isotherm and local wind during the first part of the 2016–17 record. Recall that there was significant energy in the currents in the 2–10 day energy band. This energy is likely generated elsewhere, and thus could obscure any correlation between currents and local winds. While we tested for relationships with remote winds at select sites without significant results, a more complete investigation of remote versus local forcing on the Chukchi continental slope is left for future analyses.

Finally, the C9 location is approximately 120 km from the coast north of Utqiaġvik, AK, where the coastline abruptly changes direction by ~90°. Wind at C9 is usually oriented northeast-southwest, roughly parallel to the Chukchi Sea coast (Fig. 14b; Stabeno et al., 2018), so that it often blows across, rather than along, the continental slope. This general lack of alignment of the wind and continental slope could potentially help explain the lack of correlation between the wind and observed along-slope currents at C9. In contrast, wind blowing along Alaska's Beaufort coastline, where the shelf is much narrower, appears to be effective at forcing along-slope flows (Nikolopoulos et al., 2009). Any oceanic response, however, to changes in wind forcing on the Beaufort continental slope would propagate east in the direction of coastal-trapped waves, rather than toward the C9 site. Finally, the BG is forced by basin-wide winds (the Beaufort High) and modified by the accumulation of freshwater stored in the BG (Armitage et al., 2017; Regan et al., 2019; Petty et al., 2016), so it is not surprising that the CSC at C9 is not locally wind-forced. Although we also found poor correlations between basin-averaged wind stress curl and currents at C9, the fact that the region of highest sea-surface height gradient exists along the Chukchi continental slope from Barrow Canyon to the Chukchi Borderland (Regan et al., 2019) suggests a relationship between the CSC and the BG.

We hypothesize that this northwestward flowing CSC is forced by the edge of the Beaufort Gyre. Corlett and Pickart (2017), while admitting that a dynamical connection could exist, argued that the CSC was not a manifestation of the Beaufort Gyre, citing the relatively strong currents observed on the Chukchi Slope, lack of a similar current off the Beaufort Slope and the presence of Chukchi Shelf water properties in the CSC as evidence. Spall et al. (2018) similarly suggest that the CSC is distinct from the Beaufort Gyre owing to its Bering Strait source and unique water properties. Nevertheless, the fact that the CSC flowed west in the model of Spall et al. (2018) was a result of the basin-scale circulation associated with the BG (their Fig. 16). The body of evidence indicates that the fact that the CSC flows northwestward is a result of the BG dynamics. We suggest that water exiting the Chukchi Shelf via Barrow Canyon is entrained into the western boundary current of the BG flowing northwest along the Chukchi Slope, consistent with the model results of Spall et al. (2018). Dynamically, we expect that the lateral pressure gradient associated with the BG in the region north of, and extending west from, Utqiaġvik (Figs. 4 and 5 of Regan et al., 2019) presents an effective "wall" that is more than sufficient to overcome the Coriolis force acting on the flow emanating from Barrow Canyon, resulting in the CSC flowing northwestward along the continental slope.

The shelf-slope system from Barrow Canyon to the Chukchi Borderland is a complex region. The exit of warm, saline water out of Barrow Canyon during summer is a source of subsurface heat to the Arctic Ocean basin (Aagaard and Carmack, 1989; Stabeno et al., 2018; Woodgate et al., 2012). In contrast, the Atlantic Water can enter the Chukchi Shelf via Barrow Canyon (Bourke and Paquette, 1976; Ladd et al., 2016; Wood et al., 2018). An array of moorings across the Chukchi Slope would provide insight into the variability in the boundary of the BG, its strength and the pathways of the outflowing Pacific Water. Clearly, additional observations are required to understand the system.

CRediT authorship contribution statement

Phyllis J. Stabeno: Conceptualization, Methodology, Software, Validation, Formal analysis, Investigation, Resources, Data curation, Writing - original draft, Visualization, Supervision, Project administration, Funding acquisition, Writing - review & editing. **Ryan M. McCabe:** Conceptualization, Methodology, Software, Validation, Formal analysis, Investigation, Resources, Writing - original draft, Visualization, Project administration, Writing - review & editing.

Declaration of competing interest

The authors declare that they have no known competing financial interests or personal relationships that could have appeared to influence the work reported in this paper.

Acknowledgments

Support was provided by the National Oceanic and Atmospheric Administration; the Bureau of Ocean Energy Management CHAOZ, CHAOZ-X and ArcWEST programs; the NPRB Arctic Program (A92-02a, A92-02b); and the Joint Institute for the Study of the Atmosphere and Ocean (JISAO) under NOAA Cooperative Agreement NA15OAR4320063. This is contribution No. 4990 for Pacific Marine Environmental Laboratory and Contribution No. 2019-1048 to University of Washington JISAO. We thank three anonymous reviewers for helping to improve the manuscript.

References

Aagaard, K., Carmack, E., 1989. The role of sea ice and other fresh water in the Arctic circulation. J. Geophys. Res. 94 (14), 485–14,498.

Armitage, T.W.K., Bacon, S., Ridout, A.L., Petty, A.A., Wolbach, S., Tsamados, M., 2017. Arctic Ocean surface geostrophic circulation 2003–2014. Cryosphere 11, 1767–1780. https://doi.org/10.5194/tc-11-1767-2017.

Belmonte Rivas, M., Stoffelen, A., 2019. Characterizing ERA-Interim and ERA5 surface wind biases using ASCAT. Ocean Sci. 15, 831–852. https://doi.org/10.5194/os-15-831-2019.

Bourke, R.H., Paquette, R.G., 1976. Atlantic water on the Chukchi shelf. Geophys. Res. Lett. 3 (10), 629–632. https://doi.org/10.1029/GL003i010p00629.

Coachman, L.K., Aagaard, K., Tripp, R.B., 1975. Bering Strait: the Regional Physical Oceanography. Univ. of Washington Press, Seattle, Wash.

Corlett, W.B., Pickart, R.S., 2017. The Chukchi slope current. Prog. Oceanogr. 153, 50–65. https://doi.org/10.1016/j.pocean.2017.04.005.

Danielson, S.L., Weingartner, T.J., Hedstrom, K.S., Aagaard, K., Woodgate, R., Curchitser, E., Stabeno, P.J., 2014. Coupled wind-forced controls of the Bering-Chukchi Shelf circulation and the Bering Strait throughflow: Ekman transport, continental shelf waves, and variations of the Pacific-Arctic sea surface height gradient. Prog. Oceanogr. 125, 40–61. https://doi.org/10.1016/j.pocean.2014.04.006.

Dee, D.P., Uppala, S.M., Simmons, A.J., Berrisford, P., Poli, P., Kobayashi, S., Andrae, U., Balmaseda, M.A., Balsamo, G., Bauer, P., Bechtold, P., Beljaars, A.C.M., van de Berg, L., Bidlot, J., Bormann, N., Delsol, C., Dragani, R., Fuentes, M., Geer, A.J., Haimberger, L., Healy, S.B., Hersbach, H., Hólm, E.V., Isaksen, L., Kållberg, P., Köhler, M., Matricardi, M., Mcnally, A.P., Monge-Sanz, B.M., Morcrette, J.J., Park, B. K., Peubey, C., de Rosnay, P., Tavolato, C., Thépaut, J.N., Vitart, F., 2011. The ERA-Interim reanalysis: configuration and performance of the data assimilation system. Q. J. Roy. Meteorol. Soc. 137, 553–597. https://doi.org/10.1002/qj.828.

Doddridge, E.W., Meneghello, G., Marshall, J., Scott, J., Lique, C., 2019. A Three-way balance in the Beaufort Gyre: the Ice-Ocean Governor, wind stress, and eddy diffusivity. J. Geophys. Res. Oceans 124, 3107–3124. https://doi.org/10.1029/2018JC014897.

Fine, E.C., MacKinnon, J.A., Alford, M.H., Mickett, J.B., 2018. Microstructure observations of turbulent heat fluxes in a warm-core Canada Basin eddy. J. Phys. Oceanogr. 48, 2397–2418. https://doi.org/10.1175/JPO-D-18-0028.1.

Giles, K.A., Laxon, S.W., Ridout, A.L., Wingham, D.J., Bacon, S., 2012. Western Arctic Ocean freshwater storage increased by wind-driven spin-up of the Beaufort Gyre. Nat. Geosci. 5, 194–197. https://doi.org/10.1038/ngeo1379.

Gong, D., Pickart, R.S., 2016. Early summer water mass transformation in the eastern Chukchi Sea. Deep Sea Res. Part II 130, 43–55. https://doi.org/10.1016/j.dsr2.2016.04.015.

Haiden, T., Janousek, M., Bidlot, J., Ferranti, L., Prates, F., Vitart, F., Bauer, P., Richardson, D.S., 2017. Evaluation of ECMWF forecasts, including 2016–2017 upgrades. European Centre for medium-range weather Forecasts. ECMWF Tech. Memo 817, 56. https://doi.org/10.21957/x397za5p5.

Hersbach, H., de Rosnay, P., Bell, B., Schepers, D., Simmons, et al., 2018. Operational global reanalysis: progress, future directions and synergies with NWP. In: European Centre for Medium-Range Weather Forecasts, ERA Report Series, vol. 27, p. 63.

Itoh, M., Nishino, S., Kawaguchi, Y., Kikuchi, T., 2013. Barrow Canyon volume, heat, and freshwater fluxes revealed by long-term mooring observations between 2000 and 2008. J. Geophys. Res. Oceans 118 (9), 4363–4379. https://doi.org/10.1002/jgrc.20290.

Jackson, J.M., Williams, W.J., Carmack, E.C., 2012. Winter sea-ice melt in the Canada basin, Arctic Ocean. Geophys. Res. Lett. 39, L03603. https://doi.org/10.1029/2011GL050219.

Ladd, C., Mordy, C.W., Salo, S.A., Stabeno, P.J., 2016. Winter water properties and the Chukchi Polynya. J. Geophys. Res. Oceans 121, 5516–5534. https://doi.org/10.1002/2016JC011918.

Large, W.G., Pond, S., 1981. Open ocean momentum flux measurements in moderate to strong winds. J. Phys. Oceanogr. 11, 324–336.

Li, M., Pickart, R.S., Spall, M.A., Weingartner, T.J., Lin, P., Moore, G., Qi, Y., 2019. Circulation of the Chukchi Sea shelfbreak and slope from moored timeseries. Prog. Oceanogr. 172, 14–33. https://doi.org/10.1016/j.pocean.2019.01.002.

Linders, J., Pickart, R.S., Björk, G., Moore, G.W.K., 2017. On the nature and origin of water masses in Herald Canyon, Chukchi Sea: synoptic surveys in summer 2004, 2008, and 2009. Prog. Oceanogr. 159, 99–114. https://doi.org/10.1016/j.pocean.2017.09.005.

Lindsay, R., Wensnahan, M., Schweiger, A., Zhang, J., 2014. Evaluation of seven different atmospheric reanalysis products in the Arctic. J. Clim. 27, 2588–2606. https://doi.org/10.1175/JCLI-D-13-00014.1.

Mesinger, F., DiMego, G., Kalnay, E., Mitchell, K., Shafran, P.C., Ebisuzaki, W., Jovic, D., Woollen, J., Rogers, E., Berbery, E.H., Ek, M.B., Fan, Y., Grumbine, R., Higgins, W., Li, H., Lin, Y., Manikin, G., Parrish, D., Shi, W., 2006. North American regional reanalysis. Bull. Am. Meteorol. Soc. 87, 343–360. https://doi.org/10.1175/BAMS-87-3-343.

Moore, G.W.K., 2012. Decadal variability and a recent amplification of the summer Beaufort Sea High. Geophys. Res. Lett. 39, L10807. https://doi.org/10.1029/2012GL051570.

Moore, G.W.K., Pickart, R.S., Renfrew, I.A., 2008. Buoy observations from the windiest location in the world ocean, Cape Farewell, Greenland. Geophys. Res. Lett. 35, L18802. https://doi.org/10.1029/2008GL034845.

Nikolopoulos, A., Pickart, R.S., Fratantoni, P.S., Shimada, K., Torres, D.J., Jones, E.P., 2009. The western Arctic boundary current at 152 W: Structure, variability, and transport. Deep-Sea Res. Part II 56, 1164–1181. https://doi.org/10.1016/j.dsr2.2008.10.014.

Peralta-Ferriz, C., Woodgate, R.A., 2017. The dominant role of the East Siberian Sea in driving the oceanic flow through the Bering Strait—conclusions from GRACE ocean mass satellite data and in situ mooring observations between 2002 and 2016. Geophys. Res. Lett. 44 (11) https://doi.org/10.1002/2017GL075179, 472–11,481.

Petty, A.A., Hutchings, J.K., Richter-Menge, J.A., Tschudi, M.A., 2016. Sea ice circulation around the Beaufort Gyre: the changing role of wind forcing and the sea ice state. J. Geophys. Res. Oceans 121 (5), 3278–3296. https://doi.org/10.1002/2015JC010903.

Pickart, R.S., Pratt, L.J., Torres, D.J., Whitledge, T.E., Proshutinsky, A.Y., Aagaard, K., Agnew, T.A., Moore, G.W.K., Dail, H.J., 2010. Evolution and dynamics of the flow through Herald canyon in the western Chukchi Sea. Deep-Sea Res. Part II 57 (1–2), 5–26. https://doi.org/10.1016/j.dsr2.2009.08.002.

Pisareva, M.N., Pickart, R.S., Lin, P., Fratantoni, P.S., Weingartner, T.J., 2019. On the nature of wind-forced upwelling in Barrow Canyon. Deep-Sea Res. II 162, 63–78. https://doi.org/10.1016/j.dsr2.2019.02.002.

Polyakov, I.V., Pnyushkov, A.V., Alkire, M.B., Ashik, I.M., Baumann, T.M., 2017. Greater role for Atlantic inflows on sea-ice loss in the Eurasian basin of the Arctic Ocean. Science 356 (6335), 285–291. https://doi.org/10.1126/science.aai8204.

Proshutinsky, A., Krishfield, R., Timmermans, M.-L., 2019. Preface to special issue forum for Arctic Ocean modeling and observational synthesis (FAMOS) 2: Beaufort gyre phenomenon. J. Geophys. Res. Oceans. https://doi.org/10.1029/2019JC015400 (in press).

Regan, H.C., Lique, C., Armitage, T.W.K., 2019. The Beaufort Gyre extent, shape, and location between 2003 and 2014 from satellite observations. J. Geophys. Res. Oceans 124, 844–862. https://doi.org/10.1029/2018JC014379.

Renfrew, I.A., Peterson, G.N., Sproson, D.A.J., Moore, G.W.K., Adiwidjaja, H., Zhang, S., North, R., 2009. A comparison of aircraft-based surface-layer observations over Denmark Strait and the Irminger Sea with meteorological analyses and QuikSCAT winds. Q. J. R. Meteorol. Soc. 135, 2046–2066. https://doi.org/10.1002/qj.444.

Serreze, M.C., Crawford, A.D., Stroeve, J.C., Barrett, A.P., Woodgate, R.A., 2016. Variability, trends, and predictability of seasonal sea ice retreat and advance in the Chukchi Sea. J. Geophys. Res. Oceans 121, 7308–7325. https://doi.org/10.1002/2016JC011977.

Shimada, K., Carmack, E.C., Hatakeyama, K., Takizawa, T., 2001. Varieties of shallow temperature maximum waters in the western Canada Basin of the Arctic Ocean. Geophys. Res. Lett. 28, 3441–3444.

Spall, M., Pickart, R., Li, M., Itoh, M., Lin, P., Kikuchi, T., Qi, Y., 2018. Transport of Pacific water into the Canada basin and the formation of the Chukchi slope current. J. Geophys. Res. Oceans 123, 7453–7471. https://doi.org/10.1029/2018JC013825.

Stabeno, P., Kachel, N., Ladd, C., Woodgate, R., 2018. Flow patterns in the eastern Chukchi Sea: 2010–2015. J. Geophys. Res. Oceans 123, 1177–1195. https://doi.org/10.1002/2017JC013135.

Stabeno, P.J., Danielson, S.L., Kachel, D.G., Kachel, N.B., Mordy, C.W., 2016b. Currents and transport on the Eastern Bering Sea shelf: an integration of over 20 years of data. Deep-Sea Res. II 134, 13–29. https://doi.org/10.1016/j.dsr2.2016.05.010.

Stabeno, P.J., Bell, S., Cheng, W., Danielson, S., Kachel, N.B., Mordy, C.W., 2016. Long-term observations of Alaska Coastal Current in the northern Gulf of Alaska. Deep-Sea Res. II 132, 24–40. https://doi.org/10.1016/j.dsr2.2015.12.016. Understanding Ecosystem Processes in the Gulf of Alaska: Volume 1.

Stabeno, P.J., Bond, N.A., Hermann, A.J., Kachel, N.B., Mordy, C.W., Overland, J.E., 2004. Meteorology and oceanography of the northern Gulf of Alaska. Continent. Shelf Res. 24, 859–897. https://doi.org/10.1016/j.csr.2004.02.007.

Stabeno, P.J., Reed, R.K., 1994. Circulation in the Bering Sea basin observed by satellite-tracked drifters: 1986–1993. J. Phys. Oceanogr. 24 (4), 848–854.

Steele, M., Morison, J., Ermold, W., Rigor, I., Ortmeyer, M., Shimada, K., 2004. Circulation of summer Pacific halocline water in the Arctic Ocean. J. Geophys. Res. 109, C02027. https://doi.org/10.1029/2003JC002009.

Steele, M., Ermold, W., Zhang, J., 2008. Arctic Ocean surface warming trends over the past 100 years. Geophys. Res. Lett. 35, L02614. https://doi.org/10.1029/2007GL031651.

Stegall, S.T., Zhang, J., 2012. Wind field climatology, changes, and extremes in the chukchi-beaufort seas and Alaska north slope during 1979–2009. J. Clim. 25, 8075–8089. https://doi.org/10.1175/JCLI-D-11-00532.1.

Timmermans, M.-L., Proshutinsky, A., Golubeva, E., Jackson, J.M., Krishfield, R., McCall, M., Platov, G., Toole, J., Williams, W., Kikuchi, T., Nishino, S., 2014. Mechanisms of Pacific summer water variability in the Arctic central Canada basin. J. Geophys. Res. Oceans 119, 7523–7548. https://doi.org/10.1002/2014JC010273.

Timmermans, M.-L., 2015. The impact of stored solar heat on Arctic sea ice growth. Geophys. Res. Lett. 42, 6399–6406. https://doi.org/10.1002/2015gl064541.

Timmermans, M.-L., Toole, J., Krishfield, R., 2018. Warming of the interior Arctic Ocean linked to sea ice losses at the basin margins. Sci. Adv. 4 (8), eaat6773 https://doi.org/10.1126/sciadv.aat6773.

Torrence, C., Compo, G.P., 1998. A practical guide to wavelet analysis. Bull. Am. Meteorol. Soc. 79, 61–78. https://doi.org/10.1175/1520-0477(1998)079<0061:APGTWA>2.0.CO;2.

Tsukada, Y., Ueno, H., Ohta, N., Itoh, M., Watanabe, E., Kikuchi, T., Nishino, S., Mizobata, K., 2018. Interannual variation in solar heating in the Chukchi Sea, Arctic Ocean. Polar Sci. 17, 33–39. https://doi.org/10.1016/j.polar.2018.06.003.

Watanabe, E., Onodera, J., Itoh, M., Nishino, S., Kikuchi, T., 2017. Winter transport of subsurface warm water toward the Arctic Chukchi Borderland. Deep-Sea Res. I 128, 115–130. https://doi.org/10.1016/j.dsr.2017.08.009.

Weingartner, T., Aagaard, K., Woodgate, R., Danielson, S., Sasaki, Y., Cavalieri, D., 2005. Circulation on the north central Chukchi Sea shelf. Deep-Sea Res. Part II 52 (24–26), 3150–3174. https://doi.org/10.1016/j.dsr2.2005.10.015.

Wood, K.R., Jayne, S.R., Mordy, C.W., Bond, N., Overland, J.E., Ladd, C., Stabeno, P.J., Ekholm, A.K., Robbins, P.E., Schreck, M., Heim, R., Intrieri, J., 2018. Results of the first Arctic heat open science Experiment. Bull. Am. Meteorol. Soc. 99, 513–520. https://doi.org/10.1175/BAMS-D-16-0323.1.

Woodgate, R.A., Aagaard, K., Weingartner, T.J., 2005a. Monthly temperature, salinity, and transport variability of the Bering Strait through flow. Geophys. Res. Lett. 32, L04601. https://doi.org/10.1029/2004GL021880.

Woodgate, R.A., Aagaard, K., Weingartner, T.J., 2005b. A year in the physical oceanography of the Chukchi Sea: moored measurements from autumn 1990–1991. Deep-Sea Res. Part II 52 (24–26), 3116–3149. https://doi.org/10.1016/j.dsr2.2005.10.016.

Woodgate, R.A., Weingartner, T.J., Lindsay, R., 2012. Observed increases in Bering Strait oceanic fluxes from the Pacific to the Arctic from 2001 to 2011 and their impacts on the Arctic Ocean water column. Geophys. Res. Lett. 39, L24603. https://doi.org/10.1029/2012GL054092.

Woodgate, R.A., Aagaard, K., Muench, R.D., Gunn, J., Bjork, G., Rudels, B., Roach, A.T., Schauer, U., 2001. The Arctic Ocean boundary current along the Eurasian slope and the adjacent Lomonosov Ridge: water mass properties, transports and transformations from moored instruments. Deep-Sea Res. Part I 48 (8), 1757–1792.

Yang, J., Proshutinsky, A., Lin, X., 2016. Dynamics of an idealized Beaufort Gyre: 1. The effect of a small beta and lack of western boundaries. J. Geophys. Res. Oceans 121, 1249–1261. https://doi.org/10.1002/2015JC011296.

Zhang, J., Steele, M., Runciman, K., Dewey, S., Morison, J., Lee, C., Rainville, L., Cole, S., Krishfield, R., Timmermans, M., Toole, J., 2016. The Beaufort Gyre intensification and stabilization: a model-observation synthesis. J. Geophys. Res. Oceans 121, 7933–7952. https://doi.org/10.1002/2016JC012196.

Deep–Sea Research II 177 (2020) 104742

Contents lists available at ScienceDirect

Deep-Sea Research Part II

journal homepage: http://www.elsevier.com/locate/dsr2

Stratification, plankton layers, and mixing measured by airborne lidar in the Chukchi and Beaufort seas

James H. Churnside [a,*], Richard D. Marchbanks [b], Svein Vagle [c], Shaun W. Bell [d], Phyllis J. Stabeno [e]

[a] NOAA Earth System Research Laboratory, Boulder, CO, USA
[b] Cooperative Institute for Research in the Environmental Sciences, University of Colorado and NOAA Earth System Research Laboratory, Boulder, CO, USA
[c] Institute of Ocean Sciences, Fisheries and Oceans Canada, Sidney, British Columbia, Canada
[d] Joint Institute for the Study of the Atmosphere and Oceans, University of Washington and NOAA Pacific Marine Environmental Laboratory, Seattle, WA, USA
[e] NOAA Pacific Marine Environmental Laboratory, Seattle, WA, USA

ARTICLE INFO

Keywords:
Ocean lidar
Arctic ocean
Subsurface plankton layers
Ocean optics
Barrow canyon
Turbulence
Ocean remote sensing

ABSTRACT

A total of 4.9 million vertical profiles of optical backscattering were measured by airborne lidar in July of 2014 and July of 2017 in the Chukchi and Beaufort seas. We found very different ice conditions in the study area between July 2014 and July 2017, but the characteristics of subsurface plankton layers measured by the lidar and their dependence on ice cover were similar for the two years. In both years, the prevalence of subsurface plankton layers exponentially decreased with increasing ice cover. The average depths were similar for both years, with layers in open water deeper than those in the pack ice. The depths of subsurface plankton layers were consistent with mixed layer depth in areas where *in situ* density profiles were available. A noticeable difference in layer strength (defined as the ratio of the layer signal to the background) was likely caused by higher background phytoplankton concentrations in 2017. Differences in layer thickness were observed, which could be the result of higher current shears in 2017. Turbulent mixing of phytoplankton and zooplankton in Barrow Canyon was inferred from the power spectral density of lidar and acoustic scattering. Lidar measurements suggested that the level of turbulence and its vertical distribution were affected by local upwelling-favorable winds. The vertical distribution of acoustic scattering was different from that of the lidar, which we interpret as different vertical distributions of phytoplankton and zooplankton.

1. Introduction

The climate of the Arctic is rapidly changing as a result of several amplifying feedback mechanisms (Pithan and Mauritsen, 2014; Serreze and Barry, 2011; Taylor et al., 2013). These include decreases in surface albedo, increases in cloud cover, and increased atmospheric transport from the south. The largest factor in determining surface albedo is sea ice, which has been shrinking in extent, becoming thinner, and drifting more rapidly (Comiso, 2011; Kwok and Rothrock, 2009; Spreen et al., 2011; Vaughan et al., 2013). In turn, the reduction in sea ice affects the timing and distribution of phytoplankton blooms. Satellite observations suggest that the primary productivity of the Arctic Ocean is increasing as the area of open water and the length of growing season increase (Arrigo and van Dijken, 2015; Arrigo et al., 2008). In addition, thinning ice and more melt ponds allow increased primary productivity under the ice (Arrigo et al., 2014).

Sub-surface phytoplankton layers are common in the Arctic Ocean in summer (Ardyna et al., 2013; Cota et al., 1996; Coupel et al., 2011). As nutrients are depleted at the surface, a plankton layer develops at the pycnocline formed by melting ice (Brown et al., 2015; Hill and Cota, 2005; Martin et al., 2010; Naoya et al., 2018). While the depth of these layers is generally consistent with measured pycnocline depths, some can be much deeper. Brown reported depths ranging from 3 to 106 m, but with a mode of 15–20 m in July. This is consistent with a previous suggestion that there might be shallow layers associated with the pycnocline, but also deep layers that might be associated with the deeper nutricline (Churnside and Marchbanks, 2015; Martin et al., 2013). While this work is all in the Arctic Ocean, we should note that thin plankton layers associated with a salinity-driven pycnocline have also been observed in Magellan Strait in the Southern Ocean (Ríos et al., 2016).

* Corresponding author.
E-mail address: james.h.churnside@noaa.gov (J.H. Churnside).

https://doi.org/10.1016/j.dsr2.2020.104742
Received 29 May 2019; Received in revised form 25 January 2020; Accepted 26 January 2020
Available online 31 January 2020

Subsurface plankton layers affect primary productivity. In the northern Barents Sea, productivity in the subsurface plankton layer was measured to be similar to that during the spring bloom (Hegseth, 1998). In the central North Sea, 58% of the total column productivity in August was in a subsurface plankton layer, and 37% of the annual average was in this layer (Weston et al., 2005, 2011). Measurements in the Beaufort Sea found 55% of the productivity in the subsurface layer (Retamal et al., 2008), and models suggest that 35–90% of the coastal productivity in the Beaufort Sea is within the subsurface layer (Martin et al., 2013). A comparison of 32 models found that the models generally performed better in regions where there was no subsurface layer (Lee et al., 2015). It has been noted that models often overestimate primary production, and this can compensate for not including production of the subsurface layer, resulting in an overall estimate that might be better than expected (Arrigo et al., 2011; Lee et al., 2015). In fact, column integrated productivity can be negatively correlated with surface chlorophyll, because low surface chlorophyll is often associated with a subsurface chlorophyll layer with high productivity (Jacox et al., 2015).

Within the Arctic Ocean, Barrow Canyon is a region that has received a lot of attention. Much of the water flowing northward through the Bering Strait passes through the canyon, especially in summer. Summertime estimates range from 50% (Stabeno et al., 2018) to 80% (Gong and Pickart, 2015), and an annual average of 55% has been reported (Itoh et al., 2013). Together with this influx of water from the south, Barrow Canyon is also biologically active and has been designated as one of eight regions of the Distributed Biological Observatory, which was implemented to monitor changes in the Arctic Ocean (Grebmeier et al., 2010; Moore and Grebmeier, 2018). Flow through the canyon might also be expected to generate turbulent mixing, and a direct measurement of turbulent kinetic energy dissipation near the head of the canyon along the 70-m isobath on the northern side showed elevated levels near the pycnocline and also within the boundary layer near the bottom (Shroyer et al., 2014).

There have been a number of investigations of plankton using lidar (Churnside, 2014; Churnside and Ostrovsky, 2005; Churnside and Donaghay, 2009; Churnside et al., 2012), but few in the Arctic. Hill and Zimmerman (2010) used model results to show that primary production estimates in the Arctic could be improved with lidar. Goldin et al. (2007) used an airborne lidar to detect subsurface layers in the Barents Sea in August of 2003. We used a similar lidar to provide more details of the structure of subsurface layers in the Chukchi and Beaufort seas in 2014 (Churnside and Marchbanks, 2015). Beherenfeld et al. (2017) estimated phytoplankton biomass in the Arctic using the depth-integrated return from a space-based lidar that lacks depth resolution required for profiling. That same lidar has been used to detect sea ice (Lu et al., 2017). We should note that lidar provides vertical profiles of phytoplankton backscattering, while many of the plankton layer studies listed above were based on chlorophyll measurements, (e.g. Arrigo et al., 2011; Hill et al., 2005; Weston et al., 2005) The depth distributions of the two quantities can be different because of photo-acclimation by phytoplankton (Kitchen and Zaneveld, 1990).

In this paper, we report the results of lidar surveys in 2017 and compare these with our 2014 results. These results are based on 4.9 million lidar profiles of optical backscattering in the ocean. The survey periods were the same for the two years, but the ice conditions were very different. Because these measurements were only three years apart, the differences were well within the range of natural variability. However, to the extent that the results depend on ice cover, they can be used to predict the characteristics of subsurface plankton layers in July as Arctic sea ice continues to retreat.

2. Materials and methods

The study area and period (15–31 July) of investigation were the same as in 2014, except that the flight locations were adjusted in response to the different ice conditions. Fig. 1 shows the flight tracks for the two years, along with the ice extent at the beginning (July 15) and end (July 31) of the study. Only airborne lidar is capable of measuring subsurface plankton layers over this geographical extent within a two-week period. In both years, the objective of each flight was to fly from open water to full ice cover or the reverse along as many lines as possible consistent with weather conditions. The platform was a National Oceanographic and Atmospheric Administration (NOAA) Twin Otter flying at 300 m altitude at a speed of about 60 m s^{-1}. Ice-extent values are from satellite-derived maps of the marginal ice zone from the US National Ice Center. These are provided for context, and were not used in the analysis. Additionally, daily ice-extent values were obtained from the National Snow and Ice Data Center (Fetterer et al., 2010) and averaged over the period July 15–31 for each year.

The primary instrument for this investigation, as in 2014, was the NOAA airborne oceanographic lidar (Fig. 2). This lidar transmitted 12 ns pulses of linearly polarized green (532 nm) light at a rate of 30 Hz. Two receiver channels detected the co- and cross-polarized light scattered from the ocean with a 1 GHz sample rate. Processing of the lidar data to obtain layer parameters has been described in detail in (Churnside and Marchbanks, 2017). Briefly, the technique assumes that, for every lidar return, the lidar attenuation and scattering parameters can be expressed as the sum of a component that is constant with depth and a perturbation that is depth dependent (Churnside and Marchbanks, 2017). A linear regression of the logarithm of the return with depth is used to find the constant components. We then assume that the integral of the attenuation coefficient perturbation from the surface to each depth is small, although the perturbation itself at any depth need not be. Layers were identified visually from plots of the scattering perturbation parameter with depth. For each identified layer, the averages of the depth of the maximum of the scattering perturbation (layer depth), the full width at half maximum of the perturbation peak (layer thickness), and the value of the maximum divided by the constant return (layer strength) were calculated. Fractional ice cover was also obtained from the lidar, based on the fraction of pulses in each kilometer of flight track where the surface return saturated the detector.

To investigate turbulent mixing in Barrow Canyon, five transects of the canyon were selected (Fig. 3). Bathymetric data were obtained from the International Bathymetric Chart of the Arctic Ocean (IBCAO) Version 3.0 (Jakobsson et al., 2012), and the flight segment where the depth is greater than 70 m was used to define the canyon. Within the inertial subrange of spatial wavelengths, the power-spectral density (*psd*) of a passive scalar sampled along a line through a turbulent field is given by (Sreenivasan, 1996)

$$psd = TK^{-5/3}, \tag{1}$$

where T is a measure of turbulence strength that depends on the units of the measured quantity and K is the spatial wavelength. In our case, we calculated the *psd* of data series constructed by taking a single sample of the lidar return at the same depth from each pulse across the canyon. To investigate depth differences, depths of 10 and 20 m were used for each transect. To obtain large spatial scales, we used the full length of each transect, so no information about the distribution of mixing along transects is possible. A linear regression of the logarithm of the *psd* to the logarithm of spatial wavelength was calculated for each transect at each of the two depths.

Water density profiles were measured at 71.219°N, 164.257°W using the NOAA Prawler (PRofiling crAWLER) (Osse et al., 2015; Tabisola et al., 2017). This instrument provided CTD (Conductivity Temperature Depth) profiles at 3 h intervals beginning July 29, 2017, and data through August 5, 2017 were considered in the analysis. For each profile, potential density was calculated from temperature and salinity, and the depth where the derivative of potential density with depth was maximum (maximum Brunt-Väisälä frequency) was used as a measure of the mixed layer depth (Bourgain and Gascard, 2011). Each profile of potential density was plotted and inspected to ensure that the measured

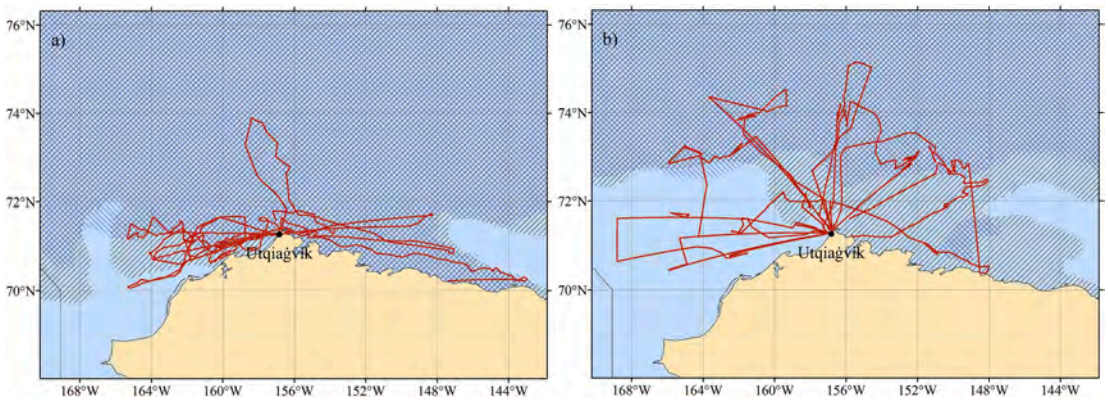

Fig. 1. Map of study area near northern Alaska in **a)** July 2014 and **b)** July 2017. Black///denotes the area covered by ice on July 15, and blue \\ denotes the area covered by ice on July 31 of each year. Red lines are the aircraft flight tracks, and the black circle marks the airport in Utqiaġvik.

Fig. 2. Photos of lidar in aircraft (left) showing the optics package in center of the cabin at the rear and the electronics rack and laptop computer in the foreground. On the right are the ADCP (top) and the installation on the side of the vessel (bottom).

depth was at the bottom of the surface mixed layer. Lidar flights came within 50 km of this mooring on three days, July 22, 26, and 28, 2017.

Water density was also measured by CTD cast from the USCGC *Healy* at 71.223°N, 164.262°W on July 29, 2017 and 72.473°N, 156.567°W on August 3, 2017. The first position was within 500 m of the Prawler position. Lidar flights came within 50 km of the second position on July 18, 27, and 29, 2017.

We also have CTD casts from 10 positions across Barrow Canyon (Fig. 2) measured on July 21 and 22, 2017 from the CCGS *Sir Wilfrid Laurier*. In addition to calculating mixed layer depths for these casts, we calculated the positions of various water masses across the canyon according to the classifications of Gong and Pickard (2015).

During the same period, a 150 kHz Acoustic Doppler Current Profiler (ADCP, Fig. 2) was operated from the ship, which made four passes along the CTD line in Fig. 2. To see if the ADCP measured turbulence over a range of wavelengths similar to the lidar, we calculated the power spectral density of the acoustic backscatter intensity at three depths – 11, 19, and 39 m. Because the scattering mechanisms are different, we were not interested in comparing the magnitude of mixing between lidar and ADCP. As with the lidar, a single sample was used from each acoustic ping to create the data series for each spectrum. The 8° two-way beam width of the ADCP implies that spatial wavelengths greater than 650, 380, and 180 km^{-1} cannot be measured at the three depths used. These wavelengths were greater than the noise limit for all cases.

Large-scale winds were obtained from the National Centers for Environmental Prediction (NCEP) North American Regional Reanalysis (Mesinger et al., 2006). These were averaged over the period of the flights (July 15–31) for each year. Only values over water and between −170° and −168° longitude were used in the analysis. This roughly corresponds to the longitudinal extent of the Bering Strait.

The Bakun upwelling index (Bakun, 1973, 1990) was calculated using the hourly wind speed and direction at the Wiley Post-Will Rogers Memorial Airport in Utqiaġvik, Alaska. For this calculation, a value of 34° from the east-west direction was used for the orientation of the coastline. This is the angle of a line from Point Barrow to Point Hope along the northwest coast of Alaska.

3. Results

An example of layers in broken ice (Fig. 4) shows two layers – one at

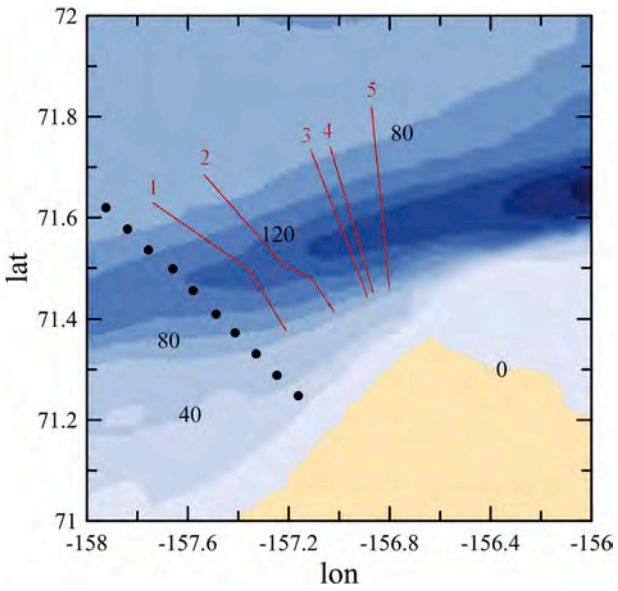

Fig. 3. Map of region near Point Barrow, Alaska, with bathymetry denoted by color scale at depth intervals of 20 m. Flight segments from 2017 are denoted by red lines and numbered from west to east. Ship stations are denoted by black circles. (For interpretation of the references to color in this figure legend, the reader is referred to the Web version of this article.)

a depth of about 20 m and another at a depth of about 30 m. The lidar does not penetrate through ice, but layers are visible wherever the lidar is able to penetrate between ice floes; they appear as vertical white bands in the image. They can even be seen in the first km of the image, where the ice fraction is 86%. Note also that the penetration into the water does not depend on ice fraction. This figure illustrates the ability of airborne lidar to measure subsurface plankton layers with high horizontal and vertical resolution, even in broken ice.

The ice conditions were very different in the latter half of July in the two years (Fig. 1), and this difference shows up in survey conditions (Fig. 5a). The surveys in 2017 were much more likely to be over open water (ice fraction < 0.1), less likely to be over broken ice, and slightly more likely to be over complete ice cover (ice fraction > 0.9). Qualitatively, we noticed that the transition from open water to tightly packed floes occurred much more rapidly in the 2017 flights. This figure was included to acknowledge that sampling bias might be a factor in our results. Clearly, the smaller sample sizes in broken ice in 2017 produce larger error bars in the probability of detecting a layer (Fig. 5b).

The probability of encountering a subsurface plankton layer in 2017 was greater than in 2014, except in open water (Fig. 5b). For 2014, the

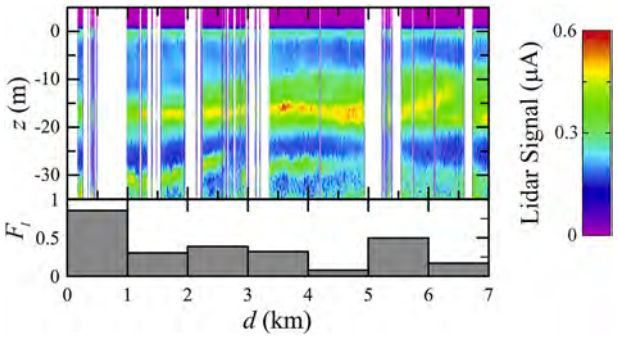

Fig. 4. Top is lidar signal current as a function of depth, z, and position along the flight track, d, for a 7 km segment of data. Color scale at the right shows signal current levels. Vertical white regions denote regions of ice. Bottom is a bar chart of the corresponding ice fraction, F_I, in 1 km segments.

layer probability decreased with increasing ice fraction, with a coefficient of determination of $R^2 = 0.52$ ($p = 0.02$). Without the open water value, the correlation was much higher, with $R^2 = 0.90$ ($p < 10^{-4}$). For 2017, the correlation was much higher when all values were used, with $R^2 = 0.83$ ($p < 0.001$). Without the open water point, the correlation was slightly less than in 2014, with $R^2 = 0.86$ ($p < 0.001$).

For both years, an exponential model for the relationship between ice fraction and the probability of encountering a subsurface plankton layer explained most of the variance in the latter. Within the region of broken ice (fraction > 0.1), the exponential model explained 90% of the observed variability in 2014 and 86% of the variability in 2017. The rate of decay for the two years was very similar, although the overall levels were different. In general, $P_L = A \exp(-2.32 F_I)$, where P_L is the probability of a layer and F_I is the ice fraction. The difference in the coefficient of F_I between the two years was about 5% of the reported mean value. The constant, A, was 0.18 in 2014 and twice as large (0.37) in 2017.

The mean characteristics of the layers for both years are listed in Table 1, including a column for layers south of 72° N. This area, where most of the 2014 surveys took place (Fig. 1), was almost entirely open water in 2017. The most notable feature is the difference in layer strength; the average and median strength of the layers was much weaker in 2017 than 2014. For both years, layers in open water were stronger than those in broken ice. Open water layers south of 72° were stronger than the overall average, but still only about half as strong as open water layers in 2014. Average layer depths were about the same for both years, with open water layers slightly deeper than those in broken ice. Layers in 2017 were thinner than those in 2014, with little difference between the thickness in open water and ice in either year.

The average depth of layers within 50 km of the Prawler was 27.0 m with a standard deviation of 8.8 m. The average depth of the mixed layer inferred from the Prawler data was 25.6 m with a standard deviation of 1.7 m. The difference in the average depths, 1.4 m, is about 13% of the combined standard deviations.

The mixed layer depths inferred from the two ship-based casts were 23 m and 29 m. Note that the first cast was within 500 m of the Prawler, so the same lidar data were compared with the Prawler and with the first ship cast. The average (±standard deviation) depth of the plankton layers in these data was 27.0 ± 8.8 m. For the other cast, the average layer depth was 16.2 ± 8.1 m, which is well above the mixed layer depth of 29 m inferred from the CTD cast. However, there was a second density gradient at about 14 m, which is much closer to the average layer depth. The Brunt-Väisälä frequency at this depth was 0.041 s^{-1}, which is of a similar magnitude to the peak value of 0.053 s^{-1} at 29 m.

The average mixed layer depth across the Barrow Canyon casts was 11.9 m, with a standard deviation of 4.0 m. Stratification was weak, with the mean of the peak Brunt-Väisälä frequency only 5.4×10^{-3} s^{-1} and the standard deviation 3.1×10^{-3} s^{-1}. The average depth of plankton layers across the five lidar transects of the canyon was 17.8 m, with a standard deviation of 7.4 m. The layers were also weak, with a mean and standard deviation of 1.98 ± 1.06 times the background scattering level. Both depth and strength of layers increased as the distance from the mouth of the canyon increased.

Using the CTD data, three water masses were found across Barrow Canyon (Fig. 6). Alaskan Coastal Water (ACW), warm (>3 °C) and moderately salty (30–32.5 psu), covered the surface and extended to the bottom on the south side of the canyon. Winter Water (WW), cold (<−1.6 °C) and salty (31.5–33.6 psu), was below 30 m on the north side of the canyon. Chukchi Summer Water (CSW), with intermediate temperature (-1 – 3 °C) and salinity (30–32.8), was found primarily in a layer around 25 m on the north side of the canyon and to the bottom in the deepest part of the canyon.

The power spectral density of the fluctuations in lidar signal were very close to a power law with exponent of −5/3 for all five passes over Barrow Canyon and for both depths. A typical spectrum (Fig. 7) shows a power-law shape until the lidar noise limit is reached at high spatial wavelengths. For this case, the fit was performed up to a wavelength of

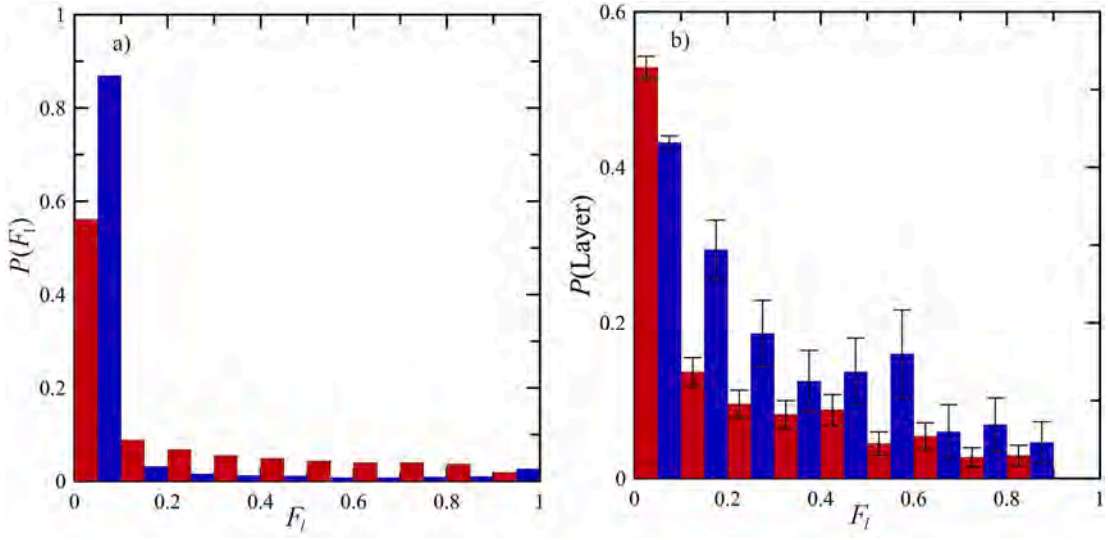

Fig. 5. a) Probability of encountering a given fractional ice cover, F_I, in increments of 0.1 for 2014 (red) and 2017 (blue). **b)** Probability of encountering a subsurface plankton layer as a function of ice fraction for 2014 (red) and 2017 (blue). Error bars represent ±1 standard deviation of the values. (For interpretation of the references to color in this figure legend, the reader is referred to the Web version of this article.)

Table 1
Strength (average, standard deviation, and median in next line), average and standard deviation depth, and average and standard deviation thickness for layers identified in 2014 and 2017. Columns present values for open water and broken ice for each year, and open water south of 72°N for 2017 (In, 2014, all open water was south of 72°N).

2014	Open Water	Ice >0.1	2017:	Open Water	Ice >0.1	South of 72°
Strength	27.0 ± 44.7	8.9 ± 14.0		10.7 ± 48.9	4.1 ± 5.6	13.4 ± 55.3
Median	12	5.1		2.6	2.2	3.0
Depth (m)	19.6 ± 6.0	15.6 ± 6.2		18.5 ± 8.1	15.5 ± 7.0	20.1 ± 8.2
Thickness (m)	3.8 ± 1.5	3.4 ± 2.0		2.4 ± 1.6	2.8 ± 1.7	2.3 ± 1.6

40 km^{-1}, and the exponent of −1.70 is within 2% of the expected value.

The characteristics of power spectral density for the five passes and two depths are presented in Table 2, along with the Bakun upwelling index estimated from Utqiaġvik winds. The correlation between upwelling and turbulence level was 0.91 (P = 0.03) at 10 m and 0.88 (P = 0.05) at 20 m. During periods of downwelling (negative index), turbulence levels were all below 10^{-17}, and the differences between the

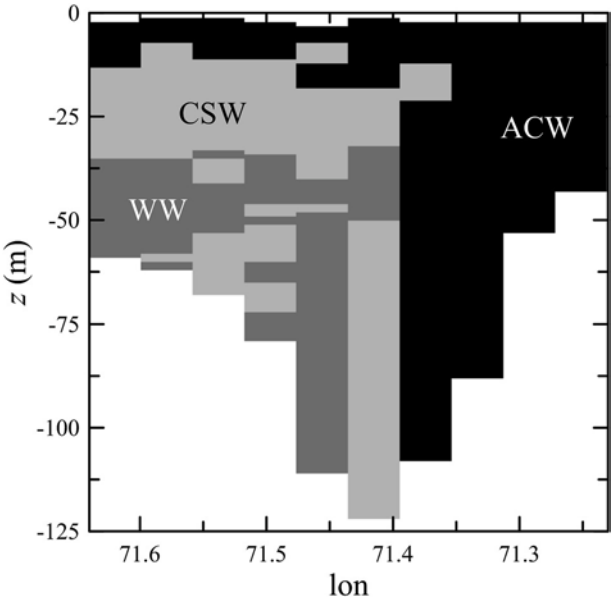

Fig. 6. Distribution of Gong-Pickard water masses across Barrow Canyon. Colors represent Alaskan Coastal Water (ACW, black), Winter Water (WW, dark gray), and Chukchi Summer Water (CSW, light gray).

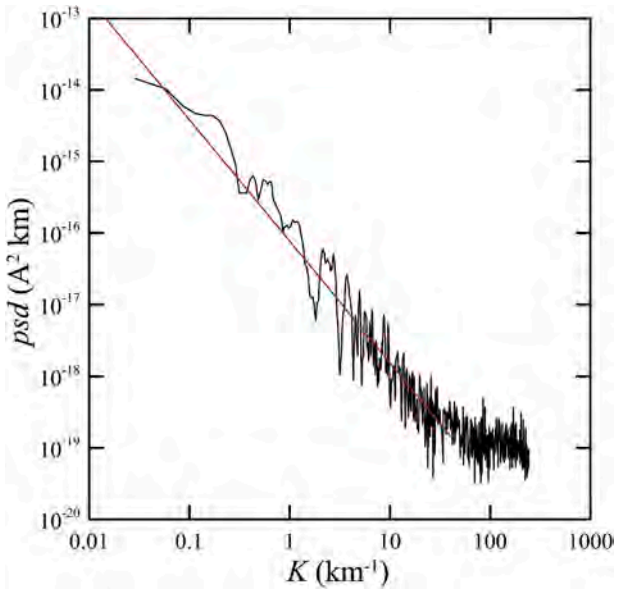

Fig. 7. Power spectral density, *psd*, as a function of spatial wavelength, *K*, for lidar data collected at 10 m depth on July 28, 2017. Red line is the result of a linear regression from the first value to 40 km^{-1}. (For interpretation of the references to color in this figure legend, the reader is referred to the Web version of this article.)

Table 2
Line number (from west to east in Fig. 2), date (July 2017) of the measurement, Bakun upwelling index ($m^3\ s^{-1}$ per 100 m of coastline), turbulence level, T (A^2 km) at 10 m and 20 m depths, and the percent difference between them.

Line (W to E)	Date	Upwelling	T_{10}	T_{20}	Difference (%)
1	21	−177	7.96×10^{-18}	7.45×10^{-18}	6
2	28	58	1.12×10^{-16}	4.50×10^{-17}	60
3	29	−509	3.43×10^{-18}	3.08×10^{-18}	10
4	31	−310	2.95×10^{-18}	3.11×10^{-18}	5
5	18	64	4.09×10^{-17}	1.31×10^{-17}	68

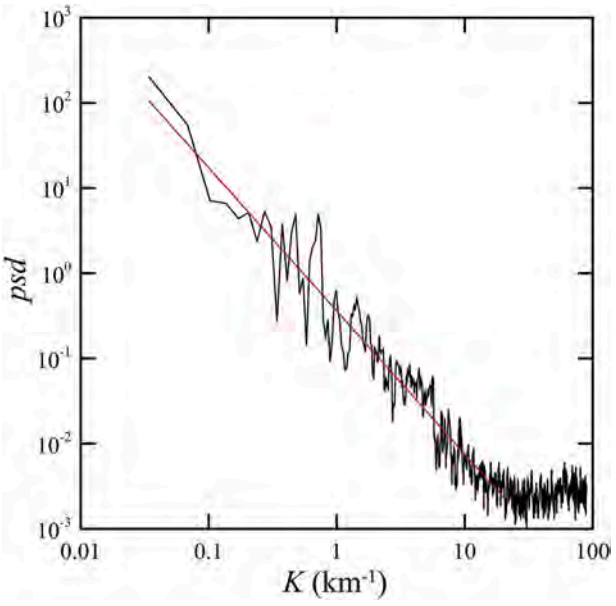

Fig. 8. Power spectral density, *psd*, as a function of spatial wavelength, *K*, for acoustic data collected at 39 m depth on July 22, 2017. Red line is the result of a linear regression from the first value to 20 km^{-1}. (For interpretation of the references to color in this figure legend, the reader is referred to the Web version of this article.)

levels at the two depths were 10% or less of the value at 10 m. During upwelling conditions, turbulence levels were higher ($>10^{-17}$) and the difference was 60% or greater.

The acoustic spectra (Fig. 8) are very similar to the lidar spectra; a power law with slope near −5/3 and a nearly white noise floor at high wavelengths. While the spatial scales are similar to those measured by the lidar, the magnitudes are very different; this is simply because we used different measures of signal level for the two instruments, and they have different units. For the case presented, the slope of −1.68 was within 1% of the expected value out to a wavelength of 20 km^{-1}. These data were collected over too short a time period to investigate the effects of upwelling on turbulence level, but we did find a significant increase of turbulence with depth ($R = 0.76$, $P = 0.005$) over the three depths investigated.

4. Discussion

Much of the difference in ice cover can be explained by a difference in winds between 2014 and 2017. On the northern Chukchi Shelf, the mean winds (NCEP reanalysis) in June and July of 2014 were toward the southwest at ~0.7 m s^{-1}. In sharp contrast, in June and July of 2017 the winds were toward the west-northwest at > 2 m s^{-1}. Thus, during the months of strong melt-back on the northern Chukchi Shelf, we would expect the sea ice to be pushed farther north in 2017 and pushed weakly southward in 2014. The transport of sea ice in 2014 southward is limited by relatively warm surface temperatures and by relatively weak northward transport through Barrow Canyon (Stabeno et al., 2018). We would also expect individual floes to be pushed together by the winds in 2017, resulting in smaller areas with partial ice cover and more areas with almost complete ice cover. These features are consistent with the differences seen in Fig. 3. This is also consistent with visual observations of areas of complete ice cover from the aircraft; in 2014, these areas appeared to be mostly solid ice, while in 2017, they appeared to be mostly closely packed ice floes. The change in ice conditions seems less likely to be related to global changes. For the northern hemisphere, the average ice extent over the last half of July only decreased by 1.5% from 2014 to 2017, while the corresponding decrease in the Chukchi Sea was 20% (Fetterer et al., 2010).

It is not clear why so much of the variability would be explained by ice fraction. One possibility is that the stratification increases as the ice melts, so the density gradients that support thin plankton layers increase as the ice fraction decreases.

The biggest difference in plankton layer properties between the two years was the layer strength in both open water and in broken ice. Because the layer strength is defined as the ratio of the layer signal to the background, this difference could be because the concentrations of phytoplankton within the layers were lower in 2017, the background concentrations were greater, or some combination of the two. To answer this question, we used chlorophyll concentration composites for the month of July in each year from the Visible and Infrared Imager/Radiometer Suite (VIIRS). We assumed that this average of surface chlorophyll concentration would be correlated with the average of the background lidar scattering parameter obtained from the perturbation inversion of the lidar depth profiles. For pixels (at 4-km resolution) in US Arctic waters with data for both years, the average increase in surface chlorophyll concentration from 2014 to 2017 was 72%. The mean layer strength in open water south of 72°N was 50% of the strength in open water in 2014, all of which was south of 72°. This would suggest that much of the difference was caused by an increase in background levels, coupled with a smaller decrease in phytoplankton concentrations within the layers.

The average depths of layers in open water and in broken ice were nearly the same for both years, and, in both cases, slightly deeper in open water (Table 1). In 2017, the depths agreed with available measurements of pycnocline depth to within the variability of the measurements. In general, layer depths were slightly greater than pycnocline depth, however. Our depths are also consistent with *in situ* measurements of layer depths that range from 15 to 25 m (Brown et al., 2015; Coupel et al., 2011; Hill and Cota, 2005; Martini et al., 2016).

The average layer thickness was slightly less in 2017 than in 2014. This difference may also be at least partially explained by the difference in winds. A model of layer thickness based on current shear predicts a minimum thickness of (Birch et al., 2008)

$$t = 2.4\alpha^{-1/3}\kappa_\nu^{1/3}L_0^{1/3}, \quad (2)$$

where α is vertical current shear, κ_ν is the vertical diffusivity of plankton, and L_0 is the initial horizontal extent of the plankton patch before thinning by shear. In this simple model, the initial vertical extent does not matter. The factor of 2.4 is the result of converting from a Gaussian radius to full width at half maximum. Using typical parameters from Birch et al. (2008), the predicted minimum thickness is approximately

what we observed in 2017. The thicker layers in 2014 could be explained by a current shear of about one fourth of the 2017 values. One might expect that the weaker winds in 2014 would produce lower surface drift currents and less shear. However, current shear measurements from ADCP moorings east of Barrow Canyon (31 km from shore in 45 m of water at 71.2°N, 158.0°W) were generally higher during the last half of July in 2014 than in the same period of 2017. It is not clear whether the current shear measured at this location is not representative of the larger survey area or if some other mechanism is controlling layer thickness.

The difference between the ice conditions is mainly due to interannual variability, but our results suggest what may happen in the future as the July ice edge moves farther north. The prevalence of subsurface plankton layers might increase, while their intensity relative to the background concentration might decrease. The exponential decrease in layer prevalence should continue with the same dependence on ice cover. Similarly, the depth of layers would not be expected to change significantly. From a biological perspective, the increased prevalence of subsurface plankton layers could lead to increases in both primary and secondary productivity (Durham and Stocker, 2011). The higher density of phytoplankton in the layer, relative to the nutrient-depleted surface water, produces faster recycling of nutrients and higher grazing rates by zooplankton and pelagic fish. Conceivably, this could support a northward expansion of some pelagic fish species.

Except at the very limit of depth penetration, the lidar measurements in Barrow Canyon were made in either Alaskan Coastal Water or Chukchi Summer Water. This is consistent with previous measurements of water masses in Barrow Canyon in summer, although some authors used different identifiers and different parameter ranges (Coachman and Barnes, 1961; Crawford et al., 2012; Weingartner et al., 1998). Therefore, it is mixing of these two water masses that provides the turbulence observed by the lidar and the ADCP at the two shallower depths. At 40 m, the ADCP is also influenced by Winter Water (Fig. 6).

Turbulent mixing of phytoplankton in Barrow Canyon is enhanced by wind-driven upwelling. Another hypothesis, that tidal currents might be a factor, was not considered, because tidal currents are very small in Barrow Canyon (Itoh et al., 2013; Mountain et al., 1976). We also observed that measured turbulence levels were higher at 10 m than at 20 m during upwelling, but nearly the same during downwelling conditions. This result is probably related to greater vertical gradients during upwelling conditions. For our data, the average lidar signal across the canyon was 19% higher at 10 m than at 20 m during upwelling, but 2.6% lower during downwelling.

While the lidar return is dominated by phytoplankton (Churnside and Thorne, 2005), the ADCP return is mostly from zooplankton (Flagg and Smith, 1989; Ressler, 2002). This might explain why the turbulence levels observed by the ADCP increase with increasing depth. The spectrum of zooplankton can also be affected by individuals swimming, but the observed −5/3 power law is strong evidence that this has a minimal effect. Zooplankton can be detected by lidar (Churnside and Thorne, 2005), but the required processing reduces the signal to noise ratio, and it was not possible to obtain clear spectra of the zooplankton return.

For a passive scalar quantity, θ, the turbulence level defined above is given by

$$T = C_\theta \langle \varepsilon \rangle^{-1/3} \langle \chi \rangle, \tag{3}$$

where C_θ is the Obukhov-Corrsin constant (~0.4), $\langle \varepsilon \rangle$ is the mean energy dissipation rate, and the dissipation rate of the variance of the scalar is given by

$$\langle \chi \rangle = 2\kappa_\nu \langle |\nabla \theta|^2 \rangle, \tag{4}$$

where κ_ν is the scalar diffusivity and $\nabla\theta$ is the scalar gradient (Sreenivasan, 1996). This suggests that the difference in the vertical distribution of turbulence level observed by the lidar and the ADCP is because of differences in the vertical distribution of gradients of phytoplankton and zooplankton.

5. Conclusions

Ice conditions were very different in the study area in July of 2014 and 2017, but the characteristics of subsurface plankton layers and their dependence on ice cover were similar for the two years. In both years, the prevalence of subsurface plankton layers exponentially decreased with increasing ice cover. The average depths were similar for both years, with layers in open water deeper than those in the pack ice. The depths of subsurface plankton layers were consistent with the mixed layer depth in areas where *in situ* density profiles were available. A noticeable difference in layer strength relative to the background water was likely caused by higher background phytoplankton concentrations in 2017. Differences in layer thickness were observed, which could be the result of higher current shears in 2017.

Turbulent mixing of phytoplankton and zooplankton in Barrow Canyon was inferred from the power spectral density of lidar and acoustic scattering. Lidar measurements suggested that the level of turbulence and its vertical distribution were affected by local upwelling winds. The vertical distribution of acoustic scattering was different from that of the lidar, which we interpret as different vertical distributions of phytoplankton and zooplankton gradients.

Declaration of competing interest

The authors declare that they have no known competing financial interests or personal relationships that could have appeared to influence the work reported in this paper.

CRediT authorship contribution statement

James H. Churnside: Conceptualization, Methodology, Investigation, Writing - original draft. **Richard D. Marchbanks:** Investigation, Software. **Svein Vagle:** Investigation, Writing - review & editing. **Shaun W. Bell:** Software, Data curation, Writing - review & editing. **Phyllis J. Stabeno:** Investigation, Writing - review & editing.

Acknowledgments

We would like to acknowledge our pilots, Shanae Coker and Frank Centinello III, mechanic, Robert Miletic, and the captain and crew of CCGS Sir Wilfrid Laurier. Satellite ice extent were obtained from the US National Ice Center (https://www.natice.noaa.gov/). Large-scale wind data were obtained from the NOAA Earth System Research Laboratory Physical Sciences Division (https://www.esrl.noaa.gov/psd/cgi-bin/data/narr/plothour.pl). Hourly wind speed and direction at the Wiley Post-Will Rogers Memorial Airport were obtained from the Weather Underground archive (https://www.wunderground.com/history/). Satellite chlorophyll data were obtained from the NASA Goddard Space Flight Center, Ocean Ecology Laboratory, Ocean Biology Processing Group. Visible and Infrared Imager/Radiometer Suite (VIIRS) Ocean Color Data; 2018 Reprocessing. NASA OB.DAAC, Greenbelt, MD, USA. https://doi.org/10.5067/NPP/VIIRS/L2/OC/2018, accessed on 08/22/2018. The authors have no conflict of interest. Lidar data from this study are available at https://data.nodc.noaa.gov/cgi-bin/iso?id=gov.noaa.nodc:0187514. This publication is contribution #4896 from the Pacific Marine Environmental Laboratory. This work was partially supported by the United States National Aeronautics and Space Administration grant NNH16AD24I.

Appendix A. Supplementary data

Supplementary data to this article can be found online at https://doi.org/10.1016/j.dsr2.2020.104742.

References

Ardyna, M., Babin, M., Gosselin, M., Devred, E., Bélanger, S., Matsuoka, A., Tremblay, J.É., 2013. Parameterization of vertical chlorophyll a in the Arctic Ocean: impact of the subsurface chlorophyll maximum on regional, seasonal, and annual primary production estimates. Biogeosciences 10, 4383–4404. https://doi.org/10.5194/bg-10-4383-2013.

Arrigo, K.R., van Dijken, G.L., 2015. Continued increases in Arctic Ocean primary production. Prog. Oceanogr. 136, 60–70. https://doi.org/10.1016/j.pocean.2015.05.002.

Arrigo, K.R., van Dijken, G., Pabi, S., 2008. Impact of a shrinking Arctic ice cover on marine primary production. Geophys. Res. Lett. 35, L19603. https://doi.org/10.1029/2008gl035028.

Arrigo, K.R., Matrai, P.A., van Dijken, G.L., 2011. Primary productivity in the Arctic Ocean: impacts of complex optical properties and subsurface chlorophyll maxima on large-scale estimates. J. Geophys. Res. Oceans 116, C11022. https://doi.org/10.1029/2011jc007273.

Arrigo, K.R., et al., 2014. Phytoplankton blooms beneath the sea ice in the Chukchi sea. Deep Sea Res. II 105, 1–16. https://doi.org/10.1016/j.dsr2.2014.03.018.

Bakun, A., 1973. Coastal Upwelling Indices, West Coast of North America, 1946-71. NOAA Technical Report Rep. NMFS SSRF-693. U.S. Department of Commerce, Seattle, Washington.

Bakun, A., 1990. Global climate change and intensification of coastal ocean upwelling. Science 247, 198.

Behrenfeld, M.J., et al., 2017. Annual boom–bust cycles of polar phytoplankton biomass revealed by space-based lidar. Nat. Geosci. 10, 118. https://doi.org/10.1038/ngeo2861. https://www.nature.com/articles/ngeo2861#supplementary-information.

Birch, D.A., Young, W., Franks, P., 2008. Thin layers of plankton: formation by shear and death by diffusion. Deep Sea Res. I 55, 277–295. https://doi.org/10.1016/j.dsr.2007.11.009.

Bourgain, P., Gascard, J.C., 2011. The Arctic Ocean halocline and its interannual variability from 1997 to 2008. Deep Sea Res. I 58, 745–756. https://doi.org/10.1016/j.dsr.2011.05.001.

Brown, Z.W., Lowry, K.E., Palmer, M.A., van Dijken, G.L., Mills, M.M., Pickart, R.S., Arrigo, K.R., 2015. Characterizing the subsurface chlorophyll a maximum in the Chukchi Sea and Canada basin. Deep Sea Res. II. https://doi.org/10.1016/j.dsr2.2015.02.010.

Churnside, J.H., 2014. Review of profiling oceanographic lidar. Opt. Eng. 53 https://doi.org/10.1117/1.oe.53.5.051405, 051405-051405.

Churnside, J.H., Thorne, R.E., 2005. Comparison of airborne lidar measurements with 420 kHz echo-sounder measurements of zooplankton. Appl. Optic. 44, 5504–5511. https://doi.org/10.1364/AO.44.005504.

Churnside, J.H., Ostrovsky, L.A., 2005. Lidar observation of a strongly nonlinear internal wave train in the Gulf of Alaska. Int. J. Rem. Sens. 26, 167–177. https://doi.org/10.1080/01431160410001735076.

Churnside, J.H., Donaghay, P.L., 2009. Thin scattering layers observed by airborne lidar. ICES J. Mar. Sci. 66, 778–789. https://doi.org/10.1093/icesjms/fsp029.

Churnside, J.H., Marchbanks, R.D., 2015. Sub-surface plankton layers in the Arctic Ocean. Geophys. Res. Lett. 42, 4896–4902. https://doi.org/10.1002/2015GL064503.

Churnside, J.H., Marchbanks, R.D., 2017. Inversion of oceanographic profiling lidars by a perturbation to a linear regression. Appl. Optic. 56, 5228–5233. https://doi.org/10.1364/AO.56.005228.

Churnside, J.H., Marchbanks, R.D., Lee, J.H., Shaw, J.A., Weidemann, A., Donaghay, P. L., 2012. Airborne lidar detection and characterization of internal waves in a shallow fjord. J. Appl. Remote Sens. 6 https://doi.org/10.1117/1.jrs.6.063611, 063611-063615.

Coachman, L.K., Barnes, C.A., 1961. The contribution of Bering sea water to the Arctic Ocean. Arctic 14, 147–161.

Comiso, J.C., 2011. Large decadal decline of the Arctic multiyear ice cover. J. Clim. 25, 1176–1193. https://doi.org/10.1175/jcli-d-11-00113.1.

Cota, G., Pomeroy, L., Harrison, W., Jones, E., Peters, F., Sheldon, W.J., Weingartner, T., 1996. Nutrients, primary production and microbial heterotrophy in the southeastern Chukchi Sea: Arctic summer nutrient depletion and heterotrophy. Mar. Ecol. Prog. Ser. 135, 247–258. https://doi.org/10.3354/meps135247.

Coupel, P., Jin, H.Y., Ruiz-Pino, D., Chen, J.F., Lee, S.H., Li, H.L., Rafizadeh, M., Garçon, V., Gascard, J.C., 2011. Phytoplankton distribution in the Western Arctic Ocean during a summer of exceptional ice retreat. Biogeosci. Discuss. 8, 6919–6970. https://doi.org/10.5194/bgd-8-6919-2011.

Crawford, R.E., Vagle, S., Carmack, E.C., 2012. Water mass and bathymetric characteristics of polar cod habitat along the continental shelf and slope of the Beaufort and Chukchi seas. Polar Biol. 35, 179–190. https://doi.org/10.1007/s00300-011-1051-9.

Durham, W.M., Stocker, R., 2011. Thin phytoplankton layers: characteristics, mechanisms, and consequences. Annu. Rev. Mar. Sci. 4, 177–207. https://doi.org/10.1146/annurev-marine-120710-100957.

Fetterer, F., Savoie, M., Helfrich, S., Clement-Colon, P., 2010. Multisensor analyzed sea ice extent - northern hemisphere (MASIE-NH), Version 1. In: Daily Ice Extent. National Ice Center and National Snow and Ice Data Center, Boulder, Colorado, USA. https://doi.org/10.7265/N5GT5K3K.

Flagg, C.N., Smith, S.L., 1989. On the use of the acoustic Doppler current profiler to measure zooplankton abundance. Deep Sea Res. A. 36, 455–474. https://doi.org/10.1016/0198-0149(89)90047-2.

Goldin, Y.A., Vasilev, A.N., Lisovskiy, S.S., Chernook, V.I., 2007. Results of Barents Sea airborne lidar survey. In: Proc. 6615, Current Research on Remote Sensing, Laser Probing, and Imagery in Natural Waters. SPIE, Bellingham, p. 66150E. https://doi.org/10.1117/12.740456.

Gong, D., Pickart, R.S., 2015. Summertime circulation in the eastern Chukchi Sea. Deep Sea Res. II 118, 18–31. https://doi.org/10.1016/j.dsr2.2015.02.006.

Grebmeier, J.M., Moore, S.E., Overland, J.E., Frey, K.E., Gradinger, R., 2010. Biological response to recent Pacific Arctic sea ice retreats. Eos, Trans. Am. Geophys. Union 91, 161–162. https://doi.org/10.1029/2010EO180001.

Hegseth, E.N., 1998. Primary production of the northern Barents Sea. Polar Res. 17, 113–123. https://doi.org/10.1111/j.1751-8369.1998.tb00266.x.

Hill, V., Cota, G., 2005. Spatial patterns of primary production on the shelf, slope and basin of the Western Arctic in 2002. Deep Sea Res. II 52, 3344–3354. https://doi.org/10.1016/j.dsr2.2005.10.001.

Hill, V., Cota, G., Stockwell, D., 2005. Spring and summer phytoplankton communities in the Chukchi and eastern Beaufort seas. Deep Sea Res. II 52, 3369–3385. https://doi.org/10.1016/j.dsr2.2005.10.010.

Hill, V.J., Zimmerman, R.C., 2010. Estimates of primary production by remote sensing in the Arctic Ocean: assessment of accuracy with passive and active sensors. Deep Sea Res. I 57, 1243–1254. https://doi.org/10.1016/j.dsr.2010.06.011.

Itoh, M., Nishino, S., Kawaguchi, Y., Kikuchi, T., 2013. Barrow Canyon volume, heat, and freshwater fluxes revealed by long-term mooring observations between 2000 and 2008. J. Geophys. Res. Oceans 118, 4363–4379. https://doi.org/10.1002/jgrc.20290.

Jacox, M.G., Edwards, C.A., Kahru, M., Rudnick, D.L., Kudela, R.M., 2015. The potential for improving remote primary productivity estimates through subsurface chlorophyll and irradiance measurement. Deep Sea Res. II 112, 107–116. https://doi.org/10.1016/j.dsr2.2013.12.008.

Jakobsson, M., et al., 2012. The international bathymetric chart of the Arctic Ocean (IBCAO) Version 3.0. Geophys. Res. Lett. 39, L12609 https://doi.org/10.1029/2012GL052219.

Kitchen, J.C., Zaneveld, J.R.V., 1990. On the noncorrelation of the vertical structure of light scattering and chlorophyll α in case I waters, 95, pp. 20237–20246. https://doi.org/10.1029/JC095iC11p20237.

Kwok, R., Rothrock, D.A., 2009. Decline in Arctic sea ice thickness from submarine and ICESat records: 1958–2008. Geophys. Res. Lett. 36, L15501. https://doi.org/10.1029/2009gl039035.

Lee, Y., et al., 2015. An assessment of phytoplankton primary productivity in the Arctic Ocean from satellite ocean color/in situ chlorophyll-a based models. J. Geophys. Res. Oceans 120, 6508–6541. https://doi.org/10.1002/2015jc011018.

Lu, X., Hu, Y., Liu, Z., Rodier, S., Vaughan, M., Lucker, P., Trepte, C., Pelon, J., 2017. Observations of Arctic snow and sea ice cover from CALIOP lidar measurements. Remote Sens. Environ. 194, 248–263. https://doi.org/10.1016/j.rse.2017.03.046.

Martin, J., Dumont, D., Tremblay, J.-É., 2013. Contribution of subsurface chlorophyll maxima to primary production in the coastal Beaufort Sea (Canadian Arctic): a model assessment. J. Geophys. Res. Oceans 118, 5873–5886. https://doi.org/10.1002/2013JC008843.

Martin, J., Tremblay, J., Gagnon, J., Tremblay, G., Lapoussi, A., Jose, C., Poulin, M., Gosselin, M., Gratton, Y., Michel, C., 2010. Prevalence, structure and properties of subsurface chlorophyll maxima in Canadian Arctic waters. Mar. Ecol. Prog. Ser. 412, 69–84. https://doi.org/10.3354/meps08666.

Martini, K.I., Stabeno, P.J., Ladd, C., Winsor, P., Weingartner, T.J., Mordy, C.W., Eisner, L.B., 2016. Dependence of subsurface chlorophyll on seasonal water masses in the Chukchi Sea. J. Geophys. Res. Oceans 121, 1755–1770. https://doi.org/10.1002/2015JC011359.

Mesinger, F., et al., 2006. North American regional reanalysis. Bull. Am. Meteorol. Soc. 87, 343–360. https://doi.org/10.1175/bams-87-3-343.

Moore, S.E., Grebmeier, J.M., 2018. The distributed biological observatory: linking physics to biology in the Pacific Arctic region. Arctic 71, 1–7. https://doi.org/10.14460/arctic4606.

Mountain, D.G., Coachman, L.K., Aagaard, K., 1976. On the flow through Barrow canyon. J. Phys. Oceanogr. 6, 461–470. https://doi.org/10.1175/1520-0485(1976)006<0461:otftbc>2.0.co;2.

Naoya, K., Shin, S., Yoshihiko, O., Daiki, S., Yasushi, F., Daiki, N., 2018. Upwelling of macronutrients and dissolved inorganic carbon by a subglacial freshwater driven plume in Bowdoin Fjord, northwestern Greenland. J. Geophys. Res. Biogeosci. 123, 1666–1682. https://doi.org/10.1029/2017JG004248.

Osse, T.J., Meinig, C., Stalin, S., Milburn, H., 2015. The PRAWLER, a vertical profiler powered by wave energy. In: Paper Presented at OCEANS 2015. MTS/IEEE, Washington, 19-22 Oct. 2015.

Pithan, F., Mauritsen, T., 2014. Arctic amplification dominated by temperature feedbacks in contemporary climate models. Nat. Geosci. 7, 181–184. https://doi.org/10.1038/ngeo2071.

Ressler, P.H., 2002. Acoustic backscatter measurements with a 153kHz ADCP in the northeastern Gulf of Mexico: determination of dominant zooplankton and micronekton scatterers. Deep Sea Res. I 49, 2035–2051. https://doi.org/10.1016/S0967-0637(02)00117-6.

Retamal, L., Bonilla, S., Vincent, W.F., 2008. Optical gradients and phytoplankton production in the mackenzie river and the coastal Beaufort sea. Polar Biol. 31, 363–379. https://doi.org/10.1007/s00300-007-0365-0.

Ríos, F., Kilian, R., Mutschke, E., 2016. Chlorophyll-a thin layers in the Magellan fjord system: the role of the water column stratification. Continent. Shelf Res. 124, 1–12. https://doi.org/10.1016/j.csr.2016.04.011.

Serreze, M.C., Barry, R.G., 2011. Processes and impacts of Arctic amplification: a research synthesis. Global Planet. Change 77, 85–96. https://doi.org/10.1016/j.gloplacha.2011.03.004.

Shroyer, E.L., Benoit-Bird, K.J., Nash, J.D., Moum, J.N., 2014. Stratification and mixing regimes in biological thin layers over the Mid-Atlantic Bight. Limnol. Oceanogr. 59, 1349–1363. https://doi.org/10.4319/lo.2014.59.4.1349.

Spreen, G., Kwok, R., Menemenlis, D., 2011. Trends in Arctic sea ice drift and role of wind forcing: 1992–2009. Geophys. Res. Lett. 38, L19501. https://doi.org/10.1029/2011gl048970.

Sreenivasan, K.R., 1996. The passive scalar spectrum and the Obukhov-Corrsin constant. Phys. Fluids 8, 189–196. https://doi.org/10.1063/1.868826.

Stabeno, P., Kachel, N., Ladd, C., Woodgate, R., 2018. Flow patterns in the eastern Chukchi Sea: 2010–2015. J. Geophys. Res. Oceans 123, 1177–1195. https://doi.org/10.1002/2017JC013135.

Tabisola, H.M., Stabeno, P.J., Mordy, C.W., 2017. Using a biophysical mooring as a sentinel for ecosystem change: the story of M2. In: paper presented at OCEANS 2017, Anchorage, 18–21 Sept. 2017.

Taylor, P.C., Cai, M., Hu, A., Meehl, J., Washington, W., Zhang, G.J., 2013. A decomposition of feedback contributions to polar warming amplification. J. Clim. 26, 7023–7043. https://doi.org/10.1175/jcli-d-12-00696.1.

Vaughan, D.G., et al., 2013. Observations: cryosphere. In: Stocker, T.F., Qin, D., Plattner, G.-K., Tignor, M., Allen, S.K., Boschung, J., Nauels, A., Xia, Y., Bex, V., Midgley, P.M. (Eds.), Climate Change 2013: the Physical Science Basis. Contribution of Working Group I to the Fifth Assessment Report of the Intergovernmental Panel on Climate Change. Cambridge University Press, Cambridge, pp. 317–382.

Weingartner, T.J., Cavalieri, D.J., Aagaard, K., Sasaki, Y., 1998. Circulation, dense water formation, and outflow on the northeast Chukchi Shelf. J. Geophys. Res. Oceans 103, 7647–7661. https://doi.org/10.1029/98JC00374.

Weston, K., Fernand, L., Mills, D.K., Delahunty, R., Brown, J., 2005. Primary production in the deep chlorophyll maximum of the central North Sea. J. Plankton Res. 27, 909–922. https://doi.org/10.1093/plankt/fbi064.

Weston, K., Fernand, L., Mills, D.K., Delahunty, R., Brown, J., 2011. Primary production in the deep chlorophyll maximum of the central North Sea. J. Plankton Res. 33, 1627–1628. https://doi.org/10.1093/plankt/fbr067.

Deep–Sea Research II 177 (2020) 104807

Contents lists available at ScienceDirect

Deep-Sea Research Part II

journal homepage: http://www.elsevier.com/locate/dsr2

Seasonal and interannual variability of nitrate in the eastern Chukchi Sea: Transport and winter replenishment

Calvin W. Mordy [a,b,*], Shaun Bell [a,b], Edward D. Cokelet [b], Carol Ladd [b], Geoff Lebon [a,b], Peter Proctor [a,b], Phyllis Stabeno [b], David Strausz [a,b], Eric Wisegarver [b], Kevin Wood [a,b]

[a] Joint Institute for the Study of the Atmosphere and Ocean, Box 355672, University of Washington, Seattle, WA, 98105-5672, USA
[b] Pacific Marine Environmental Laboratory, NOAA, 7600 Sand Point Way, NE, Seattle, WA, 98115, USA

ARTICLE INFO

Keywords:
Chukchi sea
Bering sea
Nitrate
Transport
Replenishment
Nitrate flux
Net community production
NCP

ABSTRACT

Rapid changes in sea ice and ocean properties are occurring in the Chukchi Sea, and there is considerable uncertainty how these changes might influence nutrient distributions and ultimately primary productivity. Although inorganic nitrogen is a limiting nutrient, there are few reports on seasonal or interannual variability of nitrate, especially those focused on wintertime replenishment of nitrate. This study examined six years of hourly measurements of nitrate at multiple mooring locations off Icy Cape between 2010 and 2018 with a focus on winter replenishment in relation to northward transport. Nitrate concentrations are lowest in newly formed winter water, and rates of local nitrate replenishment appear low relative to the nutrient flux through Bering Strait. There is considerable interannual variability in transport over the northeastern shelf of the Chukchi Sea that is driven by northerly (weakens transport) and southerly (strengthens transport) wind events. Anomalously low nitrate concentrations were observed in the winter of 2011–2012 when transport was negligible, and locally formed, low nitrate winter water remained on the shelf. During winters with the highest transport (2010–2011, 2017–2018), pre-bloom (15 May) nitrate concentrations were high and closely resembled nitrate concentrations in the Bering Sea from the previous fall. In recent years, there has been an increase in southerly wind events. As these conditions enhance total transport and nutrient flux through Bering Strait, contemporary Bering Sea water is advected onto the northern Chukchi Sea shelf. In the presence of southerly wind events, nutrient measurements in the northern Bering Sea in fall can be used to predict pre-bloom nitrate concentrations available for sustaining primary production in the eastern Chukchi Sea the following spring. Since 2005, inorganic nitrogen concentrations in the northern Bering Sea have varied between 11 and 22 μM; an indication that net community production over the eastern Chukchi Sea may have varied between ~30 and 70 g C m^{-2} during this time.

1. Introduction

The Arctic Ocean is undergoing rapid change with warming temperatures and reductions in the extent, thickness and duration of sea ice (Zhang, 2005; Steele et al., 2008; Serreze et al., 2009; Screen and Simmonds, 2010; Cavalieri and Parkinson, 2012; Frey et al., 2015; Wang et al., 2018; Dai et al., 2019). These changes are especially striking in the Chukchi Sea where the open water season continues to increase with the later arrival of ice in fall and earlier ice retreat in spring (Frey et al., 2015; Wang and Overland, 2015; Wood et al., 2015; Serreze et al., 2016; Overland and Wang, 2018; Rolph et al., 2018; Stabeno et al., 2018b; Wang et al., 2018). Lengthening of the open-water season is projected to alter the composition and distribution of phytoplankton communities (Tremblay et al., 2009; Ardyna et al., 2011; Neeley et al., 2018) and the timing and extent of primary production (Arrigo et al., 2008; Hill et al., 2018; Selz et al., 2018; Lewis et al., 2019). These changes are primarily due to increased stratification and a reduction in vertical mixing and diffusion of nutrients from deeper water (30–40 m) into the upper water column. While primary production over the shelf has been tied to the flow of cold, nutrient-rich bottom water (Lowry et al., 2015), to date there are no direct measurements that examine interannual variability of nutrient transport across the eastern shelf of the Chukchi Sea.

The only direct pathway of flow from the Pacific Ocean into the Arctic Ocean is through Bering Strait, a narrow (~80 km), shallow (<55 m) passageway between Siberia and Alaska, which is divided into western and eastern channels by the Diomede Islands (Coachman et al.,

* Corresponding author. Cooperative Institute for Climate, Ocean, and Ecosystem Studies, Box 355672, University of Washington, Seattle, WA, 98195-5672, USA.
E-mail address: mordy@uw.edu (C.W. Mordy).

https://doi.org/10.1016/j.dsr2.2020.104807
Received 13 September 2019; Received in revised form 28 April 2020; Accepted 24 May 2020
Available online 17 June 2020

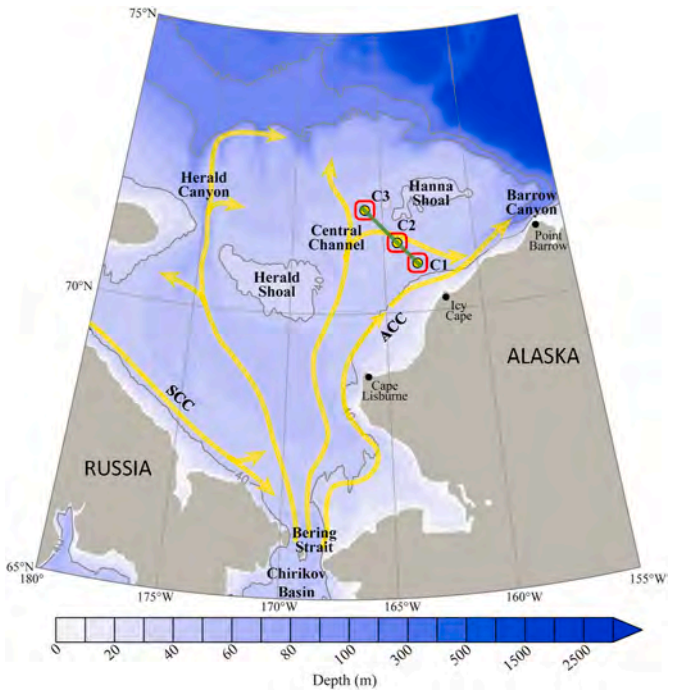

Fig. 1. Map of the Chukchi Sea (modified from Ladd et al., 2016) showing patterns of flow (yellow arrows) including the Siberian Coastal Current (SCC) and Alaskan Coastal Current (ACC), and the locations of the Icy Cape moorings (C1, C2, and C3) and the Icy Cape hydrographic line (green bar). The red boxes around each of the moorings denotes the boxes for determining ice concentration. (For interpretation of the references to color in this figure legend, the reader is referred to the Web version of this article.)

Table 1
The locations and bottom depths of the Icy Cape moorings.

Mooring	Latitude (°N)	Longitude (°W)	Depth (m)
C1	70.835	163.119	44
C2	71.222	164.250	43
C3	71.825	165.975	45

Table 2
Temperature and salinity bounds for water masses observed in this study. The classification scheme is drawn from Gong and Pickart (2015), Ladd et al. (2016), and Danielson et al. (2017).

Water Mass	Temperature (°C)	Salinity
Winter Water	$-2 < T < 0$	$30.0 \leq S \leq 33.6$
Summer Water	$0 \leq T < 7$	$30.0 \leq S \leq 33.6$
Atlantic Water	$-1.7 \leq T < 1$	$33.6 < S < 35.0$
Newly-ventilated / Brine-influenced	$T < -1.7$	$33.6 < S < 35.0$

Table 3
Mean and standard deviation of nitrate and dissolved inorganic nitrogen (DIN) concentrations in bottom water on the northern Bering Sea in spring (March–May) and summer/fall (July–October). Data are from 5 cruises in spring and 23 cruises in summer/fall spanning 2004–2018. Stations were located between 61.5° and 63.6°N and 55–90 m water depth, and samples were from the deepest Niskin bottle providing that it was <12 m from the bottom. Cruises in spring were conducted in ice-covered waters in 2007–2010 as part of the Bering Sea Ecosystem Study (BEST), and in ice-free waters in May 2018 during the NOAA-PMEL spring mooring cruise.

	Nitrate (μM)	DIN (μM)	N
March–May	13.5 ± 4.0	14.9 ± 3.6	92
July–October	10.8 ± 3.2	14.4 ± 3.5	207

1975). Three Pacific water masses enter the Chukchi Sea through Bering Strait: the saline and nutrient-rich Anadyr Water (AW) and Bering Shelf Water (BSW), and the fresher and nutrient-poor Alaskan Coastal Water (ACW) (Coachman et al., 1975). ACW originates primarily on the inner shelf (<50 m) of the Bering Sea, and includes freshwater inputs from regional rivers including the Yukon River (Woodgate et al., 2005; Aagaard et al., 2006); it generally flows along the eastern side of Bering Strait (Coachman et al., 1975; Danielson et al., 2017). AW originates on the outer shelf or slope of the Bering Sea, and flows through Chirikov Basin (Fig. 1) and along the western side of the strait (Coachman et al., 1975; Danielson et al., 2017).

In Bering Strait, BSW is generally found between ACW and AW (Coachman et al., 1975; Danielson et al., 2017). The primary source of the BSW is the northward flowing current along the 100-m isobath, which is the transition between the middle and outer domains of the Bering Sea (Stabeno et al., 2016b, 2018a). On the northern middle shelf of the Bering Sea, there is substantial interannual variability in nutrient content. For example, there was a significant decline in the concentrations of dissolved inorganic nitrogen (DIN, nitrate + nitrite + ammonium) and phosphate between 2005 and 2016, with concentrations partially rebounding in 2017 (Stabeno et al., 2018a). It is unclear if this variability extends to other portions of the Bering Sea Shelf and slope, or how it might be reflected in BSW that flows across the eastern Chukchi Sea Shelf.

In the Chukchi Sea, nitrogen is the limiting nutrient (Cota et al., 1996; Codispoti et al., 2005; Tremblay et al., 2006), although continual nutrient inputs through Bering Strait (primarily western Bering Strait) make this region analogous to a "chemostat", and one of the most productive shelves in the Arctic (Sambrotto et al., 1984; Stein and Macdonald, 2004; Hill and Cota, 2005; Sakshaug, 2004; Codispoti et al., 2005, 2013; Hill and Zimmerman, 2010; Hill et al., 2018). Transport through Bering Strait has been measured for decades (Roach et al., 1995; Woodgate et al., 2005, 2012; Woodgate, 2018). The flow is typically northward, and is thought to be driven by a sea level difference (pressure head) between the Pacific and Arctic Oceans (Coachman and Aagaard, 1966; Stigebrandt, 1984; Aagaard et al., 2006) and modified by winds (Aagaard et al., 1985; Coachman and Aagaard, 1988; Roach et al., 1995; Woodgate et al., 2005; Danielson et al., 2017). During the past 25 years, transport through Bering Strait has increased from 0.8 to 1.0 Sv (10^6 m^3 s^{-1}) (Woodgate, 2018), and this was attributed primarily to changes in westward winds along the Arctic coasts and sea-level change in the East Siberian Sea (Peralta-Ferriz and Woodgate, 2017; Woodgate, 2018).

After passing Bering Strait, Pacific Water continues into the central Arctic following three branches (Fig. 1). In the west, flow is toward Herald Canyon, with a portion of the flow exiting Herald Canyon and the remainder turning eastward and remaining on the shelf (e.g. Linders et al., 2017; Li et al., 2019). The Siberian Coastal Current (SCC) flows southwestward along the Siberian Coast with some of the SCC turning northward joining the flow toward Herald Canyon (Linders et al., 2017; Bond et al., 2018). The SCC appears intermittent and is forced by wind and buoyancy (Weingartner et al., 1999), and some of the SCC has been observed to flow southward into the western channel of Bering Strait (Roach et al., 1995; Weingartner et al., 1999). In the east, the Alaskan Coastal Current (ACC) flows northeastward along the Alaskan coast toward Barrow Canyon (Weingartner et al., 1998). BSW flows north through Central Channel with the majority of flow joining the ACC just north of Icy Cape; most of this flow exits through Barrow Canyon (Stabeno et al., 2018b).

As water flows through the Chukchi Sea, physical characteristics are seasonally modified through ice melt and ice formation (i.e. brine exclusion), and warming and cooling. Temperature and salinity signatures have been used to define seasonal water types in the Chukchi Sea including ACW, melt water (MW), summer water (SW), and winter water (WW), and used to identify the presence of saltier Atlantic Water (AtlW), which can upwell along the shelfbreak (Gong and Pickart, 2015; Ladd et al., 2016; Danielson et al., 2017).

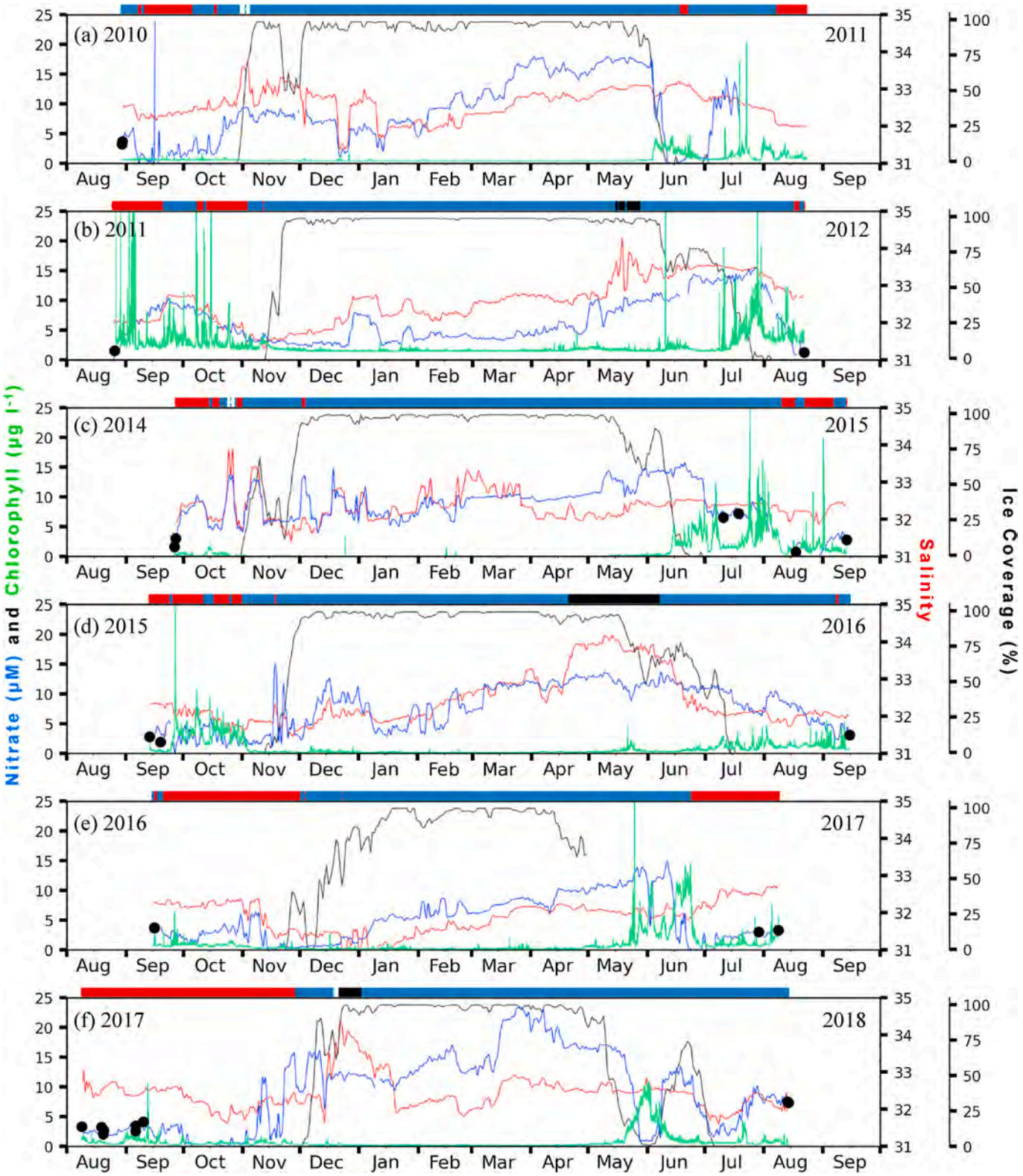

Fig. 2. Annual time series of the percent areal ice cover (black), nitrate (blue), salinity (red), chlorophyll fluorescence (green), and water mass (color bar atop each panel) from six deployments at the C2 mooring spanning 2010–2012 and 2014–2018. Filled circles indicate discrete nitrate calibration points. Water types include summer water (red), winter water (blue), Atlantic water (white), and newly-ventilated or brine-influenced water (black). (For interpretation of the references to color in this figure legend, the reader is referred to the Web version of this article.)

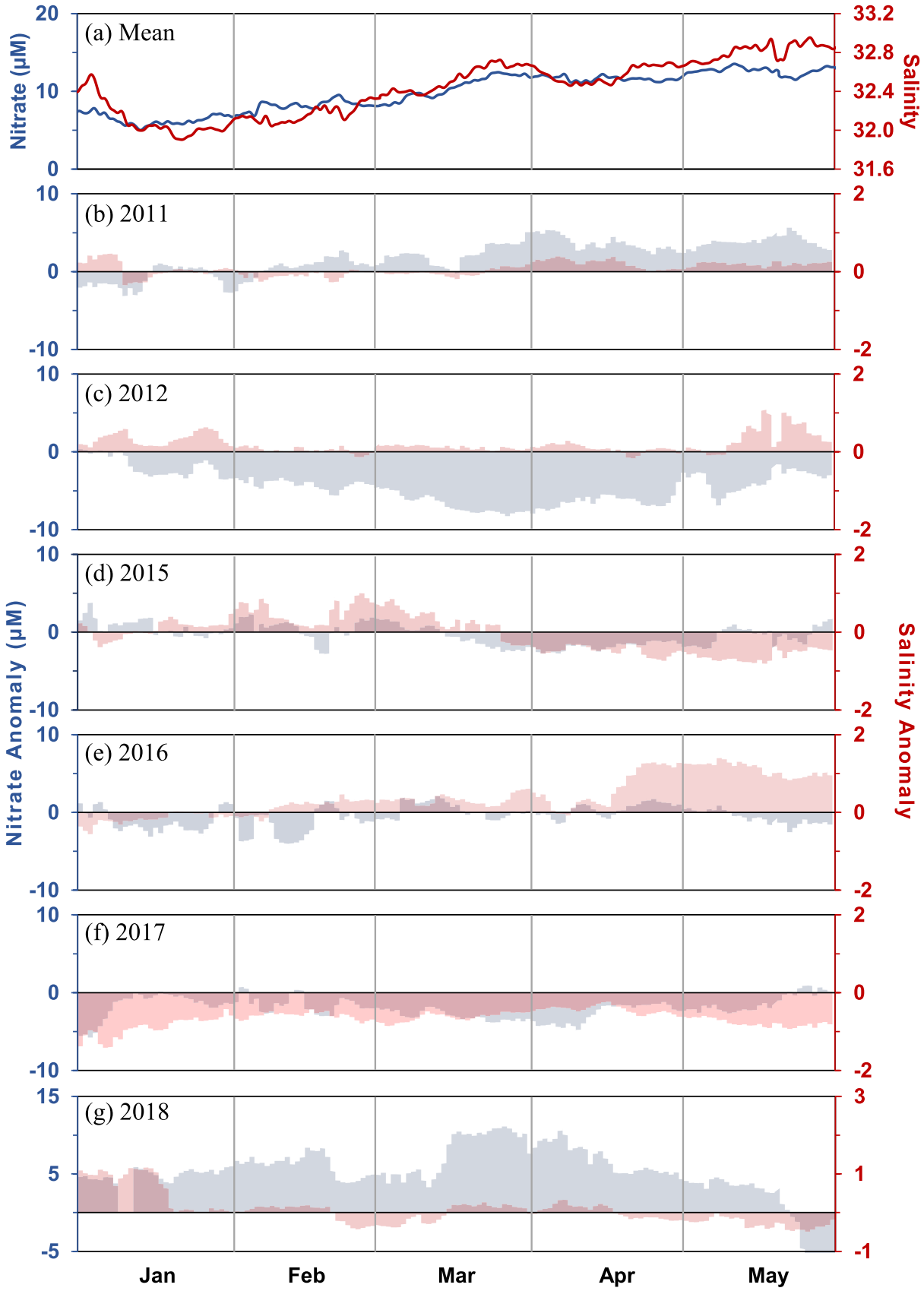

Fig. 3. Multi-year (2011, 2012, 2015–2018) hourly mean (a) and anomalies (b–g) of nitrate (blue) and salinity (red) at the C2 mooring in January through May for the six time series shown in Fig. 2. Note the change in scale in 2018. The mean does not include nitrate data from 20 to 31 May 2018, and the nitrate anomaly during this period is off-scale at −12.1 μM. (For interpretation of the references to color in this figure legend, the reader is referred to the Web version of this article.)

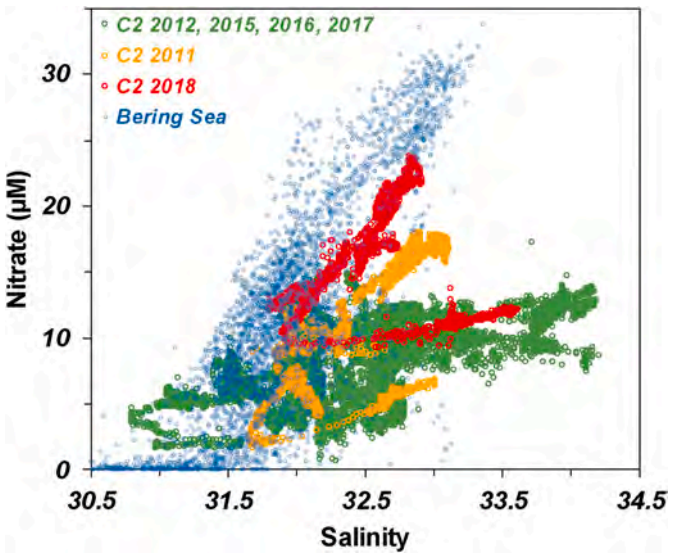

Fig. 4. Nitrate-Salinity relationship at the C2 mooring from 1 January to 31 May in 2012, 2015, 2016, and 2017 (green), and 2011 (orange). Data from 2018 (red) are shown from 1 January to 20 May as the seasonal drawdown of nitrate occurred thereafter. Data from the Bering Sea (blue) include 3973 near-bottom (<12 m from bottom) samples from the shelf (<150 m) that were collected on 53 cruises spanning March to October 2003 to 2018. (For interpretation of the references to color in this figure legend, the reader is referred to the Web version of this article.)

From 2010 to present, moorings have been deployed along the Icy Cape line (Fig. 1) providing time series of transport, nitrate, and other variables on the eastern shelf (Ladd et al., 2016; Stabeno et al., 2018b). Transport along the Icy Cape line is likely a combination of ACW near the coast and BSW farther offshore, which converge near Icy Cape (Fig. 1). There is considerable short-term variability in the time series due to local wind forcing and likely remote wind forcing (Danielson et al., 2014, 2017), as the transport and winds are significantly correlated (Stabeno et al., 2018b). While the variability in flow is dominated by the winds, monthly mean transport at Icy Cape shows a seasonal signal similar to Bering Strait with transport weakest in fall and winter (Stabeno et al., 2018b). The flow at Icy Cape accounts for ~40% of annual transport through Bering Strait, although this fraction varies on seasonal and interannual time scales (Stabeno et al., 2018b).

Several high-resolution nitrate time series have been reported on the Chukchi Shelf (Ladd et al., 2016; Hauri et al., 2018), but heretofore there has not been a study on the seasonal and interannual variability of nitrate over the shelf that includes winter replenishment. Herein, we present several years of continuous nitrate measurements at the Icy Cape mooring sites (C1, C2, C3; Fig. 1). While nitrate concentrations are modulated by numerous factors, including nitrification (oxidation of ammonium into nitrate), denitrification (nitrate reduction into nitrogen gas), brine exclusion, and primary production, this study is focused on seasonal and interannual variability, and winter replenishment in relationship to the transport of nutrients across the shelf.

2. Methods

2.1. Shipboard hydrography

Each year (2010–2018), hydrographic transects were run along the Icy Cape transect line in August or September in conjunction with mooring deployment and recovery. Profile data were collected using a Sea-Bird SBE 911plus Conductivity, Temperature, and Depth (CTD) instrument with dual temperature and salinity sensors. CTD data were recorded during the downcast, with a descent rate of 15 m min^{-1} to a depth of 30 m, and 30 m min^{-1} below that. Discrete calibration samples for salinity were collected from Niskin bottles on approximately one third of the casts on the transect line and also at the mooring sites. The samples were analyzed on a laboratory salinometer at the NOAA Pacific Marine Environmental Laboratory (PMEL) in Seattle, Washington. During hydrographic transects, discrete nutrient samples were collected from Niskin bottles at the surface, at 10-m intervals throughout the water column, and at the bottom of the cast. At the mooring sites, discrete nutrient samples were collected at the deployment depth of the nitrate sensor during mooring recovery and redeployment and used for calibration. Additional *in situ* calibration samples were collected opportunistically at other times while the nitrate sensors were deployed. Nutrient samples were filtered through 0.45 μm cellulose acetate filters, and frozen for later analysis at PMEL. Nitrate was measured using automated continuous flow analysis with a segmented flow and colorimetric detection. Standardization and analysis procedures specified by Gordon et al. (1994) were closely followed including calibration of labware, preparation of primary and secondary standards, and corrections for blanks and refractive index. In this method, nitrate + nitrite and nitrite are both measured, and nitrate is determined from the difference.

2.2. Moorings

Moorings have been deployed at three sites offshore of Icy Cape since August 2010 (C1, C2, and C3; Table 1, Fig. 1) with sensors located 4–6 m off the bottom. Measurements at each site included chlorophyll fluorescence (Sea-Bird/WetLabs ECO fluorometer), temperature and salinity (Sea-Bird SBE16), and current speed and direction (Aanderaa RCM-9, SeaGuard and/or Teledyne RD Instruments acoustic Doppler current profiler [ADCP], 300 or 600 kHz) (Stabeno et al., 2018b). Mooring data were collected at least hourly. The Sea-Bird ECO fluorometers, Sea-Bird SBE16s, and current meters were calibrated prior to deployment, and the data were processed according to manufacturers' specifications. Unless otherwise indicated, all current meter and salinity time series were low-pass filtered with a 35-h, cosine-squared, tapered Lanczos filter to remove higher-frequency variability, and resampled at 6 h intervals. Final processed time series were accurate to ±0.0005 S m^{-1} and ±0.5 cm s^{-1} for salinity and currents, respectively. At mooring site C2, the drift in the salinity of the moored SBE16 was usually minimal (<0.1) when compared to discrete samples collected from shipboard hydrographic CTD casts at the mooring site that are used for salinity calibration.

Nitrate sensors (Sea-Bird/Satlantic ISUS or SUNA) have been deployed at C2 each year, and were occasionally deployed at C1 and C3. In 2012 and 2013, the nitrate sensors deployed at C2 did not record data. To reduce biofouling, the SUNA instruments had a wiper that was activated prior to each set of hourly measurements, and the ISUS instruments were plumbed into the outflow of a Sea-Bird SBE-16 with antifouling agents mounted on either side of the ISUS flow cell. To ensure that the SBE-16 pump was triggered before the ISUS began sampling, the ISUS sampled 3 min after the pump was activated.

The hourly nitrate data included a dark frame (or reference sample) and 10–15 samples of nitrate (the number of samples has varied over the years). Each sample included the full spectrum of 255 spectrometer channels between ~200 and 400 nm, and an estimate of nitrate based upon the absorbance of ~35 spectrometer channels between 217 and 240 nm. The SUNA also provided several channels to assess potential interference from other absorbers (e.g. colored dissolved organic matter) including the absorbance at 254 and 350 nm, which was outside the absorbance range of nitrate, and the root-mean-square error between the measured and standard absorbance curves.

Spectral plots were used to assess performance of each instrument and identify data dropouts (Supplementary Fig. S1). The SUNA generally outperformed the ISUS as the SUNA had fewer data dropouts, and the spectral intensity of the SUNA was relatively strong throughout the deployment. This result was most likely due to the use of an optical wiper on the SUNA. Data processing included de-spiking by identifying

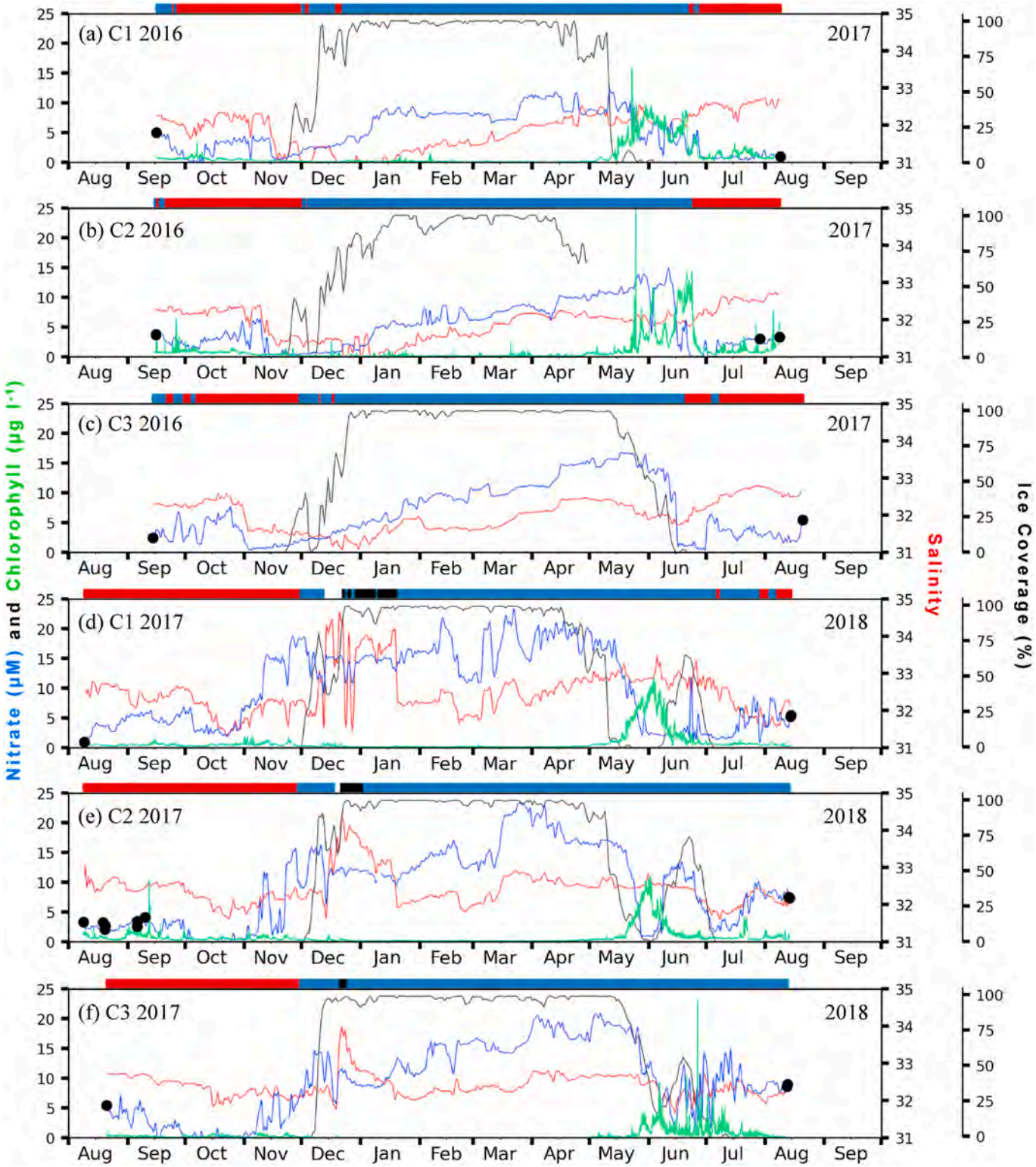

Fig. 5. Annual time series of the percent areal ice cover in 50 km × 50 km box centered on each mooring (black), nitrate (blue), salinity (red), chlorophyll fluorescence (green), and water mass (color bar atop each panel) from deployments at the C1, C2, and C3 moorings deployed in 2016 (a–c) and 2017 (d–f). Filled circles indicate discrete nitrate calibration points. Water types include summer water (red), winter water (blue), Atlantic water (white), and newly-ventilated or brine-influenced water (black). (For interpretation of the references to color in this figure legend, the reader is referred to the Web version of this article.)

deviations at 254 nm or 350 nm, calibration (discussed below), and applying a 35 h, cosine-squared, tapered Lanczos filter to remove tidal and higher-frequency variability.

The ISUS and SUNA optical nitrate sensors have a reported accuracy of ~2 μM, and do not have internal standards. Based upon numerous deployments since 2001, while these sensors provide relative changes in nitrate concentrations on tidal to seasonal scales (Mordy et al., 2005, 2019), absolute values are unreliable and the sensors must be calibrated against discrete field samples collected while the sensors are deployed. Each moored dataset was calibrated by determining the difference

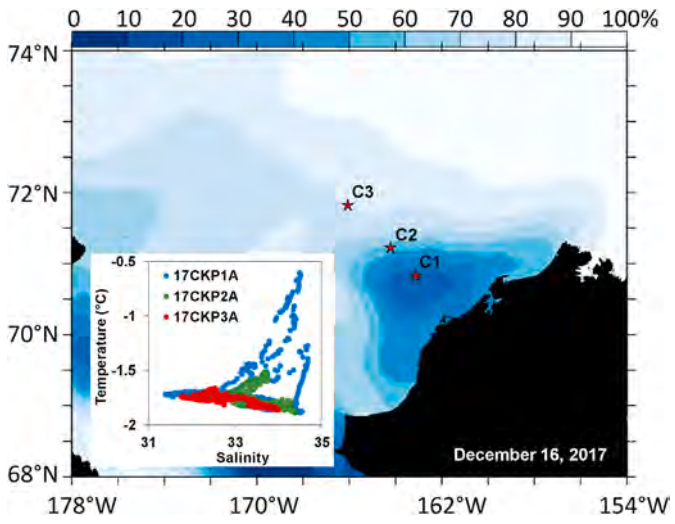

Fig. 6. Percent ice cover (blue is open water, white is ice) on December 16, 2017 showing a polynya near the C1 mooring. The inset is the T-S diagram from December 15, 2017 to January 31, 2018 for the C1 (blue), C2 (green), and C3 (red) moorings. The warmest temperatures (−0.6 °C) were observed at the C1 mooring on December 16, 2017. (For interpretation of the references to color in this figure legend, the reader is referred to the Web version of this article.)

between the moored and discrete data at each calibration point, then regressing these differences against the discrete sample time to correct for sensor drift. During the deployment at C2 in 2010–2011, the ISUS often recorded negative values and the sensor failed in July 2011, eliminating the possibility of an *in-situ* calibration from the recovery CTD cast. In this instance, the calibration drift correction used the initial *in-situ* calibration point and the most negative daily mean value (observed on 12 June), which was set to zero. The resulting pattern was similar to the nitrate time series at C1, which had a double maximum between late March and late May, and ~9 μM drop in nitrate on 4–7 June (not shown). After calibration, the C2 time series 2016–2017 had periods of negative values. For this time series, a secondary drift correction was applied by setting the most negative daily mean value (observed on 14 November) to zero.

2.3. Transport

Estimates of total transport were obtained as described in Stabeno et al. (2018b). This approach was used to calculate transport of the ACC in the Gulf of Alaska (Schumacher et al., 1989; Stabeno et al., 1995, 2016a) and the Alaskan Stream (Stabeno and Hristova, 2014). Transport was calculated from current measurements along a line of moorings (C1, C2, C3) across the region of interest. Using low-pass filtered currents, the component of velocity perpendicular to the mooring line was calculated. The normal component of velocity at each current meter or ADCP bin was multiplied by the cross-sectional areas. The horizontal distance of the cross-sectional area was the midpoint between two adjacent moorings, the distance between the mooring and the shore, or the outer edge of the mooring line was defined as the same half distance as between the outer mooring and its nearest neighbor (as appropriate). The vertical boundaries were the surface, the bottom at the mooring site, or the halfway point between instruments/bins, as appropriate. The individual mooring transport time series were summed across the section. In the Chukchi Sea, this method was reliable when all three moorings (C1, C2, and C3) provided current measurements. When data from one mooring were missing, the transport was calculated by selecting a calculated transport (T) when all three moorings provided data (data set D), removing the comparable missing velocities from D, and doing a multiple linear regression of the more limited data set on the transport, T. We then used the regression parameters to calculate transport for the years when there were missing velocities. See Table 3 in Stabeno et al. (2018b) for more detailed explanations.

2.4. Other measurements

Daily sea-ice concentrations at 25-km resolution were generated using the Advanced Microwave Scanning Radiometer - Earth Observing System (AMSR-E) Bootstrap Algorithm (Comiso, 2017), and are available from the National Snow and Ice Data Center (https://nsidc.org/data/nsidc-0079/versions/3). Time series of percent areal coverage were calculated in 50 km × 50 km boxes around each of the mooring sites (Fig. 1).

Wind velocity was obtained from the North American Regional Reanalysis (NARR) using the nearest gridpoint to the C2 mooring site. NARR was introduced as an extension to the National Centers for Environmental Prediction (NCEP) Reanalysis 2 (NCEPR2) for the North American Region using the high resolution NCEP Eta model (~32 km grid size compared to NCEPR2's 2.5° grid) and includes additional assimilated parameters to improve the reanalysis product (Mesinger et al., 2006). NARR winds are available at 3 hourly intervals and monthly averages were used for this study.

Several classifications of water types have been presented in the literature (Gong and Pickart, 2015; Ladd et al., 2016; Danielson et al., 2017)., Here we have combined those schemes to account for water influenced by brine exclusion (Table 2).

3. Results

3.1. C2 time series

Time series shown in Fig. 2 include sea-ice extent, classification of the bottom water mass, salinity, and concentrations of nitrate and chlorophyll-a at the C2 mooring for deployments in 2010, 2011, and 2014–2017. Moorings were deployed in mid-to-late summer at a time when the bottom water at C2 was primarily SW. The fall transition from SW to WW occurred prior to the arrival of ice (except for a brief appearance of ice in 2016), and WW persisted for ~2 months after ice retreat, except in 2011 with the arrival of warmer water for a short period soon after ice retreat.

Increases and decreases in nitrate and salinity often corresponded on event and seasonal scales. Event-scale variability is evident in the December–January time series in 2010–2011, 2011–2012, 2014–2015, and 2015–2016. Other notable events include increased nitrate and salinity on November 1, 2010, October 22, 2014, and November 10, 2014, which are related to the presence of AtlW and coastal polynyas (AtlW was observed at C1 on November 10, 2014) (Ladd et al., 2016). Other event-scale changes in salinity were not reflected in nitrate (e.g. mid-May 2012 and late February–March 2015).

Corresponding seasonal trends in nitrate and salinity included the fall transition and winter replenishment. During the fall transition, freshening and a reduction of nitrate concentrations in bottom water were common with the lowest values typically occurring in November–December. Exceptions were in October–November 2010, when salinity and nitrate increased likely due to a weak upwelling event of AtlW (Ladd et al., 2016), and the 2014 polynya events mentioned above. Winter replenishment of nitrate typically occurred between January and May. In January–May of 2011, 2016, and 2017, there was a corresponding increase in salinity and nitrate. During other years, replenishment was more variable. In 2012, winter replenishment of nitrate did not begin until April. In January–June 2015, salinities were variable but showed no seasonal trend, while nitrate steadily increased through the winter. In 2018, although salinity was variable without a considerable seasonal trend, nitrate concentrations were high through the winter reaching 24 μM in late March.

To assess interannual variability in wintertime nutrient replenishment, nitrate and salinity anomalies were determined for January–May

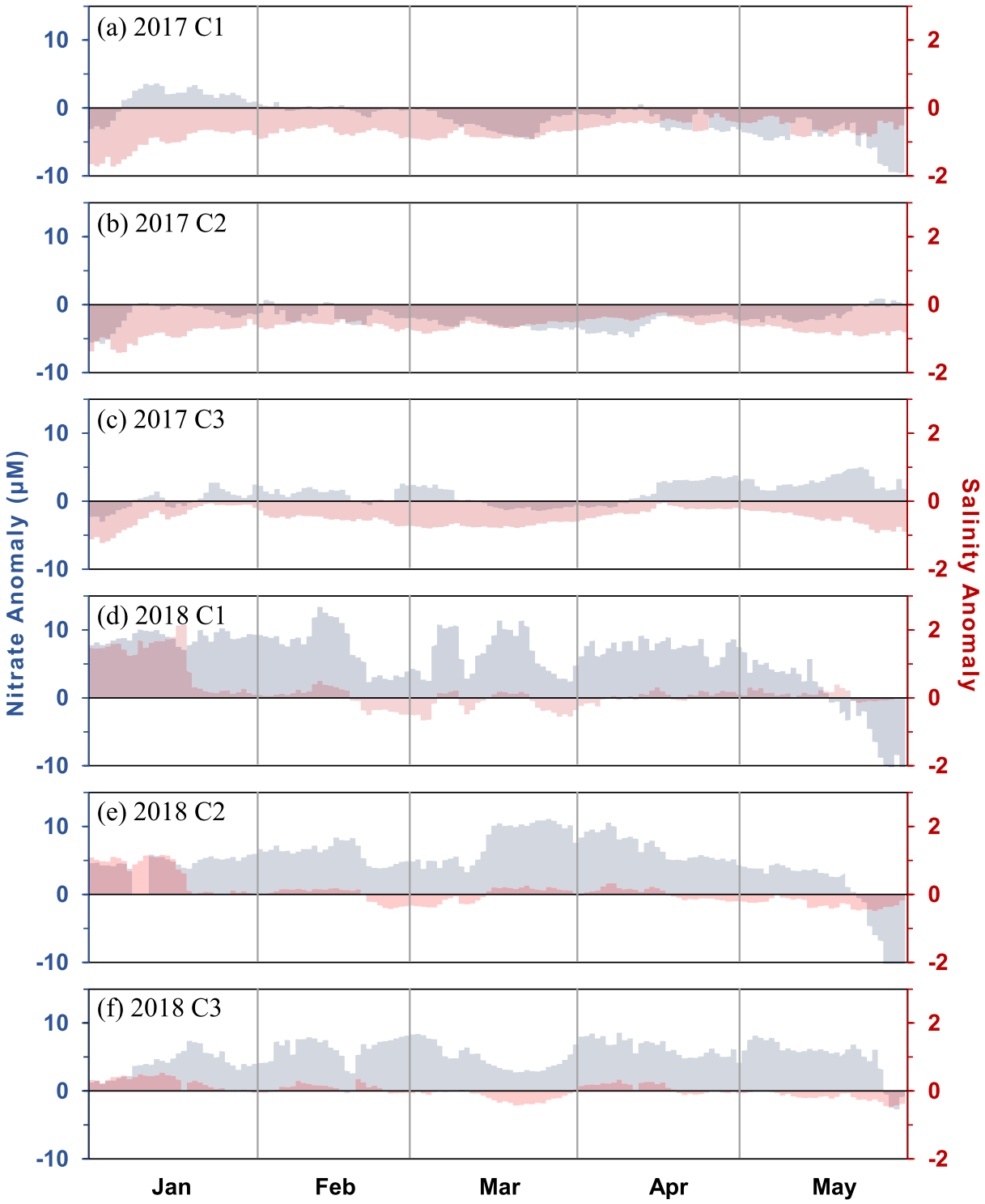

Fig. 7. Anomalies of nitrate (blue) and salinity (red) in January through May for time series at C1, C2, and C3 in 2017 (a–c) and 2018 (d–f) using the same mean values as in Fig. 3. (For interpretation of the references to color in this figure legend, the reader is referred to the Web version of this article.)

(Fig. 3). The multi-year (2011, 2012, 2015–2018) hourly means of nitrate and salinity that were used to calculate anomalies are shown in Fig. 3a. Mean nitrate did not include data from 20 to 31 May 2018, as there was a sharp decline in nitrate associated with an early ice retreat and high levels of chlorophyll (Fig. 2f, Stabeno et al., 2020). In the mean, nitrate and salinity were significantly correlated ($R^2 = 0.83$, $p < 0.0001$) with values generally increasing from January–May (Fig. 3a). While there was frequent correspondence between nitrate and salinity anomalies (e.g. early January 2018, February–April 2015, January–May 2017), at other times anomalies were of opposite sign (e.g. January 2011, May 2012). Most notable was the negative nitrate anomaly in 2012 and the positive nitrate anomaly from mid-January to mid-May 2018, both accompanied by relatively neutral salinity anomalies. The second largest positive nitrate anomaly occurred in March–May 2011. These positive nitrate anomalies were evident in the wintertime nitrate–salinity relationship (Fig. 4) wherein nitrate concentrations in 2011 and 2018 more closely resembled data from the Bering Sea, and were significantly higher ($p < 0.0001$) than in other years that had maximum

	SON	OND	NDJ	DJF	JFM	FMA	MAM
2017 – 2018	1.1	1.0	0.8	0.7	0.9	0.9	0.5
2016 – 2017	0.5	0.5	0.6	0.5	0.6	0.4	0.5
2015 – 2016	0.5	0.0	0.0	-0.1	0.1	0.1	0.2
2014 – 2015	0.4	0.1	0.1	0.1	0.3	0.2	0.3
2013 – 2014	0.5	0.5	0.1	-0.1	-0.1	0.2	0.5
2012 – 2013	0.4	0.4	0.1	-0.2	-0.2	0.0	0.3
2011 – 2012	0.1	0.0	0.0	0.0	0.1	0.0	0.1
2010 – 2011	0.2	-0.1	0.2	0.6	0.9	0.6	0.4

Fig. 8. Three-month means of transport (Sv) across the Icy Cape line. Years in gray are periods without a corresponding time series in nitrate.

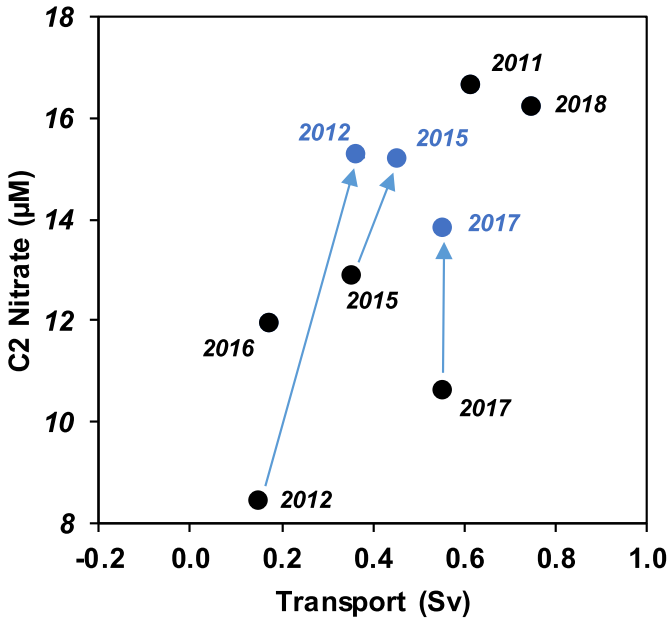

Fig. 9. Black symbols are the 3-day mean nitrate concentrations on 14–16 May at the six C2 time series shown in Fig. 2 compared to the mean seasonal (January–May) transport across the Icy Cape line. Blue symbols are the maximum 3-day mean nitrate concentration after 15 May compared to the mean transport from the prior 5 months with arrows indicating the increase in nitrate after 15 May. The standard error of the mean was within the symbols. The regression slopes in these comparisons were not significant. (For interpretation of the references to color in this figure legend, the reader is referred to the Web version of this article.)

nitrate concentrations generally <13 μM.

In spring, the timing of nitrate drawdown in bottom waters at C2 was related to ice retreat and/or increased chlorophyll concentrations (Fig. 2), but varied among the years (Stabeno et al., 2020). In June 2011, there was a sharp drop in nitrate coincident with ice retreat despite relatively low chlorophyll concentrations. In the summers of 2015 and 2017, the drawdown of nitrate occurred within a month of ice retreat coincident with relatively high chlorophyll concentrations. In summer 2016, winter water persisted until September while chlorophyll concentrations remained relatively low; nitrate concentrations slowly declined through the seasons with minimum concentrations occurring in November (observed in the subsequent deployment time series, Fig. 2e). In May–June 2018, while there was an initial reduction in nitrate associated with ice retreat and a chlorophyll peak, several pulses of ice and nitrate occurred thereafter. A similar increase in nitrate was observed in July 2011 absent ice cover. Both instances were associated with WW. In 2012, ice lingered at C2 until late July as nitrate concentrations increased from May–July.

3.2. Icy Cape time series

Time series of nitrate, salinity, and areal ice coverage at the three moorings along the Icy Cape line (C1, C2, and C3) are shown for 2016–2017 (Fig. 5a–c) and 2017–2018 (Fig. 5d–f). While episodic and seasonal variability were similar among the three moorings in individual years, there was considerable interannual variability. In the 2016–2017 time series, salinities freshened by ~1 in November 2016, and the freshest bottom water was observed in late December 2016 and January 2017 (Fig. 5a–c). Between January and August 2017 salinities increased to ~32.8 with a freshening event occurring in May and June 2017. In the 2016–2017 nitrate time series, the fall transition was similar at the three moorings with increased nitrate in mid-October 2016 followed by a minimum in November that occurred several weeks prior to the appearance of winter water. There was less correspondence among the three moorings during winter replenishment as concentrations at C1 showed step increases in January and March with concentrations of 11 μM in April; concentrations at C2 increased to 5 μM in January followed by a relatively steady increase to 13 μM in June; and concentrations at C3 steadily increased from the minimum in November to 16 μM in May. At all three moorings, nitrate concentrations declined to <5 μM in June 2017 concomitant with ice retreat and increasing chlorophyll concentrations in the bottom water, and nitrate drawdown was more gradual at C1 compared to C2 and C3.

In the 2017–2018 salinity time series at C1, C2, and C3 (Fig. 5d–f), freshening associated with the fall transition was less pronounced than in the 2016–2017 time series. Increased salinity at C1 and C2 in December 2017, was associated with upwelling of warmer AtlW, an event that slightly warmed temperatures at C2 and formed a hybrid latent/sensible heat polynya (Ladd et al., 2016) with evidence of brine exclusion (salinity > 33.6) observed at all three moorings (Fig. 6).

Nitrate concentrations at the three moorings were low in October 2017 and rapidly increased in November and December during the transition from SW to WW. Variability in nitrate was high in December 2017 concomitant with the polynya, and also in February–March 2018 with stepwise increases occurring in March. Prior to ice retreat, nitrate concentrations of 15–20 μM were observed at the three moorings. Nitrate concentrations rapidly declined upon ice retreat and increased

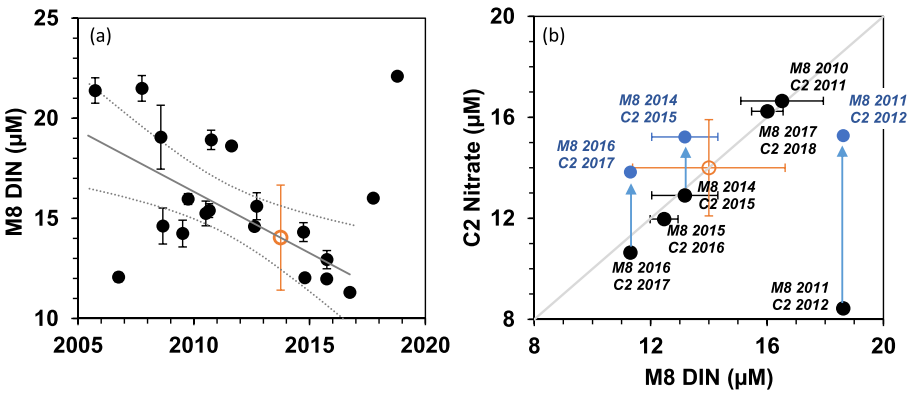

Fig. 10. (a) Summer and fall (July–October) concentrations of dissolved inorganic nitrogen (DIN) in bottom water (<12 m from the bottom except for samples collected at 50 m in 2011) within a 1° latitude × 2° longitude box (61.8°–62.8°N, 174°–176°W) around the M8 mooring in the northern Bering Sea. Data are from 20 individual cruises between 2005 and 2018. Error bars represent the standard error of the mean for each cruise. The regression line is from 2005 to 2016 and has a significant slope of 0.6 μM y^{-1} ($p = 0.005$, $F = 11$) shown with the 95% confidence bands. From this regression, the predicted DIN concentration on October 1, 2013 was 14.0 ± 2.6 μM (±SE, orange data point). (b) Black symbols are the 3-day mean nitrate concentrations at the C2 mooring on 14–16 May compared to mean DIN concentrations in bottom water at the M8 from the previous summer and/or fall. Blue symbols are the maximum 3-day mean nitrate concentration at the C2 mooring after 15 May with arrows indicating the increase in nitrate after 15 May as in Fig. 9. Error bars represent the standard error of the mean, and y-error bars are within the symbols. The gray line is the 1:1 ratio. Arrigo et al. (2017) reported that mean nitrate concentrations in bottom water over the shelf in May-June 2014 was 14.0 ± 1.9 μM (orange) shown with the SE of the prediction at M8. (For interpretation of the references to color in this figure legend, the reader is referred to the Web version of this article.)

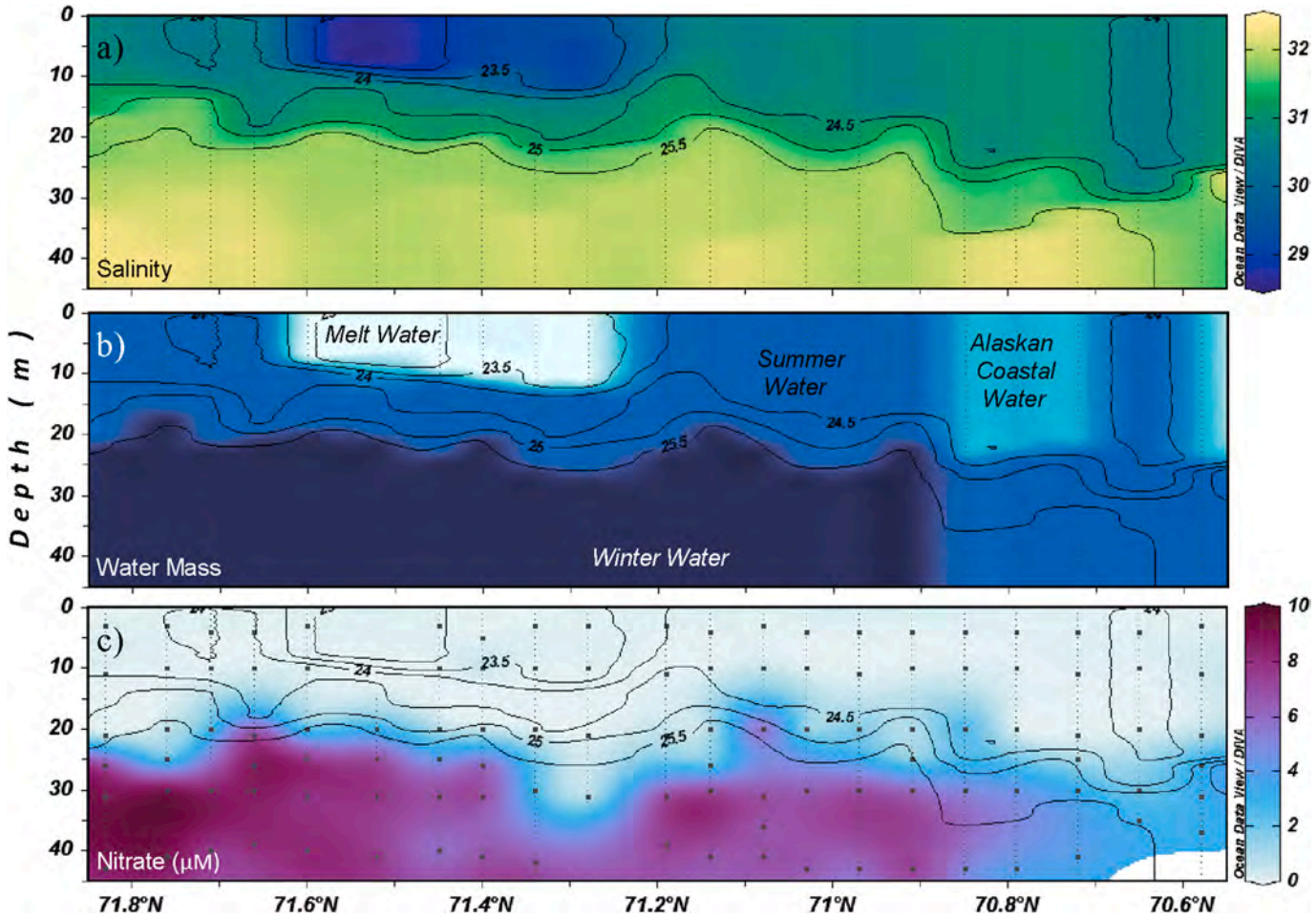

Fig. 11. Hydrographic sections along the Icy Cape line in August 2018 of salinity (a) and nitrate (c) with contours of potential density (σ_t). Identification of water types (b) are according to Danielson et al. (2017).

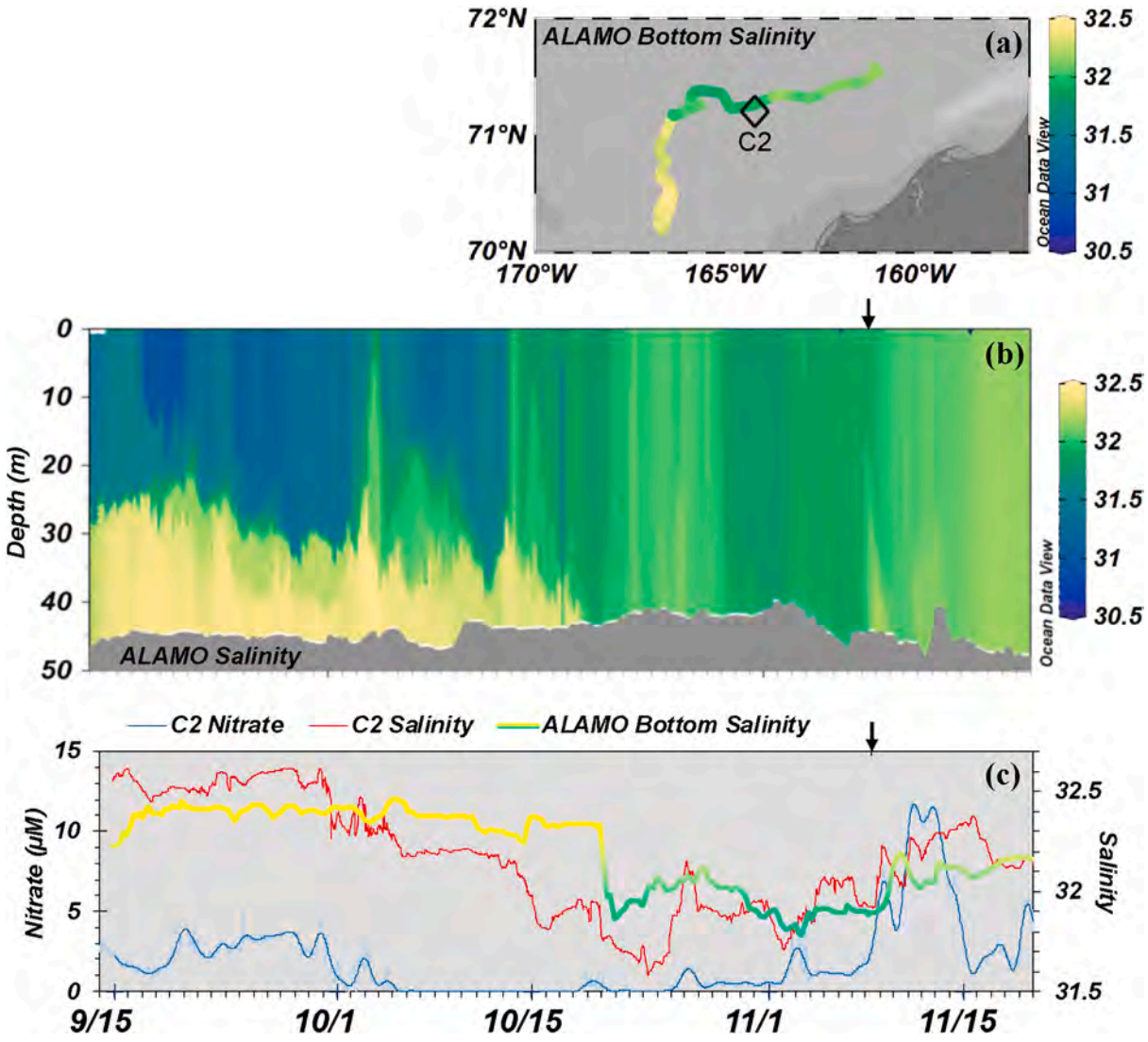

Fig. 12. (a) Drift track of ALAMO float 9119 from September 14, 2017 to November 20, 2017 colored by bottom salinity. The diamond indicates the location of the C2 mooring. (b) Vertical profile of salinity from ALAMO float 9119 during this period. (c) Time series of nitrate (blue) and salinity (red) from the C2 mooring along with bottom salinity (yellow/green) from ALAMO float 9119. The arrows in (b) and (c) indicate the nearest approach of the float to the C2 mooring. (For interpretation of the references to color in this figure legend, the reader is referred to the Web version of this article.)

bottom chlorophyll concentrations (Stabeno et al., 2020).

Anomalies for salinity and nitrate at the three moorings (Fig. 7) were determined for January–May using the mean values derived at C2 and employed in Fig. 3. In 2017, salinity anomalies were negative at all three moorings while the nitrate anomalies had greater spatial and temporal variability (Fig. 7a–c). At C1, the 2017 nitrate anomaly was positive in January, and negative in the remaining months with the seasonal drawdown of nitrate beginning in mid-May 2017. At C2, nitrate and salinity anomalies were negative. At C3, the 2017 nitrate anomaly was generally neutral or positive with the highest anomalies observed in mid-April – May. In 2018, salinity anomalies were neutral except for the high salinities observed in early January that were associated with a polynya (Fig. 7d–f). The highest nitrate anomalies at all three moorings were observed in February–April, interrupted by lower values generally associated with negative salinity anomalies.

3.3. Transport and pre-bloom nitrate concentrations

Interannual variability in transport across the shelf during winter is captured by comparing 3-month means of transport across the Icy Cape line (Fig. 8). Weak or negative transport was observed in winters spanning 2011–2012 to 2015–2016 with the weakest mean transport in 2011–2012. Moderate transport was observed in 2016–2017 and relatively high transport was observed from December 2010 to April 2011 and in the fall 2017 to spring 2018.

In years with weak transport, relatively low nitrate concentrations were observed at the C2 mooring from January–May (Fig. 4, green) indicating that early in the year the northern shelf may retain a remnant nutrient signature from the previous summer. In a year with moderate transport (Fig. 8, 2016–2017), water with a stronger Bering Sea signature was observed in May 2017 at the C3 mooring (salinity = 32.3, NO_3 = 15.5 μM; Fig. 5c), while C1 and C2 appeared to retain older water (NO_3 < 13 μM; Fig. 5a and b). This result implies that in 2017, transport through the central channel exceeded flow farther inshore, assuming all other processes being equal (e.g. brine exclusion, nitrification, and denitrification). This is consistent with findings that BSW flows through Bering Strait and northward through Central Channel, reaching C3, then C2 and finally C1 (unpublished data). In years with the largest monthly mean transports, water with a Bering Sea signature (i.e. NO_3 = 15–20 μM) was observed from mid-March–May 2011 at C2 (Fig. 4, orange) and at all three moorings in 2017–2018 (Fig. 4, red, and Fig. 5d–f).

Given the correspondence along the Icy Cape line between high

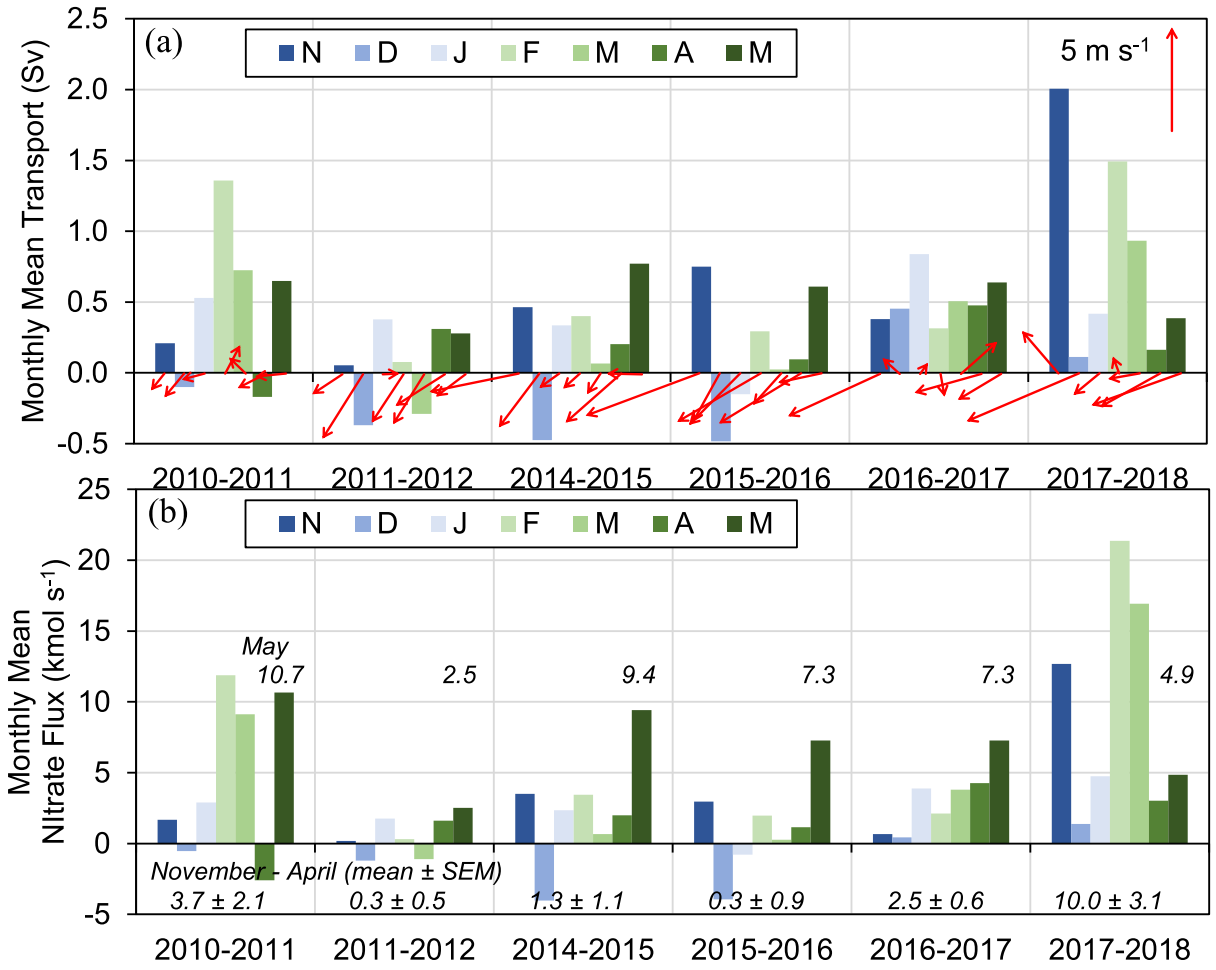

Fig. 13. Monthly mean wind (red) and transport (a) and nitrate flux (b) across the Icy Cape line from November through May for the six mooring deployments. Transport was calculated using currents from the C1, C2, and C3 moorings, and was combined with nitrate at C2 for determination of the nitrate flux with the assumption that the water column was well mixed during this period. In May 2018, nitrate was averaged from 1 to 20 May. Positive transport and nitrate flux are to the northeast, and winds are relative to north. In (b), the mean nitrate flux from November–April is shown above the x-axis, and the May nitrate flux appears above each column in May. (For interpretation of the references to color in this figure legend, the reader is referred to the Web version of this article.)

levels of multi-month mean transport and the appearance of water with Bering Sea characteristics, a comparison was made between pre-bloom nitrate content and transport (Fig. 9). Mean transport in January through May was compared to the 3-day mean nitrate concentration centered on 15 May (black symbols in Fig. 9). Note, 15 May was prior to major ice retreat at any of the C2 mooring time series and prior to large accumulations of bottom chlorophyll (Fig. 2). The regression slope in Fig. 9 was not significant ($p = 0.08$, $F = 5.4$). Most notable were the discrepancies in 2017 between relatively high-transport/low-nitrate concentrations, and the very low nitrate concentrations in 2012.

In 2012, 2015, and 2017, after 15 May, nitrate concentrations in WW continued to increase at C2 for weeks to months despite ice retreat and the accumulation of chlorophyll in bottom water (Fig. 2). This is illustrated in a second comparison between nitrate and transport in Fig. 9 (blue symbols). This comparison shows the maximum 3-day mean nitrate concentrations between 15 May and July in each of these years compared to the prior 5-month mean of transport. For example, in 2012, the maximum 3-day mean nitrate between May and July was 15.3 μM and occurred on July 27, 2012, and the mean 5-month transport from March–July was 0.37 Sv. While neither of the regression slopes in these comparisons were significant, these results illustrate that in some years, there is a continual flux of cold nitrate-rich WW over the shelf through spring and into summer (blue arrows in Fig. 9), seasons when contributions from nitrification are thought to be low (Baer et al., 2017).

In summer and fall, there is considerable variability in DIN concentrations near the M8 mooring on the northern middle shelf of the Bering Sea (Stabeno et al., 2018a). In the proximity of the M8 mooring (62.194°N, 174.688°W), concentrations of DIN in bottom water declined by ~37% between 2005 and 2016 before recovering in 2017 and 2018 (Stabeno et al., 2018a, Fig. 10a). The mechanisms forcing this variability are still undetermined. In winter, this water begins to flow over the Chukchi Shelf, and during this transit ammonium is likely nitrified and contributes to the nitrate pool (Baer et al., 2017). In the absence of primary production in winter, we might expect correspondence between summer/fall DIN concentrations at M8 in the northern Bering Sea and pre-bloom (15 May) nitrate concentrations at C2 in the Chukchi Sea the following spring (Fig. 10b). For example, the lowest values in the northern Bering Sea were observed in September 2016 (Fig. 10a), and likely resulted in the low values observed spring 2017 in the Chukchi Sea despite relatively high transport (Fig. 9). Arrigo et al. (2017) surveyed the northeastern Chukchi Sea in May–June 2014 and reported a mean pre-bloom nitrate concentration in bottom water of 14.0 ± 1.9 μM. Although DIN was not measured at M8 the previous year, their finding is consistent with regressed concentration for October 1, 2013 (14.0 μM, orange data in Fig. 10). While consistent in the mean, they observed higher concentrations in the central channel and lower concentrations near the shelf break.

While there is nearly a 1:1 correspondence between summer/fall DIN in the Bering Sea and pre-bloom nitrate in the Chukchi Sea (black symbols in Fig. 10b), there was a large discrepancy at C2 in 2012.

Despite relatively high concentrations of DIN in the Bering Sea, the winter of 2012 had the largest negative nitrate anomaly at C2 (Fig. 3c), and nitrate replenishment that year did not begin until April (Fig. 2b). These results are explained by the absence of transport across the Icy Cape line between September 2011 and May 2012 (Fig. 8). The discrepancy is much smaller on July 27, 2012 when maximum 3-day mean nitrate concentrations were observed (blue symbols in Fig. 10b); that is when water with Bering Sea characteristics arrived at Icy Cape. In 2015 and 2017, nitrate concentrations continued to increase after 15 May, and the maximum 3-day mean nitrate concentrations were greater than observed in the Bering Sea (Fig. 10b). These higher nitrate levels may be the result of ammonification-nitrification, brine rejection, or mixing with AW upstream of the Icy Cape line in winter.

4. Discussion

The seasonal water masses in the Chukchi Sea are typically defined by temperature and salinity, and the seasonal progression of these water masses over the shelf are well described (Woodgate et al., 2005; Gong and Pickart, 2015; Lowry et al., 2015; Danielson et al., 2017; Lin et al., 2019; Danielson et al., 2020). In spring and summer, WW is gradually replaced from south to north by MW, SW, and ACW (Lowry et al., 2015; Lin et al., 2019; Danielson et al., 2020) due to the seasonal progression of ice melt across the shelf and enhanced transport in summer forced by southerly winds (Woodgate et al., 2005; Stabeno et al., 2018b). During hydrographic surveys conducted in mid-to-late-summer, conditions off Icy Cape are typified by a strong two-layer system (Fig. 11). The surface layer is composed of ACW, SW, and/or MW, and is relatively fresh, warm, and nitrate-poor (Fig. 11; Danielson et al., 2017). In the bottom layer, WW and SW are the primary water types found off Icy Cape in summer, and their relative contributions depend in part on the timing of sampling (Lin et al., 2019). While SW is nutrient-poor, WW has moderate nitrate content in late summer (Lowry et al., 2015; Danielson et al., 2017; Lin et al., 2019), and this water type is thought to initiate and sustain phytoplankton blooms throughout the growing season (Lowry et al., 2015).

By October, most of the WW along the bottom has been flushed off the shelf by relatively warm ACW and SW (Lin et al., 2019; Danielson et al., 2020). During the fall transition, storms break down the two-layer system that is prevalent in summer, and mix warmer, fresher, and nutrient-poor water to depth (Fig. 12; Woodgate et al., 2005; Nishino et al., 2016). As a result, bottom salinities and nutrient concentrations are often lowest during this period (Figs. 2, 5 and 12). Exceptions to this pattern along the Icy Cape line include fall 2010 and 2014 when upwelling events in Barrow Canyon transported salt and nitrate over the shelf (Fig. 2; Ladd et al., 2016). The transition from SW to WW generally occurred in September–November prior to the arrival of ice. In 2016, there was a short period of ice cover during the fall transition, and, in 2016 and 2017, SW was evident through November (Fig. 2). This transition may be further delayed with future warming (Wood et al., 2018; Danielson et al., 2020). The rapid rates of heat loss over the shelf (e.g. Wood et al., 2018; Danielson et al., 2020) signify that the transition to WW is primarily a local or regional event rather than advective event (Lowry et al., 2015). Thus, when formed, WW is relatively fresh and nutrient poor (Figs. 2 and 5; Woodgate et al., 2005; Lowry et al., 2015).

Replenishment of nitrate over the shelf in winter occurs through brine exclusion (Aagaard et al., 1981; Anderson et al., 1988), nitrification, which has the highest rates in winter (Christman et al., 2011; Baer et al., 2017), upwelling along the shelf break (Ladd et al., 2016) and the transport of nutrients through Bering Strait (Walsh et al., 1989; Springer and McRoy, 1993), and is modulated by denitrification (Chang and Devol, 2009). In terms of nutrient transport, the majority of water flowing over the eastern Chukchi Sea shelf has its origins from the middle and outer shelf of the northern Bering Sea (Stabeno et al., 2016b). While winter nutrient concentrations in the northern Bering Sea are rarely measured, bottom water concentrations in spring and summer/fall in the Bering Sea are similar and relatively high compared to recently formed (October–November) WW in the Chukchi Sea (Table 3; Figs. 2 and 5).

Despite the relatively high nutrient concentrations in Bering Sea source waters, transport across the eastern Chukchi Sea Shelf in winter is weak and highly variable due to prevailing northerly winds that can sometimes result in southward transport (Stabeno et al., 2018b). Along the Icy Cape line, while there are periods of strong northeastward transport in fall and winter (e.g. February 2011), 5 to 20-day periods of southwestward transport are not uncommon (see Fig. 12 in Stabeno et al., 2018b). They found that while ~40% of the annual flow through Bering Strait passes the Icy Cape line, less than a fifth of this transport occurs during December–April. This is an indication that, on the eastern shelf, advective replenishment of nitrate in winter may be sporadic, and highly variable among years. Model results suggest that in the first 180 days of the year, the southern shelf of the Chukchi Sea (south of ~70°N) is filled with water that has recently (<5 mo) passed through Bering Strait (Spall, 2007), thereby introducing relatively high concentrations of nutrients from the Bering Sea into the southern Chukchi Sea. These model results also suggest that, early in the year, the northern shelf in the Chukchi Sea may retain older water (Spall, 2007), a result supported by the low nutrient-salinity relationships in Fig. 4 relative to Bering Sea water. This is also consistent with a May-June 2014 survey that observed lower nitrate concentrations on the northern shelf (Arrigo et al., 2017).

Macdonald et al. (2010) provided a mean estimate of annual new production in the Chukchi Sea of 50 g C m^{-2} y^{-1} (5–160 g C m^{-2} y^{-1}) with a corresponding annual mean nitrogen demand of 12.4 kmol N s^{-1}. Their estimate of Pacific inflow of DIN through Bering Strait was 16.5 kmol N s^{-1}. Torres-Valdés et al. (2013) used inverse modeled velocities and a July 2005 nitrate section that crossed the entire southern Chukchi Sea and determined a summertime nitrate flux of 9 ± 0.8 (±SD) kmol N s^{-1} with most of this flux occurring in the western Chukchi Sea. For contrast, a summary of monthly wintertime winds, transport, and nitrate flux in the northeastern Chukchi Sea are presented in Fig. 13. In November–April, the nitrate flux in the northeastern Chukchi Sea ranged from <1.5 kmol N s^{-1} in winters with weak transport (i.e. 2011–2012, 2014–2015, 2015–2016) to 10 kmol N s^{-1} in winters with high transport (Fig. 13). Higher transports were associated with more easterly or southerly winds, and higher fluxes generally occurred in late winter or early spring (May) as northerly winds weakened and contemporary water from the Bering Sea spread across the northeastern Chukchi Sea. The low nitrate flux in May 2012 reflected the weak transport of remnant winter water that had yet to be flushed from the region (Fig. 10b).

The wintertime nitrate flux on the northeastern shelf was often low relative to the findings of Macdonald et al. (2010) and Torres-Valdés et al. (2013). In most years contemporary water from the Bering Sea arrived at the Icy Cape line in early spring (Fig. 10b) and was perhaps modified in route from nitrate-rich AW, nitrification, or denitrification. During the growing season, nitrate in bottom water was often consumed (Fig. 2), reinforcing the notion that nitrate is the primary limiting nutrient (Cota et al., 1996; Codispoti et al., 2005; Tremblay et al., 2006; Lowry et al., 2015) and enabling an estimate of net community production (NCP) upstream of the Icy Cape line (i.e. the seasonal change in carbon or nutrients that represents production minus community respiration). Defining pre-bloom nitrate concentrations as 15 May or later (nitrate concentrations continued to increase in 2012, 2015, and 2017), concentrations at the C2 mooring range from 12.0 ± 0.3 (±SD) μM in 2016 to 16.7 ± 0.2 μM in 2011 (Fig. 10b). This corresponds to NCP of 35–48 g C m^{-2} (assuming consumption to 40 m and a C:N ratio of 6 from Hansell et al., 1993).

Arrigo et al. (2017) measured pre-bloom nitrate concentrations in the northeast Chukchi Sea in 2014, and derived NCP values of 27.8 ± 4.1, 37.6 ± 5.6, and 42.3 ± 6.9 g C m^{-2} y^{-1} for nitrate consumption to 30, 40, and 50 m, respectively. Their estimates were generally lower than prior studies in the region (40–70 g C m^{-2} y^{-1}; Hansell et al., 1993;

Codispoti et al., 2013; Mills et al., 2015). They argued that earlier estimates were unreasonably high because pre-bloom nitrate concentrations were not locally and/or rigorously determined; for example, Hansell et al. (1993) employed nitrate data from the southeast Bering Sea without consideration of denitrification over the Bering Sea shelf. Given that: i) nitrate consumption may extend to at least 40–45 m; ii) pre-bloom concentrations at C2 correspond to fall concentrations at M8 (Fig. 10b); and iii) DIN at M8 varies from ~11 to 22 μM (Fig. 10a), it is reasonable to expect NCP upstream of C2 to vary interannually between ~30 and 70 g C m^{-2} y^{-1}.

5. Conclusion

As WW warms in spring and summer to > −1.6 °C, it has been categorized as remnant winter water (Gong and Pickart, 2015; Lin et al., 2019). This definition does not distinguish between water advected through Bering Strait during winter and remnant summer water that has locally cooled, transitioned into winter water, and, in some years, is still residing over the northern shelf. This distinction is important because nitrate concentrations are lowest in newly formed WW, and rates of local nitrate replenishment appear low relative to the nutrient flux through Bering Strait. In recent years there has been an increase in southerly wind events (Stabeno, 2019; Stabeno and Bell, 2019) that may be reinforced by warming of arctic shelves (Tachibana et al., 2019; Danielson et al., 2020). These conditions enhance total transport and nutrient flux through Bering Strait, and introduce contemporary Bering Sea water into the northern Chukchi Sea shelf. As a result, in the presence of southerly wind events, nutrient measurements at the M8 mooring in the Bering Sea from the prior summer/fall should make it possible to predict pre-bloom nitrate concentrations available for sustaining primary production in the eastern Chukchi Sea. Since 2005, annual summer/fall DIN concentrations at M8 in the Bering Sea have varied between 11 and 22 μM (Fig. 10a), an indication that NCP over the eastern Chukchi Sea may have varied by 50% during this time.

Funding

This work was supported by the National Oceanic and Atmospheric Administration (NOAA), United States; the Bureau of Ocean Energy Management CHAOZ, CHAOZ-X, and ArcWEST programs, United States; the North Pacific Research Board Arctic Program grants A92-02a and A92-02b, United States; and the Joint Institute for the Study of the Atmosphere and Ocean, United States, under NOAA Cooperative Agreement NA15OAR4320063.

Declaration of competing interest

The authors declare that they have no known competing financial interests or personal relationships that could have appeared to influence the work reported in this paper.

CRediT authorship contribution statement

Calvin W. Mordy: Conceptualization, Methodology, Writing - original draft, Writing - review & editing, Supervision. **Shaun Bell:** Software, Formal analysis. **Edward D. Cokelet:** Software, Formal analysis, Writing - original draft. **Carol Ladd:** Formal analysis, Writing - original draft. **Geoff Lebon:** Resources. **Peter Proctor:** Investigation, Validation. **Phyllis Stabeno:** Conceptualization, Methodology, Writing - original draft, Supervision. **David Strausz:** Software, Formal analysis. **Eric Wisegarver:** Investigation, Formal analysis. **Kevin Wood:** Investigation, Validation.

Acknowledgements

This is contribution No. 5016 for Pacific Marine Environmental Laboratory, contribution No. 2019–1024 for JISAO, and contribution No. EcoFOCI-0935 for NOAA's Ecosystem Fisheries Oceanography Coordinated Investigations. We thank the officers, captains and crew of the USCGC *Healy*, NOAA Ships *Oscar Dyson* and *Ronald H. Brown*, the R/Vs *Aquila* and *Ocean Starr*, and F/V *Mystery Bay*. We thank W. Floering, N. Kachel, and M. Langis for assistance with field operations, M. Sullivan for archival of data and metadata, and S. Bigley, M. Lomas and several anonymous reviewers for comments that greatly helped to improve this manuscript.

Appendix A. Supplementary data

Supplementary data to this article can be found online at https://doi.org/10.1016/j.dsr2.2020.104807.

References

Aagaard, K., Coachman, L.K., Carmack, E., 1981. On the halocline of the Arctic Ocean. Deep-Sea Res. Part A-Oceanogr. Res. Pap. 28 (6), 529–545. https://doi.org/10.1016/0198-0149(81)90115-1.

Aagaard, K., Roach, A.T., Schumacher, J.D., 1985. On the wind-driven variability of the flow through Bering Strait. J. Geophys. Res.-Oceans 90 (C4), 7213–7221. https://doi.org/10.1029/JC090iC04p07213.

Aagaard, K., Weingartner, T.J., Danielson, S.L., Woodgate, R.A., Johnson, G.C., Whitledge, T.E., 2006. Some controls on flow and salinity in Bering Strait. Geophys. Res. Lett. 33 (19), L19602. https://doi.org/10.1029/2006GL026612.

Anderson, L.G., Jones, E.P., Lindegren, R., Rudels, B., Sehlstedt, P.I., 1988. Nutrient regeneration in cold, high salinity bottom water of the Arctic shelves. Continent. Shelf Res. 8 (12), 1345–1355. https://doi.org/10.1016/0278-4343(88)90044-1.

Ardyna, M., Gosselin, M., Michel, C., Poulin, M., Tremblay, J.É., 2011. Environmental forcing of phytoplankton community structure and function in the Canadian High Arctic: Contrasting oligotrophic and eutrophic regions. Mar. Ecol. Prog. Ser. 442, 37–57. https://doi.org/10.3354/meps09378.

Arrigo, K.R., Mills, M.M., van Dijken, G.L., Lowry, K.E., Pickart, R.S., Schlitzer, R., 2017. Late spring nitrate distributions beneath the ice-covered northeastern Chukchi Shelf. J. Geophys. Res. Biogeosci. 122 (9), 2409–2417. https://doi.org/10.1002/2017JG003881.

Arrigo, K.R., van Dijken, G., Pabi, S., 2008. Impact of a shrinking Arctic ice cover on marine primary production. Geophys. Res. Lett. 35 (19), L19603. https://doi.org/10.1029/2008GL035028.

Baer, S.E., Sipler, R.E., Roberts, Q.N., Yager, P.L., Frischer, M.E., Bronk, D.A., 2017. Seasonal nitrogen uptake and regeneration in the western coastal Arctic. Limnol. Oceanogr. 62 (6), 2463–2479. https://doi.org/10.1002/lno.10580.

Bond, N., Stabeno, P., Napp, J., 2018. Flow patterns in the Chukchi Sea based on an ocean reanalysis. June through October 1979–2014. Deep-Sea Res. Part II-Top. Stud. Oceanogr. 152, 35–47. https://doi.org/10.1016/j.dsr2.2018.02.009.

Cavalieri, D.J., Parkinson, C.L., 2012. Arctic sea ice variability and trends. 1979–2010. Cryosphere 6 (4), 881–889. https://doi.org/10.5194/tc-6-881-2012.

Chang, B.X., Devol, A.H., 2009. Seasonal and spatial patterns of sedimentary denitrification rates in the Chukchi Sea. Deep-Sea Res. Part II Top. Stud. Oceanogr. 56 (17), 1339–1350. https://doi.org/10.1016/j.dsr2.2008.10.024.

Christman, G.D., Cottrell, M.T., Popp, B.N., Gier, E., Kirchman, D.L., 2011. Abundance, diversity, and activity of ammonia-oxidizing prokaryotes in the coastal Arctic Ocean in summer and winter. Appl. Environ. Microbiol. 77 (6), 2026–2034. https://doi.org/10.1128/AEM.01907-10.

Coachman, L.K., Aagaard, K., 1966. On the water exchange through Bering Strait. Limnol. Oceanogr. 11 (1), 44–59. https://doi.org/10.4319/lo.1966.11.1.0044.

Coachman, L.K., Aagaard, K., 1988. Transports through Bering Strait: annual and interannual variability. J. Geophys. Res.-Oceans 93 (C12), 15535–15539. https://doi.org/10.1029/JC093iC12p15535.

Coachman, L.K., Aagaard, K., Tripp, R.B., 1975. Bering Strait: the Regional Physical Oceanography. University of Washington Press, Seattle, WA.

Codispoti, L.A., Flagg, C., Kelly, V., Swift, J.H., 2005. Hydrographic conditions during the 2002 SBI process experiments. Deep-Sea Res. Part II Top. Stud. Oceanogr. 52 (24–26), 3199–3226. https://doi.org/10.1016/j.dsr2.2005.10.007.

Codispoti, L.A., Kelly, V., Thessen, A., Matrai, P., Suttles, S., Hill, V., Steele, M., Light, B., 2013. Synthesis of primary production in the Arctic Ocean: III. Nitrate and phosphate-based estimates of net community production. Prog. Oceanogr. 110, 126–150. https://doi.org/10.1016/j.pocean.2012.11.006.

Comiso, J.C., 2017. Bootstrap sea ice concentrations from nimbus-7 SMMR and DMSP SSM/I-SSMIS, version 3.Boulder, Colorado USA. NASA National Snow and Ice Data Center Distributed Active Archive Center. https://doi.org/10.5067/7Q8HCCWS4I0R.

Cota, G.F., Pomeroy, L.R., Harrison, W.G., Jones, E.P., Peters, F., Sheldon Jr., W.M., Weingartner, T.R., 1996. Nutrients, primary production and microbial heterotrophy in the southeastern Chukchi Sea: arctic summer nutrient depletion and heterotrophy. Mar. Ecol. Prog. Ser. 135, 247–258. https://doi.org/10.3354/meps135247.

Dai, A., Luo, D., Song, M., Liu, J., 2019. Arctic amplification is caused by sea-ice loss under increasing CO_2. Nat. Commun. 10 (1), 121. https://doi.org/10.1038/s41467-018-07954-9.

Danielson, S.L., Ahkinga, O., Ashjian, C., Basyuk, E., Cooper, L.W., Eisner, L., Farley, E., Iken, K.B., Grebmeier, J.M., Juranek, L., Khen, G., Jayne, S., Kikuchi, T., Ladd, C., Lu, K., McCabe, R., Moore, G.W.K., Nishino, S., Okkonen, S.R., Ozenna, F., Pickart, R.S., Polyakov, I., Stabeno, P.J., Wood, K., Williams, W.J., Woodgate, R.A., Weingartner, T.J., 2020. Manifestation and consequences of warming and altered heat fluxes over the Bering and Chukchi Sea continental shelves. This issue Deep-Sea Res. Part II Top. Stud. Oceanogr.

Danielson, S.L., Eisner, L., Ladd, C., Mordy, C., Sousa, L., Weingartner, T.J., 2017. A comparison between late summer 2012 and 2013 water masses, macronutrients, and phytoplankton standing crops in the northern Bering and Chukchi Seas. Deep-Sea Res. Part II Top. Stud. Oceanogr. 135, 7–26. https://doi.org/10.1016/j.dsr2.2016.05.024.

Danielson, S.L., Weingartner, T.J., Hedstrom, K.S., Aagaard, K., Woodgate, R., Curchitser, E., Stabeno, P.J., 2014. Coupled wind-forced controls of the Bering–Chukchi shelf circulation and the Bering Strait throughflow: Ekman transport, continental shelf waves, and variations of the Pacific–Arctic sea surface height gradient. Prog. Oceanogr. 125, 40–61. https://doi.org/10.1016/j.pocean.2014.04.006.

Frey, K.E., Moore, G.W.K., Cooper, L.W., Grebmeier, J.M., 2015. Divergent patterns of recent sea ice cover across the Bering, Chukchi, and Beaufort seas of the pacific arctic region. Prog. Oceanogr. 136, 32–49. https://doi.org/10.1016/j.pocean.2015.05.009.

Gong, D., Pickart, R.S., 2015. Summertime circulation in the eastern Chukchi Sea. Deep-Sea Res. Part II Top. Stud. Oceanogr. 118, 18–31. https://doi.org/10.1016/j.dsr2.2015.02.006.

Gordon, L.I., Jennings, J.C., Ross, A.A., Krest, J.M., 1994. A suggested protocol for continuous flow analysis of seawater nutrients (phosphate, nitrate, nitrite, and silicic acid) in the WOCE Hydrographic Program and the Joint Global Ocean Fluxes Study. WHP Office Report 91 (1).

Hansell, D.A., Whitledge, T.E., Goering, J.J., 1993. Patterns of nitrate utilization and new production over the Bering-Chukchi shelf. Continent. Shelf Res. 13 (5–6), 601–627. https://doi.org/10.1016/0278-4343(93)90096-G.

Hauri, C., Danielson, S., McDonnell, A.M.P., Hopcroft, R.R., Winsor, P., Shipton, P., Lalande, C., Stafford, K.M., Horne, J.K., Cooper, L.W., Grebmeier, J.M., Mahoney, A., Maisch, K., McCammon, M., Statscewich, H., Sybrandy, A., Weingartner, T., 2018. From sea ice to seals: a moored marine ecosystem observatory in the Arctic. Ocean Sci. 14 (6), 1423–1433. https://doi.org/10.5194/os-14-1423-2018.

Hill, V., Ardyna, M., Lee, S.H., Varela, D.E., 2018. Decadal trends in phytoplankton production in the pacific arctic region from 1950 to 2012. Deep-Sea Res. Part II Top. Stud. Oceanogr. 152, 82–94. https://doi.org/10.1016/j.dsr2.2016.12.015.

Hill, V., Cota, G., 2005. Spatial patterns of primary production on the shelf, slope and basin of the Western Arctic in 2002. Deep-Sea Res. Part II Top. Stud. Oceanogr. 52 (24–26), 3344–3354. https://doi.org/10.1016/j.dsr2.2005.10.001.

Hill, V.J., Zimmerman, R.C., 2010. Estimates of primary production by remote sensing in the Arctic Ocean: assessment of accuracy with passive and active sensors. Deep-Sea Res. Part I Oceanogr. Res. Pap. 57 (10), 1243–1254. https://doi.org/10.1016/j.dsr.2010.06.011.

Ladd, C., Mordy, C.W., Salo, S.A., Stabeno, P.J., 2016. Winter water properties and the Chukchi polynya. J. Geophys. Res.-Oceans 121 (8), 5516–5534. https://doi.org/10.1002/2016JC011918.

Lewis, K.M., Arntsen, A.E., Coupel, P., Joy-Warren, H., Lowry, K.E., Matsuoka, A., Mills, M.M., van Dijken, G.L., Selz, V., Arrigo, K.R., 2019. Photoacclimation of Arctic Ocean phytoplankton to shifting light and nutrient limitation. Limnol. Oceanogr. 64 (1), 284–301. https://doi.org/10.1002/lno.11039.

Li, M., Pickart, R.S., Spall, M.A., Weingartner, T.J., Lin, P., Moore, G.W.K., Qi, Y., 2019. Circulation of the Chukchi Sea shelfbreak and slope from moored timeseries. Prog. Oceanogr. 172, 14–33. https://doi.org/10.1016/j.pocean.2019.01.002.

Lin, P., Pickart, R.S., McRaven, L.T., Arrigo, K.R., Bahr, F., Lowry, K.E., Stockwell, D.A., Mordy, C.W., 2019. Water mass evolution and circulation of the northeastern Chukchi Sea in summer: Implications for nutrient distributions. J. Geophys. Res.-Oceans 124 (7), 4416–4432. https://doi.org/10.1029/2019JC015185.

Linders, J., Pickart, R.S., Björk, G., Moore, G.W.K., 2017. On the nature and origin of water masses in Herald Canyon, Chukchi Sea: Synoptic surveys in summer 2004, 2008, and 2009. Prog. Oceanogr. 159, 99–114. https://doi.org/10.1016/j.pocean.2017.09.005.

Lowry, K.E., Pickart, R.S., Mills, M.M., Brown, Z.W., van Dijken, G.L., Bates, N.R., Arrigo, K.R., 2015. The influence of winter water on phytoplankton blooms in the Chukchi Sea. Deep-Sea Res. Part II Top. Stud. Oceanogr. 118, 53–72. https://doi.org/10.1016/j.dsr2.2015.06.006.

Macdonald, R.W., Anderson, L.G., Christensen, J.P., Miller, L.A., Semiletov, I.P., Stein, R., 2010. The Arctic Ocean. In: Liu, K.-K., Atkinson, L., Quiñones, R., Talaue-McManus, L. (Eds.), Carbon and Nutrient Fluxes in Continental Margins: A Global Synthesis. Springer Berlin Heidelberg, pp. 291–303.

Mesinger, F., DiMego, G., Kalnay, E., Mitchell, K., Shafran, P.C., Ebisuzaki, W., Jović, D., Woollen, J., Rogers, E., Berbery, E.H., Ek, M.B., Fan, Y., Grumbine, R., Higgins, W., Li, H., Lin, Y., Manikin, G., Parrish, D., Shi, W., 2006. North American regional reanalysis. Bull. Am. Meteorol. Soc. 87 (3), 343–360. https://doi.org/10.1175/BAMS-87-3-343.

Mills, M.M., Brown, Z.W., Lowry, K.E., van Dijken, G.L., Becker, S., Pal, S., Benitez-Nelson, C.R., Downer, M.M., Strong, A.L., Swift, J.H., Pickart, R.S., Arrigo, K.R., 2015. Impacts of low phytoplankton NO_3^-:PO_4^{3-} utilization ratios over the Chukchi shelf, Arctic Ocean. Deep-Sea Res. Part II Top. Stud. Oceanogr. 118, 105–121. https://doi.org/10.1016/j.dsr2.2015.02.007.

Mordy, C.W., Stabeno, P.J., Kachel, N.B., Kachel, D., Ladd, C., Zimmermann, M., Hermann, A.J., Coyle, K.O., Doyle, M., 2019. Patterns of flow in the canyons of the northern Gulf of Alaska. Deep-Sea Res. Part II Top. Stud. Oceanogr. 165, 203–220. https://doi.org/10.1016/j.dsr2.2019.03.009.

Mordy, C.W., Stabeno, P.J., Ladd, C., Zeeman, S.I., Wisegarver, D.P., Hunt Jr., G.L., 2005. Nutrients and primary production along the eastern Aleutian Island Archipelago. Fish. Oceanogr. 14, 55–76. https://doi.org/10.1111/j.1365-2419.2005.00364.x.

Neeley, A.R., Harris, L.A., Frey, K.E., 2018. Unraveling phytoplankton community dynamics in the northern Chukchi Sea under sea-ice-covered and sea-ice-free conditions. Geophys. Res. Lett. 45 (15), 7663–7671. https://doi.org/10.1029/2018GL077684.

Nishino, S., Kikuchi, T., Fujiwara, A., Hirawake, T., Aoyama, M., 2016. Water mass characteristics and their temporal changes in a biological hotspot in the southern Chukchi Sea. Biogeosciences 13 (8), 2563–2578. https://doi.org/10.5194/bg-13-2563-2016.

Overland, J.E., Wang, M., 2018. Arctic-midlatitude weather linkages in North America. Pol. Sci. 16, 1–9. https://doi.org/10.1016/j.polar.2018.02.001.

Peralta-Ferriz, C., Woodgate, R.A., 2017. The dominant role of the East Siberian Sea in driving the oceanic flow through the Bering Strait—Conclusions from GRACE ocean mass satellite data and in situ mooring observations between 2002 and 2016. Geophys. Res. Lett. 44 (22), 11472–11481. https://doi.org/10.1002/2017GL075179.

Roach, A.T., Aagaard, K., Pease, C.H., Salo, S.A., Weingartner, T., Pavlov, V., Kulakov, M., 1995. Direct measurements of transport and water properties through the Bering Strait. J. Geophys. Res.-Oceans 100 (C9), 18443–18457. https://doi.org/10.1029/95JC01673.

Rolph, R.J., Mahoney, A.R., Walsh, J., Loring, P.A., 2018. Impacts of a lengthening open water season on Alaskan coastal communities: deriving locally relevant indices from large-scale datasets and community observations. Cryosphere 12 (5), 1779–1790. https://doi.org/10.5194/tc-12-1779-2018.

Sakshaug, E., 2004. Primary and secondary production in the arctic seas. In: Stein, R., MacDonald, R.W. (Eds.), The Organic Carbon Cycle in the Arctic Ocean. Springer Publishing Company, Berlin, pp. 57–81.

Sambrotto, R.N., Goering, J.J., McRoy, C.P., 1984. Large yearly production of phytoplankton in the western Bering Strait. Science 225 (4667), 1147–1150. https://doi.org/10.1126/science.225.4667.1147.

Schumacher, J.D., Stabeno, P.J., Roach, A.T., 1989. Volume transport in the Alaska coastal current. Continent. Shelf Res. 9 (12), 1071–1083. https://doi.org/10.1016/0278-4343(89)90059-9.

Screen, J.A., Simmonds, I., 2010. The central role of diminishing sea-ice in recent Arctic temperature amplification. Nature 464, 1334–1337. https://doi.org/10.1038/nature09051.

Selz, V., Laney, S., Arnsten, A.E., Lewis, K.M., Lowry, K.E., Joy-Warren, H.L., Mills, M.M., van Dijken, G.L., Arrigo, K.R., 2018. Ice algal communities in the Chukchi and Beaufort Seas in spring and early summer: composition, distribution, and coupling with phytoplankton assemblages. Limnol. Oceanogr. 63 (3), 1109–1133. https://doi.org/10.1002/lno.10757.

Serreze, M.C., Barrett, A.P., Stroeve, J.C., Kindig, D.N., Holland, M.M., 2009. The emergence of surface-based Arctic amplification. Cryosphere 3, 11–19. https://doi.org/10.5194/tc-3-11-2009.

Serreze, M.C., Stroeve, J., Barrett, A.P., Boisvert, L.N., 2016. Summer atmospheric circulation anomalies over the Arctic Ocean and their influences on September sea ice extent: a cautionary tale. J. Geophys. Res. Atmos. 121 (19), 11463–11485. https://doi.org/10.1002/2016JD025161.

Spall, M.A., 2007. Circulation and water mass transformation in a model of the Chukchi Sea. J. Geophys. Res.-Oceans 112 (C5), C05025. https://doi.org/10.1029/2005JC003364.

Springer, A.M., McRoy, C.P., 1993. The paradox of pelagic food webs in the northern Bering Sea—III. Patterns of primary production. Continent. Shelf Res. 13 (5–6), 575–599. https://doi.org/10.1016/0278-4343(93)90095-F.

Stabeno, P.J., 2019. The Eastern Bering Sea: Declining ice, warming seas, and a changing ecosystem, in *State of the Climate in 2018*. Bull. Am. Meteorol. Soc. 100 (9), S148–S149.

Stabeno, P.J., Bell, S.W., 2019. Extreme conditions in the Bering Sea (2017-2018): record breaking low sea-ice extent. Geophys. Res. Lett. 46, 8952–8959. https://doi.org/10.1029/2019GL083816.

Stabeno, P.J., Bell, S.W., Bond, N.A., Kimmel, D.G., Mordy, C.W., Sullivan, M.E., 2018a. Distributed biological observatory region 1: physics, chemistry and plankton in the northern Bering Sea. Deep-Sea Res. Part II Top. Stud. Oceanogr. 162, 8–21. https://doi.org/10.1016/j.dsr2.2018.11.006.

Stabeno, P.J., Bell, S., Cheng, W., Danielson, S., Kachel, N.B., Mordy, C.W., 2016a. Long-term observations of Alaska coastal current in the northern Gulf of Alaska. Deep-Sea Res. Part II Top. Stud. Oceanogr. 132, 24–40. https://doi.org/10.1016/j.dsr2.2015.12.016.

Stabeno, P.J., Danielson, S.L., Kachel, D.G., Kachel, N.B., Mordy, C.W., 2016b. Currents and transport on the eastern Bering Sea shelf: an integration of over 20 years of data. Deep-Sea Res. Part II Top. Stud. Oceanogr. 134, 13–29. https://doi.org/10.1016/j.dsr2.2016.05.010.

Stabeno, P.J., Hristova, H.G., 2014. Observations of the Alaskan Stream near Samalga pass and its connection to the Bering Sea: 2001– 2004. Deep-sea res. Part I-oceanogr. Res. Pap. 88, 30–46. https://doi.org/10.1016/j.dsr.2014.03.002.

Stabeno, P., Kachel, N., Ladd, C., Woodgate, R., 2018b. Flow patterns in the eastern Chukchi Sea: 2010–2015. J. Geophys. Res. 123 (2), 1177–1195. https://doi.org/10.1002/2017JC013135.

Stabeno, P., Mordy, C.W., Sigler, M., 2020. Seasonal patterns of primary production at the seafloor in the eastern Chukchi Sea based upon *in-situ* chlorophyll fluorescence measurements. this issue Deep-Sea Res. Part II Top. Stud. Oceanogr.

Stabeno, P.J., Reed, R.K., Schumacher, J.D., 1995. The Alaska coastal current: Continuity of transport and forcing. J. Geophys. Res.-Oceans 100 (C2), 2477–2485. https://doi.org/10.1029/94JC02842.

Steele, M., Ermold, W., Zhang, J., 2008. Arctic Ocean surface warming trends over the past 100 years. Geophys. Res. Lett. 35 (2), L02614. https://doi.org/10.1029/2007GL031651.

Stein, R., Macdonald, R.W., 2004. The Organic Carbon Cycle in the Arctic Ocean. Springer Publishing Company, Berlin. https://doi.org/10.1007/978-3-642-18912-8.

Stigebrandt, A., 1984. The North Pacific: a global-scale estuary. J. Phys. Oceanogr. 14 (2), 464–470.

Tachibana, Y., Komatsu, K.K., Alexeev, V.A., Cai, L., Ando, Y., 2019. Warm hole in Pacific Arctic sea ice cover forced mid-latitude Northern Hemisphere cooling during winter 2017–18. Sci. Rep. 9 (1), 5567. https://doi.org/10.1038/s41598-019-41682-4.

Torres-Valdés, S., Tsubouchi, T., Bacon, S., Naveira-Garabato, A.C., Sanders, R., McLaughlin, F.A., Petrie, B., Kattner, G., Azetsu-Scott, K., Whitledge, T.E., 2013. Export of nutrients from the Arctic Ocean. J. Geophys. Res.-Oceans 118 (4), 1625–1644. https://doi.org/10.1002/jgrc.20063.

Tremblay, G., Belzile, C., Gosselin, M., Poulin, M., Roy, S., Tremblay, J.-É., 2009. Late summer phytoplankton distribution along a 3500 km transect in Canadian Arctic waters: strong numerical dominance by picoeukaryotes. Aquat. Microb. Ecol. 54 (1), 55–70. https://doi.org/10.3354/ame01257.

Tremblay, J.-É., Michel, C., Hobson, K.A., Gosselin, M., Price, N.M., 2006. Bloom dynamics in early opening waters of the Arctic Ocean. Limnol. Oceanogr. 51 (2), 900–912. https://doi.org/10.4319/lo.2006.51.2.0900.

Walsh, J.J., McRoy, C.P., Coachman, L.K., Goering, J.J., Nihoul, J.J., Whitledge, T.E., Blackburn, T.H., Parker, P.L., Wirick, C.D., Shuert, P.G., Grebmeier, J.M., Springer, A.M., Tripp, R.D., Hansell, D.A., Djenidi, S., Deleersnijder, E., Henriksen, K., Lund, B.A., Andersen, P., Müller-Karger, F.E., Dean, K., 1989. Carbon and nitrogen cycling within the Bering/Chukchi Seas: source regions for organic matter effecting AOU demands of the Arctic Ocean. Prog. Oceanogr. 22 (4), 277–359. https://doi.org/10.1016/0079-6611(89)90006-2.

Wang, M., Overland, J.E., 2015. Projected future duration of the sea-ice-free season in the Alaskan Arctic. Prog. Oceanogr. 136, 50–59. https://doi.org/10.1016/j.pocean.2015.01.001.

Wang, M., Yang, Q., Overland, J.E., Stabeno, P., 2018. Sea-ice cover timing in the Pacific Arctic: the present and projections to mid-century by selected CMIP5 models. Deep-Sea Res. Part II Top. Stud. Oceanogr. 152, 22–34. https://doi.org/10.1016/j.dsr2.2017.11.017.

Weingartner, T.J., Cavalieri, D.J., Aagaard, K., Sasaki, Y., 1998. Circulation, dense water formation, and outflow on the northeast Chukchi shelf. J. Geophys. Res.-Oceans 103 (C4), 7647–7661. https://doi.org/10.1029/98JC00374.

Weingartner, T.J., Danielson, S., Sasaki, Y., Pavlov, V., Kulakov, M., 1999. The Siberian Coastal Current: a wind- and buoyancy-forced Arctic coastal current. J. Geophys. Res.-Oceans 104 (C12), 29697–29713. https://doi.org/10.1029/1999JC900161.

Wood, K.R., Bond, N.A., Danielson, S.L., Overland, J.E., Salo, S.A., Stabeno, P.J., Whitefield, J., 2015. A decade of environmental change in the Pacific Arctic region. Prog. Oceanogr. 136, 12–31. https://doi.org/10.1016/j.pocean.2015.05.005.

Wood, K.R., Jayne, S.R., Mordy, C.W., Bond, N., Overland, J.E., Ladd, C., Stabeno, P.J., Ekholm, A.K., Robbins, P.E., Schreck, M.-B., Heim, R., Intieri, J., 2018. Results of the first arctic heat open science experiment. Bull. Am. Meteorol. Soc. 99 (3), 513–520. https://doi.org/10.1175/BAMS-D-16-0323.1.

Woodgate, R.A., 2018. Increases in the Pacific inflow to the Arctic from 1990 to 2015, and insights into seasonal trends and driving mechanisms from year-round Bering Strait mooring data. Prog. Oceanogr. 160, 124–154. https://doi.org/10.1016/j.pocean.2017.12.007.

Woodgate, R.A., Aagaard, K., Weingartner, T.J., 2005. A year in the physical oceanography of the Chukchi Sea: moored measurements from autumn 1990–1991. Deep-Sea Res. Part II Top. Stud. Oceanogr. 52 (24–26), 3116–3149. https://doi.org/10.1016/j.dsr2.2005.10.016.

Woodgate, R.A., Weingartner, T.J., Lindsay, R., 2012. Observed increases in Bering Strait oceanic fluxes from the Pacific to the Arctic from 2001 to 2011 and their impacts on the Arctic Ocean water column. Geophys. Res. Lett. 39 (24), L24603. https://doi.org/10.1029/2012GL054092.

Zhang, J., 2005. Warming of the arctic ice-ocean system is faster than the global average since the 1960s. Geophys. Res. Lett. 32 (19), L19602. https://doi.org/10.1029/2005GL024216.

Deep–Sea Research II 177 (2020) 104842

Contents lists available at ScienceDirect

Deep-Sea Research Part II

journal homepage: http://www.elsevier.com/locate/dsr2

Seasonal patterns of near-bottom chlorophyll fluorescence in the eastern Chukchi Sea: 2010–2019

Phyllis J. Stabeno [a,*], Calvin W. Mordy [a,b], Michael F. Sigler [c]

[a] NOAA Pacific Marine Environmental Laboratory, 7600 Sand Point Way NE, Seattle, WA, 98115-0070, USA
[b] University of Washington, JISAO, 7600 Sand Point Way NE, Seattle, WA, 98115-0070, USA
[c] NOAA Alaska Fisheries Science Center, Retired, 17109 Point Lena Loop Road, Juneau, AK, 99801-8344, USA

ARTICLE INFO

Keywords:
Chukchi Sea
Sea ice
Fluorescence
Ice algae

ABSTRACT

The Chukchi Sea consists of a broad, shallow (<45 m) shelf that is seasonally (November–July) covered by sea ice. This study characterizes the seasonal patterns of near-bottom primary production using moored instruments measuring chlorophyll fluorescence, oxygen, nitrate, and photosynthetically active radiation. From 2010 to 2018, moorings were deployed at multiple sites each year. Instruments were restricted to within 10 m of the seafloor due to ice keels, which can reach 30 m below the surface in this region. Near-bottom blooms were common at all mooring sites. The bloom onset directly followed ice retreat whereas the end of the bloom followed loss of light in September. The intensity of light at the seafloor (~40 m deep) was similar to levels observed under 1–2 m thick ice floes in the spring/early summer, and was sufficient to support photosynthesis near the seafloor, utilizing nitrate and producing oxygen. We hypothesize that the near bottom bloom originated from aggregates of ice algae that sank during ice retreat. As a consequence of climate warming and earlier ice retreat, we predict that the near-bottom bloom onset will occur earlier, but the timing of the end of the near-bottom bloom will remain the same pending a sufficient nutrient supply. The Chukchi Sea is highly productive even though the growing season is short. This production is promoted by a shallow seafloor, which allows multiple production layers (surface open water, bottom of the mixed layer, under-ice algae, and disassociated ice algae which settles near the seafloor). We term this the Multiple Production Layers (MPL) hypothesis.

1. Introduction

The Chukchi Sea consists of a broad shallow shelf, extending >800 km northward from the Bering Strait to the shelf break and the Arctic basin. It is characterized as an inflow shelf for the Arctic (Carmack and Wassmann, 2006) and is the sole source of Pacific water to the Arctic Ocean. The flow through Bering Strait provides heat, freshwater, and salt, including nutrients, to the Chukchi Sea and the Arctic Basin. The northward flow divides into two primary branches — the western branch flows into the Arctic basin through Herald Canyon and the eastern branch flows through Barrow Canyon (Coachman et al., 1975).

Sea-ice algae are a major source of carbon to the benthic ecosystem (Grebmeier, 2012; Koch et al., 2020) with an estimated production during spring of 1–2 g C m^{-2} (Gradinger, 2009). Production of ice algae is primarily limited by light (Michel et al., 1988; Welch and Bergmann, 1989) and nutrients (Cota et al., 1987; Castellani et al., 2017).

The spring plankton bloom likely initiates under and within the sea ice (Hill and Cota, 2005; Arrigo et al., 2012; Lowry et al., 2018; Tedesco et al., 2019). Seasonal ice retreat favors the export of aggregates of under-ice algae directly to the benthos (Ambrose et al., 2005; Boetius et al., 2013; Katlein et al., 2015; Koch et al., 2020). This, together with benthic microalgae, support the Chukchi's rich, benthic-dominated ecosystem (Dunton et al., 2014).

There has been a dramatic loss of sea ice in the Chukchi Sea during the last 15 years (Wood et al., 2015, 2018; Serreze et al., 2016; Frey et al., 2015), with earlier ice retreat in the spring/summer and later ice arrival in the fall. This loss of sea ice (including multi-year ice) has increased the atmospheric heat-flux into the Chukchi Sea (Danielson et al., 2020). Earlier ice retreat also impacts the timing of export of ice algae to the seafloor and the timing of open water phytoplankton production (Arrigo et al., 2008; Hill et al., 2017), and favors open water phytoplankton primary production that benefits a pelagic ecosystem (Grebmeier et al., 2006, 2015; Moore and Stabeno, 2015). A longer open-water season is predicted to alter the composition and distribution

* Corresponding author.
E-mail address: phyllis.stabeno@noaa.gov (P.J. Stabeno).

https://doi.org/10.1016/j.dsr2.2020.104842
Received 6 September 2019; Received in revised form 11 July 2020; Accepted 16 July 2020
Available online 25 July 2020

of phytoplankton communities (Tremblay et al., 2009; Neeley et al., 2018).

The focus in this paper is to examine the relationship among chlorophyll fluorescence, arrival and departure of sea ice, and photosynthetically active radiation (PAR). We utilize a variety of data sources, including hydrographic casts, pop-up buoys (a newly developed technology that measures properties underneath the ice), and a variety of time series collected on moorings. Chlorophyll fluorescence, PAR, oxygen, and nitrate were measured near the seafloor at multiple mooring sites on the U.S. Chukchi Shelf over a 9-year period (Fig. 1). These instruments were all deployed within 8 m of the seafloor to avoid the deep ice keels that can occur on this shelf.

Preliminary analysis indicated that the large export of ice algae to the seafloor coincides with ice retreat (Berchok et al., 2015). In their analysis, an increase in percent oxygen saturation and/or decrease in nitrate concentration were often associated with this export event, suggesting that net primary production due to ice algae continues at depth. We contend that this continued production is not due to subsurface phytoplankton, which lie shallower, but rather near-bottom disassociated ice algae. We present evidence to support this distinction in the results and discussion.

Our objective was to test the multiple production layer or MPL, 'maple', hypothesis that ice algae fall to the seafloor as ice retreats and continue to photosynthesize for weeks or longer (Fig. 2). According to this hypothesis, this near-bottom layer of continued photosynthesis by disassociated ice algae adds to the other layers of primary production (i.e. sympagic algal production, and surface and sub-surface phytoplankton blooms) that together account for the high primary productivity found on the Chukchi Shelf (Hill and Cota, 2005; Arrigo et al., 2012; Codispoti et al., 2013; Hill et al., 2017).

2. Data and methods

2.1. Moorings

Moorings (Fig. 1) were deployed at 8 sites (C1–C8) on the Chukchi Shelf during late summer and recovered the following summer, when new moorings were usually deployed. Listed in Table 1 are the deployment years at each site, mooring locations and instrumentation. All moorings were short, taut wire moorings. During winter and spring, sea-ice keels can be as deep as 30 m below the surface (Stabeno et al., 2018). To avoid these ice keels, each mooring was <10 m tall, keeping the upper float at least 30 m below the surface. This height limitation resulted in two moorings being deployed at each site, because of the limited amount of vertical wire space. Instruments on the moorings collected hourly measurements of the following variables: temperature (SeaBird SBE-37, SBE-39, SeaCat); currents (Acoustic Doppler Current Profiler, RCM-9); salinity (SBE-37, SeaCat); chlorophyll fluorescence (Sea-Bird/WET Labs FLSB ECO Fluorometer); nitrate (Sea-Bird/Satlantic ISUS or SUNA; at selected sites); and PAR (Biospherical Instruments QSP2300). Excluding the ADCP that was deployed at the top of the mooring, the rest of the instruments were deployed 4–8 m above the bottom. All instruments were prepared according to manufacturers' specifications and calibrated prior to deployment (except for calibration of the nitrate sensors which is discussed below). While chlorophyll samples were taken at the mooring sites on deployment and recovery of the moorings, there were insufficient data to improve the conversion of fluorescence to chlorophyll.

To reduce biofouling, optical wipers on the Eco Fluorometer and SUNA were engaged prior to each hourly set of measurements, and the ISUS sensors were plumbed into the outflow of a Sea-Bird Scientific SBE-16 with anti-fouling agents mounted on either side of the ISUS flow cell. See Mordy et al. 2020 for further details of data processing of nitrate sensors.

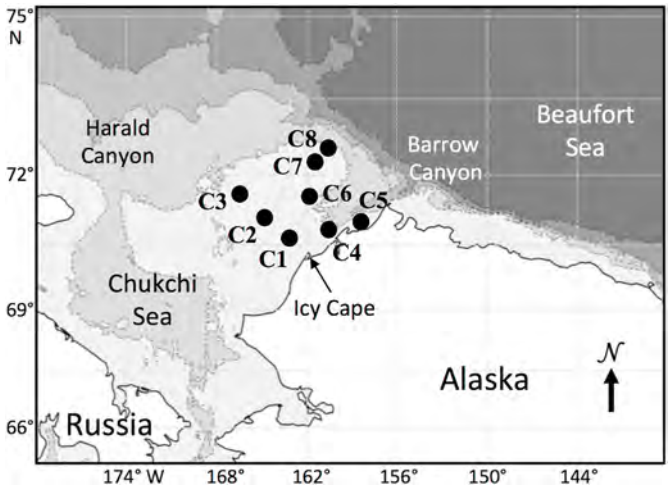

Fig. 1. Map of the Chukchi Sea shelf with bathymetry and place names. The eight shelf mooring sites (C1–C8) are indicated by black dots. The periods of deployments are listed in Table 1.

2.2. Hydrography

The conductivity-temperature-depth (CTD) instrument package consisted of a Sea-Bird 911plus with dual sensors measuring temperature, conductivity and oxygen, and single sensors measuring, pressure, and chlorophyll fluorescence. Hydrographic casts were done at each mooring site upon deployment and/or recovery of moorings. While the optical nitrate sensors (ISUS and SUNA) have a reported accuracy of ~2 μM, they must be calibrated with discrete samples. At the depth of the nitrate sensor, discrete samples for nutrients were collected from Niskin bottles and filtered through 0.45 μm cellulose acetate filters. Samples were frozen for analysis at our laboratory in Seattle, WA. See Mordy et al. 2020 for details of the analysis.

On July 18, 2015, aboard the USCGC Healy cruise HE1501, a GoPro camera was attached to the top of the CTD frame and a movie was taken simultaneously with the CTD downcast near the C2 mooring (164.3°W, 71.2°N). Three representative frames were selected from this movie and presented herein, and a short video segment is included in the supplemental material (Supplemental Video).

2.3. Pop-up buoy

During the last four years, pop-up buoys have been developed at the Pacific Marine Environmental Laboratory (Langis et al., 2018). The purpose of this effort was to develop an inexpensive, expendable buoy to make under-ice measurements that could be deployed in summer or fall and rise to the surface in the following winter or spring on a prearranged day. Eventually, when the ice melted, the buoy surfaced and transmitted data back to the laboratory. The instruments collect data during three unique periods: (1) on the seafloor; (2) on the vertical profile as it rises to the surface; and (3) under the ice.

The buoy presented in this manuscript is Generation 3. It consisted of a spherical float (30 cm in diameter). The upper ~5 cm of top had been cut off, and a flat plate (cap) attached at the top. One thermistor (±0.01 °C) was located on the top-cap and a second one at the bottom of the float. A fluorometer (±2%) was located on the bottom of the float facing downwards, while the PAR sensor (±3%) and pressure sensor (±0.21 m) were located on the top-cap. The camera (UCAM III Low-Resolution Digital Camera) was tilted upward at 45° and positioned ~10 cm from the bottom of the ice.

2.4. Sea ice

The Advanced Microwave Scanning Radiometer (AMSR-E) data

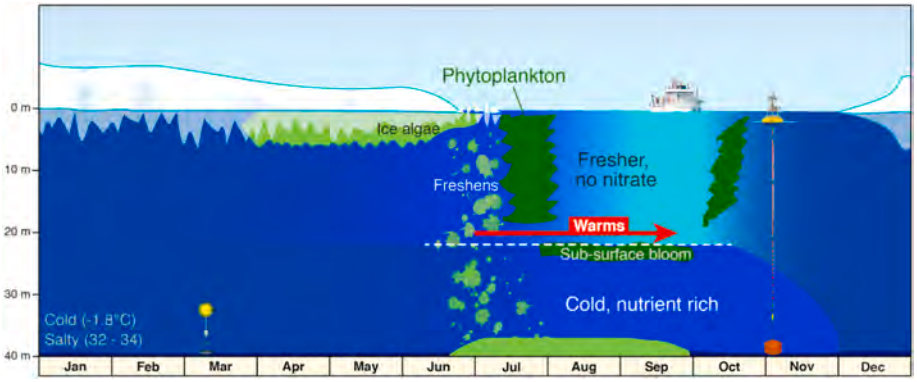

Fig. 2. Seasonality of the lower trophic level of the ecosystem on the northeastern Chukchi Sea Shelf. Ice algae bloom occurs beneath the ice in spring, and with ice melt it is exported to the bottom, where there is sufficient light and nutrients to support further production. With ice retreat/melt the water stabilizes with a relatively warm, low salinity surface layer overlaying a colder, more saline bottom layer. With this stabilization, a surface phytoplankton bloom can occur consuming the remainder of surface nutrients and support a subsurface bloom. With surface mixing in late summer a fall phytoplankton bloom may occur (Adapted from Fig. 136, Berchok et al., 2015).

Table 1
List of moorings (with depth in parentheses) and instruments deployed between 2010 and 2017. F indicates the fluorometer functioned correctly providing data for the entire deployment. Similarly, N is a nitrate sensor, O an oxygen sensor and P a PAR sensor. Bold indicates that the instrument recorded data for only part of the deployment cycle. "Yes" indicates that there was production in the near bottom; "No" indicates that there was no production; and "-" indicates that there were insufficient data to decide. In addition to the variables listed below, currents were measured at most sites. The depths of each instrument were 4–8 m above the bottom.

Site (depth) Lat. Long.	Aug 2010	Aug 2011	Aug 2012	Aug 2013	Sep 2014	Sep 2015	Aug 2016	Aug 2017
C1 (45 m) 70.835 163.119	FNO**P** yes	F**O** –		**FNOP** –	NP –	FNOP yes	FNOP yes	FNP yes
C2 (44 m) 71.222 164.250	F**N**OP yes	FN**OP** yes	FOP yes	FOP yes	FN**OP** yes	FN**OP** yes	FNOP yes	FNOP yes
C3 (45 m) 71.825 165.975	OP –	FN**O** yes					NP –	FNOP yes
C4 (48 m) 71.042 160.493			OP –	F**OP** –	FNP yes	FOP yes	FP –	FOP yes
C5 (45 m) 71.207 157.999				FON yes	**F**NOP yes		FP –	FP –
C6 (43 m) 71.777 161.875				FN no	**F**N –			
C7 (43 m) 72.424 161.604				FN yes	FN yes			
C8 (46 m) 72.586 161.215					FO yes			

(available from the National Snow and ice Data Center, http://nsidc.org/data/amsre/) were used in this manuscript. AMSR is a dataset of sea-ice extent and areal concentration consisting of daily ice concentration data at 12.5 km resolution. Time series of percent areal coverage were calculated in 50 km × 50 km boxes around each mooring site (C1–C8).

2.5. Data analysis

Time series of sea-ice coverage (percent) values were used to determine the timing and duration of the ice-free period in summer. These records were plotted, and the retreat and return dates were assigned (Table S1, Fig. S1). Ice retreat was considered to have occurred when areal sea-ice cover fell below 15% for the first time during each year. Ice return was considered to have occurred when areal ice cover increased above 15% for the last time during each year. The duration of the ice-free period was computed as the difference in days between ice retreat and ice return.

PAR values near the seafloor for each mooring and year were examined to determine the time and duration of the photic period in summer. These records were plotted and the onset, end and maximum value of PAR were assigned (Table S1, Fig. S1). Onset and end of the PAR period were considered to have occurred when the PAR value crossed a threshold of 0.1 μE m^{-2} s^{-1} (Hancke et al., 2018). PAR duration was computed as the difference in days between PAR end and PAR onset.

Chlorophyll values near the seafloor for each mooring and year were examined to determine the time and duration of the bloom in summer (herein we use "bloom" to indicate increased chlorophyll fluorescence). These records were plotted and the onset, end and maximum value of the summer bloom were assigned (Table S1, Fig. S1). Onset and end of the near-seafloor summer bloom ('bloom end') were considered to have occurred when the concentration of chlorophyll crossed 1 μg l^{-1} (Arrigo and van Dijken, 2011). Bloom duration was computed as the difference in days between bloom end and bloom onset.

Annual values of ice retreat, ice return, PAR onset, PAR end, bloom onset, and bloom end were plotted by year and mooring using box plots and the R package 'ggplot2'. The relationships between values (e.g. between bloom onset and ice retreat) were plotted by year and mooring using the R package 'ggplot2' scatter plots. Their relatedness was examined by computing Pearson correlation coefficients *r* (e.g., between bloom onset and ice retreat) and the statistical significance of the *r*-values were estimated using the R package 'Hmisc'.

3. Results

3.1. Sea ice

Typically, ice cover was at or near 100% during winter for most mooring sites (Fig. 3a, Fig. S1). The exceptions were the three most coastal moorings—primarily C4 and C5 and, to a lesser extent, C1. At these sites, winter and spring sea-ice cover was usually reduced when strong winds were out of the east and/or northeast (referred to as a wind-driven polynya) or when warm Atlantic water surfaced (referred to as a sensible heat polynya) (Ladd et al., 2016; Hirano et al., 2016). At these coastal moorings, areal ice concentration during winter was smallest in 2013, 2014, and 2016 (Fig. 3a). The greatest variability in areal ice cover was at C4 and C5, the two moorings nearest the shelf break (Figs. 1 and 3b). At all the mooring sites discussed herein, sea ice eventually retreated in summer, and returned in late summer or fall (Fig. S1).

The timing of sea-ice retreat varied among years with later retreats in 2012–2014 and earlier retreats in 2010–2011 and 2015–2017 (Fig. 4a). The median day of ice retreat was approximately day 170 (mid-June) for 2010–2011, day 205 (late July) for 2012–2014, day 190 (early July) for 2015–2016, and day 135 (mid-May) for 2017. This pattern of two years of early retreat, three of late, two of mid-range, and finally one year of early ice retreat largely occurred regardless of location, with some exceptions. For example, ice retreat at C7 and C8 in 2010 was similar to the later ice retreat observed in 2012–2014. At C4, the early ice retreat in 2012 reflects a brief period of low ice followed by a return of sea ice lasting several weeks (Fig. S1).

The timing of sea-ice return varied less than sea-ice retreat, with most returns occurring between days 300 and 330 (November; Fig. 4d). The range of sea-ice return was much narrower (~50 days, day 294–345) than the range of sea-ice retreat (~100 days, day 133–232) (Table S1). Thus, variability in the duration of the ice-free period was dictated more by ice retreat than ice return and ranged from 67 to 203 days. The median duration of the ice-free period was 127 days.

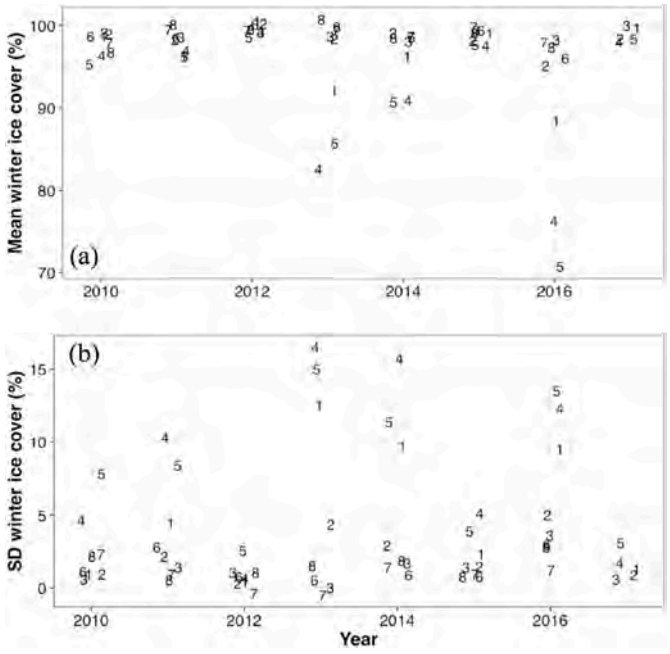

Fig. 3. (a) The mean winter (January–March) ice cover at each mooring site as a function of year. (b) The standard deviation of the mean winter ice cover shown in (a). The individual moorings are indicated by number, so "4" refers to the mooring site C4. The points are randomly offset to reduce overlap. The coastal moorings C1, C4, and C5 had periods of low ice cover and the greatest variability.

3.2. Ice algae

3.2.1. Under-ice data from pop-up buoy

An under-ice (water-ice interface) bloom was observed during spring 2019 from a pop-up buoy that floated to the surface and came to rest at the bottom of an ice floe for approximately two months (May and June). The pop-up buoy was deployed in August 2018 near the C2 mooring (71.2°N, 164.3°W). It remained anchored to the sea floor until April 30, 2019, when the pop-up buoy was released (as designed) and rose to the surface underneath a large (~20 km long) ice floe (Fig. 5a). This distinctive floe was tracked *via* satellite images until 20 June, when the ice floe began to break apart. The floe traveled a distance of ~400 km over a period of 60 days (blue line, Fig. 5b). During this period, the pop-up buoy successfully collected hourly temperature, PAR and fluorescence data just below the bottom of the ice. The top of the buoy rested immediately below the ice at a depth of ~1.5 m (an indication of ice thickness) during the first ~25 days and then began to shoal (an indication of ice thinning) (Fig. 5c).

Chlorophyll fluorescence near the ice-seawater interface began to increase on ~14 May and the bloom continued through early June (Fig. 5d). This bloom occurred under low light conditions (max 2–3 μE m^{-2} s^{-1} prior to 27 May); PAR increased reaching 4–8 μE m^{-2} s^{-1} in early June. In mid-June, the fluorescence disappeared and PAR increased to 20 μE m^{-2} s^{-1}. It was unlikely that the disappearance of the bloom was related to photoinhibition because Cota and Horne (1989) found that, even for ice algae adapted to low light, photo inhibition does not occur until ~40 μE m^{-2} s^{-1}. While nutrient depletion and grazing cannot be discounted, the expectation is that the bloom sank toward the sea floor once the ice substrate began to erode (Fig. 5c), which is consistent with loss of color in the under-ice images (Fig. 5f and g) (Riebesell et al., 1991; Ambrose et al., 2005; Boetius et al., 2013; Fernández-Méndez et al., 2014; Katlein et al., 2015).

The pop-up buoy remained in the vicinity of moorings C2 and C3 for ~25 days (Fig. 5b). This provided simultaneous time series of fluorescence underneath the ice and near the seafloor (Fig. 6). While in the vicinity of C2 (red line Fig. 6a), the under-ice chlorophyll fluorescence was near-zero as was the near-bottom chlorophyll fluorescence. As the buoy came closer to C3, under-ice fluorescence began to increase (green line). The near bottom fluorescence began to increase at C3 ~20 days after it began to increase at the ice-water interface (green line in Fig. 6b). This lag is consistent with estimates of settling rates of ice algae (0.4–2.7 m d^{-1}, Michel et al., 1993).

3.2.2. Water column data from CTD and video

Vertically, there can be multiple layers of significant chlorophyll fluorescence in the Chukchi Sea (Martini et al., 2016). This multilayer pattern was evident in a hydrographic cast done in 2015 (Fig. 7, left), when a camera was attached to the CTD frame (photos in Fig. 7, right). This CTD cast (164.3°W, 71.2°N on July 18, 2015) was taken near C2, approximately 3 days after the ice retreated. Two increases in chlorophyll fluorescence are evident in the cast data, a relatively small one at ~15 m and a larger one below 20 m. The photos show the different quality of the blooms. The photo of the upper water column appears fairly clear (Fig. 7, photo A); the middle photo shows a diffuse chlorophyll peak and likely represents a subsurface phytoplankton bloom associated with the pycnocline (Fig. 7, photo B), while the bottom photo (Fig. 7, photo C) has larger aggregates of cells and extends over ~10 m depth (Fig. 7, left). As the CTD passed the halfway point through the lower layer of fluorescence (~28 m), PAR was fully attenuated. These aggregates are better viewed and clearly visible by video (Supplementary Video), and consistent with reports of sinking aggregates of disassociated ice algae (Riebesell et al., 1991; Ambrose et al., 2005; Boetius et al., 2013; Fernández-Méndez et al., 2014; Katlein et al., 2015; Koch et al., 2020).

Identifying these aggregates as disassociated ice algae at our moorings is supported by observations at a nearby sediment trap deployed on

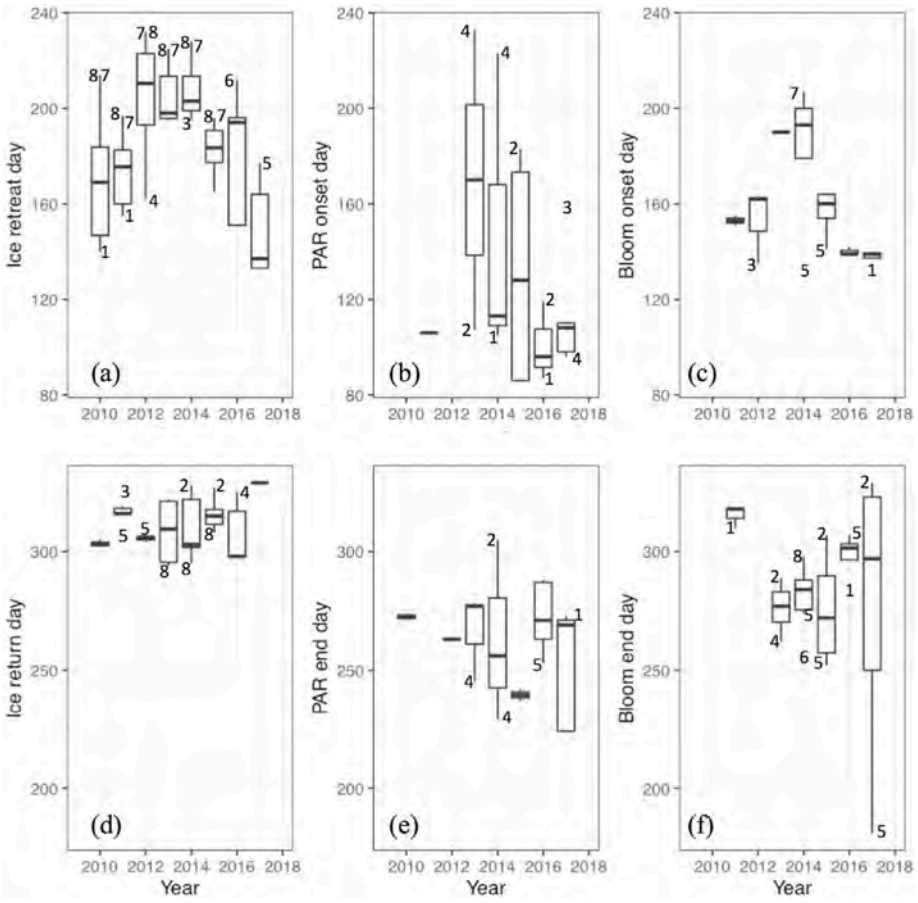

Fig. 4. Box plots indicating (a) day of ice-retreat, (b) day on which the onset of PAR > 0.1 μE m^{-2} s^{-1}, (c) day of bloom onset, (d) day of ice-return, (e) day on which PAR falls below 0.1 μE m^{-2} s^{-1}, and (f) day of bloom end day, all versus year of mooring deployment. The data shown herein are from S1. The numbers in each panel indicate the mooring sites (e.g. "4" refers to C4) that are outside the interquartile range.

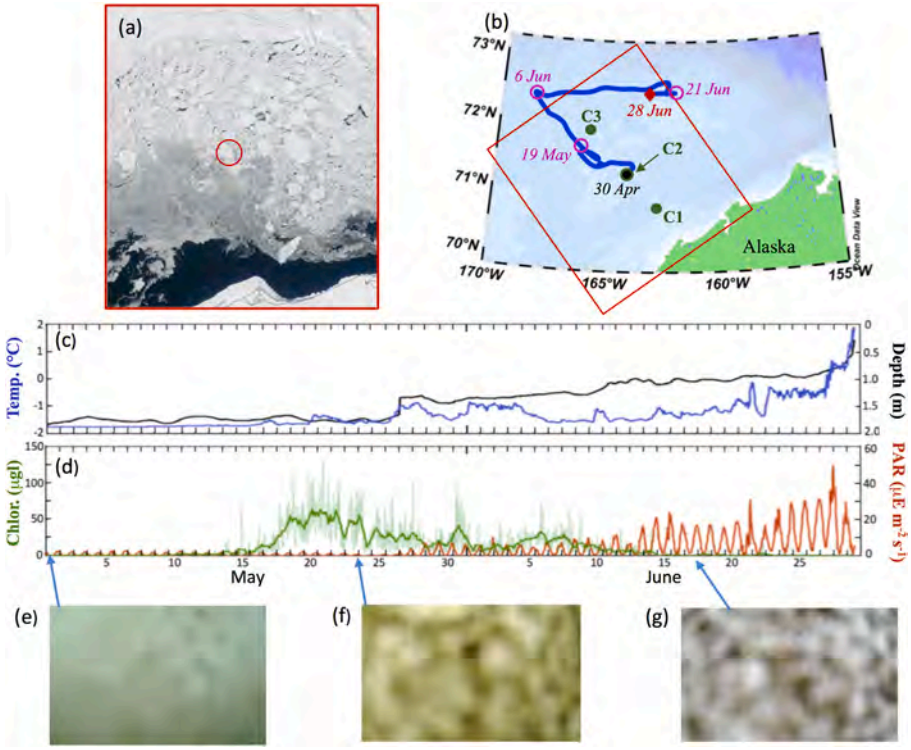

Fig. 5. (a) Satellite image of sea ice on April 30, 2019 when the pop-up buoy surfaced. The red circle indicates the location of where the pop-up buoy was deployed. (b) The trajectory of the ice floe from 30 April to 28 June when it broke apart and the buoy began to transmit location and data (red dot). Selected dates are indicated in purple. Mooring locations are shown and color-coded. The red box is the area shown in (a). (c) Time series of temperature beneath the sea ice and the depth of buoy. The depth of buoy is effectively the thickness of the sea ice at that point because the buoy sits immediately beneath the ice. (d) Time series of chlorophyll fluorescence and PAR measured below the ice by instruments on the pop-up buoy. (e–g) Photos of the water column. (For interpretation of the references to color in this figure legend, the reader is referred to the Web version of this article.)

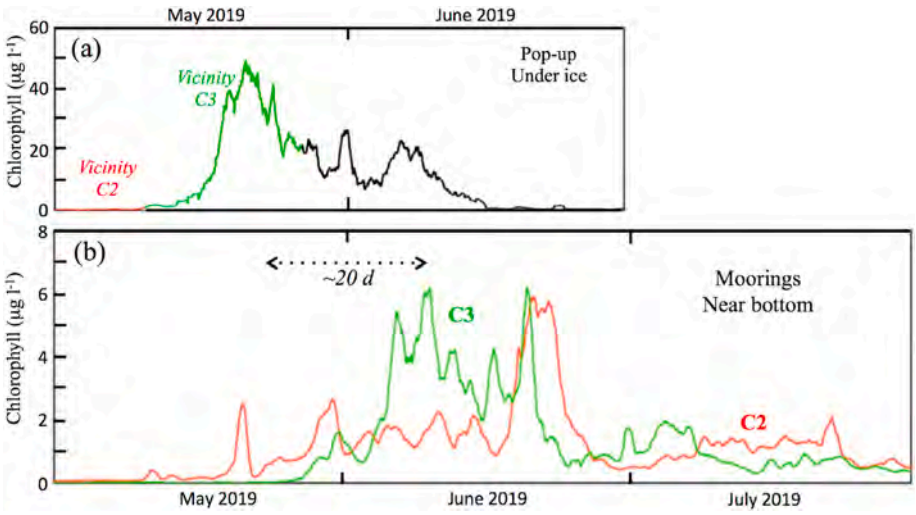

Fig. 6. (a) Low-pass filtered time series of chlorophyll fluorescence measured by pop-up buoy under the ice. It is color coded with red indicating when the buoy was in the vicinity of C2, green in the vicinity of C3, and black in the vicinity of no mooring. (b) Low-pass filtered time series of near-bottom chlorophyll fluorescence measured at C2 (red) and C3 (green). (For interpretation of the references to color in this figure legend, the reader is referred to the Web version of this article.)

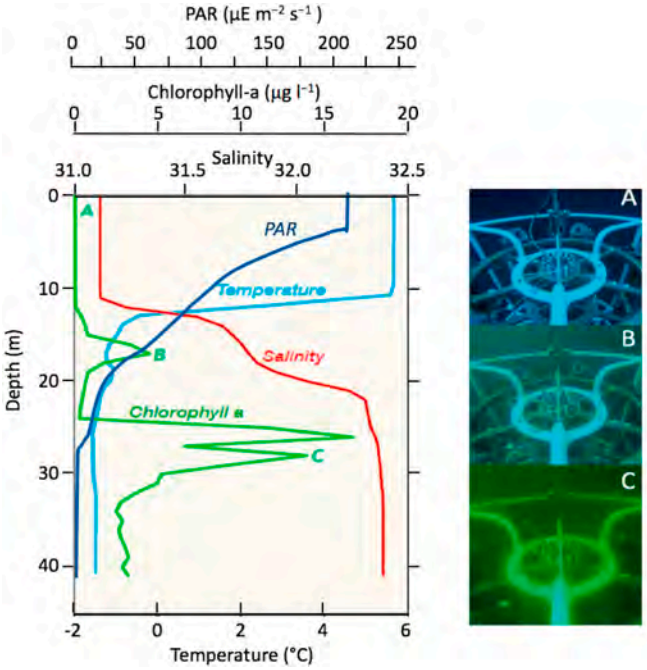

Fig. 7. (left) Hydrographic cast in 2015 near C2 showing multiple subsurface chlorophyll maxima. A smaller subsurface maximum was observed just below the pycnocline, and a larger maximum was observed in the bottom layer. (right) Photos of the water column (taken from a video in the supplemental material): upper layer of relatively clear water; first chlorophyll maximum below the pycnocline; and at the top of the large maximum. The letters A, B, and C correspond to the appropriate depth shown on the left.

the northern Chukchi Shelf in 2016 (Koch et al., 2020). Koch et al. (2020) found that as ice retreated, the flux of sea-ice exclusive diatoms (*Nitzschia frigida* and *Melosira arctica*) increased from ~2 million cells m^{-2} d^{-1} in early June to ~ 30 million cells m^{-2} d^{-1} in early July. This was accompanied by a 10-fold increase in the flux of lipids that are specific to sympagic organisms (from ~100 to 1000 ng m^{-2} d^{-1}). The timing of this flux was concurrent with the increased concentrations of chlorophyll observed at two nearby moorings, C2 (60 km away) and C4 (80 km) (Fig. S1).

3.2.3. Near-bottom data from mooring C2 in 2018

The fate of these sinking aggregates can be seen in the time series (oxygen, nitrate, PAR and fluorescence) collected at the moorings. For example, in 2018 at mooring C2, the ice retreated in mid-May (Fig. 8a), an early date for ice retreat, and there was a sharp increase in chlorophyll fluorescence in the near-bottom water (30–40 m below the surface; Fig. 8b). Accompanying this increase in fluorescence was a sharp increase in the percent saturation of oxygen, from ~90% to >120%, and, at the same time, a decrease in nitrate from ~15 μM to near 0 μM

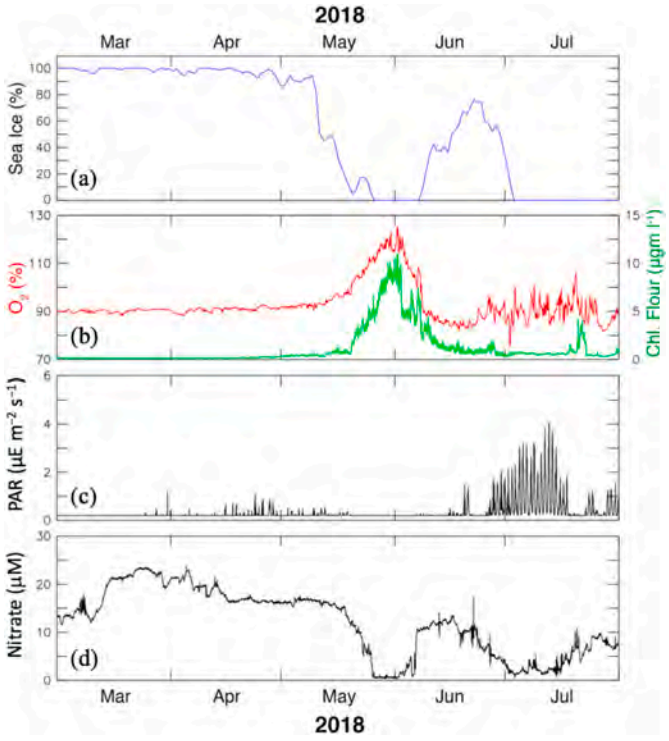

Fig. 8. Time series of: (a) percent ice cover in 50 km × 50 km box centered on C2; (b) percent oxygen saturation (red) and chlorophyll fluorescence (green); (c) PAR; and (d) nitrate. Except for (a), all time series were measured on mooring at C2 within 8 m of the bottom. (For interpretation of the references to color in this figure legend, the reader is referred to the Web version of this article.)

(Fig. 8d) consistent with active photosynthesis in the bottom waters. Light (PAR) was very weak (<2 μE m^{-2} s^{-1}), but measurable through mid-May, decreasing to near zero during the period of high chlorophyll fluorescence; it increased markedly in early July with the disappearance of fluorescence. We suspect that the decrease in PAR to near zero in mid-May was a result of disassociated ice algae descending as a mass through the water column, and the resulting shading prevented most of the light from reaching the seafloor. Such a shading (sharp decrease in PAR) effect was also evident in Fig. 7a, when the CTD entered the region with high chlorophyll. The highest PAR values (Fig. 8c) occurred in July when near-bottom chlorophyll concentrations were low and ice was absent. Vertical mixing in the bottom ~8 m during late May - early June likely exposes the ice algae to sufficient light to continue production; that is, sometimes cells are at the top of the layer and exposed to sufficient light and then mixed downward in this bottom mixed layer.

Near the seafloor, chlorophyll fluorescence began decreasing between 1–6 June, perhaps due to nutrient limitation or grazing (Fig. 8b, d). On 7 June, sea ice returned, and there was a sharp increase in nitrate, and reductions in chlorophyll fluorescence and oxygen saturation (<90%), results consistent with advection of water past the mooring (Mordy et al., 2020) and net respiration. When the ice retreated for the second time in early July, the highest PAR was recorded and yet there was no clear evidence of active photosynthesis as chlorophyll fluorescence remained low and oxygen saturation, while variable, was <100%. Finally, in mid-July there was a small pulse of chlorophyll fluorescence that once again shaded near-bottom waters (low PAR), was coincident with a 5 μM drop in nitrate, and resulted in a short period of >100% oxygen saturation.

3.3. Near-bottom chlorophyll and its relationship to sea ice and light level

Continued fluorescence and photosynthesis near the seafloor following ice retreat was common in our time series. This pattern (described in the previous section for mooring C2 in 2018) of ice retreat, increased fluorescence, increased oxygen (by >20%) and/or decreased nitrate dominates at the mooring sites over the years (2010–2018), occurring 22 out of 23 times (96%) when there are sufficient data to detect this pattern (Table 1). Each of these locations is shallow (<48 m) with measurable light (PAR) reaching the bottom. In MPL, we have hypothesized that the increased fluorescence was likely due to continued photosynthesis by disassociated ice algae near the seafloor, as evidenced by accumulation of sea-ice exclusive diatoms in a sediment trap (Koch et al., 2020) and increasing percent oxygen saturation and/or decreasing nutrients (Fig. 8). In the next few paragraphs, we explore the relationship among the timing and duration of the chlorophyll fluorescence bloom, ice retreat and duration, and the magnitude of PAR.

The timing of PAR onset (>0.1 μE m^{-2} s^{-1}) was earlier for 2011, variable and often later for 2013–2015, and earlier for 2016–2017 (Fig. 4b). The median of PAR onset was approximately days 95–130 for all years except in 2013, when the median was about day 170. Unlike the timing of PAR onset, the timing of PAR end was similar regardless of the year. In general, the range of PAR end (~80 days, day 224–305) was much narrower than the range of PAR onset (~150 days, day 86–233) (Supplemental Table S1). Thus, the duration of the PAR period was dictated more by the timing of PAR onset than the timing of PAR end, ranging from 6 (C4 in 2014) to 200 days. The median duration of the PAR period was 151 days (Table S1).

The timing of the algal bloom onset was earlier for 2011–2012, later for 2013–2014, and earlier for 2015–2017 (Fig. 4c). The median day of bloom onset was approximately day 160 for 2011–2012, 190 for 2013–2014, and 150 for 2015–2017. The timing of bloom end was later for 2011, earlier for 2013–2015, and mid-range for 2016–2017 (Fig. 4f). The median day of the end of the bloom was about day 320 for 2011, 280 for 2013–2015, and 300 for 2016–2017. The median duration of the bloom was 128 days and the range was 41–190 days (Table S1). One unusual observation was mooring C5 in 2014, which had a much earlier bloom onset (approximately day 130) than that year's median (approximately day 190). This bloom began during a period of variable ice cover, but the ice was not so reduced that it reached the 15% threshold that defined ice retreat (Fig. S1).

Comparing the timing of ice, light and the bloom provides evidence that the near-bottom bloom onset occurs at, or prior to, ice retreat, whereas the end of the bloom followed the loss of light in September (Fig. 9). The timing of bloom onset was related to ice retreat ($r = 0.54$, $p = 0.007$) and weakly related to PAR onset ($r = 0.51$, $p = 0.065$) (Fig. 9). The timing of bloom end was weakly related to PAR end ($r = 0.46$, $p = 0.098$) and unrelated to ice return ($r = 0.26$, $p = 0.199$) (Fig. 9). Based on these results, we computed an alternate index of the growing period, the interval between ice retreat and PAR end. We termed this interval the ice retreat-PAR end duration and found that bloom duration is strongly related to ice retreat-PAR end duration ($r = 0.72$, $p = 0.013$) (Fig. 10).

3.4. Annual fluorescence variation during summer

The growing season near the seafloor typically began with the following sequence: ice retreat, a slight increase in PAR, followed by a reduction of PAR concomitant with an increase in near-bottom chlorophyll fluorescence (e.g. Fig. 8). As the ice melted, ice algae were released from the underside of the ice and dropped to the bottom. During the period of the near-bottom bloom (high fluorescence), PAR was particularly low due to self-shading of the bloom. In addition, open-water phytoplankton blooms in the surface layer or below the surface mixed layer (subsurface), common on the northern Chukchi Shelf (Martini et al., 2016), likely contributed to shading of the water column. Another good example of this sequence of events is mooring C2 in 2013 (Fig. S1), where ice cover decreased to 50% in early July and was quickly followed by increased near-bottom chlorophyll concentration. PAR increased concomitant with declining chlorophyll.

As discussed above, sea-ice return did not determine the end of the growing season. Instead the near-bottom bloom was terminated by the seasonal reduction in light during early fall that preceded ice return during our sample years. The usual sequence at the end of the growing season was: PAR becoming undetectable around days 250–270; the near-bottom bloom ending around days 270–300; and ice returning around days 300–320 (Fig. 4).

The near-bottom bloom onset followed directly on ice retreat whereas the end of the bloom followed loss of light in September. As a result, the growing season (bloom duration) near the seafloor was significantly related to the duration of the period between ice retreat and PAR end. In fact, because there was relatively low variability in the ice return day, the PAR end day, and the bloom end day (Fig. 4), the durations of the bloom, PAR, and the ice-free periods were dictated by the timing of their onsets and not their ends.

3.5. Earlier blooms, polynyas and ice-cover variability

Areas of open water during winter and spring occurred in some years. Most often, this happened at mooring sites C1, C4, and C5 (2010, 2011, 2013, 2014, and 2016; Fig. 3). Each of these moorings is near the coast where the Chukchi polynya occurs (Ladd et al., 2016). Intrusion of warmer, saltier Atlantic Water can contribute to or even cause this polynya (Ladd et al., 2016). Earlier blooms were more common in the Chukchi polynya area (C1, C4, and C5) than outside this area. Using the median bloom onset day (day 154) as a threshold to differentiate "early" from "late" bloom onset, 8 of 12 bloom onsets were early in the Chukchi polynya area and only 4 of 12 bloom onsets from this area were late.

Ice retreat is primarily a result of ice melt or of advection forced by local winds and local currents, or a combination of melt and advection (Ladd et al., 2016). The timing of ice retreat (defined here as the first occurrence of areal ice concentration < 15%) varied among the five primary moorings (C1–C5 for the period 2001–2016), with earliest

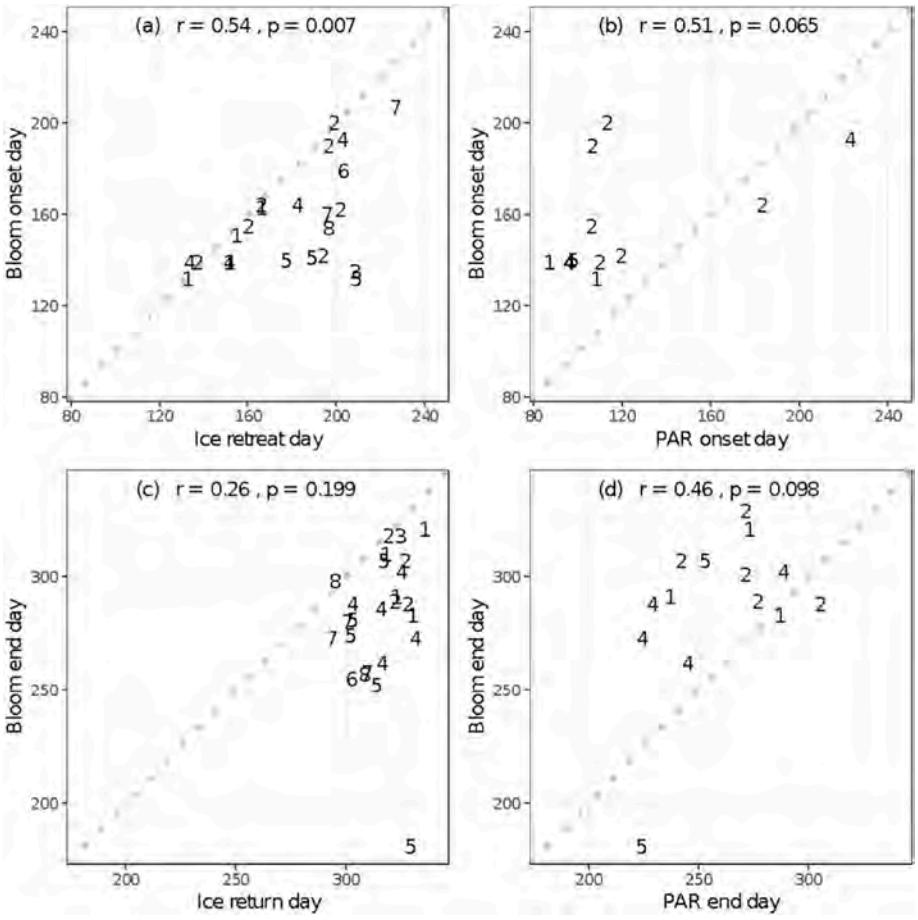

Fig. 9. Scatter plots of the timing of: (a) bloom onset versus ice retreat; (b) bloom onset versus PAR onset; (c) bloom end versus ice return; and (d) bloom end versus PAR end based on near-bottom measurements. The dashed grey line is the 1:1 line.

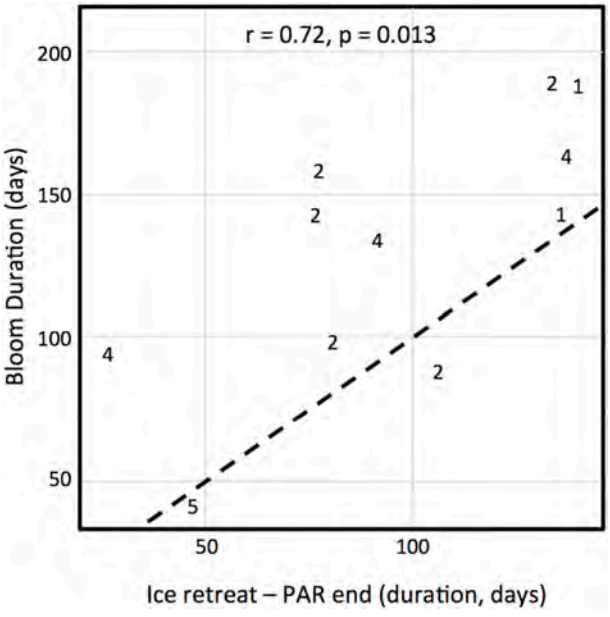

Fig. 10. Scatter plot of the duration of the bloom versus the length of time between ice retreat and PAR end based on near-bottom measurements. The dashed grey line is the 1:1 line.

mean retreat occurring at C1 followed by C4, C2, C3 and, finally, C5. The date of retreat among these five moorings was related with the highest correlation ($r = 0.86$, $p < 0.01$) between the coastal moorings C1 and C4 and the weakest, but still significant, between C1 and C5 ($r = 0.71$, $p < 0.01$). Noting this relationship, the expectation (Fig. 9a) would be that blooms occur earliest at C1 and latest at C3 and C5. Unfortunately, directly examining the timing of the blooms is difficult, because of the limited number of concurrent time series.

Bloom onset was early during years when ice retreated earlier (Fig. 9a) or was episodic in nature. Occasionally ice retreated early, partially returned and then retreated fully for the summer (e.g. mooring C1 in 2012). In this case, a bloom began with the initial ice retreat and continued during the partial return. In other years (e.g. mooring C2 in 2018; Fig. 8) the bloom began with ice retreat and stopped when ice returned. In some years, ice cover was variable during winter and spring (e.g. 2016), PAR increased early (April) and the spring bloom occurred after the early PAR increase (Fig. S1).

Even if ice retreat occurred earlier, an associated chlorophyll maximum was not guaranteed. The earliest observed chlorophyll maxima were during May. For example, a May bloom followed early ice retreat at mooring C5 in 2014 and 2015 (Fig. S1). This can be seen in the 2016 time series; ice cover was irregular in April at moorings C1, C2, and C4, yet substantial fluorescence increases did not occur until May. The lack of a bloom may indicate that either little ice algae were present or the sea ice was advected away (taking its ice algae with it) as opposed to melted.

4. Discussion

4.1. Primary production continues at the seafloor through summer

We found that primary production continued at the seafloor through summer, adding to the primary productivity of the Chukchi Sea, which together with the Chirikov Basin (the region of the northern Bering Sea northeast of St. Lawrence Island) are the most productive regions in the Pacific Arctic (Hill and Cota, 2005; Arrigo et al., 2012; Codispoti et al., 2013; Hill et al., 2017). Virtually all the moorings that successfully measured chlorophyll fluorescence, and either oxygen or nitrate, showed a clear signal of continued production near the seafloor during the summer (Table 1).

We propose that this near-bottom production is due to disassociated ice algae. In most regions with seasonal sea ice, ice algae descend below the photic zone, and thus discontinue to photosynthesize (e.g. Boetius et al., 2013; Rapp et al., 2018). In contrast, much of the Chukchi Sea Shelf is less than 45 m deep and lies within the photic zone. The magnitude of PAR at the Chukchi seafloor was comparable to what was measured beneath the sea ice (Figs. 5d and 8c). Because ice algae can photosynthesize at low levels (Hancke et al., 2018), it is not surprising that photosynthesis by disassociated ice algae may continue near the seafloor. This conclusion is consistent with Koch et al. (2020) who identified disassociated ice algae species together with chlorophyll fluorescence for several months at the seafloor. In addition, the concentration of nitrate in spring and summer is variable, but nitrate usually is sufficient to support some production (see Figs. 2 and 5 in Mordy et al., 2020. With both light and nutrients, the contribution of continued primary production on the seafloor can be substantial and should be considered in estimating primary production in the Chukchi Sea.

4.2. MPL hypothesis

Our results support the hypothesis that continued photosynthesis by disassociated ice algae at the seafloor provides another source of primary production in addition to the spring phytoplankton bloom in the surface mixed layer (Arrigo et al., 2012; Lowry et al., 2014, 2018), the subsurface phytoplankton blooms in the nutrient rich water beneath the surface mixed layer (Lowry et al., 2015; Martini et al., 2016), and the sympagic algal bloom (Gradinger, 2009; Poulin et al., 2011). There is also evidence of a late summer phytoplankton bloom, when summer/fall storms entrain water from the nutrient-rich lower layer (Hill et al., 2017; Ardyna et al., 2014). Together, the various blooms form Multiple Productive Layers that we term the MPL Hypothesis. The MPL hypothesis explains why the Chukchi Sea is highly productive even with a short growing season.

The Chukchi Sea is an inflow shelf (Carmack and Wassmann, 2006). The Arctic Marine Pulses Model describes the Chukchi Sea ecosystem as being dominated by various pulses from the Bering Sea into the Chukchi Sea and from the Arctic basin onto the Chukchi Shelf (Moore et al., 2018). On monthly time scales, inflow through Bering Strait is typically weak in the winter, but in summer this changes with a strong northward flow ($>1 \times 10^6$ m^3 s^{-1}) of relatively warm nutrient-rich, Bering Sea water into the Chukchi Sea (Coachman et al., 1975; Mordy et al., 2020. With the melting of sea ice, a strong pulse of carbon (e.g. ice algae) is exported to the benthic community—an important pelagic-benthic coupling that supports the rich benthic community of the Chukchi Sea (Grebmeier, 2012; Koch et al., 2020). Herein, we add that while there is a sudden pulse of ice algae to the bottom with sea ice melting; in the Chukchi Sea, this near-bottom water remains productive for weeks to months.

4.3. Comparison of Chukchi and Bering Seas

The relationship between the onset of the growing season and ice retreat for the Chukchi Sea also occurs in the northern Bering Sea, but not in the southeastern Bering Sea (Sigler et al., 2014). In the southeastern Bering Sea, the timing of the spring bloom (ice algae and phytoplankton) is dependent on ice and winds (Sigler et al., 2014). If ice retreats early (prior to March 15) or is not present at all, storms continue to mix the upper water column, and the spring bloom commences only after surface waters have warmed enough to stratify the vertical structure. This bloom is only composed of phytoplankton. If ice retreat is late, melt water stabilizes the water column and promotes an early spring, under-ice algal bloom, as well as an open-water phytoplankton bloom near the ice edge. The latter pattern is what occurs in the northern Bering Sea, at least until 2018 (Stabeno and Bell, 2019; Stabeno et al., 2019). In 2018, the lack of sea ice in the northern Bering Sea (mooring M8; 62.2°N, 174.7°W) resulted in a late (June) open water bloom, similar to what occurs in the southeastern Bering Sea during years when there is no ice on the southern shelf after 15 March. While subsurface blooms are uncommon in the southeastern Bering Sea, the northern Bering Sea is similar to the Chukchi Sea, with subsurface blooms being common (Stabeno et al., 2012).

The timing of the spring bloom in the southeastern Bering Sea affects the zooplankton species of the ecosystem, a phenomenon described as the Oscillating Control Hypothesis (OCH) (Hunt et al., 2002, 2011; Stabeno and Hunt, 2002). This control likely is spatially determined and related to the location of the ice edge (Siddon et al., 2013; Sigler et al., 2016). The region where the OCH is effective appears to be moving north as climate warms. For example, the entire eastern Bering Sea Shelf was largely ice free in the winter of 2017–2018, a radical change that was not predicted to occur for at least a few decades (Stabeno et al., 2012; Stabeno and Bell, 2019). The lack of ice had widespread effects on the survival of large crustacean zooplankton and juvenile walleye pollock (Duffy-Anderson et al., 2017). Whether and when the OCH region will move into the Chukchi Sea remains to be examined.

Continued productivity of ice algae that has sunk to the seafloor is probably much greater for the Chukchi Sea Shelf than the eastern Bering Sea Shelf, because the latter's bottom depth is mostly below the photic zone. The eastern Bering Sea Shelf deepens from east to west and the mid-shelf is 50–100 m deep whereas the eastern Chukchi Sea Shelf is predominantly shallower than 45 m. Thus, in the Bering Sea, primary production is limited to under-ice algal blooms, surface mixed layer phytoplankton blooms and subsurface phytoplankton blooms, while in the Chukchi Sea, there is evidence of additional disassociated ice algal production near the seafloor.

4.4. What are the consequences of a shorter ice season?

Sea ice in the Chukchi Sea has been arriving later and retreating earlier for ~30 years (Wood et al., 2015; Serreze et al., 2016; Stroeve et al., 2014) and this pattern is expected to continue (Wang et al., 2018). How changes in ice arrival and retreat will impact primary production in the Chukchi ecosystem is dependent upon how other ecosystem characteristics change. Consider two scenarios (from Berchok et al., 2015). As ice retreats earlier, there will be an earlier export of ice algae to the benthos, but the timing of the spring phytoplankton bloom depends upon wind conditions. If winds are strong, then the water column will be well mixed and the spring phytoplankton bloom will not set up until after winds weaken and water becomes stratified. In contrast, if winds are weak the water column will stratify with a warm, fresher (from ice melt) surface layer. This would support an earlier spring phytoplankton bloom. The first scenario will result in weaker stratification than the second scenario, allowing more short summer blooms supported by input of nutrients during wind events. The complexity of the system makes it difficult to predict how this ecosystem will react to changing ice conditions, but there is consensus on some changes.

With climate warming, there will be a decrease in the duration of sea ice over the Chukchi Sea (Wang et al., 2018). Earlier ice retreat will result in earlier export of ice algae to the seafloor, where there should be sufficient nutrients and light to support a near bottom algal bloom

(Tedesco et al., 2019). The one caveat to this scenario is: can the sea-ice retreat occur "too early". Considering that from our analysis there is insufficient light after the fall equinox to support algal production on the seafloor, it is likely that any ice algae dropping to the seafloor before the spring equinox, also will be non-productive. Ice retreat prior to the spring equinox, however, is not predicted to occur prior to 2050 (Wang et al., 2018). In contrast to earlier ice retreats, delayed ice return will have little impact on near-bottom algal blooms, since they are largely controlled by the availability of light.

Ice algae, however, is only one component in primary production in the Chukchi Sea. Changes in phytoplankton blooms in spring (upper mixed layer), in the summer (sub-pycnocline) and fall (near surface) have been discussed by others. In open water, phytoplankton production may increase, because of a longer growing season (Arrigo and van Dijken, 2015; Arrigo et al., 2008; Brown et al., 2015), although nutrients could be limiting. Once nutrients are consumed in the surface layer, a bloom often forms below the surface mixed layer (e.g. Martini et al., 2016; Lowry et al., 2015). This bloom can be substantial, providing more than a third of primary productivity in the Beaufort Sea (Martin et al., 2013). Churnside et al. (2020) suggest that with reduction in sea ice, the occurrence of these subsurface blooms could increase. These subsurface phytoplankton blooms would likely compete for nutrients with the near-bottom algal blooms and may reduce near-bottom algal production through shading.

5. Summary

The Chukchi Sea is highly productive even though the growing season is short. We provide evidence of production at multiple layers and hypothesize that near-bottom production is a result of disassociated ice algae near the seafloor. On the basis of this evidence, we propose the MPL hypothesis, where high production is promoted by a shallow seafloor, which allows multiple production layers (surface, sub-surface, sympagic ice algae, and disassociated ice algae near the seafloor; Fig. 2). High production occurs because the amount of light near the seafloor in mid-spring to early fall is similar to that measured beneath a 1.5-m thick ice floe. With sufficient light near the seafloor (~40 m deep), ice algae continue to photosynthesize, utilizing nitrate and producing oxygen through summer; a unique feature that pertains to this shallow shelf.

Bloom onset occurred in summer following ice retreat, whereas the end of the bloom occurred in September following loss of light. While this is a complex system, with multiple feedbacks and thus difficult to predict, our results do suggest certain possibilities. Even in a changing system with ice retreating later and arriving earlier, the primary change will be the timing of the export of ice algae to the bottom. Thus, the duration of near-bottom primary productivity will lengthen, because bloom onset occurs earlier.

CRediT authorship contribution statement

Phyllis J. Stabeno: Conceptualization, Methodology, Validation, Resources, Formal analysis, Investigation, Data curation, Writing - original draft, Writing - review & editing, Funding acquisition, Supervision, Visualization. **Calvin W. Mordy:** Conceptualization, Methodology, Validation, Resources, Investigation, Data curation, Funding acquisition, Writing - original draft, Writing - review & editing. **Michael F. Sigler:** Conceptualization, Methodology, Formal analysis, Writing - original draft, Writing - review & editing, Supervision, Visualization.

Declaration of competing interest

The authors declare that they have no known competing financial interests or personal relationships that could have appeared to influence the work reported in this paper.

Acknowledgements

Support was provided by the National Oceanic and Atmospheric Administration; the Bureau of Ocean Energy Management CHAOZ, CHAOZ-X and ArcWEST programs; the NPRB Arctic Program (A92-02a, A92-02b); and the Joint Institute for the Study of the Atmosphere and Ocean (JISAO) under NOAA Cooperative Agreement NA15OAR4320063. We thank S. Bell for data analysis; S. Donohoe for building the pop-up buoys; Leo MacLeod for tracking the ice floe; C. Berchok for being principal investigator on the three BOEM programs, and S. Salo, D. Strausz, G. Lebon, and S. Grassia, for preparing equipment, processing data, and deploying and recovering the moorings. This manuscript is included as part of the North Pacific Research Board (NPRB) Arctic Integrated Ecosystem Research Program, NPRB publication ArcticIERP-09. It is contribution No. 5010 for Pacific Marine Environmental Laboratory, contribution No. 2020–1064 for JISAO, and contribution No. 0933 for NOAA's Ecosystem Fisheries Oceanography Coordinated Investigations.

Appendix A. Supplementary data

Supplementary data to this article can be found online at https://doi.org/10.1016/j.dsr2.2020.104842.

References

Ambrose, W.G., Von Quillfeldt, C., Clough, L.M., Tilney, P.V., Tucker, T., 2005. The sub-ice algal community in the Chukchi sea: large-and small-scale patterns of abundance based on images from a remotely operated vehicle. Polar Biol. 28 (10), 784–795.

Ardyna, M., Babin, M., Gosselin, M., Devred, E., Rainville, L., Tremblay, J.-É., 2014. Recent Arctic Ocean sea ice loss triggers novel fall phytoplankton blooms. Geophys. Res. Lett. 41 (17), 6207–6212. https://doi.org/10.1002/2014GL061047.

Arrigo, K.R., van Dijken, G.L., 2011. Secular trends in Arctic Ocean net primary production. J. Geophys. Res. Oceans 116(C9), C09011. https://doi.org/10.1029/2011JC007151.

Arrigo, K.R., van Dijken, G., 2015. Continued increases in Arctic Ocean primary production. Prog. Oceanogr. 136, 60–70. https://doi.org/10.1016/j.pocean.2015.05.002.

Arrigo, K.R., van Dijken, G., Pabi, S., 2008. Impact of a shrinking Arctic ice cover on marine primary production. Geophys. Res. Lett. 35, L19603. https://doi.org/10.1029/2008GL035028.

Arrigo, K.R., Perovich, D., Pickart, R., Brown, Z., van Dijken, G., Lowry, K., et al., 2012. Massive phytoplankton blooms under Arctic sea ice. Science 336(6087) 1408. https://doi.org/10.1126/science.1215065.

Berchok, C.L., Crance, J.L., Garland, E.C., Mocklin, J.A., Stabeno, P.J., Napp, J.M., Rone, B.K., Spear, A.H., Wang, M., Clark, C.W., 2015. Chukchi Offshore Monitoring In Drilling Area (COMIDA): Factors Affecting the Distribution and Relative Abundance of Endangered Whales and Other Marine Mammals in the Chukchi Sea. Final Report of the Chukchi Sea Acoustics, Oceanography, and Zooplankton Study, OCS Study BOEM 2015-034. National Marine Mammal Laboratory, Alaska Fisheries Science Center, NMFS, NOAA, 7600 Sand Point Way NE, Seattle, WA 98115-6349.

Boetius, A., Albrecht, S., Bakker, K., Bienhold, C., Felden, J., Fernández-Méndez, M., Hendricks, S., Katlein, C., Lalande, C., Krumpen, T., Nicolaus, M., 2013. Export of algal biomass from the melting Arctic sea ice. Science 339 (6126), 1430–1432.

Brown, Z.W., Lowry, K.E., Palmer, M.A., van Dijken, G.L., Mills, M.M., Pickart, R.S., Arrigo, K.R., 2015. Characterizing the subsurface chlorophyll *a* maximum in the Chukchi sea and Canada basin. Deep-Sea Res. Part II 118 (A), 88–104. https://doi.org/10.1016/j.dsr2.2015.02.010.

Carmack, E., Wassmann, P., 2006. Food webs and physical-biological coupling on pan-Arctic shelves: unifying concepts and comprehensive perspectives. Prog. Oceanogr. 71, 446–477.

Castellani, G., Losch, m., Lange, B., Flores, H., 2017. Modeling Arctic sea-ice algae: physical drivers of spatial distribution and algae phenology. J. Geophys. Res. Oceans 122, 7466–7487. https://doi.org/10.1002/2017JC012828.

Churnside, J.H., Marchbanks, R.D., Vagle, S., Bell, S.W., Stabeno, P.J., 2020. Stratification, plankton layers, and mixing measured by airborne lidar in the Chukchi and Beaufort seas. Deep-Sea Res. Part II this issue.

Coachman, L.K., Aagaard, K., Tripp, R.B., 1975. Bering Strait: The Regional Physical Oceanography. University of Washington Press, Seattle, WA.

Codispoti, L.A., Kelly, V., Thessen, A., Matrai, P., Suttles, S., Hill, V., Steele, M., Light, B., 2013. Synthesis of primary production in the Arctic Ocean: III. Nitrate and phosphate based estimates of net community production. Prog. Oceanogr. 110, 126–150.

Cota, G.F., Horne, E.P.W., 1989. Physical control of arctic ice algal production. Mar. Ecol. Prog. Ser 52, 111–121.

Cota, G.F., Prinsenberg, S.J., Bennett, E.B., Loder, J.W., Lewis, M.R., Anning, J.L., et al., 1987. Nutrient fluxes during extended blooms of Arctic ice algae. J. Geophys. Res.: Oceans 92 (C2), 1951–1962.

Danielson, S.L., Ahkinga, O., Ashjian, C., Basyuk, E., Cooper, L.W., Eisner, L., et al., 2020. Manifestation and consequences of warming and altered heat fluxes over the Bering and Chukchi Sea continental shelves. Deep-Sea Res. Part II this issue.

Duffy-Anderson, J.T., Stabeno, P.J., Siddon, E.C., Andrews, A.G., Cooper, D.W., Eisner, L. B., Farley, E.V., Harpold, C.E., Heintz, R.A., Kimmel, D.G., Sewall, F.F., Spear, A.H., Yasumishii, E.C., 2017. Return of warm conditions in the southeastern Bering Sea: phytoplankton–fish. PLoS ONE 12(6), e0178955. https://doi.org/10.1371/journal.pone.0178955.

Dunton, K.H., Grebmeier, J.M., Trefry, J.H., 2014. The benthic ecosystem of the northeastern Chukchi Sea: an overview of its unique biogeochemical and biological characteristics. Deep-Sea Res. Part II 102, 1–8. https://doi.org/10.1016/j.dsr2.2014.01.001.

Fernández-Méndez, M., Wenzhöfer, F., Peeken, I., Sørensen, H.L., Glud, R.N., Boetius, A., 2014. Composition, buoyancy regulation and fate of ice algal aggregates in the Central Arctic Ocean. PloS One 9 (9), e107452. https://doi.org/10.1371/journal.pone.0107452.

Frey, K.E., Moore, G.W.K., Cooper, L.W., Grebmeier, J.M., 2015. Divergent patterns of recent sea ice cover across the bering, Chukchi, and Beaufort seas of the pacific arctic region. Prog. Oceanography 136, 32–49.

Gradinger, R., 2009. Sea-ice algae: major contributors to primary production and algal biomass in the Chukchi and Beaufort Seas during. Deep-Sea Res. Part II 56 (17), 1201–1212. https://doi.org/10.1016/j.dsr2.2008.10.016. May/June 2002.

Grebmeier, J., 2012. Shifting patterns of life in the Pacific Arctic and sub-arctic seas. Annu. Rev. Mar. Sci. 4, 16, 1–16.6.

Grebmeier, J., Overland, J.E., Moore, S.E., Farley, E.V., Carmack, E.C., Cooper, L.W., Frey, K.E., Helle, J.H., McLaughlin, F.A., McNutt, S.L., 2006. A major ecosystem shift in the northern Bering Sea. Science 311, 1461–1464. https://doi.org/10.1126/science.1121365.

Grebmeier, J., Bluhm, B., Cooper, L., Denisenko, S., Iken, K., Kędra, M., Serratos, C., 2015. Time-series benthic community composition and biomass and associated environmental characteristics in the Chukchi Sea during the RUSALCA 2004–2012 program. Oceanography 28 (3), 116–133.

Hancke, K., Lund-Hansen, L.C., Lamare, M.L., Højlund Pedersen, S., King, M.D., Andersen, P., Sorrell, B.K., 2018. Extreme low light requirement for algae growth underneath sea ice: a case study from Station Nord, NE Greenland. J. Geophys. Res.: Oceans 123, 985–1000. https://doi.org/10.1002/2017JC013263.

Hill, V., Cota, G., 2005. Spatial patterns of primary production on the shelf, slope and basin of the Western Arctic in 2002. Deep Sea Res. Part II 52 (24–26), 3344–3354.

Hill, V., Ardyna, M., Lee, S., Varela, D., 2017. Decadal trends in phytoplankton production in the Pacific Arctic region from 1950 to 2012. Deep-Sea Res. Part II 152, 82–94. https://doi.org/10.1016/j.dsr2.2016.12.015.

Hirano, D., Fukamachi, Y., Watanabe, E., Ohshima, K.I., Iwamoto, K., Mahoney, A.R., Eicken, H., Simizu, D., Tamura, T., 2016. A wind-driven, hybrid latent and sensible heat coastal polynya off Barrow, Alaska. J. Geophys. Res. Oceans 121, 980–997. https://doi.org/10.1002/2015JC011318.

Hunt Jr., G.L., Stabeno, P., Walters, G., Sinclair, E., Brodeur, R.D., Napp, J.M., Bond, N. A., 2002. Climate change and control of the southeastern Bering Sea pelagic ecosystem. Deep-Sea Res. Part II 49 (26), 5821–5853. https://doi.org/10.1016/S0967-0645(02)00321-1.

Hunt Jr., G.L., Coyle, K.O., Eisner, L., Farley, E.V., Heintz, R., Mueter, F., Napp, J.M., Overland, J.E., Ressler, P.H., Salo, S., Stabeno, P.J., 2011. Climate impacts on eastern Bering Sea foodwebs: a synthesis of new data and an assessment of the Oscillating Control Hypothesis. ICES J. Mar. Sci. 68 (6), 1230–1243. https://doi.org/10.1093/icesjms/fsr036.

Katlein, C., Fernández-Méndez, M., Wenzhöfer, F., Nicolaus, M., 2015. Distribution of algal aggregates under summer sea ice in the Central Arctic. Polar Biol. 38 (5), 719–731.

Koch, C.W., Cooper, L.W., Lalande, C., Brown, T.A., Frey, K.E., Grebmeier, J.M., 2020. Seasonal and latitudinal variations in sea ice algae deposition in the Northern Bering and Chukchi Seas determined by algal biomarkers. PLoS ONE 15(4), e0231178. https://doi.org/10.1371/journal.pone.0231178.

Ladd, C., Mordy, C.W., Salo, S.A., Stabeno, P.J., 2016. Winter water properties and the Chukchi polynya. J. Geophys. Res. 121 (8), 5516–5534. https://doi.org/10.1002/2016JC011918.

Langis, D., Stabeno, P.J., Meinig, C., Mordy, C.W., Bell, S.W., Tabisola, H.M., October 2018. 2018. Low-cost expendable buoys for under ice data collection. In: Oceans 2018 MTS/IEEE Charleston, Marine Technology Society and IEEE Oceanic Engineering Society. IEEE, Charleston, SC, pp. 22–25. https://doi.org/10.1109/OCEANS.2018.8604752.

Lowry, K.E., van Dijken, G.L., Arrigo, K.R., 2014. Evidence of under-ice phytoplankton blooms in the Chukchi sea from 1998 to 2012. Deep Sea Res. Part II 105, 105–117. https://doi.org/10.1016/j.dsr2.2014.03.013.

Lowry, K.E., Pickart, R.S., Mills, M.M., Brown, Z.W., van Dijken, G.L., Bates, N.R., Arrigo, K.R., 2015. The influence of winter water on phytoplankton blooms in the Chukchi Sea. Deep-Sea Res. Part II 118, 53–72.

Lowry, K.E., Pickart, R.S., Selz, V., Mills, M.M., Pacini, A., Lewis, K.M., et al., 2018. Under-ice phytoplankton blooms inhibited by spring convective mixing in refreezing leads. J. Geophys. Res. Oceans 123 (1), 90–109.

Martin, J., Dumont, D., Tremblay, J.-É., 2013. Contribution of subsurface chlorophyll maxima to primary production in the coastal Beaufort Sea (Canadian Arctic): a model assessment. J. Geophys. Res. Oceans 118 (11), 5873–5886. https://doi.org/10.1002/2013JC008843.

Martini, K.I., Stabeno, P.J., Ladd, C., Winsor, P., Weingartner, T.J., Mordy, C.W., Eisner, L.B., 2016. Dependence of subsurface chlorophyll on seasonal water masses in the Chukchi Sea. J. Geophys. Res. 121 (3), 1755–1770. https://doi.org/10.1002/2015JC011359.

Michel, C., Legendre, L., Demers, S., Therriault, J.-C., 1988. Photoadaptation of sea-ice microalgae in springtime: photosynthesis and carboxylating enzymes. Mar. Eco. Prog. Ser 50, 177–185.

Michel, C., Legendre, L., Therriault, J._C., Demers, S., Vandevelde, T., 1993. Springtime coupling between ice algal and phytoplankton assemblages in southeastern Hudson Bay, Canadian Arctic. Polar Biol. 13, 441–449. https://doi.org/10.1007/BF00233135.

Moore, S.E., Stabeno, P.J., 2015. Synthesis of arctic Research (SOAR) in marine ecosystems of the pacific arctic. Prog. Oceanography 136, 1–11. https://doi.org/10.1016/j.pocean.2015.05.017.

Moore, S.E., Stabeno, P.J., Grebmeier, J.M., Okkonen, S.R., 2018. The arctic marine pulses model: linking annual oceanographic processes to contiguous ecological domains in the pacific arctic. Deep-sea res. Part II 152. SOAR II 8–21. https://doi.org/10.1016/j.dsr2.2016.10.011.

Mordy, C., Bell, S., Cokelet, E., Ladd, C., Lebon, G., Proctor, P., Stabeno, P., Strausz, D., Wisegarver, E., 2020. This Issue. Seasonal Variability of Nitrate in the Eastern Chukchi Sea. Deep-Sea Res. Part II.

Neeley, A.R., Harris, L.A., Frey, K.E., 2018. Unraveling phytoplankton community dynamics in the northern Chukchi Sea under sea-ice-covered and sea-ice-free conditions. Geophys. Res. Lett. 45 (15), 7663–7671.

Poulin, M., Daugbjerg, N., Gradinger, R., Ilyash, L., Ratkova, T., von Quillfeldt, C., 2011. The pan-Arctic biodiversity of marine pelagic and sea-ice unicellular eukaryotes: a first-attempt assessment. Mar. Biodivers. 41, 13–28. https://doi.org/10.1007/s12526-010-0058-8.

Rapp, J.Z., Fernández-Méndez, M., Bienhold, C., Boetius, A., 2018. Effects of ice-algal aggregate export on the connectivity of bacterial communities in the central Arctic Ocean. Front. Microbiol. 9, 1035.

Riebesell, U., Schloss, I., Smetacek, V., 1991. Aggregation of algae released from melting sea ice: implications for seeding and sedimentation. Polar Biol. 11 (4), 239–248.

Serreze, M.C., Crawford, A.D., Stroeve, J.C., Barrett, A.P., Woodgate, R.A., 2016. Variability, trends, and predictability of seasonal sea ice retreat and advance in the Chukchi Sea. J. Geophys. Res. Oceans 121 (10), 7308–7325. https://doi.org/10.1002/2016jc011977.

Siddon, E., Heintz, R., Mueter, F., 2013. Conceptual model of energy allocation in walleye pollock (*Theragra chalcogramma*) from age-0 to age-1 in the southeastern Bering Sea. Deep-Sea Res. Part II 94, 140–149. https://doi.org/10.1016/j.dsr2.2012.12.007.

Sigler, M.F., Stabeno, P.J., Eisner, L.B., Napp, J.M., Mueter, F.J., 2014. Spring and fall phytoplankton blooms in a productive subarctic ecosystem, the eastern Bering Sea, during 1995–2011. Deep-Sea Res. Part II 109, 71–83. https://doi.org/10.1016/j.dsr2.2013.12.007.

Sigler, M.F., Napp, J.M., Stabeno, P.J., Heintz, R.A., Lomas, M.W., Hunt Jr., G.L., 2016. Variation in annual production of copepods, euphausiids, and juvenile walleye pollock in the southeastern Bering Sea. Deep-Sea Res. Part II 134, Understanding Ecosystem Processes in the Eastern Bering Sea IV 223–234. https://doi.org/10.1016/j.dsr2.2016.01.003.

Stabeno, P.J., Bell, S.W., 2019. Extreme conditions in the Bering Sea (2017–2018): record-breaking low sea-ice extent. Geophys. Res. Lett. 46 (15), 8952–8959. https://doi.org/10.1029/2019GL083816.

Stabeno, P.J., Hunt Jr., G.L., 2002. Overview of the inner front and southeast Bering Sea carrying capacity programs. Deep-Sea Res. Part II 49 (26), 6157–6168. https://doi.org/10.1016/S0967-0645(02)00339-9.

Stabeno, P.J., Farley, E., Kachel, N., Moore, S., Mordy, C., Napp, J.M., Overland, J.E., Pinchuk, A.I., Sigler, M.F., 2012. A comparison of the physics of the northern and southern shelves of the eastern Bering Sea and some implications for the ecosystem. Deep-Sea Res. Part II 65–70, 14–30. https://doi.org/10.1016/j.dsr2.2012.02.019.

Stabeno, P., Kachel, N., Ladd, C., Woodgate, R., 2018. Flow patterns in the eastern Chukchi sea: 2010–2015. J. Geophys. Res. 123 (2), 1177–1195. https://doi.org/10.1002/2017JC013135.

Stabeno, P.J., Bell, S., Bond, N., Kimmel, D., Mordy, C., Sullivan, M., 2019. Distributed biological observatory region 1: physics, chemistry and plankton in the northern Bering Sea. Deep-Sea Res. Part II 162, 8–21. https://doi.org/10.1016/j.dsr2.2018.11.006.

Stroeve, J.C., Markus, T., Boisvert, L., Miller, J., Barret, A., 2014. Changes in Arctic melt season and implications for sea ice loss. Geophys. Res. Lett. 41, 1216–1225. https://doi.org/10.1002/2013GL058951.

Tedesco, L., Vichi, M., Scoccimarro, E., 2019. Sea-ice algal phenology in a warmer Arctic. Sci. Adv 5 (5), eaav4830. https://doi.org/10.1126/sciadv.aav4830.

Tremblay, G., Belzile, C., Gosselin, M., Poulin, M., Roy, S., Tremblay, J.É., 2009. Late summer phytoplankton distribution along a 3500 km transect in Canadian Arctic waters: strong numerical dominance by picoeukaryotes. Aquat. Microb. Ecol. 54 (1), 55–70.

Wang, M., Yang, Q., Overland, J.E., Stabeno, P.J., 2018. Sea-ice cover timing in the Pacific Arctic: the present and projections to mid-century by selected CMIP5 models. Deep-Sea Res. Part II 152. SOAR II 22–34. https://doi.org/10.1016/j.dsr2.2017.11.017.

Welch, H.E., Bergmann, M.A., 1989. Seasonal development of ice algae and its prediction from environmental factors near Resolute, NWT, Canada. Can. J. Fish. Aquat. Sci. 46 (10), 1793–1804.

Wood, K.R., Bond, N.A., Overland, J.E., Salo, S.A., Stabeno, P., Whitefield, J., 2015. A decade of environmental change in the Pacific Arctic region. Prog. Oceanography 136, 12–31. https://doi.org/10.1016/j.pocean.2015.05.005.

Wood, K.R., Jayne, S.R., Mordy, C.W., Bond, N., Overland, J.E., Ladd, C., Stabeno, P.J., Ekholm, A.K., Robbins, P.E., Schreck, M.-B., Heim, R., Intrieri, J., 2018. Results of the first. Arctic Heat Open Science Experiment. Bull. Am. Meteorol. Soc. 99 (3), 513–520. https://doi.org/10.1175/BAMS-D-16-0323.1.

Deep–Sea Research II 177 (2020) 104730

Contents lists available at ScienceDirect

Deep-Sea Research Part II

journal homepage: http://www.elsevier.com/locate/dsr2

Annual cycle of export fluxes of biogenic matter near Hanna Shoal in the northeast Chukchi Sea

Catherine Lalande [a,*], Jacqueline M. Grebmeier [b], Russell R. Hopcroft [c], Seth L. Danielson [c]

[a] Amundsen Science, Université Laval, Québec, QC, Canada
[b] Chesapeake Biological Laboratory, University of Maryland Center for Environmental Science, Solomons, MD, USA
[c] College of Fisheries and Ocean Sciences, University of Alaska Fairbanks, Fairbanks, AK, USA

ARTICLE INFO

Keywords:
Arctic Ocean
Chukchi Sea
Export
Sediment trap
Microalgae
Zooplankton
Observatory

ABSTRACT

The Chukchi Ecosystem Observatory (CEO), a mooring array of subsurface oceanographic instruments, was established on the northeast Chukchi Sea continental shelf to obtain time-series measurements of physical, biogeochemical, and biological parameters. A sequential sediment trap was deployed on a CEO mooring 8 m above seafloor to measure export fluxes of chlorophyll *a* (chl *a*), microalgal cells, zooplankton fecal pellets, total particulate matter (TPM), particulate organic carbon (POC), and zooplankton actively entering the trap from August 2015 to July 2016. These time-series measurements allowed us to monitor sympagic and pelagic algal production, the seasonal development of the zooplankton community, pelagic-benthic coupling, and particulate matter export in relation to snow and sea-ice cover on the shallow Chukchi Sea continental shelf. Notably, chl *a* and algal fluxes were nearly as high from August to October 2015 as in June–July 2016, indicating substantial autumn production. Autumn algal fluxes were dominated by the epipelic *Cylindrotheca closterium* while summer fluxes were dominated by pennate diatoms, including *Fossula arctica* and *Neodenticula seminae*. Peaks in the export of the exclusively sympagic diatom *Nitzschia frigida* in May and June 2016 indicated the release of ice algae due to snow and ice melt events. While pelagic copepods *Calanus glacialis/marshallae*, *Pseudocalanus* spp. and *Oithona similis* were the dominant copepods collected in the sediment trap, meroplanktonic stages of benthic organisms displayed the largest abundances and reflected mixing of pelagic stages and resuspension events on the shallow Chukchi Sea shelf. Enhanced fecal pellet carbon fluxes reflected zooplankton grazing in August and September 2015 and in July 2016. Despite the grazing pressure, high chl *a*, diatom and POC fluxes during these periods allowed strong pelagic-benthic coupling in the northeast Chukchi Sea. Persistent summer and autumn production also suggest that the local benthic community benefits from a sustained food supply rather than episodic flux events. Overall, these observations demonstrate the importance of year-round monitoring for fully understanding the phenology of marine processes and set a baseline for understanding the impact of environmental changes on Arctic marine ecosystems.

1. Introduction

Decades of physical and biological sampling in the Pacific Arctic region have revealed that the abundant nutrient supply of Pacific waters flowing into the Chukchi Sea through the Bering Strait supports one of the most productive marine ecosystems of the Arctic Ocean (Grebmeier and Maslowski, 2014). The constant input of nutrient-rich waters leads to sympagic algae production (~1–2 g C m^{-2}) and large pelagic blooms (up to ~200 g C m^{-2} yr^{-1}) on the southern Chukchi Shelf just north of Bering Strait (Gradinger, 2009; Hill et al., 2018; Wang et al., 2018). On the northern Chukchi Shelf, stratification following ice melt results in a seasonally nutrient-depleted surface layer over much of the shelf but production at or below the mixed layer depth may persist to the end of summer and reach up to 90 g C m^{-2} yr^{-1} (Hill and Cota, 2005; Questel et al., 2013; Danielson et al., 2017a). The high levels of primary production at several regional hotspots in the Chukchi Sea support large populations of zooplankton, pelagic fishes, seabirds, and marine mammals (Ershova et al., 2015; Kuletz et al., 2015; Logerwell et al., 2015; De Robertis et al., 2017; Moore and Kuletz, 2019), and lead to large export fluxes of biogenic matter sustaining rich benthic communities (Grebmeier et al., 1988, 2006b, 2015; Lalande et al., 2007). Similar to the northern Bering Sea, the Chukchi Sea has recently experienced a rapid

* Corresponding author.
E-mail address: catherine.lalande@as.ulaval.ca (C. Lalande).

https://doi.org/10.1016/j.dsr2.2020.104730
Received 17 January 2019; Received in revised form 4 January 2020; Accepted 5 January 2020
Available online 7 January 2020

reduction in seasonal sea-ice cover and an increase in air and ocean temperatures that may result in a shift from Arctic to subarctic conditions (Grebmeier et al., 2006b, 2018; Shimada et al., 2006; Woodgate et al., 2012; Baker et al., 2020).

Except for a few notable programs with shipboard operations early (May–June) in the productive season (e.g. Hill and Cota, 2005; Arrigo et al., 2012; Baker and Dickson, 2020; Danielson et al., 2020), most of the sampling effort in the Chukchi Sea takes place closer to the annual minimum sea ice cover period (July-August-September), providing snapshots of the physical conditions and marine ecosystem only relatively late in the growing season. The lack of regular ship-based observations between October and June results in a critical observational gap for the majority of the seasonal cycle. This gap motivated the establishment of the Chukchi Ecosystem Observatory (CEO), an array of subsurface oceanographic instruments deployed on the northeast Chukchi Sea continental shelf near Hanna Shoal (71° 35.976′ N, 161° 31.621' W), to obtain continuous, high-resolution, and year-round measurements of physical, biogeochemical, and biological parameters (Fig. 1; Danielson et al., 2017b; Hauri et al., 2018). The CEO moorings are equipped with sensors that collectively measure temporal variations in sea-ice cover and thickness, light, currents, waves, water column structure, dissolved oxygen, nitrate, inorganic carbon, particulate matter, sympagic and pelagic algal export, and local zooplankton communities, fish populations, and marine mammal vocalizations (Danielson et al., 2017b; Hauri et al., 2018).

Here, we present results on the continuous export fluxes of biogenic matter obtained from a sequential sediment trap deployed at the CEO from August 18, 2015 to July 31, 2016. Export fluxes were used to evaluate the phenology and makeup of algal production, the seasonal development of the zooplankton community, pelagic-benthic coupling, and particulate matter export in relation to snow and sea-ice cover on the shallow Chukchi Sea continental shelf. Due to the nature of mooring deployment and recovery in seasonally ice-covered regions, the time frame of the annual cycle from late August to the following July prevented the analysis of a complete production cycle. This constraint will be eliminated by maintaining consecutive sediment trap deployments at the CEO. In the current context of a period of rapid changes, this annual cycle of export fluxes provides a benchmark against which to assess natural variability and the impact of climate change on this productive Arctic marine ecosystem.

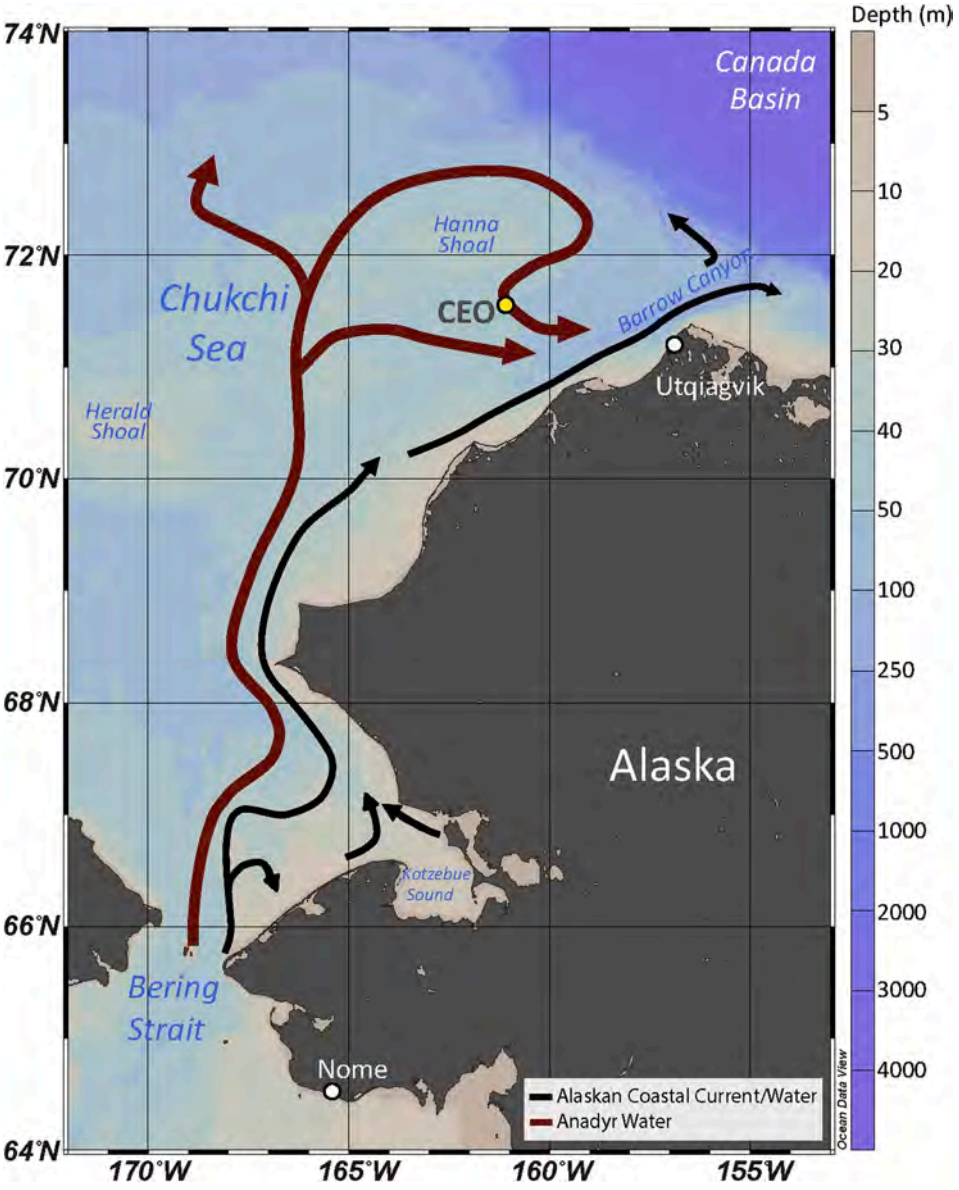

Fig. 1. Location of the Chukchi Ecosystem Observatory in the Chukchi Sea (71° 35.976′ N, 161° 31.621′ W).

2. Methods

2.1. Remote sensing

Daily averaged sea-ice concentrations were retrieved at a 12.5-km resolution from the Centre ERS d'Archivage et de Traitement (CERSAT) service of the French Research Institute for Exploitation of the Sea (http://cersat.ifremer.fr/). Snow depth on top of sea ice was retrieved at a 25-km resolution from the Northern Hemisphere snow depth files derived from the Scanning Multichannel Microwave Radiometer (SMMR) and the Special Sensor Microwave/Imager (SSM/I) of the National Aeronautics Space Agency (https://neptune.gsfc.nasa.gov; Comiso et al., 2003). Daily sea-ice concentration and snow depth were averaged for a delimited region above the mooring (44 × 44 km; 71.4–71.8°N; 161.4–161.9°W; Fig. 1).

2.2. Sequential sediment trap

A sequential sediment trap (Hydro-Bios, Germany) was deployed at 37 m depth, 8 m above seafloor, on the biogeochemistry mooring of the CEO (Fig. 1). CEO moorings were deployed from the R/V *Norseman II* in August 2015 and recovered from the USCGC *Healy* in August 2016. Collection cups rotated at pre-programmed intervals ranging from one week during spring and summer to one month during winter. Because the sediment trap was recovered before the completion of the last rotation, the last open sample was excluded from the study. Collection cups were filled with filtered seawater adjusted to a salinity of 38 with NaCl and fixed with formalin (4% final solution) to preserve samples during deployment and after recovery.

In the laboratory, zooplankton and meroplankton actively entering the collection cups (swimmers) were removed from a fraction of the samples with forceps and identified to the lowest taxonomic level possible using a dissecting microscope. Sample cups were then gently mixed before subsamples (0.1–3 ml) were taken with a modified micropipette to enable the collection of large particles for measurements of chl *a*, microalgal cells, zooplankton fecal pellets, total particulate matter (TPM), and particulate organic carbon (POC). Subsamples for chl *a* measurements were filtered onto GF/F filters (0.7 μm), extracted in acetone for 24 h at −20 °C and measured on a Turner Design fluorometer following the methods outlined in Welschmeyer (1994). Samples were kept cool and in the dark prior to chl *a* measurements but may have experienced some degradation, even when preserved in a formalin solution. For the enumeration of algal cells, subsample volumes were adjusted to 3 ml with filtered seawater when needed before being placed in an Utermöhl chamber. A minimum of 300 algal cells were counted and identified by inverted microscopy at 100X, 200X or 400X depending on cell size according to the Utermöhl method (Utermöhl, 1931). Subsamples for the enumeration and measurement of zooplankton fecal pellets were sieved to remove small sandy particles before observation using a dissecting scope. The length and width of fecal pellets (broken or intact) were measured with an ocular micrometer and fecal pellet volumes were calculated according to their shape. Cylindrical pellets were attributed to calanoid copepods while ellipsoidal pellets were attributed to appendicularians (González et al., 1994). Fecal pellet volumes were converted to fecal pellet carbon (FPC) using a volumetric carbon conversion factor of 0.057 mg C mm^{-3} for copepod pellets and 0.042 mg C mm^{-3} for appendicularian pellets (González et al., 1994). Subsamples for TPM measurements were filtered onto pre-combusted (500 °C overnight) and pre-weighed GF/F filters (0.7 μm), rinsed with distilled water to remove salt, dried at 60 °C overnight, and weighed on a microbalance. The same filters were then exposed to 1N HCl overnight for removal of inorganic carbon and dried once again at 60 °C overnight before encapsulation for POC measurements. POC measurements were conducted on a PerkinElmer CHNS 2400 Series II elemental analyzer. All measurements were converted to daily flux rates depending on the open cup duration of each sample and integrated to annual fluxes.

3. Results

3.1. Sunlight, snow, sea ice, air temperature

The northeast Chukchi Sea was ice free and had >18 daylight hours at the start of the sediment trap deployment in August 2015 (Fig. 2a). Sea-ice cover began to form and snow started to accumulate at the CEO site on November 7, a few days before the CEO site entered the polar night on November 20 (sunrise and sunset times; https://aa.usno.navy.mil). Six months later in May 2016, satellite-derived snow depths revealed an early season snow melt event coinciding with the onset of the polar day on May 12, followed by gradual snow melt through June and July (Fig. 2b). The cause of the mid-May snow melt event was linked to the air temperature recorded at the nearby coastal city of Utqiaġvik (170 km east of the CEO), where air temperatures increased and remained above 0 °C for 83 consecutive hours over May 10–14, with maximum temperatures exceeding 5 °C (Fig. 2a). Although low-salinity sea-ice melt waters at the mooring position were first observed at the end of June (Hauri et al., 2018), sea ice remained in the region until the last sample collection in July 2016 (Fig. 2b).

3.2. Algal fluxes

The contribution of diatoms ranged from ~93 to 100% of the total microalgal flux at 8 m above the seafloor, with 30–73% of diatoms containing chloroplasts (data not shown). High chl *a* and diatom fluxes (>1.5 mg m^{-2} d^{-1} and >2000 million cells m^{-2} d^{-1}, respectively) were observed from August to October and in late June and July (Fig. 3a and b). Chlorophyll *a* fluxes drastically decreased below 0.3 mg m^{-2} d^{-1} by the end of October but a low diatom flux of ~35 million cells m^{-2} d^{-1} persisted from November to March (Fig. 3b). The lowest diatom flux, with ~3.5 million cells m^{-2} d^{-1} containing chloroplasts, was observed during the second half of March just before the onset of spring production. The epipelic diatom *Cylindrotheca closterium* contributed ~60–95% of the diatom fluxes from August to mid-November and 20–45% from mid-November to April (Fig. 3b and c).

The composition of the diatom fluxes gradually shifted to a greater diversity during spring (Fig. 3c). The exclusively sympagic algae *Nitzschia frigida* was first collected in the sediment trap at the end of March, and peaks of *N. frigida* fluxes were observed during May and June (Fig. 3c and d). The onset of *N. frigida* export was quickly followed by the export of *Melosira arctica*, another exclusively sympagic algae, with most of the cells exported as resting spores (Fig. 3c and d). *Synedropsis hyperborea*, a common epiphyte on *M. arctica* (Hasle et al., 1994; von Quillfeldt et al., 2003), was present from May to July, similar to *M. arctica*. Export fluxes of *Gyrosigma-Pleurosigma-Haslea*, a group of physiologically similar sea-ice diatoms constituting a minor proportion of the ice assemblage, were observed from February to early July (Fig. 3c). The ice-associated pennate diatoms *Achnantes taeniata*, *Fragilariopsis* spp. and *Pseudonitzschia* spp. first appeared in March and April and significantly contributed to the diatom fluxes during spring and summer (Fig. 3c). Unidentified pennate diatoms dominated algal fluxes during the bloom in June and July, including large contributions of *Fossula arctica* and *Neodenticula seminae*. The exclusively pelagic centric diatoms *Chaetoceros* spp. and *Thalassiosira* spp. increasingly contributed to the diatom fluxes at the end of July, while *Proboscia* spp. significantly contributed to the diatom fluxes from November to January (Fig. 3c).

3.3. Zooplankton and meroplankton

The suspension-feeding copepods *Calanus glacialis/Calanus marshallae* and *Pseudocalanus* spp. and the omnivorous copepod *Oithona similis* were the dominant copepods collected at the CEO site. As adults and juveniles (copepodite stages) of the Arctic *C. glacialis* and the Pacific *C. marshallae* are difficult to distinguish, *C. glacialis* and *C. marshallae* were aggregated and identified as *C. glacialis/marshallae* (Hopcroft et al.,

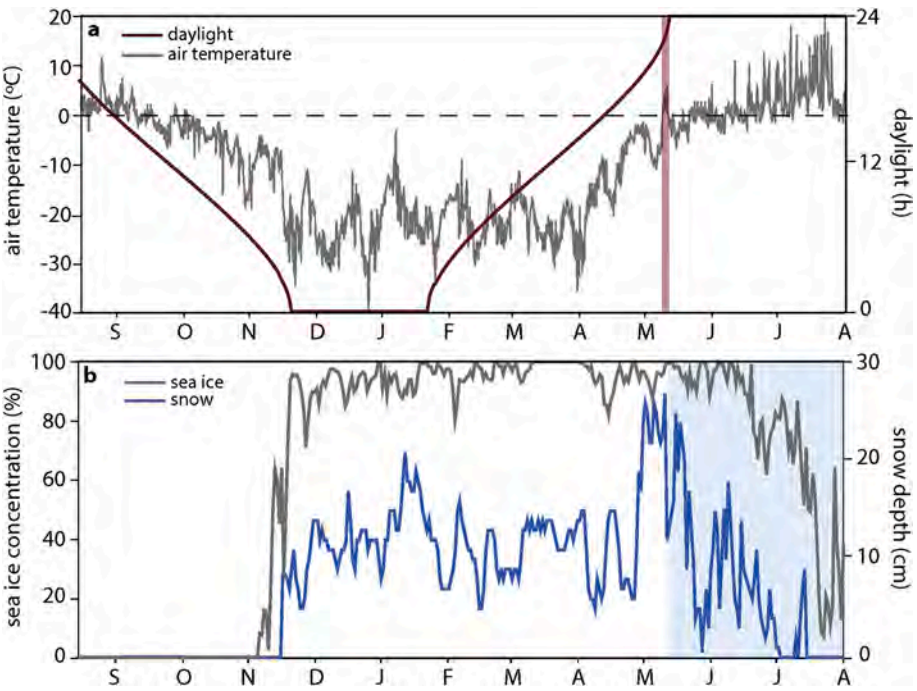

Fig. 2. a) Daylight duration and air temperature recorded at the coastal city of Utqiaġvik (170 km east of the CEO), and b) satellite-derived daily sea-ice concentration and snow depth above the mooring position (71.4–71.8°N, 161.4–161.9°W) during the CEO sediment trap sampling period. Shaded areas represent the early warm air temperature episode (red) and the snow and sea ice melt period (blue). (For interpretation of the references to colour in this figure legend, the reader is referred to the Web version of this article.)

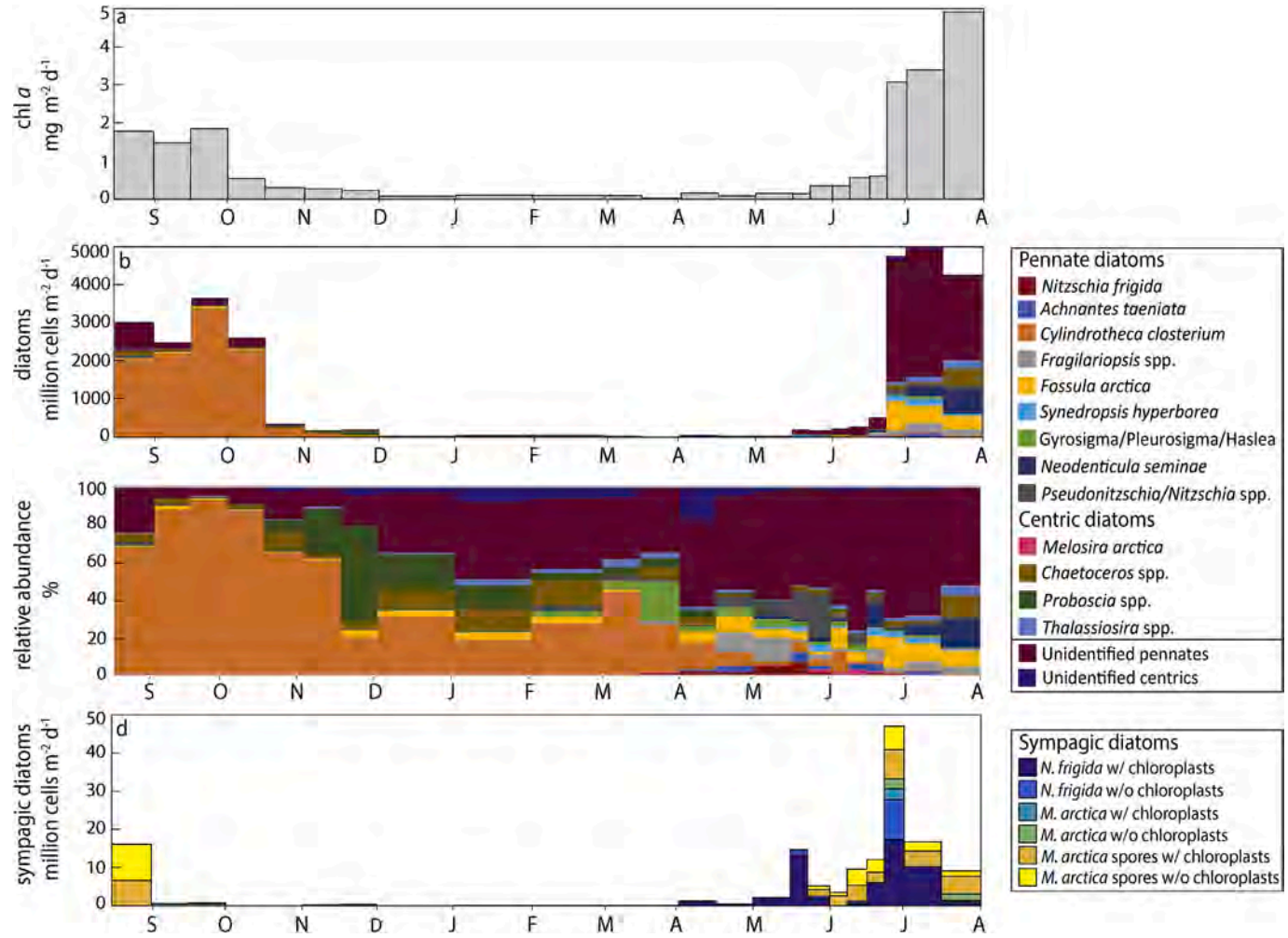

Fig. 3. Annual cycles of a) chlorophyll *a* fluxes, b) diatom fluxes, c) relative abundance of dominant diatom species and groups, and d) sympagic diatoms *N. frigida* and *M. arctica* fluxes at the CEO site from August 2015 to July 2016.

2010; Questel et al., 2013; Ashjian et al., 2017). *Calanus glacialis/marshallae* copepodite stages C2, C3 and C4 were abundant at the beginning of the deployment in August 2015 (Fig. 4a). The *C. glacialis/marshallae* population shifted to a dominance of C5 in September and decreased in abundance from September to March (Fig. 4a). Adult females of *C. glacialis/marshallae* were collected in the sediment trap in April (Fig. 4a). *C. glacialis/marshallae* nauplii of feeding stages N3 to N6 were observed at the end of August 2015 and from the end of June 2016 until the end of the trap deployment in July 2016 (Fig. 4b).

Pseudocalanus spp., most likely a combination of *P. minutus*, *P. acuspes* and *P. newmani* (Darnis et al., 2008), were a constant blend of adult females and males, adult females with eggs, and all copepodite stages from August to January and in July (Fig. 4c). Adult females were present from August to October and at the end of April-beginning of May (Fig. 4c). Nauplii stages of *Pseudocalanus* spp. were mostly abundant from August to December and in July (Fig. 4d). The abundance of all copepodite stages of *O. similis* increased in November and December, a few weeks later than peak in abundances of *C. glacialis/marshallae* and *Pseudocalanus* spp. (Fig. 4e). Nauplii of *O. similis* were nearly absent, apart from a few nauplii of an unidentified stage observed at the beginning of November (Fig. 4f).

High abundances of appendicularians were collected at 37 m in July 2016 (Fig. 4g). While the majority of appendicularians were identified as *Fritillaria borealis* (~95%), a few *Oikopleura vanhoeffeni* (~5%) were observed from September to February (data not shown). Meroplanktonic stages of benthic organisms were also abundant in the sediment trap, with bivalve veliger, polychaete larvae, barnacle larvae, and even polychaetes observed from August to November 2015 (Fig. 4h). Polychaete larvae and a few barnacle larvae were also observed at the end of June and in July 2016 (Fig. 4h).

3.4. Particulate matter and carbon fluxes

FPC fluxes declined from 21.6 to 4.9 mg C m^{-2} d^{-1} from August to October, with copepod FPC contributing to >58% of the FPC fluxes during this period (Fig. 5a). A peak in copepod FPC flux (12.9 mg C m^{-2} d^{-1}) contributing to 98% of the total FPC flux was recorded at the end of May (Fig. 5a). Highest FPC fluxes were recorded in early July (28 mg C m^{-2} d^{-1}), with appendicularian FPC contributing to >70% of the FPC flux at that time (Fig. 5a). TPM and POC fluxes (~60 g m^{-2} d^{-1} and ~1.0 g C m^{-2} d^{-1}, respectively) were 15–20 times higher during August than at their lowest values at the end of March (Fig. 5b). TPM and POC fluxes steadily decreased until the end of March and remained low until the end of May except for a short period of increased fluxes in the first half of April (Fig. 5b). TPM and POC fluxes increased from the beginning of June until the end of the deployment in July (Fig. 5b).

4. Discussion

4.1. Algal fluxes

Continuous export fluxes obtained at the CEO site from August 2015 to July 2016 reflected pelagic processes occurring over a year, encompassing the full range of annual sunlight and sea-ice conditions on the shallow Chukchi Sea shelf. These year-long measurements provide an invaluable dataset to track the seasonal development of the Chukchi marine ecosystem, particularly for the rarely-sampled winter and early spring periods. Enhanced chl *a* (3–5 mg m^{-2} d^{-1}) and diatom fluxes (>4000 million cells m^{-2} d^{-1}) during June and July 2016 were higher than daily chl *a* fluxes (<2.5 mg m^{-2} d^{-1}) obtained from May to August 2004 in the Chukchi Sea (Lalande et al., 2007) and than under-ice algal fluxes (~120 million cells m^{-2} d^{-1}) recorded in April and May 2008 and 2009 in the Bering Sea (Szymanski and Gradinger, 2016). Elevated chl *a* (>1 mg m^{-2} d^{-1}) and diatom fluxes (>2000 million cells m^{-2} d^{-1}) were also observed in the absence of ice cover from mid-August to October 2015 at the CEO site. These results reflect exceptionally high algal biomass and export during summer and autumn that led to annual fluxes of chl *a* and diatoms reaching 225 mg m^{-2} yr^{-1} and ~320 billion cells

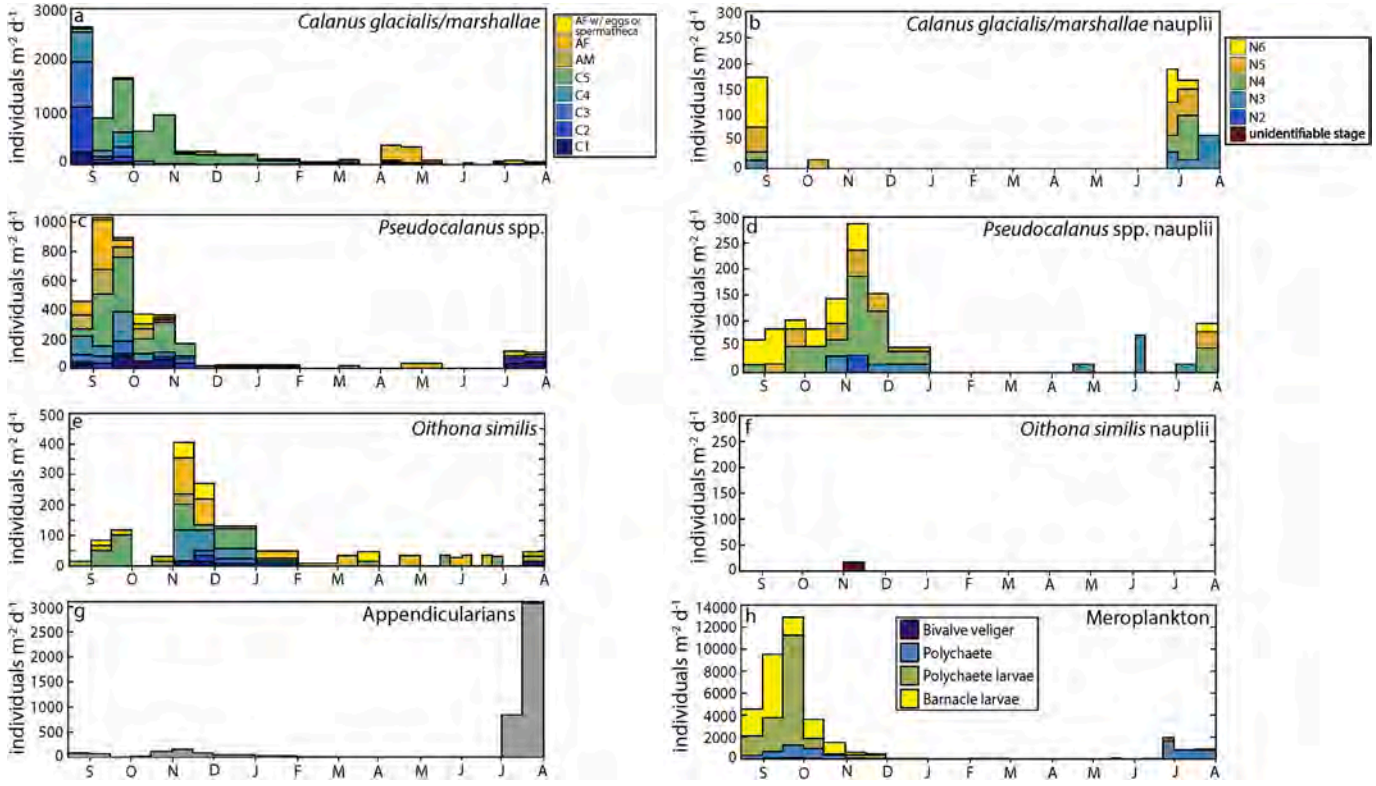

Fig. 4. Annual cycles of the abundance of a) *C. glacialis/marshallae*, b) *C. glacialis/marshallae* nauplii, c) *Pseudocalanus* spp., d) *Pseudocalanus* spp. nauplii, e) *O. similis*, f) *O. similis* nauplii, g) appendicularians, and h) meroplankton individuals at the CEO site from August 2015 to July 2016.

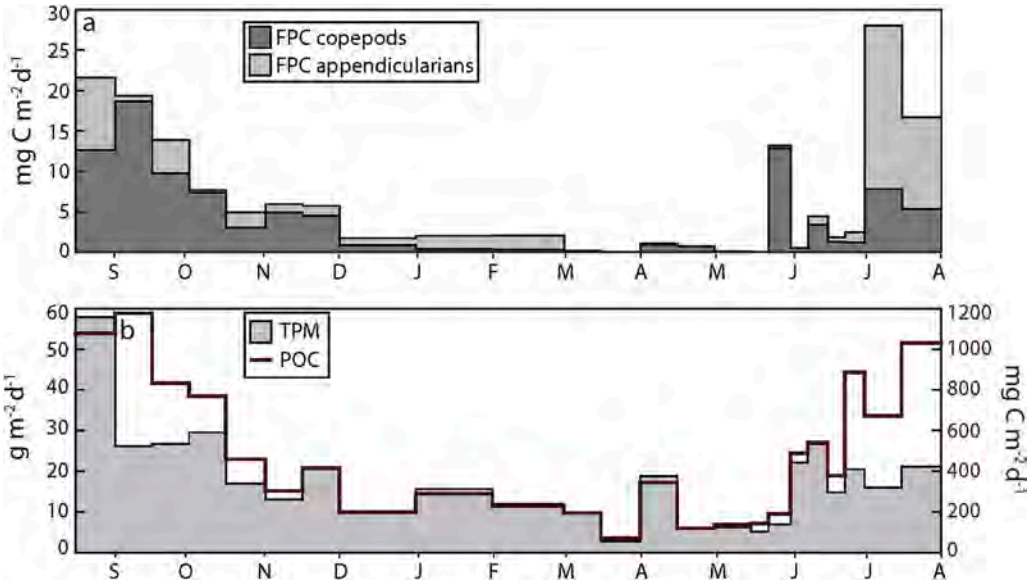

Fig. 5. Annual cycles of a) fecal pellet carbon (FPC) fluxes and b) total particulate matter (TPM) and particulate organic carbon (POC) fluxes from August 2015 to July 2016.

m^{-2} yr^{-1}, respectively, on the shallow northeast Chukchi Sea shelf.

Diatoms have been reported as the dominant or the second most abundant taxa (after flagellates) in the Chukchi Sea (Sukhanova et al., 2009; Giesbrecht et al., 2019). Whereas small flagellates have low sinking rates, diatom aggregates may sink at rates >100 m d^{-1} and rapidly reach the seafloor on the shallow continental shelf, therefore contributing to the majority of algal flux, pelagic-benthic coupling, and potential carbon sequestration (Legendre et al., 1992; McDonnell and Buesseler, 2010). Since most diatom cells exported in autumn and summer contained chloroplasts, these fluxes clearly reflected the export of recent and local algal production.

Commonly found on shallow shelves, *C. closterium* has a rapid growth rate when transported into the euphotic zone during mixing events (Kingston, 2009). Strong winds (>10 m s^{-1}) and frequent wind direction reversals recorded in Utqiaġvik were associated with periodic depressions of the pycnocline from August to November 2015 at the nearby CEO freeze-up detection mooring (Hauri et al., 2018). The strong wind-induced mixing of surface waters was accompanied by elevated chl *a* fluorescence under decreasing levels of photosynthetically active radiation until November at the same site, supporting an autumn bloom (Hauri et al., 2018). The elevated fluxes of *C. closterium* containing chloroplasts observed from August to October reflected the enhanced algal production when ice was absent and sunlight was sufficient for growth on the shallow Chukchi Sea shelf. The large proportion of *C. closterium* and other diatom cells without chloroplasts composing the algal flux during winter suggested a sustained resuspension of sedimented material beneath the ice cover. However, the constant contribution of diatoms with chloroplasts to these wintertime diatom fluxes (at least 10 million cells m^{-2} d^{-1}) indicated that a considerable fraction of resuspended diatoms remained alive throughout the polar night, providing a continual carbon source for benthic suspension feeders and surface deposit feeders. In contrast, ~5 million diatom cells with chloroplasts m^{-2} d^{-1} reached the seafloor at 2430 m during a spring peak diatom export event in the deep Fram Strait (Lalande et al., 2016). The close proximity of the seafloor and the extended periods of algal export clearly factor into the tight pelagic-benthic coupling and elevated benthic biomasses reported for the Chukchi continental shelf (Grebmeier et al., 2006a).

Sea-ice algal production in nutrient-rich waters such as in the Chukchi Sea is often limited by light, either related to photoperiod or snow cover (Legendre et al., 1992; Rysgaard et al., 2001). Sea-ice algae grow and accumulate at the bottom of the ice, in melt ponds, or in the ice brine channel matrix from the time sunlight is sufficient until their release into the water column at the onset of melting processes. In the Chukchi Sea, high sea-ice algal abundance has previously been observed in early March (Szymanski and Gradinger, 2016). Peaks in the ice algal bloom have been reported from mid to late May (Selz et al., 2018). While many diatom species composing the ice algal community in the Arctic Ocean are both sympagic and pelagic, key species such as *N. frigida* and *M. arctica* are exclusively sympagic (Poulin et al., 2011, 2014). *Nitzschia frigida*, a pennate diatom forming arborescent colonies, usually dominates the biomass on the ice underside and sinks out of the water relatively quickly when melt is initiated, without maintaining a planktonic population (Michel et al., 1993; von Quillfeldt et al., 2003; Olsen et al., 2017; Lalande et al., 2019). The two distinct peaks in *N. frigida* fluxes observed in May and June therefore reflected ice algae release. These two peaks coincided with the snow melt event recorded on May 15 and with the combined snow and ice melt observed at the end of June. While *M. arctica*, a chain-forming centric diatom, has been reported as sporadically abundant in the Chukchi Sea (Ambrose et al., 2005; Wang et al., 2018), only low fluxes of *M. arctica* were measured during the 2015–2016 deployment, most of them at the onset of ice melt at the end of June. The constant, albeit relatively low fluxes of *N. frigida*, *M. arctica* and *Gyrosigma-Pleurosigma-Haslea* observed from February to July reflected a continuous release of ice algae from the drifting sea ice above the mooring site, contrasting with model-derived results that suggest a brief sea-ice algal seeding period in the Chukchi Sea (Selz et al., 2018).

The ice-associated pennate diatoms *Achnantes taeniata*, *Fragilariopsis* spp. and *Pseudonitzschia* spp., common phytoplankton spring bloom taxa thriving in both ice and the water column in the Chukchi Sea (Sukhanova et al., 2009; Selz et al., 2018; Wang et al., 2018), first appeared in March and April and significantly contributed to the diatom fluxes during spring and summer. The boreal pennate diatom *Neodenticula seminae*, a common species in the northern North Pacific and Bering Sea (Reid et al., 2007), increasingly contributed to the export fluxes from May to July, reflecting the influence of inflowing Pacific waters from the Bering Sea into the study area. The substantial increase of chl *a* and diatom fluxes at the end of June clearly reflected a large bloom during snow and ice melt. The dominant diatom exported at the onset of the bloom was the pennate diatom *Fossula arctica*, another species known to thrive well in both ice and water and common in early phytoplankton blooms (Szymanski and Gradinger, 2016). The exclusively pelagic

centric diatoms *Chaetoceros* spp. and *Thalassiosira* spp. increasingly contributed to the diatom fluxes at the end of July. However, while *Chaetoceros* spp. and *Thalassiosira* spp. have been reported as dominant components of pelagic algal blooms in the Chukchi Sea (Sukhanova et al., 2009; Arrigo et al., 2012; Wang et al., 2018), they never dominated diatom fluxes during summer, rather reflecting a steady contribution from August 2015 to July 2016. *Proboscia* spp., a genus observed in late summer blooms following wind forcing or the influence of small eddies (Sukhanova et al., 2009), significantly contributed to the diatom fluxes from November to January. A similar increase in the relative abundance of *Proboscia* was observed at ~200 m over the Northwind Abyssal Plain, north of the CEO site, in October and November 2011 (Onodera et al., 2015).

4.2. Zooplankton and meroplankton

Year-round studies on zooplankton abundance and stage succession are rare in the Arctic Ocean due to the remoteness and difficult accessibility of polar regions (e.g. Kosobokova, 1982; Darnis and Fortier, 2014). Although sediment traps are not designed to quantitatively collect zooplankton, zooplankton entering the traps have effectively been identified to partly reflect the seasonal development of the zooplankton community (e.g. Dezutter et al., 2019). On a very shallow shelf, swimmers are more likely to be trapped and thereby accurately reflect the relative abundance and composition of the zooplankton community. In the Chukchi Sea, the copepods *C. glacialis/marshallae*, *Pseudocalanus* spp., and *O. similis* dominate the zooplankton communities in terms of abundance and biomass (Hopcroft et al., 2010; Questel et al., 2013; Ashjian et al., 2017). Accordingly, they were the dominant copepods collected in the CEO sediment trap. A few individuals of *C. hyperboreus,* the most abundant copepod in the adjacent deep Arctic basin (Campbell et al., 2009), were collected in January (~5–10 individuals) and March (~30–35 individuals; data not shown), possibly reflecting the aperiodic upwelling of deep continental slope waters onto the shallow shelf (Ashjian et al., 2017; Danielson et al., 2017a). Pacific copepods *Eucalanus bungii* and *Metridia pacifica* were also sporadically collected from August to October (data not shown). Although zooplankton typical of Pacific origin water can be absent near Hanna Shoal (Lane et al., 2008), other studies do find them on occasion (Hopcroft et al., 2010).

The large proportion of young copepodite stages of *C. glacialis/marshallae* collected at the beginning of the deployment in August corroborated with the dominance of *C. glacialis/marshallae* copepodite stages C1–C3 collected using vertical net tows on Hanna Shoal in August 2012 and 2013 (Ashjian et al., 2017). The gradual transition from a high abundance of *C. glacialis/marshallae* C2, C3 and C4 to a low abundance of C5 during autumn may have reflected high predation and/or early life stage mortality. It also reflects the accrual of energy and growth of *C. glacialis/marshallae* into a lipid-rich stage for the winter (Falk-Petersen et al., 2009). While *C. glacialis/marshallae* typically attempts to enter diapause within cold bottom-water pools in the region (Ashjian et al., 2017; Elliott et al., 2017), it is unclear to what extent the decline of C5s after November reflected decreased swimming activity, permanent descent below the depth of the trap, or advection into deeper waters off the shelf. The limited but lasting presence from September to January of *C. glacialis/marshallae* C5 on the shallow Chukchi Sea shelf suggests the advection of the overwintering stage from nearby deeper areas into the region (Darnis et al., 2008; Ashjian et al., 2017). After months of quiescence, *C. glacialis/marshallae* rapidly develops its gonads using internal lipid reserves (Falk-Petersen et al., 2009), reflected by the collection of *C. glacialis/marshallae* adult females in the sediment trap in April (Fig. 4a). The near complete absence of *C. glacialis/marshallae* at 37 m following their maturation presumably reflected their distribution nearer the ice-water interface to feed on ice algae and spawn prior to the pelagic bloom, and in the subsurface chlorophyll maximum during the bloom (Niehoff et al., 2002; Campbell et al., 2009; Søreide et al., 2010; Leu et al., 2011; Daase et al., 2013; Darnis and Fortier, 2014; Durbin and Casas, 2014). The subsequent collection of *C. glacialis/marshallae* nauplii of feeding stages N3 to N6 at the onset on the pelagic bloom 8–10 weeks later reflected nauplii development in the region in time to feed on the pelagic bloom to fuel their growth (Søreide et al., 2008, 2010; Leu et al., 2011; Wold et al., 2011; Dezutter et al., 2019). The presence of *C. glacialis/marshallae* nauplii during August 2015 may have reflected the production of nauplii by populations advected in the region from the Bering Sea, or an extended nauplii production period on the Chukchi Sea shelf.

In contrast to *C. glacialis/marshallae,* the period of high abundance of *Pseudocalanus* spp. copepodites coincided with high abundance of their nauplii from August to December. The presence of young nauplii stages N2, N3 and N4 during November and December suggested sustained spawning until ice formation on the Chukchi Sea shelf. The *Pseudocalanus* spp. complex exploited the prolonged productive period to sustain growth, maturation, lipid accumulation, and reproduction during autumn before a rapid decline of the population occurred at the beginning of the polar night. Similar to *C. glacialis/marshallae*, the lower abundance of *Pseudocalanus* spp. in spring and summer likely indicated their distribution at the ice-water interface to feed on ice algae from the bottom of the ice (Conover et al., 1986; Campbell et al., 2009).

An increased abundance of the small omnivorous copepod *O. similis* was observed in November and December, a few weeks later than peak in abundances of *C. glacialis/marshallae* and *Pseudocalanus* spp. The increased abundance matched with a seasonal peak in the abundance of *O. similis* in November in Kongsfjorden (Lischka and Hagen, 2005) and suggests that *O. similis* thrives when larger copepods are not present (Zamora-Terol et al., 2014). Relatively high abundances of adult females and males during winter support previous reports that *O. similis* uses a year-round reproduction strategy and remains active during winter (Zamora-Terol et al., 2013), although only a few unidentified nauplii were collected in November. The presence of all copepodite stages from November to January and scattered throughout the sampling period reflected the continuous reproduction of *O. similis*, with all stages typically present throughout the year (Ashjian et al., 2003; Lischka and Hagen, 2005; Zamora-Terol et al., 2013).

Appendicularians and meroplankton may contribute to a large proportion of the zooplankton community in terms of abundance and biomass during summer on the Chukchi Sea shelf, but are also extremely variable in their abundances from year to year (Hopcroft et al., 2010; Questel et al., 2013; Ashjian et al., 2017). While nearly all appendicularians were collected in July during the bloom, extremely large abundances of larvae of polychaetes and barnacles from mid-August to November suggest that meroplanktonic stages exploited the autumn production during resuspension events. Ashjian et al. (2017) also reported high abundances of barnacle larvae and polychaete larvae in the water column in August on Hanna Shoal. The presence of adult polychaetes 8 m above seafloor from August to November and in June and July further reflects resuspension and the rich benthic ecosystem of the Chukchi Sea.

4.3. Pelagic-benthic coupling

Elevated chl *a*, diatom and POC fluxes reflected a tight coupling between water column primary production and benthic secondary production on the shallow Chukchi Sea shelf. These fluxes (annual POC flux: ~145 g C m^{-2} yr^{-1}) are more than sufficient to support the rich benthic biomass (<20 g C m^{-2}) of amphipods and bivalves that constitute the food base for benthic-feeding marine mammals in the Hanna Shoal region (Grebmeier and Barry, 1991; Grebmeier et al., 2015). Campbell et al. (2009) reported a low grazing impact of the zooplankton community on algal production due to low zooplankton biomass during spring in the Chukchi Sea, concluding that grazers are not able to exert much control over algal blooms in this region. Therefore, the majority of the water column primary production is directly available for local

export to the benthos or for offshore transport into the adjacent basin. Acoustics-derived data recently obtained north of the Bering Strait also reflected low zooplankton biomass during the spring phytoplankton bloom on the Chukchi Sea shelf, further implying that low grazing impact resulted in tight pelagic-benthic coupling in the region (Kitamura et al., 2017). Export fluxes of rapidly-sinking fecal pellets at the CEO showed a peak in copepod FPC fluxes reaching ~13 mg C m^{-2} d^{-1} at the end of May. This peak followed the appearance of *C. glacialis/marshallae* and *Pseudocalanus* spp. adult females in April and reflected enhanced grazing by copepods after the onset of ice algae release in May. Similar FPC fluxes (up to ~25 mg C m^{-2} d^{-1}) were previously obtained from under-ice drifting sediment trap deployments at nearby East Hanna Shoal and Barrow Canyon during May and June (Lalande et al., 2007). A peak in appendicularian FPC fluxes in July 2016 coincided with the large abundance of *Fritillaria borealis* in the sediment trap, reflecting the high grazing and growth rates of these filter feeders (Deibel, 1998). The summertime peak in FPC fluxes on the shallow Chukchi Sea shelf was 30 times higher than at 200 m in the eastern Fram Strait in June and five times higher than at 25 m in the Central Arctic Ocean in July and August (Lalande et al., 2014, 2016). Elevated FPC fluxes at the CEO from August to November also indicated enhanced grazing pressure during autumn, consistent with high abundance of copepods, mostly of older stages. Overall, FPC fluxes indicated that a fair proportion of algal production was channeled into the pelagic ecosystem during autumn and summer. Despite this grazing pressure, the prolific chl *a*, diatom and POC fluxes clearly indicate that tight pelagic-benthic coupling prevails on the shallow Chukchi Sea shelf, in agreement with acoustics-derived and experimental results (Campbell et al., 2009; Kitamura et al., 2017).

4.4. Particulate matter and carbon fluxes

Elevated TPM and POC fluxes throughout the mooring deployment show that multiple processes combine to regulate the export of particulate matter on the Chukchi Sea shelf. In agreement with elevated *C. closterium* fluxes, high TPM and POC fluxes during autumn can be attributed to resuspension of sediments and diatoms blooming as a result of fall storms in the absence of ice cover. Despite substantial fecal pellet export (~2 g C m^{-2} yr^{-1}), the annual FPC flux only contributed to a small fraction (<2%) of the annual POC flux, and the annual POC flux (~145 g C m^{-2} yr^{-1}) represented <3% of the annual TPM flux (~5600 g m^{-2} yr^{-1}). Enhanced TPM and POC fluxes in April and from the beginning of June until the end of the deployment in July 2016 likely corresponded to the release of particulate matter during snow and ice melt events. A large quantity of particulate matter is incorporated into ice during freeze-up on shallow shelves and is later released during melt (Wegner et al., 2005; Lalande et al., 2014). Because the potential for incorporation of particulate matter into sea ice likely increases with decreasing depth, ice-released material likely contributed considerably to TPM and POC fluxes during spring and summer on the very shallow Chukchi Sea shelf. High diatom fluxes during the spring bloom from the end of June to the end of the deployment in July likely contributed to enhanced POC fluxes for that period. Overall, export fluxes on the shallow Chukchi Shelf were extremely high relative to fluxes recorded in deeper Arctic regions, displaying winter fluxes as high as spring and summer fluxes in the Beaufort Sea, northern Baffin Bay, Laptev Sea, and Fram Strait (Lalande et al., 2009, 2016). These substantial export fluxes of biogenic matter reflected the combined effect of extensive primary production driven by high nutrient loads, ice-released material, and resuspension on a shallow Arctic shelf.

5. Conclusions

Continuous export flux measurements of biogenic matter obtained at intervals ranging from one week to one month from August 2015 to July 2016 captured the local products of elevated primary production during summer and autumn. While autumn fluxes obtained at the end of the productive cycle of 2015 were possibly affected by different wind-forcing, water masses and circulation patterns than in autumn 2016, these fluxes nonetheless set a baseline for production dynamics in the northeast Chukchi Sea. These collections documented the release of ice algae due to snow melt during spring, the onset of the under-ice phytoplankton bloom triggered by ice melt enabling stratification during summer, high appendicularian grazing in the presence of ice during summer, and high copepod grazing in the absence of ice cover during autumn. These high-resolution biological time-series measurements provided critical information to track biodiversity, phytoplankton phenology, seasonal development of zooplankton communities, and food supply to the benthos. Most importantly, these results showed a 4-month period of sustained elevated primary and secondary production on the Chukchi Sea shelf validated by elevated fluorescence and intense acoustic backscatter of zooplankton at the CEO during the same period (Hauri et al., 2018), suggesting that the local benthic community benefits from a sustained food supply rather than episodic flux events. In spite of the apparent continuous food supply during the polar day, the benthic macrofauna near the CEO site only reach half the biomass of benthic communities found in the southeast Chukchi Sea (Grebmeier et al., 2006a, 2015), possibly due to lower nutrient content (Giesbrecht et al., 2019). Long-term biological and biogeochemical measurements such as these are uncommon but imperative for fully understanding the impact of environmental changes such as warmer water temperature and reduced sea-ice cover. With the need to better monitor and understand the rapidly changing Arctic coupled with technological advances that enable reliable year-round observations, we anticipate better biological monitoring at high latitudes through the future addition of sequential sediment traps on year-round moorings.

Declaration of competing interest

There is no conflict of interest.

CRediT authorship contribution statement

Catherine Lalande: Conceptualization, Resources, Formal analysis, Visualization, Writing - original draft, Writing - review & editing. **Jacqueline M. Grebmeier:** Conceptualization, Writing - review & editing, Funding acquisition. **Russell R. Hopcroft:** Writing - review & editing. **Seth L. Danielson:** Conceptualization, Investigation, Resources, Writing - review & editing, Project administration, Funding acquisition.

Acknowledgements

A broad consortium of academic, agency, and industry partners are contributing to the success of the CEO program. Financial support comes from the National Pacific Research Board Long-Term Monitoring (NPRB LTM) program (project #1426, NPRB publication #ArcticIERP–SI–1-02), the Alaska Ocean Observing System (award #NA11NOS0120020), and the University of Alaska Fairbanks. National Ocean Partnership Program (NOS Integrated Ocean Observations Systems (IOOS), award number: NA14NOS0120158) with funding from NOAA, Shell Oil Company, and BOEM (Bureau of Ocean Energy Management) also supported efforts by J.G. C.L. was supported through the Long-Term Oceanic Observatories project funded by ArcticNet, a Network of Centres of Excellence of Canada. For at-sea support and assistance, we thank the captains, crews, and scientists of the 2015 Arctic Marine Biodiversity Observation Network (AMBON) cruise on *R/V Norseman II* and the 2016 Chukchi Borderlands Hidden Ocean cruise on USCGC *Healy*. We thank Peter Shipton for mooring preparation, deployment and recovery, Marie Parenteau, Gabrielle Nadaï, Thibaud Dezutter, and Cyril Aubry for laboratory work, and Louis Fortier for access to his laboratory at Université Laval.

Appendix A. Supplementary data

Supplementary data to this article can be found online at https://doi.org/10.1016/j.dsr2.2020.104730.

References

Ambrose, W.G., Quillfeldt, C.v., Clough, L.M., Tilney, P.V.R., Tucker, T., 2005. The sub-ice algal community in the Chukchi sea: large- and small-scale patterns of abundance based on images from a remotely operated vehicle. Polar Biol. 28, 784–795.

Arrigo, K.R., Perovich, D.K., Pickart, R.S., Brown, Z.W., van Dijken, G.L., Lowry, K.E., Mills, M.M., Palmer, M.A., Balch, W.M., Bahr, F., Bates, N.R., Benitez-Nelson, C., Bowler, B., Brownlee, E., Ehn, J.K., Frey, K.E., Garley, R., Laney, S.R., Lubelczyk, L., Mathis, J., Matsuoka, A., Mitchell, B.G., Moore, G.W.K., Ortega-Retuerta, E., Pal, S., Polashenski, C.M., Reynolds, R.A., Schieber, B., Sosik, H.M., Stephens, M., Swift, J. H., 2012. Massive phytoplankton blooms under arctic sea ice. Science 336, 1408-1408.

Ashjian, C.J., Campbell, R.G., Welch, H.E., Butler, M., Van Keuren, D., 2003. Annual cycle in abundance, distribution, and size in relation to hydrography of important copepod species in the western Arctic Ocean. Deep-Sea Res Pt I 50, 1235–1261.

Ashjian, C.J., Campbell, R.G., Gelfman, C., Alatalo, P., Elliott, S.M., 2017. Mesozooplankton abundance and distribution in association with hydrography on Hanna shoal, NE Chukchi Sea, during August 2012 and 2013. Deep-Sea Res Pt II 144, 21–36.

Baker, M.R., Dickson, D., 2020. Arctic integrated ecosystem Research program. Deep-Sea Res Pt II. Special Issue I – Understanding ecosystem processes, timing, and changes in the Pacific Arctic.

Baker, M.R., Kivva, K.K., Pisareva, M., Watson, J., Selivanova, J., 2020. Shifts in the physical environment in the Pacific Arctic and implications for ecological timing and conditions. Deep-Sea Res Pt II Special Issue I – Understanding ecosystem processes, timing, and changes in the Pacific Arctic.

Campbell, R.G., Sherr, E.B., Ashjian, C.J., Plourde, S., Sherr, B.F., Hill, V., Stockwell, D. A., 2009. Mesozooplankton prey preference and grazing impact in the western Arctic Ocean. Deep-Sea Res Pt II 56, 1274–1289.

Comiso, J.C., Cavalieri, D.J., Markus, T., 2003. Sea ice concentration, ice temperature, and snow depth using AMSR-E data. IEEE T Geosci Remote 41, 243–252.

Conover, R.J., Herman, A.W., Prinsenberg, S.J., Harris, L.R., 1986. Distribution of and feeding by the copepod *Pseudocalanus* under fast ice during the Arctic spring. Science 232, 1245–1247.

Daase, M., Falk-Petersen, S., Varpe, Ø., Darnis, G., Søreide, J.E., Wold, A., Leu, E., Berge, J., Philippe, B., Fortier, L., 2013. Timing of reproductive events in the marine copepod *Calanus glacialis*: a pan-Arctic perspective. Can. J. Fish. Aquat. Sci. 70, 871–884.

Danielson, S., Ahkinga, O., Ashjian, C., Basyuk, E., Cooper, L., Eisner, L., Iken, K., Grebmeier, J., Juranek, L., Khen, G., Jayne, S., Kikuchi, T., Ladd, C., Lu, K., McCabe, R., Moore, K., Nishino, S., Ozenna, F., Pickart, R., Polyakov, I., Stabeno, P., Thoman, R., Williams, B., Wood, K., Weingartner, T., 2020. Manifestation and consequences of warming and altered heat fluxes over the Bering and Chukchi Sea continental shelves. Deep-Sea Res Pt II Special Issue I - Understanding ecosystem processes, timing, and changes in the Pacific Arctic.

Danielson, S.L., Eisner, L., Ladd, C., Mordy, C., Sousa, L., Weingartner, T.J., 2017. A comparison between late summer 2012 and 2013 water masses, macronutrients, and phytoplankton standing crops in the northern Bering and Chukchi Seas. Deep-Sea Res Pt II 135, 7–26.

Danielson, S.L., Iken, K., Hauri, C., Hopcroft, R.R., McDonnell, A.M.P., Winsor, P., Lalande, C., Grebmeier, J.M., Cooper, L.W., Horne, J.K., Stafford, K.M., 2017. Collaborative approaches to multi-disciplinary monitoring of the Chukchi shelf marine ecosystem: Networks of networks for maintaining long-term Arctic observations. OCEANS 2017 - Anchorage 1–7.

Darnis, G., Barber, D.G., Fortier, L., 2008. Sea ice and the onshore–offshore gradient in pre-winter zooplankton assemblages in southeastern Beaufort Sea. J. Mar. Syst. 74, 994–1011.

Darnis, G., Fortier, L., 2014. Temperature, food and the seasonal vertical migration of key arctic copepods in the thermally stratified Amundsen Gulf (Beaufort Sea, Arctic Ocean). J. Plankton Res. 36, 1092–1108.

De Robertis, A., Taylor, K., Wilson, C.D., Farley, E.V., 2017. Abundance and distribution of arctic cod (Boreogadus saida) and other pelagic fishes over the U.S. Continental shelf of the northern bering and Chukchi seas. Deep-Sea Res Pt II 135, 51–65.

Deibel, D., 1998. Feeding and metabolism of appendicularia. In: Bone, Q. (Ed.), The Biology of Pelagic Tunicates. Oxford University Press, pp. 139–149.

Dezutter, T., Lalande, C., Dufresne, C., Darnis, G., Fortier, L., 2019. Mismatch between microalgae and herbivorous copepods due to the record sea ice minimum extent of 2012 and the late sea ice break-up of 2013 in the Beaufort Sea. Prog. Oceanogr. 173, 66–77.

Durbin, E.G., Casas, M.C., 2014. Early reproduction by Calanus glacialis in the Northern Bering Sea: the role of ice algae as revealed by molecular analysis. J. Plankton Res. 36, 523–541.

Elliott, S.M., Ashjian, C.J., Feng, Z., Jones, B., Chen, C., Zhang, Y., 2017. Physical control of the distributions of a key arctic copepod in the northeast Chukchi Sea. Deep-Sea Res Pt II 144, 37–51.

Ershova, E.A., Hopcroft, R.R., Kosobokova, K.N., 2015. Inter-annual variability of summer mesozooplankton communities of the western Chukchi Sea: 2004–2012. Polar Biol. 38, 1461–1481.

Falk-Petersen, S., Mayzaud, P., Kattner, G., Sargent, J.R., 2009. Lipids and life strategy of Arctic Calanus. Mar. Biol. Res. 5, 18–39.

Giesbrecht, K.E., Varela, D.E., Wiktor, J., Grebmeier, J.M., Kelly, B., Long, J.E., 2019. A decade of summertime measurements of phytoplankton biomass, productivity and assemblage composition in the Pacific Arctic Region from 2006 to 2016. Deep-Sea Res Pt II 162, 93–113.

González, H.E., Gonzalez, S.R., Brummer, G.-J.A., 1994. Short-term sedimentation pattern of zooplankton, faeces and microplankton at a permanent station in the Bjornafjorden (Norway) during April-May 1992. Mar. Ecol. Prog. Ser. 105, 31–45.

Gradinger, R., 2009. Sea-ice algae: major contributors to primary production and algal biomass in the Chukchi and Beaufort Seas during May/June 2002. Deep-Sea Res Pt II 56, 1201–1212.

Grebmeier, J.M., McRoy, C.P., Feder, H.M., 1988. Pelagic-benthic coupling on the shelf of the northern Bering and Chukchi Seas. I. Food supply source and benthic biomass. Mar. Ecol. Prog. Ser. 48, 57–67.

Grebmeier, J.M., Barry, J.P., 1991. The influence of oceanographic processes on pelagic-benthic coupling in polar regions: a benthic perspective. J. Mar. Syst. 2, 495–518.

Grebmeier, J.M., Cooper, L.W., Feder, H.M., Sirenko, B.I., 2006. Ecosystem dynamics of the pacific-influenced northern bering and Chukchi seas in the amerasian arctic. Prog. Oceanogr. 71, 331–361.

Grebmeier, J.M., Overland, J.E., Moore, S.E., Farley, E.V., Carmack, E.C., Cooper, L.W., Frey, K.E., Helle, J.H., McLaughlin, F.A., McNutt, S.L., 2006. A major ecosystem shift in the northern Bering Sea. Science 311, 1461–1464.

Grebmeier, J.M., Maslowski, W.E., 2014. The Pacific Arctic Region: Ecosystem Status and Trends in a Rapidly Changing Environment. Springer, Berlin-Heidelberg-New York.

Grebmeier, J.M., Bluhm, B.A., Cooper, L.W., Danielson, S., Arrigo, K.R., Blanchard, A.L., Clark, J.T., Day, R.H., Frey, K.E., Gradinger, R.R., Kędra, M., Konar, B., Kuletz, K.J., Lee, S.H., Lovvorn, J.R., Norcross, B.L., Okkonen, S.R., 2015. Ecosystem characteristics and processes facilitating persistent macrobenthic biomass hotspots and associated benthivory in the Pacific Arctic. Prog. Oceanogr. 136, 92–114.

Grebmeier, J.M., Frey, K.E., Cooper, L.W., Kędra, M., 2018. Trends in benthic macrofaunal populations, seasonal sea ice persistence, and bottom water temperatures in the Bering Strait region. Oceanography 31, 136–151.

Hasle, G.R., Medlin, L.K., Syvertsen, E.E., 1994. Synedropsis gen. nov., a genus of araphid diatoms associated with sea ice. Phycologia 33, 248–270.

Hauri, C., Danielson, S., McDonnell, A.M.P., Hopcroft, R.R., Winsor, P., Shipton, P., Lalande, C., Stafford, K.M., Horne, J.K., Cooper, L.W., Grebmeier, J.M., Mahoney, A., Maisch, K., McCammon, M., Statscewich, H., Sybrandy, A., Weingartner, T., 2018. From sea ice to seals: a moored marine ecosystem observatory in the Arctic. Ocean Sci. 14, 1423–1433.

Hill, V., Cota, G., 2005. Spatial patterns of primary production on the shelf, slope and basin of the Western Arctic in 2002. Deep-Sea Res Pt II 52, 3344–3354.

Hill, V., Ardyna, M., Lee, S.H., Varela, D.E., 2018. Decadal trends in phytoplankton production in the pacific arctic region from 1950 to 2012. Deep-Sea Res Pt II 152, 82–94.

Hopcroft, R.R., Kosobokova, K.N., Pinchuk, A.I., 2010. Zooplankton community patterns in the Chukchi Sea during summer 2004. Deep-Sea Res Pt II 57, 27–39.

Kingston, M.B., 2009. Growth and motility of the diatom *Cylindrotheca closterium*: implications for commercial applications. JNCAS 125, 138–142.

Kitamura, M., Amakasu, K., Kikuchi, T., Nishino, S., 2017. Seasonal dynamics of zooplankton in the southern Chukchi Sea revealed from acoustic backscattering strength. Cont. Shelf Res. 133, 47–58.

Kosobokova, K.N., 1982. Composition and distribution of the biomass of zooplankton in the central Arctic Basin. Oceanology 22, 744–750.

Kuletz, K.J., Ferguson, M.C., Hurley, B., Gall, A.E., Labunski, E.A., Morgan, T.C., 2015. Seasonal spatial patterns in seabird and marine mammal distribution in the eastern Chukchi and western Beaufort seas: identifying biologically important pelagic areas. Prog. Oceanogr. 136, 175–200.

Lalande, C., Grebmeier, J.M., Wassmann, P., Cooper, L.W., Flint, M.V., Sergeeva, V.M., 2007. Export fluxes of biogenic matter in the presence and absence of seasonal sea ice cover in the Chukchi Sea. Cont. Shelf Res. 27, 2051–2065.

Lalande, C., Forest, A., Barber, D.G., Gratton, Y., Fortier, L., 2009. Variability in the annual cycle of vertical particulate organic carbon export on arctic shelves: contrasting the Laptev Sea, northern Baffin Bay and the Beaufort Sea. Cont. Shelf Res. 29, 2157–2165.

Lalande, C., Nöthig, E.-M., Somavilla, R., Bauerfeind, E., Shevchenko, V., Okolodkov, Y., 2014. Variability in under-ice export fluxes of biogenic matter in the Arctic Ocean. Glob. Biogeochem. Cycles 28, 571–583.

Lalande, C., Nöthig, E.-M., Bauerfeind, E., Hardge, K., Beszczynska-Möller, A., Fahl, K., 2016. Lateral supply and downward export of particulate matter from upper waters to the seafloor in the deep eastern Fram Strait. Deep-Sea Res Pt I 114, 78–89.

Lalande, C., Nöthig, E.-M., Fortier, L., 2019. Algal export in the Arctic Ocean in times of global warming. Geophys. Res. Lett. 46, 5959–5967.

Lane, P.V.Z., Llinás, L., Smith, S.L., Pilz, D., 2008. Zooplankton distribution in the western Arctic during summer 2002: hydrographic habitats and implications for food chain dynamics. J. Mar. Syst. 70, 97–133.

Legendre, L., Ackley, S.F., Dieckmann, G.S., Gulliksen, B., Horner, R., Hoshiai, T., Melnikov, I.A., Reeburgh, W.S., Spindler, M., Sullivan, C.W., 1992. Ecology of sea ice biota. Polar Biol. 12, 429–444.

Leu, E., Søreide, J.E., Hessen, D.O., Falk-Petersen, S., Berge, J., 2011. Consequences of changing sea-ice cover for primary and secondary producers in the European Arctic shelf seas: timing, quantity, and quality. Prog. Oceanogr. 90, 18–32.

Lischka, S., Hagen, W., 2005. Life histories of the copepods Pseudocalanus minutus, P. acuspes (Calanoida) and Oithona similis (Cyclopoida) in the arctic Kongsfjorden (Svalbard). Polar Biol. 28, 910–921.

Logerwell, E., Busby, M., Carothers, C., Cotton, S., Duffy-Anderson, J., Farley, E., Goddard, P., Heintz, R., Holladay, B., Horne, J., Johnson, S., Lauth, B., Moulton, L., Neff, D., Norcross, B., Parker-Stetter, S., Seigle, J., Sformo, T., 2015. Fish communities across a spectrum of habitats in the western Beaufort Sea and Chukchi Sea. Prog. Oceanogr. 136, 115–132.

McDonnell, A.M.P., Buesseler, K.O., 2010. Variability in the average sinking velocity of marine particles. Limnol. Oceanogr. 55, 2085–2096.

Michel, C., Legendre, L., Therriault, J.-C., Demers, S., Vandevelde, T., 1993. Springtime coupling between ice algal and phytoplankton assemblages in southeastern Hudson Bay, Canadian Arctic. Polar Biol. 13, 441–449.

Moore, S.E., Kuletz, K.J., 2019. Marine birds and mammals as ecosystem sentinels in and near Distributed Biological Observatory regions: an abbreviated review of published accounts and recommendations for integration to ocean observatories. Deep-Sea Res Pt II 162, 211–217.

Niehoff, B., Madsen, S., Hansen, B., Nielsen, T., 2002. Reproductive cycles of three dominant Calanus species in Disko Bay, West Greenland. Mar. Biol. 140, 567–576.

Olsen, L.M., Laney, S.R., Duarte, P., Kauko, H.M., Fernández-Méndez, M., Mundy, C.J., Rösel, A., Meyer, A., Itkin, P., Cohen, L., Peeken, I., Tatarek, A., Różańska-Pluta, M., Wiktor, J., Taskjelle, T., Pavlov, A.K., Hudson, S.R., Granskog, M.A., Hop, H., Assmy, P., 2017. The seeding of ice algal blooms in Arctic pack ice: the multiyear ice seed repository hypothesis. J Geophys Res-Biogeo 122, 1529–1548.

Onodera, J., Watanabe, E., Harada, N., Honda, M.C., 2015. Diatom flux reflects water-mass conditions on the southern Northwind Abyssal Plain. Arctic Ocean. Biogeosciences 12, 1373–1385.

Poulin, M., Daugbjerg, N., Gradinger, R., Ilyash, L., Ratkova, T., von Quillfeldt, C., 2011. The pan-Arctic biodiversity of marine pelagic and sea-ice unicellular eukaryotes: a first-attempt assessment. Mar. Biodivers. 41, 13–28.

Poulin, M., Underwood, G.J.C., Michel, C., 2014. Sub-ice colonial Melosira arctica in Arctic first-year ice. Diatom Res. 29, 213–221.

Questel, J.M., Clarke, C., Hopcroft, R.R., 2013. Seasonal and interannual variation in the planktonic communities of the northeastern Chukchi Sea during the summer and early fall. Cont. Shelf Res. 67, 23–41.

Reid, P.C., Johns, D.G., Edwards, M., Starr, M., Poulin, M., Snoeijs, P., 2007. A biological consequence of reducing Arctic ice cover: arrival of the Pacific diatom Neodenticula seminae in the North Atlantic for the first time in 800000 years. Glob. Chang. Biol. 13, 1910–1921.

Rysgaard, S., Kühl, M., Glud, R.N., Hansen, J.W., 2001. Biomass, production and horizontal patchiness of sea ice algae in a high-Arctic fjord (Young Sound, NE Greenland). Mar. Ecol. Prog. Ser. 223, 15–26.

Selz, V., Laney, S., Arnsten, A.E., Lewis, K.M., Lowry, K.E., Joy-Warren, H.L., Mills, M.M., van Dijken, G.L., Arrigo, K.R., 2018. Ice algal communities in the Chukchi and Beaufort Seas in spring and early summer: composition, distribution, and coupling with phytoplankton assemblages. Limnol. Oceanogr. 63, 1109–1133.

Shimada, K., Kamoshida, T., Itoh, M., Nishino, S., Carmack, E., McLaughlin, F., Zimmermann, S., Proshutinsky, A., 2006. Pacific Ocean inflow: influence on catastrophic reduction of sea ice cover in the Arctic Ocean. Geophys. Res. Lett. 33, L08605, 08610.01029/02005GL025624.

Søreide, J.E., Falk-Petersen, S., Hegseth, E.N., Hop, H., Carroll, M.L., Hobson, K.A., Blachowiak-Samolyk, K., 2008. Seasonal feeding strategies of Calanus in the high-Arctic Svalbard region. Deep-Sea Res Pt II 55, 2225–2244.

Søreide, J.E., Leu, E.V.A., Berge, J., Graeve, M., Falk-Petersen, S., 2010. Timing of blooms, algal food quality and *Calanus glacialis* reproduction and growth in a changing Arctic. Glob. Chang. Biol. 16, 3154–3163.

Sukhanova, I.N., Flint, M.V., Pautova, L.A., Stockwell, D.A., Grebmeier, J.M., Sergeeva, V.M., 2009. Phytoplankton of the western Arctic in the spring and summer of 2002: structure and seasonal changes. Deep-Sea Res Pt II 56, 1223–1236.

Szymanski, A., Gradinger, R., 2016. The diversity, abundance and fate of ice algae and phytoplankton in the Bering Sea. Polar Biol. 39, 309–325.

Utermöhl, v.H., 1931. Neue Wege in der quantitativen Erfassung des Planktons (Mit besondere Beriicksichtigung des Ultraplanktons). Verh Int Verein Theor Angew Limnol 5, 567–595.

von Quillfeldt, C.H., Ambrose, W.G., Clough, L.M., 2003. High number of diatom species in first-year ice from the Chukchi Sea. Polar Biol. 26, 806–818.

Wang, Y., Xiang, P., Kang, J.-h., Ye, Y.-y., Lin, G.-m., Yang, Q.-l., Lin, M., 2018. Microphytoplankton community structure in the western Arctic Ocean: surface layer variability of geographic and temporal considerations in summer. Hydrobiologia 811, 295–312.

Wegner, C., Hölemann, J.A., Dmitrenko, I., Kirillov, S., Kassens, H., 2005. Seasonal variations in arctic sediment dynamics—evidence from 1-year records in the Laptev Sea (Siberian arctic). Glob. Planet. Chang. 48, 126–140.

Welschmeyer, N.A., 1994. Fluorometric analysis of chlorophyll a in the presence of chlorophyll b and pheopigments. Limnol. Oceanogr. 39, 1985–1992.

Wold, A., Darnis, G., Søreide, J.E., Leu, E., Philippe, B., Fortier, L., Poulin, M., Kattner, G., Graeve, M., Falk-Petersen, S., 2011. Life strategy and diet of Calanus glacialis during the winter–spring transition in Amundsen Gulf, south-eastern Beaufort Sea. Polar Biol. 34, 1929–1946.

Woodgate, R.A., Weingartner, T.J., Lindsay, R., 2012. Observed increases in Bering Strait oceanic fluxes from the Pacific to the Arctic from 2001 to 2011 and their impacts on the Arctic Ocean water column. Geophys. Res. Lett. 39.

Zamora-Terol, S., Nielsen, T.G., Saiz, E., 2013. Plankton community structure and role of Oithona similis on the western coast of Greenland during the winter-spring transition. Mar. Ecol. Prog. Ser. 483, 85–102.

Zamora-Terol, S., Kjellerup, S., Swalethorp, R., Saiz, E., Nielsen, T.G., 2014. Population dynamics and production of the small copepod Oithona spp. in a subarctic fjord of West Greenland. Polar Biol. 37, 953–965.

Deep–Sea Research II 177 (2020) 104814

Contents lists available at ScienceDirect

Deep-Sea Research Part II

journal homepage: http://www.elsevier.com/locate/dsr2

Advection and in situ processes as drivers of change for the abundance of large zooplankton taxa in the Chukchi Sea

Adam Spear *, Jeff Napp, Nissa Ferm, David Kimmel

Alaska Fisheries Science Center, National Marine Fisheries Service, National Oceanic and Atmospheric Administration, 7600 Sand Point Way NE, Seattle, WA, 98115-6349, USA

ARTICLE INFO

Keywords:
Zooplankton
Euphausiids
Climate
Chukchi sea
Sea ice
Arctic food webs

ABSTRACT

The Chukchi Sea has recently experienced increased water temperatures, increased advection of water from the Bering Sea, declines in sea-ice concentration, and shorter periods of ice coverage. These physical changes are expected to impact trophic food-webs and ecosystem attributes. In this study, a series of research surveys were conducted in the summers of 2011–2015 to characterize the physical environment and its relation to the abundance of large zooplankton. Large zooplankton are key prey for many higher trophic level organisms including seabirds, marine mammals, and fishes. Yearly advection from the Bering Sea influenced the adult large zooplankton abundance, but this influence was less apparent in the earlier development stages. Known development times of stages of zooplankton, along with their location within the study area, suggested that a fraction of the zooplankton standing stock was the result of local production. Decreased advection and later ice retreat resulted in higher abundances of the lipid-rich copepod *Calanus glacialis*. Warmer conditions with increased advection from the Bering Sea resulted in higher abundances of euphausiids. Warming, sea-ice melting, and increases in transport of Bering Sea water and plankton into the Chukchi Sea are ongoing, and changes in food-web structure are likely to result.

1. Introduction

The zooplankton of the Chukchi Sea shelf consist of taxa that are more similar to the Pacific Ocean community than the Arctic Ocean community (Ashjian et al., 2010, 2017; Hopcroft et al., 2010; Eisner et al., 2013; Questel et al., 2013; Pinchuk and Eisner, 2017), a result of the transport of North Pacific water through the Bering Strait into the Arctic. Northward advection through the Bering Strait combines several water masses that results in the transport of relatively warm, nutrient-rich water, as well as primary and secondary producers into the Arctic (Woodgate et al., 2005; Gong and Pickart, 2015; Danielson et al., 2017; Stabeno et al., 2018). Northward advection through the Bering Strait in the summer, along with sea-ice melting and episodic upwelling from the Beaufort Sea on to the shelf and Barrow Canyon, results in a highly productive and complex shelf ecosystem that responds to local, regional and global forcing (e.g. Bond et al., 2018). Adding to the complexity of the Chukchi Sea shelf ecosystem, recent reports have shown dramatic changes in timing and extent of sea-ice coverage, along with considerable increases in sea surface temperatures (National Snow and Ice Data Center, nsidc.org; Timmermans and Ladd, 2019; Perovich et al., 2019).

In summer, the northern Bering and Chukchi seas experience increased day length and melting sea ice, resulting in a phytoplankton bloom. The bulk of the bloom sinks to the bottom due to the shallow depth (<50 m) and relatively low grazing impact on phytoplankton (Campbell et al., 2009), supporting a robust benthic community. Recent studies, however, have shown a temporal decrease in benthic biomass in the northern Bering Sea, suggesting a possible weakening of benthic-pelagic coupling as the ice retreat now occurs earlier in the season (Grebmeier et al., 2006a; Grebmeier et al., 2006b; Grebmeier, 2012). Concurrently, zooplankton biomass in the Chukchi Sea has increased over the past seven decades (Ershova et al., 2015), which can be explained, in part, by increasing temperatures, reduction in sea ice, and an increase in northward water transport through the Bering Strait (Ershova et al., 2015; Woodgate et al., 2015; Woodgate, 2018). These trends suggest a potential ecosystem regime shift is underway in the Pacific Arctic, with consequences for local food webs. These changes emerge from both direct and indirect effects on both the indigenous biota residing in the ecosystem as well as the introduced species. Changes in the timing and type of production within the pelagic and

* Corresponding author.
E-mail address: Adam.Spear@noaa.gov (A. Spear).

https://doi.org/10.1016/j.dsr2.2020.104814
Received 31 July 2019; Received in revised form 3 June 2020; Accepted 3 June 2020
Available online 11 June 2020
0967-0645/Published by Elsevier Ltd.

benthic communities, will result in changes in benthic-pelagic coupling that have the potential to effect higher trophic levels such as birds, marine mammals, fish, and the people who live in the region.

One specific taxon of interest for our studies were bowhead whales (*Balaena mysticetus*) that forage as they migrate southwestward in the fall through the Utqiagvik (formerly known as Barrow) region from the Beaufort Sea (Moore et al., 2010; Quakenbush et al., 2010; Citta et al., 2012). Studies have reported improvements in bowhead body condition in association with earlier ice retreat and increase in the area of open water (George et al., 2015). The observed improvements in bowhead body condition may be the result of increased prey populations, specifically euphausiids and copepods that dominate the prey in stomachs of bowhead whales harvested near Utqiagvik, Alaska (Lowry et al., 2004; Ashjian et al., 2010; Moore et al., 2010; George et al., 2015). Previous studies suggested that euphausiids are advected along the bottom from the northern Bering Sea into the Chukchi Sea, and subsequently concentrated into dense aggregations through upwelling onto the Beaufort Sea shelf towards Barrow Canyon (Berline et al., 2008; Ashjian et al., 2010). Zooplankton sampling in the Chukchi Sea has generally underestimated populations of euphausiids because estimates were based on collections from small (0.25–0.6 cm diameter) aperture size plankton bongo nets (Hopcroft et al., 2010; Eisner et al., 2013; Questel et al., 2013; Ashjian et al., 2017; Pinchuk and Eisner, 2017) and because the predominantly daytime vertical or oblique sampling failed to target krill layers near the bottom (Coyle and Pinchuk, 2002).

The main objectives of this study were 1) to understand the transport pathways of euphausiids from the Bering Strait to Barrow Canyon, 2) evaluate the abundance of other large planktonic prey for whales in the region, and 3) provide data on the status and trends of Chukchi Sea zooplankton communities. This study builds on other research based on conceptualized modeling to explain the dynamics of late-summer euphausiid populations in this region (Berline et al., 2008; Ashjian et al., 2010) by providing empirical data collected from epibenthic and plankton tows that should more accurately reflect the abundance of euphausiid and other epibenthic taxa. We compared epibenthic and pelagic zooplankton abundances to assess whether they were significantly different and to explore whether epibenthic tows were a more accurate reflection of near-bottom taxa. We hypothesized that advection of zooplankton from the Bering Sea to be the main driver of zooplankton abundance in the region. To test this, we compared zooplankton abundance across years and locations, and calculated krill development times to see if euphausiids captured in this study could have reached that stage after having been advected from the Bering Sea.

2. Methods

2.1. Study area

The Chukchi Sea has a broad, mostly shallow (<50 m) shelf situated between Alaska and Siberia (Fig. 1). Survey transects varied among years, 2011–2015, depending on the scientific focus for the year, available ship time, and ice distribution. Surveys were conducted in the late summer, lasting approximately 30 days (~August 5th – September 5th), except for 2014, which was September 22nd – October 12th. For analysis and description purposes, the study area was divided into 'Beaufort', 'Southwest,' 'Central,' and 'Northeast' regions that are established from statistically different oceanographic conditions (Eisner et al., 2013; Randall et al., 2019).

2.2. Physical data

Hydrographic data, including temperature and salinity, were collected using a SBE 911plus and FastCAT SBE 49 systems (SeaBird Electronics). Sea Surface temperatures (SST) were averaged from 5 – 10 m depth. We quantified broad-scale patterns in sea-ice concentration using satellite data. Sea-ice concentration (percentage of ocean covered by sea-ice) and extent data were obtained after the surveys from a Scanning Multichannel Microwave Radiometer (SMMR) on the Nimbus-7 satellite and from the Special Sensor Microwave/Imager (SSM/I) sensors on the Defense Meteorological Satellite Program's (https://nsidc.org; Comiso, 1999). Bering Strait volume transport data were acquired from moored Acoustic Doppler Current Profiler (ADCP)

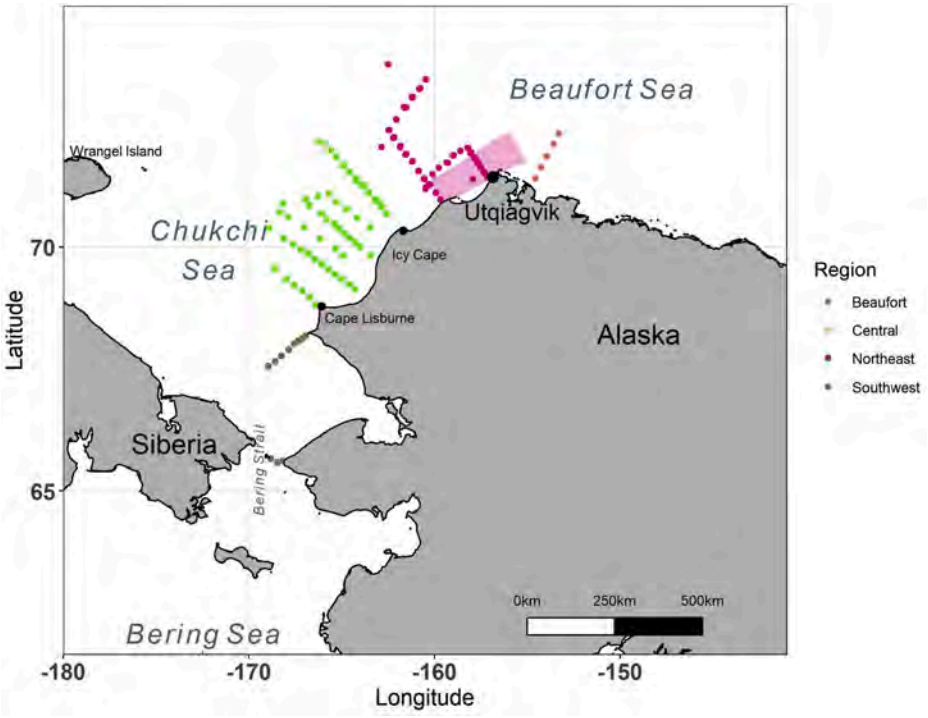

Fig. 1. Study area in the Chukchi Sea. Each region is symbolized by a colored circle. The study area was split up into southwest, central, northeast, and Beaufort regions. The pink shaded region indicates Barrow Canyon.

measurements (Woodgate et al., 2015; Woodgate, 2018). Northeastward water column volume transport, in Sverdrups (Sv), was calculated according to Stabeno et al. (2018) from current data measured at C1, C2, and C3 moorings along the Icy Cape transect. Transport was averaged over 14 and 30 days leading up to the date that the station was sampled.

2.3. Zooplankton net data

Zooplankton were collected primarily during daylight hours using a multiple-opening and closing 1 m^2 Tucker Sled trawl equipped with a FastCAT, and sled-like runners at the bottom so that samples could be taken in close proximity to the bottom. A 505 μm (2013–2015) or a 333 μm (2011–2012) mesh net sampled while the sled was towed at a speed of 1.5–2.0 knots along the bottom for 2 min, then mechanically tripped to close and simultaneously open a second net to sample the entire water column from the bottom to the surface (wire retrieval rate 20 m min^{-1}). For smaller taxa, a 25 cm net with 150 μm mesh was suspended in the larger net that profiled the entire water column. Note that this setup is not ideal in cases where clogging in the 20- cm net occurs, thus the possibility of inaccurate volume filtered readings exist in this study. Samples that appeared questionable (e.g. low flowmeter readings, large jellyfish in the net) were excluded from the analysis. Smaller taxa such as *C. glacialis* and euphausiid furcilia were enumerated in the water column only and not in the epibenthic samples. Both Tucker nets were equipped with a separate calibrated General Oceanics flow meter to estimate volume filtered. Plankton captured by the nets were washed into the cod-ends, sieved through appropriately-sized wire mesh screens and preserved in glass jars with sodium borate-buffered 5% Formalin. Samples were inventoried at the end of the cruise and then sent to the Plankton Sorting and Identification Center in Szczecin, Poland, for processing. Subsampled taxa were enumerated and identified to lowest possible genera and life stage and returned to the Alaska Fisheries Science Center for verification. Ten percent of the returned samples were checked for quality assurance/quality control of species identification and enumeration.

2.4. Zooplankton data analysis

Zooplankton abundance was reported as four general categories in the context of known bowhead whale prey in the region (Lowry et al., 2004; Moore et al., 2010), including: euphausiids (primarily *Thysanoessa raschii*), amphipods (dominant species included *Themisto libellula* and unidentified Gammaridea), mysids (dominant species included *Neomysis rayii* and *Pseudomma truncatum*), and copepods (*Calanus glacialis*). Analysis of variance (ANOVA) was used to examine epibenthic and pelagic variation across years in *T. raschii*, mysid, and amphipod abundance.

Development times of *Thysanoessa* spp. stages were estimated using the formula:

$$R_2 = R_1 * Q_{10}^{\frac{T_2 - T_1}{10}}$$

where R_1 and R_2 are the development rates (d^{-1}) at temperature T_1 and T_2 (°C), respectively (Teglhus et al., 2015). We used the Q_{10} of 2.04 (Pinchuk and Hopcroft, 2006). The calculated temperature (T_2) and development rate (R_2) were normalized to 5 °C and 0.016 d^{-1} (for furcilia; 0.045 d^{-1} for calyptopis), obtained from Teglhus et al. (2015). We chose the measured rates from Teglhus et al. (2015) because of the similar temperature conditions (5–8 °C) and because a mixed population of krill was used as we also have a mixed community. These were also the slowest known development rates for *Thysanoessa* spp. furcilia compared to previous studies (see Table 3 in Teglhus et al., 2015); this prevented an overestimation of development rates of *Thysanoessa* spp. under conditions that may be significantly influenced by availability of food such as phytoplankton (Pinchuk and Hopcroft, 2007). Development times were then compared to satellite-tracked drifter data (Stabeno et al., 2018) to explore the possibility of recent reproduction in the Chukchi Sea.

We used the mgcv package (Wood, 2011) in R (R Core Team, 2019) to fit generalized additive models (GAM) with Gaussian distribution to relate changes in C2 and C5 stages of *C. glacialis, T. raschii* (adult and juvenile), and euphausiid furcilia mean abundance to environmental variables. These two particular stages in each species were chosen to contrast different ages, with C2 representing younger and C5 representing older *C. glacialis*, and furcilia representing younger and adults/juveniles representing older *T. raschii*. For simplicity, we excluded stages C3 and C4 from the analysis as these stage abundances are correlated to the C5 stage (data not shown). We chose to exclusively use epibenthic abundances of *T. raschii* since most of our sampling occurred primarily during the day and when the vast majority of euphausiids would be at or near the bottom. Restricted Maximum Likelihood (REML) method was used as the smoothing parameter estimation. The model selection was done by assessing deviance explained, R^2, and Akaike information criterion (AIC). Residuals were analyzed to ensure there were no obvious deviations from normal distributions, and we examined the response versus. fitted value for patterns. We assessed ten environmental variables for inclusion in the GAMs including: latitude, longitude, bottom temperature, surface temperature, bottom salinity, surface salinity, 14 and 30-day northeastward transport, year, and day of the year (hereinafter referred to as ordinal day).

3. Results

3.1. Environmental conditions

Sea surface temperatures (SST) were warmest in 2011 (mean SST 6.89 ± 1.35 °C) and coldest in 2013 (mean SST 2.64 ± 2.61 °C). Both 2012 (mean SST 5.46 ± 2.41 °C) and 2015 (mean SST 6.13 ± 2.18 °C) had similar warm SSTs towards the central and southwest portion of the survey, and colder SSTs across the northeast portion; however, 2012 was colder in the northeast region (Fig. 2). Sea surface temperatures in 2014 (mean SST 3.09 ± 1.62 °C) were colder over the entire survey area and had substantially less northeast to southwest variability. Randall et al. (2019) using the mean bottom temperatures in the central region, found 2013 (−1.4 °C) to be the coldest year, with 2011–2012 and 2014–2015 having similar warmer bottom temperatures (~2 °C). Similarly, differences between years were evident from initial dates at which ice concentration was less than 10% (Table 1). Sea-ice remained in the northeast region until mid to late August in years 2012–2014, and melted in mid-to late July in 2011 and 2015.

Monthly mean northward transport (Sv) through the Bering Strait tended to peak in the spring and summer (~May–August), with lower transport in the winter (Fig. 3). Higher spring/summer transport occurred in 2011and 2015, peaking at around 1.92 (±0.09) Sv in May and 1.87 (±0.06) Sv in July of 2015 and 1.91 (±0.10) Sv in June of 2011. Spring and summer transport was moderate in 2014 and lower in 2012 and 2013, with mean values as low as 1.14 (±0.18) and 1.18 (±0.14) in August of 2012 and 2013, respectively.

3.2. Zooplankton abundance

Average pelagic amphipod abundances increased from 2011 to 2015; average benthic abundances were generally higher than pelagic abundances but also increased over the same period (Fig. 4a). Overall, 2013, 2011 had the highest and lowest average amphipod abundance respectively. Mysid epibenthic and pelagic abundances were relatively low across all years (Fig. 4b), but epibenthic abundances were relatively higher in all years and there were no increasing or decreasing trends across the years. The euphausiids community consisted of four species of the genus *Thysanoessa*: *T. inermis, T. longipes, T. spinifera, and T. raschii*; the latter, being the most abundant (approximately 70% of total abundance) of the four, was singled out in this study for purposes of

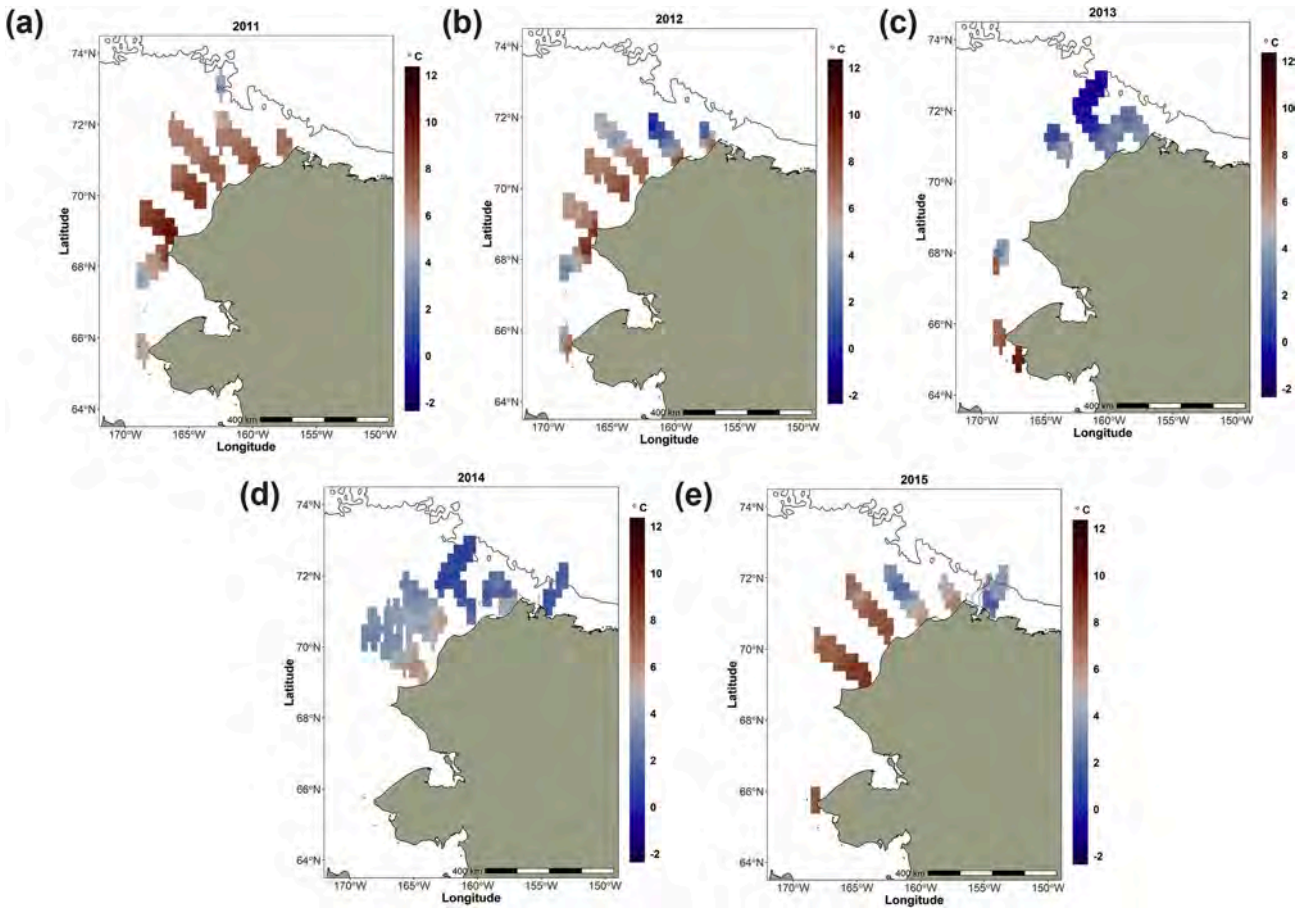

Fig. 2. Sea surface temperature (°C) averaged from 5-10 m for each year.

Table 1
Estimate of the initial date at which ice concentration was less than 10% within the southwest and northeast region of the sampling area.

	Southwest	Northeast
2011	3 June	15 July
2012	22 June	19 August
2013	29 June	31 August
2014	16 June	16 August
2015	14 June	18 July

simplicity. Epibenthic *T. raschii* abundances were lowest in 2013 and highest in 2014 (Fig. 4c). Pelagic *T. raschii* abundance was lowest in 2011 and highest in 2015.

There were no consistent differences in the abundance of *T. raschii*, mysid, and amphipods between the bottom layer and water column when we took into account year and a depth-year interaction in our analyses. ANOVA results did not show significant differences between epibenthic and pelagic *T. raschii* abundances independent of year. However, *T. raschii* abundance did show significant differences between years ($F = 3.20$, $p = 0.01$), independent of depth and depth/year interactions ($F = 5.56$, $p < 0.001$). Similarly, ANOVA results did not show significant differences between epibenthic and pelagic amphipods independent of year ($F = 2.16$, $p = 0.14$). However, amphipod abundances did show significant differences among years independent of depth ($F = 4.467$, $p = 0.001$) and depth/year interactions ($F = 3.294$, $p = 0.01$). ANOVA results showed significant differences between epibenthic and pelagic mysids independent of year ($F = 9.59$, $p = 0.002$), years independent of depth ($F = 4.80$, $p = 0.0008$), and depth/year interactions ($F = 0.84$, $p = 0.50$). Time of day was hypothesized to influence euphausiid

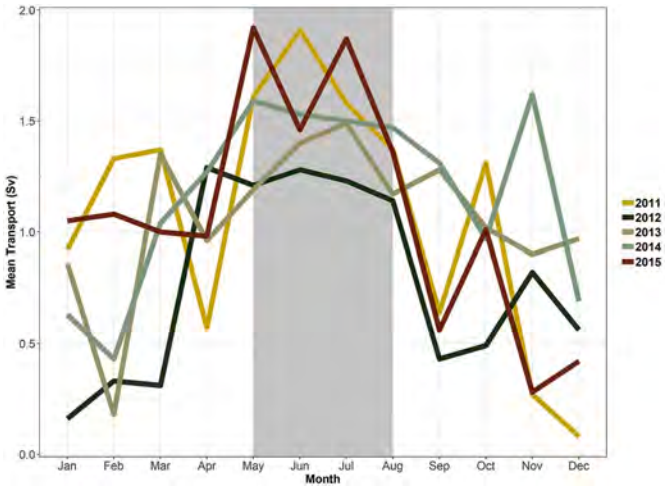

Fig. 3. Mean transport (Sv) of water by month for each year through the Bering Strait. The grey underlay highlights the approximate peak transport months.

abundance, however, ANOVA results did not find differences in day/night sampling abundances of *T. raschii* at the $p < 0.05$ significance level.

A post-hoc Tukey's 'Honest Significant Difference' test of depth-year interactions of *T. raschii*, mysids, and amphipods showed 2014 and 2015 were significantly ($p < 0.05$) different from most previous years (Table 3). Within years 2014 and 2015, *T. raschii* showed significant ($p < 0.05$) differences between epibenthic and pelagic depths. Similarly, both mysids and amphipods showed significant ($p < 0.05$) differences

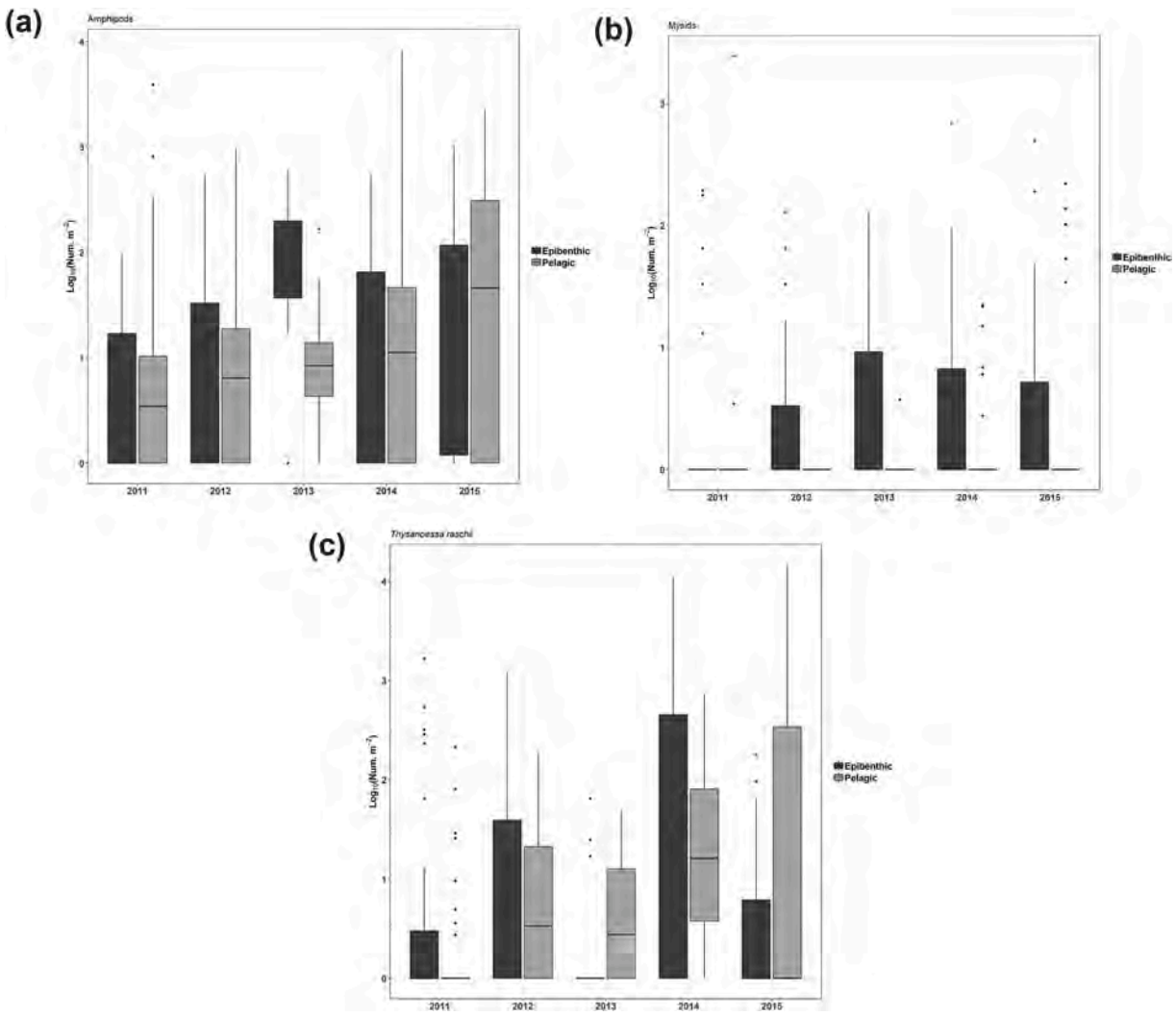

Fig. 4. Yearly epibenthic and pelagic total abundance (Log_{10}(Num m^{-2})) for amphipods (a), mysids (b), and *Thysanoessa raschii* (c).

between epibenthic and pelagic depths within 2014. Overall, we cannot independently assess year without noting whether *T. raschii*, mysids, or amphipods samples were caught in the water column or just above the bottom.

There was a lack of spatial differences among years for amphipods, with positive catches across all regions (Fig. 5a). The highest amphipod frequency of occurrence was in 2013, with complete absence in only one station (epibenthic and pelagic combined). Mysid abundance was low for each year across all regions (Fig. 5b); within years, more mysids were captured in the northeast than other regions. Mysid had the highest frequency of occurrence in 2014 with animals captured at stations in 3 of the 4 regions (epibenthic and pelagic combined). A lack of spatial differences of *T. raschii* among years was evident (Fig. 5c), with positive catches appearing across most regions. The highest *T. raschii* frequency of occurrence was in 2014, with presence detected from at least one station in three of the four areas (epibenthic and pelagic combined). There were no obvious trends in presence/absence or abundance as a function of distance from land.

Abundances of *C. glacialis* were lower in warmer years (2011, 2014, and 2015) and higher in colder years (2012, 2013; Fig. 6). *Calanus glacialis* were ubiquitous across all regions, with presence detected at most stations (Fig. 7).

3.3. Early life stages

Development time calculations suggest that it takes approximately 51 and 78 days at 8 and 2 °C water temperature, respectively, for *Thysanoessa* spp. stages to develop from eggs to furcilia (Table 2). Note that the furcilia counted in this study were not identified to species. Euphausiid furcilia stages were most abundant in the central and southwestern regions of each year (Fig. 8). Euphausiid furcilia were completely absent from the northeastern region in 2012 and 2013. Both 2011, 2014 had similar abundances along the central and southeastern regions, with 2011 having slightly higher abundances in the northeast. In 2015, highest abundances were located in the central region, with lower abundances extending into the northeast. Euphausiid calyptopis, a developmental stage of much shorter duration (~40 days shorter; Teglhus et al., 2015), were only caught in very low abundances (~1.0 log_{10} (Num. m^{-2})) in 2011 at 3 stations (map not shown) from the northeast and southwest regions.

Spear et al. (2019) estimated *C. glacialis* egg to C2 stages have approximate development times of 8 to 12 days at temperatures ranging between 12 and -1.5 °C respectively. *Calanus glacialis* C2 stages were almost exclusively caught in the northeast region, including Icy Cape (Fig. 9). Higher total abundances appeared in both 2012 (4.92 log_{10} (Num. m^{-2})) and 2013 (5.19 log_{10} (Num. m^{-2})), while the lowest total abundances were in 2011 (3.38 log_{10} (Num. m^{-2})).

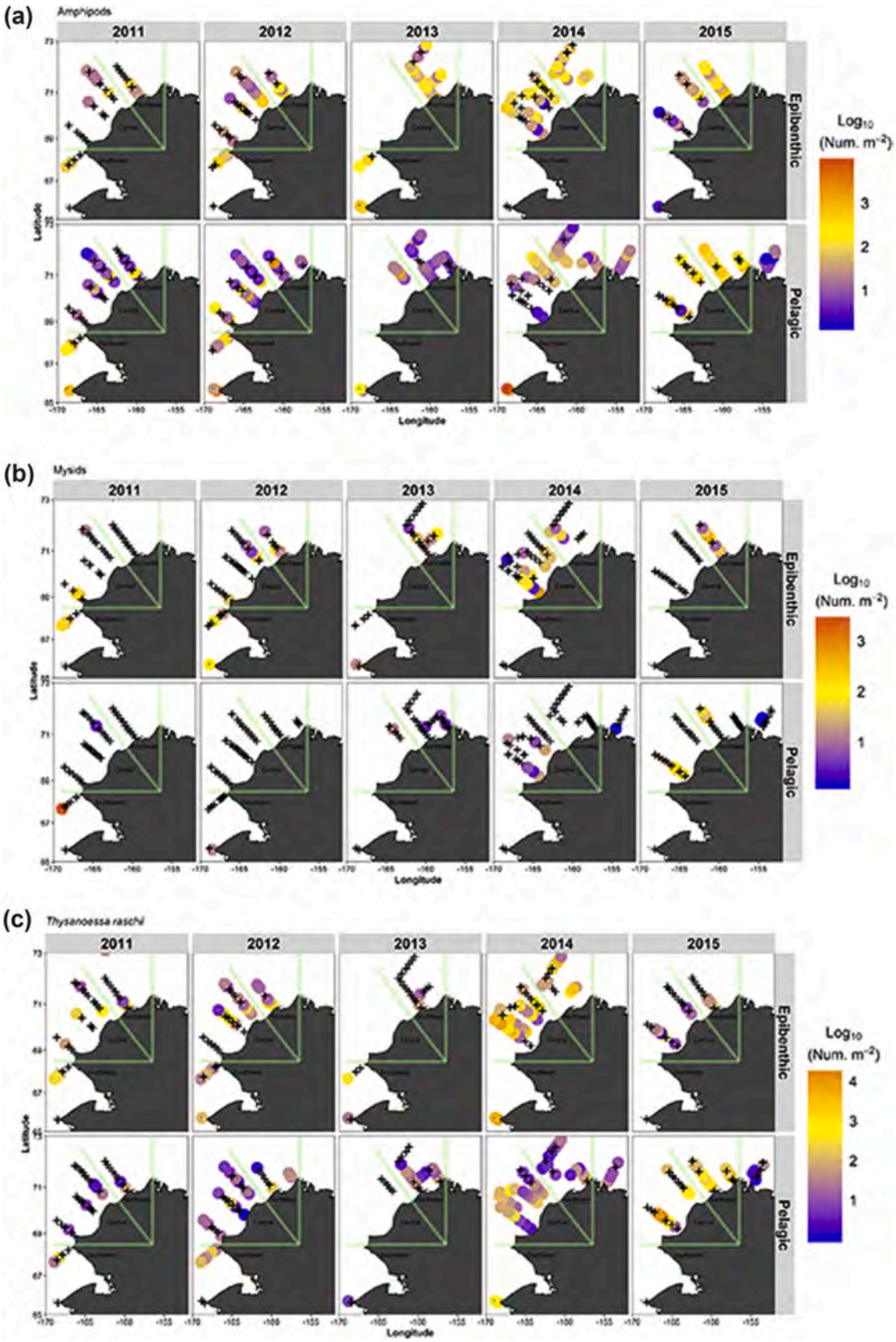

Fig. 5. Yearly maps of epibenthic and pelagic total abundance (Log_{10}(Num m^{-2}))for amphipods (a), mysids (b), and *Thysanoessa raschii* (c). The letter "X" denotes tows where the taxon was absent. Note that the scale differs among taxa.

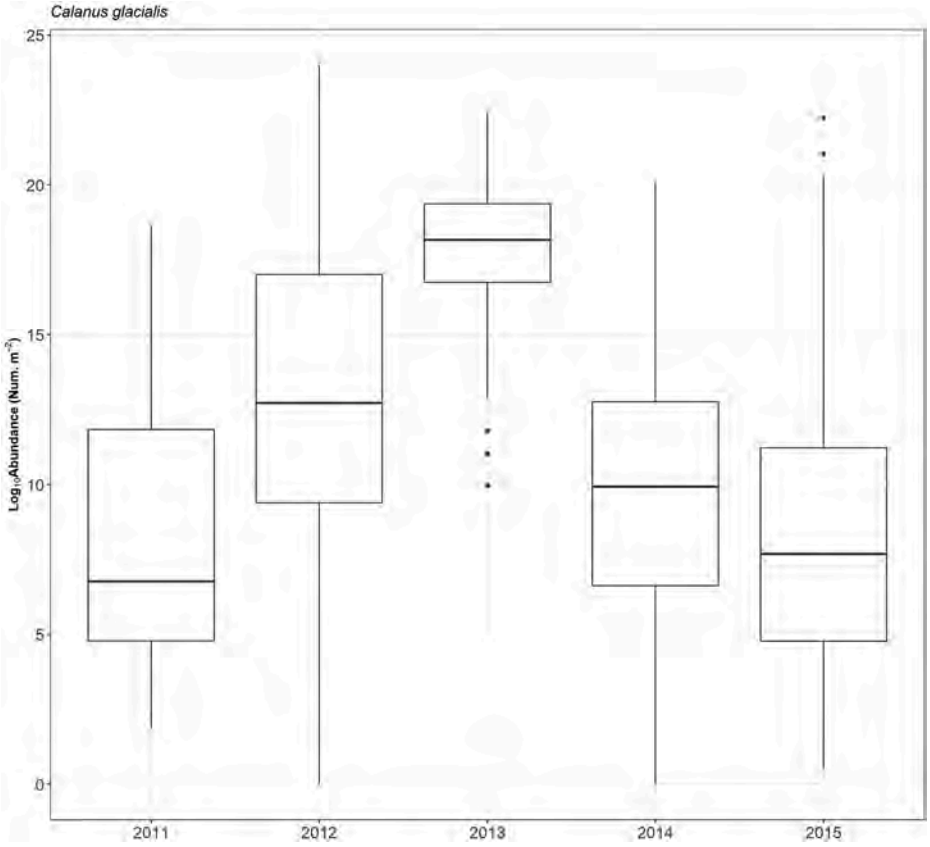

Fig. 6. Yearly pelagic total abundance (Log_{10}(Num m^{-2})) of *Calanus glacialis*.

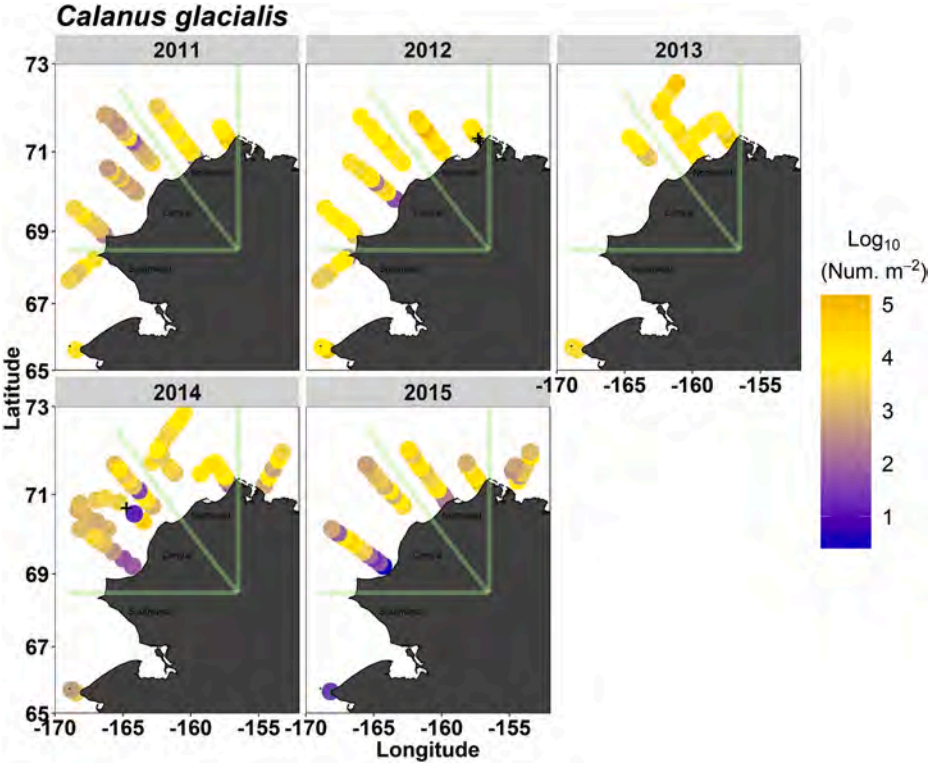

Fig. 7. Yearly maps of pelagic total abundance (Log_{10}(Num m^{-2})) of *Calanus glacialis*. The letter "X" denotes tows where the taxon was absent.

Table 2
Amount of days at different temperatures for *Thysanoessa* spp. stages to develop from eggs.

Stage	12 °C	8 °C	2 °C	−1.5 °C
Calyptopis	13.4	17.8	27.3	35
Furcilia	38.2	50.9	78	100

3.4. Relationships between plankton abundance and physical variables

Bottom temperature, 30-day northeastward transport, longitude, and ordinal day were the most significant variables associated with mean *T. raschii* abundance (Table 4). The model helped explain 42.3% of the deviance with an r^2 of 0.38. Extreme lower and higher bottom temperature conditions were associated with lower *T. raschii* abundance (Fig. 10). There was a positive relationship between 30-day northeastward transport and *T. raschii* abundance. The longitude parameter also showed that *T. raschii* abundance was positively associated with the northeastern and southwestern portions of the study area. The strong positive relationship with ordinal day showed that higher abundances showed up later in the year in 2014. This is because the only year in which we sampled past day of year 260 was 2014. Furcilia abundance had significant relationships with bottom temperature, 14-day northeastward transport, year, ordinal day, and longitude. The model explained 56.8% deviance in abundance for euphausiid furcilia with an r^2 of 0.53 (Table 4). There was not a clear abundance pattern in relation to the bottom temperature (Fig. 11). In contrast to the relationship between transport and *T. raschii* adults, there was a negative relationship with furcilia abundance and 14-day northeastward transport.

The model helped explain 43% of the deviance with an r^2 of 0.39 of the *C. glacialis* C5 stage (Table 4). The most significant parameters included surface salinity, surface temperature, bottom temperature, 14-day transport, ordinal day, and year. Higher surface temperatures had a positive association, while lower surface had a slightly negative association, with C5 abundances (Fig. 12). Conversely, lower bottom temperatures had a positive relationship and higher bottom temperatures had a negative relationship with C5 abundance. Stage C5 abundance was also negatively associated with lower salinity seawater. There was a slight negative association with strong northeastward transport and C5 abundance. Interestingly, there was not a significant association with northeastward transport and *C. glacialis* C2 stages. The C2 stage was similar to C5 stages in the relationship with bottom temperatures, as there was a negative relationship with higher bottom temperatures and a positive relationship lower bottom temperatures (Fig. 13). There was positive association of C2 stages with higher longitudes. Overall, C2 stages had the strongest GAM model, which explained 57% of the deviance and a r^2 of 0.55 (Table 4).

4. Discussion

4.1. Euphausiid transport

T. raschii is an amphiboreal species whose distribution also extends to the Arctic Ocean and associated continental shelves. We observed the presence of *T. raschii* in all years near Utqiagvik, with relatively high abundances in 2014 and 2015. The annual presence of euphausiids there is important as they are a dominant component of the diet for bowhead whales in the region (Lowry et al., 2004; Moore et al., 2010). A positive association with northeastward transport and a positive association with higher longitudes, implies that *T. raschii* were advected from the south. The positive association with lower longitudes may be the result of krill being advected into the Chukchi Shelf from the Beaufort Sea as described by Ashjian et al. (2010); other explanations include lack of sampling in the central region in 2013, sampling later in the 2014, or because of the current patterns that tend to extend farther offshore in the central region (Stabeno et al., 2018), resulting in animal presence just outside of the sampled transect. Overall, these findings support the hypothesis of Berline et al. (2008) and Ashjian et al. (2010) that the

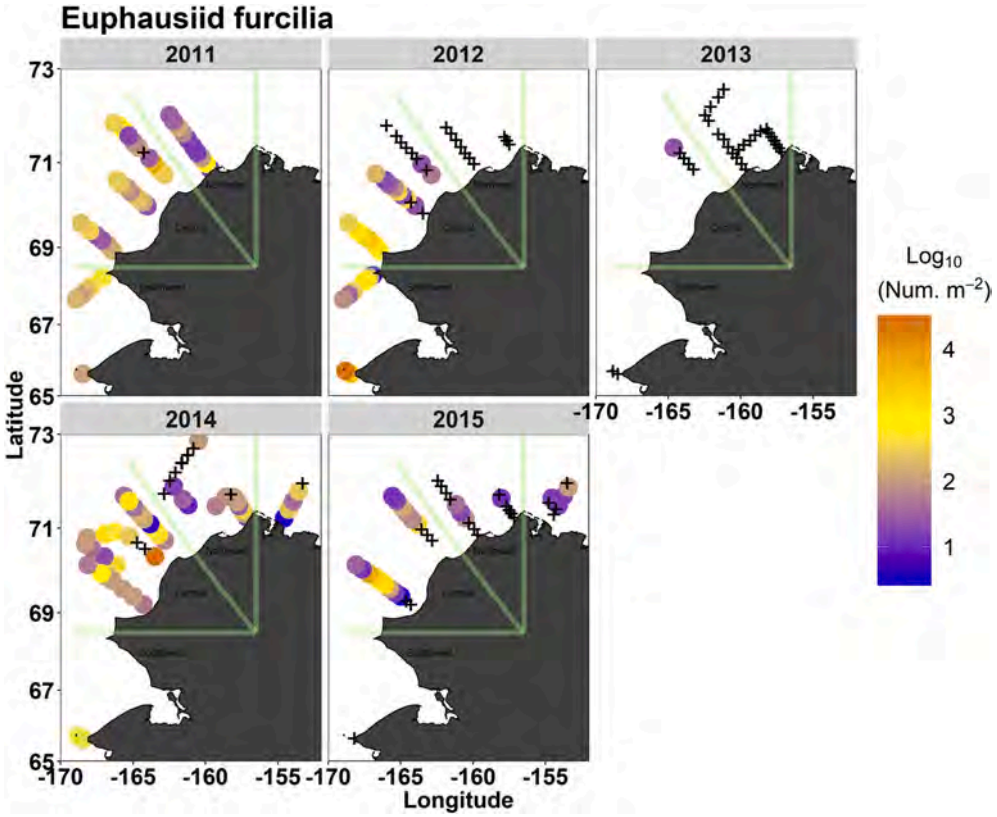

Fig. 8. Yearly maps of pelagic total abundance (Log_{10}(Num m^{-2})) of euphausiid furcilia. The letter "X" denotes tows where the taxon was absent.

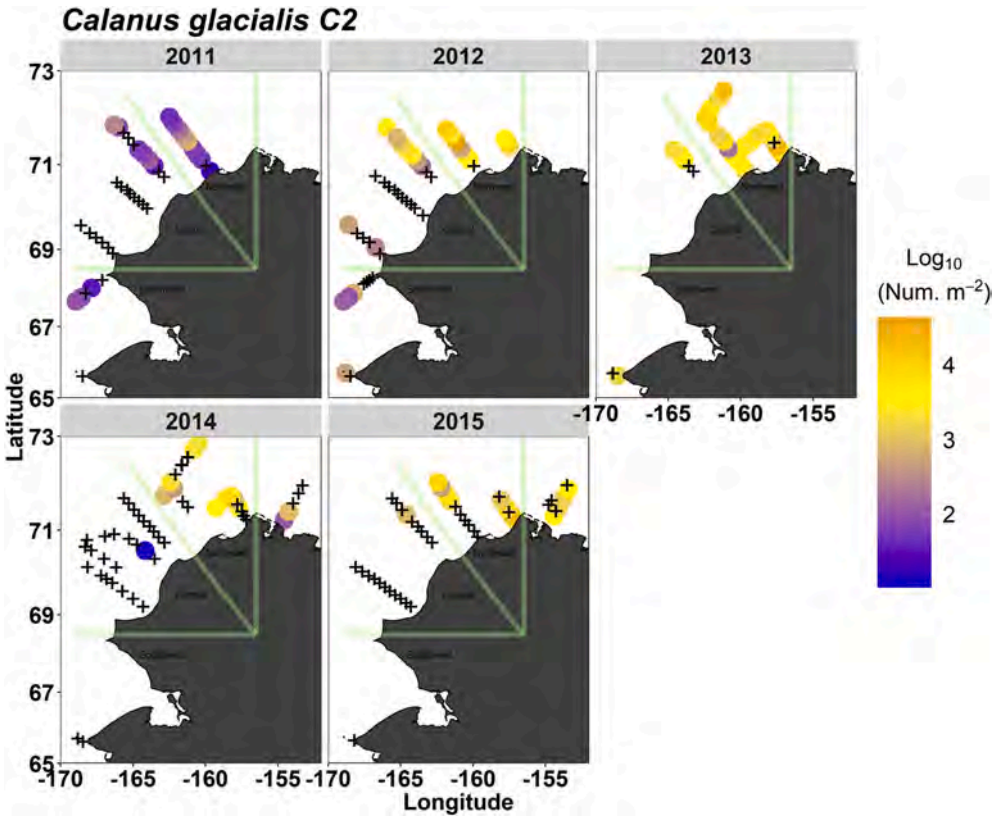

Fig. 9. Yearly maps of pelagic total abundance (Log_{10}(Num m^{-2})) of *Calanus glacialis* C2 stage. The letter "X" denotes tows where the taxon was absent.

Table 3
Post-hoc Tukey's test significant *p* values for the depth-year interactions of each taxon.

	Depth:Year	*p* value
T. raschii	Epibenthic:2014 – Pelagic:2011	0.0200
	Pelagic:2015 – Pelagic:2011	0.0252
	Epibenthic:2014 – Epibenthic:2011	0.0462
	Epibenthic:2014 – Pelagic:2012	0.0179
	Pelagic:2015 – Pelagic:2012	0.0234
	Epibenthic:2014 – Epibenthic:2012	0.0417
	Pelagic:2015 – Epibenthic:2011	0.0494
	Epibenthic:2014 – Pelagic:2014	0.0235
	Pelagic:2015 – Pelagic:2014	0.0307
	Epibenthic:2015 – Epibenthic:2014	0.0342
	Epibenthic:2015 – Pelagic:2015	0.0390
Mysids	Epibenthic:2014 – Pelagic:2011	0.0000
	Epibenthic:2014 – Epibenthic:2011	0.0001
	Epibenthic:2014 – Pelagic:2012	0.0000
	Epibenthic:2014 – Epibenthic:2012	0.0001
	Epibenthic:2014 – Pelagic:2013	0.0008
	Epibenthic:2014 – Epibenthic:2013	0.0009
	Epibenthic:2014 – Pelagic:2014	0.0000
	Epibenthic:2014 – Epibenthic:2015	0.0001
	Epibenthic:2014 – Pelagic:2015	0.0001
Amphipods		
	Epibenthic:2014 – Pelagic:2011	0.0060
	Epibenthic:2014 – Epibenthic:2011	0.0017
	Epibenthic:2014 – Pelagic:2012	0.0010
	Epibenthic:2014 – Epibenthic:2012	0.0014
	Epibenthic:2014 – Pelagic:2013	0.0101
	Epibenthic:2014 – Epibenthic:2013	0.0087
	Epibenthic:2014 – Pelagic:2014	0.0063
	Epibenthic:2014 – Pelagic:2015	0.0312
	Epibenthic:2014 – Epibenthic:2015	0.0010

Table 4
GAM model significant terms for each taxon with R^2 and the percentage of deviance explained. $*p < 0.05$; $**p < 0.01$; $***p < 0.001$.

	Significant terms	R^2	Deviance explained
***Calanus glacialis* C5**	Surface Salinity***	0.394	43%
	Surface Temperature*		
	14-day Transport*		
	Bottom Temperature***		
	Ordinal Day***		
	Year***		
***Calanus glacialis* C2**	Mean Bottom Temperature***	0.551	57%
	Mean Surface Temperature**		
	Longitude*		
	Julian Day*		
	Year*		
Thysanoesssa raschii	Mean Bottom Temperature**	0.375	42.3%
	30-day Transport*		
	Longitude***		
	Ordinal Day ***		
Euphausiid furcilia	Mean Bottom Temperature ***	0.53	55.8%
	14-day Transport***		
	Longitude***		
	Ordinal Day***		
	Year***		

euphausiids concentrated by physical processes near Barrow Canyon likely originated from the northern Bering Sea.

Conversely, temperature-dependent euphausiid furcilia development times suggest their extent into the central and northeast regions in warmer conditions was a result of spawning in the Chukchi Sea. Transport of water takes ~90 days to reach Icy Cape from the Bering

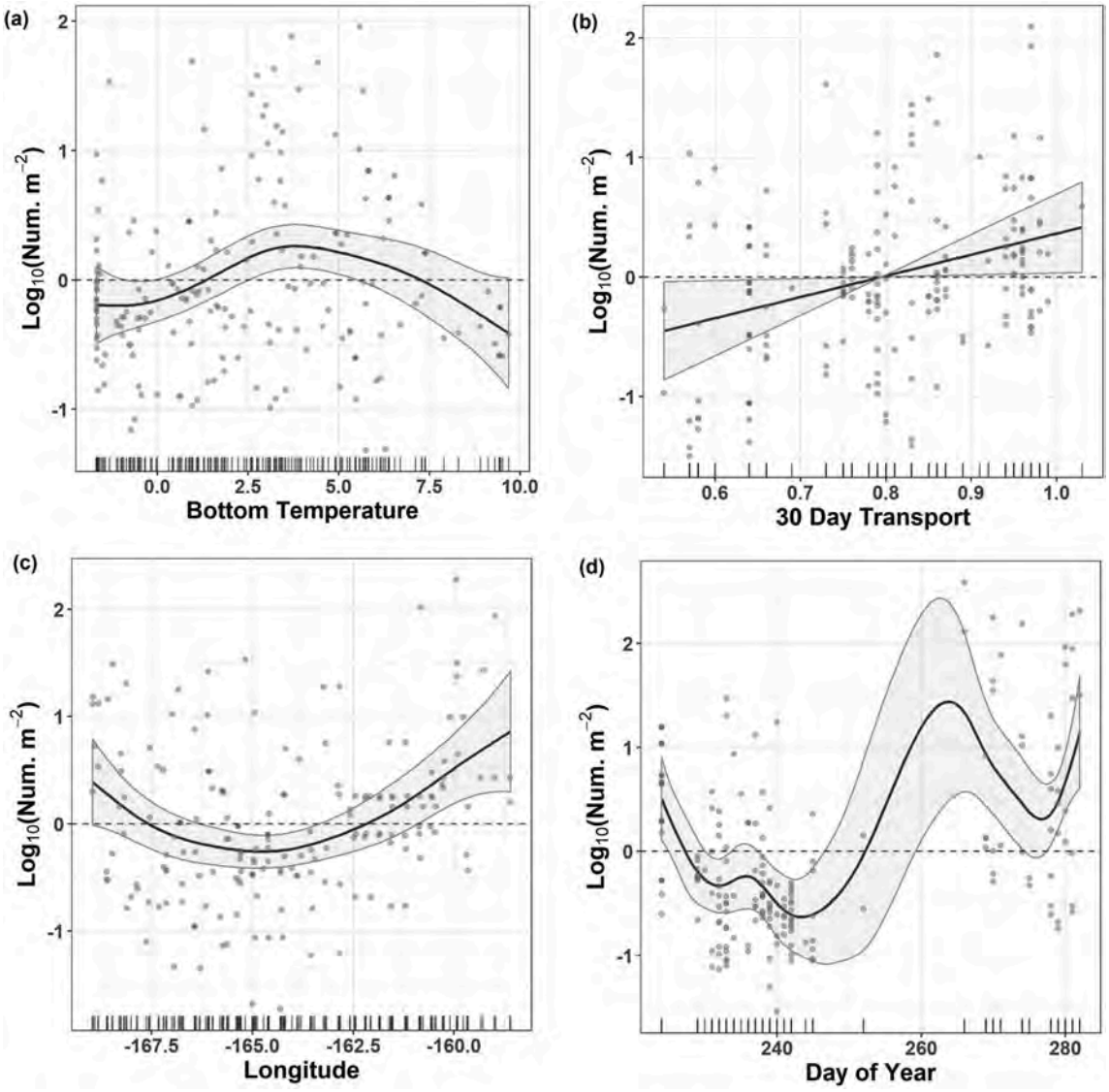

Fig. 10. GAM smooth for the distribution of *Thysanoessa raschii* epibenthic abundance (Log_{10}(Num m^{-2})), 2011–2015. Variables included mean bottom temperature (a), 30-day transport (b), longitude (c), and day of year (ordinal day) (d).

Strait (Stabeno et al., 2018). This is roughly 12 to 40 days longer than the development time from egg to furcilia at comparable temperatures. The hypothesis of local production is also supported by the negative relationship with 14-day transport or lack of clear relationship with bottom temperatures. In particular, the negative relationship with 14-day transport (in addition to a lack of association with 30-day transport) showed that the greater and more recent transport resulted in reduced abundances, suggesting they were likely recently spawned nearby and subsequently transported away.

Adult euphausiids were present in the northeast region in 2012 and 2013, even though overall transport during those years was low. The absence of younger stages could have resulted from a change in the timing of reproduction relative to our sampling, failed spawning, or very high mortality of the larvae because of cold temperatures or high predation. Euphausiid eggs were present in the northeast region in 2014 and 2015, but were absent in 2012 and 2013 (egg data not collected in 2011), suggesting reproduction only occurred when this region was not occupied by colder water masses.

The higher pelagic abundances of euphausiids in 2013 and 2015 were not due to a day/night effect as a comparison of day/night abundances found no significant differences (not shown). The significant increase in abundance of *T. raschii* in 2014, compared to remaining years, suggests that sampling later in the season likely had considerable impact. This is evidenced by the relationship between ordinal day and euphausiid abundance in 2014. Other environmental and physical results did not suggest any other anomalous features that may have caused this significant jump in abundance. Thus, it suggests that because we sampled later in 2014 we observed more euphausiids compared to other years. This is most likely the result of advection timing (as explained in Berline et al., 2008), but may also reflect local recruitment. Alternative explanations for increased abundance include local production or retained for a longer period of time. Most historical surveys have not sampled later than mid-September to avoid disturbing subsistence hunting by Iñupiat whalers as the whales migrate westward from the Beaufort. Thus previous surveys (Grebmeier and Harvey, 2005; Lane et al., 2008) reporting low numbers of euphausiids could be due to the mismatch between euphausiid transport from the south and survey timing.

Our estimates of adult euphausiid abundance may be somewhat improved over prior estimates derived from small mouth plankton nets towed only in the water column (e.g. Eisner et al., 2013). However, euphausiids are difficult to accurately estimate even with larger nets

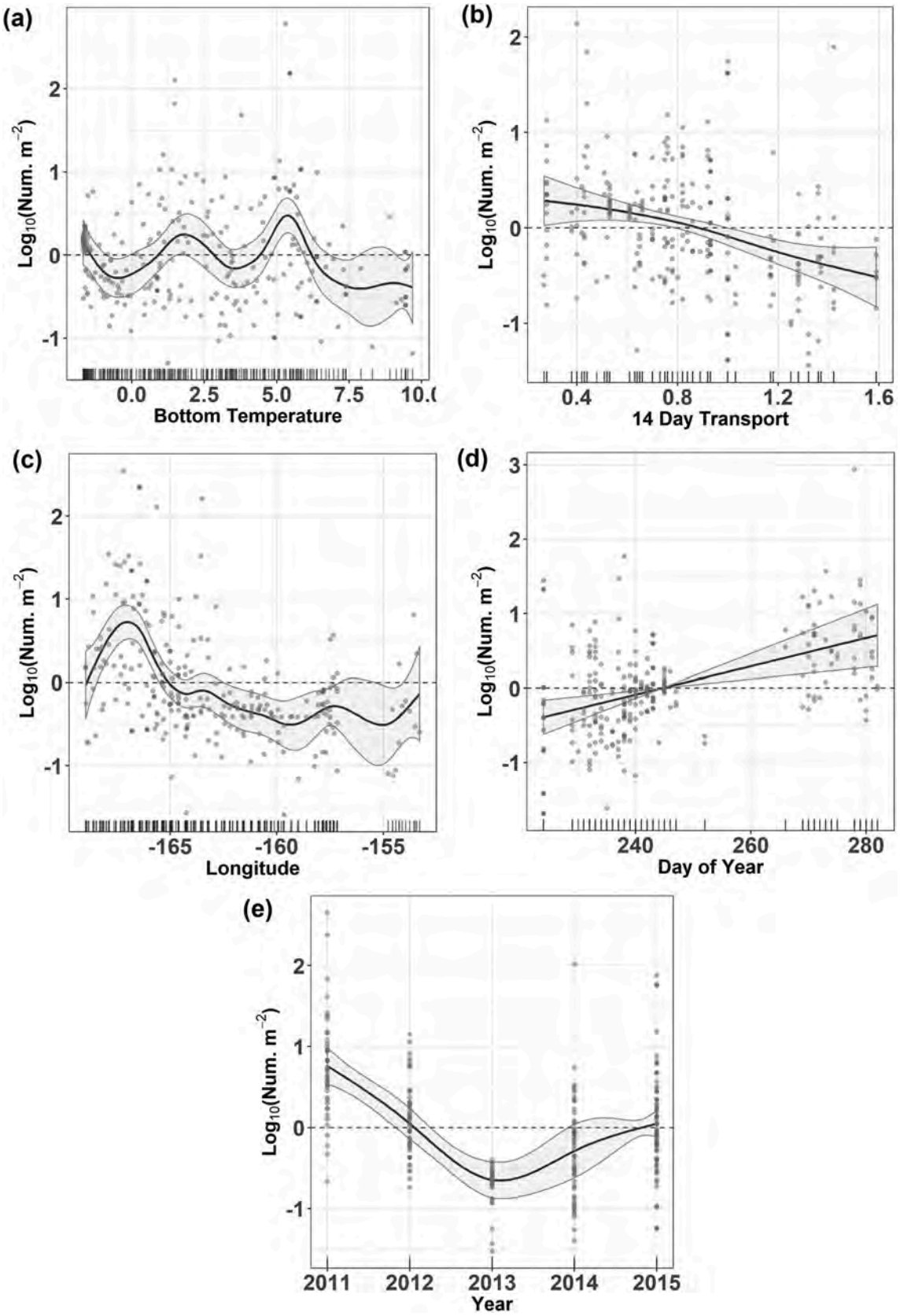

Fig. 11. GAM smooth for the distribution of euphausiid furcilia pelagic abundance (Log_{10}(Num m^{-2})), 2011–2015. Variables included mean bottom temperature (a), 14- day transport (b), longitude (c), day of year (ordinal day) (d), and year (e).

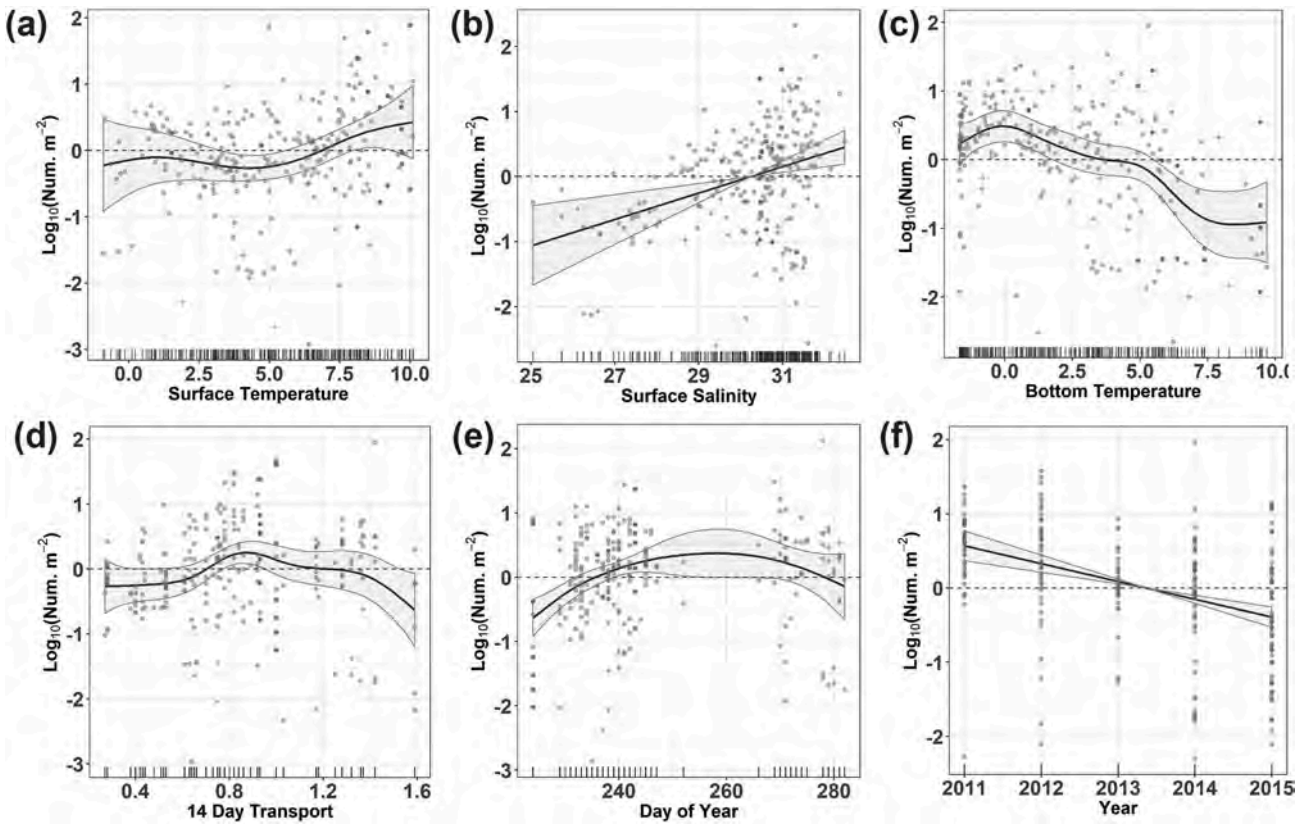

Fig. 12. GAM smooth for the distribution of *Calanus glacialis* C5 stage pelagic abundance (Log_{10}(Num m^{-2})), 2011–2015. Variables included mean surface temperature (a), surface bottom salinity (b), bottom temperature (c), 14-day transport (d), day of year (ordinal day) (e), and year (f).

that sample at faster tow speeds. (e.g. Hunt et al., 2016). Net avoidance by euphausiids has long been recognized as chronic problem in oceanographic studies (e.g. Brinton, 1967; Sameoto et al., 2011; Wiebe et al., 2013). Net avoidance abilities may even extend to the young stages (e.g. Smith, 1991). Future work using acoustical or optical techniques may be able to provide better estimates of euphausiid abundance, although as this study demonstrated there is a need to sample very close to the seafloor.

4.2. Other large zooplankton

We found that *C. glacialis* were most abundant in colder conditions, with the abundance increase being driven by earlier development stages. This finding is supported by research showing that *C. glacialis* were strongly tied to the ice edge algae production, which is increased in colder years (Søreide et al., 2010). Both C2 and C5 stages showed a significant positive association with colder bottom temperatures. The C5 stage, as opposed to the C2 stage, also had a positive association with warmer surface temperatures and significant relationship with northeastward transport, suggesting that C5 stages were more likely to be influenced by advection. The C2 stage had significantly higher abundances in the northeast region, a negative relationship with higher surface temperatures, and lack of a significant relationship with transport, suggesting local production rather than transported from the south. This is supported by previous research showing *C. glacialis* having approximate development times of 8 to 12 days at temperatures between 12 and -1.5 °C, respectively, from egg to C2 stage (Hirst and Lampitt, 1998; Kiørboe and Hirst, 2008; Spear et al., 2019). As described earlier, transport times from the Bering Sea to the northeast region were much longer than development times from egg to C2 Stage. C2 copepodites were also more abundant in 2012 and 2013, when temperatures were coldest in the northeast. This suggests that the overall abundance increases in *C. glacialis* in 2012 and 2013, when temperatures were colder, sea ice melted later in the northeast region, and advection was lower, was primarily due to local reproduction. Abundance increases in the northeast region could also be due to upwelling onto the Chukchi Shelf from the Beaufort Sea (Ashjian et al., 2010). Conversely, the lower abundances of C2 stages in warmer conditions may be a result of faster and earlier development into later stages. Thus the various stages of *C. glacialis* region likely have multiple sources (in situ reproduction and transport from the south and east), and the absolute abundance is a function of local and regional processes. This is a notable result; later stages of *C. glacialis* are known to be the primary prey of bowhead whales around West Greenland (Heide-Jørgensen et al., 2013), and a significant contribution to their diet in the Chukchi and Beaufort seas (Lowry et al., 2004; Moore et al., 2010). In addition, if *C. glacialis* are developing faster, they may enter into diapause earlier creating a mismatch with migrating whales.

The significant differences in pelagic and epibenthic abundance in both mysids and amphipod highlights the importance of sampling near the bottom. Mysids and some amphipod species may spend time in the water column; therefore, sampling the water column and epibenthic layer will yield improved estimates of their abundance. Epibenthic amphipod abundance was significantly higher in 2013 than any other year sampled in this study. This is a notable observation in the context of a changing climate, given that 2013 was also the coldest year and certain species of amphipods, in particular, have known ice-associated and bottom dwelling habits (Vinogradov, 1999; Gradinger and Bluhm, 2004). Both amphipods and mysids are prey for multiple marine mammals, including bearded seals (*Erignathus barbatus*; Cameron et al., 2010), Pacific walrus (*Odobenus rosmarus divergens*; Sheffield and Grebmeier, 2009), beluga whales (*Delphinapterus leucas*; Quakenbush et al., 2015), grey whales (*Eschrichtius robustus*; Nerini, 1984; Darling et al., 1998), and bowhead whales (Lowry et al., 2004). Given the

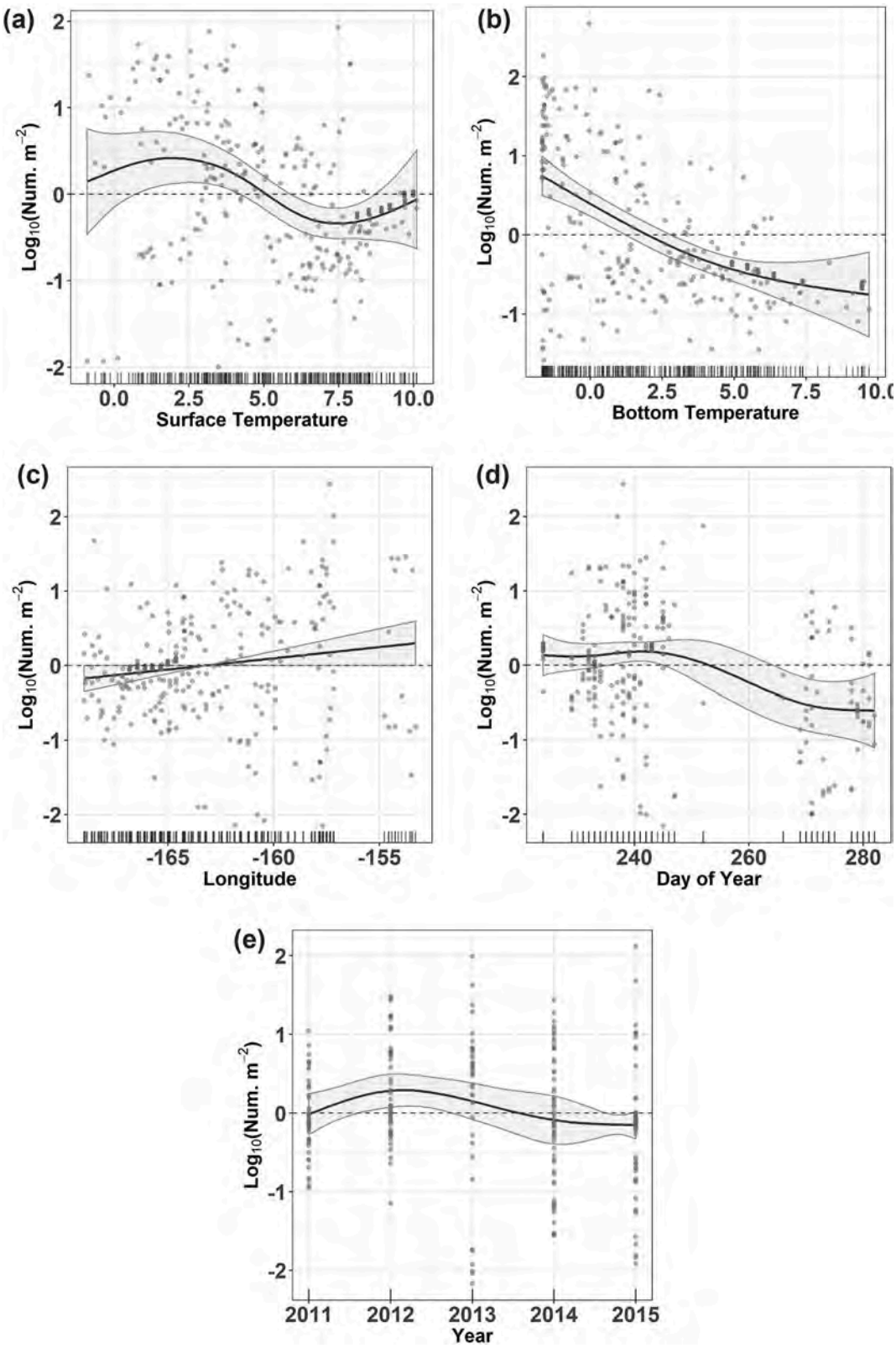

Fig. 13. GAM smooth for the distribution of *Calanus glacialis* C2 stage pelagic abundance (Log_{10}(Num m^{-2})), 2011–2015. Variables included mean surface temperature (a), bottom temperature (b), longitude (c), day of year (ordinal day) (d), and year (e).

importance of mysids and amphipods to Arctic food webs, it is important to monitor their response to changes in ice cover and water temperatures.

4.3. Chukchi Sea large zooplankton status and trends

The findings of this study are relevant to the potential response of lower trophic levels to climate warming, including changes in Arctic

food webs. Recent studies have found a 50% increase in water volume transport through the Bering Strait to the Chukchi Sea from 2001-2014; the immediate impact to the physical environment is an increase in heat flux that is a potential trigger for Arctic sea-ice melt and retreat (Woodgate et al., 2010; 2015; Woodgate, 2018). As the climate warms, increases in primary and secondary production will result in changes in abundance of lipid-rich zooplankton, but it remains to be seen what the overall lipid availability will be (Renaud et al., 2018). Two of the species targeted in this study, *C. glacialis* and *T. raschii*, have an average percent lipid content of approximately 11–15% and 3–5%, respectively, both having a higher average percent lipid content in colder years (Heintz et al., 2013). There is a general consensus that densities of sea ice-associated, lipid-rich *C. glacialis* are expected to decline due to loss of ice in the region. (Tremblay et al., 2012; Grebmeier et al., 2006a; Grebmeier, 2012; Moore and Stabeno, 2015; Renaud et al., 2018). In addition, this study provides evidence that increases in large zooplankton abundance such as euphausiids (which also contain depot lipids) is likely to occur, either via advection from lower latitudes or changes in local production. This is supported by previous studies which found an increase in zooplankton biomass over several decades in the Chukchi Sea (Ershova et al., 2015). An increase in abundance of prey such as euphausiids will likely benefit higher trophic level predators such as planktivorous fish, seabirds and marine mammals. Recently, studies have suggested that the abundance of other planktivores in the northern Bering Sea and Chukchi appear to be changing. For example, in the Bering Sea, there has been a decrease in the lipid-rich nodal species Arctic cod (*Boreogadus saida*) and an increase in the commercial species walleye pollock (*Gadus chalcogrammus*) and Pacific cod (*Gadus macrocephalus*; Stevenson and Lauth, 2019). Walleye pollock have been observed in the Chukchi and Beaufort seas (e.g. Logerwell et al., 2015) and is an important planktivore in the southeastern Bering Sea ecosystem consuming both euphausiids and large copepods (Dwyer et al., 1987; https://access.afsc.noaa.gov/REEM/WebDietData/DietDataIntro.php). Walleye pollock could become an effective competitor for large zooplankton with other fishes, seabirds, and marine mammals if its abundance continues to increase in the northern Bering, Chukchi and Beaufort seas. At present, however, there is evidence of improved body condition of bowhead whales returning from the Beaufort (George et al., 2015). This suggests that the plankton community in their summer feeding grounds has changed in either biomass, species composition or both.

The strong interaction between top-predators (whales, seabirds, and Arctic cod) and copepods/krill in the northern Chukchi appeared to be mediated by both advection and local production related to sea-ice dynamics. What remains to be seen is whether arctic shelf ecosystems will continue to be bottom-up forced by sea-ice dynamics or whether climate-mediated impacts on intermediate trophic levels (e.g. large zooplankton and small fishes) could become the predominant controlling mechanism, e.g. wasp-waist control (Gaichas et al., 2015; Griffiths et al., 2013; Fauchald et al., 2011). If warming continues, the bottom-up dynamics in this location would likely be disrupted by increased advection over longer time-periods as well as a lack of localized, lipid-rich, ice-associated production. Such a shift would greatly impact the trophic dynamics in the region.

5. Conclusions

This study analyzed five successive years of zooplankton abundance over a wide range of physical oceanographic characteristics in the Chukchi Sea to better understand the status and trends in prey availability for baleen whales, seabirds, and planktivorous fish. The coldest year (2013) was highlighted by later summer sea-ice melt, colder sea surface and bottom temperatures, and lower northward transport through the Bering Strait during the spring and summer months. Generally, the warmest years accompanied with earlier summer sea-ice melt, warmer sea surface and bottom temperatures, and higher Bering Strait transport during the spring and summer months. Adult euphausiid abundances differed across warm and cold conditions. These differences appeared most pronounced regionally (NE-SW gradient) and were related to transport, which suggests that most of these euphausiids are transported to the Chukchi Sea from the Bering Sea. The lack of furcilia in 2012 and 2013, (except in the SW), and the presence of furcilia in 2011 and 2014–15, suggests that only in these warmer years with higher advection were earlier stages transported to the northeast region of the Chukchi Sea. We also found that some euphausiids might be locally produced based on the development times. In contrast, the *C. glacialis* C5 stages were found across all years, but C2 stages were found primarily in the northeast and were more abundant under colder conditions which suggests local production of copepods. Thus, the large numbers of euphausiids and copepods that dominate the prey in stomachs of bowhead whales harvested near Utqiagvik, Alaska (Lowry et al., 2004; Ashjian et al., 2010; Moore et al., 2010; George et al., 2015) are likely the result of transport of euphausiids to this location and the contribution of locally produced *C. glacialis,* although *Calanus* found in the region potentially come from several sources or origins.

Declaration of competing interest

The authors declare that they have no known competing financial interests or personal relationships that could have appeared to influence the work reported in this paper.

CRediT authorship contribution statement

Adam Spear: Investigation, Conceptualization, Methodology, Data curation, Formal analysis, Writing - original draft, Visualization. **Jeff Napp:** Investigation, Conceptualization, Methodology, Writing - review & editing, Supervision. **Nissa Ferm:** Data curation, Visualization, Formal analysis. **David Kimmel:** Conceptualization, Methodology, Writing - review & editing.

Acknowledgements

The authors would like to thank Captain Fred Roman, F/V *Mystery Bay*, Captain Kale Garcia, R/V *Aquila*, and Captain/C.O. Robert A. Kamphaus, NOAA ship *Ronald H. Brown*, as well as all crew members. Special thanks also go to Catherine Berchok and Nanci Kachel for their leadership; Bill Floering and David Strausz for assistance at sea, Rebecca Woodgate for suggestions and sharing physical data; the Bering Strait mooring project; Polish Plankton Sorting and Identification Center for processing and enumerating zooplankton samples; and North Pacific Climate Regimes and Ecosystem Productivity (NPCREP) program for support. This research was part of the Chukchi Sea Acoustics, Oceanography and Zooplankton Extension (CHAOZ-X) and Arctic Whale Ecology Study (ArcWEST) which were funded by the Bureau of Ocean Energy Management (BOEM; Contract No. M13PG00026 and M12PG00021). Reference to trade names does not imply endorsement by the National Marine Fisheries Service, NOAA.

References

Ashjian, C.J., Braund, S.R., Campbell, R.G., Gearge, J.C., Kruse, J., Maslowski, W., Moore, S.E., Nicolson, C.R., Okkonen, S.R., Sherr, B.F., 2010. Climate variability, oceanography, bowhead whale distribution, and Iñupiat subsistence whaling near Barrow, Alaska. Arctic 179–194. https://doi.org/10.14430/arctic973.

Ashjian, C.J., Campbell, R.G., Gelfman, C., Alatalo, P., Elliott, S.M., 2017. Mesozooplankton abundance and distribution in association with hydrography on Hanna Shoal. NE Chukchi Sea, during August 2012 and 2013. Deep-Sea Res. II 144, 21–36. https://doi.org/10.1016/j.dsr2.2017.08.012.

Berline, L., Spitz, Y.H., Ashjian, C.J., Campbell, R.G., Maslowski, W., Moore, S.E., 2008. Euphausiid transport in the western Arctic Ocean. Mar. Ecol. Prog. Ser. 360, 163–178. https://doi.org/10.3354/meps07387.

Bond, N., Stabeno, P., Napp, J., 2018. Flow patterns in the Chukchi sea based on an oceano reanalysis. Deep-Sea Res. II 152, 35–47. https://doi.org/10.1016/j.dsr2.2018.02.009. June through October 1979 – 2014.

Brinton, E., 1967. Vertical migration and avoidance capability of euphausiids in the California Current. Limnol. Oceanogr. 12, 451–483. https://doi.org/10.4319/lo.1967.12.3.0451.

Cameron, M.F., Bengtson, J.L., Boveng, P.L., Jansen, J.K., Kelly, B.P., Dahle, S.P., Logerwell, E.A., Overland, J.E., Sabine, C.L., Waring, G.T., Wilder, J.M., 2010. Status review of the bearded seal (*Erignathus barbatus*). U.S. Dep. Commer. NOAA Tech Memo NMFS-AFSC- 211, 246.

Campbell, R.G., Sherr, E.B., Ashjian, C.J., Plourde, S., Sherr, B.F., Hill, V., Stockwell, D. A., 2009. Mesozooplankton prey preference and grazing impact in the western Arctic Ocean. Deep-Sea Res. II 56, 1274–1289. https://doi.org/10.1016/j.dsr2.2008.10.027.

Citta, J.J., Quakenbush, L.T., George, J.C., Small, R.J., Heide-Jorgensen, M.P., Brower, H., Adams, B., Brower, L., 2012. Winter movements of bowhead whales (*Balaena mysticetus*) in the Bering Sea. Arctic 65, 13–34. https://doi.org/10.14430/arctic4162.

Comiso, J., 1999. Bootstrap Sea Ice Concentrations for NIMBUS-7 SMMR and DMSP SSM/I. Digital Media. National Snow and Ice Data Center 10.

Coyle, K., Pinchuk, A., 2002. Climate-related differences in zooplankton density and growth on the inner shelf of the southeastern Bering Sea. Prog. Oceanogr. 55, 177–194. https://doi.org/10.1016/S0079-6611(02)00077-0.

Danielson, S.L., Eisner, L., Ladd, C., Mordy, C., Sousa, L., Weingartner, T.J., 2017. A comparison between late summer 2012 and 2013 water masses, macronutrients, and phytoplankton standing crops in the northern Bering and Chukchi Seas. Deep-Sea Res. II 135, 7–26. https://doi.org/10.1016/j.dsr2.2016.05.024.

Darling, J.D., Keogh, K.E., Steeves, T.E., 1998. Gray whale (*Eschrichtius robustus*) habitat utilization and prey species off Vancouver Island, BC. Mar. Mamm. Sci. 14, 692–720. https://doi.org/10.1111/j.1748-7692.1998.tb00757.x.

Dwyer, D.A., Bailey, K.M., Livingston, P.A., 1987. Feeding habits and daily ration of walleye pollock (*Theragra chalcogramma*) in the eastern Bering Sea with special reference to cannibalism. Can. J. Fish. Aquat. Sci. 44, 1972–1984. https://doi.org/10.1139/f87-242.

Eisner, L., Hillgruber, N., Martinson, E., Maselko, J., 2013. Pelagic fish and zooplankton species assemblages in relation to water mass characteristics in the northern Bering and southeast Chukchi seas. Polar Biol. 36, 87–113. https://doi.org/10.1007/s00300-012-1241-0.

Ershova, E.A., Hopcroft, R.R., Kosobokova, K.N., Matsuno, K., Nelson, R.J., Yamaguchi, A., Eisner, L.B., 2015. Long-term changes in summer zooplankton communities of the western Chukchi Sea, 1945–2012. Oceanography 28, 100–115. https://doi.org/10.5670/oceanog.2015.60.

Fauchald, P., Skov, H., Skern-Mauritzen, M., Johns, D., Tveraa, T., 2011. Wasp-waist interactions in the north Sea ecosystem. PloS One 6, e22729. https://doi.org/10.1371/journal.,pone.0022729.

Gaichas, S., Aydin, K., Francis, R.C., 2015. Wasp waist or beer belly? Modeling food web structure and energetic control in Alaskan marine ecosystems, with implications for fishing and environmental forcing. Prog. Oceanogr. 138, 1–17. https://doi.org/10.1016/j.pocean.2015.09.010.

George, J.C., Druckenmiller, M.L., Laidre, K.L., Suydam, R., Person, B., 2015. Bowhead whale body condition and links to summer sea ice and upwelling in the Beaufort Sea. Prog. Oceanogr. 136, 250–262. https://doi.org/10.1016/j.pocean.2015.05.001.

Gong, D., Pickart, R.S., 2015. Summertime circulation in the eastern Chukchi sea. Deep-Sea Res. II. 118, 18–31. https://doi.org/10.1016/j.dsr2.2015.02.006.

Gradinger, R.R., Bluhm, B.A., 2004. In-situ observations on the distribution and behavior of amphipods and Arctic cod (*Boreogadus saida*) under the sea ice of the High Arctic Canada Basin. Polar Biol. 27, 595–603. https://doi.org/10.1007/s00300-004-0630-4.

Grebmeier, J.M., Harvey, H.R., 2005. The western arctic shelf? Basin interactions (SBI) project: an overview. Deep-Sea Res. II. 52, 3109–3115. https://doi.org/10.1016/j.dsr2.2005.10.004.

Grebmeier, J.M., Cooper, L.W., Feder, H.M., Sirenko, B.I., 2006a. Ecosystem dynamics of the pacific-influenced northern bering and Chukchi seas in the amerasian arctic. Prog. Oceanogr. 71, 331–361. https://doi.org/10.1016/j.pocean.2006.10.001.

Grebmeier, J.M., Overland, J.E., Moore, S.E., Farley, E.V., Carmack, E.C., Cooper, L.W., Frey, K.E., Helle, J.H., McLaughlin, F.A., McNutt, S.L., 2006b. A major ecosystem shift in the northern Bering Sea. Science 311, 1461–1464. https://doi.org/10.1126/science.1121365.

Grebmeier, J.M., 2012. Shifting patterns of life in the pacific arctic and sub-arctic seas. Ann. Rev. Mar. Sci. 4, 63–78. https://doi.org/10.1146/annurev-marine-120710-100926.

Griffiths, S.P., Olson, R.J., Watters, G.M., 2013. Complex wasp-waist regulation of pelagic ecosystems in the Pacific Ocean. Rev. Fish Biol. Fish. 23, 459–475. https://doi.org/10.1007/s11160-012-9301-7.

Heide-Jørgensen, M.P., Laidre, K.L., Nielsen, N.H., Hanson, R.G., Røstand, A., 2013. Winter and spring diving behavior of bowhead whales relative to prey. Anim. Biotel. 1, 15. https://doi.org/10.1186/2050-3385-1-15.

Heintz, R.A., Siddon, E.C., Farley, E.V., Napp, J.M., 2013. Correlation between recruitment and fall condition of age-0 pollock (*Theragra chalcogramma*) from the eastern Bering Sea under varying climate conditions. Deep-sea Res II 94, 150–156. https://doi.org/10.1016/j.dsr2.2013.04.006.

Hirst, A.G., Lampitt, R.S., 1998. Towards a global model of in situ weight-specific growth in marine planktonic copepods. Mar. Biol. 132, 247–257. https://doi.org/10.1007/s002270050390.

Hopcroft, R.R., Kosobokova, K.N., Pinchuk, A.I., 2010. Zooplankton community patterns in the Chukchi Sea during summer 2004. Deep-Sea Res. II 57, 27–39. https://doi.org/10.1016/j.dsr2.2009.08.003.

Hunt, G.L., Ressler, P.H., Gibson, G.A., De Robertis, A., Aydin, K., Sigler, M.F., Ortiz, J., Lessard, E.J., Williams, B.C., Pinchuk, A., Buckley, T., 2016. Euphausiids in the eastern Bering Sea: a synthesis of recent studies of euphausiid production, consumption, and population control. Deep-Sea Res. II 134, 204–222. https://doi.org/10.1016/j.dsr2.2015.10.007.

Kiørboe, T., Hirst, A.G., 2008. Optimal development time in pelagic copepods. Mar. Ecol. Prog. Ser. 367, 15–22. https://doi.org/10.3354/meps07572.

Lane, P.V., Llinás, L., Smith, S.L., Pilz, D., 2008. Zooplankton distribution in the western Arctic during summer 2002: hydrographic habitats and implications for food chain dynamics. J. Mar. Syst. 70, 97–133. https://doi.org/10.1016/j.jmarsys.2007.04.001.

Logerwell, E., Busby, M., Carothers, C., Cotton, S., Duffy-Anderson, J., Farley, E., Goddard, P., Heintz, R., Holladay, B., Horne, J., Johnson, S., Lauth, B., Moulton, L., Neff, D., Norcross, B., Parker-Stetter, S., Siegle, J., Sformo, T., 2015. Fish communities across a spectrum of habitats in the western Beaufort sea and Chukchi sea. Prog. Oceanogr. 136, 115–132. https://doi.org/10.1016/j.pocean.2015.05.013.

Lowry, L.F., Sheffield, G., George, J.C., 2004. Bowhead whale feeding in the Alaskan Beaufort Sea, based on stomach contents analyses. J. Cetacean Res. Manag. 6, 215–223.

Moore, S.E., Stafford, K.M., Munger, L.M., 2010. Acoustic and visual surveys for bowhead whales in the western Beaufort and far northeastern Chukchi seas. Deep-Sea Res. II 57, 153–157. https://doi.org/10.1016/j.dsr2.2009.08.013.

Moore, S.E., Stabeno, P.J., 2015. Synthesis of arctic research (SOAR) in marine ecosystems of the pacific arctic. Prog. Oceanogr. 136, 1–11. https://doi.org/10.1016/j.pocean.2015.05.017.

Nerini, M., 1984. A review of gray whale feeding ecology. The gray whale, Eschrichtius robustus 423–450.

Perovich, D.K., Farrell, S., Gerland, S., Hendricks, S., Kaleschke, L., Meier, W., Ricker, R., Tian-Kunze, X., Tschudi, M., Webster, M., Wood, K., 2019. sea ice [in Arctic Report Card 2019]. http://www.arctic.noaa.gov/reportcard.

Pinchuk, A.I., Eisner, L.B., 2017. Spatial heterogeneity in zooplankton summer distribution in the eastern Chukchi Sea in 2012–2013 as a result of large-scale interactions of water masses. Deep-Sea Res. II 135, 27–39. https://doi.org/10.1016/j.dsr2.2016.11.003.

Pinchuk, A.I., Hopcroft, R.R., 2006. Egg production and early development of *Thysanoessa inermis* and *Euphausia pacifica* (Crustacea: Euphausiacea) in the northern Gulf of Alaska. J. Exp. Mar. Biol. Ecol. 332, 206–215. https://doi.org/10.1016/j.jembe.2005.11.019.

Pinchuk, A.I., Hopcroft, R.R., 2007. Seasonal variations in the growth rates of euphausiids (*Thysanoessa inermis, T. spinifera*, and *Euphausia pacifica*) from the northern Gulf of Alaska. Mar. Biol. 151, 257–269. https://doi.org/10.1007/s00227-006-0483-1.

Questel, J.M., Clarke, C., Hopcroft, R.R., 2013. Seasonal and interannual variation in the planktonic communities of the northeastern Chukchi Sea during the summer and early fall. Continent. Shelf Res. 67, 23–41. https://doi.org/10.1016/j.csr.2012.11.003.

Quakenbush, L.T., Citta, J.J., George, J.C., Small, R.J., Heide-Jørgensen, M.P., 2010. Fall and winter movements of bowhead whales (*Balaena mysticetus*) in the Chukchi Sea and within a potential petroleum development area. Arctic 63, 289–307. https://doi.org/10.14430/arctic1493.

Quakenbush, L., Suydam, R.S., Bryan, A.L., Lowry, L.F., Frost, K.J., Mahoney, B.A., 2015. Diet of beluga whales (*Delphinapterus leucas*) in Alaska from stomach contents, March–November. Mar. Fish. Rev. 77, 70–84.

R Core Team, 2019. R: A Language and Environment for Statistical Computing. R Foundation for Statistical Computing, Vienna, Austria. https://www.R-project.org/.

Randall, R.J., Busby, M.S., Spear, A., Mier, K.L., 2019. Spatial and temporal variation of summer ichthyoplankton assemblage structure in the eastern Chukchi Sea 2010-2015. Polar Biol. 42, 1811–1824. https://doi.org/10.1007/s00300-019-02555-8.

Renaud, P.E., Daase, M., Banas, N.S., Gabrielsen, T.M., Søreide, J.E., Varpe, Ø., Cottier, F., Falk-Petersen, S., Halsband, C., Vogedes, D., Heggland, K., Berge, J., 2018. Pelagic food-webs in a changing Arctic: a trait-based perspective suggests a mode of resilience. ICES J. Mar. Sci. 75, 1871–1881. https://doi.org/10.1093/icesjms/fsy063.

Sameoto, D., Cochrane, N.A., Herman, A., 2011. Convergence of acoustic, optical, and net-catch estimates of euphausiid abundance: use of artificial light to reduce net avoidance. Can. J. Fish. Aquat. Sci. 50, 334–346. https://doi.org/10.1139/f93-039.

Sheffield, G., Grebmeier, J.M., 2009. Pacific walrus (*Odobenus rosmarus divergens*): differential prey digestion and diet. Mar. Mamm. Sci. 25, 761–777. https://doi.org/10.1111/j.1748-7692.2009.00316.x.

Smith, S.L., 1991. Growth, development and distribution of the euphausiids *Thysanoessa raschii* (M.Sars) and *Thysanoessa inermis* (Kroyer) in the southeastern Bering Sea. Polar Res. 10, 461–478. https://doi.org/10.3402/polar.v10i2.6759.

Søreide, J.E., Leu, E., Berge, J., Graeve, M., Falk-Petersen, S., 2010. Timing of blooms, algal food quality and *Calanus glacialis* reproduction and growth in a changing Arctic. Global Change Biol. 16, 3154–3163. https://doi.org/10.1111/j.1365-2486.2010.02175.x.

Spear, A., Duffy-Anderson, J., Kimmel, D., Napp, J., Randall, J., Stabeno, P., 2019. Physical and biological drivers of zooplankton communities in the Chukchi Sea. Polar Biol. 42, 1107–1124. https://doi.org/10.1007/s00300-019-02498-0.

Stabeno, P., Kachel, N., Ladd, C., Woodgate, R., 2018. Flow patterns in the eastern Chukchi sea: 2010–2015. J. Geophys. Res.-Oceans 123, 1177–1195. https://doi.org/10.1002/2017JC013135.

Stevenson, D.E., Lauth, R.R., 2019. Bottom trawl surveys in the northern Bering Sea indicate recent shifts in the distribution of marine species. Polar Biol. 42, 407–421. https://doi.org/10.1007/s00300-018-2431-1.

Teglhus, F.W., Agersted, M.D., Akther, H., Nielsen, T.G., 2015. Distributions and seasonal abundances of krill eggs and larvae in the sub-Arctic Godthåbsfjord, SW Greenland. Mar. Ecol. Prog. Ser. 539, 111–125. https://doi.org/10.3354/meps11486.

Timmermans, M.-L., Ladd, C.. Sea Surface temperature [in Arctic Report Card 2019]. http://www.arctic.noaa.gov/reportcard.

Tremblay, J.-É., Robert, D., Varela, D.E., Lovejoy, C., Darnis, G., Nelson, R.J., Sastri, A.R., 2012. Current state and trends in Canadian Arctic marine ecosystems: I. Primary production. Climatic Change 115, 161–178. https://doi.org/10.1007/s10584-012-0496-3.

Vinogradov, G.M., 1999. Deep-sea near-bottom swarms of pelagic amphipods *Themisto*: observations from submersibles. Sarsia 84, 465–467. https://doi.org/10.1080/00364827.1999.10807352.

Wiebe, P.H., Lawson, G.L., Lavery, A.C., Copley, N.J., Horgan, E., Bradley, A., 2013. Improved agreement of net and acoustical methods for surveying euphausiids by mitigating avoidance using a net-based LED strobe light system. ICES J. Mar. Sci. 70, 650–664. https://doi.org/10.1093/icesjms/fst005.

Wood, S.N., 2011. Fast stable restricted maximum likelihood and marginal likelihood estimation of semiparametric generalized linear models. J. Roy. Stat. Soc. B 73, 3–36.

Woodgate, R.A., Aagaard, K., Weingartner, T.J., 2005. A year in the physical oceanography of the Chukchi Sea: moored measurements from autumn 1990–1991. Deep-Sea Res. II 52, 3116–3149. https://doi.org/10.1016/j.dsr2.2005.10.016.

Woodgate, R.A., Weingartner, T., Lindsay, R., 2010. The 2007 Bering Strait oceanic heat flux and anomalous Arctic sea-ice retreat. Geophys. Res. Lett. 37 (1) https://doi.org/10.1029/2009GL041621.

Woodgate, R.A., Stafford, K.M., Prahl, F.G., 2015. A synthesis of year-round interdisciplinary mooring measurements in the Bering Strait (1990–2014) and the RUSALCA years (2004–2011). Oceanography 28, 46–67. https://doi.org/10.5670/oceanog.2015.57.

Woodgate, R.A., 2018. Increases in the Pacific inflow to the Arctic from 1990 to 2015, and insights into seasonal trends and driving mechanisms from year-round Bering Strait mooring data. Prog. Oceanogr. 160, 124–154. https://doi.org/10.1016/j.pocean.2017.12.007.

Deep–Sea Research II 177 (2020) 104784

Contents lists available at ScienceDirect

Deep-Sea Research Part II

journal homepage: http://www.elsevier.com/locate/dsr2

The effect of oceanographic variability on the distribution of larval fishes of the northern Bering and Chukchi seas

Elizabeth A. Logerwell [a,*], Morgan Busby [a], Kathryn L. Mier [a], Heather Tabisola [b], Janet Duffy-Anderson [a]

[a] Resource Assessment and Conservation Division, Alaska Fisheries Science Center, National Marine Fisheries Service, NOAA, 7600 Sand Point Way NE, Seattle, WA, 98105, USA
[b] Pacific Marine Environmental Laboratory, NOAA, 7600 Sand Point Way NE, Seattle, WA, 98115, USA

ARTICLE INFO

Keywords:
USA
Alaska
Chukchi sea
Fish larvae
Climate changes
Polar waters
Habitat

ABSTRACT

We investigated the pelagic habitat requirements of Arctic larval fish and the effects of interannual variability of ocean conditions on their distribution. We examined the distribution of larval Arctic cod, Bering flounder, yellowfin sole and capelin in the Chukchi and northern Bering seas during two years with different oceanographic conditions. We found that despite marked changes in water mass distribution, the distributions of larval fishes were not significantly different between the two years. In both years, Arctic cod and Bering flounder were found in cold, high salinity shelf waters advected from the south and influenced by winter cooling (Chukchi Winter Water and Anadyr Water mix). Yellowfin sole and capelin distributions were also similar from year-to-year but they were only found in warm, low salinity Alaska Coastal Water. The cold, high salinity water masses had elevated large copepod biomass, and the Alaska Coastal Water had elevated small copepod biomass. Thus, we propose that these water masses provided different but nonetheless potentially profitable foraging habitat for the four species of larval fishes. We conclude by suggesting that the timing and location of spawning of these species has evolved such that larval offspring are distributed in suitable foraging habitat despite interannual variability in ocean conditions. This study provides a baseline of Arctic larval fish distribution and insight into the degree of climate variability that might be expected to impact early life history stages of larval fish. Our results also increase the knowledge of the mechanistic links between oceanography and the early life history of fish. Because growth and survival of early life stages of fish often drives population change, our results contribute to the understanding of the impacts of climate change on Arctic fish populations.

1. Introduction

The Arctic climate is rapidly changing. Ocean temperatures have been warming at over two times the global rate since the mid-20th century (Huang et al., 2017). Sea ice extent, duration and thickness have been declining at an increasing pace (Kwok and Rothrock, 2009; Meier et al., 2012; Wang and Overland, 2015). Embedded within these long-term trends is a high degree of interannual variability in sea ice timing, duration, extent and thickness, as well as ocean temperature and currents (Day et al., 2013; Wang and Overland, 2015; Woodgate et al., 2015).

It is not known with certainty how changes in Arctic climate will impact fish, although impacts are expected. Increased water temperatures may affect growth rates negatively or positively depending on the fish's optimum growth temperature and food availability (Björnsson et al., 2001; Laurel et al., 2015). Reductions in sea-ice extent may negatively impact fish that depend on sea ice for spawning, such as Arctic cod (Rass, 1968). On the other hand, an increase in the open water period due to loss of sea ice may result in increased primary production which could benefit fish feeding (Arrigo et al., 2008). The timing of spring season sea ice retreat is also an important factor. Earlier sea-ice retreat with ocean warming may change the timing and intensity of the spring bloom of phytoplankton resulting in a reduction in productivity and/or a mismatch between the timing of larval first feeding and the availability of prey (Grebmeier, 2012).

The survival of early life history stages of fish is generally thought to be an important determinant of variability in the abundance of subsequent older age classes (Hjort, 1914; Lasker, 1981). Furthermore, early

* Corresponding author.
E-mail address: libby.logerwell@noaa.gov (E.A. Logerwell).

https://doi.org/10.1016/j.dsr2.2020.104784
Received 26 April 2019; Received in revised form 15 April 2020; Accepted 16 April 2020
Available online 30 April 2020
0967-0645/Published by Elsevier Ltd.

life stages of fish are particularly sensitive to changes in their environment such as variability in transport to nursery habitat, exposure to predators and changes in food availability (e.g. Siddon et al., 2011). Thus, an understanding of the impacts of interannual variability and long-term climate trends on Arctic fish populations benefits from information on Arctic fish early life history.

Our work was part of the Arctic Ecosystem Integrated Survey (Arctic Eis), a University of Alaska College of Fisheries and Ocean Sciences program conducted in 2012 and 2013 to document physical and biological oceanography, zooplankton, ichthyoplankton, demersal fish and pelagic fish. The overarching goals of the program were to understand the environmental forcing that impacts northern Bering and Chukchi sea ecosystems and to predict the future effects of reduced sea ice and ocean warming on these ecosystems (Mueter et al., 2017). The goal of the work presented here was to study Arctic fish larval distributions and oceanographic habitat associations.

The northern Bering and Chukchi seas are mostly shallow shelves (<60 m depth) with currents typically flowing northward due to the difference in sea level between the Pacific and the Arctic (Aagaard et al., 2006). Local winds can slow the northward flow or even redirect the flow to the south or west, depending on the direction of the winds (Panteleev et al., 2010). Water masses in the northern Bering and Chukchi seas include warmer, fresher Alaska Coastal Water flowing along the eastern shore and Anadyr/Bering Summer Water flowing across the shelf with moderate temperatures and salinities (Fig. 1). The Anadyr/Bering Summer Water transforms to Chukchi Summer Water as it flows north over the Chukchi Sea shelf. Near-bottom cold and salty Bering and Chukchi Winter Waters are the result of previous winter cooling and are resident to each shelf area. Finally, Melt Water is colder, fresher water at the surface formed by melting of sea ice and in summer is only found in the northern Chukchi Sea (Danielson et al., 2017). These different water masses have different nutrient concentrations and productivity. The colder shelf and winter waters are typically nutrient-rich and productive whereas the Alaska Coastal Water is low in nutrients and productivity (Danielson et al., 2017; Springer and McRoy, 1993).

Atmospheric and oceanographic conditions observed during the Arctic Eis surveys were different between 2012 and 2013, leading to subsequent variations in water mass distribution (Danielson et al., 2017). Sea level pressure and the resulting wind fields strongly contrasted between years. In 2012, low pressure was centered over the northwestern Chukchi Sea resulting in the typical winds from the southwest. In 2013, zonally (longitudinally) elongated low pressure over the Bering Sea resulted in zonal winds from the east. Drifter and high-frequency radar data suggest that the result of these wind differences was that the freshwater core of the Alaska Coastal Current was mostly absent from the Northeast Chukchi Sea during 2013. These differences in winds and currents resulted in pronounced differences in the distribution of water masses. In 2012, Alaska Coastal Water was observed close to shore from the northern Bering Sea all the way to the Northeast Chukchi Sea (Point Barrow). In contrast, in 2013, Alaska Coastal Water was only observed as far north as Ledyard Bay in the Chukchi Sea; and it spread at least 100 km farther offshore in the Northern Bering Sea compared to 2012. Along with more extensive northerly distribution of Alaska Coastal Water in 2012 the Anadyr/Bering Summer Water/Chukchi Summer Water mix extended farther north in 2012 than in 2013.

There were also interannual differences in temperature, salinity, nutrients and chlorophyll biomass (Danielson et al., 2017). Surface

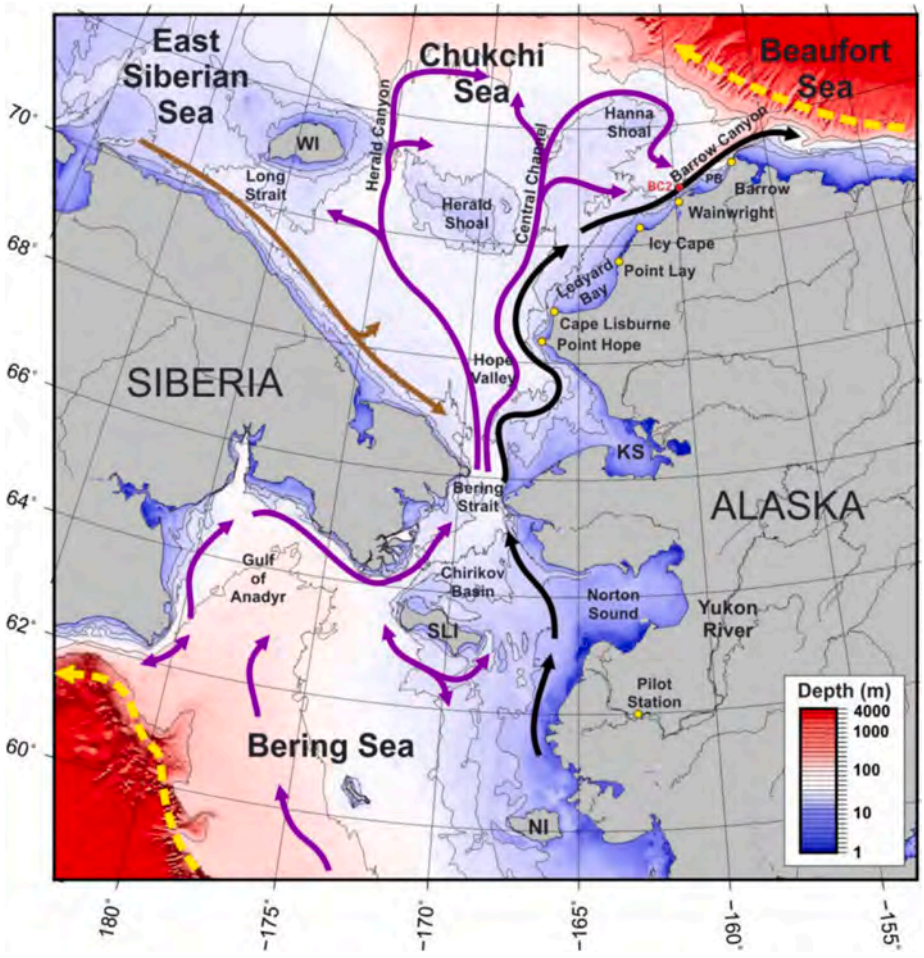

Fig. 1. Study area map with bathymetric depths and overview of general currents in the region. Mean flow pathways are color coded to denote current systems. Yellow = Bering Slope Current and Beaufort Gyre; Black = Alaska Coastal Current; Brown = Siberian Coastal Current; Purple = pathways of Bering shelf, Anadyr, and Chukchi shelf waters (Danielson et al., 2017). (For interpretation of the references to color in this figure legend, the reader is referred to the Web version of this article.)

waters were warmer and near-bottom waters were less saline in 2013 than 2012. Macronutrients, particularly in surface waters, were also different between years: there was less surface nitrate, ammonium and phosphate in 2013 than in 2012, likely leading to nutrient limitation of phytoplankton growth in 2013. In fact, average integrated chlorophyll was lower in 2013 than in 2012 (Danielson et al., 2017). Sea-ice conditions in 2012 and 2013 were similar. Winter sea ice was relatively high but June sea-ice concentrations were below normal in both years.

To investigate the potential impact of interannual variability in water mass distribution, we compared the spatial distribution of fish larvae collected in the northern Bering and Chukchi seas in 2012 and 2013. Our expectation was that larvae would be distributed farther north in 2012, and farther offshore in 2013. We propose that this would be a result of spawning location and subsequent advection within the water masses. To understand larval fish habitat associations, we mapped the distribution of larvae relative to water mass and to explore the potential foraging value of water masses, we examined their biological characteristics in terms of chlorophyll and zooplankton biomass. We also mapped the distribution of eggs and compared larval length frequency distributions for clues about spawn timing and location. The overall goal of our research presented here is to define larval oceanographic habitat and to improve our understanding of the mechanisms and the magnitude of climate variability that impact Arctic fish early life history.

2. Methods

Ichthyoplankton and oceanographic data were collected at stations spaced 28 or 55 km apart, depending on location, over a survey grid that spanned the U.S. northeastern Bering Sea and Chukchi Sea shelves (157–170°W, 60–72°N, Fig. 2). Sampling occurred from 7 August – 24 September in both years, with a similar order of station occupations.

Ichthyoplankton were collected at the primary stations (55-km spacing) and at the higher resolution stations (28-km) with a 60-cm bongo sampler fitted with two 0.505 mm mesh nets with detachable codends at 138 stations in 2012 and 143 stations in 2013. During all cruises, quantitative oblique tows were made to a maximum depth of 200 m (or to within 10 m of the substratum), resulting in vertically integrated estimates of larval fish abundance. The ship speed was monitored and adjusted (1.5–2.5 knots) throughout each tow to maintain a wire angle of 45° from the ship to the bongo net. The nets were equipped with a calibrated flow meter; therefore, catch rates were standardized to effort and converted to catch 10 m^{-2} of sea surface area (CPUE; number 10 m^{-2}). Sampling occurred during daylight hours as per ship protocol. Samples were preserved in 5% formaldehyde-sea water solution buffered with sodium borate.

Samples were sorted and fish eggs, larvae and juveniles identified to the lowest taxonomic level possible at the Plankton Sorting and Identification Center in Szczecin, Poland. Taxonomic identifications were verified at the Alaska Fisheries Science Center (AFSC) in Seattle, WA, following Matarese et al. (1989), Busby et al. (2017), and the Ichthyoplankton Information System (https://access.afsc.noaa.gov/ichthyo/). Some fish eggs and larvae were categorized as taxonomic groups (e.g. *Limanda* spp., *Liparis* spp.) due to limitations associated with identifying egg and larval stages to the species level. In the case of *Limanda* spp. eggs, *Limanda aspera* were by far the most common species of *Limanda* larvae, so we treated *Limanda* spp. eggs as *L. aspera* in the analyses. In some cases, identifications of damaged specimens were made at the family level. In these instances, the identifications were not included in counts of species richness or diversity because they were considered to be of taxa that could normally be successfully identified. Taxonomic nomenclature follows (Mecklenburg et al., 2018), except for Bering flounder (*Hippoglossoides robustus*) which, according to Mecklenburg et al. should now be classified as flathead sole (*Hippoglossoides elassadon*) in the Arctic. However, the American Fisheries Society (Page et al., 2013) still lists the occurrence of flathead sole as Pacific only, and Bering flounder as Pacific and Arctic. We defer to the latter source and use Bering flounder in this paper. We use Arctic cod for the common name of *Boreogadus saida* after Mecklenburg and Steinke (2015).

Fish were measured for standard length (SL) to the nearest 1.0 mm.

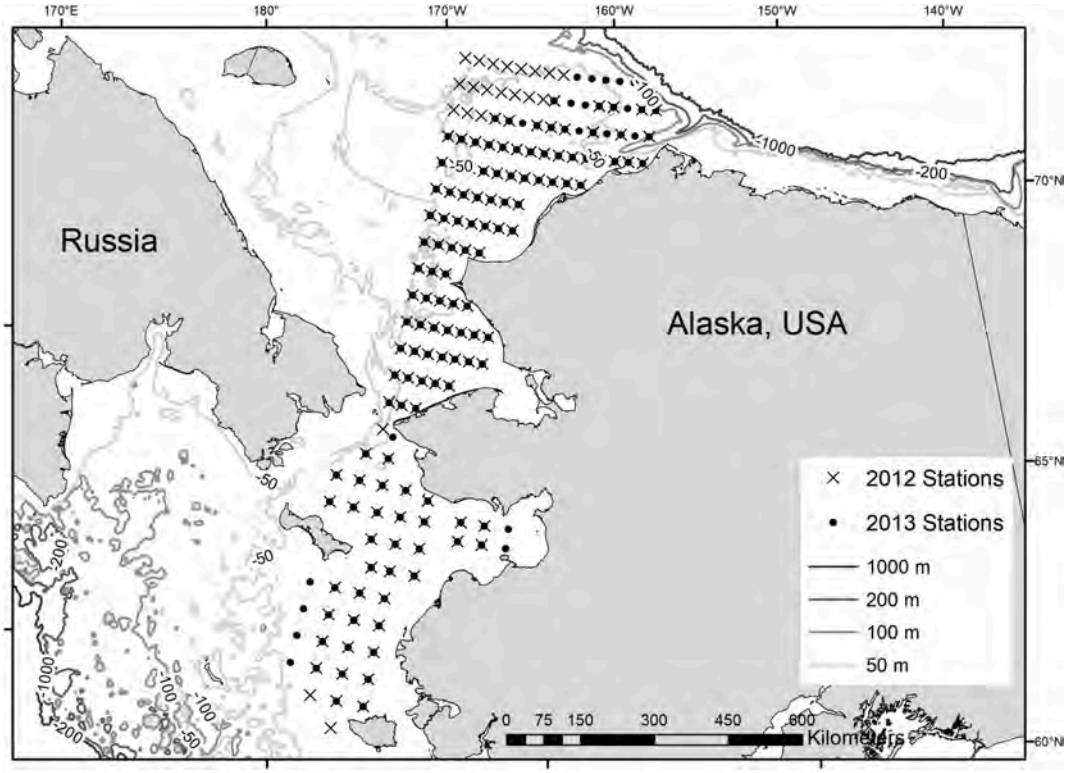

Fig. 2. Survey area and stations sampled in 2012 (x-symbols) and 2013 (solid circles). Depth contours in meters.

The separation point between the larval and juvenile stages for *B. saida* is 25.0 mm standard length (SL) based on the size at transformation of *Gadus chalcogrammus* determined by Brown et al. (2001). For other taxa, definition of the juvenile stage follows Kendall et al. (1984) as a fish having complete adult complements of fin elements, scales and "the appearance of a small adult". The only taxa for which we caught juveniles was *B. saida*.

Macro- and mesozooplankton were also collected with the 60-cm bongo frame (505 μm mesh). Meso- and microzooplankton were sampled with a 20-cm PairVet net with 150 μm mesh attached to the array with the 60-cm frame. PairVet samples were only analyzed for the 2012 cruise, due to loss of data sheets at sea during 2013. All samples were preserved in 5% formalin, buffered with seawater for later processing. In the laboratory, each net sample was subsampled and taxa were identified, staged, counted and weighed. All animals in the samples were identified to the lowest taxonomic category possible. Sibling species *Calanus marshallae* and *C. glacialis* co-occurring in the Bering and Chukchi seas (e.g. Nelson et al., 2009) were not discriminated and are named as *C. glacialis* hereafter. Recent studies confirm that the vast majority of *Calanus* spp. in the northern Bering Sea are *C. glacialis* (Campbell et al., 2014). Copepodites stages were identified and recorded. Biomass values by station were computed for each species in grams m^{-3}. See Pinchuk and Eisner (2016) for details of zooplankton sampling and laboratory analyses.

At the primary stations (55-km spaced), ocean temperature and salinity were determined from conductivity-temperature-depth measurements collected with a Sea-Bird (SBE) 911 or SBE 25 CTD equipped with a Wetlabs Wet-Star fluorimeter to estimate in vivo Chl*a*. In addition, a SBE 49 or SBR19+ CTD was towed with the bongo net to obtain hydrographic data at higher spatial resolution (between primary stations). At the primary stations, water samples for total Chl*a* were collected at ~10 m depth intervals.

– Danielson et al. (2017) identified four different bottom water masses-based on T/S diagrams derived from the survey oceanographic data: Alaska Coastal Water (ACW), Anadyr Water/Bering Shelf Water/Chukchi Shelf Water (AW Mix), Bering Winter Water (BWW) and Chukchi Winter Water (CWW). ACW was the warmest and freshest (7–12 °C; 20–32 salinity). CWW and BWW were the coldest and most saline (−2.0 to 0 °C; 30–33.5 salinity). The AW Mix was intermediate in temperature and high in salinity (0–7 °C; 30–33.5 salinity). Surface water masses were: Melt Water, which was relatively cool and fresh (-2 – 7 °C; 25–30 salinity); and AW Mix and ACW (as defined above). Ichthyoplankton distributions were overlaid on water mass distributions using ArcMap 10.5 (ver 10.5.0.6491).

A statistical test based on a generalized two-sample Cramér-von Mises test was employed to test for differences between the spatial distributions of ichthyoplankton between years (Syrjala, 1996). The null hypothesis for this specific test is that across the study area, the distributions of the populations are the same. The alternative hypothesis for this test is that there is some unspecified difference in the underlying distributions. The distributions are normalized so the test is sensitive to differences in the way populations are distributed across space, but insensitive to differences in abundance. The test is nonparametric, so no assumptions are required about the distributions of the populations. The test was implemented in R version 3.3.2 (R Core Team, 2016) using the "syrjala" function. The Kruskal-Wallis rank sum test was employed to test for differences in chlorophyll and zooplankton biomass density among water masses. A non-parametric test was used because the skewed distributions and heterogeneity of variances could not be remedied by data transformation. The test was implemented in R version 3.3.2 (R Core Team, 2016).

3. Results

A total of 1057 individuals and 31 taxa of larvae and juveniles were sampled by the ichthyoplankton nets in 2012 and 2013 (Table 1). The four most abundant taxa collected were Pacific capelin (*Mallotus catervarius*), Arctic cod (*Boreogadus saida*), Bering flounder (*Hippoglossoides robustus*) and yellowfin sole (*Limanda aspera*). These four taxa were the focus of further analysis. Juvenile fish caught in the nets were all Arctic cod. Eggs of only 5 taxa were caught, mostly Bering flounder and yellowfin sole. Walleye pollock (*Gadus chalcogrammus*) eggs were only caught in the northern Bering Sea.

Bering flounder eggs were distributed in the north Chukchi Sea over the shelf during 2012 (Fig. 3 a). Very few eggs were caught in 2013, but they were found in a similar area as in 2012 (Fig. 3 b). In contrast, yellowfin sole eggs were found farther south, in the northern Bering Sea, and in the south/central Chukchi Sea, and relatively close to shore compared to Bering flounder (Fig. 4). No eggs of either Arctic cod or Pacific capelin were caught during the surveys.

Arctic cod larvae and juveniles were distributed in the north and northeast area of the survey in both years (Fig. 5a and b.). Arctic cod were the only taxa for which we caught juvenile fish. The distributions of the two life stages overlapped, such that for further analyses, we combined the data. The Cramer von-Mises test indicated that there was not enough evidence to support a statistically significant difference in the distribution of Arctic cod between years ($\psi = 3.233$, $P = 0.165$). Bering flounder larvae were distributed throughout the Chukchi Sea, and in the northern Bering Sea (Fig. 5b and c). The catch density of Bering flounder in 2013 was much less than 2012. Similar to Arctic cod, the Cramer von-Mises test indicated that there was not enough evidence to support a statistically significant difference in the distributions between 2012 and 2013 ($\psi = 1.498$, $P = 0.767$).

Yellowfin sole and capelin larvae had more southerly distributions than Arctic cod and Bering flounder (Fig. 6). Similar to the other two taxa, there was no statistically significant difference in the distributions between 2012 and 2013 (yellowfin sole: $\psi = 3.216$, $P = 0.065$; capelin: $\psi = 2.462$, $P = 0.779$).

Flatfish larval length-frequency distributions were examined along with their egg distributions (reported above) for information on spawning locations that could explain the distribution of larvae. No eggs of either Arctic cod or capelin were caught. Bering flounder larvae distribution was discontinuous around 70°N in 2012 (Fig. 5c). Very few larvae were caught in 2013. There was little overlap in the length-frequency distributions north and south of 70°N (Fig. 7) – larvae were smaller north of 70°N and larger south. Yellowfin sole larvae distribution was discontinuous at around 65.5°N (Fig. 6a and b). However, in contrast with Bering flounder, the length-frequency distributions of yellowfin sole larvae were similar north and south of 65.5°N in both years (Fig. 8).

Overlaying the distribution of ichthyoplankton on bottom water masses shows that Arctic cod were only present in the CWW and AW Mix in both years (Fig. 5a and b). Similarly, Bering flounder were most abundant in the CWW and AW Mix (Fig. 5c and d). The relatively northerly extension of the AW Mix and ACW in 2012, reported by Danielson et al. (2017), is also evident. The distributions of yellowfin sole and capelin (Fig. 6) are shown overlaid on surface water mass distributions because there was spatial coherence between larvae and both bottom and surface ACW and the oceanographic signal of ACW was more pronounced in surface waters. BWW and CWW were not evident in surface waters (Fig. 6), only in waters at depth (Fig. 5). The ichthyoplankton tows were not depth-discrete, so it is unknown at which depths the larvae occurred. Yellowfin sole and capelin were distributed in the southern two-thirds of the study area and were virtually restricted to ACW in both years (Fig. 6), in contrast to the more northerly Arctic cod and Bering flounder, which occurred in the cold, high salinity water masses as described above.

The difference in integrated chlorophyll biomass among water masses was statistically significant in 2012 (Kruskal-Wallis Chi-squared = 12.085, p-value = 0.002), but not in 2013 (Kruskal-Wallis Chi-squared = 3.4023, p-value = 0.182) (Fig. 9 a, b). Post-hoc tests showed that chlorophyll biomass was significantly greater in ACW compared to

Table 1
Numbers of fish eggs, larvae, and juveniles collected in bongo tows from the Chukchi and northern Bering seas (NBS) during the 2012 and 2013 Arctic Ecosystem Integrated Survey (Arctic Eis) surveys.

Family	Scientific Name	Common Name	Chukchi			NBS			Chukchi			NBS				
			7 August - 9 September			10–24 September			7 August - 8 September			7 August, 10–24 September				
			2012 (n = 100 stations)			2012 (n = 38 stations)			2013 (n = 100 stations)			2013 (n = 43 stations)			Totals	
			Eggs	Larvae	Juveniles	Eggs	Larvae	Juveniles	Eggs	Larvae	Juveniles	Eggs	Larvae	Juveniles	Eggs	Larvae + Juveniles
Clupeidae	*Clupea pallasi*	Pacific herring					2									2
Osmeridae	*Mallotus catervarius*	Pacific capelin		22			16			7			3			48
Gadidae		unidentified cods								1						1
	Boreogadus saida	Arctic cod		9	4					22	15					50
	Eleginus gracilis	saffron cod		1						1	5					7
	Gadus chalcogrammus	walleye pollock		1		25		1		2		1	1		26	5
Gasterosteidae	*Pungitius pungitius*	ninespine stickleback						1								1
Hexagrammidae	*Hexagrammos stelleri*	whitespotted greenling											1			1
Cottidae	*Gymnocanthus tricuspis*	Arctic stagehorn sculpin		2						6						8
	Hemilepidotus papilio	butterfly sculpin					3									3
	Icelus spatual	spatulate sculpin		1												1
Agonidae	*Aspidophoroides monopterygius*	alligatorfish		1												1
	Aspidophoroides olrikii	Arctic alligatorfish		2						1						3
	Podothecus veternus	veteran poacher								1						1
Liparidae	*Liparis* spp.	unidentified snailfish		3						2						5
	Liparis fabricii	gelatinous seasnail		1						2						3
	Liparis gibbus1	variegated snailfish		13						7						20
	Liparis tunicatus	kelp snailfish		3			1			11						15
Stichaeidae		unidentified pricklebacks		1												1
	Acantholumpenus mackayi	blackline prickleback					1									1
	Eumesogrammus praecisus	fourline snakeblenny		7						1						8
	Anisarchus medius	stout eelblenny		1						2						3
	Leptoclinus maculatus	daubed shanny		2						3						5
	Lumpenus fabricii	slender eelblenny		1						1						2
	Stichaeus punctatus	Arctic shanny		17						19						36
Ammodytidae	*Ammodytes hexapterus*	Arctic sand lance		4						13			1			18
		unidentified flounders	6						1				2		7	2
Pleuronectidae	*Hippoglossoides robustus*	Bering flounder	156	66			7		3	10			1		159	84
	Lepidopsetta polyxystra	northern rock sole		1												1
	Limanda spp.	unidentified *Limanda*	370						333			10	1		713	1
	Limanda aspera	yellowfin sole		76		1	321			36			221		1	654
	Limanda proboscidea	longhead dab		15									4			19
	Limanda sakhalinensis	Sakhalin sole		9						1						10
	Pleuronectes quadrituberculatus	Alaska plaice		5						1						6
		total number of taxa	3	25	1	2	7	2	3	21	2	2	8	0	5	31
		total number of individuals	532	264	4	16	351	2	337	150	30	11	235	0	906	1057

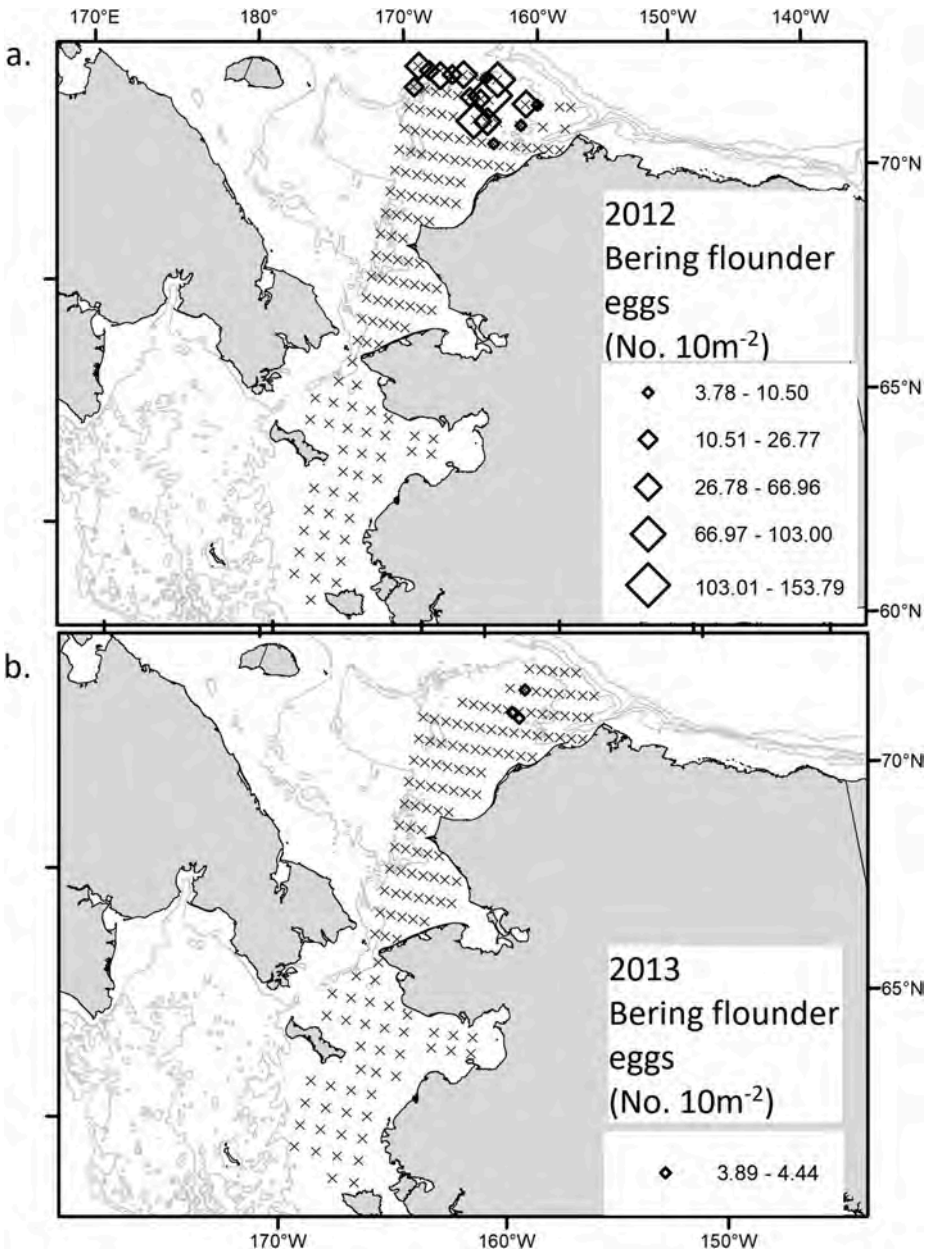

Fig. 3. Distribution of Bering flounder egg catch density (No./10 m^2) in a) 2012 and b) 2013.

CWW and greater in AW Mix compared to CWW in 2012 (Fig. 9 a). There was no significant difference in chlorophyll biomass between ACW and AWMix. Post-hoc tests comparing BWW with other water masses were not conducted, because BWW was only observed at one station (n = 1).

The difference in *Calanus glacialis* biomass density among all water masses was significant in 2012 (Kruskal-Wallis Chi-squared = 25.724, p-value <0.001), and marginally significant in 2013 (Kruskal-Wallis Chi-squared = 4.5013, p-value = 0.10) (Fig. 9 c, d). Post-hoc tests showed that *Calanus glacialis* biomass density was significantly greater in AW Mix than ACW in both years; and significantly greater in CWW than ACW in 2012. The smaller-sized stages of *Calanus glacialis* copepodites (C2 and C3) were proportionally most abundant in CWW in 2012 (Fig. 10) and even more so in 2013 (Fig. 11). C2 stages were only found in CWW in both years.

In contrast to *Calanus glacialis,* the biomass density of nauplii and smaller taxa of copepods (sampled with the PairVet net) was similar or higher in ACW compared to the other water masses in 2012. The PairVet net samples collected in 2013 were not analyzed due to loss of data sheets at sea. Calanoida nauplii biomass density was significantly different among water masses (Fig. 12 a; Kruskal-Wallis Chi-squared = 8.1041, p-value < 0.05). Post-hoc tests showed that nauplii biomass density was significantly greater in ACW compared to AW Mix. *Pseudocalanus* spp. biomass density was not significantly different among water masses (Fig. 12 b; Kruskal- Wallis Chi-squared = 1.8085, p-value = 0.40). *Acartia* spp. and *Oithona* spp. biomass densities were significantly different among water masses (*Acartia*: Kruskal-Wallis Chi-squared = 34.34, p-value <0.001. *Oithona*: Kruskal-Wallis Chi-squared = 32.5, p-value < 0.001) (Fig. 12 c, d). Post-hoc tests showed that *Acartia* and *Oithona* biomass densities were greater in ACW compared to AW Mix and compared to CWW. *Oithona* biomass density was also significantly greater in AW Mix compared to CWW.

In summary, Arctic cod and Bering flounder were most abundant in cold, high salinity water masses (AW Mix and CWW), which had elevated large copepod (*Calanus glacialis*) biomass density compared to Alaska Coastal Water. In contrast, yellowfin sole and capelin were only found in warm, low salinity Alaska Coastal Water that was high in

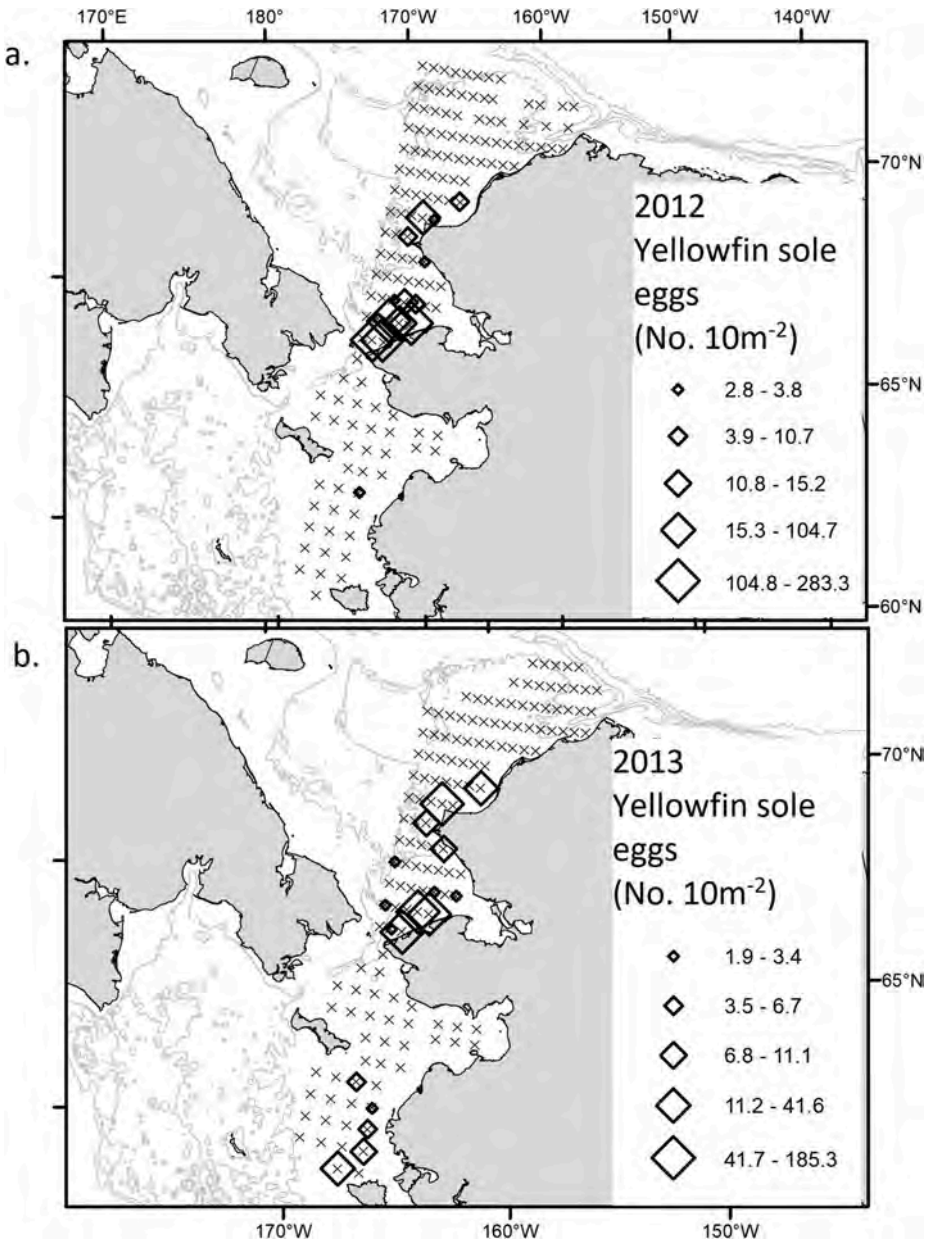

Fig. 4. Distribution of yellowfin sole egg catch density (No./10 m^2) in a) 2012 and b) 2013.

Calanoida nauplii and small copepod biomass density (*Acartia* spp. and *Oithona* spp.) compared to the cold, high salinity water masses (AW Mix and CWW).

4. Discussion

Arctic cod, Bering flounder, yellowfin sole and capelin were the four most abundant species in the ichthyoplankton catch during the 2012 and 2013 Arctic EIS surveys. Previous ichthyoplankton surveys have caught a similar mix of species (Busby et al., in review; Norcross et al., 2010; Randall et al., 2019; Wyllie-Echeverria et al., 1997), although Randall et al. (2019) also caught relatively high numbers of Arctic sand lance (*Ammodytes hexapterus*) and Arctic shanny (*Stichaeus punctatus*); and Busby et al. (in review) caught relatively high numbers of snailfish (*Liparis gibbus*).

Arctic cod and capelin are important energy-rich prey for upper trophic level predators (Hop and Gjøsæter, 2013). Arctic cod are consumed by beluga whales (*Delphinapterus leucas*), ringed seals (*Pusa hispida*), bearded seals (*Erignathus barbatus*), harp seals (*Pagophilus groenlandicus*), black guillemot (*Cepphus grylle*) and thick-billed murres (*Uria lomvia*) (Bradstreet, 1976; Bradstreet et al., 1986; Bradstreet and Cross, 1982; Huntington et al., 1999).

Alaska Arctic communities on the Chukchi Sea coast rely on many of these marine mammal species for subsistence use (Hovelsrud et al., 2008; Huntington et al., 1999). Capelin are preyed upon by mammal, bird and fish predators such as harp seals (Stenson et al., 1997), thick-billed murres (Provencher et al., 2012) and Atlantic cod (Mehl and Sunnana, 1991; Rose and O'Driscoll, 2002). Flatfishes are also important subsistence and ecological resources in the Arctic (Grebmeier et al., 2006a). Furthermore, yellowfin sole is one of the most abundant flatfish species in the eastern Bering Sea and currently is the target of the largest flatfish fishery in the world (Wilderbuer et al., 2017).

There were no statistically significant differences between 2012 and 2013 in the distributions of Arctic cod, Bering flounder, yellowfin sole and capelin larvae. This was observed despite wind-driven changes in water mass distribution between 2012 and 2013 (Danielson et al.,

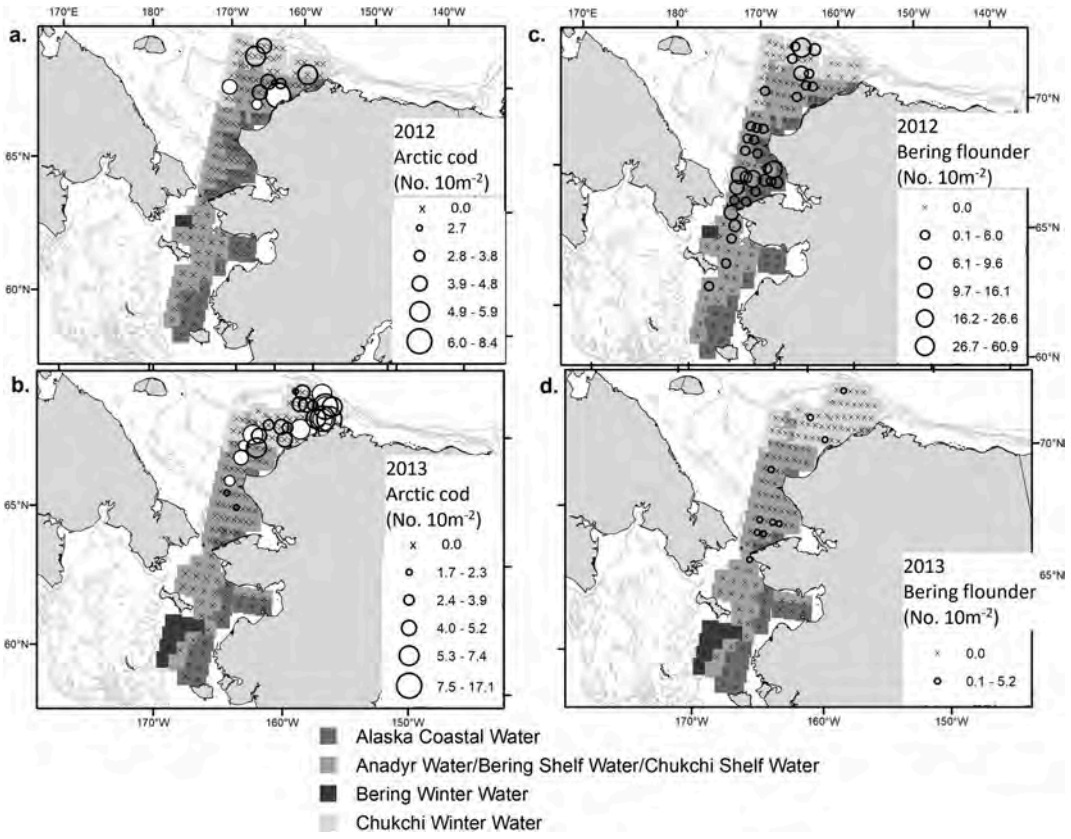

Fig. 5. Distribution of ichthyoplankton catch density (No./10 m^2) overlaid on bottom water mass type. a) 2012 Arctic cod, b) 2013 Arctic cod, c) 2012 Bering flounder, and d) 2013 Bering flounder. Open circles are larval fish, filled circles are juvenile fish. Arctic cod were the only taxa for which juvenile fish were caught. Water mass data courtesy of S. Danielson.

2017). We expected that larvae would be distributed less far north and further offshore in 2013 due to the reduced northerly extension of the Alaska Coastal Water and Anadyr Water Mix; and the offshore spread of Alaska Coastal Water. We did observe fewer Bering flounder larvae in 2013 compared to 2012. Perhaps the lower nutrient concentration and phytoplankton biomass observed in 2013 (Danielson et al., 2017) reduced the magnitude or delayed the timing of Bering flounder spawning and/or negatively impacted the survival of early larvae. The larval densities of the three other species were similar during the two years.

In both years, Arctic cod and Bering flounder larvae were found in cold water masses that we suggest provided good foraging opportunities. Arctic cod were only found in the northern third of the survey area in the Anadyr Water/Bering Shelf Water/Chukchi Shelf Water Mix (AW Mix) and Chukchi Winter Water (CWW). Bering flounder were similarly virtually restricted to these two cold and high salinity water masses. We suggest that the association of larval fish with particular water masses is the result of spawning location and subsequent entrainment of eggs and larvae in the currents that are associated with the water masses. Arctic cod spawn under the ice in late winter. Eggs are buoyant and develop near the surface, beginning under the ice cover and ending near the surface in ice-free areas after melting of the ice cover (Rass, 1968). Bering flounder spawn from April to June on the Bering and Chukchi sea shelves (Stark, 2004). It is not surprising that Arctic cod larvae are found in the north, given that they spawn under the ice in late winter. In addition, Arctic cod and Bering flounder were not found in Alaska Coastal Water which was expected given that they spawn in shelf waters.

AW Mix is formed from Bering Shelf Water, Chukchi Shelf Water and Anadyr Water. Anadyr Water is cold, saline and nutrient-rich that is delivered across the Gulf of Anadyr to the Bering Strait. This exogenous nutrient supply fuels much of the summer production on the Chukchi Sea shelf (Danielson et al., 2017). The two other components of the AW Mix, Bering Shelf Water and Chukchi Shelf Water, are cold and saline because of cycles of freezing, brine rejection and then summer warming (Danielson et al., 2017). Chukchi Winter Water (CWW) is the cold remnant of the previous winter's heat loss (Danielson et al., 2017). We found that these two cold water masses (AW Mix and CWW) had elevated large copepod (*Calanus glacialis*) biomass, compared to the warmer, fresher Alaska Coastal Water (ACW). The smallest stages of *Calanus* (C2) were proportionally most abundant in CWW.

Published information about the diets of larval Arctic cod supports the idea that the colder water masses were good foraging areas. We caught Arctic cod larvae from 10 mm to 55 mm SL, spanning flexion larvae to post-flexion larvae to juvenile stages (Ponomarenko, 2000). Arctic cod flexion larvae sampled from the Canadian Beaufort Sea consumed copepod nauplii and C1–C2 *Calanus glacialis* copepodites. Post-flexion larvae consumed copepod nauplii, *Pseudocalanus* spp. and C1–C2 *Calanus glacialis* copepodites. Arctic cod juveniles (26–55 mm length) consumed C2–C4 *Calanus glacialis* copepodites (Walkusz et al., 2011). No Arctic cod larval diet data are available for the Chukchi Sea, but if larval diets are comparable across adjacent seas, then the AW Mix and CWW could be hypothesized to be good foraging areas for Arctic cod larvae in the Chukchi Sea.

There is no published information on larval Bering flounder diets. In a review of latitudinal and taxonomic patterns in larval feeding ecology, Llopiz (2013) found that 85% of the diet of flatfish (Order: Pleuronectiformes) was comprised of appendicularians, nauplii, and calanoids. Other studies of specific flatfish taxa showed similar results. American plaice (*Hippoglossoides platessoides*) and Yellowtail flounder (*Limanda ferruginea*) relied on nauplii and copepodites of *Pseudocalanus*, *Oithona similis* and *Temora longicornis* (Pepin and Penney, 1997). Copepods

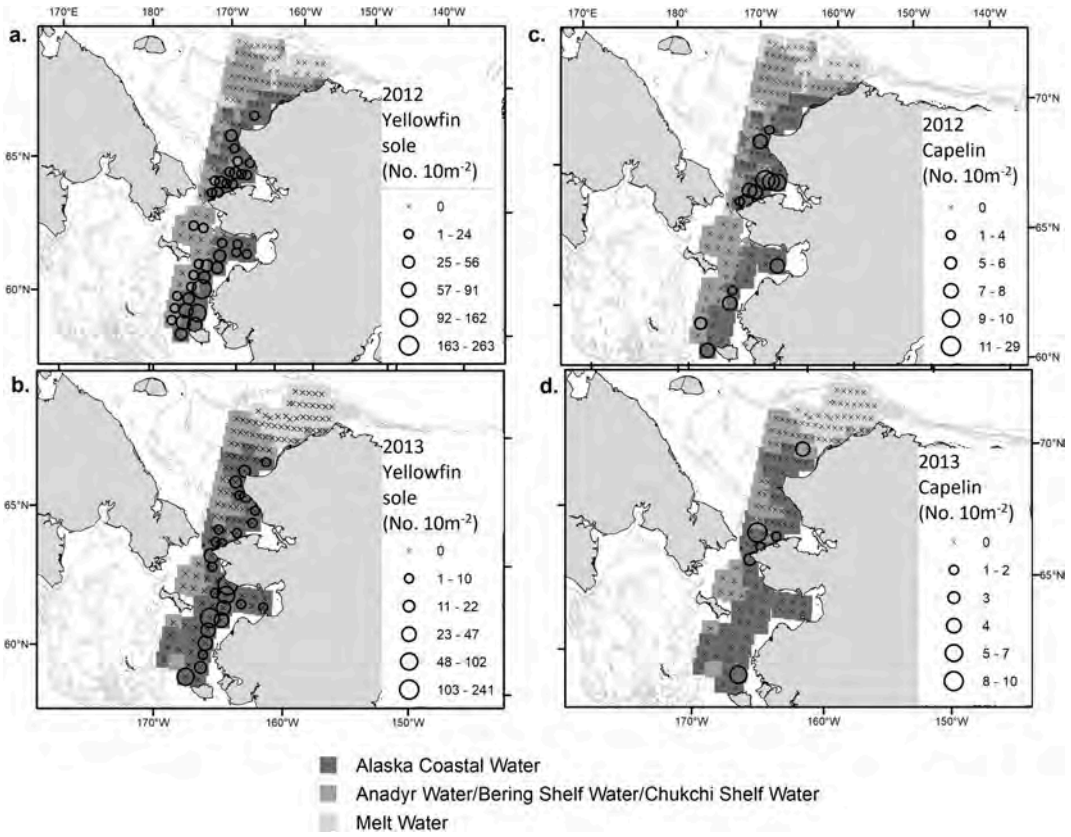

Fig. 6. Distribution of ichthyoplankton catch density (No./10 m^2) overlaid on surface water mass type. a) 2012 yellowfin sole, b) 2013 yellowfin sole, c) 2012 capelin, and d) 2013 capelin ichthyoplankton. Water mass data courtesy of S. Danielson.

(*Copepoda*) have been found to make up 88%–99% of the total gut contents of Greenland halibut (*Rheinhardtius hippoglossoides*) (Simonsen et al., 2006). Bering flounder likely consume smaller prey than Arctic cod, however the colder water masses could provide sufficient biomass of some smaller prey taxa such as *Pseudocalanus* spp. and C2 stages of *Calanus glacialis*.

Advection and the timing of seasonal sea-ice retreat contribute to the formation and productivity of the cold, high salinity water masses (AW Mix and CWW), which we suggest are good foraging habitat for Arctic cod and Bering flounder. Advection through the Bering Strait brings nutrients and plankton-rich Pacific Ocean water into the Chukchi Sea, across the shelf and through Barrow Canyon (Pickart et al., 2005; Woodgate et al., 2015). The seasonal sea-ice zone provides ice algae and early stabilization of the water column by melting ice, which initiates a spring bloom of phytoplankton. Both of these features, advection and sea ice retreat, have been shown to be impacted by global climate change. Ocean warming has resulted in reduction in seasonal sea-ice extent and earlier sea-ice retreat (Frey et al., 2014; Grebmeier et al., 2006b). This change in timing of ice break up means that although ice melt still stabilizes the water column, sunlight is not sufficient to initiate an intense spring bloom (Clement, 2004), suggesting a lowering of overall primary production. Alternatively, earlier sea-ice breakup could result in increased primary production due to a longer growing season, as has been observed in the Arctic Ocean (Arrigo et al., 2008). The second process of interest here, advection through the Bering Strait, has increased by almost 50% from 2001 to the present (Woodgate et al., 2015). A larger-scale analysis of flow patterns from 1979 to 2014 shows, in contrast, that there was slightly less poleward advection across the Chukchi Sea shelf since the turn of the century (Bond et al., 2018). Although the present study from two years' surveys suggests some potential mechanisms, further research over multiple years and over a broader study area is needed to confirm how the dynamics of advection and sea-ice retreat impact the habitat of larval fishes.

In contrast to Arctic cod and Bering flounder, yellowfin sole and capelin larvae were found more towards the south and exclusively in nearshore Alaska Coastal Water (ACW) in both years. Yellowfin sole spawn in June and July in nearshore waters (Nichol and Acuna, 2001), and capelin spawn in summer on beaches (Frost and Lowry, 1987). So it is perhaps not surprising that the larvae of both species would be entrained in the ACW. Alaska Coastal Water was the warmest and freshest water observed in the survey, and it is typically low in nutrients, chlorophyll-*a* and phytoplankton productivity after the spring bloom of phytoplankton and associated nutrient depletion (Springer and McRoy, 1993). We observed reduced large copepod (*Calanus glacialis*) biomass in ACW during our surveys. However, copepod nauplii and small copepod biomass (*Acartia* spp. and *Oithona* spp.) were relatively high, compared to the other water masses.

Due to a paucity of relevant published diet information, it is difficult to assess whether ACW could be good foraging habitat for larval yellowfin sole and capelin. There are no published diet data for yellowfin sole larvae. The larval diets of a related species, common dab (*Limanda limanda*) collected in the southern North Sea, were comprised mainly of nauplii and copepodites of the copepod *Temora longicornis* (Last, 1978). Yellowtail flounder (*Limanda ferruginea*) caught off the coast of Newfoundland similarly relied on nauplii and copepodites of *Pseudocalanus*, *Oithona similis* and *Temora longicornis* (Pepin and Penney, 1997). There are no studies of capelin diets in the Pacific arctic or subarctic. Studies of capelin diets in the Barents and Norwegian seas showed that larvae were feeding on *Calanus* eggs and nauplii (Bjorke, 1976; Karamushko and Reshetnikov, 1994). Capelin diets off the coast of Newfoundland were comprised of nauplii and copepodites of *Pseudocalanus*, *Oithona similis* and *Temora longicornis* (Pepin and Penney, 1997). Other forage fish taxa, such as Pacific herring (*Clupea harengus*) and sandlance (*Ammodytes* spp.) similarly consume copepod nauplii and

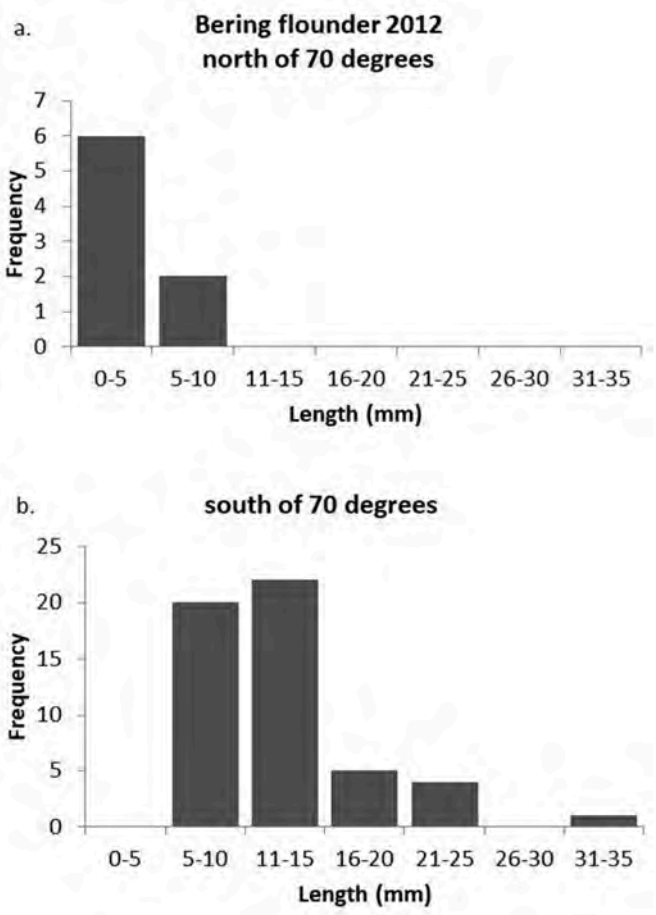

Fig. 7. Length-frequency distributions (number of fish) of Bering flounder larvae from 2012: a) north of 70° latitude (n = 8) and b) south of 70° latitude (n = 52).

copepodites, including *Acartia* spp. (Fortier et al., 1995; Robert et al., 2013). If copepod nauplii and small copepods such as *Acartia* and *Oithona* are suitable prey for yellowfin sole and capelin larvae in the Chukchi Sea and Northern Bering Sea, then the ACW could provide good foraging habitat.

Previous ichthyoplankton surveys of the Chukchi Sea have made similar conclusions about the distribution of Arctic fish larvae in relation to water masses. Surveys in 1990–1991 (Wyllie-Echeverria et al., 1997) and in 2004 (Norcross et al., 2010) found Arctic cod in cold offshore water and yellowfin sole in nearshore ACW. Wyllie-Echeverria et al. (1997) also found capelin in ACW; Norcross et al. (2010) did not catch any capelin in 2004. One conflict among these results is that Norcross et al. (2010) found Bering flounder larvae in cold offshore waters, similar to what we observed, but Wyllie-Echeverria et al. (1997) showed Bering flounder associated with ACW. Randall et al. (2019) documented species assemblages of ichthyoplankton during marine mammal and plankton surveys in 2010–2015 and found interannual associations between communities and the dominant water masses similar to our results. For instance, in years where ACW occupied more of the study area, the ichthyofauna was characterized by a yellowfin sole-driven community. In years when there was more cold water on the shelf, a community typified by Arctic cod was present at most stations.

The distribution and large size of Arctic cod larvae was expected given what is known about the timing and location of Arctic cod spawning. The transport pathways between Arctic cod hatching locations and larval distributions have been investigated using a biophysical transport model that simulates larval growth and dispersal (Vestfals

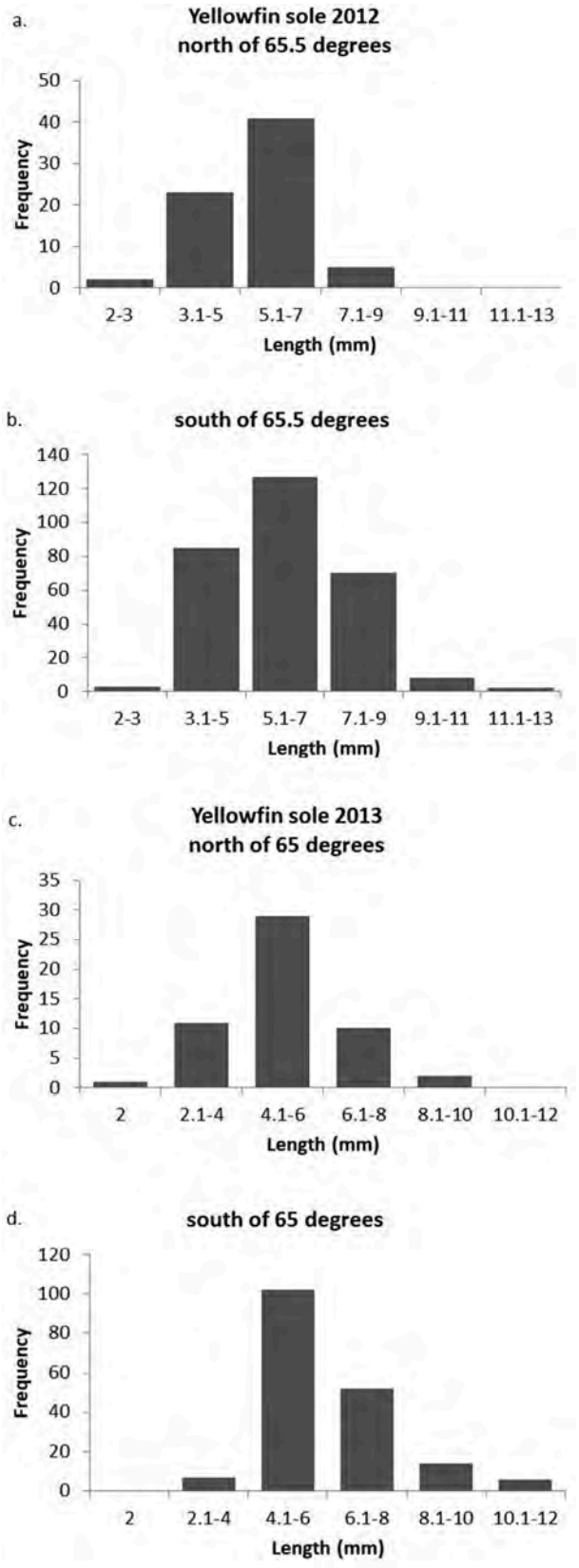

Fig. 8. Length-frequency distributions (number of fish) of yellowfin sole larvae from: a) 2012, north of 65.5° latitude (n = 71); b) 2012, south of 65.5° latitude (n = 295); c) 2013, north of north of 65.5° latitude (n = 53); and d) 2013, south of 65.5° (n = 181).

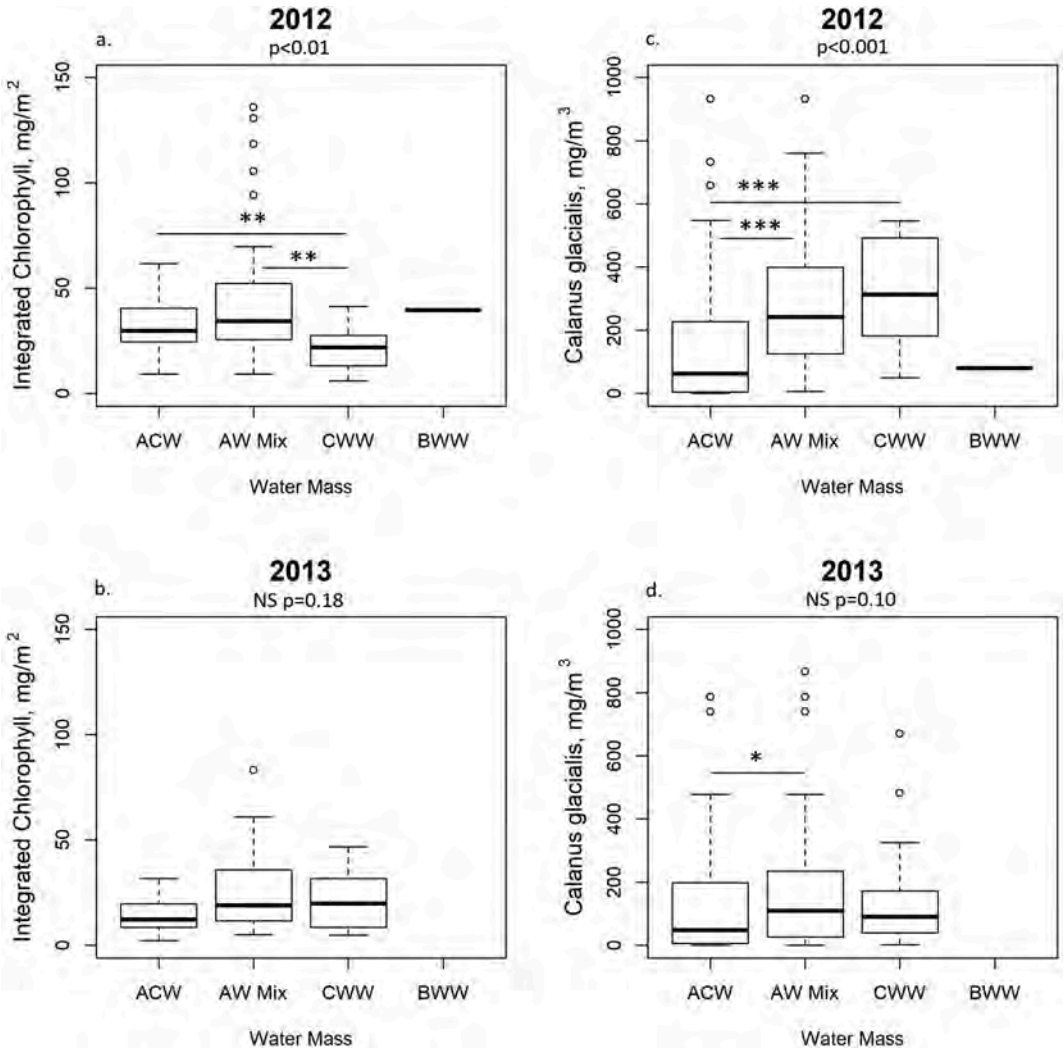

Fig. 9. Water mass characteristics for Alaska Coastal Water (ACW) at the surface; and Anadyr Water/Bering Shelf Water/Chukchi Shelf Water (AW Mix), Chukchi Winter Water (CWW) and Bering Winter Water (BWW) at depth. Box plots show median (horizontal line), first and third quartile (box), minimum and maximum (whiskers) and outliers (points). p-value from Kruskal-Wallis rank sum test for comparisons among all water masses is shown at upper right of each box plot. Significant p-values for post-hoc Kruskal-Wallis rank sum test comparisons between pairs of water masses are indicated by bars and asterix. *$p < 0.05$, **$p < 0.01$, ***$p < 0.001$; a) 2012 integrated chlorophyll (mg m^{-2}), b) 2013 integrated chlorophyll (mg m^{-2}), c) 2012 *Calanus glacialis* (mg m^{-3}), and d) 2013 *Calanus glacialis* (mg m^{-3}).

et al., in prep). The results of this modeling effort indicate that Arctic cod larvae caught during the Arctic Eis surveys were likely spawned in the northern Bering Sea or southern Chukchi Sea in winter and then transported to the north by late summer.

Flatfish larvae in the Chukchi Sea could have resulted from local (Chukchi Sea) or remote (Bering Sea) spawning. Our data on egg distributions and larval length-frequency patterns provided clues about flatfish spawning areas. Bering flounder eggs were caught in the northern Chukchi Sea and there was an aggregation of larvae in the same area. There were also Bering flounder larvae in the southern Chukchi Sea and northern Bering Sea, but no eggs were found in those areas. The length-frequency distributions of the northern versus the southern Bering flounder larvae were different. The larvae to the north were smaller, consistent with later spawning and/or slower larval growth rates. The larvae to the south were larger, consistent with earlier spawning and/or faster growth rates. These patterns in egg distribution and larval length-frequencies could indicate that Bering flounder larvae in the northern Chukchi Sea were spawned locally, in the northern Chukchi Sea, later than flounder to the south and in colder water resulting in slower growth and smaller size. In contrast, larvae in the southern Chukchi Sea could have been spawned to the south in the Bering Sea earlier and in warmer water resulting in faster growth rate, and were then transported north, in the Bering Shelf and/or Anadyr Current. It is unlikely that larvae in the south were advected from the north where we caught eggs because this is in the opposite direction of the prevailing currents. An alternative mechanism is that Bering flounder larvae in the southern Chukchi Sea were spawned locally, but sufficiently earlier that eggs were no longer present when that area was surveyed.

Yellowfin sole eggs were found throughout the survey area and larval length-frequency distributions were similar to the north and south. This is consistent with local spawning of yellowfin sole larvae in the southern Chukchi Sea and northern Bering Sea at the same time of year. An alternative mechanism is that yellowfin sole spawning only occurred in the southern Bering Sea and their eggs and larvae were transported to the northern Bering Sea and Chukchi Sea in the Alaska Coastal Current.

Currents across the Chukchi Sea shelf are slow, on average, around 5 cm s^{-1} (Stabeno et al., 2018; Weingartner et al., 2005; Woodgate et al., 2005), such that it is less likely that larval flatfish found in the Chukchi Sea were transported from the south. At 5 cm s^{-1} (4.32 km day^{-1}), it would take an egg or larvae 179 days to transit the 777 km from the Bering Strait to the northernmost station in the survey. Pelagic durations

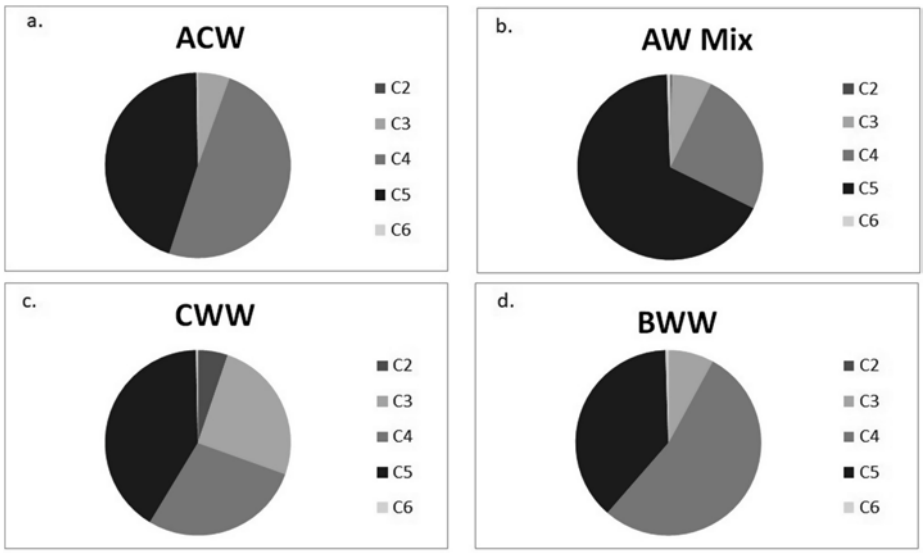

Fig. 10. Proportion of *Calanus glacialis* copepodite stages C2–C6 in each water mass in 2012: a) Alaska Coastal Water (ACW), b) Chukchi Winter Water (CWW), c) Anadyr Water/Bering Shelf Water/Chukchi Shelf Water (AW Mix), d) Bering Winter Water.

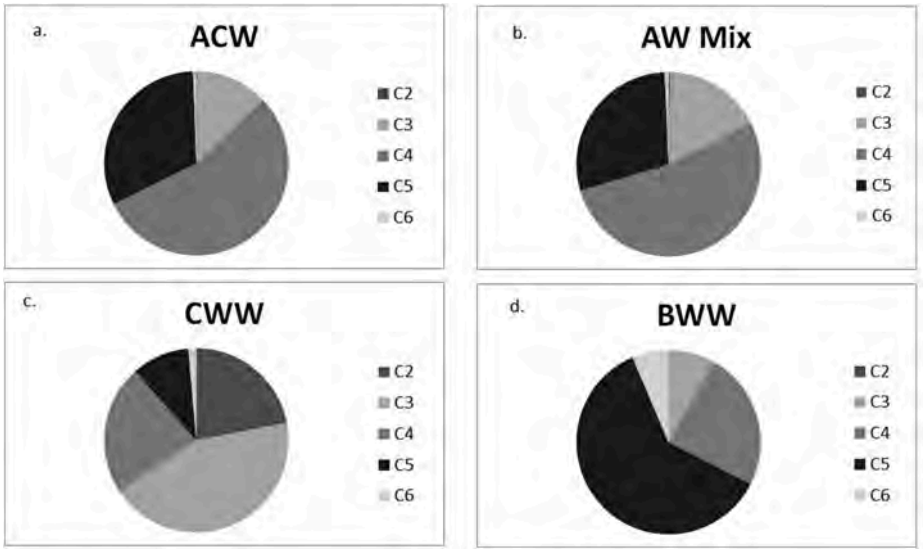

Fig. 11. Proportion of *Calanus glacialis* copepodite stages C2–C6 in each water mass in 2013: a) Alaska Coastal Water (ACW), b) Chukchi Winter Water (CWW), c) Anadyr Water/Bering Shelf Water/Chukchi Shelf Water (AW Mix), d) Bering Winter Water.

of flatfish larvae are less than that transit time, on the order of 30–60 days for yellowfin sole in the Gulf of Alaska, and 30–120 days for *Hippoglossoides platessoides* (American plaice) in the North Atlantic (Duffy-Anderson et al., 2015). Randall et al. (2019), analyzing data from a collection of other ichthyoplankton surveys conducted in 2010–2015 as part of marine mammal studies (CHAOZ and ArcWest), similarly concluded that Bering flounder in the Chukchi Sea were likely to have been spawned locally.

5. Conclusions

The distributions of Arctic fish larvae were not statistically different between 2012 and 2013 despite the differences in water mass distribution between the two years. Larvae of Arctic cod, Bering flounder, yellowfin sole and capelin were found in similar locations in both years and were associated with water masses that had elevated biomass of zooplankton taxa that could potentially have been prey. We suggest that the distribution of larvae is a product of spawning behavior that results in the larvae being located in habitat suitable for successful foraging even as oceanographic processes vary from year-to-year. In other words, Arctic fishes have evolved spawn timing and location such that larval distributions are resilient to the degree of interannual climate variability observed between 2012 and 2013. Biophysical transport models such as Vestfals et al. (in prep) can demonstrate the advective connections between spawning location and larval distribution and can be used to explore this hypothesis. This study describes the habitat for larval Arctic cod, Bering flounder, capelin and yellowfin sole and provides baseline information on their early life history. Understanding the associations between larval oceanographic habitat and spawning-related resilience helps us to better understand the mechanisms and the degree of oceanographic change due to ocean warming and loss of sea ice which may have the potential to impact the early life histories of Arctic fishes.

Funding

This work was supported by the Coastal Impact Assistance Program

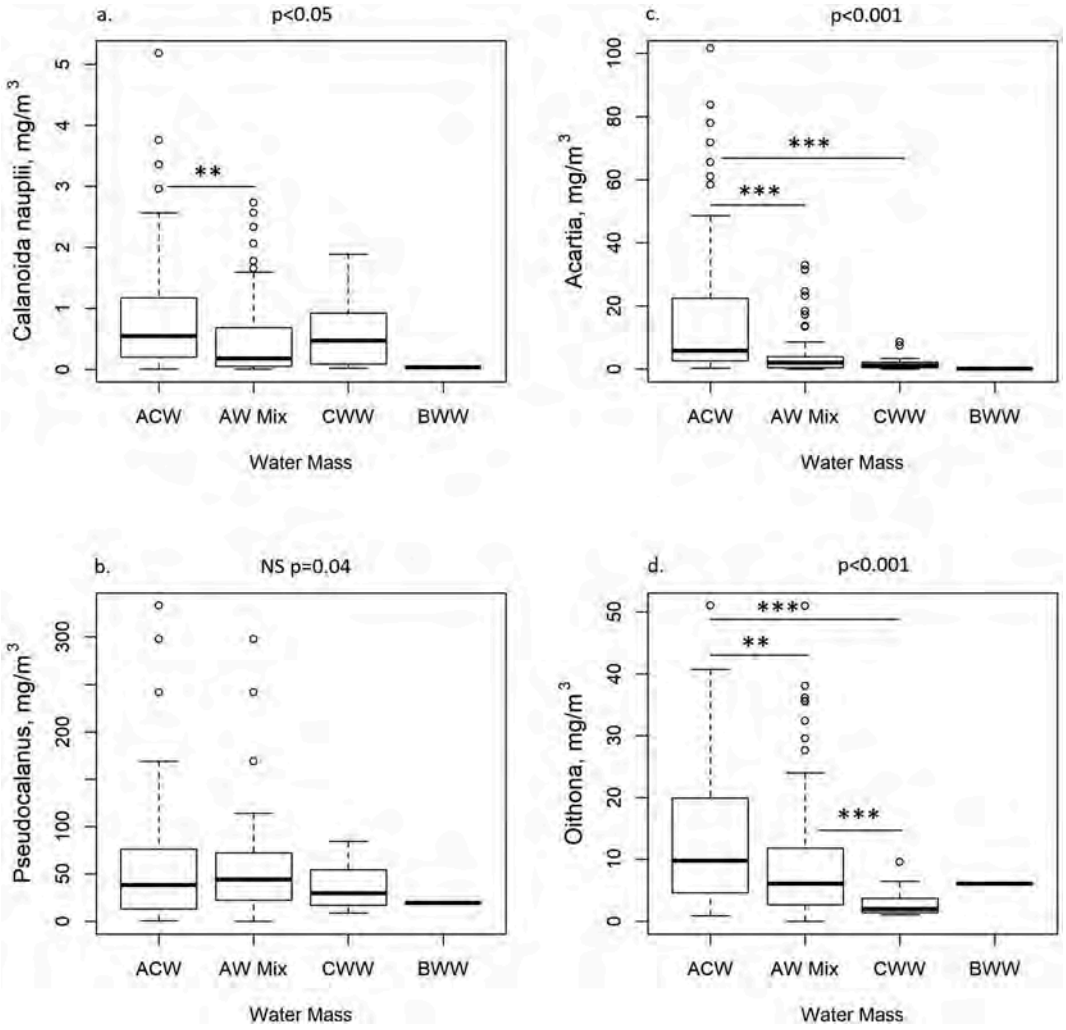

Fig. 12. Biomass density (mg m^{-3}) of small copepods in Alaska Coastal Water (ACW), Anadyr Water/Bering Shelf Water/Chukchi Shelf Water (AW Mix), Chukchi Winter Water (CWW) and Bering Winter Water (BWW) in 2012. No small (20-mm) PairVet net samples were analyzed for 2013 due to loss of data sheets at sea. Box plots show median (horizontal line), first and third quartile (box), minimum and maximum (whiskers) and outliers (points). p-value from Kruskal-Wallis rank sum test for comparisons among all water masses is shown at upper right of each box plot. Significant p-values for post-hoc Kruskal-Wallis rank sum test for comparisons between pairs of water masses are indicated by bars and asterix. *$p < 0.05$, **$p < 0.01$, ***$p < 0.001$; a) Calanoida nauplii, b) *Pseudocalanus* sp., c) *Acartia* spp., and d) *Oithona* spp.

(AKDNR/USFWS), the University of Alaska Fairbanks [10-CIAP-010 and F12AF00188], Bureau of Ocean Energy Management and the University of Alaska Fairbanks [M12AC00009].

This manuscript builds on research associated with the North Pacific Research Board Arctic (NPRB) Integrated Ecosystem Research Program and is NPRB publication ArcticIERP-11.

Declaration of competing interest

The authors declare that they have no known competing financial interests or personal relationships that could have appeared to influence the work reported in this paper.

CRediT authorship contribution statement

Elizabeth A. Logerwell: Conceptualization, Methodology, Formal analysis, Writing - original draft, Visualization. **Morgan Busby:** Conceptualization, Investigation, Writing - review & editing. **Kathryn L. Mier:** Formal analysis, Writing - review & editing. **Heather Tabisola:** Conceptualization, Writing - review & editing. **Janet Duffy-Anderson:** Conceptualization, Resources, Supervision, Project administration, Funding acquisition, Writing - review & editing.

Acknowledgments

We thank the captain and crew of the FV *Bristol Explorer*, and all of the Arctic Eis scientists who helped carry this program forward, particularly Franz Mueter and Jared Weems. Thanks also to the Bureau of Ocean and Energy Management program manager Catherine Coon. Thank you to C. Ladd and C. Vestfals for reviews of earlier drafts of this manuscript and to two anonymous reviewers and the editor for journal review. This is Eco-FOCI contribution #0920. Reference to trade names does not imply endorsement by the National Marine Fisheries Service, NOAA.

Appendix A. Supplementary data

Supplementary data to this article can be found online at https://doi.org/10.1016/j.dsr2.2020.104784.

References

Aagaard, K., Weingartner, T.J., Danielson, S.L., Woodgate, R.A., Johnson, G.C., Whitledge, T.E., 2006. Some controls on flow and salinity in Bering Strait. Geophys. Res. Lett. 33, 1–5. https://doi.org/10.1029/2006GL026612.

Arrigo, K.R., van Dijken, G., Pabi, S., 2008. Impact of a shrinking Arctic ice cover on marine primary production. Geophys. Res. Lett. 35, 1–6. https://doi.org/10.1029/2008GL035028.

Bjorke, H., 1976. Some preliminary results on food and feeding of young capelin larvae. ICES Counc 1–12. Meet. 1976/H 3e.

Björnsson, B., Steinarsson, A., Oddgeirsson, M., 2001. Optimal temperature for growth and feed conversion of immature cod (Gadus morhua L.). ICES J. Mar. Sci. 58, 29–38. https://doi.org/10.1006/jmsc.2000.0986.

Bond, N., Stabeno, P., Napp, J., 2018. Flow patterns in the Chukchi sea based on an ocean reanalysis, June through October 1979–2014. Deep. Res. Part II Top. Stud. Oceanogr. 152, 35–47. https://doi.org/10.1016/j.dsr2.2018.02.009.

Bradstreet, M.S.W., 1976. Summer Feeding Ecology of Seabirds in Eastern Lancaster Sound. LGL Ltd, Toronto, 1976. Report.

Bradstreet, M.S.W., Cross, W.E., 1982. Trophic relationships at high Arctic ice edges. Arctic 35, 1–12.

Bradstreet, M.S.W., Finley, K.J., Sekerak, A.D., Griffiths, W.B., Evans, C.R., Fabijan, F.F., Stallard, H.E., 1986. Aspects of the biology of Arctic cod (*Boreogadus saida*) in Arctic marine food chains. Can. Tech. Rep. Fish. Aquat. Sci. 1491.

Brown, A.L., Busby, M.S., Mier, K.L., 2001. Walleye pollock *Theragra chalcogramma* during transformation from the larval to juvenile stage: otolith and osteological development. Mar. Biol. 139, 845–851. https://doi.org/10.1007/s002270100641.

Busby, M.S., Holladay, B.A., Mier, K.L., and Norcross, B.L., in reviw. Ichthyoplankton of the Chukchi sea 2004-2012: Russian-American long-term census of the arctic. Polar Biol..

Busby, M.S., Blood, D.M., Matarese, A.C., 2017. Identification of larvae of three arctic species of Limanda (family pleuronectidae). Polar Biol. 40, 2411–2427. https://doi.org/10.1007/s00300-017-2153-9.

Campbell, R.G., Gelfman, C., Dennis, M., McCoy, I., Ashjian, C.J., 2014. Population genetics of the *Calanus glacialis/marshallae* species complex in the Bering and Western Arctic seas. In: Proceedings of the Ocean Sciences Meeting. Honolulu, Hawaii, USA, pp. 23–28 (February).

Clement, J.L., 2004. Late winter water column and sea ice conditions in the northern Bering Sea. J. Geophys. Res. 109, 1–16. https://doi.org/10.1029/2003JC002047.

Danielson, S.L., Eisner, L., Ladd, C., Mordy, C., Sousa, L., Weingartner, T.J., 2017. A comparison between late summer 2012 and 2013 water masses, macronutrients, and phytoplankton standing crops in the northern Bering and Chukchi Seas. Deep Sea Res. II 135, 7–26.

Day, R.H., Weingartner, T.J., Hopcroft, R.R., Aerts, L.A.M., Blanchard, A.L., Gall, A.E., Gallaway, B.J., Hannay, D.E., Holladay, B.a., Mathis, J.T., Norcross, B.L., Questel, J. M., Wisdom, S.S., 2013. The offshore northeastern Chukchi Sea, Alaska: a complex high-latitude ecosystem. Cont. Shelf Res. 67, 147–165. https://doi.org/10.1016/j.csr.2013.02.002.

Duffy-Anderson, J.T., Bailey, K.M., Cabral, H.N., Nakata, H., Van Der Veer, H.W., 2015. The planktonic stages of flatfishes: physical and biological interactions in transport processes. In: Gibson, R.N., Nash, R.D.M., Geffen, A.J., Van der Veer, H.W. (Eds.), Flatfishes: Biology and Exploitation, second ed., pp. 132–170. https://doi.org/10.1002/9781118501153.ch6.

Fortier, L., Ponton, D., Gilbert, M., 1995. The match/mismatch hypothesis and the feeding success of fish larvae in ice-covered southeastern Hudson Bay. Mar. Ecol. Prog. Ser. 120, 11–27. https://doi.org/10.3354/meps120011.

Frey, K.E., Maslanik, J.A., Kinney, J.C., Maslowski, W., 2014. Recent variability in sea ice cover, age, and thickness in the Pacific Arctic region. In: Grebmeier, J.M., Maslowski, W. (Eds.), The Pacific Arctic Region: Ecosystem Status and Trends in a Rapidly Changing Environment. Springer-Verlag, Dordrecht, pp. 31–64.

Frost, K.J., Lowry, L.F., 1987. Marine mammals and forage fishes in the southeastern Bering Sea. In: Conference Proceedings of Forage Fishes of the Southeastern Bering Sea. 4-5 November 1986, Anchorage, AK. Prepared for U.S. Department of the Interior, Mineral Management Service, Alaska OCS Region, pp. 11–18.

Grebmeier, J.M., 2012. Shifting patterns of life in the pacific arctic and sub-arctic seas. Annu. Rev. Mar. Sci. 44, 63–78. https://doi.org/10.1146/annurev-marine-120710-100926.

Grebmeier, J.M., Cooper, L.W., Feder, H.M., Sirenko, B.I., 2006a. Ecosystem dynamics of the pacific-influenced northern Bering and Chukchi seas in the Amerasian arctic. Prog. Oceanogr. 71, 331–361. https://doi.org/10.1016/j.pocean.2006.10.001.

Grebmeier, J.M., Overland, J.E., Moore, S.E., Farley, E.V., Carmack, E.C., Cooper, L.W., Frey, K.E., Helle, J.H., McLaughlin, F.A., McNutt, S.L., 2006b. A major ecosystem shift in the northern Bering Sea. Science 311, 1461–1646 (80-.).

Hjort, J., 1914. Fluctuation in the great fisheries of northern Europe. Rapp. Proc.-Verb. des Reun. Cons. Int. Explor. Mer. 20, 1–228.

Hop, H., Gjøsæter, H., 2013. Polar cod (*Boreogadus saida*) and capelin (*Mallotus villosus*) as key species in marine food webs of the Arctic and the Barents Sea. Mar. Biol. Res. 9, 878–894. https://doi.org/10.1080/17451000.2013.775458.

Hovelsrud, G., McKenna, M., Huntington, H.P., 2008. Marine mammal harvests and other interactions with humans. Ecol. Appl. 18, 135–147.

Huang, J., Zhang, X., Zhang, Q., Lin, Y., Hao, M., Luo, Y., Zhao, Z., Yao, Y., Chen, X., Wang, L., Nie, S., Yin, Y., Xu, Y., 2017. Recently amplified arctic warming has contributed to a continual global warming trend. Nat. Clim. Chang. 7, 875–880. https://doi.org/10.1038/s41558-017- 0009-5.

Huntington, H.P., The communities of Buckland, Elim, Koyuk, Lay, Point, S, 1999. Traditional knowledge of the ecology of beluga whales (*Delphinapterus leucas*) in the eastern Chukchi and northern Bering seas, Alaska. Arctic 52, 49–61.

Karamushko, O., Reshetnikov, Y., 1994. Daily Rations of larval capelin , *Mallotus villosus villosus*, and cod , *Gadus morhua morhua* , in the Barents and Norwegian Seas. J. Ichthyol. 34, 112–127.

Kendall, A.W., Ahlstrom, E.H., Moser, H.G., 1984. Early life history stages and their characters. In: Moser, H.G., Richards, W.J., Cohen, D.M., Fahay, M.P., Kendall, A.W., Richardson, S.L. (Eds.), Ontogeny and Systematics of Fishes - Ahlstrom Symposium, 15-18 August, 1983, La Jolla, CA, vol. 1. Am Soc Ich Herpetol Special Publ 1, pp. 11–22. Am Soc Ich Herpetol Special Publ.

Kwok, R., Rothrock, D.A., 2009. Decline in Arctic sea ice thickness from submarine and ICESat records: 1958-2008. Geophys. Res. Lett. 36, 1–5. https://doi.org/10.1029/2009GL039035.

Lasker, R., 1981. Factors contributing to variable recruitment of the Northern Anchovy (*Engraulis mordax*) in the California current: contrasting years, 1975 through 1978. Rapp. P.-V. Reun. Cons. int. Mer 178, 375–388.

Last, J.M., 1978. The food of four species of pleuronectiform larvae in the eastern English Channel and southern North Sea. Mar. Biol. 45, 359–368.

Laurel, B.J., Spencer, M., Iseri, P., Copeman, L.A., 2015. Temperature-dependent growth and behavior of juvenile Arctic cod (*Boreogadus saida*) and co-occurring North Pacific gadids. Polar Biol. https://doi.org/10.1007/s00300-015-1761-5.

Llopiz, J.K., 2013. Latitudinal and taxonomic patterns in the feeding ecologies of fi sh larvae : a literature synthesis. J. Mar. Syst. 109– 110, 69–77. https://doi.org/10.1016/j.jmarsys.2012.05.002.

Matarese, A.C., Kendall Jr., A.W., Blood, D.M., Vinter, B.M., 1989. Laboratory guide to early life history stages of northeast Pacific fishes. In: NOAA Technical Report NMFS, vol. 80.

Mecklenburg, C., Lynghammar, A., Johannesen, E., Byrkjedal, I., Christiansen, J.S., Karamushko, O.V., Mecklenburg, T.A., Møller, P.R., Steinke, D., Wienerroither, R.M., 2018. Marine Fishes of the Arctic Region Vol I and II. CAFF Monitoring Series Report 28. Conservation of Arctic Flora and Fauna (Akureyi, Iceland).

Mecklenburg, C.A., Steinke, D., 2015. Ichthyofaunal baselines in the Pacific Arctic region and RUSALCA study area. Oceanography 28, 158–189.

Mehl, S., Sunnana, K., 1991. Changes in growth of Northeast Arctic cod in relation to food consumption in 1984-1988. ICES Mar. Sci. Symp. 193, 103–112.

Meier, W.N., Stroeve, J., Barrett, A., Fetterer, F., 2012. A simple approach to providing a more consistent Arctic sea ice extent time series from the 1950s to present. Cryosphere 6, 1359–1368. https://doi.org/10.5194/tc-6-1359-2012.

Mueter, F.J., Weems, J., Farley, E.V., Sigler, M.F., 2017. Arctic ecosystem integrated survey (arctic Eis): marine ecosystem dynamics in the rapidly changing pacific arctic gateway. Deep Sea Res. II 135, 1–6. https://doi.org/10.1016/j.dsr2.2016.11.005.

Nelson, R.J., Carmack, E.C., McLaughlin, F.A., Cooper, G.A., 2009. Penetration of pacific zooplankton into the western arctic ocean tracked with molecular population genetics. Mar. Ecol. Prog. Ser. 381, 129–138. https://doi.org/10.3354/meps07940.

Nichol, D.G., Acuna, E.I., 2001. Annual and batch fecundities of yellowfin sole, Limanda aspera, in the eastern Bering Sea. Fish. Bull. 99, 108–122.

Norcross, B.J., Holladay, B.A., Busby, M.S., Mier, K.L., 2010. Demersal and larval fish assemblages in the Chukchi Sea. Deep Sea Res. II 57, 57–70.

Page, L.M., Espinosa-Perez, H., Findley, L.T., Gilbert, C.R., Lea, R.N., Mandrak, N.E., Mayden, R.L., Nelson, J.S., 2013. Common and Scientific Names of Fishes from the United States, Canada, and Mexico, vol. 34. American Fisheries Society Special Publication.

Panteleev, G., Nechaev, D.A., Proshutinsky, A., Woodgate, R., Zhang, J., 2010. Reconstruction and analysis of the Chukchi sea circulation in 1990-1991. J. Geophys. Res. Ocean. 115, 1–22. https://doi.org/10.1029/2009JC005453.

Pepin, P., Penney, R.W., 1997. Patterns of prey size and taxonomic composition in larval fish: are there general size-dependent models? J. Fish. Biol. 51, 84–100. https://doi.org/10.1111/j.1095-8649.1997.tb06094.x.

Pickart, R.S., Weingartner, T., Pratt, L.J., Zimmerman, S.T., Torres, D.J., 2005. Flow of winter-transformed Pacific water into the western Arctic. Deep Sea Res. II 52, 3175–3198.

Pinchuk, A.I., Eisner, L.B., 2016. Spatial heterogeneity in zooplankton summer distribution in the eastern Chukchi Sea in 2012–2013 as a result of large-scale interactions of water masses. Deep Sea Res. Part II Top. Stud. Oceanogr. 0– 1 https://doi.org/10.1016/j.dsr2.2016.11.003.

Ponomarenko, V.P., 2000. Eggs, larvae, and juveniles of polar cod Boreogadus saida in the Barents, Kara and white seas. J. Ichthyol. 40, 165–173.

Provencher, J.F., Gaston, A.J., O'Hara, P.D., Gilchrist, H.G., 2012. Seabird diet indicates changing Arctic marine communities in eastern Canada. Mar. Ecol. Prog. Ser. 454, 171–182. https://doi.org/10.3354/meps09299.

R Core Team, 2016. R: A Language and Environment for Statistical Computing.

Randall, J.R., Busby, M.S., Spear, A.H., Mier, K.L., 2019. Spatial and temporal variation of late summer ichthyoplankton assemblage structure in the eastern Chukchi Sea : 2010 – 2015. Polar Biol. 42, 1811–1824. https://doi.org/10.1007/s00300-019-02555-8.

Rass, T.S., 1968. Spawning and development of polar cod. Rapp. Procés-Verbaux des Réunions du Cons. Int. pour l'Exploration la Mer 158, 135–137.

Robert, D., Murphy, H.M., Jenkins, G.P., Fortier, L., 2013. Poor taxonmical knowledge of larval fish prey preference is impeding our ability to assess the existence of a "critical period" driging year-class strength. ICES J. Mar. Sci. https://doi.org/10.1093/icesjms/fst198.

Rose, G.A., O'Driscoll, R.L., 2002. Multispecies interactions capelin are good for cod: can the northern stock rebuild without them? ICES J. Mar. Sci. 59, 1018–1026. https://doi.org/10.1006/jmsc.2002.1252.

Siddon, E.C., Duffy-Anderson, J.T., Mueter, F.J., 2011. Community-level response of fish larvae to environmental variability in the southeastern Bering Sea. Mar. Ecol. Prog. Ser. 426, 225–239. https://doi.org/10.3354/meps09009.

Simonsen, C., Munk, P., Folkvord, A., Pedersen, S., 2006. Feeding ecology of Greenland halibut and sandeel larvae off West Greenland. Mar. Biol. 149, 937–952. https://doi.org/10.1007/s00227-005-0172-5.

Springer, A.M., McRoy, C.P., 1993. The paradox of pelagic food webs in the northern Bering Sea. III. Patterns of primary production. Cont. Shelf Res. 13, 575–579.

Stabeno, P.J., Kachel, N.B., Ladd, C., Woodgate, R.A., 2018. Flow patterns in the eastern Chukchi sea: 2010-2015. J. Geophys. Res. Ocean. 123, 1177–1195. https://doi.org/10.1002/2017JC013135.

Stark, J.W., 2004. A comparison of the maturation and growth of female flathead sole in the central Gulf of Alaska and south-eastern Bering Sea. J. Fish. Biol. 64, 876–889. https://doi.org/10.1111/j.1095-8649.2004.00356.x.

Stenson, G.B., Hammill, M.O., Lawson, J.W., 1997. Predation by harp seals in Atlantic Canada: preliminary consumption estimates for Arctic cod, capelin and Atlantic Cod. J. Northwest Atl. Fish. Sci. 22, 137–154. https://doi.org/10.2960/J.v22.a12.

Syrjala, S.E., 1996. A statistical test for a difference between the spatial distributions of two populations. Ecology 77, 75–80.

Vestfals, C.D., Mueter, F.J., Hedstrom, K.S., Laurel, B.J., Petrik, C.M., Duffy-Anderson, J. T., Danielson, S.L., De Robertis, A., and E.N. Curchitser Vestfals, C.D., Mueter, F.J., Hedstrom, K.S., Laurel, B.J., Petrik, C.M., Duffy-Anderson, J.T., Danielson, and E.N. C., in prep. Modeling the dispersal of Arctic cod (Boreogadus saida) and saffron cod (Eleginus gracilis) early life stages in the Pacific Arctic using a biophysical transport model. Polar Biol..

Walkusz, W., Paulic, J.E., Williams, W.J., Kwasniewski, S., Papst, M.H., 2011. Distribution and diet of larval and juvenile Arctic cod (Boreogadus saida) in the shallow Canadian Beaufort Sea. J. Mar. Syst. 84, 78–84. https://doi.org/10.1016/j.jmarsys.2010.09.001.

Wang, M., Overland, J.E., 2015. Projected future duration of the sea-ice-free season in the Alaskan Arctic. Prog. Oceanogr. 136, 50–59. https://doi.org/10.1016/j.pocean.2015.01.001.

Weingartner, T., Okkonen, S.R., Danielson, S.L., 2005. Circulation and Water Property Variations in the Nearshore Alaskan Beaufort Sea, Final Report. OCS Study MMS.

Wilderbuer, T.K., Nichol, D.G., Ianelli, J.N., 2017. Assessment of the yellowfin sole stock in the Bering sea and Aleutian Islands. In: Bering Sea and Aleutian Islands Stock Assessment and Fishery Evaluation Report to the North Pacific Fishery Management Council, 605 W. 4th Avenue, Anchorage AK 99510.

Woodgate, R., Stafford, K., Prahl, F.G., 2015. A synthesis of year-round interdisciplinary mooring measurements in the Bering Strait (1990-2014) and the RUSALCA years (2004-2011). Oceanography 28, 46–67. https://doi.org/10.5670/oceanog.2015.57.

Woodgate, R.A., Aagaard, K., Weingartner, T.J., 2005. A year in the physical oceanography of the Chukchi Sea: Moored measurements from autumn 1990-1991. Deep. Res. Part II Top. Stud. Oceanogr. 52, 3116–3149. https://doi.org/10.1016/j.dsr2.2005.10.016.

Wyllie-Echeverria, T., Barbera, W.E., Wylle-Echeverria, S., 1997. Water masses and transport of young-of-the-year fish into the northeastern Chukchi Sea. In: Reynolds, J. (Ed.), Fish Ecology in Arctic North America Symposium. American Fisheries Society, Fairbanks, AK, pp. 60–67.

Deep–Sea Research II 177 (2020) 104779

Contents lists available at ScienceDirect

Deep-Sea Research Part II

journal homepage: http://www.elsevier.com/locate/dsr2

Documenting growth parameters and age in Arctic fish species in the Chukchi and Beaufort seas

Caitlin E. Forster [a,*], Brenda L. Norcross [a], Ingrid Spies [b]

[a] University of Alaska Fairbanks, College of Fisheries and Ocean Sciences, USA
[b] Alaska Fisheries Science Center, NOAA Fisheries, USA

ARTICLE INFO

Keywords:
Arctic fishes
Chukchi sea
Beaufort sea
Length-weight relationships
Age

ABSTRACT

Basic life history parameters of Arctic fishes have not been well characterized for many species in the Chukchi and Beaufort seas. Increasing environmental and anthropogenic changes in the Arctic may impact the biology of Arctic fishes and can best be evaluated if a benchmark is available against which to evaluate future changes in the biology of Arctic fishes. We used data from over 45,000 individual fishes to determine the length and weight relationships of 28 species, and further determined ages of 17 species of Arctic fishes. Specimens that we captured in the Pacific Arctic tended to be small in size, often less than 300 mm, and generally showed positive allometric growth. Despite their small sizes, individuals of some species, especially in Agonidae, Zoarcidae and Stichaeidae, were long-lived, reaching ages of up to 26 years. In the Chukchi Sea, individuals were shorter-lived and tended to be larger and longer-at-age. In contrast, the species that lived longer than a decade reached their maximum ages in the Beaufort Sea. While these long-lived species were smaller at age in the Beaufort Sea, they ultimately reached a greater maximum age than their Chukchi Sea conspecifics. Growth variation can have a large effect on management reference points, and understanding species-specific parameters would be required before any management action is considered, as mandated in the 2009 U.S. Arctic Fisheries Management Plan.

1. Introduction

There is a lack of information on the basic life history parameters, distribution, and life history strategies of Arctic fishes in the Chukchi and Beaufort seas. The remote, ice-covered environment where these Arctic species reside has historically impeded sampling during much of the year. In recent years, the combination of warmer waters, longer open-ice periods, and the existence of commercial fisheries in portions of the Atlantic Arctic have provided opportunities for consistent sampling of Arctic fishes in the Arctic region (Norcross et al., 2013; Logerwell et al., 2017). This has resulted in a larger body of knowledge about fishes in this area (Olsen et al., 2009; Johannesen et al., 2012), and presents an opportunity to better understand the life history parameters of these species.

In a preemptive move, the North Pacific Fisheries Management Council, the managing body for fisheries off the coast of Alaska, U.S., approved the Arctic Fisheries Management Plan (FMP) in 2009. The FMP provides a unique opportunity for precautionary management of Arctic fish resources (NPFMC, 2009) because it closed the U.S. Arctic to commercial fishing. Stock assessments are rarely conducted on U.S. Arctic fishes, in part due to the commercial fishery closure, and also because basic information such as length, weight, and age, is not available for this region. Species-specific biological data are fundamental to establishing parameters that are incorporated into fisheries stock assessments. Basic stock assessment techniques such as virtual population analysis (VPA) require length, weight, and age, which makes the determination of these parameters for Arctic fish species essential for future management actions (Gulland, 1965; Maunder and Punt, 2013). Furthermore, modern stock assessments are moving beyond single species analysis and are increasingly incorporating multi-species interactions (Plagányi et al., 2014). Therefore, the length, weight, and age information assembled in this study for both potentially target and non-target species is vital to stock assessment efforts in the Arctic.

Analysis of fish length, weight, and age can be used to infer attributes of Arctic fish life history and provide insight into the susceptibility of a species to environmental change. The relationship between fish length and weight is one way to characterize growth patterns through the calculation of the allometric growth coefficient (Huxley, 1950; Froese, 2006). Growth patterns include isometric, negative allometric, and positive allometric, and indicate whether fish body length increases at

* Corresponding author.
E-mail addresses: ceforster@alaska.edu (C.E. Forster), bnorcross@alaska.edu (B.L. Norcross), ingrid.spies@noaa.gov (I. Spies).

https://doi.org/10.1016/j.dsr2.2020.104779
Received 18 July 2019; Accepted 27 March 2020
Available online 31 March 2020

the same relative rate as weight, growing long and thin, or short and stout, respectively. This allometry coefficient can be used to compare geographic variation in growth for a species across regions (Mendes et al., 2004). Fish age and maximum life expectancy have not been established for most Pacific Arctic fishes, with a few exceptions (Rand and Logerwell, 2011; Helser et al., 2017). The von Bertalanffy growth model is the most widely used growth curve in age-structured fisheries stock assessments and can be parameterized to the relationship between length and age (Quinn and Deriso, 1999). Both the overall lifespan of a species as well as the relative frequency of ages in a population permits assessment of a species' vulnerability to environmental disturbances (Berkeley et al., 2004). The difficulty of obtaining direct observation of Arctic fish biology renders indirect inference via length, weight, and age relationships especially useful.

Within the Pacific Arctic, the Chukchi and Beaufort seas form two habitats with distinct environmental conditions as a result of their widely differing physical oceanography. The Chukchi Sea has a wide and shallow shelf and receives an inflow of water from three primary water masses: Alaska Coastal Water, Bering Shelf Water and Anadyr Water (Weingartner, 1997; Weingartner et al., 2013). Nutrient-rich water originating from the Bering Sea creates areas of high production and rich benthic habitats on the Chukchi shelf (Dunton et al., 2005). In contrast, the Beaufort Sea has a narrow shelf that quickly drops off into deeper water. The Beaufort gyre, freshwater input from the Mackenzie River, and input from Atlantic Ocean water influence oceanographic processes in the Beaufort Sea, reducing the influence of nutrient-rich waters from the Pacific Ocean. Without these nutrient subsidies from richer sub-Arctic waters, production in the Beaufort Sea is much lower than in the Chukchi (Dunton et al., 2005).

It is understood that the Arctic is changing rapidly as a result of climate change (IPCC, 2018). Therefore, establishing a benchmark is necessary against which to evaluate the impacts of those changes on Arctic fish biology. With reduced sea ice, there is increasing interest in the Arctic for oil and gas exploration, shipping, and commercial fishing opportunities, which could significantly disturb the ecosystem (Gautier et al., 2009; Smith and Stephenson, 2013; Frey et al., 2015). In the absence of a formal stock assessment, knowledge of basic life history parameters of length, weight, and age is essential. In conjunction with growth type analysis, these parameters can provide a metric to evaluate the impact of these environmental changes. To determine these foundational life history parameters for Arctic fish species, this study analyzed more than a decade of length, weight, and age data collected from 28 species across the Pacific Arctic in the Chukchi and Beaufort seas (Table 1). Fishes collected spanned pelagic and benthic habitats and included ecologically critical species, such as Arctic Cod (*Boreogadus saida*), as well as species which are relatively undescribed (Table 2). Length, weight, and age were compared among species and across seas. By determining life history parameters of Arctic fish species, we have established a metric for future comparison in the data-poor region of the Pacific Arctic marine ecosystem.

2. Methods

Research cruises were conducted 2007–2015 in the Chukchi and Beaufort seas from July to October (Table 1). In the Chukchi Sea, sample locations spanned U.S. and Russian waters from approximately 174°E, to Point Barrow, 156°W, and extended from the Bering Strait at 66°N to approximately 76°N. In the Beaufort Sea, station locations covered the Alaskan coast from Point Barrow into Canadian waters past the Mackenzie River, 137°W, and extended northward to approximately 72°N (Fig. 1). The Chukchi Sea has a wide and shallow shelf, while the Beaufort Sea is characterized by a narrow shelf and a steep slope; thus, samples collected along the shelf and slope extend farther offshore in the Chukchi Sea, when compared to the Beaufort Sea. A variety of demersal and pelagic trawl gears, as well as beach seines were deployed to collect fish. Not all gear types were deployed on every cruise or at every sample

Table 1
List of sampling events by year, date range, ship, cruise designator, and sea.

Year	Start Date	End Date	Ship	Cruise	Region
2007	4-Sep	16-Sep	*R/V Oscar Dyson*	OD0710	Chukchi
2008	7-Jul	13-Jul	*T/S Oshoro-Maru IV*	OS190	Chukchi
2009	27-Jul	11-Aug	*R/V Alpha Helix*	COMIDA_2009	Chukchi
2009	4-Sep	29-Sep	*R/V Professor Khromov*	RUSALCA_2009	Chukchi
2009	13-Aug	29-Aug	*F/V Westward Wind*	WWW0902	Chukchi
2009	26-Sep	7-Oct	*F/V Westward Wind*	WWW0904	Chukchi
2010	21-Aug	4-Sep	*R/V Norseman II*	AKCH10	Chukchi
2010	1-Sep	18-Sep	*F/V Westward Wind*	WWW1003	Chukchi
2011	4-Sep	17-Sep	*R/V Norseman II*	AKCH11	Chukchi
2012	9-Aug	24-Sep	*F/V Alaska Knight*	Arctic Eis_2012	Chukchi
2012	27-Aug	16-Sep	*R/V Professor Khromov*	RUSALCA_2012	Chukchi
2016	2-Jul	10-Aug	*USCGC Healy*	HLY1601	Chukchi
2010	22-Sep	28-Sep	*F/V Westward Wind*	WWW1004	Beaufort
2011	15-Aug	4-Sep	*R/V Norseman II*	BOEM_2011	Beaufort
2012	20-Sep	1-Oct	*R/V Norseman II*	TB_2012	Beaufort
2013	12-Aug	2-Sep	*R/V Norseman II*	TB_2013	Beaufort
2014	14-Jul	2-Sep	*R/V Norseman II*	TB_2014	Beaufort
2013	14-Jul	25-Aug	*Nearshore Beach Seine*	ACES-2013	Chukchi, Beaufort
2014	15-Jul	27-Aug	*Nearshore Beach Seine*	ACES-2014	Chukchi, Beaufort
2014	15-Jul	28-Jul	*R/V Launch 1273*	ACES-2014	Chukchi, Beaufort
2015	14-Jul	15-Sep	*Nearshore Beach Seine*	AFF-2015	Chukchi, Beaufort

Table 2
List of taxa included in analysis.

Family	Scientific Name	Common Name
Osmeridae	*Mallotus catervarius*	Capelin
Gadidae	*Boreogadus saida*	Arctic cod
	Eleginus gracilis	saffron cod
Cottidae	*Artediellus scaber*	Hamecon
	Gymnocanthus tricuspis	Arctic staghorn sculpin
	Icelus bicornis	twohorn sculpin
	Icelus spatula	spatulate sculpin
	Myoxocephalus scorpius	shorthorn sculpin
	Triglops pingelii	ribbed sculpin
Hemitripteridae	*Nautichthys pribilovius*	eyeshade sculpin
Agonidae	*Aspidophoroides olrikii*	Arctic alligatorfish
	Podothecus veternus	veteran poacher
Liparidae	*Liparis fabricii*	gelatinous seasnail
	Liparis gibbus	variegated snailfish
	Liparis tunicatus	kelp snailfish
Zoarcidae	*Gymnelus hemifasciatus*	halfbarred pout
	Lycodes adolfi	Adolf's eelpout
	Lycodes polaris	Canadian eelpout
	Lycodes raridens	Marbled eelpout
	Lycodes sagittarius	archer eelpout
	Lycodes seminudus	longear eelpout
Stichaeidae	*Anisarchus medius*	stout eelblenny
	Lumpenus fabricii	slender eelblenny
	Stichaeus punctatus	Arctic shanny
Ammodytidae	*Ammodytes hexapterus*	Pacific sand lance
Pleuronectidae	*Hippoglossoides robustus*	Bering flounder
	Limanda aspera	Yellowfin sole
	Limanda proboscidea	longhead dab

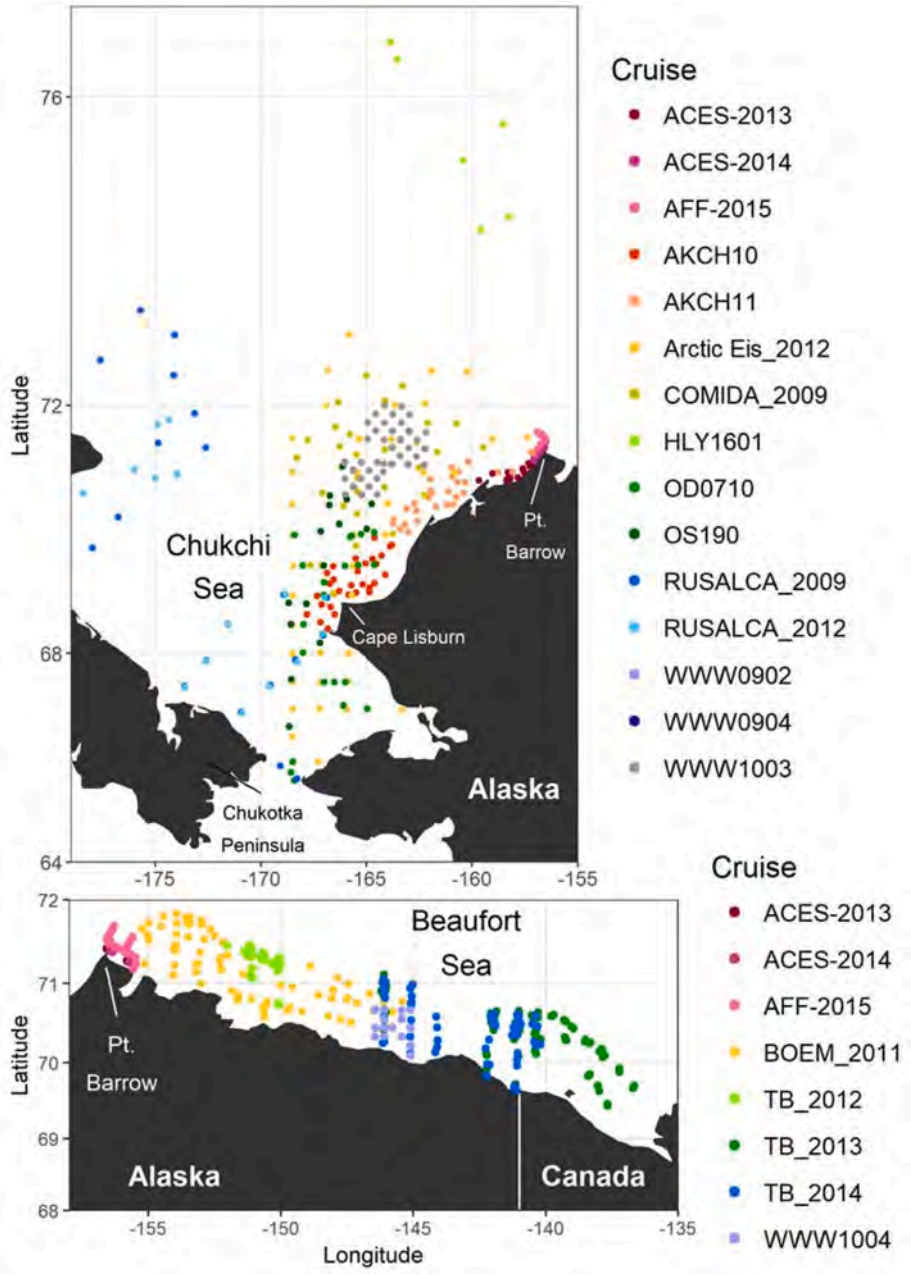

Fig. 1. Stations sampled in the Chukchi and Beaufort seas, 2007–2015. Colors correspond with cruise identity. Division between Chukchi and Beaufort seas occurs at Pt. Barrow. (For interpretation of the references to colour in this figure legend, the reader is referred to the Web version of this article.)

location. Codend mesh sizes ranged from 3 mm to 38 mm. By deploying a variety of gear types and mesh sizes, catches represented a wide range of sizes of the species we considered.

Fish were frozen in the field and sent to the Fisheries Oceanography Lab in Fairbanks, Alaska, U.S., for analysis. In the lab, field identification of fish specimens was confirmed using Mecklenburg et al., (2002); measurements were taken of total fish length (mm) with a fish measuring board and wet weight (g) with a top-loading balance. A size-based selection process was used to establish a subset of individuals for age estimation. Twenty individuals from each 10 mm size bin were randomly selected for aging from each cruise for each species if sufficient specimens were available. Sagittal otoliths were mounted on glass slides using Crystalbond™ (Ted Pella, Inc., Redding, CA, U.S.) thermoplastic glue and transversely sectioned under continuous water flow using a Buehler (Reno, NV, U.S.) rotating wheel with 1200 grit sandpaper. Once sectioned, the otolith was reheated, flipped onto the flattened edge, remounted, and sanded to ~200–400 μm. Transverse cross sections of otoliths were photographed under transmitted light using a Leica DFC295 digital camera mounted on a Leica M165 C microscope at 5x magnification (Leica Biosystems DM1000, Wetzlar, Germany). Otoliths were aged from photographs by two independent readers (Helser et al., 2017); a full year of growth consisted of one translucent ring of slower growth and one opaque ring of faster growth (Matta and Kimura, 2012). For the <5% of otoliths when readers disagreed on an age, the otolith in question was re-aged by both readers; most disagreements were rectified at this stage. If the disagreement persisted, readers worked together to agree on the best age for each fish; therefore, a statistical approach to reader agreement was not used here. Using this protocol, 100% of ages were checked.

Length and weight relationships were established using the standard fisheries allometric growth equation:

$$W = a * L^{b}$$

where W is fish weight, a is the y-intercept, L is total fish length, and b is the allometric growth coefficient (Huxley, 1950; Froese, 2006). The parameters a and b were estimated by log-transforming weight (W) and length (L) data and conducting a linear regression analysis. The fishes were generally small and lengths were measured in mm instead of cm, with the resulting a parameter expressed as 10^{-5}. Length-weight relationships were calculated for species where 50 or more individuals were collected in at least one sea. Approximately 99.7% of all measurements are expected to fall within ± three standard deviations for a normal distribution; measurements outside that threshold could have been due to measurement or identification error. As a QA/QC procedure, following the methods outlined by (Giacalone et al., 2010), scatter plots of weight-at-length and age-at-length were visually examined for each fish species. Using the standardized residuals obtained from the initial weight-at-length regressions, we examined points >3 standard deviations from the mean. We inspected raw field data sheets and compared to lab data sheets to check for transposed numbers, lines, and handwriting interpretations. Errors were corrected when possible. Final length-weight regressions were refit after the removal of outliers, of which there were only <1.0%.

For each species, growth type was compared between the Chukchi Sea and the Beaufort Sea using the following criteria. Growth was characterized using three criteria: if the growth coefficient, i.e., slope b, was 3 ± 0.1 growth was considered isometric, $b < 2.9$ was negative allometric growth, and $b > 3.1$ was positive allometric growth (Froese, 2006). To test for differences in growth between the Chukchi and Beaufort seas, a Student's t-test ($p < 0.05$) was performed comparing the growth coefficient b between seas.

Maximum ages were reported by region, when available, for all species for which a length-weight relationship was established. Species were selected for additional length-at-age and regional age analysis if more than 50 individuals had been collected in both the Beaufort and Chukchi seas (100 total). Eight species met these requirements (*Boreogadus saida, Eleginus gracilis, Gymnocanthus tricuspis, Myoxocephalus scorpius, Aspidophoroides olrikii, Lycodes polaris, Anisarchus medius, Lumpenus fabricii)*. For each of these eight species, average length-at-age was calculated by region. We followed the same QA/QC protocol as for length-weight relationship, i.e., checking raw data. For the remaining ages >3 standard deviations outside of the mean, otoliths were examined again by two readers. Ages that could not be corrected (<0.75%) were considered outliers and excluded from analysis. Because few data exist for these Arctic species, we use the term "outlier" without certainty that these data were necessarily incorrect.

Data for these eight species were fit to growth curves and compared to determine whether growth differed among the Chukchi and Beaufort fishes. The von Bertalanffy growth curve was selected because it is commonly used to describe fish growth and provides parameter estimates that are used in other relationships, (e.g., Beverton-Holt yield model, Beverton, 1954; Ricker, 1975). Data were fit in R using the R package *fishmethods* (http://derekogle.com/fishR/). When the von Bertalanffy relationship did not fit the data, the logistic growth model was chosen as an alternative (Quinn and Deriso, 1999).

Length-at-age data were first fit to a general model, with a separate parameter for each sea (Chukchi, Beaufort) for each of the three parameters in the von Bertalanffy model (*Linf*, *K*, and t_0). The general model was the most complex, and was examined to ensure that residuals were normally distributed and randomly dispersed around the horizontal axis (Appendix Fig. A1). If this was true for the general model, it also applied to other subset models. A subset of seven simpler models were fit to the data for each species, with hierarchically fewer parameters, and an analysis of variance (ANOVA) was employed to examine whether a more parsimonious model could provide an equally good fit to the data. The seven simpler models were as follows: three "one-parameter models" models which combined L_{inf}, K, or t_0 among the Beaufort and Chukchi samples; three "two-parameter" models with separate parameters for L_{inf}, K, or t_0 and combined parameters for the other two; and one combined model with all parameters combined for the Beaufort and Chukchi data. As each one parameter model was simpler than the general model, a one-parameter model that was not significantly different (alpha = 0.05) from the general model was considered more parsimonious and a better model. If two or three one-parameter models were better than the general model, then the model with the smallest residual sum of squared was selected. The Akaike Information Criteria (AIC) was also used to compare models, as the same data were used in each nested model.

3. Results

We examined 28 common Arctic fish species from 10 families (Table 2) and more than 45,000 individuals for analysis of length-weight relationships (Table 3). The sizes of fishes collected in the Pacific Arctic were small, often no larger than 300 mm. Sizes of individuals ranged from 13 mm (*Limanda proboscidea*) to 465 mm (*Lycodes sagittarius*). Of the 16 species caught in both seas, individuals of 11 species grew to a larger maximum size in the Chukchi Sea, though the size difference was minimal for *Liparis tunicatus* (Table 3). Only two species, *Triglops pingelii* and *Gymnelus hemifasciatus*, had isometric growth, both in the Beaufort Sea. Negative allometric growth types were found for *Podothecus veternus* and *Anisarchus medius*; in contrast to isometric growth, negative allometric growth was only detected in the Chukchi Sea. Positive allometric growth was the most common pattern and was found in 24 species in both the Chukchi and Beaufort seas (Table 3). Significant inter-sea differences of the parameter b were found for six species (Student's t-test, $p < 0.05$). The growth parameter b was larger in the Chukchi Sea in four species: *Boreogadus saida* (3.24 > 3.12), *Icelus spatula* (3.35 > 3.15), *Myoxocephalus scorpius* (3.30 > 3.13), *Gymnelus hemifasciatus* (3.16 > 2.92). The b parameter was significantly larger in the Beaufort Sea for *Lycodes polaris* (3.32 > 3.22) and *Anisarchus medius* (3.31 > 2.88).

The range of estimated ages of fish was 0–26 (Table 4). Of the 17 species for which ages were estimated (n = 7585), six species, one Agonidae, all four Zoarcidae, and one Stichaeidae, lived to a maximum age of more than a decade; the oldest were all in the Beaufort Sea. The remaining 11 species had maximum ages in the single digits.

Fish species with the greatest maximum ages were not necessarily the largest fish. Although the two oldest species, *Lycodes sagittarius* (age-26, max size 427 mm) and *L. seminudus* (age-24, max size 465 mm) also displayed the greatest maximum total length, the next two oldest species, *Anisarchus medius* (age-19, max size 158 mm) and *Aspidophoroides olrikii* (age-15, max size 80 mm) were less than a third as long (Table 3). In comparison, *Eleginus gracilis* grew to a length of 112 mm by age-1.

Patterns in species' mean length-at-age differed between the Chukchi and Beaufort seas for some of the eight species for which sufficient data were available (Table 5). Growth curves and length frequency data indicate that most species grew more quickly in the Chukchi sea (*Eleginus gracilis*, *Gymnocanthus tricuspis*, *Myoxocephalus scorpius*, *Anisarchus medius*, *Lumpenus fabricii*, *Aspidophoroides olrikii*, and *Lycodes polaris*). *Boreogadus saida* was the exception; it appeared to grow more quickly in the Beaufort Sea (Fig. 2, Table 5). There were no instances where a species' size-at-age was more frequently larger in the Beaufort Sea than in the Chukchi Sea (Table 5). Three species reached a maximum age, as estimated in the current study, in the Chukchi Sea (*Eleginus gracilis, Myoxocephalus scorpius, Lumpenus fabricii*). For the species *Eleginus gracilis* and *Myoxocephalus scorpius*, the largest individuals were not retained and aged; however, these large individuals were only caught in the Chukchi Sea and were much larger than conspecifics caught in the Beaufort (Table 3), which is consistent with the oldest individuals being found in the Chukchi Sea. Four species obtained a maximum age in the Beaufort Sea (*Gymnocanthus tricuspis*, *Aspidophoroides olrikii*, *Lycodes*

Table 3
Length-weight relationships for 28 species, calculated individually for the Beaufort and Chukchi seas. n = number of individuals analyzed, a = intercept, b = allometry parameter, r^2 = correlation coefficient. Growth type determined as allometric positive ($b > 3.1$), isometric ($b = 3.0 \pm 0.1$), or allometric negative ($b < 2.9$). * indicates significant differences in growth (b) between the Chukchi and Beaufort seas, $p < 0.05$

Family	Species	Sea	n	Length Range (mm)	Weight Range (g)	a	b	r^2	Growth Type
Osmeridae	*Mallotus catervarius*	Chukchi	341	37–147	0.082–15.991	−7.214	3.909	0.9814	positive
Gadidae	*Boreogadus saida*	Chukchi	6538	11–252	0.008–98.680	−5.698	3.237*	0.983	positive
		Beaufort	6288	14–240	0.011–106.130	−5.444	3.119*	0.977	positive
	Eleginus gracilis	Chukchi	560	15–268	0.022–189.580	−5.828	3.341	0.966	positive
		Beaufort	95	20–62	0.028–1.590	−5.883	3.453	0.922	positive
Cottidae	*Artediellus scaber*	Chukchi	1157	17–113	0.040–25.800	−5.074	3.186	0.9472	positive
		Beaufort	420	14–95	0.030–13.630	−5.167	3.223	0.9762	positive
	Gymnocanthus tricuspis	Chukchi	5856	22–167	0.078–88.270	−5.578	3.360	0.976	positive
		Beaufort	1901	21–117	0.110–27.100	−5.493	3.323	0.928	positive
	Icelus bicornis	Beaufort	105	29–87	0.230–10.940	−5.462	3.304	0.9745	positive
	Icelus spatula	Chukchi	72	25–98	0.090–12.610	−5.605	3.345*	0.9593	positive
		Beaufort	838	23–111	0.090–19.830	−5.191	3.150*	0.9273	positive
	Myoxocephalus scorpius	Chukchi	4911	20–250	0.072–138.470	−5.471	3.302*	0.9684	positive
		Beaufort	275	31–141	0.220–36.300	−5.092	3.128*	0.8714	positive
	Triglops pingelii	Chukchi	198	33–161	0.200–26.920	−5.899	3.364	0.9688	positive
		Beaufort	543	26–151	0.150–27.690	−5.210	3.041	0.9807	isometric
Hemitripteridae	*Nautichthys pribilovius*	Chukchi	87	24–85	0.159–9.400	−5.419	3.313	0.964	positive
Agonidae	*Aspidophoroides olrikii*	Chukchi	446	15–75	0.013–3.696	−6.247	3.596	0.921	positive
		Beaufort	826	22–80	0.040–3.690	−6.402	3.715	0.959	positive
	Podothecus veternus	Chukchi	90	30–133	0.130–11.180	−5.052	2.862	0.8919	negative
Liparidae	*Liparis fabricii*	Beaufort	319	15–212	0.040–112.530	−5.279	3.118	0.9775	positive
	Liparis gibbus	Beaufort	154	24–211	0.180–159.500	−5.350	3.246	0.9789	positive
	Liparis tunicatus	Chukchi	191	25–133	0.080–40.590	−5.474	3.294	0.9809	positive
		Beaufort	383	19–134	0.090–28.150	−5.455	3.261	0.9231	positive
Zoarcidae	*Gymnelus hemifasciatus*	Chukchi	158	33–131	0.100–8.060	−5.773	3.164*	0.9551	positive
		Beaufort	116	43–139	0.200–12.150	−5.293	2.922*	0.9392	isometric
	Lycodes adolfi	Beaufort	234	38–205	0.190–29.320	−5.730	3.104	0.9811	positive
	Lycodes polaris	Chukchi	371	32–229	0.100–65.010	−5.811	3.219*	0.9815	positive
		Beaufort	231	39–271	0.170–121.400	−5.948	3.318*	0.9632	positive
	Lycodes raridens	Chukchi	134	27–372	0.070–445.600	−5.849	3.264	0.9845	positive
		Beaufort	81	41–294	0.330–176.300	−5.528	3.148	0.9871	positive
	Lycodes sagittarius	Beaufort	187	44–427	0.330–347.600	−5.666	3.119	0.9896	positive
	Lycodes seminudus	Beaufort	176	41–465	0.300–535.990	−5.696	3.170	0.9918	positive
Stichaeidae	*Anisarchus medius*	Chukchi	1163	38–158	0.100–9.880	−5.301	2.877*	0.932	negative
		Beaufort	311	43–145	0.100–9.780	−6.124	3.308*	0.957	positive
	Lumpenus fabricii	Chukchi	4790	21–243	0.019–31.660	−5.931	3.205	0.960	positive
		Beaufort	507	26–164	0.030–11.680	−5.886	3.199	0.950	positive
	Stichaeus punctatus	Chukchi	486	15–122	0.0143–15.340	−6.000	3.444	0.9654	positive
		Beaufort	171	17–67	0.0128–2.400	−5.931	3.378	0.8381	positive
Ammodytidae	*Ammodytes hexapterus*	Chukchi	2031	19–167	0.016–17.190	−6.380	3.418	0.9618	positive
		Beaufort	615	24–146	0.022–9.280	−6.818	3.683	0.9461	positive
Pleuronectidae	*Hippoglossoides robustus*	Chukchi	577	15–226	0.017–104.800	−5.728	3.312	0.9693	positive
	Limanda aspera	Chukchi	395	14–217	0.034–131.230	−5.507	3.292	0.9842	positive
	Limanda proboscidea	Chukchi	156	13–171	0.014–70.910	−5.403	3.214	0.9783	positive

Table 4
Maximum age (years) for 17 species in the Chukchi Sea and Beaufort Sea. n = number of individuals aged species, - indicates no fish available.

		Chukchi		Beaufort	
Family	Species	Max Age	n	Max Age	n
Osmeridae	*Mallotus catervarius*	3	100	1	9
Gadidae	*Boreogadus saida*	5	1514	5	1230
	Eleginus gracilis	1	115	0	59
Cottidae	*Gymnocanthus tricuspis*	6	759	7	395
	Icelus spatula	–	–	6	70
	Myoxocephalus scorpius	5	260	3	69
Agonidae	*Aspidophoroides olrikii*	9	83	15	258
Liparidae	*Liparis fabricii*	–	–	5	125
Zoarcidae	*Lycodes adolfi*	–	–	12	178
	Lycodes polaris	9	215	11	162
	Lycodes sagittarius	–	–	26	116
	Lycodes seminudus	–	–	24	114
Stichaeidae	*Anisarchus medius*	12	281	19	214
	Lumpenus fabricii	7	726	5	234
Pleuronectidae	*Hippoglossoides robustus*	8	247	11	16
	Limanda aspera	4	36	–	–
	Limanda proboscidea	3	4	–	–

polaris, *Anisarchus medius*), and *Boreogadus saida* reached age-5 in both seas (Table 5). For the three oldest species (*Aspidophoroides olrikii*, *Lycodes polaris*, and *Anisarchus medius)*, the maximum age occurred in the Beaufort Sea.

Growth data for all species presented unbiased and normally distributed residuals, with the exception of *Anisarchus medius,* which presented slightly skewed residuals (Appendix Fig. A1). Length-at-age data for this species indicated either high variability at older ages (5 and higher) or two distinct groups with different growth patterns (Fig. 2). *Myoxocephalus scorpius* data included a single age-3 individual from the Beaufort Sea. This age-3 individual was 141 cm, which was 54.4 cm larger than the mean size of the eight age-2 individuals in the dataset from the Beaufort Sea. The model did not converge when the age-3 individual was included because the length of the age-3 individual was so much larger than the length of the mean age-2 year old; therefore the age-3 individual was not included in the growth fitting. Overall the model indicated that *M. scorpius* from the Chukchi grew faster than from the Beaufort, and the data confirmed this result even without the anomalously large 3 year old from the Beaufort Sea; the mean length of age-2 *M. scorpius* from the Beaufort was 86.6 cm and the mean length from the Chukchi was 108.5 cm. The only species that could not be fit to the von Bertalanffy data was *Lycodes polaris*, likely because the length

Table 5
Length-at-age for eight species collected in both the Chukchi Sea (CS) and Beaufort Sea (BS). Rows include sample size (n), average length-at-age (mm), minimum length-at-age (mm) and maximum length-at-age (mm). If no min or max is shown, only one fish was measured.

Estimated Age (yrs)		*Boreogadus saida*		*Eleginus gracilis*		*Gymnocanthus tricuspis*		*Myoxocephalus scorpius*		*Aspidophoroides olrikii*		*Lycodes polaris*		*Anisarchus medius*		*Lumpenus fabricii*	
		CS	BS	CS	BS	CS	BS	CS	BS	CS	BS	CS	BS	CS	BS	CS	BS
0	**N**	**516**	**489**	**103**	**59**	**259**	**128**	**104**	**48**	**26**	**24**	**41**	**37**	**27**	**51**	**149**	**95**
	Avg	55	49	59	37	38	35	46	47	38	38	41	47	73	59	61	59
	Min	20	15	18	24	25	24	34	31	34	28	31	39	61	49	46	46
	Max	92	103	95	62	57	47	69	56	45	44	45	60	87	69	93	80
1	**N**	**496**	**397**	**12**	**-**	**151**	**81**	**121**	**12**	**23**	**45**	**15**	**25**	**27**	**22**	**168**	**59**
	Avg	99	98	97	–	57	52	77	73	46	43	66	57	76	70	90	76
	Min	54	48	85	–	39	38	36	51	41	32	39	39	63	54	64	51
	Max	151	163	112	–	75	75	113	89	51	58	92	74	95	85	136	106
2	**N**	**370**	**273**	**-**	**-**	**174**	**99**	**30**	**8**	**9**	**25**	**48**	**18**	**34**	**29**	**239**	**33**
	Avg	127	135	–	–	77	64	103	87	52	50	77	75	97	87	120	104
	Min	62	71	–	–	60	41	60	60	43	44	56	62	64	72	87	47
	Max	197	194	–	–	101	90	156	126	58	60	131	99	130	108	175	148
3	**N**	**100**	**52**	**-**	**-**	**109**	**66**	**4**	**1**	**6**	**39**	**45**	**29**	**42**	**25**	**84**	**41**
	Avg	143	163	–	–	94	81	136	141	57	57	91	77	98	94	149	123
	Min	76	117	–	–	66	61	121	141	53	45	68	66	71	77	73	83
	Max	229	213	–	–	129	110	155	141	62	64	146	104	139	104	218	173
4	**N**	**31**	**15**	**-**	**-**	**50**	**11**	**-**	**-**	**10**	**35**	**17**	**20**	**55**	**10**	**53**	**3**
	Avg	141	197	–	–	116	103	–	–	61	59	102	99	102	107	155	128
	Min	80	175	–	–	80	70	–	–	54	48	71	69	81	91	112	87
	Max	212	231	–	–	167	127	–	–	66	69	133	145	131	127	209	162
5	**N**	**1**	**4**	**-**	**-**	**9**	**5**	**1**	**-**	**5**	**39**	**24**	**13**	**35**	**24**	**23**	**3**
	Avg	230	206	–	–	126	105	130	–	60	59	116	103	113	107	176	134
	Min	–	163	–	–	94	98	130	–	54	50	81	76	89	60	137	96
	Max	–	240	–	–	148	115	130	–	63	69	150	160	152	128	243	203
6	**n**	**-**	**-**	**-**	**-**	**7**	**3**	**-**	**-**	**1**	**26**	**10**	**11**	**21**	**13**	**7**	**-**
	Avg	–	–	–	–	138	103	–	–	63	62	142	128	114	110	181	–
	Min	–	–	–	–	108	89	–	–	–	52	108	89	55	68	132	–
	Max	–	–	–	–	156	113	–	–	–	71	168	205	134	127	223	–
7	**n**	**-**	**-**	**-**	**-**	**-**	**2**	**-**	**-**	**1**	**9**	**10**	**3**	**24**	**16**	**3**	**-**
	Avg	–	–	–	–	–	124	–	–	65	66	168	138	122	103	164	–
	Min	–	–	–	–	–	101	–	–	–	58	139	109	108	64	135	–
	Max	–	–	–	–	–	147	–	–	–	72	200	183	146	135	195	–
8	**n**	**-**	**-**	**-**	**-**	**-**	**-**	**-**	**-**	**1**	**3**	**2**	**2**	**8**	**6**	**-**	**-**
	Avg	–	–	–	–	–	–	–	–	68	73	149	191	127	106	–	–
	Min	–	–	–	–	–	–	–	–	–	68	132	176	120	73	–	–
	Max	–	–	–	–	–	–	–	–	–	76	165	205	139	139	–	–
9	**n**	**-**	**-**	**-**	**-**	**-**	**-**	**-**	**-**	**1**	**1**	**3**	**1**	**2**	**5**	**-**	**-**
	Avg	–	–	–	–	–	–	–	–	69	68	178	177	127	109	–	–
	Min	–	–	–	–	–	–	–	–	–	–	162	–	123	94	–	–
	Max	–	–	–	–	–	–	–	–	–	–	196	–	131	123	–	–
10	**n**	**-**	**-**	**-**	**-**	**-**	**-**	**-**	**-**	**-**	**2**	**-**	**2**	**4**	**2**	**-**	**-**
	Avg	–	–	–	–	–	–	–	–	–	68	–	130	131	118	–	–
	Min	–	–	–	–	–	–	–	–	–	66	–	117	123	105	–	–
	Max	–	–	–	–	–	–	–	–	–	70	–	142	136	130	–	–
11	**n**	**-**	**-**	**-**	**-**	**-**	**-**	**-**	**-**	**-**	**4**	**-**	**1**	**1**	**2**	**-**	**-**
	Avg	–	–	–	–	–	–	–	–	–	71	–	271	140	123	–	–
	Min	–	–	–	–	–	–	–	–	–	65	–	–	–	116	–	–
	Max	–	–	–	–	–	–	–	–	–	74	–	–	–	130	–	–
12	**n**	**-**	**-**	**-**	**-**	**-**	**-**	**-**	**-**	**-**	**3**	**-**	**-**	**1**	**4**	**-**	**-**
	Avg	–	–	–	–	–	–	–	–	–	71	–	–	128	120	–	–
	Min	–	–	–	–	–	–	–	–	–	66	–	–	–	94	–	–
	Max	–	–	–	–	–	–	–	–	–	75	–	–	–	145	–	–
14	**n**	**-**	**-**	**-**	**-**	**-**	**-**	**-**	**-**	**-**	**2**	**-**	**-**	**-**	**1**	**-**	**-**
	Avg	–	–	–	–	–	–	–	–	–	73	–	–	–	135	–	–
	Min	–	–	–	–	–	–	–	–	–	66	–	–	–	–	–	–
	Max	–	–	–	–	–	–	–	–	–	80	–	–	–	–	–	–
15	**n**	**-**	**-**	**-**	**-**	**-**	**-**	**-**	**-**	**-**	**1**	**-**	**-**	**-**	**1**	**-**	**-**
	Avg	–	–	–	–	–	–	–	–	–	75	–	–	–	145	–	–
16	**n**	**-**	**-**	**-**	**-**	**-**	**-**	**-**	**-**	**-**	**-**	**-**	**-**	**-**	**1**	**-**	**-**
	Avg	–	–	–	–	–	–	–	–	–	–	–	–	–	130	–	–
17	**n**	**-**	**-**	**-**	**-**	**-**	**-**	**-**	**-**	**-**	**-**	**-**	**-**	**-**	**1**	**-**	**-**
	Avg	–	–	–	–	–	–	–	–	–	–	–	–	–	107	–	–
19	**n**	**-**	**-**	**-**	**-**	**-**	**-**	**-**	**-**	**-**	**-**	**-**	**-**	**-**	**1**	**-**	**-**
	Avg	–	–	–	–	–	–	–	–	–	–	–	–	–	131	–	–

data did not asymptote at older ages. The logistic function provided a better fit for this species (Quinn and Deriso, 1999). A second species, *Eleginus gracilis* was excluded from growth modeling because there were insufficient ages in the dataset (only age-0 in Beaufort and ages 0 and 1 from the Chukchi).

Of the six species fit to the von Bertalanffy growth function, *Gymnocanthus tricuspis* and *Anisarchus medius* fit the general model (Table A1). The best model for *Boreogadus saida, Myoxocephalus scorpius,* and *Aspidophoroides olrikii* used a combined parameter for Beaufort and Chukchi seas for t_0. *Lumpenus fabricii* was the only model fit to a von

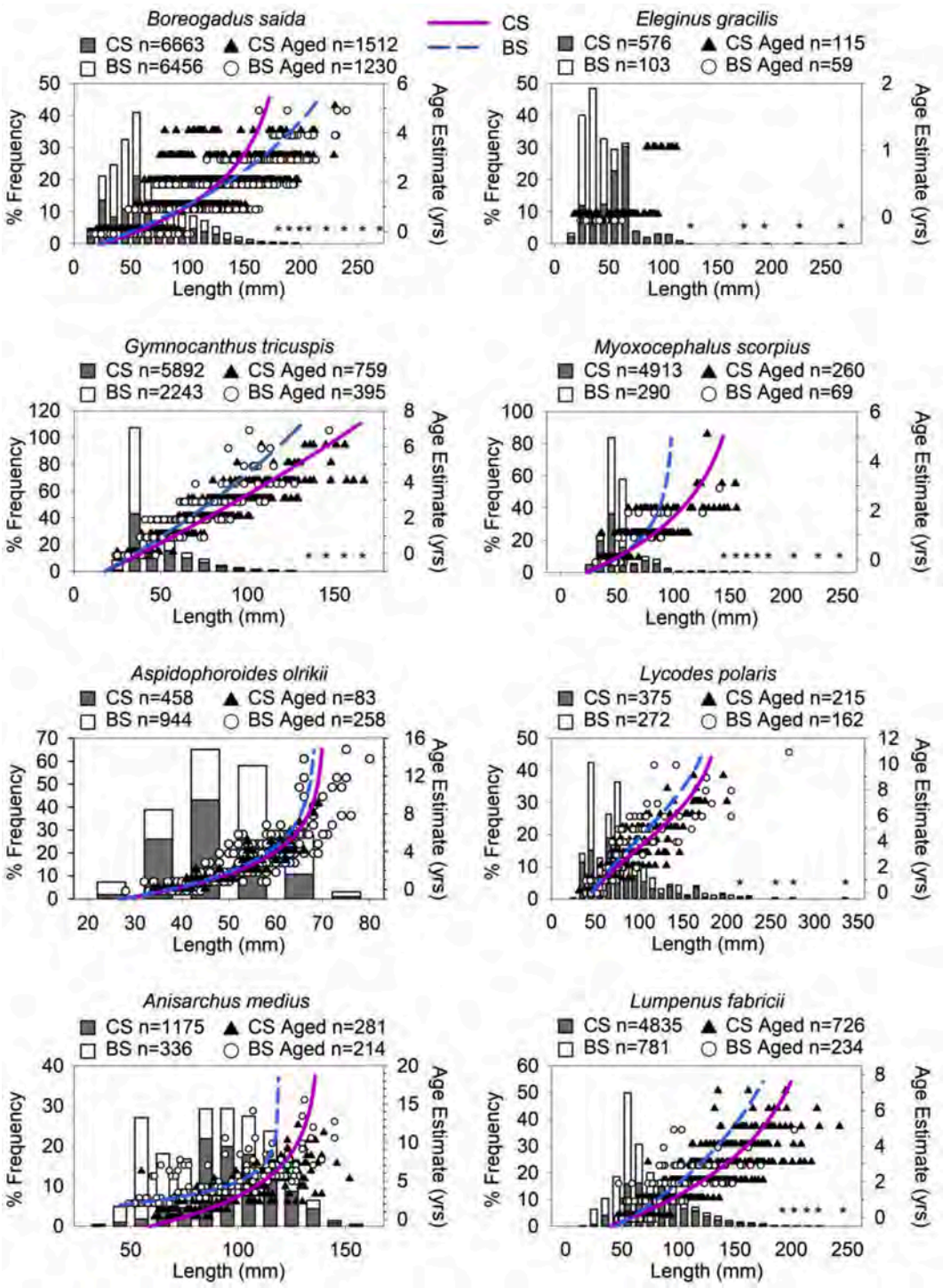

Fig. 2. Percent frequency for eight fish species of length (mm) partitioned by Chukchi Sea (CS) and Beaufort Sea (BS). Frequencies sum to 100 percent for each sea. Estimated fish age (years) are displayed on right y-axis; axes are not the same for each plot. Asterisks * above a size class indicate frequencies less than 0.4%; blanks indicate no individuals captured of that size. Lines represent growth curves (Table A1) calculated for each species in each sea, pink is CS, blue is BS. Growth curves were von Bertalanffy with the exception of *Lycodes polaris*, which used the logistic growth function, and were not generated for *Eleginus gracilis*, due to insufficient data. (For interpretation of the references to colour in this figure legend, the reader is referred to the Web version of this article.)

Bertalanffy with a single parameter for L_{inf}. The *Lycodes polaris* model with the best fit was the logistic growth function with a single L_{inf} parameter.

Growth curves showed that there were significant differences in growth ($p < 0.05$) in at least one of the three growth parameters estimated in the six species fit to von Bertalanffy and logistic growth curves among collections from the Chukchi and Beaufort Seas (Appendix Fig. A1; Table A1). The asymptotic average length differed among the Chukchi and Beaufort sea collections for *Boreogadus saida*, *Gymnocanthus tricuspis, Myoxocephalus scorpius, Aspidophoroides olrikii,* and *Anisarchus medius*; the growth rate differed for *Boreogadus saida*, *Gymnocanthus tricuspis, Myoxocephalus scorpius, Anisarchus medius, Lumpenus fabricii, and Lycodes polaris* (Appendix Table A1).

4. Discussion

New information on the length-weight relationships of 28 Arctic fish species indicates positive allometric growth, and age data show longevity over a decade despite relatively small size of some species. The knowledge gained in this study will be essential for fisheries science and stock assessment efforts in the Pacific Arctic, which may become necessary as global interest from industrial sectors, such as petroleum extraction, shipping, and potential commercial fisheries, increase in the region (Christiansen et al., 2014). Given the lack of current fisheries assessments in this region, the knowledge generated in this work provides a needed metric for comparison of future changes in the biology of Arctic fishes. Significant regional differences in growth type were detected for six species (Table 3), but neither the Chukchi nor the Beaufort seas were consistently superior for all intraspecific growth. Within the same species, differences in allometry may indicate that physical and oceanographic factors affect growth in separate geographic areas (Froese, 2006; Wund et al., 2012). Intraspecific differences in growth suggest that the environmental conditions may impact fish growth patterns, and future work should include genetic analysis to determine whether there is a genetic component to observed differences. Optimum environmental conditions for Arctic fishes vary from species to species; therefore, the impact of changes in environmental conditions in the Arctic will likely have a mosaic of species-specific effects on Arctic fish biology.

Several limitations should be considered when evaluating the results presented in this study. First, the collection of samples was not evenly distributed across gear types, years, or sampling locations. The data presented here are an opportunistic aggregation of available data. While this may introduce biases in the sizes and ages of fishes presented in this study, our goal was to present broad and foundational knowledge to support future work in the Arctic. Second, when aging otolith samples, we assumed that a dark band coupled with a light band reflect seasonal differences in growth rates and together are one year of growth as is standard practice (Campana and Stevenson, 1992). It would be good to verify this assumption by conducting age validation experiments for each species. The Arctic environment exhibits extreme seasonality, with dark, sea-ice covered winters and 24-hr daylight, open-water summers, making seasonal differences in growth more pronounced than they are for lower latitude fish species (Berge et al., 2015), thus supporting the validity of this assumption.

The size of many Arctic fish species is generally small compared to more southerly seas (Stevenson and Lauth, 2012) and is a factor that determines their ecological role in the Arctic marine ecosystem. Arctic fishes are important prey items, despite their small size, notably *Boreogadus saida*, for other marine vertebrates such as birds, seals, and beluga whales (Bluhm and Gradinger, 2008; Harter et al., 2013). In the Arctic, therefore, these small fish species play a role in the flow of energy through the ecosystem. The small sizes reported here are likely not an artifact of sampling effort failing to catch larger individuals, as a range of gear types and mesh sizes were employed to collect these specimens, and fishes as large as 525 mm were caught on the Beaufort Sea slope in a bottom trawl with 3 mm mesh (Norcross et al., 2017). Independent sampling efforts with larger nets in the Pacific Arctic also reported fish lengths similar to the values presented here (Frost and Lowry, 1983; Rand and Logerwell, 2011). Cool water temperatures generally constrain growth rates (Pörtner et al., 2001). Water temperatures in the Chukchi and Beaufort seas are cold, commonly -2–7 °C, though temperatures as warm as 13 °C have been detected (Pickart et al., 2005; Crawford et al., 2012), which potentially limits the maximum size achieved by Arctic fish species.

For six of the 28 species in this study, there are known lengths and allometry patterns from other northern collections. The size of *Mallotus catervarius* in the Chukchi Sea is equivalent to previous measurements in the Beaufort and Chukchi seas (Fechhelm et al., 1985; Wiswar and Fruge, 2006), but 60 mm smaller than in the North Pacific (Hart, 1973), and the growth parameter is similar to the Barents Sea (Gjøsæter, 1998) but less than the more southern population in the Gulf of Alaska ($b = 4.23$, Brown, 2002). Though the maximum length of *Boreogadus saida* in both seas is like other collections in the Chukchi Sea (Mecklenburg et al., 2016; Helser et al., 2017), it is 70–200 mm smaller than at lower or comparable latitudes in Iceland (Astthorsson, 2016) and the Barents Sea (Wienerroither et al., 2011). Although there was no reason to question that *B. saida* had a positive growth type in both seas in this study, that differed from isometric growth in the Chukchi Sea (Helser et al., 2017) and in the Beaufort Sea (Rand and Logerwell, 2011). The differences in the same species in the same areas over the same times could be attributable to the larger-mesh nets collecting longer, thinner fish than did the small bottom nets and beach seines we used. The largest *Lycodes raridens* in our study was less than half the size found on the Asian side of the Pacific Arctic (Balanov et al., 2006; Kulik and Gerasimov, 2016); however, the growth parameters are the same. The flatfishes *H. robustus* and *Limanda aspera* were smaller in our collections than in the Chukchi Sea (Pruter and Alverson, 1962) or northeast Pacific (Kramer and Josey, 1995). In the current study both were shorter and fatter compared to previous efforts, but while *L. aspera* displayed positive allometry (Black et al., 2013) in both studies, *H. robustus* in our study had positive growth but had been reported as negative in the Chukchi Sea earlier (Smith et al., 1997b). The differences in our findings and those of others could be due to geography.

The maximum sizes for seven of the 28 species in this study either surpass the previously recorded maximum size for the Pacific Arctic or add new knowledge as the first length measurement record for the Pacific Arctic. The 113 mm *Artediellus scaber* in our study is the largest specimen recorded in the Chukchi Sea (Thorsteinson and Love, 2016). The 212 mm specimen of *Liparis fabricii* captured in the Beaufort Sea surpasses the previous record in this sea (Mecklenburg et al., 2014), and is equal to the maximum size in the Barents Sea (Wienerroither et al., 2011). In the same Liparidae family, *L. tunicatus* is similar in maximum size to the previous record in the northern Bering Sea (Mecklenburg et al., 2016). In the Zoarcid family, many maximum lengths are reported from the Atlantic Arctic. For *Lycodes adolfi,* maximum lengths reported from east Greenland (Mecklenburg et al., 2014) and north of Spitzbergen (Byrkjedal et al., 2011) are similar to that in the Beaufort Sea from the current study. While the largest *L. seminudus* in the Beaufort Sea adds new information, it was over 100 mm smaller than the maximum reported from West Greenland (Møller and Jørgensen, 2000). In family Stichaeidae, information on *Anisarchus medius* maximum lengths fills in gaps between studies in the Western Pacific (Mecklenburg et al., 2018) and the Barents Sea (Wienerroither et al., 2011). Differential growth for *Anisarchus medius* among the Chukchi and Beaufort Seas may be a topic for future research in this species. The maximum sizes of *Stichaeus punctatus* in the current study are smaller than maximum length recorded in the North Pacific (Eschmeyer and Herald, 1983), but provide information from Arctic locations. By documenting maximum fish size, we are able to corroborate and update basic life history information for these Pacific Arctic species.

We characterized the fishes in the U.S. Chukchi and Beaufort seas as "short-lived" (<age-10) and "long-lived" (>age-10) (Tables 3 and 4). *Mallotus catervarius* may be categorized as short-lived, at a maximum of age-6 (Gjøsæter, 1998). Our values of age-3 (Chukchi Sea) and age-1 (Beaufort Sea) fit within range of both sexes in all seasons in the Barents Sea (Gjøsæter, 1998). *Boreogadus saida* is also short-lived, with maximum age-7 (Hop et al., 1997) or age-8 (Gillispie et al., 1997), and of age-5 found in this study, in the Chukchi and Bering seas (Helser et al., 2017), and in the Svalbard Archipelago (Nahrgang et al., 2016). Likewise, two of the three sculpins we found up to age-7 are short lived; this is corroborated by others finding age-9 *Gymnocanthus tricuspis* in the Chukchi Sea (Smith et al., 1997a) and age-7 *Icelus spatula* off the Kuril Islands (Tokranov and Orlov, 2005). For *Myoxocephalus scorpius,* though we only aged specimens as old as age-5, it can be found up to age-15 in Newfoundland waters (Ennis, 1970), thus it cannot be categorized as

short-lived with the other two sculpin species. *Liparis fabricii*, previously without age recorded in Pacific Arctic, now is documented as age-5, which is similar to the 6 years in the Barents Sea (Wienerroither et al., 2011).

The ages documented in this study, sometimes for the very first time in the Pacific Arctic, highlight the different life history traits of Arctic fish species. Four *Lycodes* species now have recorded ages in the Pacific Arctic, including *L. adolfi,* age-12, *L. polaris* age-11, and the two oldest species we aged, *L. sagittarius,* age-26, and *L. seminudus,* age-24. Only two of these had a previously recorded maximum ages, *L. polaris* age-5 (Frost and Lowry, 1983) and *L. seminudus* age-8 (Mecklenburg et al., 2018). One of the biggest surprises was finding that some small species were long-lived, such as *Aspidophoroides olrikii*, which are small in size (80 mm), but nevertheless long-lived, with a maximum age-15. Similarly, *Anisarchus medius,* is a long-lived (age-19) and small (134 mm) species. For both species, no other age records in the Pacific Arctic exist, highlighting the novel information gained in this study. Furthermore, the size-at-age documented here emphasizes that small body size is not necessarily an indicator of limited longevity.

Though nearly twice as many species grew to greater maximum lengths in the Chukchi Sea than the Beaufort Sea, patterns of maximum ages between the Chukchi and Beaufort seas are more nuanced than those characterizing fish maximum length and length-at-age. Species that lived longer than a decade (*Aspidophoroides olrikii*, *Lycodes polaris*, and *Anisarchus medius*), reached their maximum age in the Beaufort Sea. Although these long-lived species are smaller at age in the Beaufort Sea, they ultimately reach a greater maximum age than their Chukchi Sea conspecifics. Increased resource availability has a positive impact on fish growth (Jones, 1986; Rosenfeld et al., 2005), but rapid growth can lead to a reduction in overall lifespan (Metcalfe and Monaghan, 2003). The importance of this trade-off between growth and longevity may depend on species-specific life history. In the biologically productive Chukchi Sea (Grebmeier et al., 2006), abundant resources can foster rapid growth; for short-lived species, the benefits of growing quickly may outweigh associated metabolic costs. In contrast, the impact of these metabolic costs may be more important for long-lived fishes, explaining why species such as *Lycodes polaris* lives to its maximum age in the colder Beaufort Sea, where scarce resources promote slow growth rates. Similarly, *Lycodes reticulatus* reached a maximum age of 35 years in the cold waters of northeastern Greenland and only 19 years in the warmer waters of the Barents Sea; low resource availability leads to slower growth rates in Greenland (Hildebrandt et al., 2011). Further research into the mechanisms driving differences in fish growth and maximum age in each region is necessary to explain the physiological processes driving these patterns.

Though a current stock assessment does not exist for the U.S. Arctic, the NPFMC Arctic Fisheries Management Plan could require the development of such a plan in the future. International interest in high latitude fisheries resources may increase as other economic opportunities shift global attention towards the Arctic. A cooperative international agreement was recently reached among nine Arctic and sub-arctic nations and the European Union that prevents commercial fishing in the central Arctic Ocean (Hoag, 2017). Numerous specimens were collected and examined for this study, and we acknowledge they may already have been affected by climate change. Potential shortcomings of this research may include aging methodology and limited data on all life stages of each species. However, this work lays a solid foundation for understanding life history traits of Arctic fish species. These data will meet the increasing demand for information as both domestic and international regulatory decisions are made regarding Arctic resources. Independent of future Arctic fisheries management actions, the knowledge gained in this study establishes a benchmark of fundamental biological parameters for fishes in the Pacific Arctic.

Declaration of competing interest

The authors declare that they have no known competing financial interests or personal relationships that could have appeared to influence the work reported in this paper.

Acknowledgements

We would like to thank all captains, crew, and science teams, especially Brenda Holladay and Lorena Edenfield, who collected these fishes, as well as the students, lab technicians, and research staff of the UAF Fisheries Oceanography Lab who processed specimens and analyzed otoliths. Thank you to Dr. Thomas Helser and associates at the NOAA Alaska Fisheries Science Center for training graduate students to prepare and read otoliths. These samples were collected over 21 cruises and supported and funded by many entities: Alaska Coastal Impact Assistance Program (Arctic Eis 2012), Alaska Department of Environmental Conservation (AKCH10, AKCH11), Bureau of Ocean and Energy Management (Arctic Eis 2012, BOEM_2011, TB_12, TB_13, TB_14, Chukchi Sea Environmental Studies Program (WWW0902, WWW0904, WWW1003, WWW1004), Coastal Marine Institute (OD0710, OS190), Cooperative Institute for Alaska Research (RUSALCA_2009, RUSALCA_2012), NOAA Office of Ocean Exploration and Research (HLY1601), North Pacific Research Board (ACES-2013, ACES-2014), North Slope Borough (AFF-2015), Olgoonik Fairweather (WWW0902, WWW0904, WWW1003, WWW1004), University of Texas at Austin (COMIDA_2009), and the University of Alaska Fairbanks College of Fisheries and Ocean Sciences.

Appendix A

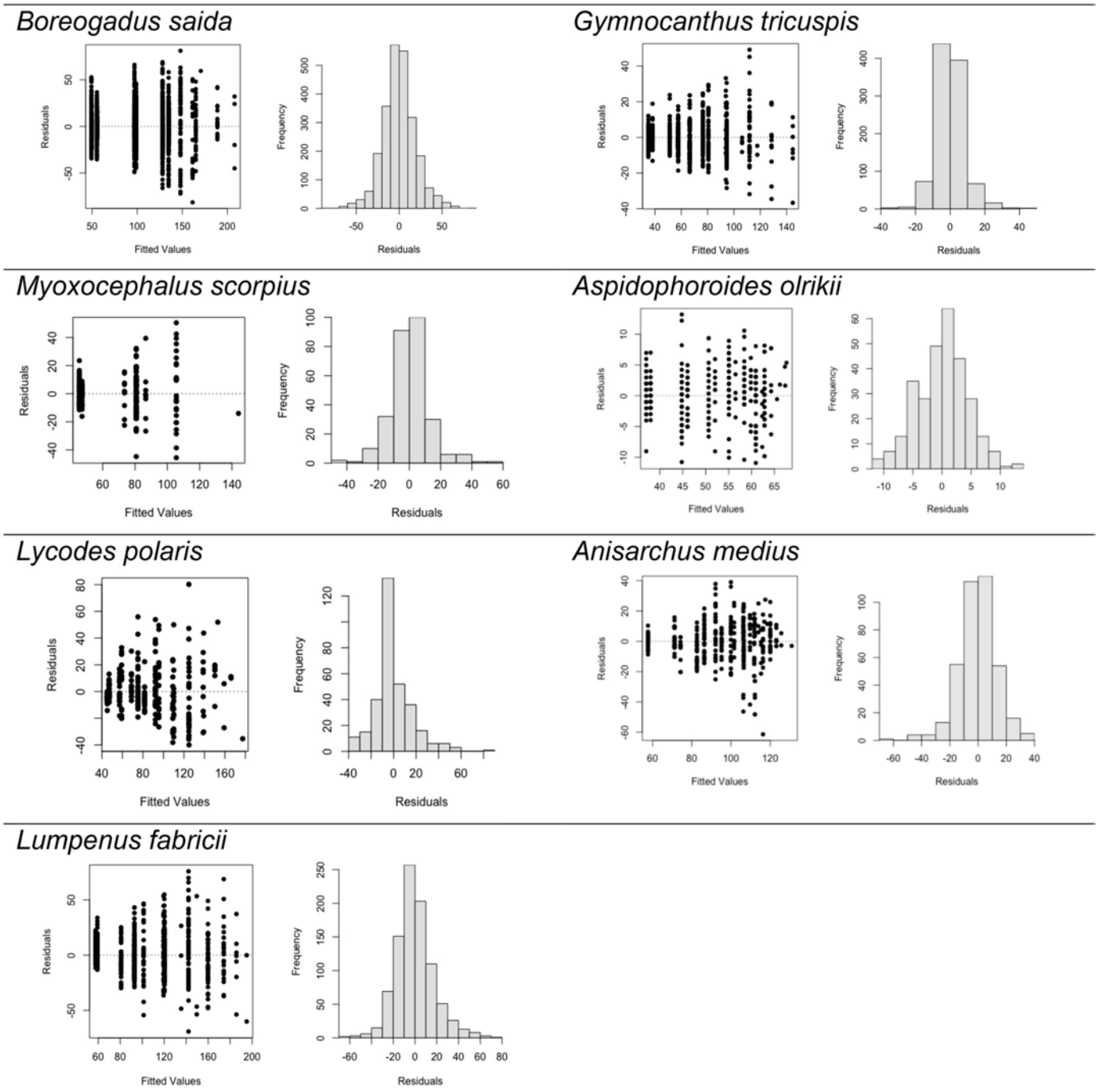

Fig. A1. Diagnostic plots for general growth models with separate parameters for the Chukchi and Beaufort Seas for seven selected species. Residual plots include data from both seas but are not differentiated. *Eleginus gracilis* was not included in the analysis because there were insufficient ages in the dataset (only age 0 in Beaufort and ages 0 and 1 from the Chukchi).

Table A1
The preferred growth model for the following species: *Boreogadus saida* (BS), *Gymnocanthus tricuspis* (GT), *Myoxocephalus scorpius* (MS), *Aspidophoroides olrikii* AO), *Lycodes polaris* (LP), *Anisarchus medius* (AM), *Lumpenus fabricii* (LF). Parameters that apply to the Beaufort (B) and Chukchi (C) Sea samples have no subscript (e.g. t_0), and a single value is presented. Parameters with separate values for the Beaufort and Chukchi Seas are given a subscript (e.g. $t_{0[sea]}$), where sea refers to Chukchi or Beaufort Seas. The von Bertalanffy growth function was used for all species, with the exception of *Lycodes polaris*, which was fit to the logistic growth function. The parameter t_l refers to total length. In the von Bertalanffy growth function, L_{inf} is the asymptotic average length, K is the Brody growth rate coefficient (units are in yr^{-1}), and t_0 represents the age when average length was zero. In the logistic growth function, L_{inf} and t_0 are as above, and G is the instantaneous growth rate at the origin of the curve

Species	Selected von Bertalanffy growth model	$L_{inf[sea=B]}$	$L_{inf[sea=C]}$	$K_{[sea=B]}$	$K_{[sea=C]}$	$t_{0[sea=B]}$	$t_{0[sea=C]}$
BS	$t_l \sim L_{inf[sea]} * (1 - \exp(-K_{[sea]} * (age - t_0)))$	290.7462	186.4611	0.2175	0.4067	−0.8603	
GT	$t_l \sim L_{inf\ [sea]} * (1-\exp(- K_{[sea]} * (age-t_{0[sea]})))$	282.5569	563.8271	0.0678	0.0378	−1.9496	−1.8555
MS	$t_l \sim L_{inf\ [sea]} * (1-\exp(- K_{[sea]} * (age - t_0)))$	99.7263	164.6567	0.6945	0.3507	−0.9216	
AO	$t_l \sim L_{inf\ [sea]} * (1-\exp(-K * (age - t_0)))$	68.5904	70.3428	0.2829		−2.7457	
AM	$t_l \sim L_{inf\ [sea]} * (1-\exp(-K_{[sea]} * (age-t_{0[sea]})))$	118.8974	138.0068	0.3164	0.1878	−2.0973	−3.8622
LF	$t_l \sim L_{inf} * (1 - \exp(-K_{[sea]} * (age-t_{0[sea]})))$	234.8108		0.1429	0.2130	−1.9646	−1.3642

Species	Selected logistic growth model	L_{inf}	$G_{[sea=B]}$	$G_{[sea=C]}$	$t_{0[sea=B]}$	$t_{0[sea=C]}$
LP	$t_l \sim L_{inf}/(1 + \exp(-(G_{[sea]} * (age - t_{0[sea]}))))$	198.6435	0.2858	0.3428	4.1995	3.4782

Appendix B. Supplementary data

Supplementary data to this article can be found online at https://doi.org/10.1016/j.dsr2.2020.104779.

References

Astthorsson, O.S., 2016. Distribution, abundance and biology of polar cod, Boreogadus saida, in Iceland–East Greenland waters. Polar Biol. 39, 995–1003.

Balanov, A., Badaev, O., Napazakov, V., Chuchukalo, V., 2006. Distribution and some biological features of Lycodes raridens (Zoarcidae) in the western part of the Bering Sea. J. Ichthyol. 46, 148–155.

Berge, J., Renaud, P.E., Darnis, G., Cottier, F., Last, K., Gabrielsen, T.M., Johnsen, G., Seuthe, L., Weslawski, J.M., Leu, E., 2015. In the dark: a review of ecosystem processes during the Arctic polar night. Prog. Oceanogr. 139, 258–271.

Berkeley, S.A., Hixon, M.A., Larson, R.J., Love, M.S., 2004. Fisheries sustainability via protection of age structure and spatial distribution of fish populations. Fisheries 29, 23–32.

Beverton, R., 1954. Notes on the Use of Theoretical Models in the Study of the Dynamics of Exploited Fish Populations (No. 2). US Fishery Laboratory.

Black, B.A., Matta, M.E., Helser, T.E., Wilderbuer, T.K., 2013. Otolith biochronologies as multidecadal indicators of body size anomalies in yellowfin sole (*Limanda aspera*). Fish. Oceanogr. 22, 523–532.

Bluhm, B.A., Gradinger, R., 2008. Regional variability in food availability for Arctic marine mammals. Ecol. Appl. 18, S77–S96.

Brown, E.D., 2002. Life history, distribution, and size structure of Pacific capelin in Prince William Sound and the northern Gulf of Alaska. ICES (Int. Counc. Explor. Sea) J. Mar. Sci. 59, 983–996.

Byrkjedal, I., Langhelle, G., de Lange Wenneck, T., Wienerroither, R., 2011. *Lycodes adolfi* nielsen and fosså, 1993 (teleostei: Zoarcidae) found in the Arctic Ocean. Polar Biol. 34, 465–467.

Campana, S.E., Stevenson, D.K., 1992. Otolith Microstructure Examination and Analysis, vol. 117. Canadian Special Publication of Fisheries and Aquatic Sciences (Department of Fisheries and Oceans, Ottawa).

Christiansen, J.S., Mecklenburg, C.W., Karamushko, O.V., 2014. Arctic marine fishes and their fisheries in light of global change. Global Change Biol. 20, 352–359. https://doi.org/10.1111/gcb.12395.

Crawford, R.E., Vagle, S., Carmack, E.C., 2012. Water mass and bathymetric characteristics of polar cod habitat along the continental shelf and slope of the Beaufort and Chukchi seas. Polar Biol. 35, 179–190. https://doi.org/10.1007/s00300-011-1051-9.

Dunton, K.H., Goodall, J.L., Schonberg, S.V., Grebmeier, J.M., Maidment, D.R., 2005. Multi-decadal synthesis of benthic–pelagic coupling in the western arctic: role of cross-shelf advective processes. Deep Sea Res. Part II Top. Stud. Oceanogr. 52, 3462–3477. https://doi.org/10.1016/j.dsr2.2005.09.007.

Ennis, G., 1970. Age, growth, and sexual maturity of the shorthorn sculpin, *Myoxocephalus scorpius*, in Newfoundland waters. Journal of the Fisheries Board of Canada 27, 2155–2158.

Eschmeyer, W.N., Herald, E.S., 1983. A Field Guide to Pacific Coast Fishes. North America (Houghton Mifflin Harcourt, New York, NY).

Fechhelm, R.G., Craig, P.C., Baker, J., Gallaway, B.J., 1985. Fish Distribution and Use of Nearshore Waters in the Northeastern Chukchi Sea, vol. 32. US Department of Commerce, NOAA, and US Department of the Interior, Minerals Management Service, pp. 121–298. Outer Continental Shelf Environmental Assessment Program Final Report.

Frey, K.E., Moore, G.W.K., Cooper, L.W., Grebmeier, J.M., 2015. Divergent patterns of recent sea ice cover across the bering, Chukchi, and Beaufort seas of the pacific arctic region. Prog. Oceanogr. 136, 32–49. https://doi.org/10.1016/j.pocean.2015.05.009.

Froese, R., 2006. Cube law, condition factor and weight-length relationships: history, meta-analysis and recommendations. J. Appl. Ichthyol. 22, 241–253. https://doi.org/10.1111/j.1439-0426.2006.00805.x.

Frost, K.J., Lowry, L.F., 1983. Demersal Fishes and Invertebrates Trawled in the Northeastern Chukchi and Western Beaufort Seas 1976-1977, vol. 764. US Department of Commerce, p. 22. NOAA Technical Report, NMFS-SSRF.

Gautier, D.L., Bird, K.J., Charpentier, R.R., Grantz, A., Houseknecht, D.W., Klett, T.R., Moore, T.E., Pitman, J.K., Schenk, C.J., Schuenemeyer, J.H., Sorensen, K., Tennyson, M.E., Valin, Z.C., Wandrey, C.J., 2009. Assessment of undiscovered oil and gas in the Arctic. Science 324, 1175–1179. https://doi.org/10.1126/science.1169467.

Giacalone, V., D'anna, G., Badalamenti, F., Pipitone, C., 2010. Weight-length relationships and condition factor trends for thirty-eight fish species in trawled and untrawled areas off the coast of northern Sicily (central Mediterranean Sea). J. Appl. Ichthyol. 26, 954–957.

Gillispie, J., Smith, R., Barbour, E., Barber, W., 1997a. Distribution, abundance, and growth of Arctic cod in the northeastern Chukchi Sea. In: Fish Ecology in Arctic North America. American Fisheries Society Symposium, pp. 81–89.

Gjøsæter, H., 1998. The population biology and exploitation of capelin (Mallotus villosus) in the Barents Sea. Sarsia 83, 453–496.

Grebmeier, J.M., Cooper, L.W., Feder, H.M., Sirenko, B.I., 2006. Ecosystem dynamics of the pacific-influenced northern bering and Chukchi seas in the amerasian arctic. Prog. Oceanogr. 71, 331–361. https://doi.org/10.1016/j.pocean.2006.10.001.

Gulland, J., 1965. Estimation of Mortality Rates. Annex to Arctic Fisheries Working Group Report. International Council for the Exploration of the Sea, CM.

Hart, J., 1973. Pacific fishes of Canada. Ottawa: fisheries research board of Canada. Bulletin 180.

Harter, B.B., Elliott, K.H., Divoky, G.J., Davoren, G.K., 2013. Arctic cod (*Boreogadus saida*) as prey: fish length-energetics relationships in the Beaufort Sea and Hudson Bay. Arctic 191–196.

Helser, T.E., Colman, J.R., Anderl, D.M., Kastelle, C.R., 2017. Growth dynamics of saffron cod (*Eleginus gracilis*) and arctic cod (*Boreogadus saida*) in the northern bering and Chukchi seas. Deep Sea Res. Part II Top. Stud. Oceanogr. 135, 66–77. https://doi.org/10.1016/j.dsr2.2015.12.009.

Hildebrandt, N., Bergmann, M., Knust, R., 2011. Longevity and growth efficiency of two deep-dwelling Arctic zoarcids and comparison with eight other zoarcid species from different climatic regions. Polar Biol. 34, 1523–1533. https://doi.org/10.1007/s00300-011-1011-4.

Hoag, H., 2017. Nations agree to ban fishing in Arctic Ocean for at least 16 years. Science Magazine. http://www.sciencemag.org/news/2017/12/nations-agree-ban-fishing-arctic-ocean-least-16-years.

Hop, H., Tonn, W.M., Welch, H.E., 1997. Bioenergetics of Arctic cod (*Boreogadus saida*) at low temperatures. Can. J. Fish. Aquat. Sci. 54, 1772–1784.

Huxley, J.S., 1950. Relative growth and form transformation. Proc. Roy. Soc. Lond. 137, 465–469.

IPCC, 2018. Summary for policymakers. Global warming of 1.5°C. An IPCC special report on the impacts of Global Warming of 1.5°C above pre-industrial levels and related global greenhouse gas emission pathways. In: The Context of Strengthening the Global Response to the Threat of Climate Change, Sustainable Development, and Efforts to Eradicate Poverty. World Meteorological Organization, Geneva, Switzerland.

Johannesen, E., Hoines, A.S., Dolgov, A.V., Fossheim, M., 2012. Demersal fish assemblages and spatial diversity patterns in the Arctic-Atlantic transition zone in

the Barents Sea. PloS One 7, e34924. https://doi.org/10.1371/journal.pone.0034924.
Jones, G., 1986. Food availability affects growth in a coral reef fish. Oecologia 70, 136–139.
Kramer, D.E., Josey, T., 1995. Guide to northeast Pacific flatfishes: families bothidae, cynoglossidae and pleuronectidae. Sea Grant.
Kulik, V., Gerasimov, N., 2016. Length–weight and length–length relationships of 11 fish species from the Sea of Okhotsk. J. Appl. Ichthyol. 32, 1326–1328.
Logerwell, E., Rand, K., Danielson, S., Sousa, L., 2017. Environmental drivers of benthic fish distribution in and around Barrow Canyon in the northeastern Chukchi Sea and western Beaufort Sea. Deep Sea Res. Part II Top. Stud. Oceanogr. 152, 170–181. https://doi.org/10.1016/j.dsr2.2017.04.012.
Matta, M.E., Kimura, D.K., 2012. Age Determination Manual of the Alaska Fisheries Science Center Age and Growth Program. NOAA Professional Papers, pp. 1–97, 13.
Maunder, M.N., Punt, A.E., 2013. A review of integrated analysis in fisheries stock assessment. Fish. Res. 142, 61–74. https://doi.org/10.1016/j.fishres.2012.07.025.
Mecklenburg, C., Mecklenburg, T., Sheiko, B., Steinke, D., 2016. Pacific arctic marine fishes. Conservation of arctic flora and fauna. CAFF monitoring series report No. 23, akureyri, Iceland.
Mecklenburg, C.W., Byrkjedal, I., Karamushko, O.V., Møller, P.R., 2014. Atlantic fishes in the Chukchi borderland. Mar. Biodivers. 44, 127–150.
Mecklenburg, C.W., Lynghammar, A., Johannesen, E., Byrkjedal, I., Christiansen, J.S., Dolgov, A.V., Karamushko, O.V., Mecklenburg, T., Møller, P.R., Steinkte, D., 2018. Marine fishes of the arctic region. Conservation of arctic flora and fauna, akureyri, Iceland.
Mecklenburg, C.W., Mecklenburg, T.A., Thorsteinson, L.K., 2002. Fishes of Alaska. American Fisheries Society, Bethesda, Maryland.
Mendes, B., Fonseca, P., Campos, A., 2004. Weight-length relationships for 46 fish species of the Portuguese west coast. J. Appl. Ichthyol. 20, 355–361. https://doi.org/10.1111/j.1439-0426.2004.00559.x.
Metcalfe, N.B., Monaghan, P., 2003. Growth versus lifespan: perspectives from evolutionary ecology. Exp. Gerontol. 38, 935–940.
Møller, P.R., Jørgensen, O.A., 2000. Distribution and abundance of eelpouts (pisces, Zoarcidae) off west Greenland. Sarsia 85, 23–48.
Nahrgang, J., Storhaug, E., Murzina, S.A., Delmas, O., Nemova, N.N., Berge, J., 2016. Aspects of reproductive biology of wild-caught polar cod (*Boreogadus saida*) from Svalbard waters. Polar Biol. 39, 1155–1164. https://doi.org/10.1007/s00300-015-1837-2.
Norcross, B.L., Apsens, S.J., Bell, L.E., Bluhm, B.A., Dissen, J.N., Edenfield, L.E., Frothingham, A., Gray, B.P., Hardy, S.M., Holladay, B.A., Hopcroft, R.R., Iken, K.B., Smoot, C.A., Walker, K.L., Wood, E.D., 2017. US-Canada transboundary fish and lower trophic communities: abundance, distribution, habitat and community analysis. US dept. Of the interior, Bureau of Ocean energy management, Alaska OCS region, Fairbanks AK. Final Report for BOEM Agreement Number M12AC00011. 435 pp + appendices.
Norcross, B.L., Raborn, S.W., Holladay, B.A., Gallaway, B.J., Crawford, S.T., Priest, J.T., Edenfield, L.E., Meyer, R., 2013. Northeastern Chukchi Sea demersal fishes and associated environmental characteristics, 2009–2010. Continent. Shelf Res. 67, 77–95. https://doi.org/10.1016/j.csr.2013.05.010.
NPFMC, 2009. Fishery Management Plan for Fish Resources of the Arctic Management Area. North Pacific Fisheries Management Council, Anchorage AK.
Olsen, E., Aanes, S., Mehl, S., Holst, J.C., Aglen, A., Gjøsæter, H., 2009. Cod, haddock, saithe, herring, and capelin in the Barents Sea and adjacent waters: a review of the biological value of the area. ICES (Int. Counc. Explor. Sea) J. Mar. Sci. 67, 87–101.
Pickart, R.S., Weingartner, T.J., Pratt, L.J., Zimmermann, S., Torres, D.J., 2005. Flow of winter-transformed pacific water into the western arctic. Deep Sea Res. Part II Top. Stud. Oceanogr. 52, 3175–3198.
Plagányi, É.E., Punt, A.E., Hillary, R., Morello, E.B., Thébaud, O., Hutton, T., Pillans, R. D., Thorson, J.T., Fulton, E.A., Smith, A.D., 2014. Multispecies fisheries management and conservation: tactical applications using models of intermediate complexity. Fish Fish. 15, 1–22.
Pörtner, H.-O., Berdal, B., Blust, R., Brix, O., Colosimo, A., De Wachter, B., Giuliani, A., Johansen, T., Fischer, T., Knust, R., 2001. Climate induced temperature effects on growth performance, fecundity and recruitment in marine fish: developing a hypothesis for cause and effect relationships in Atlantic cod (*Gadus morhua*) and common eelpout (*Zoarces viviparus*). Continent. Shelf Res. 21, 1975–1997.
Pruter, A.T., Alverson, D.L., 1962. Abundance, distribution, and growth of flounders in the south-eastern Chukchi Sea. ICES (Int. Counc. Explor. Sea) J. Mar. Sci. 27, 81–99.
Quinn, T.J., Deriso, R.B., 1999. Quantitative Fish Dynamics. Oxford University Press.
Rand, K.M., Logerwell, E.A., 2011. The first demersal trawl survey of benthic fish and invertebrates in the Beaufort Sea since the late 1970s. Polar Biol. 34, 475–488. https://doi.org/10.1007/s00300-010-0900-2.
Ricker, W., 1975. Computation and Interpretation of Biological Statistics of Fish Populations, vol. 191. Department of the Environment, Fisheries and Marine Service, Ottawa, pp. 1–382.
Rosenfeld, J.S., Leiter, T., Lindner, G., Rothman, L., 2005. Food abundance and fish density alters habitat selection, growth, and habitat suitability curves for juvenile coho salmon (*Oncorhynchus kisutch*). Can. J. Fish. Aquat. Sci. 62, 1691–1701. https://doi.org/10.1139/f05-072.
Smith, L.C., Stephenson, S.R., 2013. New Trans-Arctic shipping routes navigable by midcentury. Proc. Natl. Acad. Sci. Unit. States Am. 110, E1191–E1195. https://doi.org/10.1073/pnas.1214212110.
Smith, R., Barber, W., Vallarino, M., Gillispie, J., 1997a. Ritchie A population biology of the arctic staghorn sculpin in the northeastern Chukchi sea. In: Fish Ecology in Arctic North America. American Fisheries Society Symposium, pp. 133–139.
Smith, R., Vallarino, M., Barbour, E., Fitzpatrick, E., Barber, W., 1997b. Population biology of the bering flounder in the northeastern Chukchi sea. In: Fish Ecology in Arctic North America. American Fisheries Society Symposium, pp. 127–132.
Stevenson, D.E., Lauth, R.R., 2012. Latitudinal trends and temporal shifts in the catch composition of bottom trawls conducted on the eastern Bering Sea shelf. Deep Sea Res. Part II Top. Stud. Oceanogr. 65–70, 251–259. https://doi.org/10.1016/j.dsr2.2012.02.021.
Thorsteinson, L.K., Love, M.S., 2016. Alaska Arctic Marine Fish Ecology Catalog. U.S. Geological Survey Scientific Investigations Report 2016-5038. OCS Study, BOEM 2016-048, p. 768.
Tokranov, A., Orlov, A., 2005. Some features of the biology of Icelus spatula (cottidae) in pacific waters off the northern Kuril Islands. J. Ichthyol. 45, 229–236.
Weingartner, T., 1997. A review of the physical oceanography of the northeastern Chukchi Sea. In: Fish Ecology in Arctic North America. American Fisheries Society Symposium, pp. 40–59, 1997.
Weingartner, T., Dobbins, E., Danielson, S., Winsor, P., Potter, R., Statscewich, H., 2013. Hydrographic variability over the northeastern Chukchi Sea shelf in summer-fall 2008–2010. Continent. Shelf Res. 67, 5–22. https://doi.org/10.1016/j.csr.2013.03.012.
Wienerroither, R., Johannesen, E., Dolgov, A., Byrkjedal, I., Bjelland, O., Drevetnyak, K., Eriksen, K., Høines, Å., Langhelle, G., Langøy, H., 2011. Atlas of the Barents Sea fishes. IMR/PINRO Joint Report Series 1, 1–272.
Wiswar, D.W., Fruge, D.J., 2006. Fisheries Investigations in Western Camden Bay, Arctic National Wildlife Refuge, Alaska, 1987. US Fish and Wildlife Service, Fairbanks Fish and Wildlife Field Office.
Wund, M.A., Valena, S., Wood, S., Baker, J.A., 2012. Ancestral plasticity and allometry in threespine stickleback reveal phenotypes associated with derived, freshwater ecotypes. Biol. J. Linn. Soc. 105, 573–583.

Deep–Sea Research II 177 (2020) 104830

Contents lists available at ScienceDirect

Deep-Sea Research Part II

journal homepage: http://www.elsevier.com/locate/dsr2

Response of Pink salmon to climate warming in the northern Bering Sea

Edward V. Farley Jr. [a,*], James M. Murphy [a], Kris Cieciel [a], Ellen M. Yasumiishi [a], Karen Dunmall [b], Todd Sformo [c,d], Pete Rand [e]

[a] NOAA/NMFS, Alaska Fisheries Science Center, Ted Stevens Marine Research Institute, Auke Bay Laboratories, 17109 Point Lena Loop Road, Juneau, AK, 99801, USA
[b] Fisheries and Oceans Canada, 501 University Crescent, Winnipeg, R3T 2N6, Canada
[c] North Slope Borough Department of Wildlife Management, PO Box 69, Barrow, AK 99723, USA
[d] Institute of Arctic Biology, University of Alaska Fairbanks, 902 N. Koyukuk Dr., PO Box 757000, Fairbanks, AK 99775, USA
[e] Prince William Sound Science Center, 300 Breakwater Avenue, Cordova, AK, 99574, USA

ARTICLE INFO

Keywords:
Pink salmon
Pacific Arctic region
Abundance models
Distribution
Size

ABSTRACT

Life-history and life-cycle models of Pink salmon (*Oncorhynchus gorbuscha*) are developed to provide insight into production dynamics of northern Bering Sea Pink salmon. Arctic ecosystems, including freshwater and marine ecosystems in the northern Bering Sea, are warming at a rapid rate. Due to their short, two-year life cycle, Pink salmon are well known to respond rapidly to ecosystem change and can provide unique insight into ecosystem impacts of warming Arctic conditions. Life-cycle models suggest a lack of density-dependence for adult Pink salmon spawners in the Yukon River and potential for some density-dependence for adult Pink salmon spawners in the Norton Sound region. Life-history models identify a positive and significant relationship between the abundance index for juvenile Pink salmon and average Nome air temperature during their freshwater residency (August to June). This relationship supports the notion that warming air temperatures in this region (as a proxy for river and stream temperatures) are contributing to improved freshwater survival or increased capacity of freshwater habitats to support Pink salmon production. Life-history models also identify the number of adult Pink salmon returning to Norton Sound and the Yukon River is significantly related to the juvenile abundance in the northern Bering Sea. This result indicates that much of the variability in survival for northern Bering Sea Pink salmon occurs during early life-history stages and that juvenile abundance is an informative leading indicator of Pink salmon runs to this region.

1. Introduction

The Pacific Arctic Region (PAR), that is, the northern Bering Sea, and the Chukchi Sea to the East Siberian and Beaufort seas, is experiencing significant warming and extremes in seasonal sea ice extent and thickness (Frey et al., 2014; Baker et al., 2020; Danielson et al., 2020). Over the past two decades, record summer sea-ice minima (2007, 2011, 2012; 2017 and 2018) have occurred, and climate models project that the southern Chukchi Sea will be sea-ice free for 5 months (July to November) within a decade or two (Overland et al., 2014). In the northern Bering Sea, sea ice is projected to be less common during May, but will continue to be extensive through April (Stabeno et al., 2012). However, recent events during 2017 and 2018 in the northern Bering Sea indicate that open water in this region during winter is already occurring (Stabeno and Bell, 2019). The presence of sea ice during winter and into spring is known to influence summer bottom temperatures; however, climate models project that the loss of seasonal sea ice during spring and into fall months is currently resulting in, and expected in the future to lead to, increased sea surface temperatures during summer months in both the northern Bering Sea and Chukchi Sea (Wang et al., 2012). In addition, the reduction in seasonal sea ice is likely contributing to increased primary and secondary production (Arrigo and van Dijken, 2011) that could shift the ecosystem to a more pelagic state (Grebmeier et al., 2006).

These shifts in the PAR ecosystem are likely to have large impacts on the ecology of upper trophic level species such as fishes, birds, and mammals (Sigler et al., 2011). For instance, the community structure of some upper trophic level species already show evidence of changes in the Chukchi Sea, such as the shift from predominantly piscivorous seabirds to planktivorous seabirds in recent decades (Gall et al., 2017). Large scale distributional shifts of walleye pollock (*Gadus chalcogrammus*) and Pacific cod (*G. microcephalus*) in response to reduced cold

* Corresponding author.
E-mail address: ed.farley@noaa.gov (E.V. Farley).

https://doi.org/10.1016/j.dsr2.2020.104830
Received 16 August 2019; Received in revised form 13 July 2020; Accepted 14 July 2020
Available online 1 August 2020
0967-0645/Published by Elsevier Ltd.

pool extent in the northern Bering Sea were also found (Stevenson and Lauth, 2018). Other ecosystem consequences of continued warming have been described elsewhere, such as the Barents Sea, and include changes in zooplankton community structure as well as shifts in species distributions and relative abundances (Hop and Gjøsæter, 2013; Orlova et al., 2013; Fossheim et al., 2015). Because the upper trophic level species are typically top predators, they must adapt via biological responses to physical forcing and thereby are "sentinels" of ecosystem variability and reorganization (Moore et al., 2014). As such, there will likely be fishes that do better under climate warming and those that may not.

The most common salmon species in the PAR include Pink (*Oncorhynchus gorbuscha*) and Chum (*O. keta*) salmon (Nielsen et al., 2013; Carothers et al., 2013; Stephenson, 2006). Of these two salmon species, Pink salmon are the most abundant in the North Pacific Ocean (Ruggerone and Irvine, 2018) and have the broadest distribution in the PAR from the Yukon River to small steams from Point Hope to Point Barrow (Craig and Haldorson, 1986). Vagrants have also been found upstream in the Mackenzie River to Fort Good Hope, Northwest Territories (Dunmall et al., 2018), as far east in the Canadian western Arctic as Paulatuk, Northwest Territories (Dunmall et al., 2013) and Kugluktuk, Nunavut (Dunmall et al., 2018), and along the east coast of Greenland (Dunmall et al., 2013). Spawning Pink salmon have also been documented along the Chukotka Peninsula coastline from the northern Bering Sea into the Chukchi Sea and as far east as the Kolyma River (Radchenko et al., 2018).

Pink salmon production around the North Pacific Ocean has increased over the last decade (Radchenko et al., 2018). While some authors have expressed concern that Pink salmon may be exerting top-down control on the food web (Batten et al., 2018) and affecting growth and survival of other species reliant on the marine food web (Ruggerone et al., 2016; Oka et al., 2012; Springer et al., 2018), others have illustrated no evidence of Pink salmon abundance on marine production (Radchenko et al., 2018). While Pink salmon abundance in northern regions of their range is still quite low in relation to stocks farther south, there is evidence that the abundance of some northern stocks is increasing during this period of warming.

Pink salmon have a short 2-year life-cycle that include freshwater and marine environments (Radchenko et al., 2018). Adult Pink salmon in the northern regions return to rivers during July to September and their eggs hatch during late winter and into spring. Fry enter the marine environment during late May through June (Howard et al., 2017), and they spend the summer as juveniles in near coastal regions before migrating offshore into the North Pacific Ocean for the winter. After winter, they migrate back to their natal spawning grounds. The 2-year life-cycle creates separate even and odd year brood lines that do not overlap on spawning grounds (Radchenko et al., 2018).

Conditions in both freshwater and marine environments are important to the survival of Pink salmon. In northern regions of Pink salmon distribution, cold river and stream temperatures in the freshwater environment are believed to limit salmon production (Dunmall et al., 2016); however, continued warming air and stream temperatures, and longer periods of ice-free conditions may benefit salmon survival within this environment (Nielson et al., 2013). Two critical periods in the marine environment are believed to be important to marine survival of salmon. The first critical period is during their early marine residence where rapid growth is believed to reduce predation (Parker, 1968). The second critical period is during their first winter at sea where juvenile salmon that attain sufficient size and energy reserves (lipids) during their first summer at sea have higher probability of survival (Beamish and Mahnken, 2001). Both critical periods are linked to ecosystem function (i.e., optimum sea temperatures for growth, quantity and quality of prey resources) during their first summer at sea as juveniles, and there is evidence in the PAR that warmer sea temperatures benefit juvenile Pink salmon early marine growth (Moss et al., 2009; Andrews et al., 2009; Wechter et al., 2017). Thus, the expectation is that Pink salmon in the PAR will respond positively to the rapid warming in both freshwater and marine environments.

To better understand Pink salmon dynamics in this region, we examine the total life-cycle productivity for the Yukon River and Norton Sound area (total number of adult returns per spawner; R/S) based on models that relate abundance estimates for adult returns to the number of spawners two years earlier. We include Nome air temperatures as a proxy for river and stream temperatures and estimates of summer sea surface temperature taken from satellite measurements in the northern Bering Sea in the life-cycle productivity models to explore whether temperature in these environments is affecting production. Next, we use surface trawl survey data to examine early marine life-history periods and conditions in these environments that may impact Pink salmon survival. Juvenile Pink salmon caught during the surface trawl survey are most likely from spawning populations (previous year) in this region (Farley et al., 2005); the juveniles return as adults the following summer to western Alaska rivers. For freshwater and early marine effects, we relate juvenile Pink salmon relative abundance to the total number of spawners to the Yukon River and Norton Sound region and to Nome air temperatures as a proxy for river temperature. Strong positive relationships would suggest that the number of spawners along with warmer freshwater temperatures lead to increased relative abundance of juvenile Pink salmon in the northeastern Bering Sea region. Finally, we examine the relationship between the indices of adult Pink salmon returns to the Yukon River and Norton Sound region with the juvenile Pink salmon relative abundance, body size, and summer sea temperatures from satellite estimates. Strong positive relationships would suggest higher numbers of juveniles along with warmer temperatures and increased size lead to greater numbers of adult Pink salmon the following year.

2. Materials and methods

2.1. Life-cycle models

A time series (1995–2018) of adult Pink salmon return indices (harvest and spawners) and spawner indices to the Yukon River and Norton Sound were derived from a number of sources. The time series for the number of Yukon River and Norton Sound region Pink salmon returns are from Estensen et al. (2018) and Menard et al. (2020). For the Yukon River, the number of adult Pink salmon spawners is indexed from estimates of passage past the Pilot Station Sonar in the lower river (JTC, 2019), escapement past the East Fork Andreafsky River weir downstream of the sonar (Conitz, 2019), and total harvest of this species in the Yukon River (Estensen et al., 2018). While some lower river escapement of Pink salmon occur in systems downstream of the East Fork Andreafsky River weir and Pilot Station Sonar, a majority of total number of Pink salmon spawners in the Yukon River is accounted for by these assessment projects. For Norton Sound, the adult Pink salmon spawner index includes rivers that contain weirs or counting towers for more accurate values and have long enough time series to compare with our juvenile Pink salmon abundance index. These include the Eldorado, Snake, Kwiniuk, Nome, and North rivers. The annual indices of total Norton Sound adult Pink salmon returns are the sum of total annual harvest from the Norton Sound area, as most salmon harvest occur in marine waters downstream of spawner assessment projects, plus the sum of annual adult Pink salmon spawners to the index rivers.

Annual mean Nome air temperatures (1995–2018; August $_{(t)}$ to June $_{(t+1)}$) where t represents the year of adult Pink salmon spawning, were obtained from the National Weather Service web site: https://w2.weather.gov/climate/xmacis.php?wfo=pafg. The mean August $_{(t)}$ to June $_{(t+1)}$ air temperature represents the period of incubation (adult Pink salmon that entered freshwater streams and rivers to spawn during late July through August of year t) and rearing (over winter to when they leave freshwater as fry to enter the marine environment during late May through June of year t+1) of Pink salmon in northern regions of their

distribution. We used the annual mean air temperature as a proxy for stream and river temperatures in the northern Bering Sea region for the Pink salmon production models. Air temperatures have been used to estimate seasonal freshwater stream temperatures (McNyset et al., 2015), however we understand there are caveats given the span of seasons (includes winter) in our use of air temperatures as proxy for stream temperatures in this region.

Annual mean sea surface temperatures (1995–2018; SST_{t+1}) within the northeastern Bering Sea, where t represents the year of adult Pink salmon spawning, were estimated using data from satellite sources (NOAA Coral Reef Watch, 2018). Daily SST data were averaged within the northeastern Bering Sea (latitudes 60°N to 65°N; longitudes 166°W to 171°W) for each month. We then averaged the monthly mean sea surface temperatures for June to September for each year to represent sea temperature juvenile Pink salmon would experience during their first summer at sea.

The number of adult Pink salmon that return (R) to the river each year is a function of the number of adult spawners (S) two years prior as well as life-cycle events that occur during freshwater and marine residence. One measure of productivity is to examine the number of adults produced per spawner. Adult Pink salmon return and spawner data for the Yukon River and Norton Sound region are shown in Fig. 1a and b. There is increased variation in return indices at higher spawner index levels for both the Yukon River stocks and Norton Sound region stocks suggesting a multiplicative error structure. To understand between-stock variability in the northern Bering Sea region, we calculated the correlation of $\ln(R/S)$ between the Norton Sound region stock group and the Yukon River stock group to determine whether their productivity is synchronous. To take into account density dependent effects, we included models that relate the number of spawners to the number of adult returns (see Quinn and Deriso, 1999):

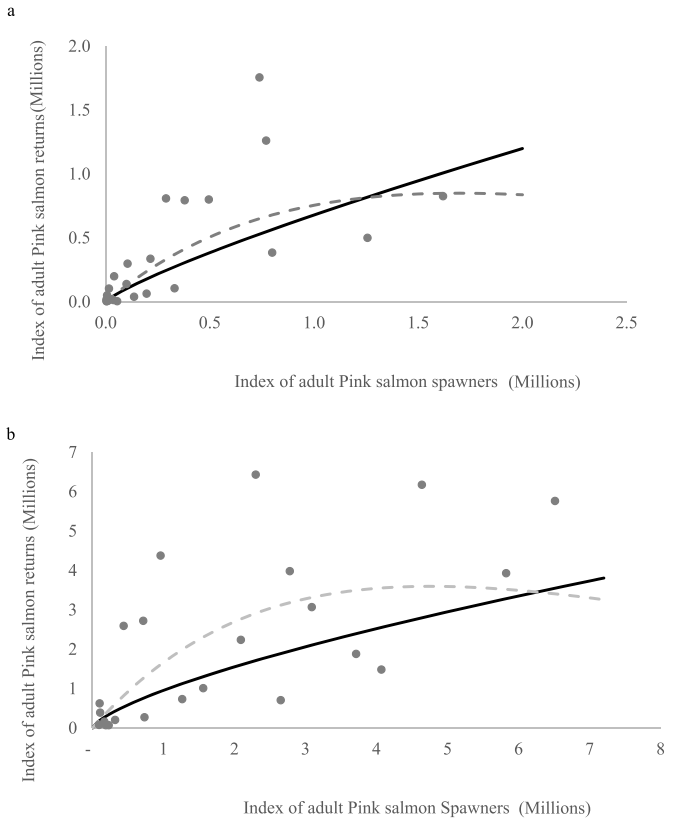

Fig. 1. Indices of adult Pink salmon spawners and returns (spawners plus harvest) to the Yukon River (a) and Norton Sound region (b). The solid line represents the Cushing model fit and the dashed line represents the Ricker model fit to the spawner and return data.

$$\ln R_{t+2} = a + \gamma \ln S_t + \varepsilon \text{ Cushing Model (Cushing, 1971)} \quad (1)$$

$$\ln (R_{t+2}/S_t) = a - \beta S_t \text{ Ricker Model (Ricker, 1975)} \quad (2)$$

where a is the natural log of the productivity parameter and γ and β are the density-dependence parameters. While the Cushing model includes a density-dependent parameter, this model lacks a peak level of recruitment (Quinn and Deriso, 1999); recruitment continues to increase as spawning level increases. To provide density dependence in the Cushing model, γ must be less than 1. The Cushing model is typically not used for salmon stocks to examine the relationship between the number of returns and spawners due to lack of density dependence at high spawning levels; however, it may be informative for northern river systems experiencing rapid warming with potential for shifts in the underlying capacity of these ecosystems to support higher production. In addition, we included the annual estimates of Nome air temperature, as a proxy for freshwater temperatures, and annual average of sea temperature in the life-cycle models to test whether their inclusion helps explain production dynamics in this region.

A step-wise selection of a linear regression model (S-plus; Insightful Corporation, 2001) was used to determine the most parsimonious life-cycle models that explain production dynamics of Pink salmon in the northern Bering Sea region. In S-plus, the effects of additional terms to the model are determined by comparing the Mallow's C_p statistic estimated by:

$$\boldsymbol{C_p} = \left(\frac{\boldsymbol{RSS}}{\widehat{\boldsymbol{\sigma}}^2}\right) + 2 * \boldsymbol{p} - n$$

where n is the sample size, $\widehat{\sigma}^2$ is the mean square error of the true regression model, RSS is the residual sum of squares and p is the number of parameters in the model, which equals the number of predictors plus 1 if the intercept is included in the model. The stepwise selection process requires an initial model often constructed explicitly as an "intercept-only" model. The step function in S-plus calculates the C_p statistic for the intercept only model as well as those for all reduced and augmented models. If any term has a C_p statistic lower than that of the intercept only model, the term with the lowest C_p statistic is dropped. We also tested the residuals of the most parsimonious models for autocorrelation between consecutive years to see if the other potential factors beyond those in the model could influence adult Pink salmon returns.

2.2. Life-history models

The information on juvenile Pink salmon marine ecology in the northern Bering Sea comes from integrated ecosystem surveys conducted during late summer and early fall months of 2003–2018 (except 2008) (Fig. 2). For this study, the northern Bering Sea consisted of stations sampled between 60°N and 65°N and juvenile Pink salmon captured in the survey region are assumed to be of wild origin originating from spawning populations within the Norton Sound region and Yukon River. Details on survey design can be found in Murphy et al. (2017). Briefly, juvenile Pink salmon were captured using a model 400/601 rope trawl, made by Cantrawl Pacific Limited of Richmond, British Columbia. The rope trawl was rigged with buoys on the headrope to sample from near surface to approximately 20–25 m depth. Sampling stations were generally completed during daylight hours (0730–2100, Alaska Daylight Savings Time). All trawl deployments lasted 30 min and covered between 2.8 and 4.6 km. A vertical (surface to near bottom depths) conductivity and temperature at depth (CTD) cast was done at each station to measure oceanographic characteristics during the survey. The surveys generally occurred during September; however, there was some variability in start and end dates among years (Table 1). The median year-day for the surface trawl survey during all years (2003–2018) was 256 (September 12).

A multi-year distribution map of juvenile Pink salmon in the north-

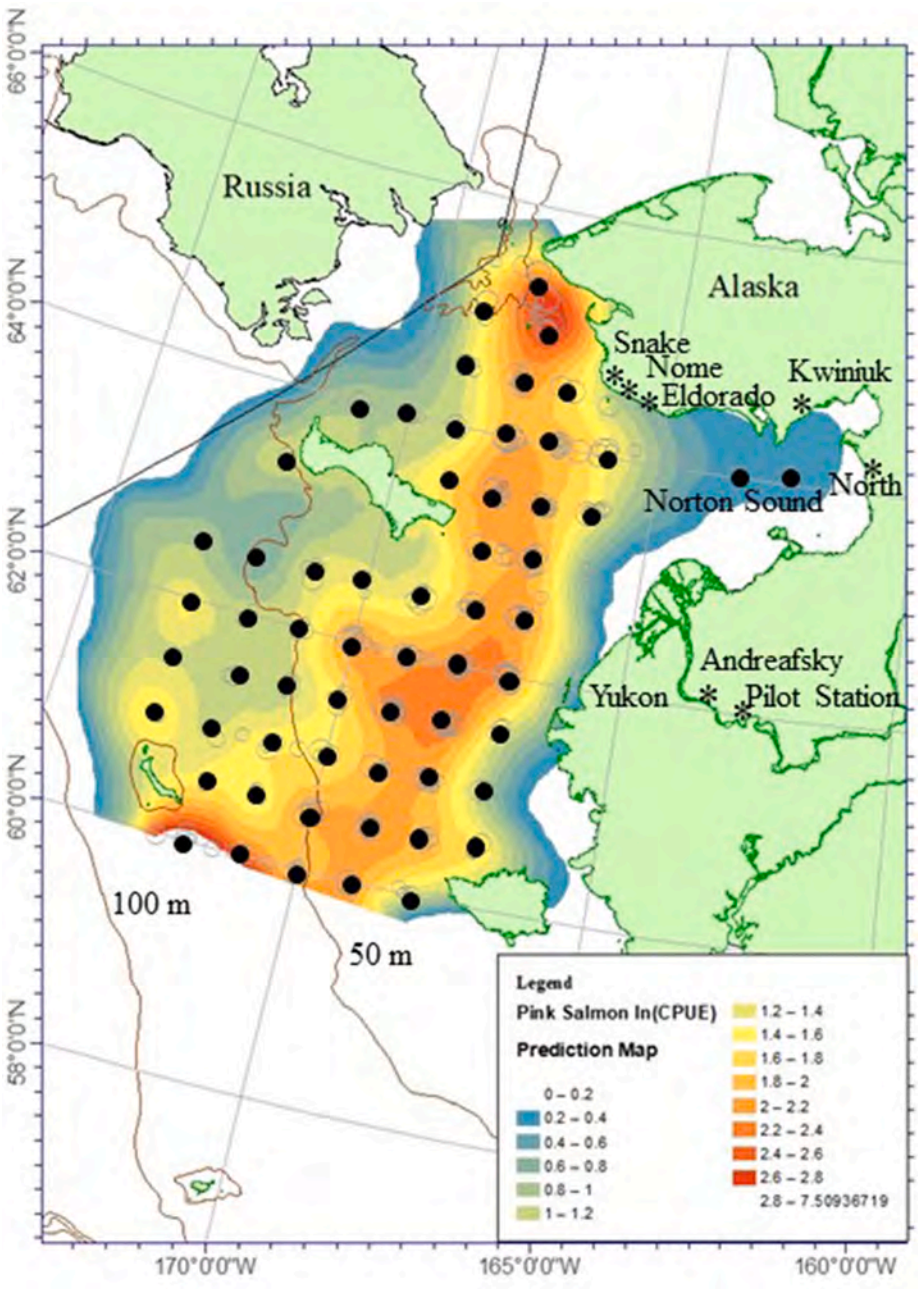

Fig. 2. Typical station grid (black dots) sampled during late August to September (2003–2018; excluding 2008) surface trawl surveys of the Northern Bering Sea. Lines indicate the 50 m and 100 m depth contours. Spatial distribution of juvenile Pink salmon based on catch data (ln CPUE, catch per unit effort, scaled to average effort km^2). Color contours are from the neighborhood kriging prediction surface of ln(CPUE). The map includes locations for Norton Sound region and Yukon River adult Pink salmon escapement index rivers (Snake, Eldorado, Kwiniuk, Yukon, Andreafsky) and the Pilot Station index.

ern Bering Sea using the standardized catch estimated as:

$$C\_std_{i,y} = \frac{C_{i,y}}{E_{i,y}}\overline{E}$$

where $C_{i,y}$ is the number of juvenile Pink salmon captured at station i during year y, $E_{i,y}$ is the area (km^2) swept by the trawl and $\overline{E}$ is the average effort (km^2) (Murphy et al., 2017). Zero catch boundary conditions were added to land masses, and the prediction surface was estimated with a neighborhood kriging model (Murphy et al., 2017).

Fish captured in the trawl were sorted to species. Subsamples of up to $n = 50$ juvenile Pink salmon were randomly selected, and these fish were measured to fork length (nearest mm) and weighed (nearest gram). Juvenile pink salmon fork length and weight were adjusted to take into account the annual differences in the surface trawl survey median year-day that could influence our interpretation of juvenile Pink salmon size due to differences in size of juveniles that could occur over the course of the survey period. We estimated adjusted length and weight by:

$$L_{J\,i,y} = \left(YD_{Capture\ j,i,y} - 256\right)*1.18mm$$

$$W_{j,i,y} = \left(YD_{Capture\ j,i,y} - 256\right)*0.2g$$

where $L_{j,i,y}$ and $W_{j,i,y}$ are the length and weight of a juvenile Pink salmon j caught at station i during year y, $YD_{Capture\ j,\ i,\ y}$ is the year-day of capture of the juvenile Pink salmon j at station i during year y, 256 is the median year-day (September 12) for all years (2003–2018) of the surface trawl survey, and 1.18 mm and 0.2 g are the estimated daily growth rate in length (Moss et al., 2009) and weight (Grant et al., 2009) for juvenile Pink salmon.

An abundance index of juvenile Pink salmon for the northern Bering Sea was based on catch per unit effort (CPUE, catch per km^2) where the number of juvenile Pink salmon caught at each station was divided by the area swept by the trawl. We used an index of relative abundance and

Table 1
The year, survey timing (start and end day), average date adjustment in days (Adj. days), average observed and adjusted (Adj.) length (L, mm), weight (W, g) and standard error (SE) for the number (N) of juvenile pink salmon sampled in the northeastern Bering Sea during 2003–2018. * no survey conducted in the NBS during 2008.

Year	Survey Timing		Adj.	N	L	SE	Adj. L	SE	W	SE	Adj. W	SE
	Start	End	(days)		(mm)		(mm)		(g)		(g)	
2003	21-Aug	8-Oct	8	550	167.0	1.4	176.6	2.4	45.9	1.1	47.5	1.3
2004	10-Sep	30-Sep	8	622	192.6	0.9	202.3	0.9	70.8	1.1	72.5	1.1
2005	17-Sep	3-Oct	16	287	188.6	1.2	207.5	1.3	63.1	1.3	66.4	1.3
2006	31-Aug	19-Sep	−2	353	150.8	0.7	148.5	0.8	29.3	0.4	28.8	0.5
2007	14-Sep	1-Oct	11	1098	186.8	0.5	199.9	0.6	64.4	0.7	66.6	0.7
2009*	30-Aug	13-Sep	−4	365	160.6	0.7	155.7	0.9	38.3	0.6	37.5	0.6
2010	10-Sep	4-Oct	10	189	179.4	1.2	190.9	1.7	54.3	1.3	56.3	1.4
2011	29-Aug	17-Sep	−8	417	145.0	0.9	135.5	1.0	27.9	0.6	26.2	0.6
2012	11-Sep	25-Sep	8	110	157.9	0.9	167.9	1.2	35.4	0.7	37.1	0.7
2013	10-Sep	24-Sep	6	684	174.2	0.5	181.3	0.6	50.6	0.5	51.7	0.5
2014	4-Sep	22-Sep	−1	372	168.7	0.8	167.8	1.0	48.5	0.8	48.3	0.8
2015	2-Sep	16-Sep	−4	983	161.4	0.8	156.2	0.9	42.4	0.7	41.6	0.7
2016	28-Aug	12-Sep	−10	395	153.9	1.2	141.9	1.4	37.3	1.1	35.2	1.2
2017	27-Aug	8-Sep	−9	848	136.4	1.0	125.4	1.0	25.7	0.6	23.9	0.7
2018	3-Sep	15-Sep	−4	1171	152.9	0.5	148.5	0.6	33.4	0.3	32.6	0.3

not actual abundance because juvenile Pink salmon captured at the outer regions of our survey may be from stocks other than Yukon River and North Sound (Farley et al., 2005). Area swept by the trawl at each station was determined by multiplying the distance (km) traveled by the horizontal distance (km) of the trawl opening that was measured by net sonar. The distance traveled was estimated using:

$$\boldsymbol{x} = \cos^{-1}(\sin(\boldsymbol{lat}_s) * \sin(\boldsymbol{lat}_e) + \cos(\boldsymbol{lat}_s) * \cos(\boldsymbol{lat}_e) * \cos(\Delta\mathbf{lon})) * 6371,$$

where lat_s is the trawl start latitude position in radians, lat_e is the trawl end latitude position in radians, Δlon is the longitude distance between the start and end trawl positions in radians, and 6371 is the earth radius in km (Murphy et al., 2017).

Mixed-layer depth expansions were applied to the area-swept indices of juvenile Pink salmon to generate an abundance index for juvenile Pink salmon as described in Murphy et al. (2017). Mixed layer depth expansions account for changes in the vertical extent of trawl sampling depths and juvenile habitat over time. Summer sea temperatures below the mixed layer depth in the northern Bering Sea are generally cold (<2 °C), which are not suitable habitat for juvenile salmon (Brett, 1952); therefore, this correction is used to provide a reasonable approximation for the vertical distribution of juvenile salmon in the northern Bering Sea (Murphy et al., 2017). Oceanographic characteristics from the CTD casts were used to determine the mixed layer depth defined as the depth where seawater density (sigma-theta) increased by 0.10 kg m^{-3} relative to the density at 5 m (Danielson et al., 2011). Mixed layer depth was set to 5 m off bottom when the entire water column was vertically mixed. The mixed layer depth adjustments applied to annual relative abundance estimates, θ_y, were estimated by

$$\boldsymbol{\theta}_y = \frac{\sum_i \boldsymbol{M}_{i,y}\boldsymbol{C}_{i,y}}{\sum_i \boldsymbol{C}_{i,y}}$$

where $C_{i,y}$ is the number of juvenile Pink salmon captured at station i during year y, and $M_{i,y}$ is equal to the ratio of mixed-layer depth to trawl depth when trawl depth is shallower than mixed layer depth, and 1.0 when trawl depth is below the mixed-layer depth. The juvenile abundance index for Pink salmon was estimated by multiplying the average ln(CPUE) by θ_y

$$\boldsymbol{N}_y = \frac{\sum_i \boldsymbol{ln}\left(\boldsymbol{CPUE}_{i,y}\right)}{\boldsymbol{n}_y} * \boldsymbol{\theta}_y$$

where n is the number of stations i sampled during year y.

Life-history models were constructed for northern Bering Sea Pink salmon using multiple sources of data. The models included the juvenile Pink salmon abundance index and adjusted average juvenile weight during the northern Bering Sea surface trawl survey. A subset (2003–2018) of Nome air temperatures and summer SSTs described above were used in the life-history models to represent freshwater and early marine conditions for relationships with juvenile Pink salmon relative abundance and adult returns. Annual estimates of adult Pink salmon returns and spawners to the Northern Bering Sea region were developed from a subset of the available annual estimates (2003–2018) of adult Pink salmon returns and spawners to the Yukon River and Norton Sound region.

Because the juvenile Pink salmon relative abundance is estimated during September, the life-history model for juvenile abundance incorporates potential freshwater and early marine effects

$$\ln(\text{juvenile relative abundance}_{\,t}) = \ln(\text{adult spawners}_{(t\text{-}1)}) + \text{Nome air temp} + \ln(\text{adjusted weight}_{\,t}) + \text{SST}_t$$

and includes the number of adult Pink salmon that spawned during the prior year, stream temperature during their freshwater life history stage, adjusted weight of juvenile salmon during year t, and summer sea surface temperatures during year t.

The life-history model relating early marine effects with adult Pink salmon returns

$$\ln(\text{adult returns}_{\,(t+1)}) = \ln(\text{juvenile relative abundance}_{\,t}) + \text{SST}_t + \ln(\text{adjusted weight}_{\,t})$$

examined the relationship between the number of adult Pink salmon returning the following year to the region with juvenile abundance, juvenile weight (condition), and sea temperature in the early marine period. We applied the step-wise variable selection procedure described above to select the most parsimonious life-history models that explain production dynamics of Pink salmon in the northern Bering Sea region.

3. Results

3.1. Life-cycle productivity

The adult Pink salmon return and spawner indices to the Norton Sound region and Yukon River during 1995–2018 ranged between a few thousand to several million (Table 2). More adult Pink salmon return during even years than odd years, especially within the Norton Sound region. However, adult returns to the Norton Sound region during the recent odd year of 2017 was much higher (>2 million) than most of the previous odd years (generally < 1 million except for 2005) within the time series. Overall, productivity (ln R/S) appears higher during the late 1990s and from 2013 to 2015 (Fig. 3). The correlation between Yukon

Table 2
Total number of returns and spawners for Pink salmon to the Norton Sound region and Yukon River (1995–2018) and the average Nome Air temperatures (°C, August $_t$ to June $_{t+1}$) and average summer sea surface temperatures during June to September (°C, SST $_{t+1}$).

Adult	**Norton Sound** Region		**Yukon River**		**Nome** Air	Summer
Year	Returns	Spawners	Returns	Spawners	Temp.	SST
1995	**169,496**	**49,409**	**55,284**	**55,137**	**−4.6**	**7.2**
1996	**3,089,682**	**2,535,593**	**216,582**	**214,837**	**−3.3**	**6.7**
1997	**189,439**	**163,728**	**4519**	**4301**	**−3.9**	**7.5**
1998	**3,712,761**	**3,070,848**	**336,166**	**330,624**	**−3.1**	**6.3**
1999	**95,302**	**73,077**	**4771**	**4716**	**−5.5**	**5.7**
2000	**2,091,074**	**1,883,867**	**105,461**	**104,866**	**−4.6**	**6.4**
2001	**109,878**	**79,706**	**3675**	**3666**	**−2.6**	**5.7**
2002	**2,300,537**	**2,239,565**	**298,111**	**289,688**	**−4.5**	**7.8**
2003	**441,387**	**392,827**	**17,864**	**15,673**	**−1.9**	**7.8**
2004	**6,513,682**	**6,432,486**	**808,739**	**799,009**	**−2.8**	**9.2**
2005	**2,652,592**	**2,594,334**	**103,255**	**100,121**	**−2.6**	**7.9**
2006	**5,825,726**	**5,763,830**	**384,274**	**379,366**	**−5.1**	**6.5**
2007	**734,723**	**708,669**	**138,492**	**136,374**	**−3.3**	**8.4**
2008	**4,069,508**	**3,932,201**	**793,747**	**770,035**	**−4.4**	**6.6**
2009	**320,631**	**275,834**	**39,225**	**36,924**	**−5.4**	**6.5**
2010	**1,560,810**	**1,484,282**	**1,261,091**	**1,256,789**	**−4.7**	**7.1**
2011	**231,000**	**206,127**	**13,298**	**10,973**	**−3.1**	**6.3**
2012	**1,265,834**	**1,013,565**	**500,227**	**495,026**	**−6.2**	**6.4**
2013	**102,117**	**73,928**	**7791**	**6715**	**−4.9**	**7.0**
2014	**960,447**	**735,843**	**799,804**	**738,121**	**−1.7**	**8.2**
2015	**716,045**	**626,383**	**50,632**	**40,473**	**−2.0**	**7.1**
2016	**4,638,943**	**4,378,422**	**1,755,412**	**1,619,366**	**−1.1**	**8.9**
2017	**2,780,199**	**2,723,866**	**199,040**	**196,573**	**−2.9**	**8.9**
2018	**6,253,239**	**6,176,411**	**825,957**	**785,957**	**−1.4**	**9.3**

River and Norton Sound region productivity was positive and significant ($r = 0.47$, $p = 0.02$).

The average Nome air temperature (proxy for freshwater temperatures) for the period covering adult Pink salmon spawning, fry emergence and smolt migration to the marine environment was below 0 °C during each year (Table 2). Coldest temperatures occurred during 1999, 2009 and 2012 with warmer temperatures occurring during 2003–2005 and 2014 to 2016. The summer SSTs covering the period of juvenile Pink salmon residence in the northeastern Bering Sea had similar trends with coolest temperatures during the late 1990s and during 2008–2012 and warmer temperatures during the early 2000s and from 2015 to 2017 (Table 2). The correlation between Nome air temperatures and summer SSTs was positive and significant ($r = 0.61$, $p = 0.002$).

The life-cycle model fits and results for the Norton Sound region and Yukon River are shown in Fig. 1a and b and Table 3. For the Yukon River, the most parsimonious Cushing model included the natural log of spawners and summer SST which explained 71% of the variation in the natural log of returning adult Pink salmon. However, the parameter estimate for summer SST is not significant ($p = 0.11$) in the model. The most parsimonious Ricker model included SST, explaining 11% of the variation in adult Pink salmon production to the Yukon River; neither parameter estimates for number of spawners and SST were significant ($p = 0.232$ and 0.124, respectively). For Norton Sound stocks, the most parsimonious Cushing model was one that included the natural log of spawners and summer SST, explaining 77% of the variation in the natural log of adult Pink salmon returns to the region. The most parsimonious Ricker model was one that contained spawners and summer SST, explaining 53% of the variation in the natural log of adult Pink salmon production to the region. No significant autocorrelation between consecutive years is evident in the residuals of the most parsimonious models (Fig. 4 a-c). In addition, the gamma parameter for the Cushing model was 0.66 for Norton Sound stocks and 0.82 for the Yukon River

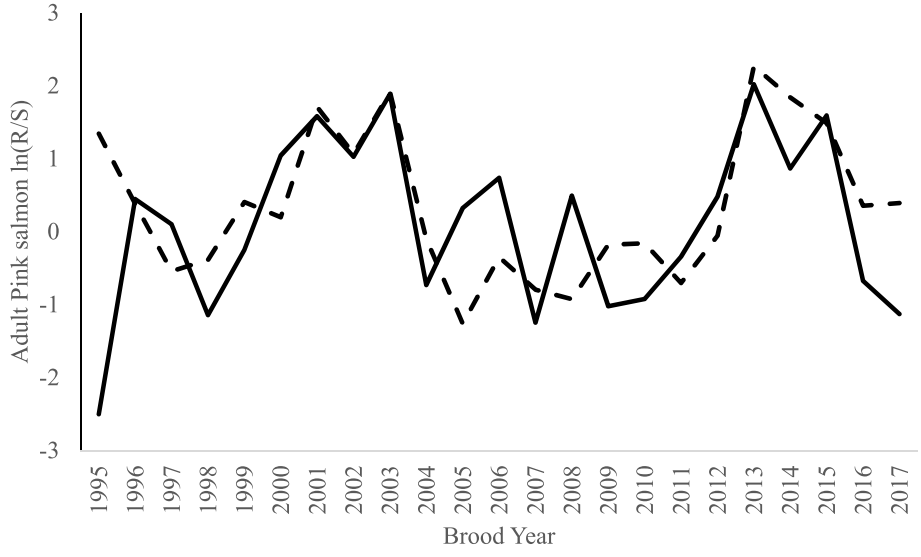

Fig. 3. The natural log of adult Pink salmon returns per spawner for the Yukon River (solid line) and Norton Sound region (dashed line) for brood years 1995–2017.

Table 3
Results of the step-wise model selection for Yukon River and Norton Sound region Pink salmon life-cycle models (1995–2018). Statistics include C_p, residual standard error (*RSS*), coefficient of variation (R^2), the mean square error of the true regression model $\hat{\sigma}^2$, parameter estimate (Estimate) and standard error (SE), *t* value of the parameter estimate and significance of the estimate (Prob).

Region	Model	*Cp*	*RSS*	$\hat{\sigma}^2$	Estimate	SE	*t* value	Prob	R^2
Yukon									
	Cushing								
				1.27					0.71
	Intercept Only	1.0	24.2		−0.47	2.07	−0.23	0.821	
	ln(spawners)	42.9	80.1		0.82	0.12	6.80	0.000	
	Summer Sea Surface Temp	1.7	27.6		0.34	0.21	1.69	0.107	
	Ricker								
				1.31					0.11
	Intercept Only	0.5	26.8		−2.44	1.61	−1.52	0.144	
	Summer Sea Surface Temp	1.0	30.1		0.35	0.22	1.60	0.124	
Norton Sound									
	Cushing								
				0.52					0.77
	Intercept Only	1.4	10.2		1.10	1.59	0.68	0.504	
	ln(spawners)	41.7	32.4		0.66	0.10	6.61	0.000	
	Summer Sea Surface Temp	13.9	17.8		0.54	0.14	3.88	0.001	
	Ricker								
				0.55					0.53
	Intercept Only	1.1	10.5		−3.36	1.04	−3.24	0.004	
	spawners	9.6	16.3		0.00	0.00	−3.32	0.003	
	Summer Sea Surface Temp	14.5	19.0		0.57	0.14	4.02	0.001	

stock suggesting that density-dependence on the spawning grounds may be more evident in the Norton Sound stocks than the Yukon River stocks.

3.2. Early life-history

Juvenile Pink salmon are distributed throughout the northern Bering Sea during late summer months (Fig. 2). The region of highest catch

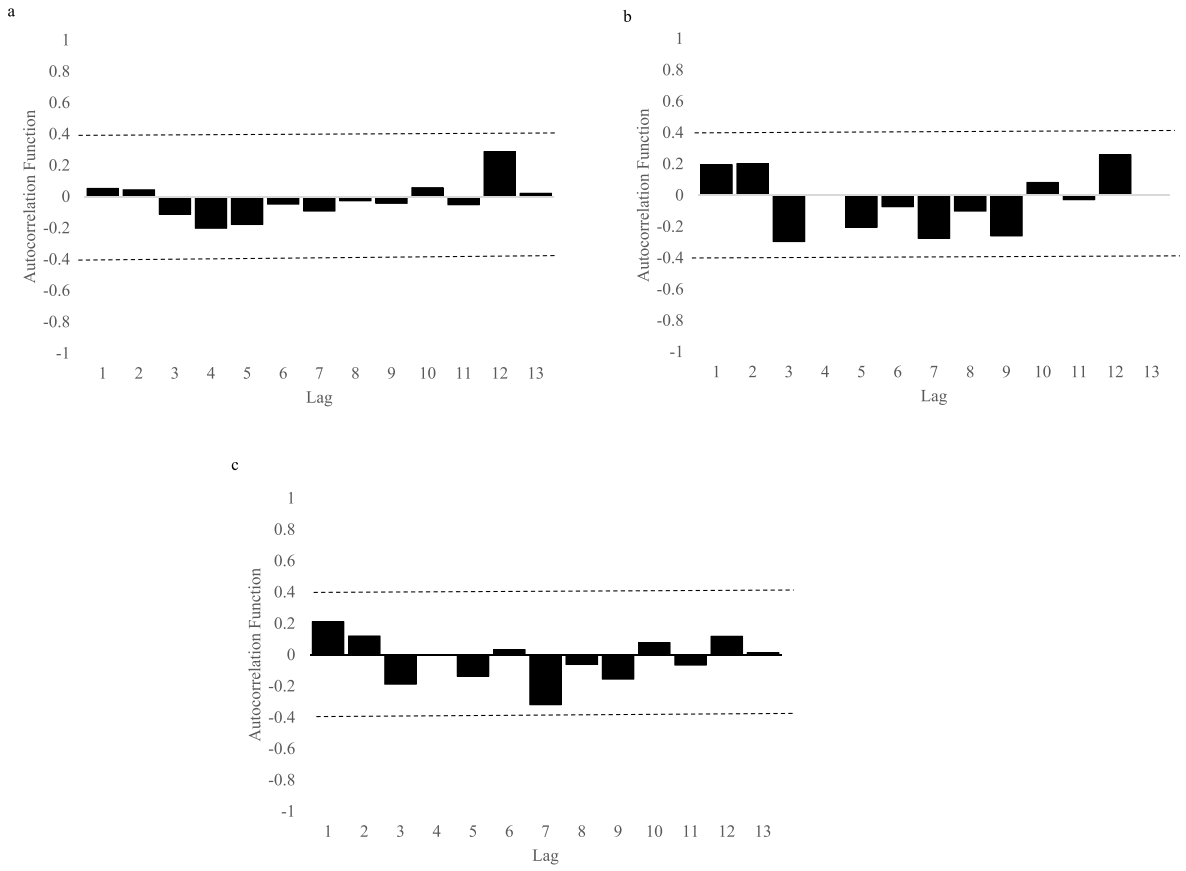

Fig. 4. The autocorrelation functions for residuals of the most parsimonious life-cycle models including the Cushing model for the Yukon River (a), the Cushing model (b) and Ricker model (c) for the Norton Sound region. The dashed lines are the upper and lower bounds for significant autocorrelation.

densities occurred within the shallow (<50 m) coastal habitats from the northern to southern margins of the northern Bering Sea survey area. Observed average size of juvenile Pink salmon varied from 136 to 193 mm (25.7–70.8 g) with an average of 164.6 mm (44.8 g) (Table 1). Adjustments for survey timing increased the overall average size of juvenile Pink salmon to 165.6 mm (44.9 g) with the largest differences occurring during 2005 and 2007. Juvenile Pink salmon were generally smaller during 2006, 2009, 2011 and from 2015 to 2018 (Fig. 5a and b). Moreover, the number of larger fish that occurred as outliers to the sample of juvenile Pink salmon was highest during 2007 and 2016 to 2018 (Fig. 5b), years that coincided with warm sea temperatures. Mixed layer depth corrections ranged from a low of 1.00 (<1%) during 2016 to a high of 1.79 (79%) during 2005 with an overall average of 1.22 (22%) to juvenile Pink salmon relative abundance estimates (Table 4). Juvenile Pink salmon relative abundance was high during 2003–2007 and again from 2013 to 2018 with lower abundance during 2009–2012.

The step-wise model selection statistics to explore life-history events that may impact Pink salmon production in fresh water and the early marine period are shown in Table 5. For the juvenile abundance model, freshwater effects including the number of spawners and Nome air temperatures were significant and explained 55% of the variation in juvenile Pink salmon relative abundance during September (Fig. 6). The step-wise selection process removed summer SST and the natural log of weight, (both represent early marine effects) as these variables did not contribute to the most parsimious model. For the adult return model, the *Cp* values for the natural log of weight and sea temperature during September were lower than the intercept only model, suggesting these variables could be removed. The most parsimonious model (Fig. 7) that included juvenile Pink salmon relative abundance explained 62% of the variation in adult Pink salmon returns to the northern Bering Sea region.

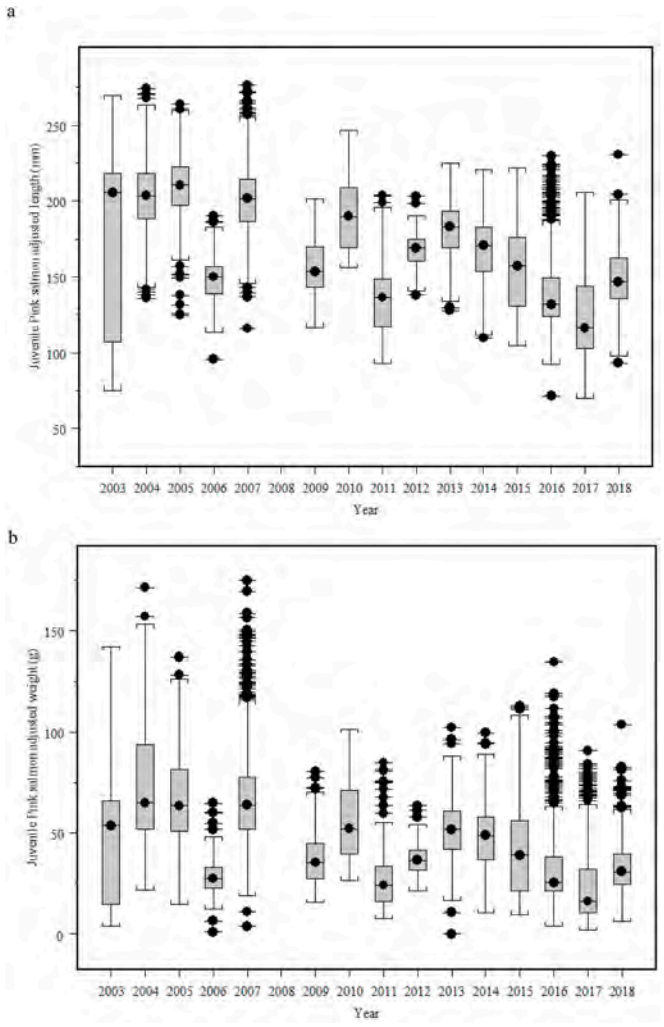

Fig. 5. Box plots of juvenile Pink salmon adjusted a) length (mm) and b) weight (g) during late August to September 2003 to 2018 (no survey was conducted during 2008) in the northeastern Bering Sea. Length and weight were adjusted to September 12 of each year. The solid horizontal line in the box plot is located at the median of the data, and the upper and lower ends of the box are located at the upper quartile and lower quartile of the data, respectively. The lines extending above and below the box indicate the variability outside the upper and lower quartiles.

Table 4
Juvenile Pink salmon natural log of the catch per unit effort (CPUE), relative abundance (defined as the natural log of the adjusted CPUE), average sea temperature above the mixed layer depth (°C), and average August$_{t-1}$ to June$_t$ air temperatures (°C) in Nome, Alaska during 2003–2018. * no ship board data available for 2008.

Juvenile Year	Mixed Layer Depth Adjustment	ln (CPUE)	Relative Abundance	Summer SST	Nome Air Temp.
2003	1.78	2.54	4.5	7.8	−1.9
2004	1.46	2.51	3.7	9.2	−2.8
2005	1.79	1.96	3.5	7.9	−2.6
2006	1.20	1.69	2.0	6.5	−5.1
2007	1.18	3.08	3.6	8.4	−3.3
2009*	1.01	1.38	1.4	6.5	−5.4
2010	1.08	1.43	1.5	7.1	−4.7
2011	1.16	1.36	1.6	6.3	−3.1
2012	1.21	0.84	1.0	6.4	−6.2
2013	1.02	3.09	3.1	7.0	−4.9
2014	1.04	2.00	2.1	8.2	−1.7
2015	1.26	4.30	5.4	7.1	−2.0
2016	1.00	2.65	2.7	8.9	−1.1
2017	1.03	3.94	4.1	8.9	−2.9
2018	1.04	4.22	4.4	9.3	−1.4

4. Discussion

Our analysis provides new insights into production dynamics of Yukon River and Norton Sound Pink salmon stocks. The best fit life-cycle models suggest that density-dependence on the spawning grounds may be low within the Yukon River but may be present within river systems draining into Norton Sound. We interpret this result to indicate that there may be potential for increased freshwater production especially within the Yukon River. The best fit life-history models suggest that the number of juvenile Pink salmon during September is a function of the number of adult Pink salmon spawners and Nome air temperature, reflecting the importance of freshwater production to overall numbers of juvenile Pink salmon. In addition, juvenile Pink salmon relative abundance during September is a good predictor of the number of adult Pink salmon that return the following year indicating that conditions in fresh water and early marine environments are key to our understanding of Pink salmon production dynamics in this region.

Our analysis of the productivity patterns highlights the synchrony (positive, significant correlation) in temporal variation among Pink salmon stocks in the northeastern Bering Sea. These patterns have been found for Pink salmon stocks across western North America (Malick and Cox, 2016) as well as other salmon stocks that show positive correlation at regional scales (Pyper et al., 2001, 2002; 2005; Peterman et al., 1998; Peterman and Dorner, 2012; Dorner et al., 2017). The synchrony in production suggests shared factors that are affecting Pink salmon stocks throughout the study region. The best fit life-cycle models included summer SSTs indicating the potential importance of sea temperature on Pink salmon production in this region. This result is similar to other analyses of salmon productivity in the Northeast Pacific Ocean (Mueter et al., 2002), illustrating the importance of summer sea temperatures to production of Pink salmon in the northeastern Bering Sea.

The best fit life-history models were those that included the number

Table 5
Results of the step-wise model selection for Pink salmon freshwater and early marine life-history events. Statistics include C_p, residual standard error (*RSS*), the mean square error of the true regression model $\hat{\sigma}^2$, coefficient of variation (R^2), parameter estimate (Estimate) and standard error (SE), *t* value of the parameter estimate and significance of the estimate (Prob).

Model	C_p	*RSS*	δ^2	Estimate	SE	*t* value	Prob	R^2
Juvenile Abundance Model								
			0.98					0.55
Intercept Only	17.2	9.8		−9.60	3.50	−2.74	0.018	
ln(spawners)	18.4	14.5		0.35	0.19	1.85	0.090	
Nome Air Temp	25.2	21.3		0.29	0.09	3.26	0.007	
Adult Return Model								
			0.75					0.62
Intercept Only	1.1	8.4		12.3	0.52	23.6	0.000	
Juvenile Index	17.3	22.0		0.74	0.16	4.6	0.000	

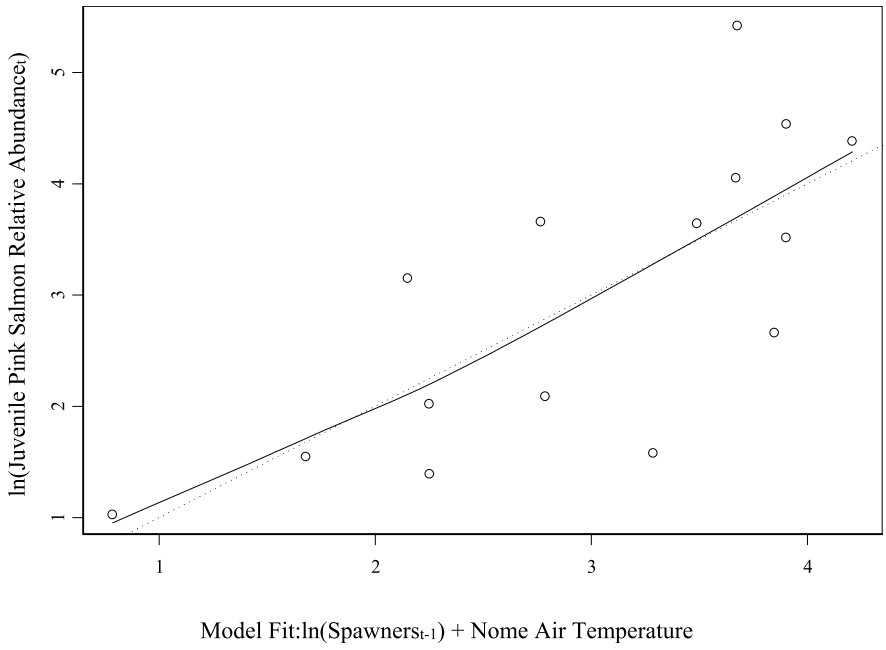

Fig. 6. The relationship (dark line) between the natural log of juvenile Pink salmon relative abundance and the natural log of adult Pink salmon spawner index with Nome Air temperature (open circles; 2003 to 2018).

of spawners, Nome air temperatures and the relative abundance of juvenile Pink salmon. For the juvenile abundance model, we found positive, significant relationships between annual juvenile Pink salmon relative abundance and the number of adult Pink salmon spawners the prior year along with annual average Nome air temperatures. This result supports the hypothesis that warming air temperatures in this region (as a proxy for river and stream temperatures) may be improving freshwater production leading to higher numbers of juvenile Pink salmon in the northern Bering Sea region during summer months. For the adult Pink salmon return model, the number of juvenile Pink salmon in the northern Bering Sea region during late summer predict the number of adults returning the following year. While summer SSTs were not included in these models, we note that there is a significant positive correlation between SSTs and Nome Air temperatures that may indicate that temperature, either fresh water or early marine are important for Pink salmon production in this region.

These relationships suggest a possible connection between changes in fresh water and early marine environments and subsequent adult production. However, the amount of variation in juvenile Pink salmon relative abundance explained by adding adult Pink salmon spawners and Nome air temperatures was less than the amount of variation explained in the adult Pink salmon returns by the juvenile index. This suggests other factors affecting early marine survival of juvenile Pink salmon in the northern Bering Sea during summer months could influence total production or that Nome air temperatures may not fully reflect the freshwater temperature dynamics thereby reducing the influence of juvenile Pink salmon relative abundance.

Although freshwater conditions in the Arctic are known to limit salmon production, it can be difficult to predict how salmon will respond to warming freshwater habitats (Nielson et al., 2013). A case study on projecting effects of climate warming on Atlantic salmon suggested that northern rivers could become more productive with increased colonization success northward and diminished production to river systems in the southern range (Reist et al., 2006). Density-dependent mortality due to too many spawners on the river, temperature, and stream flows are all factors contributing to fluctuations in freshwater survival (Heard, 1991). In addition, stream habitats with a minimum temperature of 4 °C during spawning and temperatures above 2 °C during egg incubation were found to benefit establishment of Chum and Pink salmon in high latitude and high elevation watersheds (Dunmall et al., 2016).

Nome air temperatures from August (spawning year) to June the following year were used as a proxy for freshwater stream temperatures in the region. The average air temperature was below 0 °C which is most likely colder than stream temperatures, especially during summer

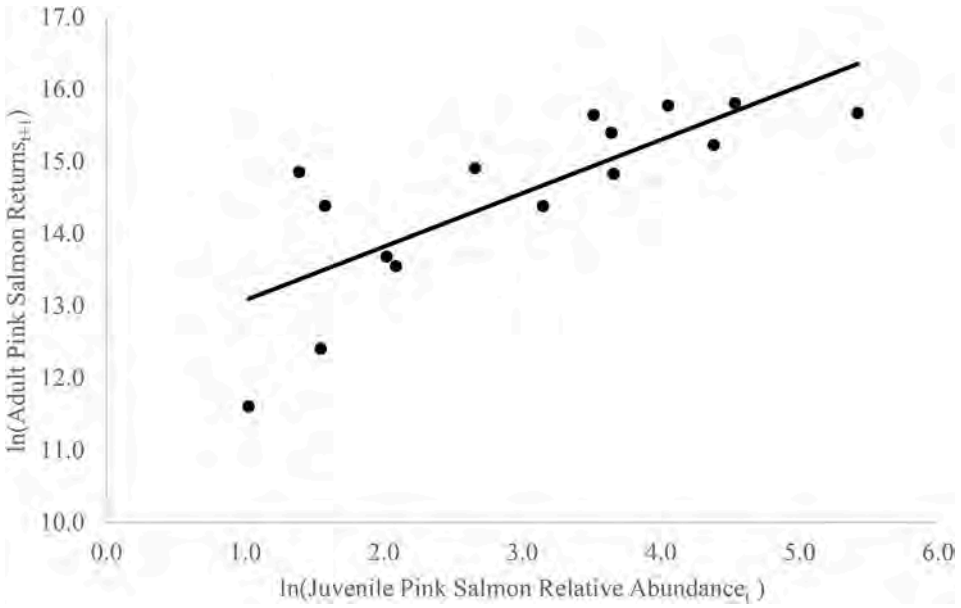

Fig. 7. The relationship (dark line) between the natural log of adult Pink salmon return index to the Yukon River and Norton Sound region and the natural log of the relative abundance of juvenile Pink salmon from the surface trawl surveys (black dots; 2003 to 2018).

months. Limited information on stream temperatures at various locations along the Pilgrim River (north of Nome, Alaska) during the summer months of 2013–2016 show that temperatures varied between 8.4 °C and 18.7 °C (Carey et al., 2019). These temperatures are well above the minimum temperature of 4 °C for successful Pink salmon spawning suggested in Dunmall et al. (2016). In addition, some river systems in the Norton Sound region experienced extremely high temperatures during summer 2019 (one river was reported near 21°C; pers. Comm. Gay Sheffield) that were believed to contribute to observed adult Pink salmon die offs on the spawning grounds. Given the nature of rapid warming in the region with respect to the marine ecosystem (Baker et al., 2020; Danielson et al., 2020; Huntington et al., 2020), it is likely that freshwater temperatures during winter and summer months in the Norton Sound and Yukon River drainage are warming enough to both improve survival and to open new areas along rivers and streams for Pink salmon to establish thereby increasing production potential in this region.

Pink salmon returns to this region are typically higher during even years (odd year juvenile Pink salmon brood), but more recently the returns to the Norton Sound region during odd years have also been high. Studies have indicated that embryonic survival of the even-year broodline for British Columbia Pink salmon is higher than the odd-year broodline in a cold (4 °C) incubation environment with higher alevin and fry growth observed (Beacham and Murray, 1988). Increasing dominance of odd-year brood lines has been documented with the inference of favorable survival during period of warming freshwater habitats (Irvin et al., 2014). The difference in temperature tolerance between the even and odd-year brood lines has been linked to dispersal after the Pleistocene Era glaciation some 10,000 years ago (Beacham et al., 2012), where even-year broodlines likely survived the glaciation in the northern refugia (Aspinwall, 1974) and the odd-year brood line may have occupied more southern refugia (McPhail and Linsey, 1970). Therefore, warming freshwater habitats in the northern regions may be improving odd-year broodline survival, leading to more adult Pink salmon returning during odd years.

Earlier studies on juvenile Pink salmon marine ecology in the northern Bering Sea found that warmer sea surface temperatures during spring and summer were positively related to their growth (Andrews et al., 2009; Farley et al., 2009; Wechter et al., 2017). Presumably, higher growth rates during their early marine period would reduce size-selective mortality and lead to higher survival for juvenile salmon (Parker, 1968). We found that juvenile Pink salmon adjusted weight and length declined over the course of our time series even though sea temperatures were increasing during the survey period. This result was counter-intuitive as growth rates typically increase with temperature. Dispersal, changes in prey quality and quantity, and migratory patterns of juvenile Pink salmon could be contributing to this apparent negative relationship between size and temperature.

Although juvenile Pink salmon were distributed throughout the northern Bering Sea survey region, the vanguard of their distribution can be under sampled, particularly during warm years. Moss et al. (2009) examined juvenile Pink salmon distribution and size within the northern Bering Sea and Chukchi Sea during 2007. They found that the highest catches of juvenile Pink salmon were in the Chukchi Sea and that these juveniles were larger than those in the northern Bering Sea region. The year 2007 was characterized by exceptionally warm sea temperatures in the Chukchi Sea and significantly increased annual mean water transport through the Bering Strait (Woodgate et al., 2010). Moreover, the water flow from the northern Bering Sea through the Bering Strait and into the Chukchi Sea has increased by 50% over the past two decades (Woodgate et al., 2015). Given that the sea temperatures have been much higher during recent years of our survey period, it is possible that juvenile Pink salmon from the northern Bering Sea region were advected north with the largest fish at the vanguard of the migration through the Bering Strait and into the Chukchi Sea and out of the northern Bering Sea survey area.

The large numbers of juvenile Pink salmon found near the Bering Strait could also be related to higher Pink salmon production in the northern regions of the PAR. Adult Pink salmon have become more prevalent in subsistence catches in the high Arctic particularly during even-numbered years (Dumnall et al., 2013; Dunmall et al., 2018). Further, the large catch of juvenile Pink salmon in the Chukchi Sea during 2007 (Moss et al., 2009) coincided with higher adult returns to the Beaufort Sea coast during 2008 (Dunmall et al., 2013, 2018). While Pink salmon appear to be poised to take advantage of warm-water thermal refugia within several watersheds of the Arctic (North American North Slope; Dunmall et al., 2016), it is unknown whether spawning has been successful in this region. Adult Pink salmon returns to the northern regions of the Kamchatka peninsula have recently increased (Klovach et al., 2018) and record returns have occurred during

most recent years to Norton Sound rivers (Menard et al., 2018). Farley et al. (2005) speculated that juvenile Pink salmon caught offshore in the northern Bering Sea could be of Russian origin. In addition, Kondzela et al. (2009) found that most of the juvenile Chum salmon caught in the Bering Strait area during 2007 were from Anady-Kanchalan rivers in the northern Kamchatka region. In any case, stock-specific juvenile data for Pink salmon are needed to better understand movement and production dynamics during this time of rapid warming.

The significant correlation between juvenile Pink salmon relative abundance and adult returns the following year suggests that the second critical period has not contributed as much to the annual variation in Pink salmon production to the northern Bering Sea region. The addition of sea surface temperature and weight did not improve our model for adult Pink salmon returns to the northern Bering Sea region. Our result is similar to studies that utilized juvenile salmon abundance indices from surface trawl data to predict adult returns. For example, a stock-specific juvenile Yukon River Chinook salmon index collected in the northern Bering Sea is used to provide management advice for expected run sizes (Murphy et al., 2017). Within southeast Alaska, adult Pink salmon returns are predicted using a juvenile Pink salmon index collected during summer months within Icy Strait (Orsi et al., 2016). Both applications are used to inform management decisions and provide more accurate outlooks than previous models.

Lastly, it is important to note results from the life-cycle models that utilize harvest and spawner data for Pink salmon to the Yukon River and Norton Sound regions are limited by incomplete data. Our estimates of Pink salmon total number of returns and spawners to the Yukon River and Norton Sound region are considered indices of abundance as total accounting of Pink salmon abundance in this region is not currently possible. Total harvest includes stocks not indexed in the spawning escapement and escapement assessment programs are designed to estimate other salmon species and do not fully account for Pink salmon abundance. Productivity values and inferences are presented here to illustrate relative change over time or relationships to environmental parameters, and should not be considered absolute values. Consequently, our interpretation of the results from these models should be considered cautiously. In addition, separate analyses of odd and even year broodlines may be warranted given that they are ecologically and reproductively isolated, suggesting that stock-recruitment relationships may differ between broodlines. The adult return and spawner time series for the region are short; therefore, combining the two broodlines allowed a more complete examination of relationships between environmental conditions and indices of productivity in the context of changing climate conditions. Additional analyses into these relationships should be explored in the future, as the extension of time series and collection of new environmental data enable such models.

Continued monitoring of salmon through life-cycle and life-history models will provide insight into how warming Arctic climate conditions are impacting critical periods in salmon production. Our analyses suggest that Pink salmon production in the northeastern Bering Sea is driven by freshwater and early marine habitat dynamics. While we used air temperature as a proxy for stream temperature, broad-scale predictive models of climate change in the Arctic provide little information about feedback processes contributing to local conditions (Nielsen et al., 2013). To explore emerging connections within freshwater habitats, local knowledge regarding stream conditions, salmon abundance and spawning locations will be needed for perspective to current observations. Further monitoring of stream temperatures, flow and ice dynamics will improve our understanding of how climate warming is impacting this important habitat and context to shifts in abundance northward into the high Arctic.

Declaration of competing interest

The authors declare that they have no known competing financial interests or personal relationships that could have appeared to influence the work reported in this paper.

Acknowledgements

The authors sincerely thank two anonymous reviewers for comments that greatly improved the manuscript. We also thank Jordan Watson for providing the summer sea surface temperatures for the northeastern Bering Sea. In addition, the authors thank all captains, crew, and science teams who collected these data. These samples were collected over 18 surveys with support and funding from many different entities including: Bering Sea Fisherman's Association, The Alaska Coastal Impact Assistance Program (Arctic Ecosystem Integrated Survey 2012, 2013), Bureau of Ocean and Energy Management, The Alaska Sustainable Salmon Fund, NCEAS – State of Alaska's Salmon and People and the Yukon River Drainage Fisherman's Association. This project is a collaborative effort with the Alaska Department of Fish and Game and the North Pacific Anadromous Fish Commission. The northern Bering Sea surface trawl survey is part of the NOAA Alaska Fisheries Science Center's, Bering Arctic Subarctic Integrated Survey (BASIS). This manuscript is a product of the North Pacific Research Board Arctic Integrated Ecosystem Research Program, NPRB publication number ArcticIERP-12.

Appendix A. Supplementary data

Supplementary data related to this article can be found at https://doi.org/10.1016/j.dsr2.2020.104830.

References

Andrews, A.G., Farley Jr., E.V., Moss, J.H., Murphy, J.M., Husoe, E.F., 2009. Energy density and length of juvenile Pink salmon (*Oncorhynchus gorbuscha*) in the eastern Bering Sea from 2004 to 2007: a period of relatively warm and cool sea surface temperatures. N. Pac. Anadrom. Fish Comm. 5, 183–189.

Arrigo, K.R., van Dijken, G.L., 2011. Secular trends in Arctic Ocean net primary production. J. Geophys. Res. 116, C09011. https://doi.org/10.1029/2011JC007151.

Aspinwall, N., 1974. Genetic analysis of North American populations of the Pink salmon, *Onchorhynchus gorbuscha*; possible evidence for the neutral mutation-random droft hypothesis. Evolution 28, 295–305.

Baker, M.R., Kivva, K.K., Pisareva, M., Watson, J., Selivanova, J., 2020. Shifts in the physical environment in the Pacific Arctic and implications for ecological timing and conditions. Deep Sea Res. II (this volume).

Batten, S.D., Ruggerone, G.T., Ortiz, I., 2018. Pink salmon induce a trophic cascade in plankton populations in the southern Bering Sea and around the Aleutian Islands. Fish. Oceanogr. 27, 548–559.

Beacham, T.D., McIntosh, B., MacConnachie, C., Spolsted, B., White, B.A., 2012. Population structure of Pink salmon (*Oncorynchus gorbuscha*) in British Columbia and Washington, determined with microsatellites. Fish. Bull. 110, 242–256.

Beacham, T.D., Murray, C.B., 1988. Variation in developmental biology of Pink salmon (*Oncorhynchus gorbuscha*) in British Columbia. Can. J. Zool. 66, 2634–2648.

Beamish, R.J., Mahnken, C., 2001. A critical size and period hypothesis to explain natural regulation of salmon abundance and the linkage to climate and climate change. Prog. Oceanogr. 49, 423–437.

Brett, J.R., 1952. Temperature tolerance in young Pacific salmon genus Oncorhynchus. J. Fish. Res. Board Can. 9, 265–323.

Carey, M.P., Keith, K.D., Schelske, M., Lean, C., McCormick, S.D., Regish, A., Zimmerman, C.E., 2019. Energy depletion and stress levels in Sockeye salmon migrating at the northern edge of their distribution. Trans. Am. Fish. Soc. 148, 785–797.

Carothers, C., Cotton, S., Moerlein, K., 2013. Subsistence use and knowledge of salmon in Barrow and Nuiqsut, Alaska. Final Report to OCS Study Bureau of Ocean and Energy Management 2013 – 0015.

Conitz, Jan, 2019. Abundance and Run Timing of Adult Pacific Salmon in the East Fork Andreafsky River, Yukon Delta National Wildlife Refuge. Alaska, 2018. Alaska Fisheries Data Series Number 2019-2.

Craig, P., Haldorson, L., 1986. Pacific salmon in the north American arctic. Arctic 39, 2–7.

Cushing, D.H., 1971. Dependence of recruitment on parent stock. J. Fish. Res. Board Can. 30, 1965–1976.

Danielson, S., Eisner, L., Weingartner, T., Aagaard, K., 2011. Thermal and haline variability over the central Bering Sea shelf: seasonal and interannual perspectives. Continent. Shelf Res. 31, 539–554.

Danielson, S.L., Ahkinga, O., Ashjian, C., Basyuk, E., Cooper, L.W., Eisner, L., Farley, E., Iken, K.B., Grebmeier, J.M., Juranke, L., Khen, G., Jayne, S., Kikuchi, T., Ladd, C., Lu, K., McCabe, R.M., Moore, G.W.K., Nishino, S., Ozenna, F., Pickart, R.S., Polyakov, I., Stabeno, P.J., Thoman, R., Williams, W.J., Wood, K., Weingartner, T.J.,

2020. Manifestation and consequences of warming and altered heat fluxes over the Bering and Chukchi Sea continental shelves. Deep Sea Res. II (this volume).
Dorner, B., Catalano, M.J., Peterman, R.M., 2017. Spatial and temporal patterns of covariation in productivity of Chinook salmon populations of the northeastern Pacific Ocean. Can. J. Fish. Aquat. Sci. 75, 1082–1095.
Dunmall, K.M., Reist, J.D., Carmack, E.C., Babluk, J.A., Heide-Jorgensen, M.P., Docker, M.F., 2013. Pacific salmon in the Arctic: harbingers of change. In: Mueter, F. J., Dickson, D.M.S., Huntington, H.P., Irvine, J.R., Logerwell, E.A., MacLean, S.A., Quankenbush, L.T., Rosa, C. (Eds.), Responses of Arctic Marine Ecosystems to Climate Change. Alaska Sea Grant. University of Alaska Fairbanks, pp. 141–163.
Dunmall, K.M., Mochnacz, N.J., Zimmerman, C.E., Lean, C., Reist, J.D., 2016. Using thermal limits to assess establishment of fish dispersing to high-latitude and high-elevation watersheds. Can. J. Fish. Aquat. Sci. 73, 1750–1758.
Dunmall, K.M., McNicholl, D.G., Reist, J.D., 2018. Community-based monitoring demonstrates increasing occurrences and abundances of Pacific salmon in the Canadian Arctic from 2000 to 2017. N. Pac. Anadr. Fish Comm. Tech. Rep. 11.
Estensen, J.L., Carroll, H.C., Larson, S.D., Gleason, C.M., Borba, B.M., Jallen, D.M., Padilla, A.J., Hilton, K.M., 2018. Annual Management Report Yukon Area, 2017. Alaska Department of Fish and Game. Fishery Management Report No. 18-28, Anchorage.
Farley Jr., E.V., Murphy, J.M., Wing, B.W., Moss, J.H., Middleton, A., 2005. Distribution, migration pathways, and size of western Alaska juvenile salmon along the eastern Bering Sea shelf. Alaska Fish. Res. Bull. 11, 15–26.
Farley Jr., E.V., Murphy, J., Moss, J., Feldmann, A., Eisner, L., 2009. Marine ecology of western Alaska juvenile salmon. In: Krueger, C.C., Zimmerman, C.E. (Eds.), Pacific Salmon: Ecology and Management of Western Alaska's Populations. American Fisheries Society, Bethesda, Maryland, pp. 307–329.
Fossheim, M., Primicerio, P.E., Johannesen, R.B., Ingvaldsen, M.M., Aschan, Dolgov, A. V., 2015. Recent warming leads to a rapid borealization of fish communities in the Arctic. Nature. https://doi.org/10.1038/NCLIMATE2647.
Frey, K.E., Maslanik, J.A., Kinney, J.C., Maslowski, W., 2014. Recent variability in sea ice cover, age, and thickness in the Pacific Arctic region. In: Grebmeier, J.M., Maslowski, W. (Eds.), The Pacific Arctic Region: Ecosystem Status and Trends in a Rapidly Changing Environment. Springer, the Netherlands, pp. 31–63.
Gall, A.E., Morgan, T.C., Day, R.H., Kuletz, K.T., 2017. Ecological shift from piscivorous to planktivorous seabirds in the Chukchi Sea, 1975 – 2012. Polar Biol. 40, 61–78.
Grant, A., Gardner, M., Nendick, L., Sackville, M., Farrell, A.P., Brauner, C.J., 2009. Growth and ionoregulatory ontogeny of wild and hatchery raised juvenile Pink Salmon (*Oncorhynchus gorbuscha*). Can. J. Zool. 87, 221–228.
Grebmeier, J.M., Overland, J.E., Moore, S.E., Farley, E.V., Carmack, E.C., Cooper, L.W., Frey, K.E., Helle, J.H., McLaughlin, F.A., McNutt, S.L., 2006. A major ecosystem shift in the Norther Bering Sea. Science 311 (5766), 1461–1464. https://doi.org/10.1126/science.1121365.
Heard, W.R., 1991. Life history of Pink salmon. In: Groot, C., Margolis, L. (Eds.), Pacific Salmon Life Histories. UBC Press.
Hop, H., Gjosaeter, H., 2013. Polar cod (*Boreogadus saida*) and capelin (*Mallotus villosus*) as key species in marine food webs of the Arctic and Barents Sea. Mar. Biol. Res. 9, 878–894.
Howard, K.G., Miller, K.M., Murphy, J., 2017. Estuarine Fish Ecology of the Yukon River Delta, 2014–2015. Alaska Department of Fish and Game, Fishery Data Series. No. 17-16, Anchorage.
Huntington, H.P., others, 2020. Evidence suggests potential transformation of the Pacific Arctic ecosystem is underway. Nat. Clim. Change. https://doi.org/10.1038/s41558-020-0695-2.
Insightful, 2001. S-plus 6 for Windows Guide to Statistics, vol. 1. Insightful Corporation, Seattle, WA.
Irvine, J.R., Michielsens, C.J.G., O'Brien, M., White, B.A., Folkes, M., 2014. Increasing dominance of odd-year returning pink salmon. Trans. Am. Fish. Soc. 143, 939–956.
Jtc (Joint Technical Committee of the Yukon River U.S./Canada Panel), 2019. Yukon River Salmon 2018 Season Summary and 2019 Season Outlook. Alaska Department of Fish and Game, Division of Commercial Fisheries, Anchorage. Regional Information Report 3A19-01.
Klovach, N.V., Temnykh, O.S., Shevlyakov, V.A., Shevlyakov, E.A., Bugaev, A.F., Ostrovskiy, V.I., Kaev, A.M., Volobuev, V.V., 2018. Current stock assessment of Pacific salmon in the far east of Russia. N. Pac. Anad. Fish Com., Tech. Rep. 11, 12–16.
Kondzela, C., Garvin, M., Riley, R., Murphy, J., Moss, J., Fuller, S.A., Gharrett, A., 2009. Preliminary genetic analysis of juvenile chum salmon from the Chukchi Sea and Bering Strait. North Pac. Anadromous Fish. Comm. Bull. 5, 25–27.
Malick, M.J., Cox, S.P., 2016. Regional-scale declines in productivity of pink and chum salmon stocks in western North America. PloS One 11 (1), e0146009. https://doi.org/10.1371/journal.pone.0146009.
McPhail, J.D., Lindsey, C.C., 1970. Freshwater fishes of northwestern Canada and Alaska. Bull. Fish. Res. Board Can. 173.
Menard, J., Leon, J., Bavilla, J., Neff, L., Joyce, S., 2018. Norton Sound salmon season summary. Alaska Department of Fish and Game, Division of Commercial Fisheries News Release. https://www.adfg.alaska.gov/static/applications/dcfnewsrelease/997457402.pdf.
Menard, J., Soong, J., Bell, J., Neff, L., Leon, J.M., 2020. 2018 Annual Management Report Norton Sound, Port Clarence, and Arctic, Kotzebue Areas. Fishery Management Report Number 20-05. Alaska Department of Fish and Game, Division of Sport Fish and Commmercial Fisheries.
Mueter, F.J., Peterman, R.M., Pyper, B.J., 2002. Opposite effects of ocean temperature on survival rates of 120 stocks of Pacific salmon (*Oncorhynchus* spp.) in the northern and southern areas. Can. J. Fish. Aquat. Sci. 59, 456–463.
Murphy, J.M., Howard, K.G., Gann, J.C., Cieciel, K.C., Templin, W.D., Guthrie III, C.M., 2017. Juvenile Chinook salmon abundance in the northern Bering Sea: implications for future returns and fisheries in the Yukon River. Deep-Sea Res. II. 1235, 156–167.
Moss, J.H., Murphy, J.M., Farley, E.V., Eisner, L.B., Andrews, A.G., 2009. Juvenile Pink and Chum salmon distribution, diet, and growth in the northern Bering and Chukchi seas. North Pac. Anadromous Fish. Comm. Bull. 5, 191–196.
Moore, S.E., Logerwell, E., Eisner, L., Farley Jr., E.V., Harwood, L.A., Kuletz, K., Lovvorn, J., Murphy, J.M., Quakenbush, L.T., 2014. Marine fishes, birds and mammals as sentinels of ecosystem variability and reorganization in the Pacific Arctic Region. In: Grebmeier, J.M., Maslowski, W. (Eds.), The Pacific Arctic Region: Ecosystem Status and Trends in a Rapidly Changing Environment, pp. 337–392.
McNyset, K.M., Volk, C.J., Jordan, C.E., 2015. Developing an effective model for predicting spatially and temporally continuous stream temperatures from remotely sensed land surface temperatures. Water 7, 6827–6846.
Nielsen, J.L., Ruggerone, G.T., Zimmerman, C.E., 2013. Adaptive strategies and life history characteristics in a warming climate: salmon in the Arctic? Environ. Biol. Fish. 96, 1187–1226. https://doi.org/10.1007/s10641-012-0082-6.
Noaa Coral Reef Watch, 2018. NOAA coral Reef Watch version 3.1 daily global 5-km satellite coral bleaching degree heating week product. updated daily. NOAA Coral Reef Watch, College Park, Maryland, USA. Jun. 3, 2013-Jun. 2, 2014. https://coastwatch.pfeg.noaa.gov/erddap/griddap/NOAA_DHW.html. (Accessed 7 January 2020).
Oka, G., Holt, C., Irvine, J.R., Trudel, M., 2012. Density-dependent growth of salmon in the North Pacific Ocean: implications of a limited, climatically varying carrying capacity for fisheries management and international governance. N. Pac. Anad. Fish Comm., Tech. Rep. 8, 112.
Orlova, E.L., Dolgov, A.V., Renaud, P.E., Boitsov, V.D., Prokopchuk, I.P., Zashihina, M.V., 2013. Structure of the macroplankton-pelagic fish-cod trophic complex in a warmer Barents Sea. Mar. Biol. Res. 9, 851–866.
Orsi, J.A., Fergusson, E.A., Wertheimer, A.C., Farley Jr., E.V., Mundy, P.R., 2016. Forecasting Pink salmon production in southeast Alaska using ecosystem indicators in times of climate change. North Pac. Anadromous Fish. Comm. Bull. 6, 483–499.
Overland, J.E., Wang, J., Pickart, R.S., Wang, M., 2014. Recent and future changes in the meteorology of the Pacific Arctic. In: Grebmeier, J.M., Maslowski, W. (Eds.), The Pacific Arctic Region: Ecosystem Status and Trends in a Rapidly Changing Environment, pp. 17–30.
Parker, R.R., 1968. Ocean Ecology of the North Pacific Salmonids. Univ. of Washington Press, Seattle, WA, p. 179.
Peterman, R.M., Pyper, B.J., Lapointe, M.F., Adkison, M.D., Walters, C.J., 1998. Patterns of covariation in survival rates of British Columbian and Alaska sockeye salmon (*Oncorhynchus nerka*) stocks. Can. J. Fish. Aquat. Sci. 55, 2503–2517.
Peterman, R.M., Dorner, B.A., 2012. A widespread decrease in productivity of sockeye salmon (*Oncorhynchus nerka*) populations in western North America. Can. J. Fish. Aquat. Sci. 69, 1255–1260.
Pyper, B.J., Mueter, F.J., Peterman, R.M., Blackbourn, D.J., Wood, C.C., 2001. Spatial covariation in survival rates of Northeast Pacific Pink salmon (*Oncorhynchus gorbushcha*). Can. J. Fish. Aquat. Sci. 58, 1501–1515.
Pyper, B.J., Mueter, F.J., Peterman, R.M., Blackbourn, D.J., Wood, C.C., 2002. Spatial covariation in survival rates of Northeast Pacific Chum salmon (*Oncorhynchus keta*). Trans. Am. Fish. Soc. 131, 343–363.
Pyper, B.J., Mueter, F.J., Peterman, R.M., 2005. Across-species comparisons of spatial scales of environmental effects on survival rates of Northeast Pacific salmon. Trans. Am. Fish. Soc. 134, 86–104.
Quinn III, T.J., Derison, R.B., 1999. Quantitative Fish Dynamics. Oxford University Press.
Radchenko, V.I., Beamish, R.J., Heard, W.R., Temnykh, O.S., 2018. Ocean ecology of pink salmon. In: Beamish, R.J. (Ed.), The Ocean Ecology of Pacific Salmon and Trout. American Fisheries Society, Bethesda, pp. 15–160.
Reist, J.D., Wrona, F.J., Prowse, T.D., Power, M., Dempson, J.B., Beamish, R.J., King, J. R., Carmichael, T.J., Sawatzky, C.D., 2006. General effects of climate change on Arctic fishes and fish populations. Ambio 35, 370–380.
Ricker, W.E., 1975. Computation and interpretation of biological statistics of fish populations. Bull. Fish. Res. Board Can. 191.
Ruggerone, G.T., Agler, B.A., Connors, B.M., Farley Jr., E.V., Irvine, J.R., Wilson, L.E., Yasumiishi, E.M., 2016. Pink and sockeye salmon interactions at sea and their influence on forecast error of Bristol Bay sockeye salmon. North Pac. Anadromous Fish. Comm. Bull. 6, 349–361.
Ruggerone, G.T., Irvine, J.R., 2018. Numbers and biomass of natural- and hatchery-origin Pink salmon, Chum salmon, and Sockeye salmon in the North Pacific Ocean, 1925 – 2015. Mar. Coast. Fish. 10, 152–168.
Sigler, M.F., Renner, M., Danielson, S.L., Eisner, L.B., Lauth, R.R., Kuletz, K.J., Logerwell, E.A., Hunt Jr., G.L., 2011. Fluxes, fins and feathers: relationships among the Bering, Chukchi, and Beaufort Seas in a time of climate change. Oceanography 24, 250–265.
Springer, A.M., van Vliet, G.B., Bool, N., Crowley, M., Fullagar, P., Lea, M., Monash, R., Price, C., Vertigan, C., Woehler, E.J., 2018. Transhemispheric ecosystem disservices of pink salmon in a Pacific Ocean macrosystem. Proc. Natl. Acad. Sci. Unit. States Am. https://doi.org/10.1073/pnas.1720577115.
Stabeno, P.J., Farley Jr., E.V., Kachel, N.B., Moore, S., Mordy, C.W., Napp, J.M., Overland, J.E., Pinchuk, A.I., Sigler, M.F., 2012. A comparison of the physics of the northern and southern shelves of the eastern Bering Sea and some implications for the ecosystem. Deep-Sea Res. II 65 – 70, 14–30.
Stabeno, P.J., Bell, S.W., 2019. Extreme conditions in the Bering Sea (2017-2018): record breaking low sea-ice extent. Geophys. Res. Lett. 46, 8952–8959. https://doi.org/10.1029/2019GL083816.
Stephenson, S.A., 2006. A review of the occurrence of Pacific salmon (*Oncorhynchus* spp) in the Canadian Western Arctic. Arctic 59, 37–46.

Stevenson, D.E., Lauth, R.R., 2018. Bottom trawl surveys in the northern Bering Sea indicate recent shifts in the distribution of marine species. Polar Biol. 42, 407–421.
Wang, M., Overland, J.E., Stabeno, P., 2012. Future climate of the Bering and Chukchi Seas projected by global climate models. Deep-Sea Res. II. https://doi.org/10.1016/j.drs2.2012.02.022.
Wechter, M.E., Beckman, B.R., Andrews III., A.G., Beaudreau, A.H., McPhee, M.V., 2017. Growth and condition of juvenile chum and pink salmon in the northeastern Bering Sea. Deep-Sea Res. II. 135, 145–155.
Woodgate, R.A., Weingartner, T., Lindsay, R., 2010. The 2007 Bering Strait oceanic heat flux and anomalous Arctic sea-ice retreat. Geophys. Res. Lett. 37 https://doi.org/10.1029/2009GL041621. L01602.
Woodgate, R.A., Stafford, K.M., Prahl, F.G., 2015. A synthesis of year-round interdisciplinary mooring measurements in the Bering Strait (1990 – 2014) and the RUSALCA years (2004 – 2011). Oceanography 28, 46–67. https://doi.org/10.5670/oceanog.2015.57.

Deep–Sea Research II 177 (2020) 104782

Contents lists available at ScienceDirect

Deep-Sea Research Part II

journal homepage: http://www.elsevier.com/locate/dsr2

Variability in fin whale (*Balaenoptera physalus*) occurrence in the Bering Strait and southern Chukchi Sea in relation to environmental factors

Erica Escajeda [a,*], Kathleen M. Stafford [b], Rebecca A. Woodgate [b], Kristin L. Laidre [a,b]

[a] School of Aquatic and Fishery Sciences, University of Washington, Seattle, WA, USA
[b] Applied Physics Laboratory, University of Washington, Seattle, WA, USA

ARTICLE INFO

Keywords:
Arctic
Bioacoustics
Fin whales
Chukchi Sea
Bering Strait
Interannual variability
Environmental factors
Marine ecology
Marine mammals

ABSTRACT

Fin whales (*Balaenoptera physalus*) are common summer visitors to the Pacific Arctic, migrating through the Bering Strait and into the southern Chukchi Sea to feed on seasonally-abundant prey. The abundance and distribution of fin whales in the Chukchi Sea varies from year-to-year, possibly reflecting fluctuating environmental conditions. We hypothesized that fin whale calls were most likely to be detected in years and at sites where productive water masses were present, indicated by low temperatures and high salinities, and where strong northward water and wind velocities, resulting in increased prey advection, were prevalent. Using acoustic recordings from three moored hydrophones in the Bering Strait region from 2009–2015, we identified fin whale calls during the open-water season (July–November) and investigated potential environmental drivers of interannual variability in fin whale presence. We examined near-surface and near-bottom temperatures (T) and salinities (S), wind and water velocities through the strait, water mass presence as estimated using published T/S boundaries, and satellite-derived sea surface temperatures and sea-ice concentrations. Our results show significant interannual variability in the acoustic presence of fin whales with the greatest detections of calls in years with contrasting environmental conditions (2012 and 2015). Colder temperatures, lower salinities, slower water velocities, and weak southward winds prevailed in 2012 while warmer temperatures, higher salinities, faster water velocities, and moderate southward winds prevailed in 2015. Most detections (96%) were recorded at the mooring site nearest the confluence of the nutrient-rich Anadyr and Bering Shelf water masses, ~35 km north of Bering Strait, indicating that productive water masses may influence the occurrence of fin whales. The disparity in environmental conditions between 2012 and 2015 suggests there may be multiple combinations of environmental factors or other unexamined variables that draw fin whales into the Pacific Arctic.

1. Introduction

The Arctic has undergone unprecedented environmental shifts as a result of climate warming (Post et al., 2019). Prominent among these shifts is the loss of sea-ice cover during the summer (Comiso et al., 2008; Cavalieri and Parkinson, 2012; Vaughan et al., 2013; Wood et al., 2015a, b; Walsh et al., 2017) along with earlier melting in the spring and delayed onset of freezing in the fall (Markus et al., 2009; Stroeve et al., 2014; Frey et al., 2015; Stabeno et al., 2019; Baker et al., this issue). Environmental shifts as a result of climate change are especially evident in the Chukchi Sea where annual sea-ice cover has declined by ~13 days each decade from 1979 to 2013 (Laidre et al., 2015), extending the open-water season (Grebmeier et al., 2010; Stroeve et al., 2014; Wood et al., 2015b; Woodgate, 2018). Declining sea ice is expected to result in range expansions of temperate and subarctic species into the Arctic (Root et al., 2003; Wassmann et al., 2011; Laidre and Heide-Jørgensen, 2012; Woodgate et al., 2015). Subarctic cetaceans, such as fin whales (*Balaenoptera physalus*), are thought to be expanding their range and residence time in the Chukchi Sea (Woodgate et al., 2015), which could lead to increased competition with Arctic cetaceans (Clarke et al., 2013).

Fin whales are a cosmopolitan mysticete whose range extends through most of the world's oceans (Mizroch et al., 1984). Though their exact migration patterns are unclear, fin whales are thought to breed in lower latitudes during winter and migrate to high-latitude areas, such as the Bering and Chukchi seas, in summer to feed on seasonally abundant prey (Mizroch et al., 1984, 2009). Fin whale diets vary seasonally and spatially across the North Pacific, but typically include euphausiids and forage fish species (Pike, 1950; Nemoto, 1959; Nemoto and Kasuya,

* Corresponding author.
E-mail address: escajeda@uw.edu (E. Escajeda).

https://doi.org/10.1016/j.dsr2.2020.104782
Received 28 February 2019; Received in revised form 13 April 2020; Accepted 15 April 2020
Available online 4 May 2020

1965; Mizroch et al., 1984; Flinn et al., 2002; Witteveen and Wynne, 2016). Fin whales are generally thought to avoid sea ice, though they have been observed swimming along the ice edge in the Arctic (Sleptsov, 1961; Mizroch et al., 1984).

Fin whales produce low frequency signals (<100 Hz), with high intensities (source levels up to 189 dB re 1 μPa at 1m) and short durations (≤1 s; Watkins, 1981; Watkins et al., 1987; Širović et al., 2007). The most commonly documented call is a short (~1 s) down-sweep generally starting around 25 Hz and ending at 15 Hz with peak energy centered near 20 Hz (Watkins, 1981; Watkins et al., 1987). The fin whale "20-Hz pulse" can occur in regular sequences, forming a stereotyped song that lasts from <1 h to ~33 h (Watkins et al., 1987). Such sequences are believed to be produced by males as a mating display starting in the fall and lasting through spring (Watkins et al., 2000; Croll et al., 2002; Stafford et al., 2007). Fin whales also produce 20-Hz and higher frequency pulses in short, irregular sequences that may serve as contact calls (Watkins, 1981; McDonald et al., 1995; Edds-Walton, 1997), especially during the summer months (Širović et al., 2013).

Historical records dating back to the early 20th century suggest fin whales commonly occurred in the southwest Chukchi Sea during the summer (Mizroch et al., 2009). Soviet and Japanese whaling expeditions in the 1930–1940s captured fin whales as far west as Cape Schmidt (68°55′18.3″N 179°27′42.7″W), and as far north as the central Chukchi Sea (69°04′N, 171°06′W) and Wrangel Island (Tomilin, 1957; Nemoto, 1959; Sleptsov, 1961; Mizroch et al., 2009, Fig. 1). Fin whales were observed in the Chukchi Sea as early as June (Nikulin, 1946) and stayed in the area until October (Nikulin, 1946; Nasu, 1960; Votrogov and Ivashin, 1980). Sleptsov (1961) describes fin whales as 'one of the numerous baleen whales that inhabit the Chukchi Sea' and reported seeing hundreds of fin whales in the span of six days between the Bering Strait and Cape Serdtse-Kamen in September 1939. By the mid-20th century, intense whaling in the North Pacific had taken a toll on fin whale populations and fin whales were rarely seen in the Chukchi Sea. Only a few sightings of fin whales were recorded between 1958 and 1981 (Nasu, 1960; Votrogov and Ivashin, 1980). More recent visual and acoustic observations of fin whales chart their presence in portions of the northeastern Chukchi Sea (Delarue et al., 2013), southcentral Chukchi Sea (Clarke et al., 2015; Brower et al., 2018), and the southern Chukchi Sea north of the Bering Strait (Tsujii et al., 2016).

We hypothesize that observed spatial variability in fin whale presence may be connected to environmental variability in the study region. In addition to the seasonal cycle of sea ice, the Chukchi Sea is characterized by the presence of distinct water masses defined by differences in temperature and salinity which vary from year to year (Coachman et al., 1975). The water masses in the Chukchi Sea have varying levels of nutrients and chlorophyll-*a* (chl-*a*), leading to distinct phytoplankton and zooplankton communities (Hopcroft et al., 2010; Eisner et al., 2013; Pisareva et al., 2015; Danielson et al., 2017; Sigler et al., 2017). Large, chain-forming diatoms are found in areas with high chl-*a* concentrations, such as the productive Anadyr Water (AW) in the western Chukchi Sea, whereas smaller phytoflagellates occur in low-nutrient areas, such as the less productive Alaskan Coastal Water (ACW) in the eastern Chukchi Sea (Springer and McRoy, 1993; Eisner et al., 2013; Danielson et al., 2017). Consequently, large copepods and other zooplankton groups are found in the AW while smaller copepods are ubiquitous in the ACW zooplankton community (Eisner et al., 2013; Sigler et al., 2017). It might be therefore expected that fin whales would occupy areas where the AW, or similarly productive water masses, dominate.

The Chukchi Sea is a highly advective ecosystem that is heavily influenced by the inflow of Pacific Water which enters through the Bering Strait (Woodgate et al., 2005a, Fig. 1). Advection from the northern Bering Sea provides the main source of zooplankton for the Chukchi Sea and is an important factor in determining zooplankton biomass and secondary production (Weingartner, 1997; Kitamura et al., 2017). High northward water velocities through the strait likely translate to increased advection of Pacific-origin prey into the Chukchi Sea. Therefore, we hypothesize that years with high detections of fin whale calls will have high northward (along-channel) water velocities.

The Bering Strait is divided into two channels by the Diomede Islands roughly mid-strait (Fig. 1). The western channel of Bering Strait is comparatively cold and salty due to the prevalence of the AW, while the eastern channel tends to be warmer and fresher due to the presence of the ACW (Coachman et al., 1975; Woodgate et al., 2005b, 2015). The cold and salty Bering Shelf Water (BSW) passes through the central strait (Coachman et al., 1975; Woodgate et al., 2005b). Variability in wind strength and direction can influence the position of these water masses

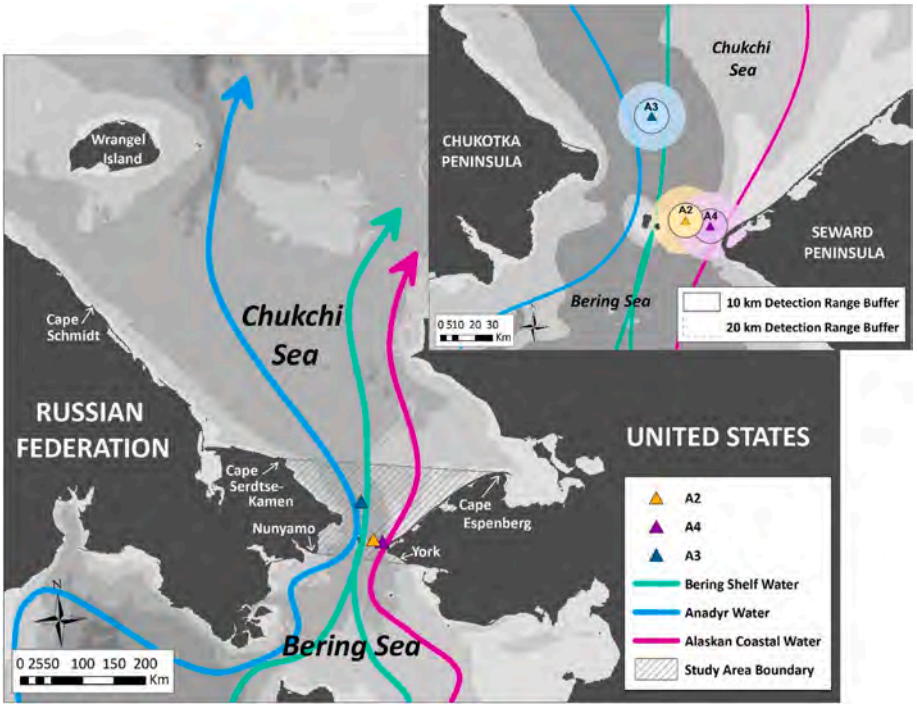

Fig. 1. Map of the study region with typical annual mean flow patterns of the three dominant water masses in the Bering Strait region and 20-m bathymetric contours (International Bathymetry Chart of the Arctic Ocean [IBCAO], v. 3; Jakobsson et al., 2012). Positions of the three moorings along with the boundaries of the study area polygon used in the sea ice concentration analysis are also displayed. Inset map shows estimated call detection range buffers around each mooring (10 and 20 km). Note that the Alaskan Coastal Water is only present seasonally.

and overall transport in the strait. Strong along-channel (northward) winds through Bering Strait may push the less productive surface ACW against the Alaskan coast via Ekman transport, allowing the more productive AW to shift east and replace it in the surface waters (Woodgate, 2018). Similarly, southward winds spread the ACW westwards across the surface of the strait and draw AW to the east at depth (Woodgate et al., 2015). Thus, wind changes could affect feeding opportunities for fin whales at different depths across the strait. Northward winds are linked to northward flow through the strait (Woodgate et al., 2005a), which leads to higher advection of prey into the Chukchi Sea, in general. Therefore, we hypothesize that fin whale occurrence may be related to northward wind velocity through the strait.

Given that the Bering Strait is the only gateway from the Pacific Ocean into the Chukchi Sea (Fig. 1), the region is an ideal study area for recording the occurrence of migrating fin whales. In this paper, we investigate whether fin whales exhibited any interannual variation in their acoustic presence during the open-water season (July–November) from 2009–2015 and explore correlations between the acoustic presence of fin whales and environmental variation in the Bering Strait region. We hypothesize that high levels of fin whale calls occur in the years when and at the mooring sites where the highly productive AW and BSW are prevalent, when/where there are higher northward water velocities (and thus primarily northward winds) through the strait, and in years when sea ice forms later in the fall, allowing fin whales to remain in the Chukchi Sea longer into the season.

2. Methods

2.1. Acoustic data

Acoustic data were collected from three AURAL-M2 hydrophones (Autonomous Underwater Recorder for Acoustic Listening-Model 2, Multi-Électronique, Inc.; sensitivity of −154 dB re 1 V/μPa and 16-bit resolution) attached to oceanographic moorings positioned within the eastern channel of the Bering Strait (A2 in the center of the eastern channel, and A4 in the Alaskan Coastal Current (ACC) on the east side of the channel), and a central strait location ~35 km north of the strait in the southern Chukchi Sea (A3; Fig. 1). Hydrophones were first installed on the moorings in September 2009 and recorded through 2015. Each hydrophone was positioned 4–8 m above the seafloor and sampled at 8192 Hz or 16384 Hz with various hourly duty cycles and recording start dates (Table 1). We assume that calls recorded during the hydrophones' duty cycle are representative of fin whale acoustic activity for the entire hour in which the calls were recorded.

We quantified fin whale calling activity as the number of hours per day with fin whale calls present, hereafter referred to as 'fin whale hours' (FWH). Note that since we were only able to detect calling whales, we could not assume the absence of fin whales during any hour, nor could we estimate the abundance of fin whales using call abundance alone. The term 'recording years' refers to years that each hydrophone actively recorded data. Analysis of the recordings was restricted to the recording start date (typically July) until the end of November, called here as the 'recording period.' Given the shallow depth of the study area, it is likely that all calls from individuals within 10–20 km of the hydrophones were recorded (Woodgate et al., 2015). If we use the conservative call detection range of 10 km, the hydrophones cover a total of 892 km^2, or ~3% of the study area (Fig. 1). Hydrophones at A2 and A4 cover ~64% of the eastern channel area (~900 km^2), while the width of the A3 10-km call detection buffer covers ~10% of the across-strait distance at its latitude north of the strait.

We identified hours with fin whale 20-Hz pulses using the spectrogram correlation tool implemented in Ishmael (2014 version; Mellinger and Clark, 2000; Mellinger, 2002). Detector parameters included a threshold of 10 to reduce the number of false detections and a smoothing time constant of 0.3 s. Each hour identified by the detector was then manually verified to contain fin whale calls by inspecting the spectrogram in Ishmael (FFT 4096, Hanning window, spectrogram equalization enabled with a time constant of 30 s) and eliminating any false positives from the dataset. The hours before and after a true positive FWH were examined to capture any hours with calls that were not picked up by the detector, adding a total of 269 FWH to our detections (~11% of the total number of FWH for all three sites).

To investigate spatial and temporal patterns in the presence of fin whales, we compared FWH between years and sites using a nonparametric two-sample Wilcoxon rank-sum test under the null hypothesis of equal distributions. Since all hydrophones recorded in October, we restricted our interannual comparisons of FWH within each mooring site and between the three sites to October only to avoid issues with unequal recording period lengths. We also compared the date of departure of calling fin whales from the study region by calculating the 95% quantile of the cumulative distribution of days with fin whale calls starting on 1 October of each year, following the procedure of Hauser et al. (2017). We used a significance threshold of 0.05 for all statistical tests and assumed independence between daily values.

2.2. Environmental data collection

Six environmental variables were recorded *in-situ* by other sensors on the same moorings, including: near-bottom temperature and salinity (40–55 m depth) measured by Sea-Bird (SBE) SBE16 and SBE37 sensors;

Table 1
Recording settings and positions of the three hydrophones. Dates are in the format 'mm/dd/yyyy.'

Mooring	Year	Latitude N	Latitude W	Record Start Date	Record End Date	Sampling Rate (Hz)	Hourly Duty Cycle
A2	2009	65.80°	168.80°	9/1/2009	1/16/2010	16384	12 min
	2010	65.80°	168.80°	8/11/2010	12/8/2010	16384	15 min
	2012	65.80°	168.80°	9/1/2012	5/15/2013	16384	10 min
	2013	65.78°	168.57°	7/15/2013	7/1/2014	8192	20 min
	2014	65.78°	168.57°	7/10/2014	7/4/2015	8192	20 min
	2015	65.78°	168.57°	7/5/2015	7/8/2016	8192	20 min
A3	2009	66.33°	168.97°	9/1/2009	3/3/2010	16384	12 min
	2010	66.33°	168.97°	8/11/2010	2/19/2011	16384	15 min
	2011	66.33°	168.97°	10/1/2011	5/25/2012	8192	10 min
	2012	66.33°	168.97°	9/1/2012	5/17/2013	16384	10 min
	2013	66.33°	168.97°	7/15/2013	7/2/202014	8192	20 min
	2014	66.33°	168.97°	7/10/2014	7/2/2015	8192	20 min
	2015	66.33°	168.97°	7/5/2015	7/8/2016	8192	20 min
A4	2012	65.75°	168.37°	9/1/2012	6/24/2013	16384	10 min
	2013	65.75°	168.26°	7/15/2013	7/2/2014	8192	20 min
	2014	65.75°	168.25°	7/10/2014	7/2/2015	8192	20 min
	2015	65.75°	168.25°	7/5/2015	7/8/2016	8192	20 min

near-surface temperature and salinity (14–19 m depth) measured by the ISCAT system developed at the University of Washington (e.g. Woodgate et al., 2015), which includes a SBE37 temperature-salinity-pressure sensor in an ice-resistant housing; and water velocity (cm s^{-1}) and direction (°) measured by Teledyne's Workhorse Acoustic Doppler Current Profilers (ADCPs). The ADCPs measured water velocity in 2-m bins from ~15 m to ~45 m depth (see Supplemental Tables S1–S3 for instrument depths). For simplicity, we used only data from the ADCP bin closest to ~30 m depth. Note that henceforth the term 'near-surface' refers to measurements taken by the ISCATs and 'near-bottom' refers to those taken by the SBEs. Some ISCAT recorders were lost/stopped recording before the 30 November cut-off date (see Woodgate et al., 2015 and Supplemental Tables S1–S3 for data gaps along with other mooring sensor information). Note that the ISCAT for A3 stopped recording in August 2014, 45 days after deployment, thus near-surface temperature and salinity data are not available for fall 2014.

In addition to the *in-situ* data, we examined northward wind velocity, and satellite-derived sea surface temperatures (SST) and sea-ice concentrations. Wind velocity data were obtained from the National Center for Environmental Prediction (NCEP) R1 dataset, with a spatial resolution at the Bering Strait of 2.5°. We used the National Oceanic and Atmospheric Administration's (NOAA) Optimum Interpolation satellite sea surface temperature (OISST) gridded product with a 0.25° resolution (https://www.esrl.noaa.gov/psd/; Reynolds et al., 2007). Daily mean SSTs were extracted from the cell containing each mooring's position.

For sea-ice concentrations, we sought datasets with the highest resolution available. We required data from different passive microwave sea-ice satellites to cover the entire duration of the study. For years 2009 and 2010, we used Advanced Microwave Scanning Radiometer – Earth Observing System (AMSR-E) sea-ice concentration data with a resolution of 6.25 km from the Integrated Climate Date Center (ICDC, icdc.cen.uni-hamburg.de; Kaleschke et al., 2001; Spreen et al., 2008). The AMSR-E satellite failed in early October 2011, consequently for 2011 and 2012 we used data from the Special Scanning Microwave/Imager (SSM/I) with a spatial resolution of 25 km (Cavalieri, 1996). High resolution Advanced Microwave Scanning Radiometer 2 (AMSR-2) data with a grid resolution of 6.25 km were used for 2013–2015 (Beitsch et al., 2014; Kaleschke and Tian-Kunze, 2016).

We derived daily mean sea-ice concentration for the area of the Chukchi Sea as defined by the International Hydrographic Organization (IHO; http://www.marineregions.org/gazetteer.php?p=details&id=4257), and for a custom study area polygon (Fig. 1). The study area polygon was defined by the bounds set by Cape Serdtse-Kamen, Russian Federation, in the northwest; Nunyamo, Russian Federation, to the southwest; York, Alaska, USA, on the Seward Peninsula to the southeast; and Cape Espenberg, Alaska, USA, to the northwest (Fig. 1). We determined the study area polygon by estimating where sea ice, if present, could potentially create a migration barrier for fin whales. All satellite-derived data were visualized in ArcMap (v. 10.1) using the WGS 1984 datum and projected in a custom polar stereographic projection with a central meridian of −171°W.

2.2.1. Environmental data analysis

To ensure consistency when comparing the environmental data over time, we calculated summary statistics for October data since there were no data gaps in the *in-situ* temperature and salinity data in this month (except for a gap in the near-surface data for 2014 at A3). For the ADCP data, we elected to compare the monthly mean northward water velocities for June to November to capture the summertime peak in transport through the Bering Strait (Woodgate et al., 2005b). We investigated correlations between days with fin whale calls present (i.e. FWH >0) and select individual environmental variables using non-parametric Kendall's rank correlation tests. The Kendall's rank coefficient, tau (τ), indicates the direction of association ($-1 < \tau < 1$) and the resulting *p*-value indicates presence of a statistically significant correlation under the null hypothesis of non-correlation between the samples.

We tested for interactions between fin whale presence and along-channel (northward) wind patterns within the Bering Strait by comparing the daily mean northward wind velocity on days when the number of FWH reached above a certain threshold (≥1 h, ≥6 h, ≥12 h, and ≥18 h) and days without any FWH. We calculated summary statistics for northward wind velocities in October only, including an overall mean along-channel wind velocity as well as mean wind velocity for days with no FWHs and days with FWHs above a threshold (see categories above). We then compared the overall October mean along-channel wind velocity to the mean wind velocities for days with and without FWHs using a Wilcoxon rank sum test.

For the sea ice analysis, we calculated the melt-out and freeze-up dates as the day of the year when the sea ice concentration within the study area decreased/increased below/above 80%, respectively, following Markus et al. (2009) and Stroeve et al. (2014). We defined an area as 'ice-free' if the mean sea ice concentration was ≤15%, a threshold commonly used to indicate the presence of sea ice (Serreze et al., 2009, 2016; Stroeve et al., 2012). We calculated the melt period length using the number of days between the initiation of melting (≤80% concentration) and when the study area was ice-free (≤15% concentration). For the freeze-up period length, we calculated the number of days between the first day sea ice concentration reached ≥15% and the first day the sea ice reached ≥80% concentration in the fall. We compared the calculated fin whale departure date and sea ice freeze-up date for each year using a two-sided Pearson correlation test after testing for normality.

2.3. Water masses

Water mass presence for each day was estimated for the near-surface and near-bottom using temperature and salinity (T/S) bounds suggested by Danielson et al. (2017). These authors distinguish five water mass categories: the Alaskan Coastal Water (ACW), Bering Chukchi Summer Water (BCSW), Bering Chukchi Winter Water (BCWW), Melt Water (MW), and water from the Atlantic layer in the Arctic (AtlW). Danielson et al. (2017) combine the Anadyr Water (AW) and the Bering Shelf Water (BSW) into one water mass, the BCSW, since the T/S properties of these three water masses are often indistinguishable from each other. Note that since the T/S bounds of these waters vary interannually (Coachman et al., 1975), there are limitations to the representativeness of the above water mass identifications.

Chi-squared tests of independence were performed for each mooring site using pooled presence/absence of fin whale calls for each day across all recording years along with the daily water mass designations to determine whether there was a significant association between the presence of fin whale calls and water mass. If a chi-squared test was inappropriate (e.g. in the case of small sample sizes), a Fisher's exact test was applied instead. Fisher's exact test evaluates the significance of association, or contingency between two categorical variables, and is insensitive to sample sizes. All analyses were performed using in the statistical software R (v. 3.5.3; R Core Team, 2019).

3. Results

3.1. Fin whale detections

We processed a total of 52,272 audio files collected from ~July to November 2009–2015 (Table 1). Fin whales were detected at all three sites, with the highest frequency and abundance of fin whale hours (FWH) at site A3 by a large margin (Fig. 2; Supplemental Figs. S1–S3). About one third (34.4%) of the total recording days at A3 had at least 1 h with fin whale calls, compared to only 4.6% at A2 and 1.5% at A4. Calling fin whales were detected in all recording years at A2 and A3, but were only detected in 2014 and 2015 at A4. October had the highest

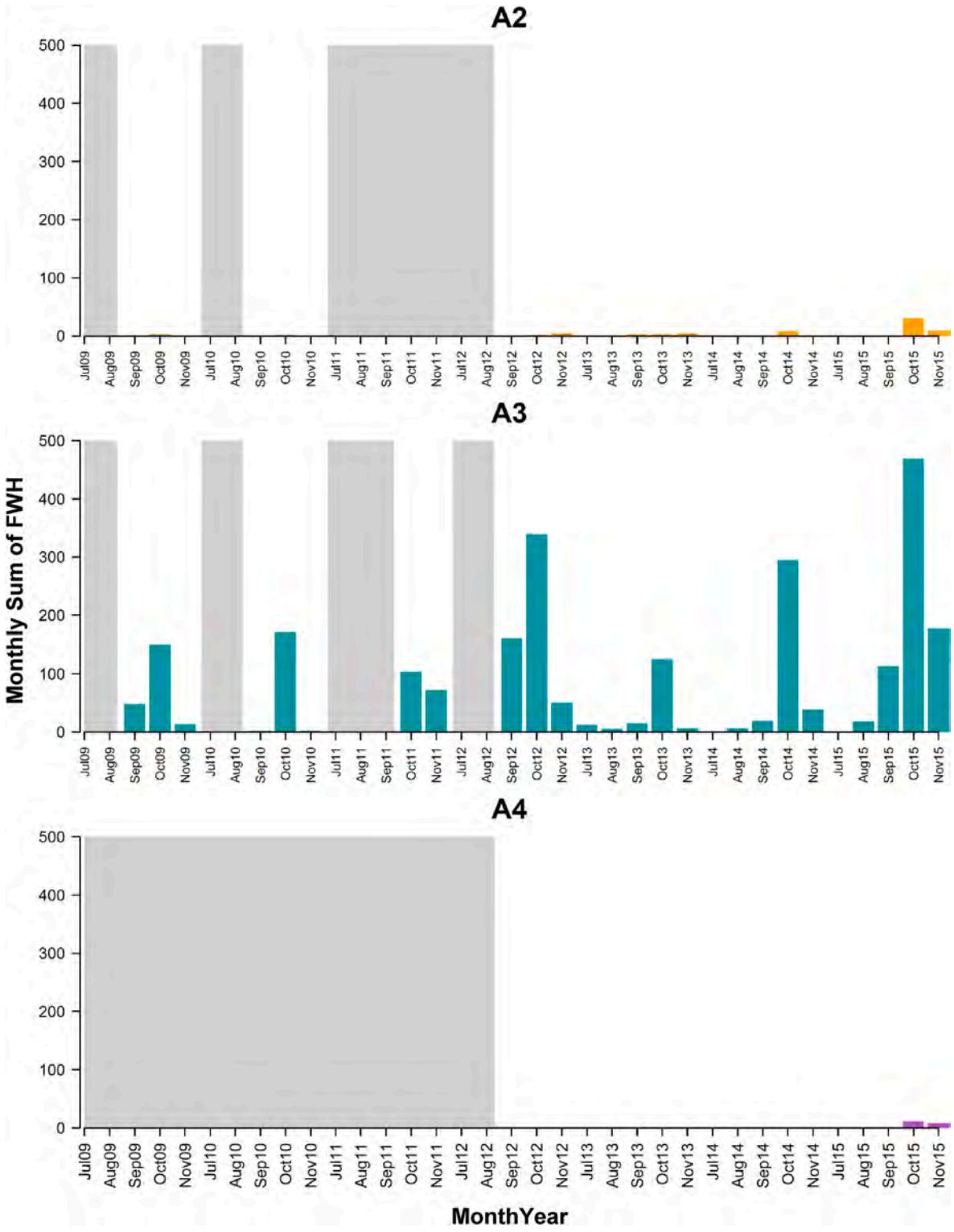

Fig. 2. Histograms of monthly sum of hours with fin whale calls ('FWH') recorded at the three mooring sites (A2, A3, and A4) within the Bering Strait region from 2009 to 2015. The gray-shaded boxes indicate periods when the hydrophones were not recording.

occurrence of FWH across all sites (68.4%), and given the hydrophones all had data from October, we restricted our statistical tests to this month. Wilcoxon rank-sum tests revealed statistically significant differences in the distribution of FWH in October at the three mooring sites (A2 and A3: $W = 5259.5$, $p < 0.001$, $n = 186$ days; A2 and A4: $W = 8423$, $p = 0.006$, $n = 124$ days; A3 and A4: $W = 1709$, $p < 0.001$, $n = 124$ days). The earliest detection of fin whale calls across all sites and years occurred on 23 July 2013 at A3, and the latest fin whale detection occurred on 20 November 2015 at A3 (Table 2). Annual fin whale departure dates using the 95% quantile were only calculated for A3 given the lack of data at A2 and A4 (see Supplemental Fig. S4 for the cumulative distribution of days with fin whale calls at A3). Fin whale departure dates at A3 did not show any statistically significant trend ($R^2 = 0.20$, $p = 0.311$; Fig. 3).

Table 2
Fin whale detection data for the three moorings, including the dates of the first and last detection, and total number of days with fin whale calls present ('FW Days'). The '.' indicates periods when the hydrophone was not actively recording.

	A2			A3			A4		
Year	First Detection Date	Last Detection Date	FW Days	First Detection Date	Last Detection Date	FW Days	First Detection Date	Last Detection Date	FW Days
2009	1 Oct	5 Nov	4	23 Sep	8 Nov	33	.	.	.
2010	14 Oct	17 Oct	2	29 Sep	5 Nov	22	.	.	.
2011	.	.	.	1 Oct	18 Nov	28	.	.	.
2012	28 Oct	2 Nov	3	1 Sep	7 Nov	52	None	None	0
2013	22 Sep	15 Nov	7	23 Jul	9 Nov	28	None	None	0
2014	17 Oct	19 Oct	3	9 Aug	13 Nov	37	2 Nov	2 Nov	1
2015	30 Sep	19 Nov	14	8 Aug	20 Nov	71	11 Oct	8 Nov	7

At A3, fin whale calling activity was highest in 2012 and 2015 (52 and 71 days with at least one FWH, respectively), while calling activity was the lowest in 2010 (22 days) followed by 2011 and 2013 (28 days). The Wilcoxon tests comparing FWH in October between years at A3 show significant differences in the distributions fin whale detections across years, with significant values ($p < 0.01$) between all consecutive years except 2009 and 2010 ($p = 0.736$) and 2010 and 2011 ($p = 0.463$; Table 3). Wilcoxon tests comparing FWH in 2012 and 2015 to the other years detected significantly different distributions ($p < 0.01$), except for the test between 2012 and 2014 ($p = 0.614$; Table 3).

Fin whale calls were less common at A2, though 2015 had relatively higher call activity with 40 h with fin whale calls compared to 2–10 h in each of the other six years. At A4, fin whale calls were only detected in 2014 (1 h) and 2015 (19 h). Insufficient sample sizes precluded any statistical comparisons of fin whale vocal activity between years for A2 and A4.

Table 3
Wilcoxon rank-sum test results comparing fin whale hours (FWH) recorded at A3 in October of each year. The *p*-values are listed in the upper section above the diagonal, and the gray shaded area below the diagonal are the W statistics from the Wilcoxon rank-sum tests (**bold** W values indicate significant results). Significant *p*-values ($p < 0.05$) are in **bold*** and indicate that the distribution of FWHs significantly differed between the two years.

Year	2009	2010	2011	2012	2013	2014	2015
2009	.	0.736	0.147	**0.002***	0.42	**0.026***	**0.000***
2010	174.5	.	0.463	**0.002***	0.554	0.062	**0.000***
2011	186	220	.	**0.002***	0.566	**0.003***	**0.000***
2012	**69**	**77**	**76**	.	**0.003***	0.614	**0.007***
2013	223	185	98.5	**399.5**	.	**0.004***	**0.000***
2014	**96**	120.5	**57.5**	257.5	**47.5**	.	**0.006***
2015	**30**	**14**	**14.5**	**110**	**21**	**106**	.

3.2. Sea-ice conditions and analyses

Sea-ice conditions within the study area were highly variable from year to year. Melt-out dates ranged from as early as 27 April (2011) to as late as 20 May (2010; Table 4). The number of days between the initiation of melting (<80% concentration) and ice-free conditions in the study area (<15% concentration) ranged from 21 days (2015) to 41 days (2013; Table 4). The study area was typically ice-free starting in late May to early June, with the earliest ice-free date occurring on 24 May 2015 and the latest on 17 June 2010. On average, freeze-up dates (≥80% concentration) occurred in early to mid-December, with the earliest freeze-up on 28 November 2009 and the latest on 25 December 2010.

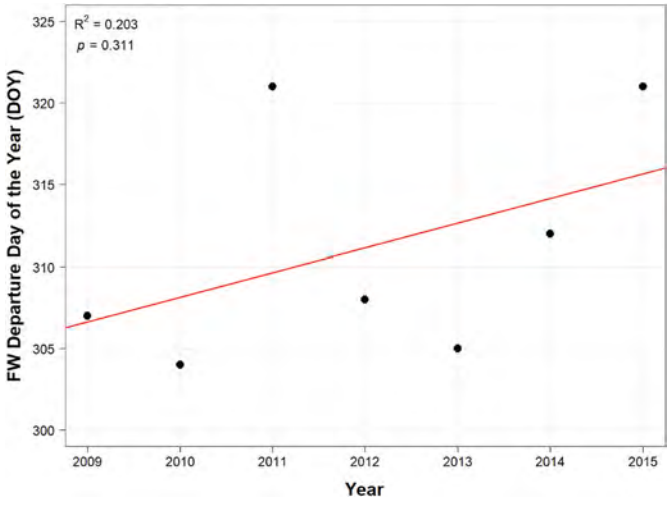

Fig. 3. Fin whale departure day of the year (DOY) for each year at the A3 mooring site, north of the Bering Strait, along with the line of best fit ($R^2 = 0.203$, $p = 0.311$).

The freeze-up periods for each year were typically much shorter than the melt periods, with the number of days between the ice-free date and freeze-up initiation ranging from five days (2014) to 23 days (2010 and 2012; Table 4).

Fin whale departure dates for each year at A3 were compared to the sea ice freeze-up date for the study area and the Chukchi Sea, as well as the day of the year when the daily mean near-surface and near-bottom temperatures first reached ≤0 °C (Fig. 4). Two-sided Pearson correlation tests indicated no significant correlation between fin whale departure date and sea ice freeze-up date for the study area ($t = -1.046$, $p = 0.344$) or the Chukchi Sea ($t = -0.308$, $p = 0.771$). The latest fin whale departure date occurred on 17 November 2011 and 2015 when the mean sea ice concentrations were ~0.8% and 4.9% in the study area, and 21.0% and 18.2% in the Chukchi Sea, respectively (Table 4).

3.3. Environmental conditions at the moorings

Environmental data at the three mooring sites exhibited strong interannual and spatial variation. The highest temperatures and lowest salinities on average were seen at A4 (e.g. 2013 October near-surface mean temperature = 3.5 °C, SD = 0.7 °C; near-surface mean salinity = 30.3 psu, SD = 1.3 psu). Conversely, A2 and A3 had lower temperatures and higher salinities than A4 (A2: 2013 October near-surface mean temperature = 3.3 °C, SD = 0.7 °C, near-surface mean salinity = 31.1 psu, SD = 1 psu; A3: 2013 October near-surface mean temperature = 2.9 °C, SD = 0.8 °C, near-surface mean salinity = 31.7 psu, SD = 0.8 psu; Fig. 5). This spatial structure, with warm fresh waters near the Alaskan Coast, typically indicates the presence of the Alaskan Coastal Current (see discussion in Woodgate et al., 2015). There were also significant interannual differences across all three sites. The lowest near-surface and near-bottom temperatures occurred in 2012 while the highest

Table 4
Sea ice statistics calculated for 2009–2015 for the study area and Chukchi Sea. Statistics for the study area include: melt initiation date ('Melt-Out Date'), melt period (number of days between 80% and 15% sea ice conc.), date when the study area was ice-free (<15% conc.; 'Ice-Free Date'), freeze-up period (number of days between 15% and 80% sea ice conc.), and mean sea ice concentration (%) in the study area on the last date fin whale calls were recorded ('Last FW'). Statistics for the Chukchi Sea include mean sea ice concentration (%) on the last date fin whale calls were recorded ('Last FWH').

	Study Area							Chukchi Sea
Year	Melt-Out Date	Ice-Free Date	Melt Period (# of days)	Freeze-up Date	Freeze-up Period (# of days)	Mean Nov. sea ice conc.	Last FW mean sea ice conc.	Last FW mean sea ice conc.
2009	14 May	5 June	23	28 Nov	12	30.2%	0.9%	1.5%
2010	20 May	17 June	29	25 Dec	23	3.4%	1.3%	4.5%
2011	27 April	30 May	34	4 Dec	12	13.3%	0.8%	21.0%
2012	16 May	10 June	25	11 Dec	23	21.3%	1.9%	18.8%
2013	5 May	14 June	41	18 Dec	19	6.3%	3.1%	12.8%
2014	1 May	31 May	31	17 Dec	5	5.4%	4.1%	7.07%
2015	4 May	24 May	21	10 Dec	17	20.1%	4.9%	18.2%

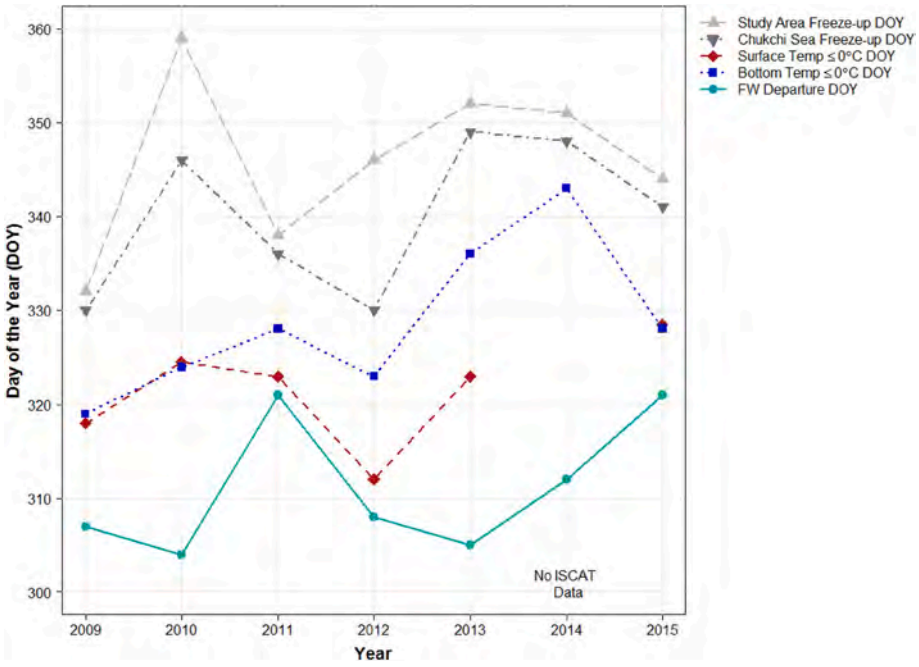

Fig. 4. Calculated fin whale departure days for each year at site A3 (light blue, solid line) with other non-solid lines indicating the day of the year (DOY) when the daily mean near-surface (ISCAT; red, medium-dashed line) and near-bottom (SBE; blue, dotted line) temperatures first reached ≤ 0 °C at the A3 mooring site. The light gray, long-dashed line represents the DOYs when sea ice concentration in the study area first reached ≥15% in each year, and the dark gray, dot-dashed line represents when sea ice concentration in the Chukchi Sea reached ≥15%. See Fig. 1 for boundaries of study area. (For interpretation of the references to color in this figure legend, the reader is referred to the Web version of this article.)

temperatures occurred in 2015 (Fig. 5; Woodgate, 2018).

Northward water velocities were on average the highest at sites A2 and A4 during the open-water season (Fig. 6), consistent with known seasonality in the flow due to weaker opposing southward winds in summer (Woodgate et al., 2005b). The year 2012 had the weakest northward water velocity throughout the open-water season while 2014 had sustained high northward velocities throughout the season (Fig. 6; Woodgate, 2018). Overall, northward water velocities weakened over the period between July and November with the slowest northward water velocities occurring in November, except in 2012 and 2014 when the seasonal minimum velocities were seen in September and October (Fig. 6). Direction of flow at all three sites was primarily northward during the open-water season (see Supplemental Fig. S5–S11 for plots of the water and wind velocity vectors along with fin whale acoustic presence at A3 during the open-water season). For a more detailed overview of variation in Bering Strait transport through 2015, see Woodgate (2018).

Due to low fin whale detections at A2 and A4, we focused our wind analysis on site A3 and used wind data from the grid point closest to the mooring (67.5°N, 190°W, ~140 km to the northwest of A3). On average, along-channel winds were mainly southward during the month of October, with the strongest mean winds occurring in 2013 (October $\bar{x}$ = −6.2 m/s, SD = 5.4 m/s) and the weakest mean winds in 2012 (October $\bar{x}$ = −0.4 m/s, SD = 8.1 m/s; Table 5). Note that the negative sign indicates a southward direction.

3.4. Environmental analyses

We focused our environmental analyses on the A3 mooring site due to the relative lack of fin whale detections at A2 and A4. The Kendall's rank correlation tests between FWH on days with fin whale calls (i.e. FWH >0) and the environmental variables produced statistically significant ($p < 0.05$) though small correlations for daily mean water speed, and along-channel wind and water velocities pooled for all seven years (2009–2015; Table 6). We ran a second test using October data only and found similar results, as well as the addition of significant correlations between FWH and near-surface temperature and SST at site A3 (Table 6).

Days with fin whale calls mostly had southward mean wind velocities while days without calls (i.e. FWH = 0) mostly had northward overall mean winds (Table 5; Fig. 7). The Wilcoxon test comparing the overall mean along-channel wind velocity for October of each year against the means for days with and without FWHs revealed that days without FWH and days with FWH ≥6 h and 12 h had statistically significant differences in along-channel wind velocities in 2011 and 2014 only (Table 5). Insufficient data precluded any tests for days with FWH

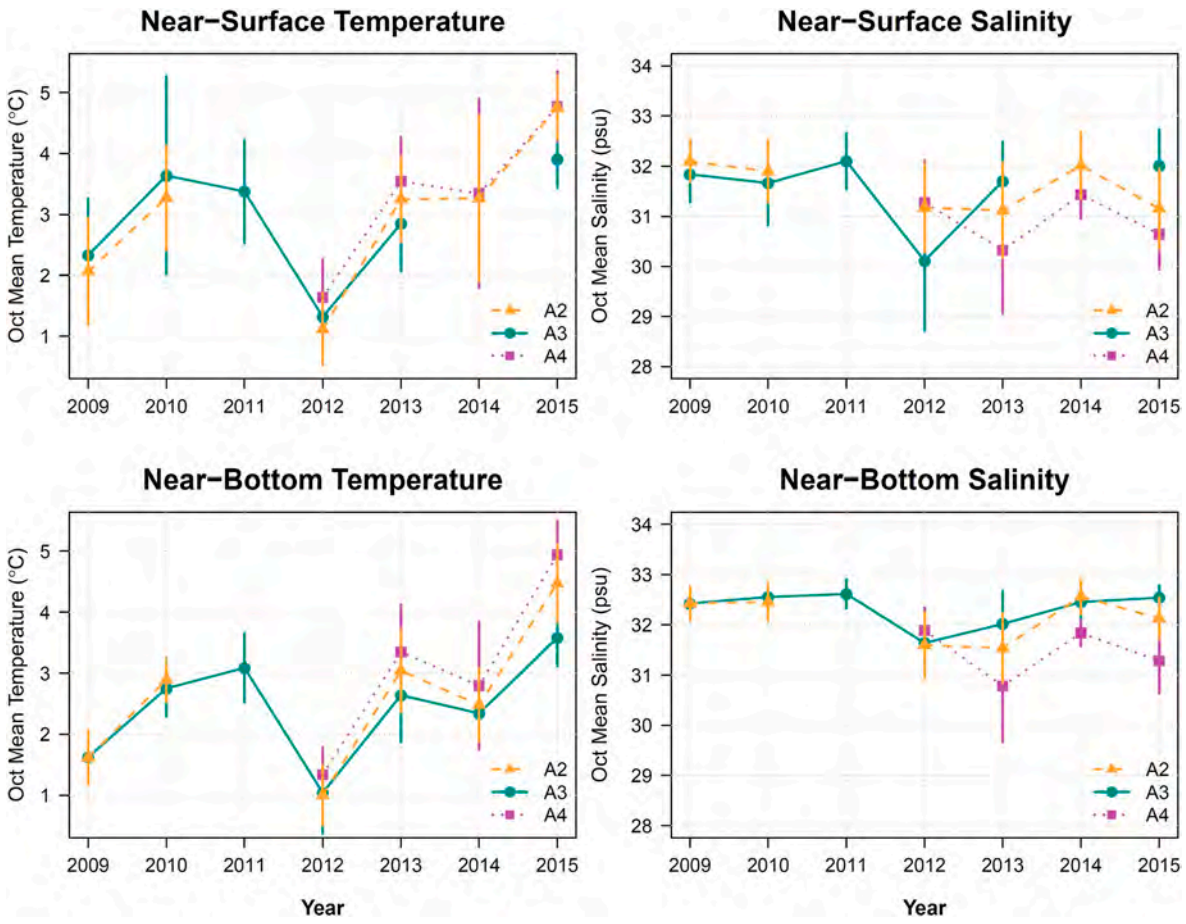

Fig. 5. Plots of the mean temperatures (°C) and salinities (psu) for October of each year for both the near-surface and near-bottom levels of the water column at each mooring site in the study area (A2, A3, and A4; see key for colors, symbols, and line styles). The vertical lines represent the standard deviation of the monthly means. (For interpretation of the references to color in this figure legend, the reader is referred to the Web version of this article.)

≥18 h.

3.5. Water mass composition at the moorings

Water mass composition at A2 and A3 during the open water season was dominated by the presence of the Bering Chukchi Summer Water (BCSW) at both the near-surface (>70% of days at both sites) and near-bottom levels (>90% of days at both sites) for all recording years (see Supplemental Figs. S12–S14 for plots with the water mass composition at the three sites during the open water season). The water mass composition at A4 was similarly dominated by BCSW at the near-bottom (73% of days in July–November) and to a lesser extent in the near-surface (51% of days in July–November). The cold and salty Bering Chukchi Winter Water (BCWW) appeared in both levels in the water column in November at all three sites, when it is assumed that fin whales are beginning their migration south. A fresher, colder signal, that falls within the Melt Water (MW) category as defined by Danielson et al. (2017), appeared in the near-surface at all three sites in September and October 2012 and 2013, with the strongest signal in 2012. However, since the sea-ice edge is far away from the mooring sites in September and October, the freshening observed in 2012 and 2013 was likely due to fresh waters from either the Alaskan Coastal Current (ACC) or the Siberian Coastal Current (SCC). The SCC is a cold, fresh current present seasonally in the Chukchi Sea only in some years (Weingartner et al., 1999). Also noteworthy was a warm Alaskan Coastal Water (ACW) signal in the near-surface at A2 in 2013, 2014, and 2015 and at A3 in 2010 and 2015.

We conducted a side-by-side comparison of the daily water mass designations for A2 and A3 and noted the number of days when at least one of the water mass designations at A2 did not match those from A3. Out of 726 days when both moorings were recording and had data for both instruments, 14 days (~2% of total days) had different water mass composition in the near-bottom water and 69 days (~10% of total days) for the near-surface water. In contrast, A2 and A4 had different water mass compositions on 203 days (~39%) for the near-surface and 127 days (24%) for the near-bottom. The comparison between A3 and A4 yielded 311 days (60%) with different water mass composition at the near-surface and 136 days (26%) at the near-bottom. These results indicate that despite close spatial proximity, A2 and A4 had very different water mass composition while A2 and A3 had similar water mass composition.

3.6. Water mass analyses

The chi-squared tests of independence between the pooled FWH and the near-surface/near-bottom water mass designations at site A3 suggest that the occurrence of fin whale calls during the study period was statistically dependent on the occurrence of water masses (both tests using near-surface and near-bottom water mass designations: $p < 0.001$). We repeated the tests of independence for each recording year at A3, using the Fisher's Exact Test to compare the daily near-surface and near-bottom water mass designations to the total FWH for each day. The results show a significant relationship for 2009, 2011, 2012, and 2015 (all $p < 0.02$), signifying that fin whale presence was statistically dependent on water mass presence for these years. We were unable to execute the Fisher's Exact test for 2013 (near-bottom water mass) and

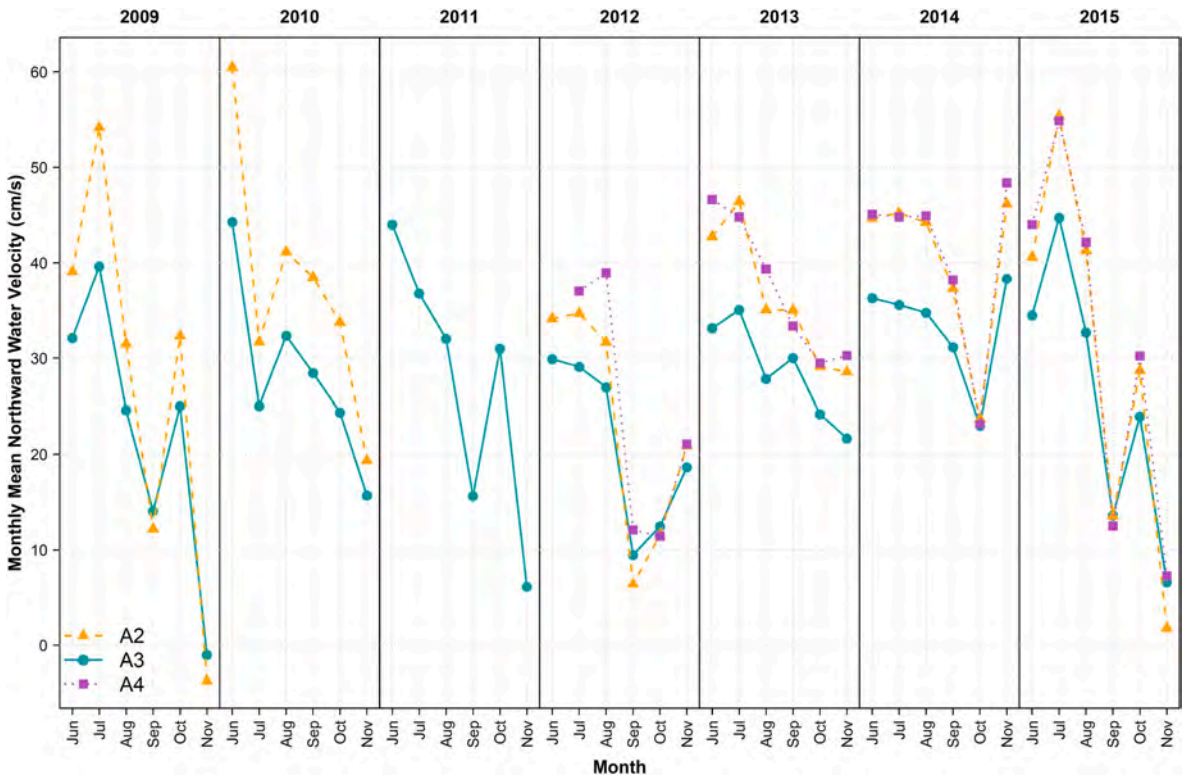

Fig. 6. Monthly mean northward water velocity (cm/s) for the June through November at each mooring site in the Bering Strait region (A2, A3, and A4; see key for colors, symbols, and line styles). See Fig. 1 for mooring locations. (For interpretation of the references to color in this figure legend, the reader is referred to the Web version of this article.)

Table 5
Summary of the overall monthly mean along-channel wind velocities (m/s) for October along with overall means for days with and without fin whale hours (FWH) in October. Wind velocities were measured at the data point at 67.5°N and 190°W. Values in parentheses are the Wilcoxon rank-sum *p*-values for the comparison between the overall October mean for each year (**bold***: significant $p < 0.05$).

Year	All October (m/s)	Days without FWH (m/s)	Days with ≥1 FWH (m/s)	Days with ≥6 FWH (m/s)	Days with ≥12 FWH (m/s)	Days with ≥18 FWH (m/s)
2009	−2.7	2.5 (**0.03***)	−5.2 (0.19)	−6.2 (0.07)	−6.6 (0.21)	NA
2010	−5.1	−3.2 (0.46)	−6.2 (0.58)	−7.3 (0.37)	−7.9 (0.25)	−9.5 (NA)
2011	−2.1	0.6 (0.12)	−4 (0.21)	−6.1 (**0.04***)	−8.7 (**0.02***)	NA
2012	−0.4	1.3 (0.97)	−0.5 (0.99)	−2.5 (0.45)	−3 (0.33)	−5.8 (NA)
2013	−6.2	−5.8 (0.88)	−6.7 (0.88)	−5.8 (0.84)	−7 (0.82)	NA
2014	−4.8	0.2 (**0.04***)	−6.2 (0.35)	−6.8 (0.25)	−7.9 (0.14)	−9.2 (NA)
2015	−4.0	5.5 (0.18)	−4.3 (0.86)	−4.7 (0.68)	−6 (0.255.3)	−7.1 (NA)

Table 6
Summary table of the Kendall's rank correlation test results for site A3. Correlation tests were conducted between the number of fin whale hours (FWH) recorded on days with fin whale calls (FWH > 0) and the daily means of: near-surface and near-bottom temperatures, along-channel wind and water velocities, water speeds, and SST. Two sets of tests were carried out: pooled data for all months for all years (2009–2015), and on October data only for all years at A3 (2009–2015).

Environmental Variable (Daily Means)	Pooled data - all months ($n = 271$)		Oct only - all years pooled ($n = 156$)	
	p	τ	*p*	τ
Near-surface Temperature	0.674	0.019	**0.012***	0.151
Near-surface Salinity	0.053	−0.087	0.851	−0.011
Near-bottom Temperature	0.82	0.01	0.129	0.084
Near-bottom Salinity	0.29	−0.044	0.507	0.037
Water Speed	**< 0.001***	**−0.167**	**< 0.001***	**−0.28**
SST	0.202	−0.054	**0.044***	**0.111**
Along-channel water velocity	**< 0.001***	**−0.15**	**< 0.001***	**−0.207**
Along-channel wind velocity	**< 0.001***	**−0.194**	**< 0.001***	**−0.231**

2014 (both near-surface and near-bottom) due to the fact that only one water mass (BCSW) was present at both levels in the water column, resulting in zeros in both the expected and observed columns of the test's contingency tables.

We were unable to perform a chi-squared test for independence for A2 and A4 due to the presence of small expected values ($E_{i,j} < 5$) in the

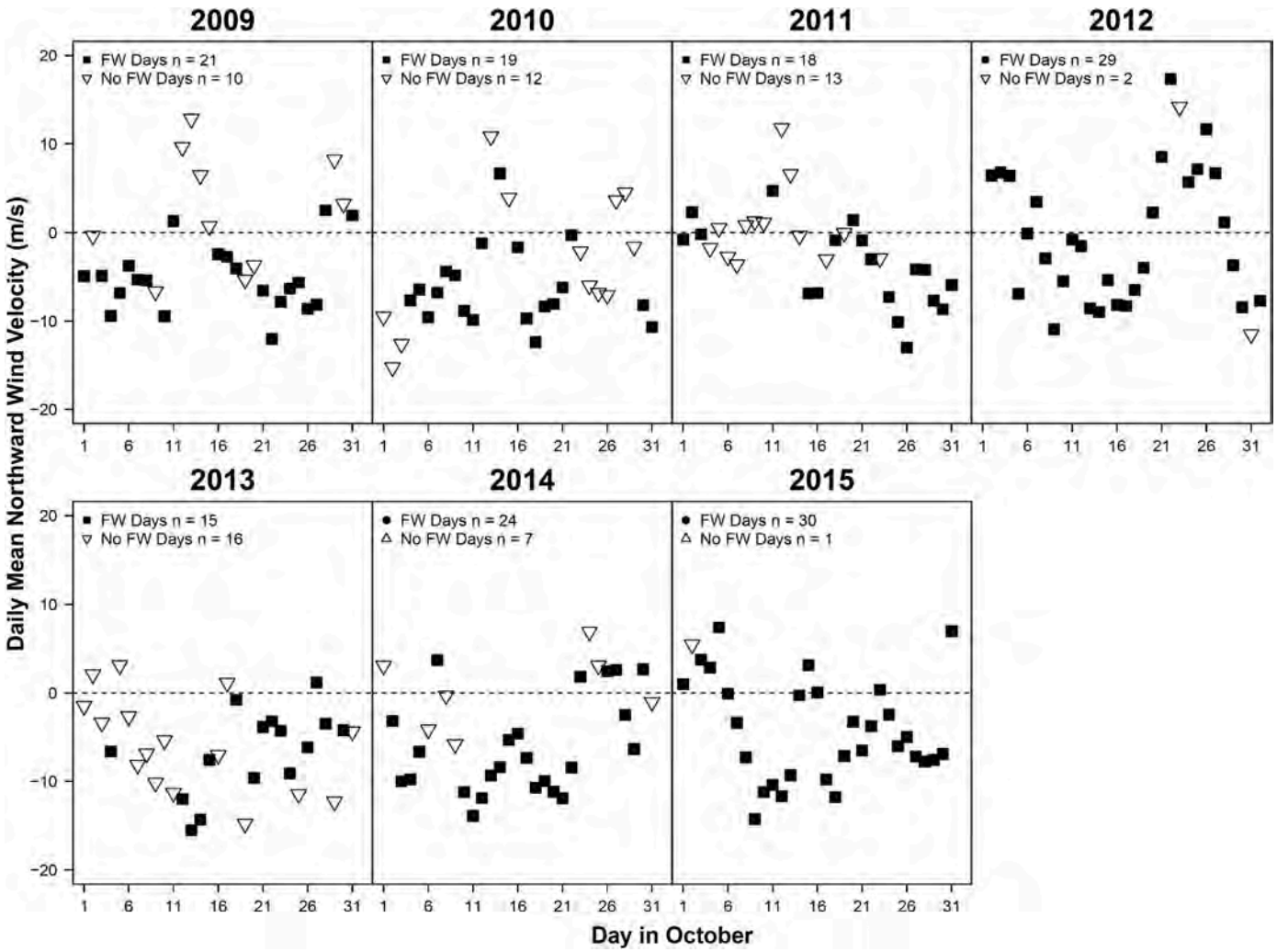

Fig. 7. Daily mean northward wind velocity for days with fin whale calls at site A3 ('FW Days', black squares) and days without fin whale calls ('No FW Days', white triangles) in October. Note that negative values signify southward wind velocities. The number of FW Days and No FW Days is included for reference.

contingency tables generated by the test. At A4, fin whale calls were only heard on days when the BCSW was present at both levels of the water column. Calling fin whales were only heard at A2 on days when the BCSW was present in the near-bottom waters. We applied a Fisher's Exact Test to the A2 near-surface water mass designations and found that fin whale calls and water mass occurrence in the near-surface waters were statistically independent of each other ($p = 0.48$).

4. Discussion

The results of this study show a pattern of interannual and spatial variation in the presence of acoustically-active fin whales in the Bering Strait region. Across all three sites, the year 2015 had the most fin whale detections followed by 2012, though these years had contrasting temperatures and salinities, sea-ice conditions, water velocity and wind patterns. Site A3, where the Anadyr Water (AW) and Bering Shelf Water (BSW) were most prevalent, had the most hours with fin whale calls, supporting our hypothesis that water masses may affect the occurrence of fin whales. We found small but significant correlations between FWH and northward wind and water velocities, near-surface temperatures and SST at site A3. However, our *p*-values for the correlation tests were potentially too low and likely overestimated the real significance of the tests given that days with fin whale calls were likely not independent of each other. In addition, the statistically significant correlations between FWH and environmental variables were small (<0.25). Thus, we conclude that it is not possible to prove a strong relationship between individual environmental parameters and FWH with our data. More data and greater spatial coverage are necessary to prove any significant association between days with fin whale calls and environmental factors in the Bering Strait region.

Most fin whale calls were heard in October, potentially due to fact that fin whale 20-Hz pulses primarily serve a reproductive purpose (Watkins et al., 2000; Croll et al., 2002; Stafford et al., 2007), and thus, tend to be heard closer to the winter mating season (Stafford et al., 2007). Consequently, fin whale vocalizations may not be a reliable indication of when fin whales first pass northwards through the Bering Strait. Additionally, the dates of departure from the Bering Strait region presented here only apply to vocal fin whales since we could not detect non-vocal whales, which could have remained in the area beyond these dates. Due to this inherent bias, the departure dates presented in this study only provide an approximation for when fin whales leave the region. The departure dates from the A3 mooring site did not exhibit a significant trend (Fig. 3), therefore it is not possible to determine whether fin whales are extending their residence time in the Chukchi Sea from our data. Perhaps this is not surprising given that we only have seven years of data, and interannual variability is substantial. In general, the fin whale departure dates at A3 occurred in early November, ranging from 31 October (2010) to 17 November (2011 and 2015). What signaled the fin whales to leave the Chukchi Sea is not clear. Sea-ice concentrations in the study area around the last detection dates were

well below 'ice-free' levels (<15%; Table 4), indicating that the Bering Strait was still navigable and free of sea ice. It is possible, though, that fin whales respond to cooling water temperatures since all departure dates occurred before near-surface and near-bottom water temperatures at A3 reached below 0 °C (Fig. 4).

The overwhelming majority of fin whale calls were detected at site A3, where calling fin whales were heard every year. There are multiple possible explanations for the spatial variability observed in fin whale detections. First, site A3 is situated at the confluence of two productive water masses, the AW and BSW, which likely provide better feeding opportunities for fin whales. The dominant water mass detected at A3 was the Bering Chukchi Summer Water (BCSW), which is composed of the AW and BSW, and thus has high nutrient levels and larger zooplankton (Eisner et al., 2013; Ershova et al., 2015; Danielson et al., 2017). Though fin whale calls were also detected on days when other fresher water masses were present at A3, including days in 2015 when Alaskan Coastal Water (ACW) was present in the near-surface (Fig. S13). Fin whale calls were also detected on days in September 2012 when a fresh, cold signal appeared in the near-surface waters at A3, possibly indicating the presence of the Siberian Coastal Current (SCC).

The SCC occasionally flows into the Bering Strait during periods with strong or persistent southward winds (Weingartner et al., 1999). Ershova et al. (2015) detected the presence of the SCC in the central Chukchi Sea in September 2012, therefore it is possible that the reach of the SCC extended to the A3 site that month. Fig. S8 shows that winds measured in September 2012 were predominantly southward, which has been shown to cause the ACW to deviate away from the Alaskan coast and towards the western Chukchi Sea (Woodgate et al., 2015; Pisareva, 2018; Morris, 2019). Often the presence of the cold and fresh SCC creates a front (Weingartner et al., 1999), which could isolate and cluster prey. In 1992–1993, Moore et al. (1995) observed bowhead whales (*Balaena mysticetus*) feeding in close association with salinity and thermal fronts along the Chukotka coast. Moreover, *Thysanoessa inermis*, a common fin whale prey (Nemoto, 1959; Witteveen and Wynne, 2016), was found to be the dominant zooplankton species collected from a dense prey patch near a front, lending support to the potential importance of the SCC in creating favorable feeding conditions for fin whales at A3.

In addition to its proximity to productive water masses, A3 may be situated close to oceanographic features created by currents, such as island wake eddies, that are known to create favorable foraging opportunities for baleen whales (Johnston et al., 2005a; Chenoweth et al., 2011). Eddies create upwelling zones which promote phytoplankton blooms (Hasegawa et al., 2009) and have been shown to be important feeding habitat for auklets and other planktivores in the Bering and Chukchi seas (Piatt and Springer, 2003). In the Bay of Fundy, Canada, island wake eddy systems were found to be important feeding grounds for fin whales as well as minke whales (*B. acutorostrata*) and harbor porpoises (*Phocoena phocoena*; Johnston et al., 2005a,b). Currents moving past the Diomede Islands generate island wake eddies (Coachman et al., 1975; Woodgate et al., 2015) that are then carried northwards towards A3, according to satellite SST data (Woodgate, pers. comm.). The island wake eddies may create opportune feeding conditions for fin whales at A3.

In contrast, site A2 had fin whale detections in all recording years but in lower abundance, while fin whale calls were largely absent from site A4. Given its position in the less-productive ACC, A4 may present lower quality feeding areas for fin whales than the other two sites. Though A2 had similar water mass composition as A3, water velocities were higher at A2, potentially transporting prey out of the area. Therefore, fin whales may be less inclined to stay at in the region around A2 due to fewer feeding opportunities. Also, the position of site A3 north and towards the middle of the Bering Strait gives it an advantage over A2 in capturing the calls of fin whales migrating through the western strait. Whereas A2 and A4 can only record the calls of fin whales passing through the east channel of the strait, A3 can potentially record calling whales migrating through both channels.

While the spatial variability in fin whale detections may be explained, the exact environmental mechanisms for the observed temporal variability are less clear. Both 2012 and 2015 stand out as years with the highest number of fin whale detections at A3, yet the two years had very different environmental conditions. The year 2012 had the coldest October mean temperatures (near-bottom October mean at A3 = 1.0 °C), late sea ice breakup (16 May), anomalously low flow (Woodgate, 2018), and weak mean northward wind velocities in the fall. On the other hand, 2015 had a very warm annual mean temperature (near-bottom October mean at A3 = 3.6 °C), earlier sea ice breakup (4 May), high flow (Woodgate, 2018), and variable northward wind velocities. Our results suggest that at A3, the occurrence of fin whale calls is more strongly related to southward winds than northward winds, but this relation does not hold for all years (Table 5). Thus, we cannot attribute interannual variation in the acoustic presence of fin whales to any one environmental predictor. Instead, we believe that a combination of conditions not only in the Chukchi Sea, but also in the Bering Sea, contributes to the abundance of fin whales in the study area. We hypothesize a series of 'push' and 'pull' factors below that may have influenced the observed interannual variation in the presence of acoustically-active fin whales.

Pull factors imply that conditions in the Chukchi Sea were favorable for zooplankton and other fin whale prey in 2012 and 2015, thus drawing more fin whales into the area to feed. The abundance of hours with fin whale calls at A3 in 2012 may point to the fact that the year was particularly cold, and thus, productive. Colder temperatures are more favorable for the secondary production of *Calanus* copepods (Kimmel et al., 2018), a prominent constituent of the Chukchi Sea zooplankton. Cold years in the Bering and Chukchi seas have been also found to have higher zooplankton biomass and abundance (Ohashi et al., 2013; Ershova et al., 2015; Pinchuk and Eisner, 2017), and thus stronger recruitment for walleye pollock (*Gadus chalcogrammus*) and Pacific cod (*G. macrocephalus*; Stabeno et al., 2012), which are zooplankton predators like fin whales. Friday et al. (2013) observed twice as many fin whales along the eastern Bering Sea shelf in 2008 and 2010 when temperatures were cold than they did in 2002, a warm year. In their August–September 2012 sampling of the Chukchi Sea, Danielson et al. (2017) observed an abnormally high biomass of large copepods as well as a predominance of the BCSW in the bottom water at multiple sampling stations. During the same sampling period, Pinchuk and Eisner (2017) report a high abundance of *Calanus glacialis* and widespread distribution of Pacific-origin zooplankton in 2012, adding evidence to our hypothesis that 2012 was a favorable year for fin whale prey.

Conversely, 2015 was a warm year with high salinities. High salinities are usually indicative of high AW content and thus are typically associated with high nutrient levels (Danielson et al., 2017). Consequently, 2015 may have had higher zooplankton abundance due to a nutrient-rich environment. Pinchuk and Eisner (2017) found a strong correlation between the biomass of Pacific-origin zooplankton and high salinities associated with the BCSW, which was the dominant water mass at A3 in 2015 (Supplementary Figs. S12–S14). It is also possible that the earlier sea-ice retreat and warmer water temperatures observed in 2015 created better conditions for Pacific-origin copepods and euphausiids. Matsuno et al. (2011) found that Pacific copepod species (e.g. *Eucalanus bungii*) expanded into the Chukchi Sea in 2007, a year with relatively early sea-ice retreat and abnormally high sea surface temperatures, similar to 2015. A notable pull factor for 2015 could also have been the strong water velocities measured in the Bering Strait. Strong velocities likely led to higher transport of both nutrients and zooplankton from the Bering Sea into the Chukchi Sea, creating better feeding opportunities for summer migrant fin whales.

In contrast to pull factors, potential push factors consist of poorer conditions in other reaches of the fin whale range, thereby sending fin whales into the Chukchi Sea in search of better conditions. Such areas include the Bering Sea and Gulf of Alaska, where fin whales are known

to occur in the summer months (Moore et al., 1998, 2000; Stafford et al., 2007). Both 2014 and 2015 were significantly warmer years in comparison to historical records for the Bering Sea (Duffy-Anderson et al., 2017). Warm years in the Bering Sea result in poor recruitment in walleye pollock due to the prevalence of small, lipid-poor copepods (Kimmel et al., 2018). In 2015, an anomalously warm water mass, nicknamed the "Blob," pervaded the North Pacific, leading to declines in krill and to northward distribution shifts of multiple marine species (Cavole et al., 2016). Concurrent with the appearance of the Blob were reports of a mass mortality event of common murres (*Uria aalge*) in the Gulf of Alaska (Piatt et al., 2018). Additionally, 12 fin whales stranded on Kodiak Island, AK, between May and June 2015 (Savage, 2017). Though the causes of death for the whales were not determined, ecological conditions rather than anthropogenic factors (e.g. ship strikes) are thought to be the culprit (Savage, 2017). Warmer temperatures observed in 2015 may have affected prey availability in other fin whale summer feeding grounds, pushing fin whales into the Chukchi Sea in search of better feeding opportunities.

Another possible explanation for the increased observation of fin whale calls in 2015 is that the North Pacific population of fin whales is increasing (Zerbini et al., 2006), and thus may be reclaiming portions of its previous range (Clarke et al., 2013; Brower et al., 2018). An increased number of fin whales observed during annual surveys conducted by the Aerial Surveys of Arctic Marine Mammals Project (ASAMM) from 2008–2016 in comparison to 1982–1991 supports this theory (Brower et al., 2018). Brower et al. (2018) report seeing the most fin whales in the south-central Chukchi Sea in 2014 (44% of observations) and in 2015 (27%). However, it is difficult to evaluate habitat reclamation of fin whales using their calls alone given that only males are thought to produce the 20-Hz pulse and we could only detect vocal fin whales.

Limitations of the present study include limited spatial coverage of the study area with hydrophones located in only the east channel and north of the Bering Strait. Since there are no recent surveys on the western side of the Bering Strait or Chukchi Sea, our knowledge of fin whale habitat use in this region is limited. Given that the productive AW is typically found mainly in the west channel of the Bering Strait, it is possible that most fin whales may traverse through the strait on the western side. However, without adequate observation platforms covering both sides of the strait, the exact migration path of fin whales in the region remains unknown.

The results of this study corroborate patterns of interannual variation in fin whale presence observed by previous studies. Like the present study, Delarue et al., 2013 noted low fin whale detections in the northeast Chukchi Sea in 2009 and 2010, attributing diminished vocal activity to poorer feeding conditions. In contrast, more fin whales were heard in 2007, a particularly warm year in the Chukchi Sea with early ice retreat and low sea-ice extent, as well as high transport through the Bering Strait (Woodgate et al., 2010; Delarue et al., 2013). The conditions in 2007 described by Delarue et al. (2013) are very similar to those we observed in 2015, when fin whale calls were the most abundant.

Our results present a preliminary examination of how environmental variations in the Bering Strait and southern Chukchi Sea may lead to interannual variability in the acoustic presence of fin whales. Though we were unable to identify a single environmental driver that explained the variation, differences in temperature, salinity, wind and water velocities likely played a role. There are potentially numerous combinations of environmental variables that create preferential feeding opportunities for fin whales. Delarue et al. (2013) hypothesize that perhaps the combination of environmental variables observed in 2007 (warm SSTs, low sea-ice concentrations, and high transport) created favorable conditions for fin whale prey. However, the abundance of calling fin whales in 2012, a period with colder water temperatures, low transport, and high spring sea-ice concentrations, suggests that alternative environmental drivers are also favorable for fin whale feeding.

Conditions in the Bering Sea may also be an important factor in determining fin whale occurrence in the Chukchi Sea. Comparing fin whale detections in the southern Chukchi Sea with those in the Bering Sea could help indicate whether fin whale presence in one region results in higher fin whale presence in the other. Also, examining environmental conditions in the Bering Sea for 2009–2015 could shed light on the patterns of fin whale occupation found in the present study. Continued monitoring of fin whale presence in the southern Chukchi and Bering seas in relation to oceanographic features is necessary for composing a more complete picture of how fin whale presence in the Pacific Arctic is changing in response to environmental shifts over time.

Declaration of competing interest

The authors declare that they have no known competing financial interests or personal relationships that could have appeared to influence the work reported in this paper.

CRediT authorship contribution statement

Erica Escajeda: Conceptualization, Methodology, Software, Formal analysis, Investigation, Visualization, Data curation, Writing - original draft, Writing - review & editing. **Kathleen M. Stafford:** Conceptualization, Validation, Supervision, Resources, Data curation, Project administration, Funding acquisition, Writing - review & editing. **Rebecca A. Woodgate:** Data curation, Validation, Resources, Project administration, Funding acquisition, Writing - review & editing. **Kristin L. Laidre:** Supervision, Resources, Writing - review & editing.

Acknowledgements

This material is based upon work supported by the National Science Foundation (NSF) Graduate Research Fellowship Program under grant number DGE-1256082. Any opinions, findings, and conclusions or recommendations expressed in this material are those of the author(s) and do not necessarily reflect the views of NSF. This work was also supported by the NSF Polar Programs Arctic Observing Network (R. Woodgate grant numbers PLR-1304052 and 1758565; K. Stafford grant number 1107106). A portion of the mooring work was supported by the Russian-American Long-term Census of the Arctic (RUSALCA), funded by the U. S. National Oceanic and Atmospheric Administration (NOAA) (grant numbers NA10OAR4320148, AM105, and AM133), the Applied Physics Laboratory at the University of Washington, and the National Science Foundation (grant number ARC-1107106). The Bering Strait mooring data are available at the permanent archives of the U.S. National Centers for Environmental Information/National Oceanographic Data Center, www.nodc.noaa.gov, and at: psc.apl.washington.edu/BeringStrait.html. This manuscript may be referenced through the North Pacific Research Board Arctic Integrated Ecosystem Research Program archives as ArcticIERP-13. We thank the four reviewers for their suggestions which improved the manuscript.

Appendix A. Supplementary data

Supplementary data to this article can be found online at https://doi.org/10.1016/j.dsr2.2020.104782.

References

Baker, M., Kivva, K., Pisareva, M., Watson, J., Selivanova, J., This issue. Shifts in the physical environment in the Pacific Arctic and implications for ecological timing and conditions. Deep Sea Res. Part II Top. Stud. Oceanogr.

Beitsch, A., Kaleschke, L., Kern, S., 2014. Investigating high-resolution AMSR2 sea ice concentrations during the February 2013 fracture event in the Beaufort Sea. Rem. Sens. 6, 3841–3856. https://doi.org/10.3390/rs6053841.

Brower, A.A., Clarke, J.T., Ferguson, M.C., 2018. Increased sightings of subArctic cetaceans in the eastern Chukchi Sea, 2008–2016: population recovery, response to climate change, or increased survey effort? Polar Biol. 41, 1033–1039. https://doi.org/10.1007/s00300-018-2257-x.

Cavalieri, D., 1996. Sea Ice Concentrations from Nimbus-7 SMMR and DMSP SSM/I-SSMIS Passive Microwave Data. https://doi.org/10.5067/8GQ8LZQVL0VL. Version 1. (Accessed 25 April 2017).
Cavalieri, D.J., Parkinson, C.L., 2012. Arctic sea ice variability and trends, 1979-2010 Cryosphere 6, 881–889. https://doi.org/10.5194/tc-6-881-2012.
Cavole, L., Diner, R., Giddings, A., Koester, I., Pagniello, C., Paulsen, M.-L., Ramirez-Valdez, A., Schwenck, S., Yen, N., Zill, M., Franks, P., 2016. Biological impacts of the 2013–2015 Warm-Water Anomaly in the northeast Pacific: winners, losers, and the future. Oceanography 29. https://doi.org/10.5670/oceanog.2016.32.
Chenoweth, E., Gabriele, C., Hill, D., 2011. Tidal influences on humpback whale habitat selection near headlands. Mar. Ecol. Prog. Ser. 423, 279–289. https://doi.org/10.3354/meps08891.
Clarke, J., Stafford, K., Moore, S., Rone, B., Aerts, L., Crance, J., 2013. Subarctic cetaceans in the southern Chukchi Sea: evidence of recovery or response to a changing ecosystem. Oceanography 26, 136–149. https://doi.org/10.5670/oceanog.2013.81.
Clarke, J.T., Ferguson, M.C., Curtice, C., Harrison, J., 2015. 8. Biologically important areas for cetaceans within U.S. waters – Arctic Region. Aquat. Mamm. 41, 94–103. https://doi.org/10.1578/AM.41.1.2015.94.
Coachman, L.K., Aagaard, K., Tripp, R.B., 1975. Bering Strait: the Regional Physical Oceanography. University of Washington Press, Seattle.
Comiso, J.C., Parkinson, C.L., Gersten, R., Stock, L., 2008. Accelerated decline in the Arctic sea ice cover. Geophys. Res. Lett. 35 https://doi.org/10.1029/2007GL031972.
Croll, D.A., Clark, C.W., Acevedo, A., Tershy, B., Flores, S., Gedamke, J., Urban, J., 2002. Only male fin whales sing loud songs. Nature 417, 809.
Danielson, S.L., Eisner, L., Ladd, C., Mordy, C., Sousa, L., Weingartner, T.J., 2017. A comparison between late summer 2012 and 2013 water masses, macronutrients, and phytoplankton standing crops in the northern Bering and Chukchi Seas. Deep Sea Res. Part II Top. Stud. Oceanogr. 135, 7–26. https://doi.org/10.1016/j.dsr2.2016.05.024.
Delarue, J., Martin, B., Hannay, D., Berchok, C.L., 2013. Acoustic occurrence and affiliation of fin whales detected in the northeastern Chukchi Sea. Arctic 66, 159–172. July to October 2007–10.
Duffy-Anderson, J.T., Stabeno, P.J., Siddon, E.C., Andrews, A.G., Cooper, D.W., Eisner, L. B., Farley, E.V., Harpold, C.E., Heintz, R.A., Kimmel, D.G., Sewall, F.F., Spear, A.H., Yasumishii, E.C., 2017. Return of warm conditions in the southeastern Bering Sea: phytoplankton - fish. PloS One x12, e0178955. https://doi.org/10.1371/journal.pone.0178955.
Edds-Walton, P.L., 1997. Acoustic communication signals of mysticete whales. Bioacoustics 8, 47–60. https://doi.org/10.1080/09524622.1997.9753353.
Eisner, L., Hillgruber, N., Martinson, E., Maselko, J., 2013. Pelagic fish and zooplankton species assemblages in relation to water mass characteristics in the northern Bering and southeast Chukchi seas. Polar Biol. 36, 87–113. https://doi.org/10.1007/s00300-012-1241-0.
Ershova, E., Hopcroft, R., Kosobokova, K., Matsuno, K., Nelson, R.J., Yamaguchi, A., Eisner, L., 2015. Long-term changes in summer zooplankton communities of the western Chukchi Sea, 1945–2012. Oceanography 28, 100–115. https://doi.org/10.5670/oceanog.2015.60.
Flinn, R.D., Trites, A.W., Gregr, E.J., Perry, R.I., 2002. Diets of fin, sei, and sperm whales in British Columbia: an analysis of commercial whaling records, 1963-1967. Mar. Mamm. Sci. 18, 663–679. https://doi.org/10.1111/j.1748-7692.2002.tb01065.x.
Frey, K.E., Moore, G.W.K., Cooper, L.W., Grebmeier, J.M., 2015. Divergent patterns of recent sea ice cover across the Bering, Chukchi, and Beaufort seas of the Pacific Arctic Region. Prog. Oceanogr. 136, 32–49. https://doi.org/10.1016/j.pocean.2015.05.009.
Friday, N.A., Zerbini, A.N., Waite, J.M., Moore, S.E., Clapham, P.J., 2013. Cetacean distribution and abundance in relation to oceanographic domains on the eastern Bering Sea shelf, June and july of 2002 2008, and 2010. Deep Sea res. Part II top. Stud. Oceanogr. 94, 244–256. https://doi.org/10.1016/j.dsr2.2013.03.011.
Grebmeier, J.M., Moore, S.E., Overland, J.E., Frey, K.E., Gradinger, R., 2010. Biological Response to Recent Pacific Arctic Sea Ice Retreats. Eos, Trans. 161–162. https://doi.org/10.1029/2010EO180001.
Hasegawa, D., Lewis, M.R., Gangopadhyay, A., 2009. How islands cause phytoplankton to bloom in their wakes. Geophys. Res. Lett. 36 https://doi.org/10.1029/2009GL039743.
Hauser, D.D.W., Laidre, K.L., Stafford, K.M., Stern, H.L., Suydam, R.S., Richard, P.R., 2017. Decadal shifts in autumn migration timing by Pacific Arctic beluga whales are related to delayed annual sea ice formation. Global Change Biol. 23, 2206–2217. https://doi.org/10.1111/gcb.13564.
Hopcroft, R.R., Kosobokova, K.N., Pinchuk, A.I., 2010. Zooplankton community patterns in the Chukchi Sea during summer 2004. Deep Sea Res. Part II Top. Stud. Oceanogr. 57, 27–39. https://doi.org/10.1016/j.dsr2.2009.08.003.
Jakobsson, M., Mayer, L.A., Coakley, B., Dowdeswell, J.A., Forbes, S., Fridman, B., Hodnesdal, H., Noormets, R., Pedersen, R., Rebesco, M., Schenke, H.-W., Zarayskaya, Y.A, Accettella, D., Armstrong, A., Anderson, R.M., Bienhoff, P., Camerlenghi, A., Church, I., Edwards, M., Gardner, J.V., Hall, J.K., Hell, B., Hestvik, O.B., Kristoffersen, Y., Marcussen, C., Mohammad, R., Mosher, D., Nghiem, S.V., Pedrosa, M.T., Travaglini, P.G., Weatherall, P., 2012. The International Bathymetric Chart of the Arctic Ocean (IBCAO) version 3.0. Geophys. Res. Lett. 39 https://doi.org/10.1029/2012GL052219.
Johnston, D., Thorne, L., Read, A., 2005a. Fin whales *Balaenoptera physalus* and minke whales *Balaenoptera acutorostrata* exploit a tidally driven island wake ecosystem in the Bay of Fundy. Mar. Ecol. Prog. Ser. 305, 287–295. https://doi.org/10.3354/meps305287.
Johnston, D., Westgate, A., Read, A., 2005b. Effects of fine-scale oceanographic features on the distribution and movements of harbour porpoises *Phocoena phocoena* in the Bay of Fundy. Mar. Ecol. Prog. Ser. 295, 279–293. https://doi.org/10.3354/meps295279.
Kaleschke, L., Lüpkes, C., Vihma, T., Haarpaintner, J., Bochert, A., Hartmann, J., Heygster, G., 2001. SSM/I sea ice remote sensing for mesoscale ocean-atmosphere interaction analysis. Can. J. Rem. Sens. 27, 526–537. https://doi.org/10.1080/07038992.2001.10854892.
Kaleschke, L., Tian-Kunze, X., 2016. AMSR2 ASI 3.125 Km Sea Ice Concentration Data, vol. 1. Institute of Oceanography, University of Hamburg. Germany, digital media (ftp-projects.zmaw.de/seaice/) [1/1/2013 - 31/12/2015].
Kimmel, D.G., Eisner, L.B., Wilson, M.T., Duffy-Anderson, J.T., 2018. Copepod dynamics across warm and cold periods in the eastern Bering Sea: implications for walleye pollock (*Gadus chalcogrammus*) and the Oscillating Control Hypothesis. Fish. Oceanogr. 27, 143–158. https://doi.org/10.1111/fog.12241.
Kitamura, M., Amakasu, K., Kikuchi, T., Nishino, S., 2017. Seasonal dynamics of zooplankton in the southern Chukchi Sea revealed from acoustic backscattering strength. Continent. Shelf Res. 133, 47–58. https://doi.org/10.1016/j.csr.2016.12.009.
Laidre, K.L., Heide-Jørgensen, M.P., 2012. Spring partitioning of Disko Bay, west Greenland, by arctic and subarctic baleen whales. ICES J. Mar. Sci. 69, 1226–1233. https://doi.org/10.1093/icesjms/fss095.
Laidre, K.L., Stern, H., Kovacs, K.M., Lowry, L., Moore, S.E., Regehr, E.V., Ferguson, S.H., Wiig, Ø., Boveng, P., Angliss, R.P., Born, E.W., Litovka, D., Quakenbush, L., Lydersen, C., Vongraven, D., Ugarte, F., 2015. Arctic marine mammal population status, sea ice habitat loss, and conservation recommendations for the 21st century: Arctic Marine Mammal Conservation. Conserv. Biol. 29, 724–737. https://doi.org/10.1111/cobi.12474.
Matsuno, K., Yamaguchi, A., Hirawake, T., Imai, I., 2011. Year-to-year changes of the mesozooplankton community in the Chukchi Sea during summers of 1991, 1992 and 2007. Polar Biol. 34, 1349–1360. https://doi.org/10.1007/s00300-011-0988-z, 2008.
Markus, T., Stroeve, J.C., Miller, J., 2009. Recent changes in Arctic sea ice melt onset, freezeup, and melt season length. J. Geophys. Res. 114 https://doi.org/10.1029/2009JC005436.
McDonald, M.A., Hildebrand, J.A., Webb, S.C., 1995. Blue and fin whales observed on a seafloor array in the Northeast Pacific. J. Acoust. Soc. Am. 98, 712–721. https://doi.org/10.1121/1.413565.
Mellinger, D.K., Clark, C.W., 2000. Recognizing transient low-frequency whale sounds by spectrogram correlation. J. Acoust. Soc. Am. 107, 3518–3529.
Mellinger, D., 2002. Ishmael 1.0 user's guide. NOAA technical memorandum OAR PMEL-120. http://www.pmel.noaa.gov/pubs/PDF/mell2434/mell2434.pdf.
Mizroch, S.A., Rice, D.W., Breiwick, J.M., 1984. The fin whale, *Balaenoptera physalus*. Mar. Fish. Rev. 46, 20–24.
Mizroch, S.A., Rice, D.W., Zwiefelhofer, D., Waite, J., Perryman, W.L., 2009. Distribution and movements of fin whales in the north Pacific Ocean. Mamm Rev. 39, 193–227. https://doi.org/10.1111/j.1365-2907.2009.00147.x.
Moore, S.E., George, J.C., Coyle, K.O., Weingartner, T.J., 1995. Bowhead whales along the Chukotka coast in autumn. Arctic 48, 155–160.
Moore, S.E., Stafford, K.M., Dahlheim, M.E., Fox, C.G., Braham, H.W., Polovina, J.J., Bain, D.E., 1998. Seasonal variation in reception of fin whale calls at five geographic areas in the North Pacific. Mar. Mamm. Sci. 14, 617–627.
Moore, S.E., Waite, J., Mazzuca, L., Hobbs, R., 2000. Mysticete whale abundance and observations of prey associations on the central Bering Sea shelf. J. Cetacean Res. Manag. 2, 227–234.
Morris, B.A., 2019. Seasonality and Forcing Factors of the Alaskan Coastal Current in the Bering Strait from July 2011 to July 2012 (Thesis). University of Washington, Seattle, WA.
Nasu, K., 1960. Oceanographic investigation in the Chukchi sea during the summer of 1958. Sci. Rep. Whales Res. Ins. 15, 143–157.
Nemoto, T., 1959. Food of baleen whales with reference to whale movements. Sci. Rep. Whales Res. Ins. 14, 149–290.
Nemoto, T., Kasuya, T., 1965. Foods of baleen whales in the Gulf of Alaska of the north pacific. Sci. Rep. Whales Res. Ins. 19, 45–51.
Nikulin, P.G., 1946. Distribution of cetaceans in the seas surrounding the Chukchi Peninsula. Izv. TINRO 22.
Ohashi, R., Yamaguchi, A., Matsuno, K., Saito, R., Yamada, N., Iijima, A., Shiga, N., Imai, I., 2013. Interannual changes in the zooplankton community structure on the southeastern Bering Sea shelf during summers of 1994–2009. Deep Sea Res. Part II Top. Stud. Oceanogr. 94, 44–56. https://doi.org/10.1016/j.dsr2.2013.03.018.
Piatt, J., Springer, A., 2003. Advection, pelagic food webs and the biogeography of seabirds in Beringia. Mar. Ornithol. 31, 141–154.
Piatt, J., Jones, T., Kuletz, K., et al., 2018. Unprecedented scale of seabird mortality in the NE Pacific during the 2015-2016 marine heatwave. In: Presented at the Alaska Marine Science Symposium. Anchorage, Alaska.
Pike, G., 1950. Stomach contents of whales caught off the coast of British Columbia. Fish. Res. Board Can. Pac. Prog. Rep. 83, 27–28.
Pinchuk, A.I., Eisner, L.B., 2017. Spatial heterogeneity in zooplankton summer distribution in the eastern Chukchi Sea in 2012–2013 as a result of large-scale interactions of water masses. Deep Sea Res. Part II Top. Stud. Oceanogr. 135, 27–39. https://doi.org/10.1016/j.dsr2.2016.11.003.
Pisareva, M.N., Pickart, R.S., Spall, M.A., Nobre, C., Torres, D.J., Moore, G.W.K., Whitledge, T.E., 2015. Flow of pacific water in the western Chukchi Sea: results from the 2009 RUSALCA expedition. Deep-Sea Res. Part I Oceanogr. Res. Pap. 105, 53–73. https://doi.org/10.1016/j.dsr.2015.08.011.

Pisareva, M.N., 2018. An overview of the recent research on the Chukchi Sea water masses and their circulation. Russ. J. Earth Sci. 18, 1–13.
Post, E., Alley, R.B., Christensen, T.R., Macias-Fauria, M., Forbes, B.C., Gooseff, M.N., Iler, A., Kerby, J.T., Laidre, K.L., Mann, M.E., Olofsson, J., Stroeve, J.C., Ulmer, F., Virginia, R.A., Wang, M., 2019. The polar regions in a 2°C warmer world. Sci. Adv. 5, eaaw9883 https://doi.org/10.1126/sciadv.aaw9883.
R Core Team, 2019. R: A language and environment for statistical computing. R Foundation for Statistical Computing, Vienna, Austria. https://www.R-project.org/.
Reynolds, R.W., Smith, T.M., Liu, C., Chelton, D.B., Casey, K.S., Schlax, M.G., 2007. Daily high-resolution-blended analyses for sea surface temperature. J. Clim. 20, 5473–5496. https://doi.org/10.1175/2007JCLI1824.1.
Root, T.L., Price, J.T., Hall, K.R., Schneider, S.H., Rosenzweig, C., Pounds, J.A., 2003. Fingerprints of global warming on wild animals and plants. Nature 421, 57–60. https://doi.org/10.1038/nature01333.
Savage, K., 2017. Alaska and British Columbia Large Whale Unusual Mortality Event Summary Report. Protected Resources Division, National Oceanic and Atmospheric Administration, Juneau, AK.
Serreze, M.C., Barrett, A.P., Stroeve, J.C., Kindig, D.N., Holland, M.M., 2009. The emergence of surface-based Arctic amplification. Cryosphere 3, 11–19. https://doi.org/10.5194/tc-3-11-2009.
Serreze, M.C., Crawford, A.D., Stroeve, J.C., Barrett, A.P., Woodgate, R.A., 2016. Variability, trends, and predictability of seasonal sea ice retreat and advance in the Chukchi Sea. J. Geophys. Res.: Oceans 121, 7308–7325. https://doi.org/10.1002/2016JC011977.
Sigler, M.F., Mueter, F.J., Bluhm, B.A., Busby, M.S., Cokelet, E.D., Danielson, S.L., Robertis, A.D., Eisner, L.B., Farley, E.V., Iken, K., Kuletz, K.J., Lauth, R.R., Logerwell, E.A., Pinchuk, A.I., 2017. Late summer zoogeography of the northern Bering and Chukchi seas. Deep Sea Res. Part II Top. Stud. Oceanogr. 135, 168–189. https://doi.org/10.1016/j.dsr2.2016.03.005.
Širović, A., Hildebrand, J.A., Wiggins, S.M., 2007. Blue and fin whale call source levels and propagation range in the Southern Ocean. J. Acoust. Soc. Am. 122, 1208–1215. https://doi.org/10.1121/1.2749452.
Širović, A., Williams, L.N., Kerosky, S.M., Wiggins, S.M., Hildebrand, J.A., 2013. Temporal separation of two fin whale call types across the eastern North Pacific. Mar. Biol. 160, 47–57. https://doi.org/10.1007/s00227-012-2061-z.
Sleptsov, M.M., 1961. O kolebaniakh chislennosti kitov v Chukotskom more v raznye gody. (On fluctuations in the number of whales in the Chukchi Sea in different years). In: Proceedings of the A.N. Severtsov Institute of Animal Morphology. Nauka, Moscow, pp. 54–64.
Spreen, G., Kaleschke, L., Heygster, G., 2008. Sea ice remote sensing using AMSR-E 89-GHz channels. J. Geophys. Res. 113, C02S03. https://doi.org/10.1029/2005JC003384.
Springer, A.M., McRoy, C.P., 1993. The paradox of pelagic food webs in the northern Bering Sea—III. Patterns of primary production. Continent. Shelf Res. 13, 575–599. https://doi.org/10.1016/0278-4343(93)90095-F.
Stabeno, P.J., Kachel, N.B., Moore, S.E., Napp, J.M., Sigler, M., Yamaguchi, A., Zerbini, A.N., 2012. Comparison of warm and cold years on the southeastern Bering Sea shelf and some implications for the ecosystem. Deep Sea Res. Part II Top. Stud. Oceanogr. 65–70, 31–45. https://doi.org/10.1016/j.dsr2.2012.02.020.
Stabeno, P.J., Bell, S.W., Bond, N.A., Kimmel, D.G., Mordy, C.W., Sullivan, M.E., 2019. Distributed biological observatory region 1: Physics, chemistry and plankton in the northern Bering Sea. Deep Sea Res. Part II Top. Stud. Oceanogr. 162, 8–21. https://doi.org/10.1016/j.dsr2.2018.11.006.
Stafford, K.M., Mellinger, D.K., Moore, S.E., Fox, C.G., 2007. Seasonal variability and detection range modeling of baleen whale calls in the Gulf of Alaska, 1999–2002. J. Acoust. Soc. Am. 122, 3378–3390. https://doi.org/10.1121/1.2799905.
Stroeve, J.C., Serreze, M.C., Holland, M.M., Kay, J.E., Malanik, J., Barrett, A.P., 2012. The Arctic's rapidly shrinking sea ice cover: a research synthesis. Climatic Change 110, 1005–1027. https://doi.org/10.1007/s10584-011-0101-1.
Stroeve, J.C., Markus, T., Boisvert, L., Miller, J., Barrett, A., 2014. Changes in Arctic melt season and implications for sea ice loss. Geophys. Res. Lett. 41, 1216–1225. https://doi.org/10.1002/2013GL058951.
Tomilin, A.G., 1957. Zveri SSSR i prilezhashchikh stran (the Mammals of the USSR and adjacent countries). Vol. IX. Kitoobraznye (cetacea). In: Proceedings of the USSR Academy of Sciences. Nauk USSR, Moscow, p. 756 [In Russian].
Tsujii, K., Otsuki, M., Akamatsu, T., Matsuo, I., Amakasu, K., Kitamura, M., Kikuchi, T., Miyashita, K., Mitani, Y., 2016. The migration of fin whales into the southern Chukchi Sea as monitored with passive acoustics. ICES J. Mar. Sci.: J. du Conseil 73, 2085–2092. https://doi.org/10.1093/icesjms/fsv271.
Vaughan, D.G., Comiso, J., Allison, I., Carrasco, J., Kaser, G., Kwok, R., et al., 2013. Observations: cryosphere. In: Stocker, T.F., Qin, D., Plattner, G.K., Tignor, M., Allen, S.K., Boschung, J., Nauels, A., et al. (Eds.), Climate Change 2013: the Physical Science Basis. Contribution of Working Group I to the Fifth Assessment Report of the Intergovernmental Panel on Climate Change Cambridge. Cambridge University Press, United Kingdom and New York, NY, USA.
Votrogov, L.M., Ivashin, M.V., 1980. Sightings of fin and humpback whales in the Bering and Chukchi seas. Rep. Int. Whal. Comm. 30, 247–248.
Walsh, J.E., Fetterer, F., Scott stewart, J., Chapman, W.L., 2017. A database for depicting Arctic sea ice variations back to 1850. Geogr. Rev. 107, 89–107. https://doi.org/10.1111/j.1931-0846.2016.12195.x.
Wassmann, P., Duarte, C.M., Agustí, S., Sejr, M.K., 2011. Footprints of climate change in the Arctic marine ecosystem. Global Change Biol. 17, 1235–1249. https://doi.org/10.1111/j.1365-2486.2010.02311.x.
Watkins, W.A., 1981. Activities and underwater sounds of fin whales. Sci. Rep. Whales Res. Ins. 33, 83–117.
Watkins, W.A., Tyack, P., Moore, K.E., Bird, J.E., 1987. The 20-Hz signals of finback whales (*Balaenoptera physalus*). J. Acoust. Soc. Am. 82, 1901–1912.
Watkins, W.A., Daher, M.A., Repucci, G.M., George, J.E., Martin, D.L., Dimarzio, N.A., Gannon, D.P., 2000. Seasonality and distribution of whale calls in the North Pacific. Oceanography 13, 62–67.
Weingartner, T., 1997. A review of the physical oceanography of the northeastern Chukchi Sea. In: Reynolds, J. (Ed.), Fish Ecology in Arctic North America. American Fisheries Society Symposium, Bethesda, MD, pp. 40–59.
Weingartner, T.J., Danielson, S., Sasaki, Y., Pavlov, V., Kulakov, M., 1999. The Siberian Coastal Current: a wind- and buoyancy-forced Arctic coastal current. J. Geophys. Res. Oceans 104, 29697–29713. https://doi.org/10.1029/1999JC900161.
Witteveen, B.H., Wynne, K.M., 2016. Trophic niche partitioning and diet composition of sympatric fin (*Balaenoptera physalus*) and humpback whales (*Megaptera novaeangliae*) in the Gulf of Alaska revealed through stable isotope analysis. Mar. Mamm. Sci. 32, 1319–1339. https://doi.org/10.1111/mms.12333.
Wood, K., Wang, J., Salo, S., Stabeno, P., 2015a. The climate of the Pacific Arctic during the first RUSALCA decade 2004–2013. Oceanography 28, 24–35. https://doi.org/10.5670/oceanog.2015.55.
Wood, K.R., Bond, N.A., Danielson, S.L., Overland, J.E., Salo, S.A., Stabeno, P.J., Whitefield, J., 2015b. A decade of environmental change in the Pacific Arctic region. Prog. Oceanogr. 136, 12–31. https://doi.org/10.1016/j.pocean.2015.05.005.
Woodgate, R.A., Aagaard, K., Weingartner, T.J., 2005a. A year in the physical oceanography of the Chukchi Sea: moored measurements from autumn 1990–1991. Deep Sea Res. Part II Top. Stud. Oceanogr. 52, 3116–3149. https://doi.org/10.1016/j.dsr2.2005.10.016.
Woodgate, R.A., Aagaard, K., Weingartner, T.J., 2005b. Monthly temperature, salinity, and transport variability of the Bering Strait through flow. Geophys. Res. Lett. 32 https://doi.org/10.1029/2004GL021880 n/a-n/a.
Woodgate, R., Stafford, K., Prahl, F., 2015. A synthesis of year-round interdisciplinary mooring measurements in the Bering Strait (1990–2014) and the RUSALCA years (2004–2011). Oceanography 28, 46–67. https://doi.org/10.5670/oceanog.2015.57.
Woodgate, R.A., 2018. Increases in the Pacific inflow to the Arctic from 1990 to 2015, and insights into seasonal trends and driving mechanisms from year-round Bering Strait mooring data. Prog. Oceanogr. 160, 124–154. https://doi.org/10.1016/j.pocean.2017.12.007.
Woodgate, Rebecca A., Weingartner, Tom, Lindsay, Ron, 2010. The 2007 Bering Strait oceanic heat flux and anomalous Arctic sea-ice retreat. Geophys. Res. Lett. 37 (1), L01602. https://doi.org/10.1029/2009GL041621.
Zerbini, A.N., Waite, J.M., Laake, J.L., Wade, P.R., 2006. Abundance, trends and distribution of baleen whales off Western Alaska and the central Aleutian Islands. Deep-Sea Res. Part I Oceanogr. Res. Pap. 53, 1772–1790. https://doi.org/10.1016/j.dsr.2006.08.009.

Deep–Sea Research II 177 (2020) 104843

Contents lists available at ScienceDirect

Deep-Sea Research Part II

journal homepage: http://www.elsevier.com/locate/dsr2

Corrigendum to "Iron from melting glaciers fuels the phytoplankton blooms in Amundsen Sea (Southern Ocean): iron biogeochemistry" (Gerringa et al., 2012)

L.J.A. Gerringa [a,*], A.-C. Alderkamp [b], P. Laan [a], C.-E. Thuróczy [c], H.J.W. de Baar [a], M.M. Mills [d], G.L. van Dijken [d], H. van Haren [a], K.R. Arrigo [d]

[a] Royal Netherlands Institute for Sea Research (NIOZ), Department of Ocean Systems, University of Utrecht, Texel, the Netherlands
[b] Biology Department, Foothill College, 12345, El Monte Road, Los Altos Hills, USA
[c] Umi Paysage, Plouarzel, France
[d] Department of Earth System Science, Stanford University, USA

There was an error in the article on iron (Fe) chemistry affecting phytoplankton blooms in the Amundsen Sea (Gerringa et al., 2012). The contribution of Fe-input of melting glaciers to the phytoplankton consumption via horizontal turbulent diffusion was overestimated by a factor of approximately three orders of magnitude, which changes the main conclusion of the paper. After correction, the new conclusion of the paper is that instead of Fe from melting glaciers, recycled Fe, due to internal regeneration, appears to be important to the persistence of the bloom. This makes the title of the paper misleading.

Gerringa et al. (2012) analyzed a large number of water sampling stations in the Amundsen Sea (Southern Ocean) to study the fate of phytoplankton blooms in relation to Fe chemistry. In particular, the daily phytoplankton growth rate, here called G, or nutrient-Fe uptake in the photic zone was compared with nutrient-Fe supply via vertical and horizontal turbulent fluxes $F_z = K_z \partial Fe/\partial z$ and $F_h = K_h \partial Fe/\partial x$, respectively. We only considered one horizontal coordinate x. The vertical K_z and horizontal K_h turbulent diffusion coefficients were determined from vertical density and horizontal Fe distributions. In mathematical form, G depends on the vertical and horizontal turbulent flux variations, or net turbulent flux of a volume in which local recycling R may take place,

$$G = -\partial F_z/\partial z - \partial F_h/\partial x + R. \quad (1)$$

The description of this calculation in Gerringa et al. (2012) is correct as well as all computed fluxes. However, to be able to compare these fluxes with biological uptake, gradients (physically named as 'divergence') of the fluxes over distance must be calculated. While this was done for the vertical turbulent flux by considering its input into the photic zone represented by the mixed layer depth (MLD, 15.2 m), this was mistakenly omitted for the horizontal flux.

Table 2 in Gerringa et al. (2012) gives horizontal flux ('lateral diffusion') computed as a function of distance from the glacier source, for example at x = 40 and 70 km $|F_h^{DFe}| = 6.6 \times 10^{-5}$ and 3.1×10^{-5} mol m^{-2} day^{-1}, respectively (we ignore the signs indicating flux-directions as in Gerringa et al., 2012). In the correction, the horizontal flux difference at x = 55 km, halfway between 70 and 40 km, divided by the distance difference multiplied by the MLD, reads $|\partial F_h^{DFe}/\partial x| = ((6.6\text{-}3.1) \times 10^{-5}/((70\text{-}40) \times 10^3)) \times 15.2 = 1.8 \times 10^{-8}$ mol m^{-2} day^{-1} (distances in m). The contributions of vertical and horizontal turbulent fluxes are now similar in equation (1), both only contribute a few percent to G. This implies that R must be of the same order as G, unless G was overestimated based on the then available knowledge in literature.

However, the corrected horizontal flux difference of total dissolvable Fe (TDFe) analyzed in unfiltered acidified samples ($|\partial F_h^{TDFe}/\partial x| = 0.9 \times 10^{-6}$ mol m^{-2} day^{-1} at x = 55 km) is ~ 40% of the assumed Fe demand of the phytoplankton bloom of 2.3×10^{-6} mol m^{-2} day^{-1}. As discussed in Gerringa et al. (2012) however, the interpretation of the role of TDFe as an Fe-source for phytoplankton is difficult because of many unknowns. For example, the upwelling flux of TDFe is often simply assumed to be twice the flux of DFe. Vertical and horizontal diffusion calculations of TDFe are problematic. Near the seabed or near the glacier, TDFe can be considered as an external Fe-source when its bio-chemical availability is properly accounted for. However, in surface waters of a polynya, a large portion of TDFe is contained in algal cells which can hardly be seen as an external source. As a result, the fluxes are calculated over a concentration gradient of different TDFe sources. Therefore, although TDFe seems to form a substantial Fe-source for phytoplankton, the actual contribution is difficult to assess from our field data.

The corrected horizontal flux contribution of DFe from Pine Island Glacier changes the conclusion in Gerringa et al. (2012). In the center of the polynya, the fluxes from vertical upwelling, vertical fluxes from the sediment and the flux from the glacier of DFe are now of the same order of magnitude. This means that recycling must be important to sustain

DOI of original article: https://doi.org/10.1016/j.dsr2.2012.03.007.
* Corresponding author.
E-mail address: Loes.Gerringa@nioz.nl (L.J.A. Gerringa).

https://doi.org/10.1016/j.dsr2.2020.104843

Available online 24 August 2020

the bloom.

Reference

Gerringa, L.J.A., Alderkamp, A.-C., Laan, P., Thuróczy, C.-E., de Baar, H.J.W., Mills, M. M., van Dijken, G.L., van Haren, H., Arrigo, K.R., 2012. Iron from melting glaciers fuels the phytoplankton blooms in Amundsen Sea (Southern Ocean); iron biogeochemistry. Deep Sea Res. Part II 71–76, 16–31.